THE PHYSICS AND CHEMISTRY OF SOLIDS

AN INTERNATIONAL JOURNAL

VOLUME 5 1958

OL.
5
958

Editor-in-Chief **HARVEY BROOKS** *Cambridge, Mass.*

Associate Editors
H. B. G. CASIMIR *Eindhoven*
G. J. DIENES *Brookhaven*
JACQUES FRIEDEL *Paris*
L. D. LANDAU *Moscow*
E. M. LIFSHITZ *Moscow*

Editorial Advisory Board

U.S.A.: L. APKER, Schenectady · J. BARDEEN, Illinois · D. S. BILLINGTON, Oak Ridge · LEO BREWER, Berkeley, Calif. · N. CABRERA, Virginia · I. ESTERMANN, Washington, D.C. · J. C. FISHER, Schenectady · CONYERS HERRING, New Jersey · A. R. VON HIPPEL, Cambridge, Mass. · J. H. HOLLOMON, Schenectady · W. V. HOUSTON, Houston · H. B. HUNTINGTON, Troy · JOHN G. KIRKWOOD, Yale · K. LARK-HOROWITZ, Purdue · A. W. LAWSON, Chicago · B. T. MATTHIAS, New Jersey · JOSEPH E. MAYER, Chicago · DAVID PINES, Princeton R. SMOLUCHOWSKI, Pittsburgh · D. TURNBULL, Schenectady · J. H. VAN VLECK, Harvard · B. E. WARREN, Cambridge, Mass. · EUGENE P. WIGNER, Princeton · B. H. ZIMM, Schenectady.

United Kingdom: A. CHARLESBY, Shrivenham, Berks · W. J. DUNNING and F. C. FRANK, Bristol · H. K. HENISCH, Reading · H. JONES, London · J. W. MITCHELL, Bristol · A. B. PIPPARD, Cambridge · M. H. L. PRYCE, Bristol F. C. TOMPKINS, London.

France: E. F. BERTAUT, Grenoble · A. GUINIER, PARIS · LOUIS NÉEL and LOUIS WEIL, Grenoble.

Germany: M. BORN, Bad Pyrmont · ULRICH DEHLINGER, Stuttgart · R. HILSCH and G. LEIBFRIED, Göttingen E. MOLLWO, Erlangen · H. PICK, Stuttgart · M. VON LAUE, Berlin · H. WELKER, Erlangen.

Italy: F. G. FUMI, Pavia.

Japan: TOSHINOSUKE MUTO, Tokyo.

The Netherlands: A. MICHELS and G. W. RATHENAU, Amsterdam. *Sweden:* J. O. LINDE, Stockholm · PER-OLOV LÖWDIN, Uppsala.

Switzerland: G. BUSCH and P. SCHERRER, Zürich. *U.S.S.R.:* G. S. ZHDANOV, Moscow.

PERGAMON PRESS NEW YORK · LONDON · PARIS · LOS ANGELES

NOTES FOR CONTRIBUTORS

I. GENERAL

1. Submission of a paper to the *Journal of the Physics and Chemistry of Solids* will be taken to imply that it represents original research not previously published (except in the form of an abstract or preliminary report), that it is not being considered for publication elsewhere, and that if accepted, it will not be published elsewhere in the same form, in any language, without the consent of the editor-in-chief. It should deal with original research work in the field of the physics and chemistry of solids.

2. Papers should be submitted to the appropriate regional editor (all English-language papers to be sent to the U.S. editor).

3. Papers will be published as quickly as possible after acceptance, and, subject to space being available, should appear in the following issue, if this is due for publication not earlier than three months after the acceptance date. Short communications under the heading of "Letters to the Editors" will receive priority for publication, and will be published in the issue following receipt, if accepted not later than the beginning of the month preceding publication.

4. Fifty free reprints of each paper are supplied. Additional copies can be obtained at a reasonable cost if ordered when proofs are returned. A reprint order form will accompany first proofs.

II. SCRIPT REQUIREMENTS

1. Papers submitted should be concise and written in a readily understandable style. Scripts should be typed and double spaced and submitted in duplicate to facilitate refereeing.

It will be appreciated if authors clearly indicate any special characters used. An abstract, not exceeding 200 words, should be provided in the language of the paper. French and German papers should be submitted with English abstract and titles, but if this is not possible the abstract will be translated by the publishers. To conserve space, authors are requested to mark less important parts of the paper, such as details of experimental technique, methods, mathematical derivations, etc. for printing in small type. The technical description of methods should be given in detail only when such methods are new. Authors will receive proofs for correction when their papers are first set; page proofs will be sent only when the amount of alteration makes it advisable.

2. Illustrations should not be included in the typescript of the paper, and legends should be typed on a separate sheet. Line drawings which require redrawing should include all relevant details and clear instructions for the draughtsman. If figures are already well drawn it may be possible to reproduce them direct from the originals, or from good photo-prints if these can be provided. It is not possible to reproduce from prints with weak lines. Illustrations for reproduction should normally be about twice the final size required. Photographs should only be included where they are essential.

Tables and figures should be so constructed as to be intelligible without reference to the text. Every table and column should be provided with an explanatory heading. Units of measure must always be clearly indicated. The same data should not be published in both tables and figures. The following standard symbols should be used on line drawings since they are easily available to the printers: ○, ●, +, ×, □, ■, △, ▲, ◇, ◆, ▽, ▼.

4. References are indicated in the text by superior numbers in parentheses, and the full reference should be given in a list at the end of the paper in the following form:

1. HILL R., *J. Iron St. Inst.* **158,** 177 (1948).
2. PEARSON C., *The Extrusion of Metals*. Chapman and Hall, London (1944).

Abbreviations of journal titles should follow those given for *Physics Abstracts*. It is particularly requested that authors' initials, and appropriate volume and page numbers, should be given in every case.

Footnotes, as distinct from literature references should be indicated by the following symbols—*, †, ‡, ‡‡, commencing anew on each page; they should *not* be included in the numbered reference system.

5. Due to the international character of the journal no rigid rules concerning notation and spelling will be observed, but each paper should be consistent within itself as to symbols and units.

VOL.
5
195

OL.
5
958

VOL.
5
1958

CONTENTS

NUMBERS 1/2

B. V. Derjaguin and I. I. Abrikossova: Direct measurements of molecular attraction of solids . 1

S. I. Pekar: Theory of electromagnetic waves in a crystal with excitons 11

R. W. Soshea, A. J. Dekker and J. P. Sturtz: X-ray-induced color centers in MgO . . . 23

Jiro Yamashita and Tatumi Kurosawa: On electronic current in NiO 34

Walter A. Harrison: Resistivity due to dislocations in copper 44

T. W. Hickmott and Gert Ehrlich: Structure-sensitive chemisorption: The mechanism of desorption from tungsten 47

P. Kisliuk: The sticking probabilities of gases chemisorbed on the surfaces of solids—II . . 78

F. J. Low and C. F. Squire: Nuclear magnetic resonance in LiF 85

William Paul and D. M. Warschauer: Optical properties of semiconductors under hydrostatic pressure—I Germanium 89

William Paul and D. M. Warschauer: Optical properties of semiconductors under hydrostatic pressure—II Silicon 102

J. B. Goodenough, D. G. Wickham and W. J. Croft: Some magnetic and crystallographic properties of the system $Li_x^{+}Ni_{1-2x}^{++}Ni_x^{+++}O$ 107

W. L. Gordon, C. H. Shaw and J. G. Daunt: Radial atomic distribution in liquid helium-4 by X-ray scattering 117

J. Hornstra: Dislocations in the diamond lattice 129

J. R. Drabble and C. H. L. Goodman: Chemical bonding in bismuth telluride 142

Letters to the Editors:

Robert E. Behringer: Note on "The band structure of aluminum: a self-consistent calculation" 145

A. S. Nowick: Defense of the strain-energy approach for small solute atoms 147

Book Review:

"Grain Boundaries in Metals", by D. McLean (reviewed by R. Smoluchowski) 148

Contents lists of Volume 3, Numbers 1–4 149

Papers to be published in future issues 155

Erratum 156

NUMBER 3

R. J. Sladek: Magnetically induced impurity banding in *n*-InSb 157

H. M. Bath and M. Cutler: Measurement of surface recombination velocity in silicon by steady-state photoconductance 171

H. A. Gersch and W. C. Koehler: Types of magnetically ordered configurations on simple lattices 180

J. W. Nielsen and E. F. Dearborn: The growth of single crystals of magnetic garnets . . 202

F. A. Kröger and H. J. Vink: Relations between the concentrations of imperfections in solids . 208

D. S. Tannhauser: Self-diffusion of bromine in silver bromide 224

Book Reviews:

"Les Transistrons dans les Amplificateurs", by Jean-Marie Moulon (reviewed by J. P. McKelvey) 236

"Sol'd State Physics", Volumes 4 and 5, edited by F. SEITZ and D. TURNBULL (reviewed by J. FRIEDEL) 236

"Rectifying Semiconductor Contacts", by H. K. HENISCH (reviewed by P. Aigrain) . . 237

Papers to be published in future issues 238

NUMBER 4

G. B. BENEDEK and T. KUSHIDA: The pressure dependence of the Knight shift in the alkali metals and copper 241

HAZIMU KAWAMURA: The deformation potential of potassium chloride 256

D. F. C. MORRIS: The lattice energy and heat of formation of lithium monosulphide . . . 264

TRUMAN O. WOODRUFF and WERNER KANZIG: Paramagnetic resonance absorption of a V center in LiF 268

JAMES C. PHILIPS and HERBERT B. ROSENSTOCK: Topological methods of locating critical points . 288

T. J. SWOBODA, R. C. TOOLE and J. D. VAUGHAN: New magnetic compounds of the ilmenite-type structure 293

R. M. BOZORTH and DOROTHY E. WALSH: Ferromagnetic moment of $CoMnO_3$ 299

D. B. FISCHBACH and A. S. NOWICK: Some transient electrical effects of plastic deformation in NaCl crystals 302

A. DAVID PEARSON: Studies on the lower oxides of titanium 316

W. G. MAISCH and H. G. DRICKAMER: The effect of pressure on color centers in alkali halide crystals 328

D. SAINT-JAMES: Détermination des lois de force dans les cristaux du type du diamant . . . 337

Papers to be published in future issues 355

AUTHOR INDEX TO VOLUME 5

(B) denotes a book review

ABRIKOSSOVA, I. I. 1
AIGRAIN, P. 237 (B)
BATH, H. M. 171
BEHRINGER, ROBERT E. 145
BENEDEK, G. B. 241
BOZORTH, R. M. 299
CROFT, W. J. 107
CUTLER, M. 171
DAUNT, J. G. 117
DEARBORN, E. F. 202
DEKKER, A. J. 23
DERJAGUIN, B. V. 1
DRABBLE, J. R. 142
DRICKAMER, H. G. 328
EHRLICH, GERT 47
FISCHBACH, D. B. 302
FRIEDEL, J. 236 (B)
GERSCH, H. A. 180
GOODENOUGH, J. B. 107
GOODMAN, C. H. L. 142
GORDON, W. L. 117
HARRISON, WALTER A. 44
HICKMOTT, T. W. 47
HORNSTRA, J. 129
KANZIG, WERNER 268
KAWAMURA, HAZIMU 256
KISLIUK, P. 78
KOEHLER, W. C. 180
KRÖGER, F. A. 208
KUROSAWA, TATUMI 34
KUSHIDA, T. 241
LOW, F. J. 85
MAISCH, W. G. 328
MORRIS, D. F. C. 264
MCKELVEY, J. P. 236 (B)
NIELSEN, J. W. 202
NOWICK, A. S. 147
NOWICK, A. S. 302
PAUL, WILLIAM 89
PAUL, WILLIAM 102
PEARSON, A. DAVID 316
PEKAR, S. I. 11
PHILLIPS, JAMES C. 288
ROSENSTOCK, HERBERT B. 288
SAINT-JAMES, D. 337
SHAW, C. H. 117
SLADEK, R. J. 157
SMOLUCHOWSKI, R. 148 (B)
SOSHEA, R. W. 23
SQUIRE, C. F. 85
STURTZ, J. P. 23
SWOBODA, T. J. 293
TANNHAUSER, D. S. 224
TOOLE R. C. 293
VAUGHAN, J. D. 293
VINK, H. J. 208
WALSH, DOROTHY E. 299
WARSCHAUER, D. M. 89
WARSCHAUER, D. M. 102
WICKHAM, D. G. 107
WOODRUFF, TRUMAN O. 268
YAMASHITA, JIRO 34

VOL. 5 1958

OL.
5
958

VOL.
5
1958

J. Phys. Chem. Solids Pergamon Press 1958. Vol. 5. pp. 1–10.

DIRECT MEASUREMENTS OF MOLECULAR ATTRACTION OF SOLIDS

B. V. DERJAGUIN and I. I. ABRIKOSSOVA

Institute of Physical Chemistry, Academy of Sciences of the U.S.S.R., Moscow

(*Received* 5 *June* 1957)

Abstract—Beam balances were constructed with a photoelectromagnetic negative feedback coupling which made it possible to measure directly the resulting force of molecular attraction between plane and spherical surfaces of two plates separated by a narrow gap, as a function of the width of this gap. The width of the gap was determined from the diameter of Newton's rings. Using a simple equation, it was then possible to determine the energy of interaction per unit area of infinite plane surfaces of the same nature as a function of the width of the gap.

Measurements were made for the pairs: quartz–quartz, mixed thallium halide–mixed thallium halide, and chromium–quartz in a range of gap widths from 0·07 to 0·3 microns. In all cases, within the limits of experimental error, the results agree with the values derived from the equations of the theory of molecular attraction of macro bodies developed by E. M. LIFSHITZ. At the same time, the LONDON–HAMAKER equation, which assumes the additivity of molecular interaction, is shown to be inapplicable.

In the measurements, special attention was paid to the removal of surface electrical charges by means of ionization of the air, and also to the removal of dust particles and to decreasing the effect of vibrations and the viscosity of the air on the measurements.

The discrepancy between the present results for quartz and those of OVERBEEK and SPARNAAY, who obtained forces 5000 times greater than the values corresponding to the LIFSHITZ equations, is apparently explained by the incomplete removal of surface charges in their measurements.

1. INTRODUCTION

IN addition to the well-known valency forces, which have a comparatively small radius of action and which practically disappear at interatomic distances equal to a few ångstroms, between all atoms or molecules there exist forces of attraction, the magnitude of which falls off much more slowly with distance. These so-called molecular forces form the basis of the fundamental phenomena of molecular physics and physical chemistry: surface tension, capillarity, capillary condensation, physical adsorption, etc. Molecular forces determine most of the properties of liquids—their viscosity, heat of vaporization, and mutual solubility.

The presence of forces of attraction between atoms and molecules naturally also gives rise to analogous forces "of molecular attraction" between two macroscopic bodies, the surfaces of which approach to within very small distances. The existence of such forces between colloidal particles and their role in coagulation, was assumed by KALLMANN and WILLSTÄTTER[1] and later considered in the first quantitative theory of the stability of colloids,[2,3] together with the forces of repulsion of diffuse double ionic layers of the adjacent particles. Thus, calculating the force or energy of molecular interaction of macro particles as a function of the distance between them is one of the main problems in the theory of stability and coagulation of colloids. In addition to its practical significance in the field of surface phenomena (problems of stability and coagulation of colloid and aerosol systems, the development of the theory of flotation, dyeing, and also in the understanding of the properties of thin films and processes of condensation and polymolecular adsorption), the experimental investigation of molecular interaction between bodies makes it possible to determine the physical nature of the forces of molecular attraction and may serve as a check on the theories relating to them.

2. EXAMINATION AND CRITICISM OF EXISTING THEORIES OF MOLECULAR FORCES

According to the calculations of LONDON,[4] the energy of interaction between separate atoms or molecules at distances large compared with their own dimensions is inversely proportional to the sixth power of the distance between them. The LONDON law can be written in the form:

$$U_{\text{disp.}} = -\frac{C}{r^6} \tag{1}$$

where $U_{\text{disp.}}$ is the energy of molecular interaction of two particles separated by a distance r, and C is a positive constant, which is the same for a given sort of atom; since the force is given by the expression $F=(-dU/dr)$, the van der Waals forces of attraction vary inversely with the seventh power of the distance between the molecules.

The LONDON theory has its limits of application in that the calculation becomes unjustifiable not only at very small distances between the atoms, when their wave functions overlap, but also at fairly large distances, when it becomes necessary to consider the effect of electromagnetic retardation, due to the finite velocity of propagation of the electromagnetic waves $\bar{C}$. The electromagnetic retardation was considered by CASIMIR and POLDER,[5] using quantum electrodynamics. According to their theory, when $r \gg \lambda_i$, where λ_i is the wavelength of absorption (emission) of a given atom, the energy of interaction between two atoms with static polarizability α is

$$U = -\left(\frac{23}{4\pi}\right)\hbar\bar{c}\alpha^2/r^7,$$

or

$$U = -c_1/r^7, \text{ where } c_1 = 251e^2\alpha^2. \tag{2}$$

Here $\hbar$, c and e have their usual meanings. The force of attraction between two atoms in this limiting case changes with distance according to the r^{-8} law.

We will now consider the molecular interaction between macroscopic bodies. Usually, in view of the additivity of the LONDON forces, the attraction between bodies consisting of a large number of molecules is calculated by considering the energy of their attraction as equal to the sum of the energies of attraction between all pairs of molecules making up the bodies. Thus, the energy of interaction between two infinite plates, per unit or surface, is found by DE BOER[6] and HAMAKER[7] to be

$$U = -A/12\pi H^2 \tag{3}$$

and the force acting on a unit of surface

$$f = A/6\pi H^3. \tag{3a}$$

Here R is the radius of the sphere and H the shortest distance between the bodies; A is a constant which depend on the nature of the bodies and is equal to the product π^2q^2C. If similar calculations are made taking into account the effect of electromagnetic retardation, then in the limiting case of sufficiently large distances we obtain for the energy per unit surface of parallel plates the expression

$$U = -A_1/30\pi H^3 \tag{4}$$

and for the force acting on unit surface the formula

$$f = A_1/10\pi H^4. \tag{4'}$$

Here

$$A_1 = \pi^2q^2C_1.$$

The validity of extending the properties of additivity of the LONDON forces has not been demonstrated, either theoretically or experimentally.

A completely new and general theory of molecular attraction between condensed bodies has been developed on a quite different basis by LIFSHITZ.[8] This theory is macroscopic, and a feature of it is the absence of any special assumptions as to the law of interaction of individual atoms. The main idea underlying the theory is that the interaction between bodies can be regarded as being caused by a fluctuating electromagnetic field, which is always present in any absorbing medium and extends beyond its boundaries. This field does not disappear even at the absolute zero of temperature, when it is bound up with the zero point oscillations of the radiation field. This method is perfectly general, i.e. it is applicable to all bodies at any temperature; it automatically takes in account the effect of electromagnetic retardation.

LIFSHITZ derives a formula for the force of attraction, f, acting on 1 cm² of surface of each of the bodies separated by a gap H. This formula is simplified in two limiting cases:

VOL. 5 1958

(1) If H is small in comparison with the principal wavelengths of the absorption spectrum of the substance, then

$$f=\frac{\hbar}{8\pi^2H^3}\int_0^\infty\left(\frac{\epsilon-1}{\epsilon+1}\right)^2 d\xi, \qquad (5)$$

i.e. the force is proportional to H^{-3}. Here $\hbar$ is Planck's constant, ϵ is the dielectric permeability of the substance, a function of the frequency ω; $i\xi$ is the imaginary part of the argument of ϵ (ω is considered in this theory as a complex number).

(2) If H is large in comparison with the principal wavelengths, then it is possible to show that

$$f=\frac{\hbar c}{H^4}\cdot\frac{\pi^2}{240}\left(\frac{\epsilon_0-1}{\epsilon_0+1}\right)^2\phi(\epsilon_0), \qquad (6)$$

where c is the velocity of light, ϵ_0 the electrostatic value of dielectric permeability, and $\phi(\epsilon_0)$ is given graphically or in a table:

$1/\epsilon_0$	0	0·025	0·1	0·25	1
$\phi(\epsilon_0)$	1	0·53	0·41	0·35	0·35

In this case, therefore, the force is proportional to H^{-4} and depends only on ϵ_0.

3. METHOD OF MEASUREMENT

The problem involved considerable experimental difficulties, the successful solution of which depended to a considerable extent on the correct choice of the form and material of the bodies for the investigation.

(a) *Objects of investigation*

For a variety of reasons it was convenient to make one of the bodies flat and the other one spherical; we therefore measured the force of attraction between a plate of area 4×7 mm^2 and a spherical lens (radius of curvature 5–25 cm). In this case the shortest distance between the bodies can be determined with sufficient accuracy from the diameter of Newton's rings. Furthermore, these bodies make it possible to study the dependence of the forces on the radius of curvature of the spherical surface and hence to separate the molecular forces, which are proportional to the radius, from the various masking effects, connected for example, with surface electrification.

The relationship establishing the proportionality of the molecular attraction to the radius of the sphere was obtained in the form[9]

$$F(H)=2\pi Ru(H), \qquad (7)$$

where $F(H)$ is the force of attraction between the sphere and the flat plate, R is the radius of the sphere, and $u(H)$ the energy of interaction (per cm^2) between two infinite plane discs of the same material in the same medium, and H the shortest distance between the surfaces.

As the main material for the preparation of specimens, we chose quartz glass, since first its transparency makes it possible to use the most accurate optical method for determining the size of the gap, secondly, its surface can be most easily polished, and thirdly, such surfaces are not affected by various cleaning methods.

In view of the smallness of the forces of attraction between macro bodies, it is also desirable to choose materials characterized by large forces of interaction, other conditions being equal. It follows from the theory of LIFSHITZ that, in the case of sufficiently large distances between bodies, the magnitude of the force of interaction depends only on the static value of the dielectric permeability ϵ_0. Of a number of dielectrics with a large value of ϵ_0, the most suitable for our measurements were the thallium halides. A series of measurements was carried out of the interaction between a disc and a lens prepared from a mixed crystal of TlBr and TlI (42·5 and 57·5 per cent respectively).

Their large force of interaction, combined with simplicity of calculation, makes metals interesting as bodies for investigation, but with metals it is essential to use a complicated method for measuring the size of the gap. Simpler, from the point of view of technique, is the case of a metal and a transparent dielectric, since it is then possible to retain the optical method for measuring the gap. In a series of such experiments we used a lens of quartz glass and a quartz plate covered with vacuum-evaporated chromium. The comparatively small coefficient of reflection of light from the chromium surface made it possible to observe sufficiently well the contrast interference rings in the gap between the surfaces of the metal and the quartz.

Measurements of the forces of attraction between the bodies selected were made in air and in vacuum. The magnitude of the force of attraction, as the theory shows, does not depend on the presence of air in the gap between the bodies, but in practice it was more convenient to conduct the experiments in vacuum (from 0·1 mm to several mm of mercury).

(b) *The method for measuring forces of interaction between solids: a balance with feedback coupling*

The main difficulties in measuring the forces of molecular attraction between bodies arise from the fact that these forces, F, detectable only at very small gaps, rapidly increase with further decrease in the gap H. Hence if we bring two surfaces sufficiently close together, they will adhere to one another. It is apparent that for a solution of the problem it is necessary to use a balance which, on the one hand, has a sufficiently large controlling moment and, on the other hand, has high sensitivity, i.e. it must satisfy requirements which are contradictory in an ordinary balance.

It was possible to overcome this difficulty by applying to the balance a method analogous to negative feedback coupling.[10] The idea of this method is that movement of the balance beam from the position of equilibrium x (or angle of deflection α) in some way or other causes an electric current i to flow, creating an electromagnetic reaction M, which acts on the beam and returns it to the position of equilibrium. In the ordinary way this would mean that the balance was less sensitive, but since the overload can be obtained not from the displacement but from the strength of the current measured by a micro-ammeter, in practice the sensitivity can be considerably increased.

The force of interaction between the flat surface of a plate P and the convex surface of a spherical lens L was measured by using a special beam-type balance[11] (Fig. 1). The length of the beam was 35 mm, the weight 0·1 g. The plate P was placed at the end of the beam, and the lens L was supported, independently of the beam, in such a way that the distance H between them was sufficiently small. A mirror S was attached to the other end of the beam. The beam was firmly connected to a coil R (15–20 turns of wire) placed in the field of a permanent magnet M (Fig. 2).

The feedback coupling was provided by passing

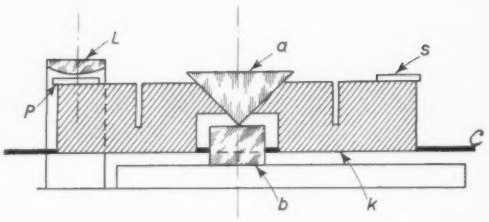

FIG. 1

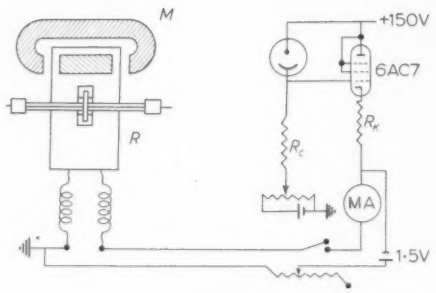

FIG. 2

through the coil a current from a sensitive photoelectric device which traced the deflection of the beam. The device for recording the deflection of the balance beam consisted of a raster photo-relay and single-cascade amplifier. A diagram of the raster photo-relay is given in Fig. 3. Through a

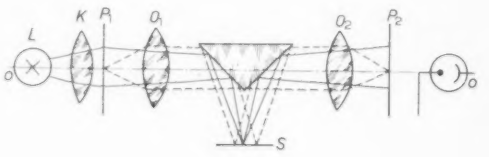

FIG. 3

condenser K, rays from the source of light L illuminated a linear (typographic) raster P_1 (a glass plate with alternate transparent and non-transparent bands of equal thickness) and, passing through the objective O_1, were focussed on the mirror S (the path of the rays is shown by a continuous line). Using the objective O_1, mirror S, and a second objective O_2 with the same focal length, a real image of the raster P_1 was thrown on to the surface of the second raster P_2 with an identical set of bands (broken line).

VOL. 5 1958

A very small rotation of the mirror altered the position of the image of the first raster with respect to the second raster, increasing or decreasing the quantity of the light transmitted. Having passed through the second raster, the light fell on an antimony–caesium vacuum photocell STsV-3, which controlled the circuit of the amplifier valve.

At the fixed zero position of the balance beam, the current in the coil was equal to zero ($i_0 = 0$). Deflection of the balance beam through a small angle α varied the passage of the light by the second raster and the illumination of the photocell, causing a current $i = K\alpha$, where K is a constant for the device.

By passing a current i in the appropriate direction through the coil of the balance situated in the field of the magnet, we set up a feedback coupling, as a result of which the balance beam came under the action of a torque

$$M = ni = nK\alpha = l\alpha$$

where n and l are constants.

By bringing the flat surface of the plate and the convex surface of the lens together by means of a fine lifting mechanism, it was possible to decrease the gap H, between them until the force of attraction F, appeared. The balance arm then rotated through an angle such that the moment of the force Fr, where r is the "shoulder" of the force of interaction, was balanced by the moment of the feedback coupling M. The required force was calculated from the formula

$$F = ni/r \qquad (8)$$

where i is the current, measured by a microammeter included in the anode circuit, and r is the distance from the edge of the fulcrum to the point on the surface of the plate P corresponding to the shortest distance between the surfaces under investigation. The method for determining n is described below.

Thus, by measuring the strength of the current, it is possible to determine the magnitude of the molecular attraction.

One of the most difficult problems in this work was to obtain a gap of a fixed width of a fraction of a micron between the surfaces and to obtain very smooth movement of one body relative to the other. Of all the methods tried for controlling the gap H, the best was found to be that using feedback coupling. A sufficiently fine ($0{\cdot}01\mu$) control of the gap width was obtained by micrometric movement of the raster P_1 in a direction perpendicular to its markings. This led to the appearance of a moment of an electromagnetic force, not compensated by gravity, which caused the balance beam to move to a new equilibrium position by rotation through an appropriate angle.

The zero current i_0 is constant and equation (8) is valid only when the moment of the balance without feedback coupling is negligibly small in comparison with the moment M. It is clear that the moment of gravity will be completely absent when the distance from the centre of gravity to the point of support (the fulcrum) is zero. For this reason, and also to minimize the sensitivity of the apparatus to vibration of the support, the centre of gravity of the balance used in our experiments was almost at the fulcrum.

Calibration of the balance (or determination of n) was carried out by means of a small glass rod C (Fig. 1), which could be placed along the balance beam. When the gap between the surfaces was large (in the absence of forces of molecular attraction), measurements were made with the microammeter of the current strength i_0, in the coil corresponding to various positions of the glass rod, as observed in the eyepiece scale of a microscope. Using a graph of the relationship between the coordinate of the end of the glass rod y and current i_0, the coefficient n was calculated from the formula

$$n = P\Delta y/\Delta i_0,$$

where P is the weight of the glass rod.

The true sensitivity of the apparatus for determining the force of interaction depends to a considerable extent on the vibration of the support on which the apparatus rests. The best results were obtained by placing the apparatus on a special table having shock absorbers, which in its turn was mounted on a cement base insulated from the foundation and sunk into the ground.

Using the method described above, it is possible to measure forces of interaction between solids in the range from $1-2\times10^{-4}$ to ~ 20 dynes when the forces fall off comparatively quickly with distance. It is thus possible to measure a force, the gradient of which is 10^6 dynes/cm with an accuracy of up to 0·02 dyne.

(c) *Method for measuring the distance between the bodies*

The size of the very small gap H between the lens L and the plate P was calculated from the diameter of Newton's rings, measured with a microscope having an eyepiece scale, the gap being illuminated with a cine lamp (300 V) through a monochromator of constant deviation and the vertical illuminator of the microscope. It is not difficult to derive a relationship between the gap H, the diameter of the m^{-th} dark ring d_m, the wavelength of the monochromatic light λ, and the radius of the spherical surface R:

$$H = \frac{\lambda}{2}\left(m - \frac{d_m^2}{4R\lambda}\right). \qquad (9)$$

From equation (9) it follows that to determine H it is necessary to know m, d_m, λ and R. To determine the number of the ring m, we used a method based on the changes in the diameter of the interference ring on varying the number m and the wavelength of the monochromatic light λ for a constant gap H. The radius of the spherical surface was measured using the same optical set-up. From equation (9) it follows that there is a linear dependence of d_m^2 on m for constant λ and H. If d_m^2 is plotted as ordinate and m as abscissa, the tangent of the angle between $d_m^2 = f(m)$ and the abscissa divided by 4λ gives R.

In calculating the size of the gap H between the quartz and metal surfaces, it was necessary to take into account the phase shift on reflection from the metal. For chromium, the metal used in our experiments, this correction to H was about 120 Å.

(d) *Preparation of specimens for measurement*

Of considerable importance in this work was the method of cleaning the glass and quartz surfaces at which interaction was studied. For a successful experiment the surfaces had to be carefully cleaned of all possible films and particles of dust. The usual methods of chemical cleaning, e.g. washing with a chromic mixture, were not used, since they sometimes spoil the polished surface of the glass. For cleaning the surfaces, we used a special method. The plate and lens were washed with distilled alcohol and ether, using cotton wool from which the fat had been removed in a Soxhlet apparatus, and then treated in a glow discharge under a glass cover. The cleanliness of the surface could be judged by its complete wetting with water. It was much more difficult to remove dust particles from the surfaces. Of all the methods which were tried (removal of dust particles with a grease-free soft brush, cotton wool, material, chamois, etc.), the best results were obtained when the surfaces (after cleaning in a glow discharge) were rubbed with grease-free cotton wool slightly moistened with pure ether. After such treatment the surfaces were clean because, as indicated by the fact that directly after cleaning in a glow discharge, they were wetted completely by water.

Preparation of the specimens for making the measurements was a very important feature of the experiment, since during removal of dust particles they became electrified, and as a result interacted with a force which was many times greater than the molecular attraction, which was thus masked. To remove the electrostatic charges, it was necessary to separate the surfaces and to ionize the air near the apparatus. Meanwhile, dust particles frequently fell on to the surfaces from the air, and it was necessary to clean them and remove charges successively until both the dust particles and the electrostatic charges were absent simultaneously. Electrostatic charges arise on clean, dry surfaces very easily even on the smallest contact with a clean brush or rubber glove. To remove the charges from the surface of quartz, we used a radioactive isotope of sulphur, ^{35}S.

4. RESULTS OF MEASUREMENTS AND COMPARISON WITH THEORY

Fig. 4 gives on a log-log scale results of a large number of experiments, separated by considerable intervals of time and conducted with various specimens of quartz. The radius of curvature of the lens was $R = 11{\cdot}1$ cm.

From equation (7) given above, the directly measured force of attraction $F(H)$ divided by $2\pi R$ gives the value of the specific energy $u(H)$ for the plane case. Fig. 5 shows the relationship between u and the distance H. The black dots refer to the experiment with a lens of radius $R = 11{\cdot}1$ cm, triangles refer to $R = 10$ cm, and white circles refer to $R = 25{\cdot}4$ cm. This graph illustrates the linear dependence of the force of attraction on the radius of the sphere and therefore shows that

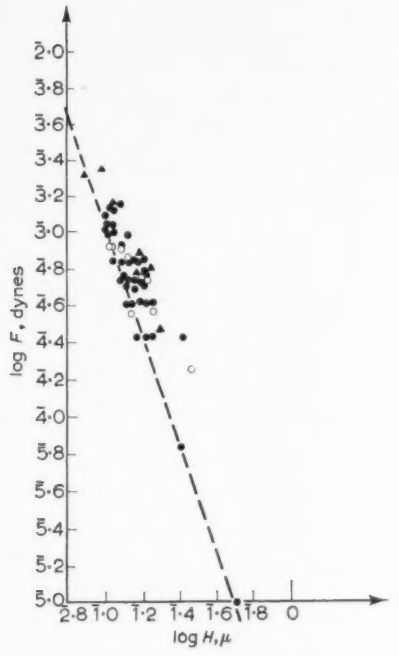

FIG. 4

the energy of attraction obtained experimentally for two plates does not depend upon which lens was used for the measurement employed in the calculation from equation (7).

If the hitherto accepted method for summing the interactions of all pairs of molecules is used, then for the energy of attraction $u(H)$ it is necessary to use equation (3). In this equation the constant A which fits our experiments has a value of 5×10^{-14} erg. The computed constant A for quartz is about 10^{-12} ergs, i.e. 20 times greater than the experimental value. This comparison shows the unsuitability, at least for distances of the order of 10^{-5} cm, of the methods of calculation used hitherto.

If the same method of summation is used and a correction made for electromagnetic delay, then equation (4) should be employed for the energy $u(H)$. Applying the results of our experiments here, we obtained for the constant A_1 a value of about 3×10^{-18} erg cm. Calculation from theory gives $A_1 = 1\times10^{-18}$ erg cm. Here again the agreement of experiment with theory is poor, but the discrepancy is considerably smaller than in the case of summation of the LONDON interactions.

An exact comparison with LIFSHITZ' theory requires a fairly complete knowledge of the optical characteristics of the substance in its regions of absorption. However, it is possible to make an approximate theoretical evaluation in view of the character of absorption of quartz—its transparency at wavelengths coinciding with the spacings used in the experiments. For this purpose the spacing in our experiments can be considered large in comparison with the wavelengths of the ultra-violet part of the absorption spectrum and small compared with the wavelengths of the remaining infra-red part of the absorption spectrum. The contribution to the measured energy of interaction arising from the second part of the absorption spectrum, as shown by its approximate evaluation, is small, and therefore the energy of interaction is as if in the quartz there existed only the first ultra-violet part of the absorption spectrum.

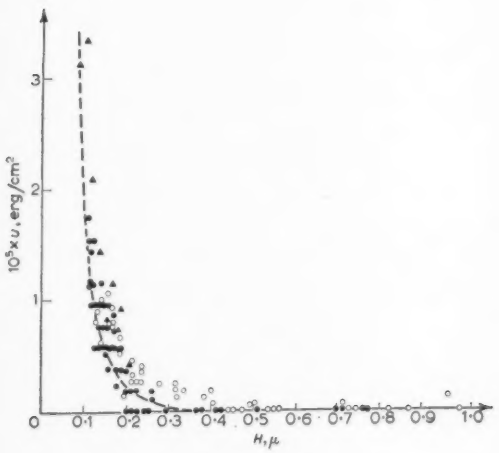

FIG. 5

However, to obtain a correct approximation in such a case it is necessary to substitute in equation (6) that value of ϵ_0 which is due only to this part of the absorption spectrum. This is equivalent to the use of the value $\epsilon_0 = n^2$, where n is the optical refractive index of the quartz. In Figs. 4 and 5 the values of force and energy calculated by using this equation are shown as dots.

Figs. 6 and 7 give results for experiments with specimens prepared from thallium halides. In Fig. 6 are presented on a log–log scale data obtained with a lens of radius $R = 12{\cdot}5$ cm; in Fig. 7 the

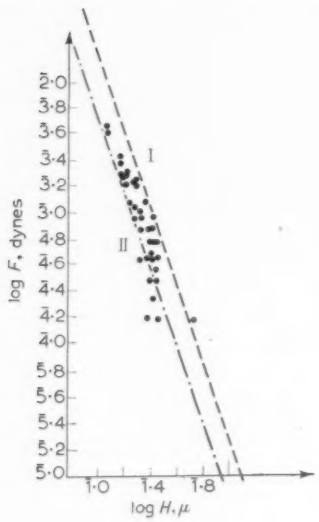

FIG. 6

dots refer to the experiment with a lens of radius $R = 12{\cdot}5$ cm, and crosses to $R = 5{\cdot}2$ cm.

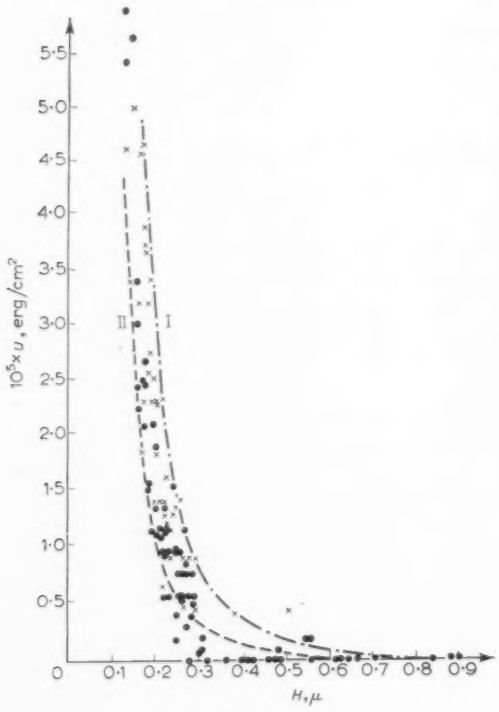

FIG. 7

Dots show the corresponding dependences obtained from the LIFSHITZ equation for the limiting case of large distances. The theoretical curves I refer to the static value of the dielectric permeability of the mixed crystal of thallium halides $\epsilon_0 \simeq 50$, and the curves II to $\epsilon = n^2 \simeq 6$, which, as with quartz, can be considered a more accurate approximation.

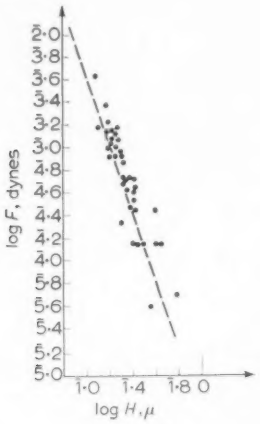

FIG. 8

Similarly, Figs. 8 and 9 show graphically the measurements in which one of the surfaces (the plate) was covered with a sufficiently thick mirror-smooth layer of chromium. The radius of curvature of the lens was 10·6 cm. In Fig. 9 the dots refer to

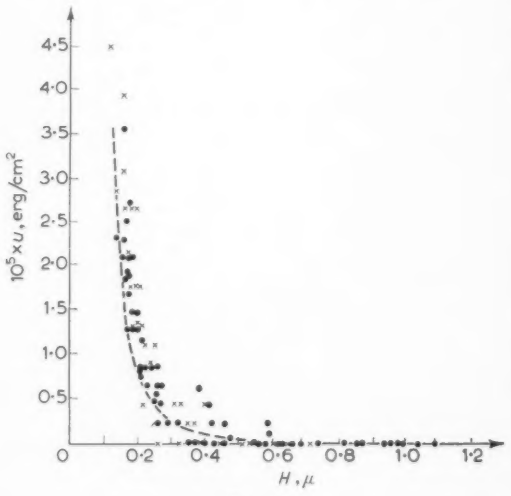

FIG. 9

VOL. 5 1958

$R = 10$ cm, and the crosses to $R = 5$ cm. LIFSHITZ' theory gives for the evaluation of the interaction of metal with dielectric for sufficiently large spacings the equation:

$$f = \frac{\hbar c}{H^4} \cdot \frac{\pi^2}{240} \cdot \frac{\epsilon_0 - 1}{\epsilon_0 + 1} \cdot \phi_1(\epsilon_0), \qquad (10)$$

where $\phi_1(\epsilon_0)$ is the function tabulated by LIFSHITZ,[12] the remaining symbols are the same as in equation (6). Considering, as above, the transparency of the quartz for wavelengths coinciding with H, we took for the calculation, the results of which are shown as dots on the graphs (Figs. 8 and 9), values of ϵ_0 equal to the square of the refractive index of quartz in the optical region.

Considering the approximate character of such theoretical evaluations, and also the error in the measurements, the agreement obtained may be considered very satisfactory.

It is interesting to observe that in LIFSHITZ' theory the electromagnetic nature of the molecular forces is fully reflected; this nature was guessed at by LEBEDEV,[13] who considered the most interesting and difficult problem of the theory to be the calculation of molecular interaction in a physical body, in which many molecules act on one another simultaneously, and their oscillations, owing to their close proximity, are not independent of one another. LEBEDEV stated that a comparison of the calculated values of molecular forces (from spectroscopic data) with observations would make it possible to solve the "main problem in molecular physics", i.e. whether the molecular forces amounted to electromagnetic forces or whether they also included other forces of hitherto unknown origin. Apparently the agreement of LIFSHITZ' theory with our measurements makes it possible to answer LEBEDEV's question: the molecular forces do in fact "amount to electromagnetic forces".

We notice that in the experiments of OVERBEEK and SPARNAAY[14] results were obtained which differ from ours. OVERBEEK and SPARNAAY measured the forces of attraction between two plates of fused quartz, using a special dynamometer in which movement of the spring was measured by a method of electrical capacity; the distance between the discs was measured using interference colours in a narrow gap.

If the calculation is made according to LIFSHITZ' theory, then for a distance between the quartz plates of 1200 Å the force of attraction is found to be about 2×10^{-4} dynes/cm^2, whereas in the experiments of OVERBEEK and SPARNAAY this distance gives a force of 1 dyne. Thus the experimental force exceeds the theoretical value by a factor of about 10^4. The poor reproducibility of the data in the work of OVERBEEK and SPARNAAY, and the very large value of the attraction are apparently due to surface electrification.

In the recently published work of PROSSER and KITCHENER,[15] the method used for the measurement of molecular attraction between solids was similar to that of OVERBEEK and SPARNAAY. The results of their measurements agree closely with ours and with the values deduced from LIFSHITZ' theory.

5. CONCLUSIONS

(1) A method has been developed which makes it possible to measure the forces of interaction between very smooth transparent solids in relation to the distance between them. The force of attraction is measured by means of a special beam balance incorporating photoelectromagnetic negative feedback coupling. The distance between the bodies is calculated from the diameter of Newton's rings. The range of forces measured is from $1-2 \times 10^{-4}$ to 20 dynes, the distances 10^{-5} to 10^{-3} cm.

(2) The molecular attraction between specimens of quartz glass was detected and measured. The energy of attraction between two plates per cm^2, $u(H)$, changes with the distance between them, H, according to an approximate H^{-3} law, and when $H = 1{\cdot}5 \times 10^{-5}$ cm the energy is about 1×10^{-5} ergs/cm^2.

(3) It is shown experimentally that the force of attraction between spherical and plane surfaces is proportional to the radius of the sphere, in agreement with the concept of the molecular nature of these forces.

(4) This work is the first direct experimental check of the theory of molecular forces of attraction between condensed bodies.

(5) An analysis has been made of the present state of the problem concerning forces of molecular reaction. It is shown that the generally

accepted idea of the additivity of forces of molecular attraction in condensed media has not been proved either experimentally or theoretically.

(6) It is shown experimentally that calculations of molecular attraction of macro bodies cannot be made by summing the interaction of all pairs of molecules, calculated from the LONDON equation, when the distance between the surfaces is 1×10^{-5} cm and greater. The best results are obtained when allowance is made for the electromagnetic delay in the propagation of the forces concerned.

(7) The experimental data agree with the predictions of LIFSHITZ' theory. This agreement supports LEBEDEV's hypothesis of the electromagnetic nature of molecular forces.

(8) Molecular attraction was measured between specimens of a mixed thallium halide and a chromium-quartz pair. The results of these measurements, within the limits of experimental error, also agree with LIFSHITZ' theory, according to which the forces in these cases are four to five times greater than for a quartz-quartz pair the same distance apart.

(9) Since the LONDON–HAMAKER H^{-2} law for $u(H)$ represents a limiting partial case of LIFSHITZ' theory for small distances, in which electromagnetic delay has no effect, confirmation of this theory makes it possible to use the H^{-2} law at small distances.

(10) Deviations from the H^{-2} law towards the low side detected at large distances (10^{-5} cm) show (as can be easily seen) the small effect of molecular forces on the rate of coagulation of aerosols with particle diameters greater than 3×10^{-5} cm.

(11) The data obtained prove the existence of forces of molecular surface action at a distance, which form one of the corner stones of the modern theory of the stability and coagulation of colloids.

(12) The data obtained also show that deviations from the sixth-power law of the charge in the HARDY–SCHULTZ rule can be expected for very low concentrations of electrolyte with highly charged counter-ions.

(13) It is shown that the measured values of the forces of molecular attraction between bodies in the experiments of OVERBEEK and SPARNAAY exceed both the theoretical values and ours by 3–4 orders of magnitude, apparently owing to the fact that in their measurements effects were present which were unconnected with molecular forces.

(14) The results obtained for quartz specimens agree with the results of the measurements PROSSER and KITCHENER obtained by using an improved OVERBEEK–SPARNAAY method.

Acknowledgements—We would like to express our sincere appreciation to Professor E. M. LIFSHITZ for discussing problems of the theory, laboratory assistant I. V. ZHADOVSKAIA for help in the measurements, and to N. I. BUTUZOV for polishing the specimens.

VOL. 5 1958

REFERENCES

1. KALLMANN H. and WILLSTÄTTER M. *Naturwissenschalften* **20,** 952 (1932); *Izv. Akad. Nauk SSSR, Otdel. Khim. Nauk.* **5,** 1153 (1937).
2. DERJAGUIN B. V. *Kolloidzschr.* **6,** 291 (1940); **7,** 285 (1941); *Trans. Faraday Soc.* **36,** 203, 730 (1940). DERJAGUIN B. V. and LANDAU L. D. *Acta Physicochim. U.R.S.S.* **14,** 633 (1941); *Zh. Eksp. Teor. Fiz.* **11,** 802 (1941); **15,** 662 (1945).
3. VERWEY E. J. W. and OVERBEEK J. Th. G. *Theory of the Stability of Lyophobic Colloids.* Elsevier, Amsterdam (1948).
4. LONDON F. *Z. phys. Chem.* B **11,** 222 (1931).
5. CASIMIR H. B. G. and POLDER D. *Phys. Rev.* **73,** 360 (1948).
6. DE BOER J. H. *Trans. Faraday Soc.* **32,** 10 (1936).
7. HAMAKER H. C. *Physica* **4,** 1059 (1937).
8. LIFSHITZ E. M. *Dokl. Acad. Nauk SSSR* **97,** 643 (1954); **100,** 879 (1955); *Zh. Eksp. Teor. Fiz.* **29,** 94 (1955).
9. DERJAGUIN, B. V. *Zh. Fiz. Khim.* **6,** 1306 (1935); *Kolloidzschr.* **69,** 155 (1934).
10. DERJAGUIN, B. V. *Dokl. Akad. Nauk SSSR* **61,** 275 (1948).
11. DERJAGUIN B. V. and ABRIKOSSOVA I. I. *Zh. Eksp. Teor. Fiz.* **21,** 425 (1951); **30,** 993 (1956); **31,** 3 (1956); *Dokl. Akad. Nauk. SSSR* **108,** 214 (1956); **90,** 1055 (1953).
12. LIFSHITZ E. M. *Zh. Eksp. Teor. Fiz.* **29,** 94 (1955).
13. LEBEDEV P. N. *Collected Works.* Moscow (1913); *Wied Ann.* **52,** 621 (1894).
14. OVERBEEK J. Th. G. and SPARNAAY M. J. *J. Colloid Sci.* **7,** 343 (1952).
15. PROSSER A. P. and KITCHENER J. A. *Nature, Lond.* **178,** 1339 (1956); *Proc. Roy. Soc.* A **242,** 403 (1957).

J. Phys. Chem. Solids Pergamon Press 1958. Vol. 5. pp. 11–22.

THEORY OF ELECTROMAGNETIC WAVES IN A CRYSTAL WITH EXCITONS

S. I. PEKAR

Physical Institute of the Ukrainian Academy of Sciences, Kiev, U.S.S.R.

(*Received* 23 *May* 1957)

Abstract—Light waves are considered the frequencies of which are close to or fall in a region of exciton absorption in a crystal. A relationship is obtained between polarization dipole moment of the crystal and electric field intensity; this relationship is not one of direct proportionality, as is usually assumed, but is expressed by a differential equation. For this reason the Maxwell equations are of a higher order and their solutions are more complex than the well-known ones which follow from the simple phenomenological theory. It is shown that a number of waves exists in the crystal all of which have the same frequency, polarization and direction but different refractive indices. This effect is different from double refraction and occurs also in isotropically polarizable (cubic) crystals. Existence of purely longitudinal electric waves in the crystal is proved. Surface exciton states, the analogues of surface electron states, are discussed.

1. THE RELATIONSHIP BETWEEN POLARIZATION DIPOLE MOMENT AND AN ELECTRIC FIELD

LET Ψ^0 be the ground state of the crystal, Ψ_k—the excited exciton states with quasimomentum $\boldsymbol{k}$ and Ψ_n—other excited states of the crystal. Here the exciton state means any excited state of the crystal among whose quantum numbers there is only one continuous (three-dimensional) quantum number $\boldsymbol{k}$. Such a general definition of the exciton includes the FRENKEL exciton,[1] the WANNIER–MOTT exciton,[2,3] just a phonon, and a wave of electron-vibrational excitation of a molecule which is propagated in the crystal.

Let H be the energy operator of the crystal and W the operator of the energy of its interaction with an external electric field. The designated wavefunctions and operators depends both on the electron co-ordinates and on the co-ordinates of the atomic nuclei in the crystal.

To discuss a crystal acted on by a weak alternating electric field we shall assume:

$$\Psi = \Psi^0 + \psi + \psi' \qquad \psi = \sum_k C_k \Psi_k$$

$$\psi' = \sum_n C_n \Psi_n. \tag{1}$$

Here all the time dependences will be included in the coefficients C_k and C_n so that Ψ_k and Ψ_n are independent of time. W, ψ and ψ' are to be regarded as quantities of the first order of smallness. Retaining in the time dependent Schrödinger equation only the terms of the first order we obtain

$$\left[i\hbar\frac{\partial}{\partial t} - H\right] C_k \Psi_k = W_{k0}\Psi_k$$

$$W_{k0} \equiv \int \Psi_k^* W \Psi^0 \, d\Omega. \tag{2}$$

The integration is carried out for co-ordinates of all particles forming the crystal.

Analogous equations are obtained for C_n, Ψ_n.

We shall assume that the electric field varies slowly in space (i.e. it changes only a little along a distance of the order of a lattice constant). We can then introduce an average dipole moment of electric polarization of the crystal $\boldsymbol{P}(\boldsymbol{r})$ induced by the external electric field

$$\boldsymbol{P}(\boldsymbol{r}) = \int \Psi^* \Psi \hat{\boldsymbol{P}}(\boldsymbol{r}) \, d\Omega \quad d\Omega = \prod_i dx_i dy_i dz_i \tag{3}$$

Here

$$\hat{\boldsymbol{P}}(\boldsymbol{r}) = \sum_i e_i (\boldsymbol{r}_i - \boldsymbol{r}) D(\boldsymbol{r}_i - \boldsymbol{r})$$

where

$$D(xyz)=\begin{cases}1 \text{ in the region} & -\tfrac{1}{2}\leqslant x\leqslant\tfrac{1}{2}\\ & -\tfrac{1}{2}\leqslant y\leqslant\tfrac{1}{2}\\ & -\tfrac{1}{2}\leqslant z\leqslant\tfrac{1}{2}\\ 0 \text{ in the remainder of space.}\end{cases} \quad (4)$$

The summation is carried out for all particles of the crystal: i = the number of the particle, e_i = its charge, $\boldsymbol{r}_i$ = its co-ordinate, $\boldsymbol{r}$ = the co-ordinate of a macroscopic point in the crystal about which the dipole moment is calculated.

To the first order of smallness we find

$$\begin{aligned}\boldsymbol{P}(\boldsymbol{r}) &= \boldsymbol{P}_1(\boldsymbol{r})+\boldsymbol{P}_2(\boldsymbol{r})+\boldsymbol{P}'(\boldsymbol{r})\\ \boldsymbol{P}_1(\boldsymbol{r}) &\equiv \int \Psi'^{0*}\psi\,\hat{\boldsymbol{P}}(\boldsymbol{r})\,d\Omega\\ \boldsymbol{P}_2(\boldsymbol{r}) &= \int \psi^*\Psi'^0\,\hat{\boldsymbol{P}}(\boldsymbol{r})\,d\Omega\\ \boldsymbol{P}'(\boldsymbol{r}) &\equiv \int (\Psi'^{0*}\psi'+\psi'^*\Psi'^0)\,\hat{\boldsymbol{P}}(\boldsymbol{r})\,d\Omega.\end{aligned} \quad (5)$$

Let T_m denote the operation of translation of all electrons and all lattice deformations by a whole-number lattice vector $\boldsymbol{m}=m_1\boldsymbol{a}_1+m_2\boldsymbol{a}_2+m_3\boldsymbol{a}_3$ ($\boldsymbol{a}_j$ = the lattice constants). In other words T_m denotes such a change of the crystal configuration in which each electron is displaced by the vector $\boldsymbol{m}(\boldsymbol{r}_i\rightarrow\boldsymbol{r}_i+\boldsymbol{m})$ and each atom (or nucleus) of l-type in a unit cell number $\boldsymbol{n}(\boldsymbol{n}=n_1\boldsymbol{a}_1+n_2\boldsymbol{a}_2+n_3\boldsymbol{a}_3)$ has now the same displacement as that possessed previously by an atom of the same type in a cell number $\boldsymbol{n}-\boldsymbol{m}[\boldsymbol{r}_n{}^l-\boldsymbol{n}\rightarrow\boldsymbol{r}_{n-m}{}^l-(\boldsymbol{n}-\boldsymbol{m})]$. As a result of such a transformation H remains invariant. Applying the well-known methods of the theory of groups we can obtain the following results: the system of eigenfunctions of the operator H may be always chosen so that

$$\left.\begin{aligned}T_m\Psi'_{\boldsymbol{f}} &= e^{i\boldsymbol{f}\boldsymbol{m}}\Psi'_{\boldsymbol{f}}\\ \text{where}\\ \boldsymbol{f} &= g_1\boldsymbol{b}_1+g_2\boldsymbol{b}_2+g_3\boldsymbol{b}_3\quad -\pi\leqslant g_1,g_2,g_3\leqslant\pi\\ \boldsymbol{b}_i &= \frac{[\boldsymbol{a}_j\boldsymbol{a}_k]}{(\boldsymbol{a}_i[\boldsymbol{a}_j\boldsymbol{a}_k])}\,i\neq j\neq\boldsymbol{k}\end{aligned}\right\} \quad (6)$$

and $\boldsymbol{b}_i$ = the reciprocal lattice constant.

The ground state wave function of the crystal Ψ'^0 should be real and constant in sign. Therefore $T_m\Psi'^0=\Psi'^0$. The exciton states should satisfy (6) in which the quantum number $\boldsymbol{f}$ should be identified with $\boldsymbol{k}$, since by definition the exciton state has only one three-dimensional continuous quantum number $\boldsymbol{k}$. Consideration of particular types of excitons shows that $\Psi'_{\boldsymbol{k}}$ and the crystal energy $E(\boldsymbol{k})$ are continuous functions of $\boldsymbol{k}$, i.e. of $\boldsymbol{f}$ in the region of values given in (6).

It follows directly from (4) that the dipole moment $\hat{\boldsymbol{P}}$ at a point $\boldsymbol{r}$ after translation assumes a value which it had before translation at a point $\boldsymbol{r}-\boldsymbol{m}$, i.e. $T_m\hat{\boldsymbol{P}}(\boldsymbol{r})=\hat{\boldsymbol{P}}(\boldsymbol{r}-\boldsymbol{m})$. By a simple interchange of integration variables it can be easily shown that $\int T_m F(\ldots\boldsymbol{r}_i\ldots)\,d\Omega=\int F(\ldots\boldsymbol{r}_i\ldots)\,d\Omega$. Using the translation properties described above we find

$$\begin{aligned}\boldsymbol{P}_{0k}(\boldsymbol{r}) &\equiv \int \Psi'^{0*}\,\hat{\boldsymbol{P}}(\boldsymbol{r})\Psi'_k\,d\Omega\\ &= \int T_m[\Psi'^{0*}\,\hat{\boldsymbol{P}}(\boldsymbol{r})\Psi'_k]\,d\Omega=e^{i\boldsymbol{k}\boldsymbol{m}}\boldsymbol{P}_{0k}(\boldsymbol{r}-\boldsymbol{m}).\end{aligned} \quad (7)$$

Since the external electric field is a slow function of the co-ordinates, the terms with small $\boldsymbol{k}$ are important, as will be shown further. In that case the quantity (7) varies slowly in a distance of the order of a lattice constant and it is permissible to put approximately $\boldsymbol{m}=\boldsymbol{r}$ in (7). Then

$$\boldsymbol{P}_{0k}(\boldsymbol{r})=\boldsymbol{P}_0e^{i\boldsymbol{k}\boldsymbol{r}} \quad (8)$$

where

$$\boldsymbol{P}_0=\boldsymbol{P}_{0k}(0)\cong[\boldsymbol{P}_{0k}(0)]_{k=0}.$$

We shall now calculate $\boldsymbol{P}_1(\boldsymbol{r})$ of equation (5). According to (1)

$$\boldsymbol{P}_1(\boldsymbol{r})=\sum_{\boldsymbol{k}}C_{\boldsymbol{k}}\int\Psi'^{0*}\Psi'_{\boldsymbol{k}}\,\hat{\boldsymbol{P}}(\boldsymbol{r})\,d\Omega=\sum_{\boldsymbol{k}}C_{\boldsymbol{k}}\boldsymbol{P}_{0k}(\boldsymbol{r}). \quad (9)$$

For simplicity the origin for energy can be taken so that the ground-state energy is zero. Then Ψ'^0 does not depend on time and from (8) and (2) we can write

$$\begin{aligned}\left[i\hbar\frac{\partial}{\partial t}-E(-i\nabla)\right]C_{\boldsymbol{k}}\boldsymbol{P}_{0k} &= \left[i\hbar\frac{\partial}{\partial t}-E(\boldsymbol{k})\right]C_{\boldsymbol{k}}\boldsymbol{P}_{0k}\\ &= \int\Psi'^{0*}\,\hat{\boldsymbol{P}}\left[i\hbar\frac{\partial}{\partial t}-H\right]C_{\boldsymbol{k}}\Psi'_{\boldsymbol{k}}\,d\Omega=\boldsymbol{P}_{0k}W_{\boldsymbol{k}0}.\end{aligned} \quad (10)$$

VOL. 5 1958

Summing this expression for all $\boldsymbol{k}$ and taking (9) into account we obtain

$$\left[i\hbar\frac{\partial}{\partial t}-E(-i\nabla)\right]\boldsymbol{P}_1(\boldsymbol{r})=\sum_{\boldsymbol{k}}\boldsymbol{P}_{0\boldsymbol{k}}(\boldsymbol{r})W_{\boldsymbol{k}0}. \quad (11)$$

The energy of interaction of the external electromagnetic field with the crystal may be written as follows:

$$W=-\frac{1}{c}\int\dot{\hat{P}}(\boldsymbol{r}')\boldsymbol{A}(\boldsymbol{r}',t)\,d\tau'$$

$$W_{\boldsymbol{k}0}=-\frac{1}{c}\int\dot{\boldsymbol{P}}_{\boldsymbol{k}0}(\boldsymbol{r}')\boldsymbol{A}(\boldsymbol{r}',t)\,d\tau'$$

$$=-\frac{i\omega_0\boldsymbol{P}_0^*}{c}\int e^{-i\boldsymbol{k}\boldsymbol{r}'}\boldsymbol{A}(\boldsymbol{r}',t)\,d\tau' \quad (12)$$

where $\boldsymbol{A}$ = the field vector-potential and $\omega_0=[E(0)]/\hbar$. We see that with increase of $\boldsymbol{k}$ the quantity $W_{\boldsymbol{k}_0}$ rapidly falls towards zero like the coefficient of the Fourier expansion of the slow function of the co-ordinates $\boldsymbol{A}$. Therefore in the right-hand side of (11) the terms with small $\boldsymbol{k}$ dominate and the approximate summation may be extended to the whole of the infinite $\boldsymbol{k}$-space. Then, substituting in (11) the results of (8) and (12), and taking into account the fact that

$$\sum_{\boldsymbol{k}}e^{i\boldsymbol{k}(\boldsymbol{r}-\boldsymbol{r}')}=V\delta(\boldsymbol{r}-\boldsymbol{r}')$$

where V = the crystal volume, we finally obtain

$$\left[i\hbar\frac{\partial}{\partial t}-E(-i\nabla)\right]\boldsymbol{P}_1(\boldsymbol{r},t)$$

$$=-\frac{i\omega_0 V}{c}\boldsymbol{P}_0[\,\boldsymbol{P}_0^*,\boldsymbol{A}(\boldsymbol{r},t)]. \quad (13)$$

Differentiating the above equation with respect to time yields

$$\left[i\hbar\frac{\partial}{\partial t}-E(-i\nabla)\right]\dot{\boldsymbol{P}}_1(\boldsymbol{r},t)=ia\mathscr{E}_\perp(\boldsymbol{r},t)$$

$$a_{xy}=\omega_0 V P_{0x}P_{0y}^* \quad (14)$$

where $\mathscr{E}_\perp=(1/c)\dot{\boldsymbol{A}}$ is the rotational part of the electric field ($\mathrm{div}\,\mathscr{E}_\perp=0$), and a = a tensor of the second rank.

An equation for the term $\boldsymbol{P}_2(\boldsymbol{r},t)$ in equation (5) can be obtained simply from (14) by taking $\boldsymbol{P}_2=\boldsymbol{P}_1^*$:

$$\left[i\hbar\frac{\partial}{\partial t}+E(-i\nabla)\right]\dot{\boldsymbol{P}}_2(\boldsymbol{r},t)=ia^*\mathscr{E}_\perp(\boldsymbol{r},t). \quad (15)$$

In most cases $E(\boldsymbol{k})$ for small $\boldsymbol{k}$ has the form

$$E(\boldsymbol{k})=E_0+\frac{\hbar^2}{2}\sum_{p,s}M_{ps}^{-1}k_pk_s+\ldots\quad p,s=1,2,3$$

$$E_0=E(0). \quad (16)$$

Here M^{-1} is called the reciprocal effective exciton mass tensor. Equation (14) can now be rewritten as

$$\left[i\hbar\frac{\partial}{\partial t}-E_0+\frac{\hbar^2}{2}\sum_{ps}M_{ps}^{-1}\frac{\partial^2}{\partial x_p\partial x_s}\right]\dot{\boldsymbol{P}}_1=ia\mathscr{E}_\perp. \quad (17)$$

We thus find that in a dielectric in which excitons may be formed the relationship between the polarization and the electric field intensity is given not by the "physical" equations of Maxwell but by the differential equations of (17). The latter equations are supplemented by the initial conditions, i.e. the values of $\boldsymbol{P}_1$ and $\dot{\boldsymbol{P}}_1$ at time $t=0$, and also by the boundary conditions, i.e. value of $\boldsymbol{P}_1$, say, at the surface of the crystal. A discussion of the boundary conditions is given in the next section.

The term $\boldsymbol{P}'$ in (5) is related to virtual transitions to non-exciton states Ψ_n. This term is not discussed here in detail but it is assumed that it can be allowed for by introduction of the usual phenomenological constant ϵ' (which is, in general, complex):

$$P'=\frac{\epsilon'-1}{4\pi}\mathscr{E} \quad (18)$$

where $\mathscr{E}$ = the electric field intensity. In practice this assumption is not always valid, and this problem needs a separate discussion.

The results given above are obtained on the assumption that the crystal when not illuminated is in its ground state Ψ^0, and on illumination some few exciton, i.e. single-momentum, states Ψ_k are added to it. This assumption is strictly correct only at the absolute zero of temperature; at temperatures other than the absolute zero there are many phonons in the crystal both when it is in the dark

and when it is illuminated. In practice the results obtained will be approximately true at non-zero temperatures provided they are sufficiently low.

2. EFFECT OF THE CRYSTAL SURFACE ON THE EXCITON STATES; THE BOUNDARY CONDITIONS FOR THE POLARIZATION DIPOLE MOMENT. SURFACE EXCITONS

To discuss the boundary conditions it is necessary to make the model of the exciton more definite. We shall discuss FRENKEL's exciton:[1] we shall assume that the interaction between the molecules of the crystal is small and therefore the many electron wave-functions of the crystal may be constructed in the zero approximation by the atomic orbital G.L.G. method. Let ϕ_n denote an antisymmetrized wave-function of the crystal when the electron-vibrational excitation is localized in the unit cell number $\boldsymbol{n}$. Since the excitation may be localized in any cell and all such ϕ_n states with different $\boldsymbol{n}$ are mutually degenerate, then, in the zero approximation, the crystal wave-function should be taken as a linear combination of all ϕ_n. It is easily shown that

$$T_m\phi_m = \phi_0 \qquad \phi_m = T_{-m}\phi_0. \tag{19}$$

Here ϕ_0 = that state of the crystal in which the excited cell is at the origin of co-ordinates. If this linear combination of wave-functions possesses the translational property (6), then the coefficients of the linear combination are obtained unambiguously from (6) and (19). As a result the zero-approximation wave-function is

$$\Psi_k = \sum_n a_n\phi_n \qquad a_n = a_0 e^{i\boldsymbol{k}\boldsymbol{n}}. \tag{20}$$

The above function can be also obtained by the method of perturbed degenerate states taking the interaction between neighbouring unit cells of the crystal to be a small perturbation. In that case for a_n we have the following systems of linear homogeneous equations

$$(E-H_0)a_n = \sum_{i=1}^{3} H_i(a_{n+a_i}+a_{n-a_i}) \tag{21}$$

where $\boldsymbol{a}_i$ are constants of the lattice

$$H_0 = \int \phi_0 H\phi_0\, d\Omega$$

$$H_i = H_{0a_i} = H_{a_i 0} = \int \phi_{a_i} H\phi_0\, d\Omega.$$

It can easily be verified that the values of a_n from (20) are the solutions of (21). For the crystal energy we find[1] a value:

$$E(\boldsymbol{k}) = H_0 + 2\sum_{i=1}^{3} H_i \cos g_i \qquad \boldsymbol{k} = g_1\boldsymbol{b}_1 + g_2\boldsymbol{b}_2 + g_3\boldsymbol{b}_3 \tag{22}$$

$$-\pi \leqslant g_i \leqslant \pi.$$

The solution (20), (22) and the results of the preceding section (Section 1) apply to an infinite crystal. Also in obtaining (21) and (22) it was assumed that each unit cell has six cells as neighbours.

We shall now consider a bounded crystal. Let it be in the form of an infinite plane-parallel plate, bounded by planes $n_3 = 1$ and $n_3 = \mathscr{G}$ ($\mathscr{G}$ = a large integer). Nodal cells will now exist only for those vectors whose third component lies in the interval $1 \leqslant n_3 \leqslant \mathscr{G}$. Of the equations which determine the coefficients a_n all the equations (21), whose vector $\boldsymbol{n}$ does not belong to the surface cells of the crystal, remain unchanged. At the crystal surface, the equations (21) are altered as follows: for $n_3 = 1$ the term a_{n-a_3} is absent on the right-hand side, and for $n_3 = \mathscr{G}$ the term a_{n+a_3} is missing, also on the right. In solving the modified system of equations for a bounded crystal we must remember that translational symmetry in the direction $\boldsymbol{a}_3$ is absent but it is still preserved in the directions $\boldsymbol{a}_1$ and $\boldsymbol{a}_2$. The wave-function should satisfy (6) with $m_3 = 0$. We now have

$$a_n = \frac{a_0}{\sqrt{2}}\left[e^{i\boldsymbol{k}\boldsymbol{n}} - e^{i\tilde{\boldsymbol{k}}\boldsymbol{n}}\right] \qquad g_3 = \pi\frac{\nu}{\mathscr{G}+1}$$

$$\nu = 1, 2, 3 \ldots \mathscr{G}. \tag{23}$$

Here vector $\tilde{\boldsymbol{k}}$ represents a mirror reflection of the vector $\boldsymbol{k}$ in the plane of the crystal surface. In other words $\tilde{\boldsymbol{k}}$ is given in terms of $\boldsymbol{k}$ by the relationships $\tilde{\boldsymbol{k}}_1\boldsymbol{a}_1 = \boldsymbol{k}\boldsymbol{a}_1$, $\tilde{\boldsymbol{k}}\boldsymbol{a}_2 = \boldsymbol{k}\boldsymbol{a}_2$, $\boldsymbol{k}\boldsymbol{a}_3 = -\boldsymbol{k}\boldsymbol{a}_3$. According to (23) and (20), an exciton wave-function in a bounded crystal can be written as

$$\phi_k = \frac{1}{\sqrt{2}}\left[\Psi_k - \Psi_{\tilde{k}}\right]. \tag{24}$$

VOL. 5 1958

If Ψ_k is taken to be an exciton wave incident on the surface, then $\Psi_{\tilde{k}}$ is a wave mirror-reflected by the surface. Ψ_k in (24) is not a wave-function for an infinite crystal but a wave-function for the plate described, with periodicity (period $\mathscr{G}\boldsymbol{a}_3$) in the direction $\boldsymbol{a}_3$. Ψ_k possesses the translational property (6) also in the direction $\boldsymbol{a}_3$. Dependence of energy on $\boldsymbol{k}$ is given by (22) as before.

The results of the preceding section (Section 1) can be obtained also for a bounded crystal. For this purpose it is sufficient to replace Ψ_k by ϕ_k in equations (1), (2), (9), (10) and (11). The final formulae (13–17) are not changed at all. Only equation (8) is altered, which for a bounded crystal becomes

$$\boldsymbol{P}_{0k}(\boldsymbol{r}) = \frac{\boldsymbol{P}_0}{\sqrt{2}}\left[e^{i\boldsymbol{k}\boldsymbol{r}} - e^{i\tilde{\boldsymbol{k}}\boldsymbol{r}}\right] \tag{25}$$

where the constant $\boldsymbol{P}_0$ has its previous numerical value.

Now we can easily obtain values of $\boldsymbol{P}_{0k}(\boldsymbol{r})$ at the crystal surfaces. One of these surfaces ($n_3 = 1$) is, in a macroscopic sense, a plane through the origin of co-ordinates. For points on this surface $\boldsymbol{r}$ is coplanar with $\boldsymbol{a}_1$ and $\boldsymbol{a}_2$ and may be represented by $\boldsymbol{r} = \boldsymbol{a}_1 r_1 + \boldsymbol{a}_2 r_2$. The difference of the exponents in (25) is given by

$$(\boldsymbol{k}-\tilde{\boldsymbol{k}}, \boldsymbol{r}) = (\boldsymbol{k}-\tilde{\boldsymbol{k}}, \boldsymbol{a}_1)r_1 + (\boldsymbol{k}-\tilde{\boldsymbol{k}}, \boldsymbol{a}_2)r_2 = 0$$

following the definition of $\tilde{\boldsymbol{k}}$. Therefore on this surface $\boldsymbol{P}_{0k}(\boldsymbol{r}) = 0$. The second bounding plane of the plate ($n_3 = \mathscr{G}$) consists of points with co-ordinates $\boldsymbol{r} = \boldsymbol{a}_1 r_1 + \boldsymbol{a}_2 r_2 + \boldsymbol{a}_3(\mathscr{G}+1)$. Now the difference of the exponents in (25) is (see equation 23):

$$\begin{aligned}(\boldsymbol{k}-\tilde{\boldsymbol{k}}, \boldsymbol{r}) &= (\boldsymbol{k}-\tilde{\boldsymbol{k}}, \boldsymbol{a}_3)(\mathscr{G}+1) \\ &= 2(\boldsymbol{k}, \boldsymbol{a}_3)(\mathscr{G}+1) = 2\pi\nu \\ \nu &= 1, 2, 3 \ldots \mathscr{G}.\end{aligned}$$

Consequently also on this surface $\boldsymbol{P}_{0k}(\boldsymbol{r}) = 0$. It follows from (9) that on the crystal surfaces also $P_1(\boldsymbol{r}) = 0$. Thus the crystal surfaces are modal planes both for the exciton waves and the dipole moment.

In a bounded crystal electrons can exist in "band" states and in surface states.[4] Similarly surface exciton states can exist in which the excited wave moves only in the surface layer of the crystal. To obtain these surface excitons in the G.L.G. approximation we shall discuss a semi-infinite crystal whose nodes are in the region $n_3 \geqslant 1$. Equation (21) is still valid for all $\boldsymbol{n}$ of those cells which are not adjacent to the surface, i.e. for $n_3 \geqslant 2$. Solution of (21) can be represented by (20), (22), as for an infinite crystal. Since the translational symmetry is rigidly preserved in the directions $\boldsymbol{a}_1$ and $\boldsymbol{a}_2$, g_1 and g_2 should be real as before and should still lie in the intervals given in (22). But g_3 may now be complex, since (21) is satisfied by (20) for any complex value of $\boldsymbol{k}$; energy in (22) is still real and the wave-function is finite if $g_3 = i\kappa + l\pi$ for $\kappa \geqslant 0$ and $l =$ integer. Thus, equations (21) have also a solution in the form:

$$\begin{gathered}a_{\boldsymbol{n}} = (-1)^l a_0 \exp[i(g_1 n_1 + g_2 n_2) - \kappa n_3] \\ -\pi \leqslant g_1, g_2 \leqslant \pi \qquad \kappa \geqslant 0\end{gathered} \tag{26}$$

$$\begin{aligned}E(\boldsymbol{k}) &\equiv E(g_1, g_2, g_3) \\ &= H_0 + 2\sum_{i=1}^{2} H_i \cos g_i + 2(-1)^l H_3 \cosh\kappa.\end{aligned} \tag{27}$$

Now it is necessary to satisfy equations for $a_{\boldsymbol{n}}$ when $\boldsymbol{n}$ refers to the cells adjacent to the surface. These equations differ from (21) in two respects: (a) for $n_3 = 1$ the term $H_3 a_{\boldsymbol{n}-\boldsymbol{a}_3}$ is missing on the right-hand side, (b) the constants H_0 and H_i have somewhat different values due to absence of the next layer $n_3 = 0$. The coefficients H_i in the G.L.G. approximation are of the first order of smallness; their variation near the surface is of the second order of smallness which can therefore be neglected. H_0 is of the zeroth order of smallness and H_0', its variation near the surface of the first order of smallness, which cannot be neglected. Thus when $\boldsymbol{n}$ refers to the surface cells ($n_3 = 1$) instead of (21) we have

$$(E - H_0 - H_0')a_{\boldsymbol{n}} = \sum_{i=1}^{3} H_i[a_{\boldsymbol{n}+\boldsymbol{a}_i} + a_{\boldsymbol{n}-\boldsymbol{a}_i}(1-\delta_{i,3})]. \tag{28}$$

The solutions of the "volume" (i.e. non-surface) equations (21), given by (26), (27), should also satisfy the "surface" equations (28). This leads to the following equation which defines κ:

$$e^{-\kappa} = l(-1)^l \frac{H_3}{H_0'}. \tag{29}$$

If κ found from the above equation is positive, i.e. if $|H_3/H_0'| \leqslant 1$, then (26), (27), (29) give solutions for a semi-infinite crystal. The probability of the presence of excitation in a cell $\boldsymbol{n}$ is equal to $|a_{\boldsymbol{n}}|^2$. This probability does not depend on n_1 or n_2 and it falls exponentially with increase of n_3 i.e. with the distance from the crystal surface. Energy of the system (27) represents a two-dimensional band since projection of the vector $\boldsymbol{k}$ in the direction $\boldsymbol{a}_3$ remains constant. The states discussed here will be called surface excitons. If $|H_3/H_0^1| > 1$ the surface excitons do not exist.

Results of the preceding section (Section 1) can be extended to the surface excitons. Equations (1) to (5) still hold if $\Psi_{\boldsymbol{k}}$ now denotes surface exciton states. Equation (6) cannot now be proved by group theory to hold for any translation $T_{\boldsymbol{m}}$ since there is no translational symmetry in the direction $\boldsymbol{a}_3$. It can be proved, however, as follows. Assume a condition of periodicity in the direction $\boldsymbol{a}_3$ with a large period $\mathscr{G}\boldsymbol{a}_3$ (as was done earlier for the plane-parallel plate). Then from (19) and (20) we obtain

$$T_{\boldsymbol{m}}\Psi_{\boldsymbol{k}} = \sum_{\boldsymbol{n}} a_{\boldsymbol{n}} T_{\boldsymbol{m}} T_{-\boldsymbol{n}} \phi_0 = \sum_{\boldsymbol{n}} a_{\boldsymbol{n}} T_{\boldsymbol{m}-\boldsymbol{n}} \phi_0$$

$$= \sum_{\boldsymbol{n}} a_{\boldsymbol{n}+\boldsymbol{m}} T_{-\boldsymbol{n}} \phi_0 = e^{i\boldsymbol{k}\boldsymbol{m}} \Psi_{\boldsymbol{k}} \qquad (30)$$

and this relationship holds for both real and complex $\boldsymbol{k}$. Thus for the surface excitons equations (6) to (12) hold but the values of $\boldsymbol{k}$ are restricted by the inequalities (26) and the condition (29). In (8) we now put $\boldsymbol{P}_0 = [\boldsymbol{P}_{0\boldsymbol{k}}(0)]_{g_1=g_2=0,\ g_3=i\kappa}$ and in (12) the integration is carried out only in the semi-space occupied by the crystal.

Substituting in (11) the expressions (8) and (12) and taking into account that

$$\sum_{g_1 g_2} e^{i(\boldsymbol{k}\boldsymbol{r}-\boldsymbol{k}^*\boldsymbol{r}')}$$

$$= \mathscr{G}^2 \exp[-\kappa(r_3+r_3')]\delta(r_1-r_1')\delta(r_2-r_2') \qquad (31)$$

where the new variables r_1, r_2, r_3 are given by $\boldsymbol{r} = \boldsymbol{a}_1 r_1 + \boldsymbol{a}_2 r_2 + \boldsymbol{a}_3 r_3$, we obtain for the surface excitons

$$\boldsymbol{P}_1 = \boldsymbol{P}_1^{(s)}(r_1, r_2)\exp(-\kappa r_3)$$

$$\left[i\hbar\frac{\partial}{\partial t} - E\left(-i\frac{\partial}{\partial r_1},\ -i\frac{\partial}{\partial r_2},\ i\kappa\right)\right]\boldsymbol{P}_1^{(s)} =$$

$$= -\frac{i\omega_0}{c}\mathscr{G}^2 v\,\boldsymbol{P}_0 \int_0^\infty \exp(-\kappa r_3')\times$$

$$\times[\boldsymbol{P}_0^*,\ \boldsymbol{A}(\boldsymbol{a}_1 r_1 + \boldsymbol{a}_2 r_2 + \boldsymbol{a}_3 r_3', t)]\,dr_3'. \qquad (32)$$

Here $v \equiv (\boldsymbol{a}_1[\boldsymbol{a}_2\boldsymbol{a}_3])$ is the volume of a unit cell and $E(g_1, g_2, g_3)$ is given by (27). When $\boldsymbol{A}(\boldsymbol{r}, t)$ in its dependence on r_3 does not change much in a distance of the order of $1/\kappa$, it is permissible to take $\boldsymbol{A}$ in (32) outside the integral sign. As a result of subsequent differentiation of (32) with respect to time, we obtain

$$\left[i\hbar\frac{\partial}{\partial t} - E\left(-i\frac{\partial}{\partial r_1},\ -i\frac{\partial}{\partial r_2},\ i\kappa\right)\right]\dot{\boldsymbol{P}}_1^{(s)}$$

$$= i a^{(s)} \mathscr{E}_\perp(\boldsymbol{a}_1 r_1 + \boldsymbol{a}_2 r_2, t) \qquad (33)$$

$$a_{xy}^{(s)} = \frac{\omega_0 \mathscr{G}^2 v}{\kappa} P_{0x} P_{0y}^*.$$

This is the analogue of (14) for the surface excitons.

In the G.L.G. approximation the constants a_{xx}, $a_{xx}^{(s)}$ may be related to the oscillator strength f_x of a given transition referred to a unit crystal cell. Thus for the excitons connected with the electronic excitation we obtain

$$a_{xx} = \frac{e^2\hbar}{2m} N f_x \qquad a_{xx}^{(s)} = 2a_{xx} \qquad (34)$$

where N = the number of cells in a unit volume and m = the free electron mass.

The above discussion was based on FRENKEL's exciton model.[1] Analogous results are obtained for other exciton models. Thus, for example, for the WANNIER–MOTT exciton,[2,3] in which a conduction electron and a hole bound by Coulomb attraction execute hydrogen-like motion, it can be shown that the exciton wave is mirror-reflected from the crystal surface. For a plane-parallel plate again equations (24) and (25) are obtained and g_3 assumes a discrete set of values given by (23). As before the crystal surface becomes a nodal plane both for the exciton waves and for the dipole moment, $\boldsymbol{P}_1(\boldsymbol{r}_1 t)$.

Also the surface exciton states are possible for electron-hole excitons. These states occur, for example, when a hole becomes attached to an electron in the surface conductivity band or,

VOL 5 195

conversely, an electron becomes attached to a hole in a surface state. An electron and a hole both belonging to surface bands may also combine to form an exciton. Again (32) and (33) are obtained.

If the exciton is a usual acoustic phonon then, for elastic waves, we have for the displacement vector an antinode on the surface (boundary between the crystal and vacuum). The dipole moment is proportional to the derivative of the displacement with respect to co-ordinates and therefore for the dipole moment we again have a node on the surface. In the case of phonons the surface excitons represent the well-known Rayleigh surface waves.

For the various models of "volume" excitons it was found that at the crystal surface $\boldsymbol{P}_1 = 0$ which is the boundary condition for (14). The exceptions to this rule are rare. Thus, for phonons, if the crystal surface is fixed (i.e. the crystal borders on a denser or heavier medium) the displacement has a node on the surface and the polarization an antinode.

For the surface excitons no boundary conditions at the crystal surface are obtained. The equations (32) and (33) do not need such conditions. For variables $\boldsymbol{r}_1$ and $\boldsymbol{r}_2$ the boundary conditions are replaced by periodicity.

3. PLANE ELECTROMAGNETIC WAVES IN A CRYSTAL

In this section solution of Maxwell's equations is given for the case when the relationship between the polarization and the electric field intensity is given by (14) or (17). Maxwell's equations may be divided into two groups: "ideal" equations which do not depend on the crystal properties

$$\operatorname{curl} \mathscr{E} = -\frac{1}{c}\dot{\mathscr{H}} \qquad \operatorname{curl} \mathscr{H} = \frac{1}{c}\dot{\mathscr{D}}$$
$$\operatorname{div} \mathscr{D} = 0 \qquad \operatorname{div} \mathscr{H} = 0 \tag{35}$$

and "physical" equations

$$\mathscr{D} = \epsilon'\mathscr{E} + 4\pi(\boldsymbol{P}_1 + \boldsymbol{P}_2)$$
$$\left[i\hbar\frac{\partial}{\partial t} - E(-i\nabla)\right]\dot{\boldsymbol{P}}_1 = ia\mathscr{E}_\perp \tag{36}$$
$$\left[i\hbar\frac{\partial}{\partial t} + E(-i\nabla)\right]\dot{\boldsymbol{P}}_2 = ia^*\mathscr{E}_\perp.$$

We shall seek a solution of these equations in the form of a plane wave assuming $\mathscr{E}$, $\mathscr{H}$, $\mathscr{D}$, $\boldsymbol{P}_1$ and $\boldsymbol{P}_2$ to be proportional to $\exp\{i\omega[(n/c)(\boldsymbol{r},\boldsymbol{s})-t]\}$. Here ω = the wave frequency; n = refractive index, $\boldsymbol{s}$ = unit vector normal to the equiphase surface. The equations (35) are satisfied when field amplitudes are related by

$$n[\boldsymbol{s}, \mathscr{E}] = \mathscr{H} \qquad n[\boldsymbol{s}, \mathscr{H}] = -\mathscr{D}. \tag{37}$$

If we eliminate $\mathscr{H}$ from these equations we obtain

$$\mathscr{D} = n^2[\mathscr{E} - \boldsymbol{s}(\boldsymbol{s}, \mathscr{E})] \tag{38}$$

Not only (37), (38) but also other relationships of the usual crystal optics, which follow from the "ideal" equations only, remain valid. These relationships are given for example by BORN[5] (pp. 296–99).

Substitution of the exponential solution into the second and third equations of (36) gives

$$\boldsymbol{P}_1 = \frac{a}{\omega}\frac{\mathscr{E}_\perp}{E[(\omega n/c)\boldsymbol{s}] - \hbar\omega}$$
$$\boldsymbol{P}_2 = \frac{a^*}{\omega}\frac{\mathscr{E}_\perp}{E[(\omega n/c)\boldsymbol{s}] + \hbar\omega} \tag{39}$$
$$\mathscr{E}_\perp = \mathscr{E} - \boldsymbol{s}(\boldsymbol{s}\mathscr{E}) \equiv \eta\mathscr{E}$$

where η = a second-rank tensor: $\eta_{xy} = \delta_{xy} - s_x s_y$. For E we can use a quadratic expansion

$$E\left(\frac{\omega n}{c}\boldsymbol{s}\right) = E_0 + \frac{\hbar^2\omega^2 n^2}{2M_s c^2} + \ldots. \tag{40}$$

Since it is assumed that the wavelength of light is much longer than the lattice constant. M_s depends on the direction of $\boldsymbol{s}$ and will be called the effective exciton mass in the direction $\boldsymbol{s}$. M_s may be linked directly with the reciprocal effective mass tensor in (17). In (39) $\boldsymbol{P}_2 \neq \boldsymbol{P}_1^*$, but if a linear combination of solutions is taken so that the fields are real (by summing the exponential with his complex conjugate, then $\boldsymbol{P}_2 = \boldsymbol{P}_1^*$.

If ω lies outside the region of exciton absorption, i.e. when ω differs considerably from $\omega_0 = E_0/\hbar$, then in (39) we can replace $E(\omega n/c\boldsymbol{s})$ by E_0. The physical Maxwell equations assume then their usual form and the usual results of crystal optics are obtained. Near the region of exciton absorption

such a replacement can be made only in $\boldsymbol{P}_2$; in $\boldsymbol{P}_1$ we must take into account dependence of E on $\boldsymbol{n}$. In this case $\boldsymbol{P}_2$ can be omitted because it is much less then $\boldsymbol{P}_1$ and the physical equations (36) can be written in the usual form $\mathscr{D} = \epsilon\mathscr{E}$. Now however ensor ϵ is equal to

$$\epsilon = \epsilon' + \frac{B\eta}{n^2-\mu} \tag{41}$$

where

$$B = \frac{8\pi M_s c^2 a}{\hbar^2\omega^3} \qquad \mu = \frac{2M_s c^2}{\hbar\omega}\left(1-\frac{E_0}{\hbar\omega}\right).$$

Thus ϵ now depends not only on the frequency ω but also on $\boldsymbol{s}$ and $\boldsymbol{n}$. Consequently for each direction of propagation and direction of polarization of the light wave there are a particular tensor $B\eta$ and particular directions of the principal axes of polarization.

Eliminating $\mathscr{D}$ from the physical equations and from (38) we find

$$\epsilon\mathscr{E} = n^2[\mathscr{E} - \boldsymbol{s}(\boldsymbol{s}\mathscr{E})]. \tag{42}$$

Equations (42) and (41) are the equivalents of Maxwell's equations (35) and (36) if the solution is in the form of plane exponential waves.

Equation (42) represents a system of three linear homogeneous equations for projections of the electric field amplitude. Equating the determinant of this system of equations to zero, we obtain an equation which determines $\boldsymbol{n}$:

$$(\boldsymbol{s},\epsilon\boldsymbol{s})n^4 + [(\boldsymbol{s},\epsilon^2\boldsymbol{s}) - (\boldsymbol{s},\epsilon\boldsymbol{s})sp\epsilon]n^2 + \Delta(\epsilon) = 0$$

$$\Delta(\epsilon) = \begin{vmatrix} \epsilon_{xx} & \epsilon_{xy} & \epsilon_{xz} \\ \epsilon_{yx} & \epsilon_{yy} & \epsilon_{yz} \\ \epsilon_{zx} & \epsilon_{zy} & \epsilon_{zz} \end{vmatrix} \tag{43}$$

In the usual crystal optics ϵ is independent of $\boldsymbol{n}$ and (43) is a quadratic equation in n^2. Two roots of this quadratic equation yield, for a given $\boldsymbol{s}$, two values of $|n|$ and consequently two plane waves in which the vectors $\mathscr{D}$ are mutually perpendicular. Near the exciton absorption region when μ is small the dependence of ϵ on $\boldsymbol{n}$, given by (41), must be taken into account. Substituting (41) in (43), introducing for the sake of brevity

$$\overline{\epsilon'} = (\boldsymbol{s},\epsilon'\boldsymbol{s}) \quad \overline{\epsilon'^2} = (\boldsymbol{s},\epsilon'^2\boldsymbol{s}) \quad \overline{\eta} = (\boldsymbol{s},\eta\boldsymbol{s})$$

$$\overline{\eta^2} = (\boldsymbol{s},\eta^2\boldsymbol{s})$$

and introducing similar quantities for the tensor $B\eta$, we can rewrite (43) as

$$\left(\overline{\epsilon'} + \frac{\overline{B\eta}}{n^2-\mu}\right)n^4 +$$

$$+\left[\overline{\epsilon'^2} - \overline{\epsilon'}sp\epsilon' + \frac{\overline{\epsilon' B\eta} + \overline{B\eta\epsilon'} - \overline{\epsilon'}sp\overline{B\eta} - B\eta sp\epsilon'}{n^2-\mu} + \right.$$

$$\left. + \frac{(\overline{B\eta})^2 - \overline{B\eta}sp B\eta}{(n^2-\mu)^2}\right]n^2 + \Delta\left(\epsilon' + \frac{B\eta}{n^2-\mu}\right) = 0.$$

This is now an equation of higher than the second degree in n^2. Therefore for a given $\boldsymbol{s}$ it gives, in general, more than two values of $|n|$ and more than two plane waves. It will be shown below that the degree of (44) depends on the crystal structure and the direction of $\boldsymbol{s}$.

As examples we shall consider rhombic, tetragonal and cubic crystals. For these crystals the calculations are simplified since the principal axes of ϵ' and B are identical with the crystalline axes of second or fourth order, and consequently the directions of the principal axes do not depend on ω, $\boldsymbol{s}$, $\boldsymbol{n}$. In these cases it is convenient to use the principal axes of ϵ' and B as the Cartesian coordinate axes and this procedure is followed below.

Rhombic Crystals

In these crystals, of all the elements of the tensor $\boldsymbol{a}$, only one is non-zero. To show this we shall note that of the three projections of the vector $\boldsymbol{P}_0$ only one can be non-zero. Indeed according to (8)

$$\boldsymbol{P}_0 = \int \Psi_0^* \hat{\boldsymbol{P}}(0)\Psi_0 \, d\Omega. \tag{45}$$

We shall first discuss crystals with $\mathscr{D}_2$ symmetry group. Let $\hat{C}_x$, $\hat{C}_y$, $\hat{C}_z$ be the operations of rotation of all electrons of the crystal and all lattice distortions by 180° about crystal axes of the second order, i.e. about the axes x, y and z. Application of any of these operators to the function under the integral sign in (45) is equivalent to change of signs in certain integration variables and therefore should not affect the value of the integral. Application of the group theory methods shows that only those projections of a matrix element in (45) may be non-zero for which the expression under the integral sign is invariant under any transformation $\hat{C}$.

To find out how the function to be integrated behaves under these rotations we shall consider how each of its three multipliers is transformed.

Ψ^0 as the ground state of the crystal should be fully symmetric and consequently invariant under all three rotations. Projection of $\hat{\boldsymbol{P}}(0)$ on the rotation axis is invariant but other projections of $\hat{\boldsymbol{P}}(0)$ change their signs. Since the point group of symmetry of rhombic crystals possesses irreducible representations of the first order only, then Ψ_0 (and Ψ^0) is certainly an eigenfunction of all three operators $\hat{C}$:

$$\hat{C}_x\Psi_0 = C_x\Psi_0 \qquad \hat{C}_y\Psi_0 = C_y\Psi \qquad \hat{C}_z\Psi_0 = C_z\Psi_0$$

Since $\hat{C}_x^{\,2} = \hat{C}_y^{\,2} = \hat{C}_z^{\,2} = 1$ the eigenvalues C_x, C_y and C_z may have only the values ± 1. Applying to Ψ_0 the left- and right-hand sides of the operator equality $\hat{C}_x\hat{C}_y = \hat{C}_z$ we obtain $C_xC_y = C_z$. It follows that either all three eigenvalues C are $+1$, or one of them is $+1$ and the other two -1.

On the basis of the above discussion of the transformation properties of the multipliers which enter the integral in (45) we can conclude:

(1) The case $C_x = C_y = C_z = 1$. In this case all projections in (45) are equal to zero.

(2) The case when one of the eigenvalues C (say C_x) is equal to $+1$ and the other two equal to -1: $C_x = 1$, $C_y = C_z = -1$. In this case $P_{0x} \neq 0$, $P_{0y} = P_{0z} = 0$. According to (14) and (41) in tensors a and B the only non-zero components are a_{xx} and B_{xx} respectively, which was to be proved. A similar result is obtained for rhombic crystals with symmetry groups C_{2v} and D_{2h}.

Thus in rhombic crystals for any direction of $\mathscr{E}$ the right-hand side of the vector equality (14) and $\boldsymbol{P}_1$ are directed along the x-axis. This does not mean that this axis is essentially different from other principal polarization axes. The above result is obtained by taking into account only one exciton band whose wave-functions possess special direction x. In rhombic crystals there are other exciton bands (not yet considered) with special directions y and z. Occurrence of several exciton bands can be taken into account by introduction into (1) of several terms of the ψ type. As a result several vector components of the $\boldsymbol{P}_1$ type including those directed along y and z will appear in the right-hand side of (5). In a rhombic crystal these exciton bands are not degenerate in energy and if the frequency of light lies in the exciton absorption region of one band then this frequency could be outside the exciton absorption regions of the other bands and the presence of the latter bands may be taken care of by change of ϵ' [see remarks preceding equation (41)].

Denoting the only non-zero component of the tensor B by b we can write as

$$\begin{vmatrix} b & 0 & 0 \\ 0 & 0 & 0 \\ 0 & 0 & 0 \end{vmatrix}$$

When $\boldsymbol{s}$ is parallel to $\boldsymbol{P}_0$, i.e. when $s_x = 1$, $s_y = s_z = 0$, then the tensor $B\eta$ is equal to zero and equation (44) has the form met in the usual crystal-optics treatment when all polarization is given by the tensor ϵ'. In this case no new solutions are obtained: 2 plane waves exist polarized along the axes y and z with refractive indices $\sqrt{(\epsilon'_{yy})}$ and $\sqrt{(\epsilon'_{zz})}$ respectively.

For a different direction of $\boldsymbol{s}$ e.g. when $s_x = s_y = 0$, $s_z = 1$ equation (44) has the following form:

$$(n^2 - \epsilon'_{yy})\left(n^2 - \epsilon'_{xx} - \frac{b}{n^2-\mu}\right) = 0. \tag{46}$$

Now the system of equations (42) has three solutions:

$$\mathscr{E}_x = \mathscr{E}_z = 0 \qquad \mathscr{E}_y \neq 0 \qquad n = \sqrt{(\epsilon'_{yy})} \tag{47}$$

$$\mathscr{E}_y = \mathscr{E}_z = 0 \qquad \mathscr{E}_x = \begin{cases} \mathscr{E}_+ & n_+^{\,2} = \tfrac{1}{2}(\mu+\epsilon'_{xx}) + \sqrt{[\tfrac{1}{4}(\mu-\epsilon'_{xx})^2 + b]} \quad (48) \\ \mathscr{E}_- & n_-^{\,2} = \tfrac{1}{2}(\mu+\epsilon'_{xx}) - \sqrt{[\tfrac{1}{4}(\mu-\epsilon'_{xx})^2 + b]}. \quad (49) \end{cases}$$

Equation (47) is identical with the usual crystal optics solution, but (48) and (49) are new solutions. To satisfy the boundary condition $\boldsymbol{P}_1 = 0$ at the crystal surface (let this surface be the plane $z = 0$) it is necessary to combine (48) and (49) linearly as follows

$$\mathscr{E}_x(z,t) = \mathscr{E}_+\{\exp[i(\omega/c)n_+z] - q\exp[i(\omega/c)n_-z]\}\exp(-i\omega t) \tag{50}$$

where

$$q=\frac{n_-^2-\mu}{n_+^2-\mu}.$$

It can be easily shown that as ω moves away from the exciton absorption region towards red or violet q becomes $\ll 1$ or $\gg 1$ respectively. Then in (50) the amplitude of one of the waves becomes negligibly small compared with the amplitude of the other wave. The wave with the dominating amplitude becomes identical with the usual crystal optics solution. Near the exciton absorption region, however, both waves in (50) have amplitudes of the same order and the solution then differs essentially from the usual crystal optics one. The new solution is a superposition of two waves with different refractive indices but polarized in the same way. Equations (48) and (49) show that neither of the refractive indices has the usual hyperbolic break in its dependence on ω in the exciton absorption region. Other formulae are also essentially different for ω in the exciton absorption range. Thus the reflection coefficient for light falling normally along the z-axis onto the crystal surface is given by

$$R=\left|\frac{1-q-n_++qn_-}{1-q+n_+-qn_-}\right|^2. \tag{51}$$

Away from the exciton absorption region when $q\ll 1$ or $q\gg 1$ equation (51) has the usual crystal optics form.

Tetragonal crystals

Let the x-axis coincide with a crystal axis of the fourth order, i.e. the lattice constants in the y and z directions are equal. Study of the exciton states by means of the group theory, analogously to the case of rhombic crystals, yields the following conclusions. The exciton bands may be divided into two types:

(a) *Non-degenerate exciton bands.* For them the vector $\boldsymbol{P}_0$ is directed along the x-axis. If ω approaches the range of absorption of light by excitons of this type, then the tensor B has the form

$$\begin{vmatrix} b & 0 & 0 \\ 0 & 0 & 0 \\ 0 & 0 & 0 \end{vmatrix}$$

The solutions of (41) and (42) are then the same as for rhombic crystals.

(b) *Paired degenerate exciton bands.* $\boldsymbol{P}_0$ along the y-axis corresponds to one of them, $\boldsymbol{P}_0$ along the z-axis corresponds to the other. We shall denote these vectors $\boldsymbol{P}_0^{(2)}$, $\boldsymbol{P}_0^{(3)}$ respectively. To discuss this case we must introduce two terms of the ψ type into the right-hand side of (1) and this leads to (14) in which now

$$a_{xy}=\omega_0 V(P_{0x}^{(2)}P_{0y}^{(2)*}+P_{0x}^{(3)}P_{0y}^{(3)*}).$$

As a result we now have

$$a=\omega_0 V|\boldsymbol{P}_0^{(2)}|^2\begin{vmatrix} 0 & 0 & 0 \\ 0 & 1 & 0 \\ 0 & 0 & 1 \end{vmatrix}$$

$$B=\begin{vmatrix} 0 & 0 & 0 \\ 0 & b & 0 \\ 0 & 0 & b \end{vmatrix} \qquad \epsilon'_{yy}=\epsilon'_{zz}\equiv\epsilon'. \tag{52}$$

We shall discuss a wave whose $\boldsymbol{s}$ lies in the yz-plane. Equation (44) assumes the form

$$(n^2-\epsilon'_{xx})\left(n^2-\epsilon'-\frac{b}{n^2-\mu}\right)=0. \tag{53}$$

Now (42) has three solutions:

$$\mathscr{E}_y=\mathscr{E}_z=0 \quad \mathscr{E}_x\neq 0 \quad n=\sqrt{(\epsilon'_{xx})} \tag{54}$$

$$\mathscr{E}=\begin{cases} \mathscr{E}_+ & n_+^2=\frac{1}{2}(\mu+\epsilon')+\sqrt{[\frac{1}{4}(\mu-\epsilon')^2+b]} \quad (55) \\ \mathscr{E}_- & n_-^2=\frac{1}{2}(\mu+\epsilon')-\sqrt{[\frac{1}{4}(\mu-\epsilon')^2+b]} \quad (56) \end{cases}$$

where $\mathscr{E}_+$ and $\mathscr{E}_-$ coincide in direction and should lie in the yz-plane and be perpendicular to $\boldsymbol{s}$. If the crystal surface is perpendicular to $\boldsymbol{s}$ then its equation is $(\boldsymbol{s}_1\boldsymbol{r})=0$. To satisfy the boundary condition $\boldsymbol{P}_1=0$ at this surface we form a linear combination of (55) and (56):

$$\mathscr{E}(\boldsymbol{r},t)=\mathscr{E}_+\{\exp[i(\omega/c)n_+(\boldsymbol{s},\boldsymbol{r})]- -q\exp[i(\omega/c)n_-(\boldsymbol{s},\boldsymbol{r})]\}\exp(-i\omega t). \tag{57}$$

The properties of the above wave are completely analogous to those of a wave given by (50).

One can now discuss a wave for which $\boldsymbol{s}$ is

directed along the x-axis. Equation (44) now has the form:

$$\left(n^2-\epsilon'-\frac{b}{n^2-\mu}\right)^2=0. \tag{58}$$

The solution of (42) is

$$\begin{aligned}\mathscr{E}(x,t)=\mathscr{E}_+\{&\exp[i(\omega/c)n_+x]-\\&-q\exp[i(\omega/c)n_-x]\}\exp(-i\omega t)\end{aligned} \tag{59}$$

if the crystal surface is the plane $x=0$. Here $\mathscr{E}_+$ is an arbitrary vector which lies in the yz-plane, n_+ and n_- have the same meanings as in (55), (56).

One can also look into the case when $\boldsymbol{s}$ has any direction in space. Then (44) is a general equation of the fourth degree in n^2. It can be solved if numerical values of $\boldsymbol{s}$ are given.

Cubic crystals

For these crystals the matrix element $\boldsymbol{P}_0$ is non-zero only for transitions to triply degenerate exciton bands. Vectors $\boldsymbol{P}_0$, all equal but directed along the axes x, y and z, correspond to three such bands. We shall denote these vectors by $\boldsymbol{P}_0^{(1)}$, $\boldsymbol{P}_0^{(2)}$ and $\boldsymbol{P}_0^{(3)}$. Introducing into the right-hand side of (1) three terms of the ψ type, which correspond to three degenerate bands, we obtain equation (14) in which, however, we put

$$a_{xy}=\omega_0 V\sum_{i=1}^{3}P_{0x}^{(i)}P_{0y}^{(i)*}.$$

Taking into account the directions of $\boldsymbol{P}_0^{(i)}$ we now obtain

$$a=\omega_0 V|\boldsymbol{P}_0^{(1)}|^2\begin{vmatrix}1&0&0\\0&1&0\\0&0&1\end{vmatrix}$$

$$B=b\begin{vmatrix}1&0&0\\0&1&0\\0&0&1\end{vmatrix}\qquad \epsilon'_{xx}=\epsilon'_{yy}=\epsilon'_{zz}\equiv\epsilon' \tag{60}$$

Thus the tensors B and ϵ' can be simply replaced by numbers b and ϵ'. Then for any direction of $\boldsymbol{s}$ (44) has the form given in (58) and consequently n_+ and n_- are given by (55) and (56).

The solution of the (42) system of equations is now

$$\begin{aligned}\mathscr{E}(\boldsymbol{r},t)=\{&\mathscr{E}_+\exp[i(\omega/c)n_+(\boldsymbol{s},\boldsymbol{r})]+\\&+\mathscr{E}_-\exp[i(\omega/c)n_-(\boldsymbol{s},\boldsymbol{r})]\}\exp(-i\omega t)\end{aligned} \tag{61}$$

where $\mathscr{E}_+$ and $\mathscr{E}_-$ should be at right angles to $\boldsymbol{s}$ but otherwise arbitrary: equation (61) contains now four linearly independent waves. All of them are solutions of a new type. If the crystal surface is perpendicular to $\boldsymbol{s}$ and coincides with the plane $(\boldsymbol{s},\boldsymbol{r})=0$ then the boundary condition $\boldsymbol{P}_1=0$ gives the connection between $\mathscr{E}_+$ and $\mathscr{E}_-$, and (61) becomes

$$\begin{aligned}\mathscr{E}(\boldsymbol{r},t)=\mathscr{E}_+\{&\exp[i(\omega/c)n_+(s,r)]-\\&-q\exp[i(\omega/c)n_-(s,r)]\}\exp(-i\omega t).\end{aligned} \tag{62}$$

Here $\mathscr{E}_+$ is any vector perpendicular to $\boldsymbol{s}$. The coefficient of reflection of light from the crystal surface is given by (51).

If the crystal surface is not perpendicular to $\boldsymbol{s}$ then to satisfy the boundary condition we must construct a linear combination of partial solutions with different $\boldsymbol{s}$. This applies also to rhombic and tetragonal crystals.

Longitudinal waves

All the above-mentioned solutions of Maxwell's equations are obtained on the assumption that in (39) the denominator of the expression for $\boldsymbol{P}_1$ is not equal to zero. There exist, however, plane exponential wave solutions of another type for which $\boldsymbol{n}$ is found by equating this denominator to zero, i.e. from the equation

$$E\left(\frac{\omega n}{c}s\right)=\hbar\omega. \tag{63}$$

In this case $\exp\{i\omega[n/c(\boldsymbol{s},\boldsymbol{r})-t]\}$ is a solution of the second equation in (36) without its right-hand part, i.e. for $a\mathscr{E}_\perp=0$. Then it follows for cubic crystals $\mathscr{E}_\perp=0$ and from (38) that $\mathscr{D}=0$ and the system of equations in (35) is satisfied when also $\mathscr{H}=0$. It remains to satisfy the first equation in (36). The solution of (35), (36) now assumes the form:

$$\mathscr{E}(\boldsymbol{r},t)=\mathscr{E}_0\exp\{i\omega[n/c(\boldsymbol{s},\boldsymbol{r})-t]\}\qquad \mathscr{E}_0\parallel\boldsymbol{s}$$

$$P_1=-\frac{1}{4\pi}\epsilon'\mathscr{E}\quad P_2\approx 0\quad \mathscr{E}_\perp=\mathscr{D}=\mathscr{H}=0. \tag{64}$$

For rhombic and tetragonal crystals there exist also solutions of such type satisfying the equation

(63), but they are longitudinal only if $\boldsymbol{S}$ has selected directions ($\boldsymbol{S}$ may lie along the principle axes of polarization). These waves are then a kind of intrinsic polarization vibrations of the crystal. They represent the macroscopic electric field of a moving exciton; their group velocity is equal to that of the exciton [this can be easily shown from (63)]. Since for these waves in cubic crystals $\mathscr{D} = 0$ but $\mathscr{E} = 0$, their dielectric constant should be zero. A simplest example of such waves are longitudinal optical vibrations of ions in a crystal. It follows from the above theory that similar waves should exist for all types of excitons.

In later work certain generalizations of crystal optics will be given in a more detailed form together with means of experimental detection of the waves of new type.

Acknowledgement—The author wishes to express his gratitude to L. D. LANDAU for very valuable discussions.

REFERENCES

1. FRENKEL Ia. I. *Phys. Rev.* **37,** 17 (1931); **37,** 1276 (1931); PEIERLS R. *Ann. Phys.* **13,** 905 (1932).
2. WANNIER G. *Phys. Rev.* **52,** 191 (1937).
3. MOTT N. F. *Trans. Faraday Soc.* **34,** 500 (1938).
4. TAMM I. E. *Sow. Phys.* **1,** 733 (1932) *Zh. éksp. teor. fiz.* **3,** 34 (1933).
5. BORN M. *Optics* O.N.T.I. (translation into Russian) Kharkov–Kiev (1937).

VOL.
5
1958

J. Phys. Chem. Solids Pergamon Press 1958. Vol. 5. pp. 23–33.

X-RAY-INDUCED COLOR CENTERS IN MgO*

R. W. SOSHEA,† A. J. DEKKER and J. P. STURTZ

Department of Electrical Engineering, Institute of Technology, University of Minnesota, Minneapolis, Minn

(*Received* 1 *July* 1957; *revised version received* 26 *August* 1957)

Abstract—An analysis is presented of the optical absorption spectrum induced in MgO crystals by heat treatment in oxygen; the analysis gives Gaussian bands near quantum energies of 5·7, 4·8 and 4·3 eV for the region investigated, which extends to 6 eV. A similar analysis of the absorption spectrum induced by X-irradiation at room temperature gives Gaussian bands near 5·7, 4·8, 4·3 and 2·3 eV, plus absorption in the region below 4 eV. Results concerning the growth and thermal decay of the optical absorption induced by X-irradiation at room temperature and at 600°C are presented. A study has also been made of the spectrum induced by X-irradiation of crystals previously colored by heat treatment in oxygen. The results are discussed in terms of a model which assumes the presence of ions of variable valence.

1. INTRODUCTION

ABOUT five years ago a study was initiated in this laboratory of the mechanism of secondary emission of single crystals and thin films of magnesium oxide. This program has gradually grown out into a broader investigation of the physical properties of MgO and presently incorporates studies of: (1) secondary emission, (2) photoemission, (3) photoconductivity, (4) color centers associated with specific impurities and with a stoichiometric excess of oxygen and magnesium, and (5) color centers resulting from X-irradiation. The present paper is confined to a discussion of the X-ray-induced color centers. A number of results obtained in the secondary-emission studies have been published previously.[1–3] The studies mentioned under (3) and (4) will be discussed by W. T. PERIA and B. V. HAXBY, respectively, in forthcoming papers. Since the studies (3), (4) and (5) are closely related, it will be necessary to refer to some of the as yet unpublished results obtained by PERIA and HAXBY. It may be mentioned here that parallel investigations on the color centers by means of electron spin resonance have been carried out by J. E. WERTZ[4] in the School of Chemistry at the University o Minnesota.

2. EXPERIMENTAL PROCEDURE

The MgO crystals were obtained from the Norton Company; only those were used which were clearly transparent in the visible region when received. Typical figures for the impurity percentages by weight are: 0·2 Ca, 0·1 Si, 0·1 Al, 0·02 Fe, 0·02 alkali metals, 0·003 Mn and 0·001 Cr. The calcium, because of its chemical similarity to magnesium, is not expected to affect appreciably the optical properties of the crystals. We believe, for reasons to be given below, that the elements which affect the optical properties most strongly are those which can occur in various valence states, such as the transition elements iron, manganese, chromium, and cobalt.

The Norton crystals as received show optical absorption bands near 5·7 and 4·3 eV; these bands are typical of crystals containing excess oxygen and can be made to disappear by firing the crystals in vacuum at 1400°C for 1 hr or more and quenching (1 hr is sufficient for crystals 0·5 mm thick). The optical density after vacuum annealing is essentially flat up to 4 eV, and thereafter increases monotonically with increasing quantum energy; in the former region, the optical density is due mostly to reflection, whereas for quantum

* Supported by the Electronic Components Laboratory of the Wright Air Development Center.

† Recipient of an RCA Predoctoral Fellowship in Electronics, 1955–56, administered by the National Academy of Sciences—National Research Council.

energies above 4 eV there is some absorption. Unless stated otherwise, the crystal plates used in these experiments were all cleaved from one large crystal, and had received identical heat treatment (2 hr at 1400°C under a pressure of 10^{-4} mm Hg).

The optical density of the crystals was measured in the range 1–6 eV with a Beckman Model DU quartz spectrophotometer; all absorption measurements discussed in this paper were made at room temperature. Also, it has been assumed throughout this paper that the reflection coefficient of the crystals does not change with treatment; consequently, the change in optical density is proportional to the change in absorption coefficient. The crystals were irradiated with X-rays from a tube operating at 50 kV and 15 mA, unless stated otherwise. The tube has a tungsten target and beryllium window. Since visible light bleaches the induced color centers, the crystals were wrapped in aluminum foil during X-irradiation to keep out the light from the tube filament, and exposure to room light during handling was kept at a minimum. The effect

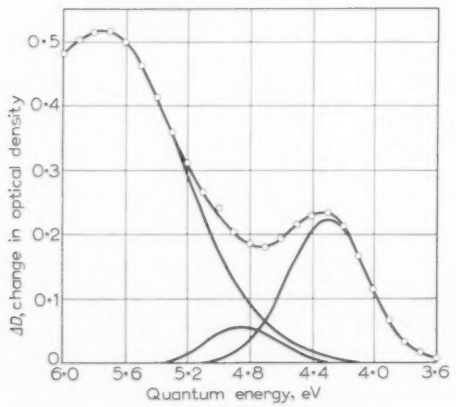

FIG. 1. The increase in optical density as function of quantum energy for an MgO crystal heated in oxygen at a pressure of 1·5 cm at 1250°C; the spectrum has been resolved into three bands of Gaussian shape.

of a small non-uniformity in color-center density resulting from the attenuation of the X-rays as they pass through the crystal was minimized by irradiating the crystals on one side during the first half of any irradiation period and on the other side for the second half.

3. ANALYSIS OF ABSORPTION SPECTRA INDUCED BY EXCESS OXYGEN AND X-IRRADIATION

The increase in optical density of an MgO crystal when heated in oxygen under a pressure of 1·5 cm at 1250°C for 11 min is shown in Fig. 1. This spectrum has been resolved into absorption bands centered near 5·7, 4·8 and 4·3 eV, which are Gaussian in shape, i.e. the induced optical density ΔD as function of the quantum energy E may be written as

$$\Delta D(E) = \sum_i \Delta D_{0i} \exp[-k_i(E-E_{0i})^2] \qquad (1)$$

Here ΔD_{0i}, k_i, and E_{0i} are constants characterizing an individual band. The analysis of the spectrum into these bands will now be discussed.*

It is assumed that all of the absorption near the peak at 5.75 eV is due to the band centered at that energy. The change in optical density in the interval between 5·75 and 5·3 eV is plotted in Fig. 2, curve A, in such a way that the data should fit a straight line if the band has a Gaussian shape; this is evidently the case. From the values of the optical density obtained from the extrapolated line, the 5·7 eV band is drawn in Fig. 1. Next, assuming that the absorption at energies less than 4·3 eV is due only to the 5·7 and 4·3 eV bands, the low-energy side of the 4·3 eV band can be drawn. Taking 4·30 eV as the center of the band, curve B in Fig. 2 was obtained. It is observed that this curve is also in agreement with a band of Gaussian shape. Finally, when the 4·3 and 5·7 eV bands are subtracted from the measured curve, one is left with a symmetrical band of Gaussian shape centered about 4·85 eV. Although the 4·8 eV band in the excess-oxygen spectrum is relatively small, it has been found in all excess-oxygen crystals studied. Thus, the bands near 5·7, 4·8, and 4·3 eV will be referred to as "excess-oxygen bands".

The absorption spectrum induced by irradiation with X-rays at room temperature for a period of 8 hr is shown in Fig. 3, analyzed into the excess-oxygen bands and a Gaussian band near 2·3 eV. The absorption near 3·6 eV represents what is left of

* For convenience we shall refer frequently to the "5·7, 4·8, and 4·3 eV bands", even though the exact position of the peaks may differ somewhat from these numbers. Measurements by P. D. JOHNSON of the General Electric Research Laboratory, Schenectady, on crystals treated in vacuum and in oxygen by R. G. LYE in our laboratory, show the existence of two more excess oxygen bands at 6·2 and near 6·7 eV. We are much indebted to Dr. JOHNSON for carrying out these measurements and providing us with the results.

VOL. 5 195

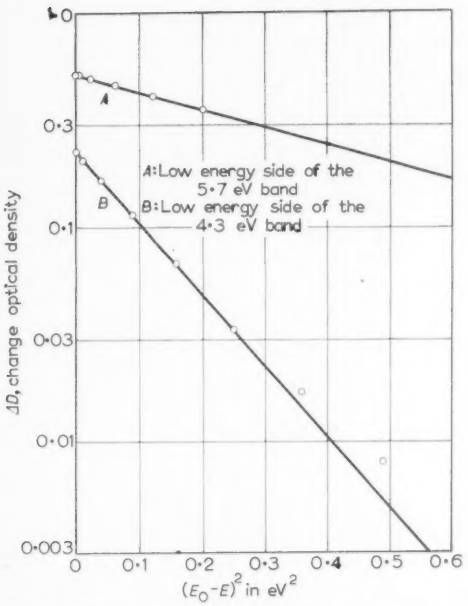

FIG. 2. Curve A represents the increase in optical density for the low-energy side of the 5·75 eV band (see Fig. 1); curve B refers to the low-energy side of the 4·30-eV band (see Fig. 1).

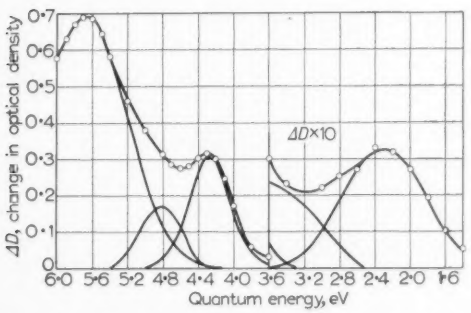

FIG. 3. Increase in optical absorption of an MgO crystal resulting from irradiation with X-rays at room temperature; the analysis shows Gaussian bands near 5·7, 4·8, 4·3 and 2·3 eV plus some absorption near 3·6 eV.

the spectrum after the 5·7, 4·8, 4·3 and 2·3 eV bands have been subtracted. The details of the analysis will be omitted here, since the procedure was similar to that described above for the excess-oxygen bands. The absorption near 3·6 eV cannot be described by a Gaussian band. When this X-rayed crystal was heated for 200 min at 100°C, the 2·3 and 3·6 eV bands decayed to about one-quarter of their initial heights; also the 5·7 eV band became more narrow and the peak shifted to 5·6 eV. The spectrum of the crystal after further heat treatment at temperatures up to 325°C is shown in Fig. 4, in which the decreased width and the shift of the 5·7 eV band are apparent.

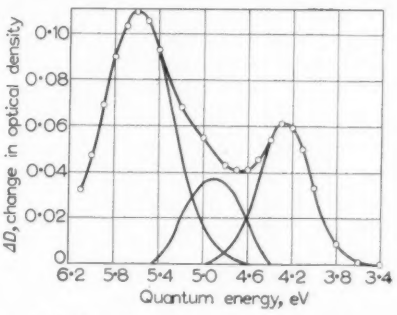

FIG. 4. Induced optical absorption spectrum resulting from X-irradiation at room temperature and subsequent bleaching at 325°C. The optical absorption spectrum induced by X-irradiation at 600°C is essentially the same as the one presented here.

The absorption spectrum induced by X-irradiation of crystals at 600°C was also measured. It was observed that the heating itself produced a Gaussian-shaped band of half-width 0·88 eV centered at 5·64 eV. The increase in the absorption coefficient, ΔK, as a function of the time of heating was independent of the thickness of the crystals and reached half its saturation value ($\Delta K_{sat} = 0{\cdot}35$ mm^{-1}) in 6 hr. This indicates that the band is not due to diffusion from or to the surface, a conclusion which was confirmed by the observation that an experiment carried out in vacuum (10^{-6} mm Hg) produced essentially the same result as the one carried out in air. The formation of this band is presumably due to electron transfer within the crystal. Thus, the absorption spectrum induced by X-irradiation at 600°C was obtained by first heating the crystals in air at 600°C for a period sufficient to saturate the 5·64 eV band. The X-ray-induced spectrum so obtained is essentially the same as that shown in Fig. 4. Note that there is very little absorption at quantum energies below 3·6 eV.

A summary of the half-widths and relative peak heights of the excess oxygen bands, as well as of the exact position of the peak of the 5·7 eV band,

is given in Table 1. It is observed that the relative height of 4·8 eV band is considerably larger in the X-irradiated crystals than in the excess-oxygen crystals. It is also noted that the change during thermal decay in width and relative height of the 5·7 eV band in the crystals irradiated with X-rays at room temperature is large compared to that of the other bands. These features, combined with the shift in the position of the peak of the 5·7 eV band upon bleaching may indicate that this band actually consists of two bands, one centered near 5·75 eV and the other near 5·6 eV, the former decaying more rapidly than the latter. The production of a single band at 5·64 eV by heating, mentioned above, may support this idea. The possibility cannot be ruled out, however, that the change in width and height of the 5·7 eV band is due to changes in the characteristics of bands centered at quantum energies beyond 6 eV.

The excess-oxygen spectrum shown in Fig. 1 and the X-ray-induced spectrum shown in Fig. 3 are essentially the same as those presented by WEBER, but the identification of the 4·8 eV band given here is different from that given by WEBER.[5] In fact, WEBER was unaware of the existence of the 4·8 eV band in the excess-oxygen spectrum, but believed it to be present in the absorption spectrum of crystals containing excess magnesium. Thus, he considered the 4·8 eV band observed in the X-ray induced spectrum as an excess-magnesium band rather than as an excess-oxygen band. Also, WEBER obtained the 4·8 eV band in the X-irradiated crystals by subtracting a scaled excess-oxygen spectrum from the X-ray-induced spectrum. Since the above analysis shows that the excess-oxygen spectrum itself contains a 4·8 eV band, it follows that WEBER must have deduced a 4·8 eV band in the X-irradiated crystals which was too small.

The following two experiments carried out by PERIA seem to provide a clue as to why WEBER was led to associate the 4·8 eV band with an excess of magnesium:

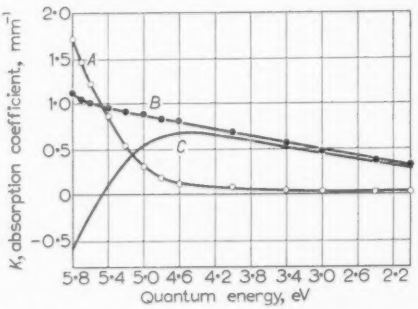

FIG. 5. Curve *A* represents the absorption spectrum of a vacuum-annealed crystal; curve *B* gives the spectrum after heating in a magnesium pressure of 2 atm for 3 hr at 1115°C. Curve *C* represents the difference between *B* and *A*.

Table 1. Comparison of the bands common to X-irradiated and excess-oxygen crystals

Crystal	Treatment	Position of peak of 5·7 eV band (eV)	Peak height relative to 4·3 eV band			Half-width* (eV)		
			5·7 eV	4·8 eV	4·3 eV	5·7 eV	4·8 eV	4·3 eV
A	Excess oxygen	5·75	2·31	0·25	1·00	1·32	0·55	0·60
B	X-rayed to saturation at room temperature	5·70	2·27	0·55	1·00	1·10	0·55	0·55
C	Crystal B bleached at 100°C	5·61	1·91	0·48	1·00	0·90	0·55	0·56
D	Crystal C bleached at 325°C	5·60	1·79	0·61	1·00	0·74	0·62	0·56
E	X-rayed to saturation at 600°C	5·62	1·88	0·40	1·00	0·88	0·56	0·59

* Half-width is defined as total width at half peak height.

(1) A crystal, about 0·7 mm thick, was heated for 3 hr in magnesium vapor at 1115°C, the magnesium pressure being approximately 2 atm. The absorption spectra before and after heating in Mg vapor are shown as curves *A* and *B*, respectively, in Fig. 5. Note that for high quantum energies the absorption after coloration with magnesium is less than before coloration with magnesium; this has been observed in a number of other similar experiments as well.

(2) A vacuum-annealed crystal was heated for 4 hr at 1115°C in about 2 atm of magnesium vapor. The absorption induced by this treatment is shown by curve *A* of Fig. 6. A further similar treatment of 5 hr was carried out. Curve *B* in Fig. 6 shows the absorption induced by the second treatment only. Note the difference between the two curves at the higher quantum energies.

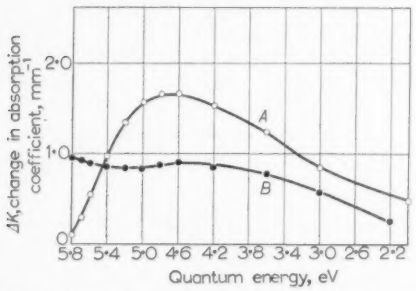

FIG. 6. Curve *A* represents the *change* in absorption due to heating an MgO crystal in a magnesium pressure of 2 atm for 4 hr at 1115°C. Curve *B* shows the *increase* in absorption resulting from further similar heat treatment for 5 hr.

Both experiments point to the fact that during the initial stages of coloration in magnesium vapor, the background absorption decreases.* This background decrease produces the apparent band at 4·8 eV in Fig. 6, curve *A*. Consequently, a spectrum representing the color centers associated with excess magnesium cannot be obtained by merely taking the difference between the absorptions before and after coloration. It is believed, however, that curve *B* in Fig. 6 represents the absorption spectrum characteristic of excess magnesium in MgO. Thus, we conclude that there is more absorption in the excess-magnesium crystals in the energy range between 4·8 and 5·8 eV than can be accounted for by the bands given by WEBER.

4. THE GROWTH OF THE OPTICAL ABSORPTION BANDS DURING X-IRRADIATION

The concentration of color centers resulting from X-irradiation at room temperature can be brought to saturation in a few hours under the irradiation conditions stated in Section 2. The growth of absorption at 5·7 and 2·3 eV is shown in Fig. 7, normalized for easier comparison. The absorption at 4·8 and 4·3 eV was proportional to that at 5·7 eV. The growth of the induced optical density at 2·3 eV follows quite accurately the expression

$$\Delta D(t) = \Delta D_s(1-e^{-t/\tau}) \qquad (2)$$

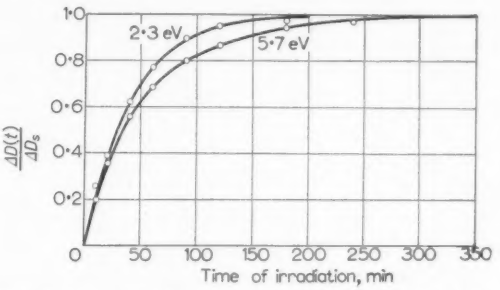

FIG. 7. Normalized representation of the growth of the optical density at 5·7 and 2·3 eV resulting from X-irradiation at room temperature.

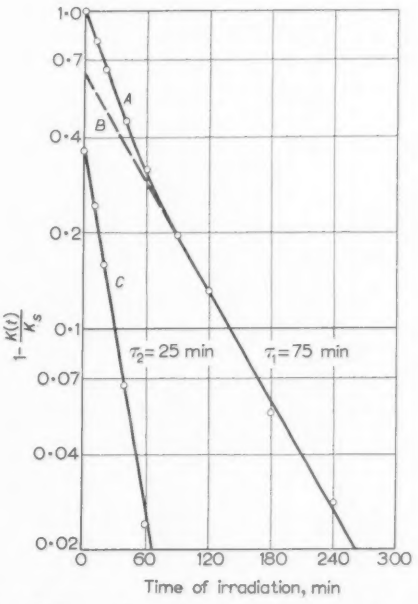

FIG. 8. Curve *A* represents the logarithm of the quantity $(1-K(t)/K_{sat})$ as a function of time for the 5·7 eV band; curve *C* is obtained as the result of subtracting *B* from *A*.

* Evidence in support of this result can be derived from optical-absorption measurements, extending to 7·4 eV, by P. D. JOHNSON of the General Electric Research Laboratory, Schenectady.

where $\tau = 40$ min for a tube current of 15 mA. The time constant τ was found to be inversely proportional to the X-ray intensity for a range of tube currents between 5 and 15 mA.

The data for the growth of the 5·7, 4·8 and 4·3 eV bands are plotted in Fig. 8, curve *A*, in such a manner that an expression such as (2) would appear as a straight line. These data can be fitted very closely to the sum of two exponential expressions, lines *B* and *C* in Fig. 8, i.e.

$$\Delta D(t) = \alpha_1 \Delta D_s(1-e^{-t/\tau_1}) + \alpha_2 \Delta D_s(1-e^{/\tau_2}) \quad (3)$$

where, for a tube current of 15 mA, $\tau_1 = 75$ min and $\tau_2 = 25$ min. Again, within the range of X-ray tube currents between 5 and 15 mA, the time constants were inversely proportional to the current. The constants α_1 and α_2 had approximately the values of 0·65 and 0·35, respectively, and were independent of the tube current in the range specified above. These results are qualitatively in agreement with those obtained by MOLNAR and HARTMAN.[6]

During X-irradiation at 600°C, the optical absorption corresponding to the 5·7 and 4·3 eV bands grows in accordance with a single exponential function with a time constant of 3·5 min for a tube current of 15 mA; saturation at this temperature is thus reached much more rapidly than at room temperature.

5. THERMAL DECAY OF THE X-RAY-INDUCED CENTERS

The color centers produced by X-irradiation at room temperatures suffer considerable thermal decay, even at room temperature. The decay of absorption at 5·7 and 2·3 eV at room temperature is shown in Fig. 9. The decay of the 4·8 and 4·3 eV bands is about the same as that of the 5·7 eV band, and the decay at 3·6 eV seems to follow that at 2·3 eV. Because the absorption in the 3·6 and 2·3 eV bands in a crystal of normal thickness (0·3 mm) is so small, the decay of these bands was studied on thick crystals (7 mm). It appears that the decay curve for the 5·7 eV band reaches a relatively stable residual level, although even after a year no asymptotic value has been reached. Since the bleaching at room temperature proceeds so slowly, the more extensive decay experiments were carried out at elevated temperatures. Thus, each of five sets of crystals (two crystals per set) was irradiated with X-rays for periods of 10, 20, 40, 90 and 300 min to obtain crystals with absorptions approximately 0·2, 0·4, 0·6, 0·8 and 1·0, respectively, of the saturation absorption. The decay at

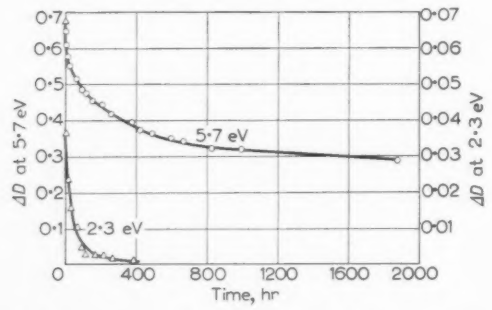

FIG. 9. Decay at room temperature of the absorption induced at 5·7 and 2·3 eV after X-irradiation at room temperature.

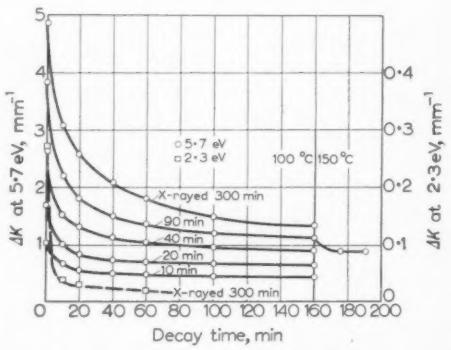

FIG. 10. Thermal decay at 100°C of the absorption induced at 5·7 and 2·3 eV by irradiation with X-rays at room temperature for various periods of time. After 160 min the temperature was raised to 150°C.

100°C of the absorption at 5·7 eV is shown in Fig. 10. The decay of the absorption at 2·3 eV in the crystal X-rayed for 300 min is included for comparison. It is observed that the rate of decay of the 5·7 eV absorption is not determined by the density of color centers alone. Also note that for a given time of irradiation, the absorption decays to a nearly constant value, as it did in Fig. 9 for the decay at room temperature. Subsequent heating to higher temperatures produced similar results. The observations described here are very similar to those of CASLER *et al.*[7] for some of the alkali halides, e.g. LiF and KBr.

The decay at 600°C of the absorption at 5·6 and 4·3 eV for a crystal irradiated with X-rays at 600°C is presented in Fig. 11.

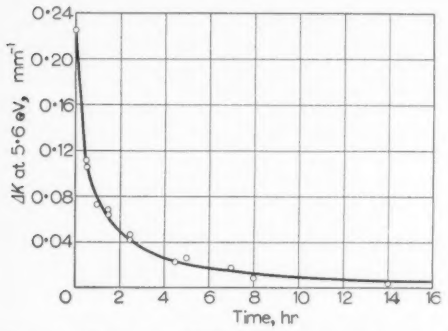

FIG. 11. Decay at 600°C of the absorption at 5·6 and 4·3 eV induced by X-irradiation at 600°C. The curve represents equation (8) with the constants C_1 and C_2 fitted for 1 and 8 hr to the curve through the experimental points.

6. X-IRRADIATION OF EXCESS-OXYGEN CRYSTALS

Since irradiation of vacuum-annealed MgO crystals produces excess-oxygen bands, it seemed of interest to study the effect of X-irradiation on crystals which had previously been colored by heat treatment in oxygen to various degrees of coloration. The crystals used were of the same stock and were given the same initial vacuum-annealing treatment as those used in the experiments previously described. The oxygen treatment consisted of heating the crystals in a quartz vessel at 1250°C for 3·5 hr, which was sufficient to bring all crystals to at least 90 per cent saturation for any particular oxygen pressure. A set of crystals was thus treated in a number of different oxygen pressures ranging between 0·01 and 1000 mm Hg at 1250°C. After the oxygen treatment, the crystals were irradiated with X-rays to saturation. The curves shown in Fig. 12 represent the X-ray-induced optical absorption, i.e. the difference between the spectrum due to the oxygen treatment plus X-irradiation treatment and the spectrum due to the heating in oxygen alone. It is observed that in the quantum range between 1·2 and 4·0 eV the increase in the optical absorption induced by X-irradiation increases as the initial excess-oxygen density is increased, whereas the opposite is true in the range between 4·0 and 6·0 eV. In the

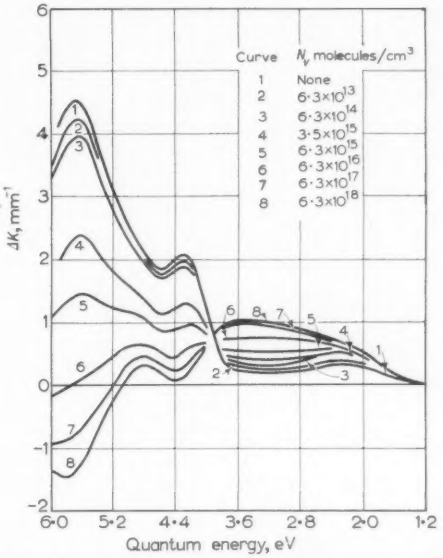

FIG. 12. Optical absorption spectra induced by X-irradiation at room temperature of crystals which had previously been colored to saturation in various densities (N_v) of oxygen at 1250°C.

range from 5·2 to 6·0 eV, the X-irradiation induces a decrease in optical absorption for high oxygen content. Fig. 13 shows that the absorption at 5·7 eV induced by X-irradiation decreases approximately linearly with the amount of excess

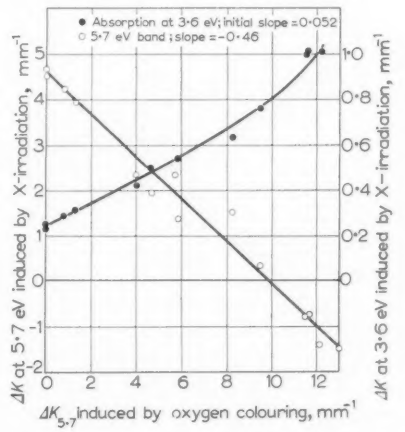
● Absorption at 3·6 eV; initial slope = 0·052
○ 5·7 eV band ; slope = −0·46
ΔK at 5·7 eV induced by X-irradiation, mm⁻¹
ΔK at 3·6 eV induced by X-irradiation, mm⁻¹
$\Delta K_{5\cdot7}$ induced by oxygen colouring, mm⁻¹

FIG. 13. Absorption at 5·7 and 3·6 eV induced by X-irradiation to saturation at room temperature as a function of the initial absorption at 5·7 eV due to heat treatment in oxygen.

oxygen present initially, whereas that corresponding to 3·6 eV increases.

7. DISCUSSION

One is, at first, tempted to interpret the data presented above in analogy with those obtained in similar experiments for the alkali halides. Thus, one would think of the excess-oxygen bands in terms of holes trapped at vacancies. Similarly, one would think of *F* and *V* centers being produced by X-irradiation. However, for the presently available MgO crystals, an interpretation on this basis leads immediately to difficulties. For example, according to WEBER[5] the saturation density of color centers obtained by heating MgO crystals in oxygen at a given elevated temperature (~ 1200°C) is proportional to the logarithm of the oxygen pressure over a range covering some five decades. Similar results have been obtained in our laboratory. For pure MgO one would expect from the law of mass action that the saturation color-center density would vary with some power of the pressure which is a rational fraction. The logarithmic variation seems to indicate that the crystals contain a certain concentration of impurities which limits the amount of oxygen that can be incorporated. In other words, the thermodynamic equilibrium of these crystals in an oxygen atmosphere cannot be discussed in analogy with, say KBr in bromine vapor. In fact, HAXBY, in our laboratory, has shown that the saturation value of the height of the excess-oxygen absorption bands in crystals intentionally doped with iron increases linearly with increasing iron content. This indicates that iron, which in the vacuum-annealed crystals may be present as Fe^{2+}, may be oxidized to Fe^{3+} during the heat treatment in oxygen. This has been confirmed by electron-spin-resonance experiments carried out on our crystals by WERTZ*; the Fe^{3+} concentration was found to increase upon heat treatment in oxygen and also upon irradiation with X-rays. WERTZ also observed an increase in the concentration of Cr^{3+} and V^{3+} ions upon heating in oxygen. Although the details of the experimental evidence will be discussed in another paper by HAXBY, it will be assumed here that the excess-oxygen bands are in some way related to the presence of transition elements in a higher valence state; for convenience the discussion will be given in terms of iron ions. It may be remarked here that there are two reasons for the greater emphasis on impurities in the interpretation of the MgO data when compared with those for the alkali halides. First, the MgO crystals are undoubtedly less pure than the alkali halide crystals which may be obtained from Harshaw. Second, the binding energies in MgO are roughly four times as high as in the alkali halides, so that for the pure crystals the density of color centers induced by heat treatment of MgO at about 1200°C in one of its constituents may be expected to be considerably smaller than for a similar experiment on the alkali halides carried out at, say, 600°C.

In order to set up an energy-level diagram suitable as a basis for discussion, a few more experimental results must be mentioned. The forbidden gap between the valence and conduction bands in MgO is approximately 10·5 eV, according to reflection measurements by NELSON.[8] It is furthermore important to point out that the 5·7, 4·8, and 4·3 eV bands do not exhibit photoconductivity at room temperature; the details of this subject will be discussed in a forthcoming paper by PERIA. The photoconductivity spectrum shows, however, one peak at 5·0 eV, and PERIA has been able to show that carriers resulting from the 5·0 eV irradiation are electrons. (Another peak at 4·0 eV leads to hole conduction.) For our purpose it is of importance to note that, according to PERIA, prolonged irradiation in the 5·0 eV band leads to the excess-oxygen absorption bands. These results lead to the postulate, in terms of the "iron-model", that irradiation with 5·0 eV quanta removes an electron from an Fe^{2+} ion, the resulting Fe^{3+} ion and its immediate surroundings exhibiting the excess-oxygen bands. The schematic energy-level diagram of Fig. 14 will therefore be adopted for a crystal annealed in vacuum.

Evidence for the electron traps *E* in Fig. 14 has been obtained from the photoconductivity data of PERIA, as well as from the spin-resonance results obtained by WERTZ. According to WERTZ, chromium occurs in MgO usually in the form of Cr^{3+} ions. Upon irradiation with X-rays, the Cr^{3+} concentration is found to decrease, presumably as a result of electron trapping; during thermal decay the Cr^{3+} concentration increases again. It thus seems that Cr^{3+} ions are responsible for a fraction

* Private communication.

VOL. 5 1958

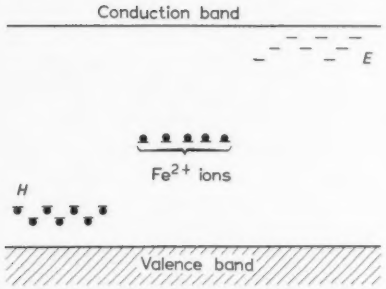

FIG. 14. Schematic energy-level diagrams for vacuum-annealed MgO. The levels E and H are, respectively, electron and hole traps. The dots indicate electrons which can be removed, e.g. by trapping of a hole.

of the E levels in Fig. 14. The existence of hole traps, indicated by H in Fig. 14, will be assumed.

The model of Fig. 14 will now be used as a basis for discussion of various aspects of the experimental results.

(a) *Effect of X-irradiation on vacuum-annealed and oxygen-colored crystals*

Irradiation with X-rays presumably produces equal numbers of trapped electrons and holes. Thus, after irradiation at room temperature of a vacuum-annealed crystal, a fraction of the Fe^{2+} ions has been transformed into Fe^{3+} ions as a result of hole trapping; the Fe^{3+} ions account for the excess-oxygen bands in the absorption spectrum. Also, according to this model, some of the free holes produced by the X-rays will have been trapped by levels H, as indicated in Fig. 15, thereby contributing to the absorption below 4 eV. The electrons trapped in levels E of Fig. 15 are presumably responsible for the remainder of the absorption below 4 eV. When the X-irradiation takes place at 600°C, the majority of the H and E levels are apparently too shallow to keep the carriers trapped, since the optical absorption below 4 eV is then found to be very small. On the other hand, the deeper E levels must have trapped a number of electrons at least equal to the number of Fe^{3+} ions. This indicates that the electron trap depths are distributed over a rather wide energy range.

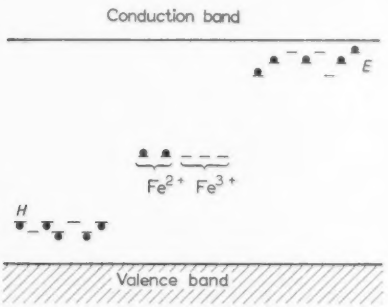

FIG. 15. Schematic representation of the crystal in Fig. 14 after X-irradiation.

For crystals which have been heated in oxygen prior to the X-irradiation, the situation is somewhat different, since these crystals contain initially an appreciable number of Fe^{3+} ions. Consequently, one expects that after X-irradiation the ratio of holes (produced by the X-rays) trapped by H levels to those trapped by Fe^{2+} ions will be larger than that for the vacuum-annealed crystals. This explains the increase in optical absorption induced below 4 eV with increasing initial Fe^{3+} content. At the same time, the probability for free electrons to be trapped by Fe^{3+} ions increases because the latter are present in larger numbers. In fact, if the initial Fe^{3+} concentration is large enough, i.e. comparable to the density of E levels, one may expect a reduction of the number of Fe^{3+} ions after X-irradiation. The fact that this is indeed observed indicates that the density of E levels is of the same order of magnitude as the density of Fe^{3+} ions initially present. This conclusion is in agreement with a conclusion drawn by PERIA from the photoconductivity data. The model presented here thus accounts qualitatively for the data of Fig. 12.

(b) *Growth and decay curves*

No attempt will be made here to interpret the details of the growth curves of the X-ray-induced optical absorption, because even for relatively simple models the problem cannot be solved exactly. It may be pointed out, however, that for the range of X-ray tube currents employed in these studies, the saturation value of the induced absorption is independent of the intensity of the beam, whereas the time constants are inversely proportional to the intensity. Thus, if n represents the density of a particular type of center, the growth curves follow a differential equation of the type

$$dn/dt = \alpha I - \beta I n = \beta I\left(\frac{\alpha}{\beta} - n\right) \qquad (4)$$

with the solution

$$n(t) = (\alpha/\beta)[1-\exp(-\beta It)]. \quad (5)$$

Here, I is the X-ray intensity, and α and β are constants. In one possible model, the term $\beta In = n/\tau$ describes the rate of destruction of centers resulting from the X-irradiation, whereas the term αI represents the rate of formation of the centers. This behaviour would result, for example, if the densities of free holes and of free electrons during irradiation were proportional to the beam intensity; if the centers were produced by trapping of holes, the rate of formation of such centers would be proportional to the density of free holes and the rate of destruction would be proportional to the density of free electrons (for a given degree of occupation of the centers, of course).

With regard to the thermal decay of the optical absorption after X-irradiation, it should be emphasized that the model of Fig. 15 allows for the possibility of decay of absorption below 4 eV without necessarily involving decay of the excess-oxygen bands. Thus, thermally released holes trapped at H levels may recombine with electrons trapped at E levels. For the excess-oxygen bands to decay, it is necessary that electrons trapped in E levels be released thermally, whereupon they can recombine with Fe^{3+} ions. The model used here can account for the residual levels of the optical absorption found after prolonged decay at a given temperature. Thus, after heating at a certain temperature, all levels E above a certain depth below the conduction band will have been emptied, and the occupied ones below have a considerable life time. When the temperature is suddenly raised, a new set of occupied E levels will be emptied, and a corresponding reduction in the excess oxygen absorption will be observed (see Fig. 10). It should be mentioned that this interpretation differs from that given by OBERLY[7] for similar results obtained with some of the alkali halide crystals. This author suggests the existence of centers which have the same optical activation energy but different thermal activation energies ("soft" and "hard" centers). This suggestion is based on the assumption that decay of color centers is a result of thermal activation of carriers in the centers themselves. In the interpretation given in the present paper, however, the decay of the excess-oxygen bands is a result of thermal excitation of carriers in traps of varying depths, and the assumption of "soft" and "hard" centers with the same optical excitation energy becomes unnecessary.

Because of the energy distribution of the trapping levels E, the theory of the decay is in general complicated. However, the decay at 600°C of the 5·7, 4·8 and 4·3 eV bands induced by X-irradiation at 600°C of vacuum-annealed crystals can be interpreted if we assume that at this temperature only the deepest of the E levels are occupied by electrons. Let N be the total number of these deep traps and let $n(t)$ of them be occupied by electrons. Also, let there be $n(t)$ Fe^{3+} ions, which implies the assumption that there are no holes in the H levels at this temperature. The probability for an electron, thermally released from an E level, to be trapped by an Fe^{3+} ion will be denoted by p; the probability for this electron to return to an E level is then 1-p, where

$$p = \frac{\alpha n}{\alpha n+\beta(N-n)}. \quad (6)$$

Here, α is the cross-section for trapping of an electron by an Fe^{3+} ion and β the same quantity for an E level. The decay is then determined by

$$dn/dt = \gamma pn \quad (7)$$

where γ is a proportionality constant depending on temperature. The solution of the equation obtained by substituting (6) into (7) may be written as

$$t = C_1 \log[n/n(0)]+(C_2/n)[1-n/n(0)] \quad (8)$$

where $C_1 = (\beta-\alpha)/\gamma\alpha$ and $C_2 = \beta N/\gamma\alpha$. Fig. 11 shows the function (8) fitted to the experimental data at the points $t = 1$ hr and $t = 8$ hr, assuming that the absorption at 5·7 and 4·3 eV is proportional to the number of Fe^{3+} ions $n(t)$; the agreement is quite good. It may be mentioned here that formula (8) was also in agreement with the decay of crystals irradiated at 600°C for periods which produced only a fraction of the saturation coloration.

In conclusion, one can say that a model of the energy-level diagram based on the presence of ions with variable valence is consistent with the results presented above. Perhaps some of the properties of color centers in alkali halides, e.g.

thermal decay of the X-ray-induced color centers, can also best be explained in terms of a distribution of trapping levels.

REFERENCES

1. Dekker A. J. *Phys. Rev.* **94,** 1179 (1954); *Physica* **21,** 29 (1954); **22,** 361 (1956).
2. Lye R. G. *Phys. Rev.* **99,** 1647 (1955).
3. Lye R. G. and Dekker A. J. *Phys. Rev.* **107,** 977 (1957).
4. Wertz J. E. and Auzins P. *Phys. Rev.* **106,** 484 (1957).
5. Weber H. *Z. Phys.* **130,** 392 (1951).
6. Molnar J. P. and Hartman C. D. *Phys. Rev.* **79,** 1015 (1950).
7. Oberly J. J. *Phys. Rev.* **83,** 228 (1951); **84,** 1257 (1951).
8. Nelson J. R. *Phys. Rev.* **99,** 1902 (1955).

OL.
5
958

J. Phys. Chem. Solids Pergamon Press 1958. Vol. 5. pp. 34–43.

ON ELECTRONIC CURRENT IN NiO*

JIRO YAMASHITA† and TATUMI KUROSAWA

Radiation Laboratory, University of Pittsburgh, Pittsburgh, Pennsylvania
The Institute of Science and Technology, University of Tokyo, Tokyo, Japan

(*Received* 29 *May* 1957; *revised* 30 *September* 1957)

Abstract—Conduction by the movement of an extra electron which is tightly bound to an ion in an ionic lattice is discussed. We assume that the wave function of the electron is localized closely around an ion and the motion of the electron is so slow that lattice polarization is induced around the electron. In this case the conduction mechanism may not be explained by the usual band theory, but it may be better to use a HEITLER–LONDON picture and to interpret the current as a result of wandering of the electron from ion to ion. We use this conduction mechanism to explain the electronic current which appears in NiO and $LaMnO_3$ crystals.

VOL.
5
195

1. INTRODUCTION

THE mechanism of electrical conduction in nickel oxide has been the subject of a good deal of theoretical speculation. From the standpoint of the simple energy-band theory it should be a good conductor, since the $(3d)^8$ configuration of the Ni^{++} ions should in the solid result in partially filled bands, even when one takes into account the probable splitting of the d levels in the cubic environment of the metal ions. In fact it seems well established experimentally that pure NiO has a very high electrical resistance when sufficient care is taken to obtain crystals of exact stoichiometric composition.[1] The available evidence suggests that the electrical conductivity is associated with the presence of Ni^{3+} ions in the lattice.[2] This idea is the basis of the so-called valence control treatment due to VERWEY.[3] In this method alloying of Li_2O with NiO in a homogenous solid solution leads to semiconducting material with a remarkable range of conductivity depending on lithium content, varying between 10^{-12} and 10 $\Omega^{-1}cm^{-1}$ at room temperature. The temperature coefficient of conductivity is also strongly dependent on lithium concentration. Thermoelectric measurements indicate that the carriers in these alloys are positive holes. A number of other crystals exhibit similar conduction properties. Several examples are listed in a paper by HEIKES,[3] an interesting case being that of $LaMnO_3$.[4]

The interpretation of the sensitivity of conduction to alloying and stoichiometry is as follows.[5] If some of the Ni^{++} ions are replaced by Li^+ ions, or are removed altogether to form vacancies, so that the crystal thus contains an excess of oxygen, then some of the remaining Ni^{++} ions must lose an electron (or capture a hole) to preserve the electrical neutrality of the crystal as a whole. The holes or Ni^{3+} ions are not, however, bound to definite positions in the lattice, but may wander through the crystal by jumping from ion to ion. This possibility of random wandering gives rise to electrical conduction. A quantitative theory of this type of conduction applicable to $LaMnO_3$ has been given by ZENER on the basis of the HEITLER–LONDON approximation.[4] This theory has been used qualitatively by HEIKES[3] to explain a correlation on ferrimagnetic materials between the spin arrangement in the lattice and the conduction properties.

A systematic study of the electrical properties of NiO and of the system NiO–Li_2O has been carried out by MORIN.[1] He measured both the Seebeck effect and the conductivity and used the data to

* This research was in part supported by the United States Air Force through the Air Force Office of Scientific Research of the Air Research and Development Command under Contract No. 18(600)-892.

† On leave from the Institute of Science and Technology, University of Tokyo, Tokyo, Japan.

Table 1. *Concentration of conduction holes* (n/cm^3) *and mobility of conduction holes* (μ : cm^2/V sec) *according to* MORIN's *analysis*

	No. 1		No. 2		No. 6	
T	n	μ	n	μ	n	μ
300					$1{\cdot}5\times10^{21}$	4×10^{-3}
500	5×10^{14}	$6{\cdot}1\times10^{-3}$	$1{\cdot}3\times10^{17}$	4×10^{-4}	5×10^{21}	2×10^{-2}
1000	1×10^{18}	$6{\cdot}4\times10^{-2}$	$2{\cdot}0\times10^{18}$	6×10^{-2}	5×10^{21}	8×10^{-2}

compute by the usual methods of semiconductor theory a carrier density and a carrier mobility. Typical results of MORIN's analysis are shown in Table 1. He found that both the carrier density and the mobility were strong functions of both lithium content and temperature. The dependence of carrier concentration on temperature is usually ascribed to the energy necessary to free a hole from a position of minimum energy near a Li^+ ion or Ni^{++} vacancy. This dissociation energy appears because either defect represents a locus of excess negative charge in the crystal and so attracts a hole. The attraction gives rise to an activation energy which varies with composition because the Coulomb interactions between defects are partially screened by the other carriers and by the statistical distribution of the defects themselves. This mechanism, however, does not explain the strong temperature-dependence and the extremely low values of the apparent mobility, which can also apparently be described in terms of an activation energy for jumping between ions.

An activation energy for jumping cannot be explained in terms of the simple HEITLER–LONDON picture of ZENER, which predicts a mobility which varies only inversely as the first power of the absolute temperature. The much larger temperature-dependence deduced by MORIN, and the sensitivity of mobility to Li^+ content suggest that the jumping of Ni^3 ions must be a thermally activated process. This cannot be explained in terms of any process which involves the motion of electrons alone, because of the small mass of the electrons. Thus we are led to the conclusion that phonons are intimately involved in the jumping process, and it is with the detailed theoretical examination of this problem that the present paper is concerned.

Briefly, the physical model with which we shall be concerned is as follows. The hole, once freed from the Coulomb field of a defect, tends to be self-trapped in the crystal as a result of the polarization of the surrounding lattice. If there is some overlap between hole wave functions localized on neighboring ions, the hole can jump, but in the ionic lattice the polarization associated with the hole must jump with it. This change in polarization, since it involves motion of the heavy ions, can give rise to an activation energy. The jumping process is then accompanied by the emission and absorption of many phonons. Because of this the hole cannot be regarded as possessing a definite momentum, and so the jumping motion has a quite different aspect from the usual motion of an electron in a periodic lattice. Indeed the conduction process bears a close analogy with ordinary ionic conduction in that each successive transition of the Ni^{3+} configuration may be regarded as uncorrelated with the previous one; the effective mean free path is of the order of the lattice constant, so that a description in terms of Bloch waves scattered by phonons is inappropriate.

In the detailed analysis of the jumping process which follows, the relative roles of the period potential and the electron phonon interaction are reversed. In ordinary conductivity theory the periodic potential is considered in zero order, and thus we start with Bloch functions and treat the electron–phonon interaction as a perturbation which produces scattering, i.e. a change in momentum. In the present theory the electron–phonon interaction is considered in zero order (to produce self-trapping), and the periodic lattice potential is treated as a perturbation which gives rise to a wandering of the self-trapped configuration through the crystal.

The theory shows that the ordinary matrix element for jumping which occurs in the simple HEITLER–LONDON approach must be multiplied by a factor which depends entirely on the lattice vibrations. When this factor is very small, leading to a very low mobility, it can also be shown to vary rapidly with temperature with the general characteristics of an activated process.

2. CONDUCTION MECHANISM OF TIGHTLY BOUND ELECTRONS

In this section we discuss the mechanism of conduction by a tightly bound hole or electron, using an idealized model. We consider an extra positive hole in a perfect lattice consisting of ions with a closed shell structure. The wave function of the hole is assumed to be localized closely around an ion. We assume that the motion of the hole is so slow that polarization of the lattice is induced around it. For simplicity we adopt a continuum model for the polarization, although this may be a poor approximation. In the absence of an external field, the Hamiltonian of the system is:

$$\mathscr{H} = \mathscr{H}_0 + \mathscr{H}_{\text{int}}, \tag{1}$$

where $\mathscr{H}_0$ is the Hamiltonian of the unperturbed system, consisting of a hole and the free field of lattice waves:

$$\mathscr{H}_0 = \mathscr{H}_{\text{el}} + \mathscr{H}_L. \tag{2}$$

where

$$\mathscr{H}_{\text{el}} = \frac{1}{2m}p^2 + U(r), \tag{3}$$

and

$$\mathscr{H}_L = \tfrac{1}{2}\sum_q \sum_{\mu=1,2} (P_{q\mu}{}^2 + \omega_q{}^2 Q_{q\mu}{}^2). \tag{4}$$

In equation (3) the first term is the kinetic energy of a hole and the second term is the potential energy of the ion to which the hole is bound, q is the wave number vector of the lattice vibration, and ω_q is the frequency. The interaction Hamiltonian consists of two terms:

$$\mathscr{H}_{\text{int}} = \mathscr{H}_1 + \mathscr{H}_2, \tag{5}$$

where

$$\mathscr{H}_1 = \sum_{n\neq 0}{}' U(\boldsymbol{r}-\boldsymbol{R}_n), \tag{6}$$

and

$$\mathscr{H}_2 = -(4\pi e)\left[\frac{1}{2\pi}\left(\frac{1}{\kappa_0}-\frac{1}{\kappa}\right)\right]^{\frac{1}{2}} \times \times \sum_q (\omega_q/q)\{Q_{q1}\sin(\boldsymbol{q}\cdot\boldsymbol{r}) + Q_{q2}\cos(\boldsymbol{q}\cdot\boldsymbol{r})\}. \tag{7}$$

Here $\mathscr{H}_1$ is the potential energy of the ions in the lattice except for the one which was already considered in equation (3). The usual periodic potential is given by the sum of these two terms.

$$U_p(\boldsymbol{r}) = U(\boldsymbol{r}) + \mathscr{H}_1 = \sum_n U(\boldsymbol{r}-\boldsymbol{R}_n). \tag{8}$$

The interaction between the hole and the lattice is assumed to be given by the usual interaction Hamiltonian (7), which should be replaced by the more rigorous one by taking into account the distortion of the lattice near the hole. For simplicity we assume that the lattice has a simple cubic structure of lattice constant a.

In the usual band approximation we regard $\mathscr{H}_2$ as a small perturbation and determine electronic energy levels by solving the equation:

$$(\mathscr{H}_0 + \mathscr{H}_1)\Phi_k(\boldsymbol{r}) = E_k\Phi_k(\boldsymbol{r}). \tag{9}$$

Then we consider $\mathscr{H}_2$ as the perturbation which gives rise to transitions between these states. The electrical resistance is explained as arising from these transitions. In the present case we regard $\mathscr{H}_1$ as a small perturbation and try to solve the equation:

$$(\mathscr{H}_0 + \mathscr{H}_2)\Psi(\boldsymbol{r}, \boldsymbol{x}) = E\Psi(\boldsymbol{r}, \boldsymbol{x}). \tag{10}$$

The wave function represents a state consisting of a bound hole and the induced polarization around it. Next we consider $\mathscr{H}_1$ as the perturbation which causes the hole to make transition to a neighbouring ion, leading to a diffusion current.

Now, let us solve equation (10) by a variational method. For this purpose we take as a trial wave function Ψ, the product of an electronic wave function $\Phi(\boldsymbol{r})$ and a lattice wave function $X(\boldsymbol{x})$:

$$\Psi = \Phi(\boldsymbol{r})\cdot X(\boldsymbol{x}), \tag{11}$$

where $\Phi(\boldsymbol{r})$ depends on the electronic co-ordinate $\boldsymbol{r}$ only, and $X(\boldsymbol{x})$ on the co-ordinates denoting the

polarization waves. It is assumed that both are normalized:

$$\int \Phi^*(\boldsymbol{r})\Phi(\boldsymbol{r})\,d\tau = 1,\ \langle X^*(\boldsymbol{x})\cdot X(\boldsymbol{x})\rangle = 1, \quad (12)$$

where $\langle\ \rangle$ indicates integration over the field variables. This approximation corresponds to that of LANDAU and PEKAR[7] in the polaron problem, and we shall follow the procedures given in FRÖHLICH's review article.[8] The variation process:

$$\delta\Big[\int \Phi^*(\boldsymbol{r})\Big(-\frac{\hbar^2}{2m}\nabla^2+U(\boldsymbol{r})-\lambda_1\Big)\Phi(\boldsymbol{r})\,d\tau+$$
$$+\sum_q \langle X^*(\boldsymbol{x})\{\tfrac{1}{2}(P_q{}^2+\omega_q{}^2Q_q{}^2)-\lambda_2\}X(\boldsymbol{x})\rangle+$$
$$+\langle X^*(\boldsymbol{x})\cdot\int \Phi^*(\boldsymbol{r})\mathscr{H}_{\rm int}\Phi(\boldsymbol{r})\,d\tau\cdot X(\boldsymbol{x})\rangle\Big]=0 \quad (13)$$

gives us the required equations. Here the λ's are the Lagrange multipliers arising from the auxiliary conditions (13). The variation with respect to $\Phi^*(\boldsymbol{r})$ yields:

$$-\frac{\hbar^2}{2m}\nabla^2\Phi(\boldsymbol{r})+U(\boldsymbol{r})\Phi(\boldsymbol{r})+$$
$$+\langle X^*\mathscr{H}_2X\rangle\Phi(\boldsymbol{r})=\lambda_1\Phi(\boldsymbol{r}). \quad (14)$$

Similarly from the variation of $X^*(\boldsymbol{x})$, we have:

$$\tfrac{1}{2}\sum_q\sum_\mu (P_{q\mu}{}^2+\omega_q{}^2Q_{q\mu}{}^2)X+$$
$$+\int \Phi^*(\boldsymbol{r})\mathscr{H}_2\Phi(\boldsymbol{r})\,d\tau\cdot X=\lambda_2 X. \quad (15)$$

Equation (14) is the Schrödinger equation for a hole moving in the field of an ion, $U(\boldsymbol{r})$, and in a self-consistent field $\langle X^*(\boldsymbol{x})\mathscr{H}_2X(\boldsymbol{x})\rangle$. Similarly equation (15) represents the motion of the field of polarization waves in a self-consistent source. If we put:

$$X=\prod\prod X_{q\mu},\ \lambda_2=\sum_{q,\mu}\lambda_{q,\mu},$$

then $X_{q,\mu}$ satisfies the following equation:

$$\tfrac{1}{2}(P_{q\mu}{}^2+\omega_q{}^2Q_{q\mu}{}^2)X_{q,\mu}-4\pi e\omega_q\times$$
$$\times\Big[\frac{1}{2\pi}\Big(\frac{1}{\kappa_0}-\frac{1}{\kappa}\Big)\Big]^{\frac{1}{2}}\frac{1}{q}Q_{q\mu}\times$$
$$\times\int \Phi^*(\boldsymbol{r})\begin{Bmatrix}\sin(\boldsymbol{q}\cdot\boldsymbol{r})\\ \cos(\boldsymbol{q}\cdot\boldsymbol{r})\end{Bmatrix}\Phi(\boldsymbol{r})\,d\tau\cdot X_{q\mu}=\lambda_{q\mu}\cdot X_{q\mu}, \quad (16)$$

which is the equation of a displaced harmonic oscillator. According to equation (5.12) of FRÖHLICH's paper $\langle X^*(\boldsymbol{x})\mathscr{H}_2X(\boldsymbol{x})\rangle$ becomes:

$$\langle X^*(\boldsymbol{x})\mathscr{H}_2X(\boldsymbol{x})\rangle$$
$$=-e^2\Big(\frac{1}{\kappa_0}-\frac{1}{\kappa}\Big)\int\frac{\Phi^*(\boldsymbol{r}')\Phi(\boldsymbol{r}')}{|\boldsymbol{r}'-\boldsymbol{r}|}\,d\tau.$$

Therefore we have:

$$-\frac{\hbar^2}{2m}\nabla^2\Phi(\boldsymbol{r})+U(\boldsymbol{r})\Phi(\boldsymbol{r})-$$
$$-e^2\Big(\frac{1}{\kappa_0}-\frac{1}{\kappa}\Big)\int\frac{\Phi^*(\boldsymbol{r}')\Phi(\boldsymbol{r}')}{|\boldsymbol{r}'-\boldsymbol{r}|}\,d\tau'\cdot\Phi(\boldsymbol{r})$$
$$=\lambda_1\Phi(\boldsymbol{r}). \quad (17)$$

Here we introduce the approximation that the potential of the ion, $U(\boldsymbol{r})$, is so large that we may write:

$$\delta U=-e^2\Big(\frac{1}{\kappa_0}-\frac{1}{\kappa}\Big)\int\frac{\Phi^*(\boldsymbol{r}')\Phi(\boldsymbol{r}')}{|\boldsymbol{r}'-\boldsymbol{r}|}\,d\tau'$$
$$=-e^2\Big(\frac{1}{\kappa_0}-\frac{1}{\kappa}\Big)\int\frac{\Phi_0{}^*(\boldsymbol{r}')\Phi_0(\boldsymbol{r}')}{|\boldsymbol{r}'-\boldsymbol{r}|}\,d\tau', \quad (18)$$

where Φ_0 represents the solution of the wave-equation of the free ion, that is, Φ_0 satisfies:

$$-\frac{\hbar^2}{2m}\nabla^2\Phi_0(\boldsymbol{r})+U(\boldsymbol{r})\Phi_0(\boldsymbol{r})=E_0\Phi_0(\boldsymbol{r}), \quad (19)$$

and is assumed to be known.
Then we have:

$$-\frac{\hbar^2}{2m}\nabla^2\Phi(\boldsymbol{r})+[U(\boldsymbol{r})+\delta U(\boldsymbol{r})]\Phi(\boldsymbol{r})=\lambda_1\Phi(\boldsymbol{r}). \quad (20)$$

The solution of this equation is more contracted than $\Phi_0(\boldsymbol{r})$ owing to the effect of the polarization potential. Next, we assume that $\Phi(\boldsymbol{r}-\boldsymbol{R}_n)$ and $\Phi(\boldsymbol{r}-\boldsymbol{R}_m)$ are approximately orthogonal ($R_n\neq R_m$).

Then equation (15) becomes:

$$\tfrac{1}{2}(P_q^2+\omega_q^2Q_q^2)X_q-4\pi e\omega_q\left[\frac{1}{2\pi}\left(\frac{1}{\kappa_0}-\frac{1}{\kappa}\right)\right]^{\frac{1}{2}}\times$$

$$\times\begin{Bmatrix}\sin(qR_n)\\ \cos(qR_n)\end{Bmatrix}\frac{Q_q}{q}\cdot X_q=\lambda_qX_q. \tag{21}$$

Through the transformation:

$$P_q'=P_q \text{ and } Q_q'=Q_q-C_q(R_n),$$

where

$$C_q(R_n)=\frac{4\pi e}{q\omega_q}\left[\frac{1}{2\pi}\left(\frac{1}{\kappa_0}-\frac{1}{\kappa}\right)\right]^{\frac{1}{2}}\begin{Bmatrix}\sin(qR_n)\\ \cos(qR_n)\end{Bmatrix}, \tag{22}$$

Equation (21) becomes the equation of an harmonic oscillator:

$$\tfrac{1}{2}(P_q'^2+\omega_q^2Q_q'^2)X_q'=E'X_q'. \tag{23}$$

Thus, we are able to determine the unperturbed wave function:

$$\Psi=\Phi_\lambda(\boldsymbol{r})\prod_q X_q^{n}(Q_q'), \tag{24}$$

where λ and n are quantum numbers. Here we must notice that Q' is a function of the lattice coordinate through $C_q(R_n)$, and $\Phi(\boldsymbol{r})$ is a function of the lattice polarization through the polarization potential $\delta U(\boldsymbol{r})$. Next we must consider the effect of the perturbation $\mathscr{H}_1$, the periodic potential aside from the given ion. As a zero-order wave function, we take a running wave constructed out of localized functions of the form (24). Such a wave is

$$\Psi_k=\sum_m e^{i\boldsymbol{k}\boldsymbol{R}_m}\Phi_\lambda(\boldsymbol{r}-\boldsymbol{R}_m)\prod_q X_q^{n}[Q_q'(R_m)]. \tag{25}$$

This would be a usual Bloch function if we replace Q' by Q, and the effect of $\mathscr{H}_1$ would correspond to the usual approximation of tight binding in the theory of metals. As a result of the perturbation $\mathscr{H}_1$, the energy of the system becomes at the absolute zero temperature ($n=0$):

$$E=E_0+2M\{\cos(k_xa)+\cos(k_ya)+$$
$$+\cos(k_za)\}e^{-S}, \tag{26}$$

where M is the transition matrix element of $\mathscr{H}_1$:

$$M=\int\Phi(\boldsymbol{r}-\boldsymbol{R}_m)\mathscr{H}_1\Phi(\boldsymbol{r}-\boldsymbol{R}_{m+1})\,d\tau. \tag{27}$$

The term $\exp(-S)$ comes from:

$$\prod_q\int X_{q0}[Q_q'(R_m)]\cdot X_q^{0}[Q_q'(R_{m+1})]\,dX_q,$$

where S is given by:

$$S=\sum_{q=1}^{N_0}\frac{\omega_q}{2\pi\hbar}\left\{C_q(R_m)-C_q(R_{m+1})\right\}^2. \tag{28}$$

and is a measure of the strength of the electron–lattice coupling. Small values of S correspond to weak coupling, and the band picture is applicable for the motion of a hole. However, if S is large, the effective mass of a hole becomes too large to regard the band picture as a suitable approximation. Moreover, the effective mass depends upon the number of phonons. If we take the number of phonons as n irrespective of q, a simple computation shows that the factor $\exp(-S)$ in equation (26) is replaced by $\exp[-(2n+1)S]$. Therefore, the effective mass increases with increasing temperature.*

Even though the band picture is not applicable for the motion of such a tightly bound hole, the hole can move to some extent from ion to ion by another mechanism. In order to explain such a motion of a hole we shall apply the HEITLER–LONDON picture to the present problem. The unperturbed wave function is given by:

$$\Psi_m=\Phi(\boldsymbol{r}-\boldsymbol{R}_m)\prod_q X_q^{n_q}[Q_q'(R_m)], \tag{29}$$

when the hole is situated around the ion R_m, and it is given by:

$$\Psi_{m+1}=\Phi(\boldsymbol{r}-\boldsymbol{R}_{m+1})\prod_q X_q^{n_q''}[Q_q'(R_{m+1})], \tag{30}$$

when the hole is situated around the ion R_{m+1}. In this case the total energy of the system in the two states Ψ_m and Ψ_{m+1} must be equal, but the wave function of phonons $X_q^{n_q'}$ and $X_q^{n_q''}$ need not to be equal. Our problem is to compute the transitio probability for transfer of the hole from the R_m ion to the R_{m+1} ion by the perturbation $\mathscr{H}_1$, when the

* This argument is not applicable for the motion of the hole with considerable kinetic energy, because the many modes of vibration can not follow the motion of the hole, so that only a small part of the polarization of the lattice can be induced around the hole and consequently S becomes small.

quantum numbers of photons of two states, n_q' and n_q'', can take any values which satisfy the condition of energy conservation:

$$\sum_{q=1}^{N_0}[(n_q''+\tfrac{1}{2})\hbar\omega_q-(n_q'+\tfrac{1}{2})\hbar\omega_q]=0. \quad (31)$$

This type of computation appears in the problem of non-radiative transitions in crystals, and has been studied by many authors[9] as "the many-phonon process". We need to apply only their results to our problem. Our transition matrix is:

$$|C_{n'\to n''}|(t)|^2 = \frac{|M|^2}{(E_n''-E_n')}|\langle X_{n_q'}(R_m)|X_{n_q''}(R_{m+1})\rangle|^2\times \times 2(1-\cos[(E_n''-E_n')t/\hbar]), \quad (32)$$

where M was defined by equation (27) and $X_{n_q'}(R_m)$ is the abbreviation of $X_q{}^{n}{}'(Q'(R_m))$. The energy differences $(E_n''-E_n')$ is given by:

$$E_n''-E_n' = \sum_q (n_q''-n_q')\hbar\omega_q. \quad (33)$$

Here we assume that the hole interact predominantly with the optical modes, and the frequency ω_q is thus approximately constant for all modes, that is,

$$\omega_q = \omega+\Delta\omega_q. \quad (34)$$

Then equation (32) becomes:

$$|C_{n'\to n''}(t)|^2 = |M|^2\cdot\prod_q|\langle X_{n_q'}(R_m)|X_{n_q''}(R_{m+1})\rangle|^2\delta(E_n''-E_n')\times \times\int_{-\infty}^{\infty}2(1-\cos[xt/\hbar])/x^2\cdot dx = \frac{2\pi}{\hbar}|M|^2\cdot\prod_q|\langle X_{n_q'}(R_m)|X_{n_q''}(R_{m+1})\rangle|^2\delta(E_n''-E_n')t. \quad (35)$$

The total transition probability W is found by averaging equation (35) over all initial states n_q' and summing over all the final n_q'':

$$W = \sum_{n'}\sum_{n''}p_{n'}|C_{n'\to n''}(t)|^2/t = \frac{2\pi}{\hbar}|M|^2\prod_q\sum_{n'}\sum_{n''}p_{n'}|\langle X_{n'q}(R_m)|X_{n_q''}(R_{m+1})\rangle|^2\times \times\delta(E_n''-E_n'), \quad (36)$$

where

$$p_{n'} = \exp(-E_n'/kT)\Big[\sum_{n'}\exp(-E_n'/kT)\Big]^{-1}. \quad (37)$$

It is also expressed as:

$$p_{n'} = \prod_q{}^{N_0}2\sinh(\beta/2)\exp\{-(n_q'+\tfrac{1}{2})\beta\}, \quad (38)$$

where

$$\beta = \hbar\omega/kT.$$

In computing the matrix element we shall disregard $\Delta\omega_q$ in equation (33). By the introduction of the integral representation of the Dirac delta function according to VASILEFF[9] we have:

$$W = \frac{2\pi}{\hbar}|M|^2\frac{1}{2\pi\hbar}\int_{-\infty}^{\infty}dtG_{n'n''}(t) = \frac{2\pi}{\hbar}|M|^2\prod_q\frac{1}{2\pi\hbar}\int_{-\infty}^{\infty}dtG_q(t) \quad (39)$$

where

$$G_{n'n''}=\prod_q \sum_{n'} \sum_{n''} |\langle X_{n_q'}(R_m)|X_{n_q''}(R_{m+1})\rangle|^2 \cdot p_{n'} \exp\left[it \sum_q (n_q''-n_q')\omega\right],$$

and

$$G_q=\sum_{n'} \sum_{n''} |\langle X_{n_q'}(R_m)|X_{n_q''}(R_{m+1})\rangle|^2 2\sin(\beta/2)\times$$

$$\times\exp\{-(n_q'+\tfrac{1}{2})(i\omega t+\beta)\}\exp\{(n_q''+\tfrac{1}{2})(i\omega t)\}. \quad (40)$$

The quantity G_q has been evaluated by many authors,[9] and we have:

$$\prod_q G_q=\exp\{-S(2n+1)\}$$

$$\exp\{2S\sqrt{n(n+1)}\cos\omega t\}, \quad (41)$$

where

$$n=1/(e^{\hbar\omega/kT}-1). \quad (42)$$

Inserting equation (41) into equation (39), we have finally:

$$W=\frac{2\pi}{\hbar}|M|^2\exp\{-S(2n+1)\}\times$$

$$\times\frac{1}{2\pi\hbar}\int_{-\infty}^{\infty}\exp\{2S\sqrt{n(n+1)}\cos\omega t\}\,dt$$

$$=\frac{2\pi}{\hbar}|M|^2\exp\{-S(2n+1)\}\left(\frac{1}{\hbar\omega}\right)\times$$

$$\times\frac{1}{2\pi}\int_{-\infty}^{\infty}\exp\{2S\sqrt{n(n+1)}\cos x\}\,dx. \quad (43)$$

Introducing the modified Bessel function $I_0(z)$ by:

$$I_0(z)=\frac{1}{2\pi}\int_0^{2\pi}\exp(Z\cos x)\,dx, \quad (44)$$

we can write equation (43) as:

$$W=\frac{2\pi}{\hbar}|M|^2\exp\{-S(2n+1)\}\times$$

$$\times\left(\frac{1}{\hbar\omega}\right)I_0\{2S\sqrt{n(n+1)}\}. \quad (45)$$

From the transition probability the diffusion coefficient D is given by:

$$D=Wa^2. \quad (46)$$

Through the Einstein relation, the mobility is given by:

$$\mu=\frac{ea^2}{kT}W. \quad (47)$$

To show the temperature-dependence of the conductivity, we have computed the factor

Table 2. Value of $\exp\{-S(2n+1)\}\ I_0[2S\sqrt{n(n+1)}]$ *as a function of* S *and* T/Θ. $n=1/[\exp(\Theta/T)-1]$

T/Θ \ S	1	3	5	10	15	20
0·0	0·3678	$4\cdot978\times10^{-2}$	$0\cdot6738\times10^{-2}$	$0\cdot0454\times10^{-3}$	$3\cdot06\times10^{-7}$	$2\cdot06\times10^{-9}$
0·3	0·3546	5·481	1·031	0·2285	$6\cdot07\times10^{-6}$	$1\cdot72\times10^{-7}$
0·5	0·3198	6·649	1·988	0·355	$1\cdot09\times10^{-4}$	$9\cdot23\times10^{-6}$
·8	0·2712	7·893	3·308	5·019	$9\cdot00\times10^{-4}$	$1\cdot70\times10^{-4}$
·0	0·2480	8·214	3·894	7·918	$1\cdot89\times10^{-3}$	$4\cdot82\times10^{-4}$
1·2	0·2286	8·284	4·216	10·6	$3\cdot12\times10^{-3}$	$9\cdot45\times10^{-4}$
1·4	0·2147	8·311	4·482	12·3	$4\cdot40\times10^{-3}$	$1\cdot56\times10^{-3}$

VOL. 5 195

$\exp\{-S(2n+1)\}I_0[2S\sqrt{n(n+1)}]$ for various temperatures, and the results are given in Table 2. As seen from the table, when S is small the value of this factor is of the order of 0·1 and it changes very slowly as a function of T, but for large values of S it becomes very small and increases very rapidly with temperature. In the first case we may expect metallic conductivity and in the second case the properties of a semiconductor. Since the quantity S is very important in our theory, its quantitative theoretical evaluation is desirable. However, our continuum model is too crude to be useful for quantitative purposes. It might be better to consider S in equation (45) as an adjustable parameter till we develop a more rigorous atomic theory of lattice vibration around the defect point. We shall evaluate S within the limit of validity of the continuum model as a rough estimate. According to the definition of S in equation (28) and that of $C_q(R)$ in equation (22), we have:

$$S=\frac{2}{\pi}\left(\frac{1}{\kappa_0}-\frac{1}{\kappa}\right)\frac{e^2}{\hbar\omega a}\left(q_0 a-\int_0^{q_0 a}(\sin x/x)\,dx\right).$$

where q_0 is the maximum value of the wave number of the lattice vibration, and it is given by (for the NaCl lattice):

$$2a^3N/(2\pi)^3\times(4\pi/3)q_0{}^3=N.$$

If we assume the following values of a, κ_0, κ, and ω:

$$a=4\times10^{-8}\text{cm},\quad K_0=3,\quad \kappa=10,\quad \omega=10^{14}\,\text{sec}^{-1},$$

we obtain the result: $S\sim 10$. We may regard this value as a rough measure of the magnitude of S, when the lithium content is very small. Let us now estimate a value for S in NiO from the temperature-dependence of the mobility. By consulting Tables 1 and 2, we estimate $S\sim 15$ for specimens No. 1 and No. 2, and $S\sim 4$—5 for the specimen No. 6. Unfortunately, the present theory cannot predict the variation of S with lithium content. However, we suppose that specimen No. 6 contains so many holes and lithium ions that the polarization around one particular hole is reduced by the effects of other holes and lithium ions which are distributed more or less uniformly in the lattice and screen the polarization.

The transition probability (45) contains the electronic matrix element M, which is not zero, either if there is direct overlap between $3d$ functions of the nearest nickel ions, or if there is an indirect or double exchange interaction between them through the intermediate oxygen. The matrix element M is also spin-dependent, because spin must be conserved in the transition. However, according to MORIN the electrical conductivity of NiO shows no sudden change at the Curie point. It is well known from specific-heat measurements, however, that a high degree of short-range order persists above the Curie temperature. Since only the matrix element between neighbouring ions is important, the transition probability will not drop abruptly above the Curie point, but will fall off only gradually with increasing temperature. In addition there is the possibility of direct overlap between nickel ions.

If we put $M=k\Theta$, equation (47) gives the correct order of magnitude of the electrical conductivity of MORIN's specimens of NiO. We may also estimate a value of S for $(LaMnO_3+SrMnO_3)$ in the case of $\delta\sim 0{\cdot}3$. We assume tentatively $\Theta=1000°K$ and $M^2/(k\Theta)^2=\frac{1}{10}$. Inserting observed values of the mobility of 0·2 cm/V-sec. ($T=300°K$), we determine a value of $\exp\{-S(2n+1)\}I_0[2S\sqrt{n(n+1)}]$ as 4×10^{-2}, which corresponds to $S=3$ or 4 in Table 2. For this case the conductivity is nearly proportional to $1/T$, as is observed.

Acknowledgements—We would like to express our gratitude to Professor A. J. ALLEN for the kind hospitality of the Radiation Laboratory. We wish to thank Professor F. KEFFER for his helpful discussions.

APPENDIX

In Section 3 we discussed electrical conduction by the HEITLER–LONDON approximation. Here we discuss the energy problem and compare the energy of the bound state of equation (39) with the energy of the polaron state. For simplicity we assume that the crystal has the simple cubic structure and the wave function of the electron is given by:

$$\Phi(r)=(\beta^3/8\pi)^{\frac{1}{2}}\exp(-\beta r/2),\qquad (A.1)$$

where β is the variational parameter. As the potential of the ion we take the simplest form:

$$U(r) = -Ze^2/r, \tag{A.2}$$

which is reasonable for a hole of the positive ion. The Hamiltonian of the system is given by equation (11). At first we solve equation (19) and the energy is given by:

$$E = E_0 + 2M\{\cos(k_x a) + \cos(k_y a) + \cos(k_z a)\}, \tag{A.3}$$

where M and E_0 are defined by equations (37) and (29), respectively. The energy of the slow electron is expressed by:

$$E = E_0 - 6|M| + |M|a^2k^2,$$

and the effective mass is defined by:

$$(m^*/m) = 6\hbar^2/ma^2\gamma, \tag{A.4}$$

where γ is the breadth of the band:

$$\gamma = 12|M|.$$

Therefore, the energy gain by the band formation is given by:

$$\Delta E_\beta = 6|M| = 3\hbar^2/m^*a^2 \tag{A.5}$$

for the slowest electron. In the next step we must consider the effect of the polarization of equation (17) for the energy. For that purpose we introduce the effective mass equation:

$$\left(\frac{\hbar^2}{2m^*}\nabla^2 + \mathscr{H}_2\right)\Psi = E\Psi. \tag{A.6}$$

By the same procedures as LANDAU and PEKAR, we can obtain the energy of the electron in the polaron state and the result is:[10]

$$E_p = E_0 - \Delta E_B - \left(\frac{e^4m^*}{\hbar^2}\right)\left(\frac{1}{\kappa_0} - \frac{1}{\kappa}\right)^3\left(\frac{25}{512}\right). \tag{A.7}$$

On the other hand, the energy of the bound state:

$$\left[\frac{\hbar^2}{2m}\nabla^2 + U(r) - e^2\left(\frac{1}{\kappa_0} - \frac{1}{\kappa}\right)\int\frac{\Phi(r')\Phi(r')}{|r'-r|}d\tau'\right]\Phi(r) = E\Phi(r) \tag{A.8}$$

is given by:

$$E_b = \frac{\hbar^3}{2m}\frac{1}{4}\beta^2 - \frac{e^2Z}{2}\beta - \frac{e^2}{2}\left(\frac{1}{\kappa_0} - \frac{1}{\kappa}\right)\frac{5}{16}\beta.$$

By determining the parameter β by the minimum condition the energy of the bound state is:

$$E_b = E_0 - \frac{me^4}{2\hbar^2}\left(\frac{1}{\kappa_0} - \frac{1}{\kappa}\right)\left[\frac{5Z}{8} + \left(\frac{5}{16}\right)^2\left(\frac{1}{\kappa_0} - \frac{1}{\kappa}\right)\right], \tag{A.9}$$

where

$$E_0 = -me^4Z^2/2\hbar^2. \tag{A.10}$$

The energy difference of these two states is:

$$E_p - E_b = \left(\frac{me^4}{\hbar^2}\right)\left(\frac{1}{\kappa_0} - \frac{1}{\kappa}\right)\left[\frac{5}{8}Z + \left(\frac{5}{16}\right)^2\left(\frac{1}{\kappa_0} - \frac{1}{\kappa}\right) - \frac{1}{2}\left(\frac{5}{16}\right)^2\left(\frac{1}{\kappa_0} - \frac{1}{\kappa}\right)\left(\frac{m^*}{m}\right) - \frac{3}{a^2}\left(\frac{\hbar^2}{me^2}\right)^2\left(\frac{m}{m^*}\right)\left(\frac{1}{\kappa_0} - \frac{1}{\kappa}\right)^{-1}\right]. \tag{A.11}$$

We see from equation (A.11) that if the effective mass is large, the increased energy of the band formation is small and the energy of the bound state becomes lower, while the band picture is a good approximation when the effective mass is small. But equation (A.11) shows that the polaron state gives lower energy for extremely large effective masses. It is the natural result of equation (A.7), in which the energy decreases continually with increase in effective mass. We do not know the physical meaning of these states, because the continuum model of dielectrics may be a very poor approximation in such cases. We show in Table 3 the values of the effective mass which satisfy the condition $E_p = E_b$. The energy of the bound state E_b is lower than E_p between these two values.

Table 3. Value of the effective mass (m^*/m), which gives the same energy for both the polaron state and the bound state as the function of the polarization of the lattice, ($1/\kappa_0 - 1/\kappa$) and the effective charge of the potential, Z

$(1/\kappa_0 - 1/\kappa)$ \ Z	0·5	1·0	2·0	3·0
0·1	3·35 28·6	1·77 54·2	0·94 103	0·64 154·00
0·2	2·25 10·7	1·00 24·0	0·50 48·5	0·33 72·6

VOL.
5
1958

REFERENCES

1. MORIN F. J. *Phys. Rev.* **93,** 1199 (1954).
2. VERWEY E. J. W. *Semiconducting Materials* (Edited by H. K. HENISCH) p. 151. Butterworths Scientific Publications, London (1951).
3. HEIKES R. R. *Phys. Rev.* **99,** 1232 (1955).
4. ZENER C. *Phys. Rev.* **82,** 403 (1951).
5. MOTT N. F. *Proc. Phys. Soc.* A **62,** 416 (1949).
6. SLATER J. C. *Phys. Rev.* **82,** 538 (1951).
7. LANDAU L. and PEKAR S. *J. Phys. U.S.S.R.* **18,** 419 (1948).
8. FRÖHLICH H. *Advanc. Phys.* **3,** 325 (1953).
9. KUBO R. *Phys. Rev.* **86,** 929 (1952).
   HUANG K. and RHYS A. *Proc. Roy. Soc.* A **204,** 406 (1950).
   LAX M. *J. Chem. Phys.* **20,** 1752 (1952).
   O'ROURKE R. C. *Phys. Rev.* **91,** 265 (1953).
   VASILEFF H. D. *Phys. Rev.* **96,** 603 (1954).
10. FRÖHLICH H. *Advanc. Phys.* **3,** 325 (1953). Eq. (5–23).

OL.
5
958

J. Phys. Chem. Solids Pergamon Press 1958. Vol. 5. pp. 44–46.

RESISTIVITY DUE TO DISLOCATIONS IN COPPER

WALTER A. HARRISON

General Electric Research Laboratory, Schenectady, N.Y.

(*Received* 27 *July* 1957; *revised* 11 *September* 1957)

Abstract—The scattering of electrons by a dislocation with a hollow core is treated. It is found that the effect of such a core upon the electrical resistivity may be many times greater than the effect of the strain field. If the change in volume of the crystal due to dislocations is set equal to the core volume (of the order of one atomic volume per interatomic distance of dislocation), a rough calculation indicates that the change in resistivity for 1 per cent change in volume is about one-half of that observed in annealing experiments on cold-worked copper. It is suggested that the general magnitude of the interaction between conduction electrons and the core may be correct, even if the specific hollow-core model is not valid. Hence it appears that a consideration of the scattering by the core provides order-of-magnitude agreement with experiment for the resistivity due to dislocations.

VOL.
5
1958

ATTEMPTS to understand the behavior of cold-worked metals in terms of the presence of dislocations and vacancies have been reasonably successful except in predicting the changes in resistivity to be associated with dislocations.[1,2] The measured resistivity changes are higher by a factor of 20–40 than those expected on the basis of the number of dislocations estimated from other considerations and of the existing calculations of the resistivity per dislocation. Although such a simple analysis of cold work is questionable, it should not lead to such order-of-magnitude discrepancies.

Among the existing calculations of the scattering of electrons by the strain fields of dislocations is the analysis by HUNTER and NABARRO,[3] which includes the effects of shear, and which gives an average increase in resistivity due to edge and screw dislocations of $0{\cdot}38\times10^{-20}N$ Ω-cm^3, where N is the density of dislocations. SEEGER and STEHLE[2] considered additional terms arising from non-linearities in the displacements of atoms, but did not find an increase in the order of magnitude of the resistivity. An order-of-magnitude increase has been obtained by attributing large scattering to ribbons of stacking fault associated with extended dislocations,[4] but there is no general agreement that scattering by stacking faults is so large. The fact that a perturbation procedure such as that of SEEGER[4] yields large scattering does not seem convincing, since calculations involving matching across the plane of the stacking fault give very small scattering.[5,6]

The above-mentioned calculations of resistivity due to dislocations have been treatments of the strain field; the effect of the dislocation core has been included only as an extrapolation of the strain field. It seems likely that the source of the discrepancy may lie within the core. The calculation described here indicates that a proper treatment of the core may easily raise the estimate of the resistivity into the range which is found experimentally.

A hollow cylinder of unknown cross-section provides a crude model for the core. This specific model is certainly questionable. However, the order of magnitude of the resulting resistivity is determined by the fact that the proposed scattering region is restricted to a region of atomic dimensions and the interaction is relatively strong. A string of interstitials or of substitutional impurities would give a similar result (see the Appendix). Thus one might expect a more precise model to give about the same magnitude of scattering.

The effect of the strain field may be neglected, since the calculations mentioned above indicate that it is small by comparison. This hollow cylinder is treated, in the effective mass approximation, as a square-well potential of the proper magnitude to give self-consistent screening in the Fermi–Thomas approximation. Since a perturbation

procedure will be used in the scattering calculation, the linearized Fermi–Thomas approximation is appropriate; that is, the potential for a vacant region is given by the density of electrons in the normal material divided by the density of states per unit energy range at the Fermi surface.

$$V_p = \tfrac{2}{3}E_F,$$

where E_F is the Fermi energy, $\hbar^2k^2/2m^*$.

The matrix element for scattering is given by:

$$V_{kk'} = \int \psi_{k'}^* \psi_k V_p \, d\tau$$

$$= (2E_F/3L^3) \int_{\text{core}} \exp(-i(k'-k)\cdot r)\, d\tau,$$

in which L^3 is the crystal volume. The integration is simplified by approximating the core cylinder by a right square prism, with one lateral face parallel to $(k'-k)$. The square cross-section is taken to have area l^2. The result is:

$$V_{kk'} = \frac{2E_F l^2 L}{3L^3} \cdot \frac{\sin|k'-k|l/2}{|k'-k|l/2},$$

if the component of k' along the dislocation line is equal to the component of k along the dislocation line, and zero otherwise. It is assumed, following MacKenzie and Sondheimer,[7] that the electron scattering by the thermal motion of the lattice is large compared to that by the dislocations. Thus the contribution to the scattering probability for an electron of wave-number k is given by the relaxation-time formula:[8]

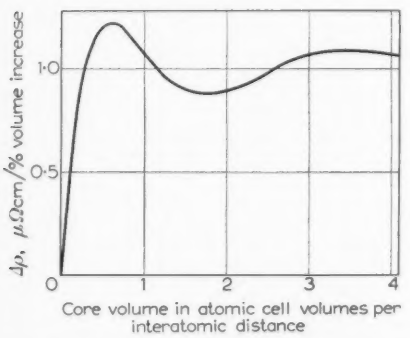

FIG. 1. Increase in resistivity/per cent increase in volume as a function of dislocation core size.

$$\frac{1}{\tau_k} = \frac{2\pi}{\hbar} \int |V_{kk'}|^2 \delta(E_{k'} - E_k) \times$$

$$\times \frac{L^3}{(2\pi)^3}(1-\cos\theta)\, dk'^3.$$

Here θ is the angle between k and k'. This scattering probability is averaged over directions of k (or over orientations of the dislocation) and multiplied by m^*NL^2/ne^2 to obtain the incremental resistivity. N is the density of dislocations and n is the density of electrons. The result is given by:†

$$\Delta\rho = \frac{\hbar k^2 l^2 N}{9e^2 n}\left(1 - \frac{\sin 2kl}{2kl}\right).$$

The factor $(1-\sin 2kl/2kl)$ equals one at a value of l corresponding to a core volume of 0·3 atomic cell volumes per interatomic distance of dislocation and fluctuates around one for larger values of l. Thus, for reasonable sizes of atomic core, this factor is approximately one. The remaining factor is directly proportional to the core volume. For a core corresponding to a line of vacancies (one atomic cell volume per interatomic distance) the resistivity becomes about $5\times10^{-20}N$ Ω-cm³, which is more than ten times the value obtained by Hunter and Nabarro[3] for the effect of the strain field.

The result may be compared rather directly with experiment by normalizing it with respect to the change in volume of the crystal, as was done by Seeger.[4] If it is assumed that the change in volume of the crystal is equal to the total core volume (NL^3l^2), the ratio of dislocation resistivity to change in specific volume becomes 1·0 $(1-\sin 2kl/2kl)$ μΩcm/per cent increase in volume for copper. In Fig. 1 this is plotted as a function of core volume. If the core volume per interatomic distance is between one-third and one atomic cell volume (for an unextended dislocation or for each half of an extended dislocation), the ratio of dislocation resistance to change in specific volume is 1·0–1·2 μΩcm/per cent increase in volume. This is about one-half the value obtained experimentally by Clarebrough *et al.*[9] from measurements of

† The integration is conveniently performed by expanding the integrand as an infinite series of sines, integrating term-by-term, and collecting terms.

resistivity and density changes during the annealing of cold-worked copper.

The fact that this model gives order-of-magnitude agreement with experiment for the resistivity due to dislocations is not to be taken as evidence that the core is in fact hollow. It does indicate, however, that with a reasonable interaction between the core and the conduction electrons, the calculated resistivity is of the order of that observed. On the other hand, if a reasonable interaction between the electrons and the *strain* field is postulated (as was done, for example, by HUNTER and NABARRO),[3] the contribution to the scattering is much smaller than that observed. Thus it is not surprising that the existing resistivity calculations, which have been treatments of the strain field, have given resistivities much smaller than those observed. Furthermore, it is reasonable to expect that a more precise treatment of the scattering by the core will restore the agreement with experiment.

Acknowledgements—The author is indebted to Drs. M. E. HARGREAVES, E. W. HART and W. G. JOHNSTON for enlightening discussions.

APPENDIX

As a check on the approximations which are made in the calculation and in order to estimate the results which might be obtained by using other models of the core, it is desirable to calculate the scattering by a single vacancy by the same method as that used for the dislocation.

The vacancy is approximated by a cube with one face parallel to $(k'-k)$. The volume of the cube is given by $l^3 = a^3/4$, where a is the lattice distance. The matrix element is given by

$$V_{kk'} = \frac{2E_F l^3}{3L^3} \cdot \frac{\sin|k'-k|l/2}{|k'-k|l/2}$$

for all values of k'. The relaxation-time formula is applied and the resistivity calculated:

$\Delta\rho = 1{\cdot}00$ $\mu\Omega$cm/atomic per cent of vacancies.

This is slightly lower than most other theoretical estimates.[10] It may also be noticed that this resistivity is of the order of calculated values for interstitials and most impurities in copper.[10] Thus the strength of interaction considered here does not seem inordinatedly large, and no change in order of magnitude should be expected to arise from refinements of the model.

REFERENCES

1. BOAS W. and SEEGER A. *Proceedings of a Conference on Dislocations and Mechanical Properties of Crystals*. John Wiley, New York (1957).
2. SEEGER A. and STEHLE H. *Z. Phys.* **146,** 242 (1956).
3. HUNTER S. C. and NABARRO F. R. N. *Proc. Roy. Soc.* A **220,** 542 (1953).
4. SEEGER A. *Canad. J. Phys.* **34,** 1219 (1956).
5. BLATT F. J., HAM F. S. and KOEHLER J. S. *Bull. Amer. Phys. Soc.* **1,** 114 (1956).
6. TWEEDALE, see discussion by ZIMAN J. *Canad. J. Phys.* **34,** 1234 (1956).
7. MACKENZIE J. K. and SONDHEIMER E. H. *Phys. Rev.* **77,** 264 (1949).
8. MOTT N. F. and JONES H. *Properties of Metals and Alloys* Chap. VII. Oxford University Press, London (1936).
9. CLAREBROUGH L. M., HARGREAVES M. E., and WEST G. W. *Proc. Roy. Soc.* A **232,** 252 (1955).
10. BLATT F. J. *Solid State Physics* Vol. 3. Academic Press, New York (1957).

VOL. 5 1958

J. Phys. Chem. Solids Pergamon Press 1958. Vol. 5. pp. 47–77.

STRUCTURE-SENSITIVE CHEMISORPTION: THE MECHANISM OF DESORPTION FROM TUNGSTEN

T. W. HICKMOTT and GERT EHRLICH

General Electric Research Laboratory, Schenectady, N.Y.

(*Received* 26 *July* 1957; *revised* 14 *October* 1957)

Abstract—The validity of measurements on evaporated tungsten films has been examined and found in doubt; the flash-filament technique has therefore been extended to yield data on the stability of binding states of gases adsorbed on metals. Qualitative results are presented for the adsorption of nitrogen, hydrogen, and oxygen on tungsten. Just as for nitrogen at room temperature, two states of binding have been isolated for both hydrogen and oxygen; for the latter two gases the pressure-measuring device seriously affects the adsorption. In the absence of atomic hydrogen produced by the ionization-gauge filament, in experiments with hydrogen only a single state of adsorption is found, which desorbs continuously from 100 to 540°K.

The methods for deriving quantitative data on rates of desorption from pressure/temperature curves obtained by the flash-filament technique are presented, and are applied to a study of the evolution of β-nitrogen from tungsten. The desorption is found to obey second-order kinetics, indicating that the nitrogen is dissociated and exists on the surface as adatoms. Although the heat of desorption is constant for all coverages examined ($n_\beta = 10\text{–}180 \times 10^{12}$ molecules/cm^2), the kinetics differ from sample to sample; heats varying between 58 and 81 kcal/mole have been measured, and a correlation between high heats and high rates of adsorption has been observed. Conditions for the maintenance of surface equilibrium are derived, and from these and the experimentally observed continuous evolution of β-nitrogen, the heterogeneities primarily responsible for variations in the heat of desorption are identified as being of a small scale, possibly associated with the presence of lattice steps. The implications of structural effects in the interpretation of the decrease in the heat of adsorption with increasing cover, reported in the past for other systems, are analysed, and it is shown that in a mobile adlayer only interactions between adatoms can bring about such a diminution. The possible structure-sensitivity of chemisorption also invalidates past attempts to establish the nature of the surface bond from measurements of the heat of adsorption on different metals; an examination of the available data shows that a simple correlation between *d*-band structure of the solid and activity in chemisorption is not warranted.

1. INTRODUCTION

CHEMISORPTION—the adsorption of a gas on a surface with a binding energy comparable to that of a primary chemical bond—has been of considerable scientific interest because of its importance in connection with such varied problems as heterogeneous catalysis, oxidation, and electron emission from metals. There is an extensive body of information dealing with the interaction of molecular gases with metals which has grown up as a result of this interest, but because of severe limitations on the experimental techniques available in the past, chemisorption of molecular gases on metals in a very dilute adsorbed layer has not been explored. Still lacking as a consequence is a thorough understanding of the nature of the chemisorption bond, its dependence upon the structure of the surface and upon the interaction with other adsorbed entities, the dependence of chemisorption upon the nature of the substrate and the gas, and the details of the kinetic processes involved in the formation, migration, and evaporation of such layers. Exploratory work on the system nitrogen on tungsten, utilizing ultra-high-vacuum techniques, has revealed two interesting facts: a very high rate of chemisorption, dependent upon the details of surface structure, and a hitherto unexpected complexity in the binding states involved.[1,2] These results suggest the power inherent in these techniques to unravel the details of surface processes,

as well as the limitations connected with attempts to interpret more standard measurements—such as those of isotherms and calorimetric heats of adsorption—and have led us to carry out a detailed study of the chemisorbed state on tungsten.

In the following we shall report upon survey experiments on evaporated films, which indicate certain limitations in this technique and which essentially motivated our own studies, based on refinements of the flash-filament method. After a summary of qualitative observations on the systems nitrogen, oxygen, and hydrogen on tungsten, we consider the quantitative measurement of the desorption of such gases from the chemisorbed state and, for the first of these systems, for which our work has been carried out in considerable detail, we shall examine the implications of our kinetic measurements for the solution of the problems we have listed above.

2. EXPERIMENTAL

(a) *Vacuum Procedures*

(i) *Flash-filament techniques*

A detailed description of the techniques for studying the kinetics of gas adsorption has been given elsewhere.[2] In the present investigation a high-vacuum system similar to that described previously has been employed. Fig. 1 shows our arrangement of traps, ionization gauges, adsorption cell and high-vacuum valve. Prior to a run, the vacuum system is repeatedly baked out, resulting in a final pressure of $\sim 5\times10^{-10}$ mm. Using valve B as a controlled leak, a constant gas flow is then established in the cell with the filament, F, hot enough that no adsorption occurs. On cooling, the filament adsorbs gas and acts as an additional pump in the system, markedly lowering the pressure in the cell. At any given time after cooling, the filament can be rapidly heated by passage of a suitable current through it (flashed), and from the pressure rise in the adsorption cell the total number of molecules adsorbed during the cold interval can be calculated. The number of molecules striking the surface per cm² per min is found from kinetic theory by monitoring the pressure during adsorption. We have used the following gauge constants to convert ion current values (in A) to pressures (in mm): nitrogen, 15 (mm Hg)$^{-1}$; oxygen, 12·7 (mm Hg)$^{-1}$[3]; hydrogen, 8 (mm Hg).$^{-1}$[3] It is the ratio of the rate of change of the number of molecules adsorbed to the number of collisions, the sticking probability, which is the quantity of interest, and from this the detailed kinetics of adsorption as a function of pressure, surface coverage, and temperature can be determined. To discriminate between different states of binding in the adsorbed layer, a knowledge of the amount of gas evolved as a function of the filament temperature during the rapid heating of the latter is desirable. The extensive tabulation by JONES and LANGMUIR[4] of the temperature-dependence of the resistance of tungsten make this a particularly convenient property to use in characterizing the filament temperature during flashing, and the techniques we have employed to extend the flash-filament method in this way will be described separately.

Three different filament samples have been used in this study. All were 0·0254 cm pre-war 218 tungsten wire, from the same spool, aged 6 hr at 2750°K and 15 min at 3000°K. The geometrical surface areas of these samples, obtained by the procedure outlined previously,[2] were as follows: Filament 1, 0·92 cm²; filament 2, 1·54 cm²; and filament 3, 1·26 cm². Qualitative results are also reported for strips of rolled 218 tungsten, of 0·00254 cm thickness, ranging in width from 0·102 to 0·152 cm; these were aged at lower temperatures.

In the early stages of the work, an Applied Physics Corporation vibrating-reed electrometer, Model 30, was used in the determination of the ion currents from the cell, in place of the less-sensitive detector previously employed. The response of this instrument proved to be too slow to follow faithfully the details of gas evolution under all the conditions of flashing, and later measurements have been made, using a Keithley Model 303 d.c. amplifier as a microammeter. For monitoring the pressure during adsorption, the ammeter is used to drive a Speedomax recorder, while during the rapid pressure rise accompanying a flash, the output is displayed on an oscilloscope. The response time of the microammeter is sufficiently rapid over the ranges of interest ($> 1\times10^{-9}$ A) to follow the changes in ion current due to the 120 cycle variations in electron emission of the a.c. heated electron source of the ionization gauge. In order to eliminate this ripple in the ion current, we have operated the electron source filament on batteries, using a regulated power supply to maintain the electron collector and electron source at +170 and +22 V with respect to ground, respectively.

(ii) *Deposition of tungsten films*

The experimental arrangement for studying pressure changes during the deposition of tungsten films differed from that employed in kinetic measurements, and shown in Fig. 1, in that trap I was followed in sequence by a high-vacuum valve, a re-entrant liquid-nitrogen trap, an ionization gauge, and the reaction vessel. The surface onto which evaporation was carried out was 1 in. Pyrex tubing cleaned with sulfuric acid–dichromate solution and thoroughly rinsed with distilled water. Evaporation was carried out from a well-outgassed, 0·0254 cm tungsten filament, 15 cm on a leg, held in 0·203 cm molybdenum clamps which were supported by 0·102 cm tungsten leads, long enough that there was no direct path from filament to ion gauge. The pumping action of the gauge was avoided by operating the grid voltage periodically, and just long enough to record the ion current, about 1 sec being required for a pressure measurement.

Before a run was made, the whole vacuum system was baked out twice at 425°C for 12 hr. Each bake-out was followed by outgassing of the filament for at least 1 hr at

OL.
5
958

FIG. 1. Vacuum system for flash-filament studies. (A) Ionization gauge, used as a trap, (B) Granville-Phillips valve, (C) flash-filament cell, (D, E) ground-glass valves, (F) flash-filament, (G, H) ionization gauges, (I) trap, and (M) cell bypass. In operation, leads L are provided with heavy copper connectors for electrical and thermal contact; cell C is thermostatted in oil bath, A in liquid nitrogen.

[*Facing page* 48

VOL.
5
1958

2600°K and outgassing of the ionization gauge to bright red heat by electron bombardment. Holding the filament at 2000°K to avoid contamination by adsorption of residual gases, the reaction vessel was thermostatted in an ice bath and liquid nitrogen was added to the trap between the valve and the gauge. The pressure was about 5×10^{-10} mm at this time. Deposition of the film was then carried out at the desired evaporation rate. After evaporation the amount of tungsten deposited was determined from the loss in filament weight.

(b) *Techniques of Temperature Measurement*

(i) *Determination of resistance*

The resistance of the filament at any instant during heating has been determined with the impedance bridge shown in Fig. 2, designed by D. S. RODBELL of this

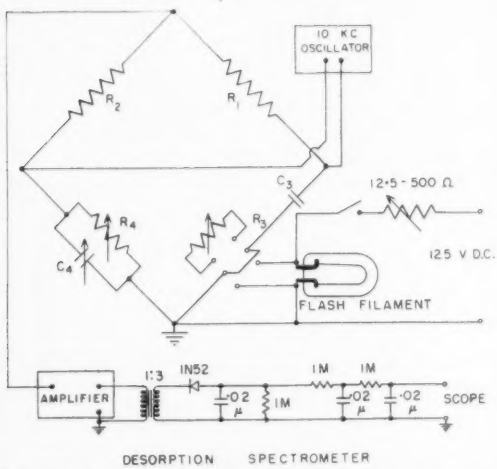

FIG. 2. Schematic diagram of desorption spectrometer. R_1, R_2, R_4 are part of standard impedance bridge: $C_3 = 30\ \mu$F, $C_4 = 0$—$100\ \mu\mu$F.

Laboratory. A somewhat similar circuit which, however, uses the d.c. potential drop developed across the filament during heating to give an oscilloscope deflection proportional to filament resistance, has been previously reported by HAGSTRUM.[5] The measurement of resistance by the latter technique requires, for convenience, that the flash-filament current remain constant during the heating. For large-diameter filaments, such as we have employed, this would entail a d.c. power supply with output voltage considerably in excess of 125 V. In the bridge described by us, the need for a constant heating current is obviated by using a high-frequency signal for the measurement of resistance, and a d.c. current for the actual heating.

In our arrangement the filament used as an adsorption sample forms one arm of a 10 kc impedance bridge; it may be heated with the current obtained by dropping 125 V d.c. through a variable-ballast resistor. The other three arms are part of a Brown Engineering Company Model 200B impedance bridge, the 10 kc signal for which is provided by a Hewlett–Packard Model 200 AB audio-oscillator. C_3 is a 30 μF blocking capacitor to prevent d.c. from passing through the bridge, and C_4 a decade capacitor for balancing. To calibrate the scope deflections R_3, a General Radio Company compensated decade resistor, may be substituted for the filament. The conditions of balance are those of a standard Wien bridge, and operating conditions are such that unbalancing of the bridge, when the filament is flashed, results in a signal proportional to filament resistance. The unbalance signal is amplified by a Hewlett–Packard Model 400D vacuum-tube voltmeter and a pulse transformer, detected, passed through a filter to remove 60 c/s noise, and displayed on one axis of an oscilloscope. The scope deflection is found to vary linearly with the calibration resistance R_3 to within 1 per cent. In determining the change of resistance with the a.c. bridge, a transient is caused by the initial current surge, but is of negligible duration compared to the total time necessary to raise the temperature to 2200°K, and does not affect measurements above 1000°K. It may, however, make it difficult to examine phenomena that occur immediately at the start of heating; wherever this has been desirable, we have used a d.c. bridge circuit, operating on a 250 V supply. The ion current from the gauge in the adsorption cell is amplified and displayed on the other axis of the scope; a Land Camera photograph of a typical trace of pressure versus filament resistance (or temperature) obtained in this fashion is shown in Fig. 6. The maximum pressure rise in the cell upon flashing is proportional to the total number of molecules adsorbed, provided that the conditions have been selected to minimize the various possible clean-up losses, and the difference between this value and the pressure at any temperature gives the number of molecules remaining on the filament at that temperature.

(ii) *Temperature calibration*

Two distinct situations arise in converting the resistance measurements obtained by the bridge technique to a measure of the filament temperature. Above 1000°K, radiation accounts for the major power losses in an electrically heated filament; for the filament in a steady state, i.e. with a temperature distribution unchanging with time, the temperature at the center can be obtained from a knowledge of the heating current, using the tables of JONES and LANGMUIR.[4] The techniques of accomplishing this, as well as for calculating the temperature distribution, are standard and have been discussed in detail.[6] In practice we have measured the unbalance of the bridge (i.e. resistance) corresponding to a range of known heating currents, thus obtaining a direct calibration of the scope deflection in terms of the central filament

temperature, T_m. The precision resistor, R_3, which can be substituted for the filament affords a convenient secondary standard, which permits us to introduce calibration marks directly on to the scope face. All temperature values above 1000°K reported here are based on this calibration of the scope deflection.

The temperature distribution over the length of the filament is established by the competition of conduction through the leads, radiation, and resistive heating; the calibration we employ assumes that the temperature distribution during a flash is actually the same as that in the steady state. However, the relaxation time for conduction through the leads is long compared to the time interval of the flash under the conditions of our experiment. This should result in a more uniform temperature distribution and therefore, also, in an estimated value for T_m higher than the actual one. That such an effect is operative under our experimental conditions has been established by photographing (at

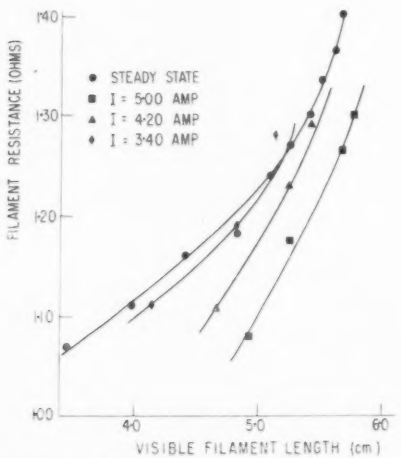

FIG. 3. Effect of heating rate on filament temperature distribution. Visible filament length above ~ 1250°K, at different values of total filament resistance. Distance measured below arbitrary point on filament.

64 frames/sec, 16 mm Tri-X film) the filament both during a flash and during steady heating, and comparing the filament images obtained at the same resistance values. Measurement of the optical density along the filament indicates that, at a fixed total resistance, the temperature distribution is more uniform at higher heating rates than in the steady state, with the central filament temperature correspondingly lowered. This is also shown in Fig. 3. Here are plotted the distance along one leg of the filament, from a fixed mark near the center to the end of the visible photographic image near the lead, corresponding to a given filament resistance, at different rates of heating obtained by varying the heating current. Under our conditions, a temperature of ~ 1250°K is necessary to obtain an image on the film, and thus the visible length gives us a measure of the filament length at a temperature above this minimum. It is apparent that the higher the heating rates the greater is the visible length, but that the difference between the temperature distributions narrows at higher temperatures, and that at the lower heating rates the temperature distribution closely approaches that of the steady state. The absolute value of T_m during a flash, obtained by our technique, may thus be in error; the maximum discrepancy would arise if *no* conduction losses occurred at all during the transient measurements, and would be ~ 130–100°K over the range 1000–2000°K. The actual error under the conditions of our measurements is significantly below this value, inasmuch as we *do* observe cooling at the leads, and can be made arbitrarily small by lowering the rate of heating. Moreover, in the quantitative evaluation of rate phenomena, only a knowledge of the variation of the temperature is required, and it will be shown in Section 3(c)(ii) that the assumption of a steady-state temperature distribution does not cause a significant error.

Below 600°K it is primarily slow heat conduction through the filament and leads which determines the steady-state temperature distribution, and we have therefore made quite the opposite assumption in the temperature calibration for this region: we have assumed that the filament does not suffer *any* end losses during the brief time interval (~ 1 sec) in which the range 100–600°K is traversed during a flash. The temperature values are obtained from the experimentally determined resistance by using the temperature/resistance scales established for an ideal tungsten filament. Below 200°K the electrical conductivity of tungsten may vary owing to imperfections and impurities;[7] we have therefore measured the resistance of the individual filaments, immersed in baths of liquid nitrogen,

VOL.
5
1958

liquid argon, solid carbon dioxide–Freon 11, and ice water, to establish our own resistance scale.

The reciprocal of T_m obtained by these procedures from the resistance/time curve, for filament 3, is shown in Fig. 4 for the range 1250–1700°K. It is of interest that over most of this region the reciprocal temperature can be adequately represented as a linear function of the time of heating, resulting in a considerable simplification in the discussion of rate processes which may occur during the heating of the filament.

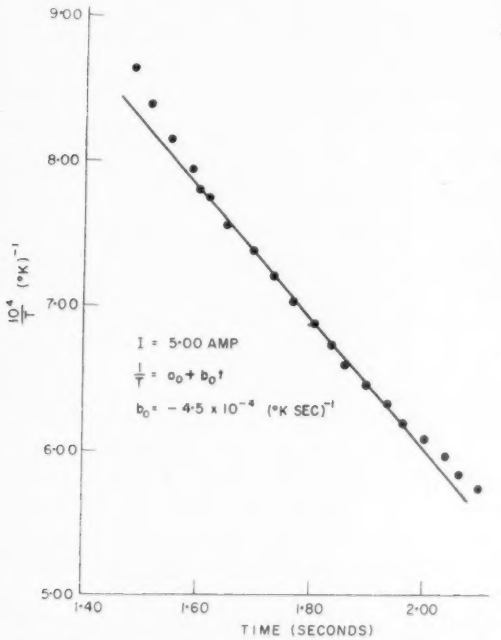

FIG. 4. Reciprocal filament temperature, $1/T_m$, versus time, during flashing.

3. EXPERIMENTAL RESULTS

(a) *The State of Contamination of Evaporated Metal Films*

Recent measurements, both qualitative and quantitative,[2,8,9,10] of the kinetics of chemisorption of gases on clean metals clearly show the high rate at which residual gases may contaminate such a surface, and as a consequence have cast some doubt upon the validity of deducing, from adsorption measurements not carried out under ultra-high-vacuum conditions, a picture of the interaction of a gas with a metal surface. The one, by now classic, technique of investigating such interactions, which has withstood these doubts well, is that of examining fairly large area evaporated metal films. Though in the past the vacuum procedures customary in the implementation of this technique do not appear to have resulted in pressures, prior to deposition, of much below 10^{-6}mm,[11] one could argue that the initial layers of the deposited metal would chemisorb the residual gases in the system, and thus create a gas density low enough to insure the cleanliness of subsequent deposits. Much basic data on the kinetics and energetics of chemisorption have been obtained by this technique, and we therefore felt it desirable to explore both the extent to which these results could be considered reliable and the applicability of this technique, with modern refinements, to the study of gas–metal interactions. We have attempted to accomplish this by observing the variations in pressure during the formation of evaporated films, following procedures analogous to those employed in past studies of adsorption,[11,12,13] though maintaining considerably better vacuum conditions.

In general, evaporated films used in catalytic and

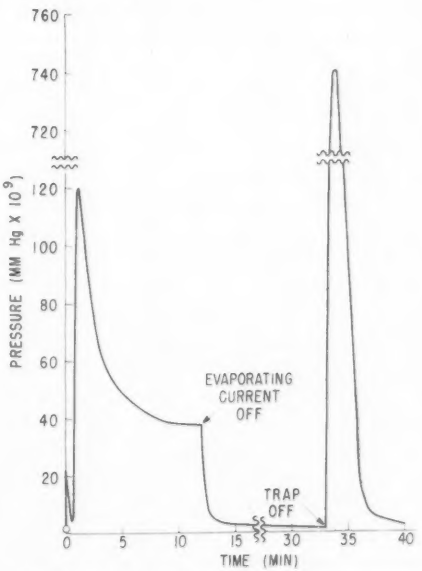

FIG. 5. Pressure change during continuous deposition of evaporated tungsten film. Evaporation rate = 0·33 mg/min.

adsorption work have been deposited by continuous evaporation at the rate of 0·2–0·5 mg/min, the total time of deposition varying with the thickness of film desired. The typical course of the pressure during and after the evaporation of a tungsten filament, at a rate of 0·33 mg/min, in the high-vacuum line described above, is shown in Fig. 5; here the evaporation cell was isolated from the pumps by means of the metal valve. Characteristic of the continuous deposition of tungsten films is the initial sharp increase from the pressure of 5×10^{-10} mm prior to evaporation, followed by a decrease in pressure lasting 35–40 sec and a second pressure peak, an order of magnitude greater, gradually diminishing to a nearly steady value. After cutting off the heating current, the pressure returns slowly to its original value before evaporation; merely lowering the liquid-nitrogen Dewar surrounding the trap situated between the gauge and the valve, a procedure which has sometimes been followed in the preparation of such films,[13] produces an instantaneous pressure burst, roughly six times the peak value during evaporation. Evaporation with the cell connected to the pumps showed the same general features, but the pressure rise on removing the trap proved to be only half as large, the second pressure burst was smaller, and the steady pressure during evaporation also was halved.

Evaporated metal films are widely used in gettering ultra-high-vacuum systems,[14] nevertheless the pressure increases found here indicate that the conditions of the evaporation, which, except for the much greater attention to cleanliness of the system, simulate those customary in adsorption studies, are still inappropriate for the production of clean surfaces. A very different behavior is found, however, when the evaporation is carried out under more stringent conditions. To achieve these, the vacuum system was baked out and outgassed for four cycles and after placing liquid nitrogen around the trap and leaving the valve open to the diffusion pumps, the evaporation of the 0·0254 cm filament was carried out intermittently, in 15 sec bursts separated by 45 sec intervals at 2300°K, at an average deposition rate of 1 mg/min. The initial pressure in the system was 3×10^{-10}mm and at *no* time did it rise above this value; removal of the liquid-nitrogen trap at the end of the run gave a much reduced pressure burst. Inasmuch as the entire operation was carried out at the lower limit of our pressure-measuring devices, we are unable to ascertain if any gettering did actually occur. We can conclude, however, that any gas that may have been evolved during the evaporation was satisfactorily taken up by the film.

The important characteristic of the pressure/time curve during the continuous deposition of tungsten films is the maintenance of an appreciable pressure of gas during the entire course of evaporation; the pressure is not reduced below its starting value, as it would be if the initial layers were gettering the system, but instead rises by several orders of magnitude. It must be noted that detailed studies of the rate of chemisorption of nitrogen, oxygen and carbon monoxide on tungsten filaments indicate that the initial rate of adsorption on a clean surface at room temperature is high, about one out of every five molecules striking the surface actually chemisorbing.[9] A clean surface should thus act as a very effective sink for gas, and this is strikingly illustrated by the very rapid pressure diminution which is found to occur, in the course of a flash-filament run, immediately upon allowing the adsorption sample to cool.[2] These studies also indicate that the rate of adsorption, after an initial plateau, diminishes rapidly, resulting in a gradual rise from the pressure minimum, during a run of the type previously described. The fact that during the continuous deposition of a tungsten film the pressure *rises* indicates that the rate of generation of gas in the system exceeds the rate at which the gas can be eliminated, by adsorption on the glass walls or the metal film, by flow out of the system, or through the occasional pumping action of the ionization gauge. If the clean evaporated layer has approximately the same activity as the filamentary samples, then this pressure rise indicates that, during its formation, the film has been covered with contaminating gas to an extent where the rate of adsorption is so small that the film no longer acts as an effective getter.

The qualitative features of the observed pressure/time curves can be readily explained by assuming that the contaminating gas is driven out of the glass substrate during deposition of the film. The initial pressure burst is presumably due to gases adsorbed on the glass walls which are desorbed on raising the filament to the evaporation temperature, the subsequent pressure decrease, of short

VOL. 5 1958

duration, being due both to clean-up by the deposited film and a reduction in the amount of desorbable gas. Assuming that the tungsten filament is at 3000°K, that the thermal conductivity of Pyrex is 0·002 cal sec^{-1} cm^{-1} $°C^{-1}$, and that the outer surface of the deposition tube is maintained at 0°C by the surrounding bath, the interior of the glass surface would be at a temperature of about 130°C. That large quantities of gas are evolved if 7740 Pyrex is heated above 100°C has been shown by CARTWRIGHT.[15] The second pressure peak during continuous evaporation, whose magnitude has been found to depend on the cleanliness of the glass and the pumping speed of the rest of the system, can thus probably be ascribed to a rise in the glass surface temperature above 100°C. The eventual establishment of a nearly steady pressure, after evaporation has been in progress for some time, is due to competition between the rates of evolution of gas from the glass surface and the pumping speed of the vacuum system and film. Comparison of the final steady pressure in evaporations carried out with the valve open to the diffusion pumps, with the final pressure with the valve closed, shows the importance of the diffusion pumps in reducing contamination. In an isolated system, all evolved gas will have to be removed by the nitrogen trap or the film itself.

It is interesting in this connection, that BEECK showed that in the deposition of nickel films the outer walls of the reaction vessel must be kept in an ice bath to avoid loss of activity of films, presumably due to sintering.[16] RIDEAL and TRAPNELL[17] have suggested that the same effect may be important for evaporated tungsten, where radiation from the evaporating filament may help to bring about sintering. However, studies in the field emission microscope have shown that tungsten does *not* have any appreciable surface mobility at temperatures below 800°K,[18] and that therefore, for tungsten at least, sintering should not occur under the conditions of evaporation. A more likely reason for the loss of activity of tungsten films is the appreciably greater rise of the temperature of the glass substrate if there is no cooling from a constant-temperature bath, resulting in greatly increased evolution of gases which contaminate the evaporated film.

From our observations on the increase in pressure during evaporation, we must conclude that evaporated films, specifically of tungsten, prepared by continuous deposition, do not present surfaces having the same degree of cleanliness which can be achieved on filaments, using current ultra-high-vacuum techniques, and that the interpretation of experiments carried out under these conditions is open to doubt. Moreover, even when the deposition of film *is* carried out under the more rigorous conditions described above, the absence of a noticeable pressure rise does not necessarily ensure a clean surface, since the adsorption of gas on the surface may just balance the rate of gas evolution. The extreme measures which are required to achieve the ultimate of cleanliness in the preparation of such films are well demonstrated by the work of ANDERSON,[19] on the determination of the photoelectric work function of metal films. In view of the difficulty in interpreting much of the past work, as well as in modifying this technique to yield unequivocal results, we have resorted to the flash-filament technique to examine the desorption steps of gases, as reported in the following.

(b) *Qualitative Observations of Binding States on Tungsten by the Flash-Filament Technique*

(i) *Nitrogen*

The general features of the interaction of nitrogen with a tungsten surface have, to a large extent, been presented in previous reports.[2,20,21] Here we wish to record a few additional observations on this system, obtained by the bridge techniques presented above, to serve as an introduction to observations on other gases, as well as to the more detailed considerations of this system which follow.

The three typical regions of desorption of nitrogen from a tungsten filament (number 3) initially at $\sim$ 100°K are shown in Fig. 6. The pressure peaks, in order of increasing temperature of appearance, are designated γ, α, and β. Under the conditions of the experiments, the first stage of desorption, γ, appears complete below 200°K and is followed by a region of constant pressure, terminated by the rise due to α, which (at low coverages) desorbs between 350 and 450°K. The last stage of gas evolution, that of the β-nitrogen, can be observed at high temperatures only and extends from 1350 to 1800°K. There are two important features of the p/T diagram that must be emphasized.

First, the temperature regions are of quantitative significance only in relation to the specific rate at which the sample is being heated. Even if the adsorbed layer on the wire can, at any given temperature, be considered in a steady state with the surrounding gas, so that the rate of adsorption is exactly compensated by that of desorption, the flow of gas into and out of the cell may still affect the shape of the curve, depending upon the heating rate. In particular, pumping out of the cell may reduce the peak height during a slow flash. If a steady state does not prevail, then the pressure in the system, even neglecting gas flow through the cell, is dependent upon the heating schedule, since it will be dictated by the rate of the desorption reaction. This will be considered in more detail in Section 3(c)(i). Second, there are indications of fine structure in the peaks shown here, the nature of which has not been fully clarified. There appears, for example, a break at the foot of the γ-peak (see Fig. 7a) which was previously identified,[20] tentatively, as a separate binding level (δ). This break cannot, however, be reproduced under all experimental conditions, and a final decision on the significance of fine-structure effects of this type must be delayed; for the moment we will consider the gas evolution as occurring in three distinct steps only.

The nature of the γ-, α- and β-peaks has already been discussed, but measurement of the p/T diagrams provides considerable new information. In Fig. 7(a) the details of the evolution of nitrogen adsorbed at $T \sim 100°K$ are isolated, and it is apparent that gas evolution does not commence immediately upon raising the filament temperature. This *suggests* that the adsorbed material in the γ-state is not in equilibrium with the gas and, in conjunction with the low pressure ($\sim 1 \times 10^{-9}$mm) and the relatively high temperature of the adsorption, ascertained by resistance measurements, leads us to surmise that the γ-peak is not due to binding of nitrogen to the tungsten surface by dispersion forces alone, but that *stronger* interactions, possibly involving charge transfer, must be considered. An irreversible adsorption effect very similar to this is observed for the material in the α-state. As previously reported,[2] the nitrogen in α goes through a maximum value as the β-peak rises monotonically. This rise of the α-peak to a maximum is again demonstrated by the sequence in Fig. 8; here we also find, however, that with increasing concentration of β the evolution of α occurs at lower temperatures, indicating that at the higher coverages exchange of molecules between α and the gas phase is occurring at a significant rate at the temperature of adsorption, 200°K. During the initial stages of the adsorption, at low coverages of β, the photographs show that it is the forward reaction that dominates and that little evaporation occurs, confirming our previous conjecture about the initial stages of the α-state. The desorption traces indicate a temperature interval of 900°K between the removal of the α-peak and the onset of evolution of β-nitrogen, and it is this discrepancy in binding energies which affords justification for considering the latter separately, without accounting for the presence of the α, as we shall do in Section 3(c).

p/T curves for nitrogen desorbed from a rolled tungsten strip, which reveal a distinct break in the β-peak, have been shown in a recent preliminary report.[21] From this break as well as from the marked diminution in the amount of material in the α-state on the strip compared with that on a filament, we deduced a dependence of the binding states of nitrogen upon the structure of the surface, supporting other evidence pointing to such an effect. We wish to note here that this break is not necessarily characteristic of rolled strips; of five examined, two did not show such a discontinuity. Moreover two of the strips were photographed during flashing, and found to heat unevenly;* such an effect makes an unequivocal assignment of the origin of the β-break difficult, and a decision must be held in abeyance. However, all of the samples examined did have a very markedly reduced α-peak, and these observations thus do bear evidence of a significant structural effect upon the desorption; a quantitative structural effect for wires will be demonstrated later on.

(ii) *Hydrogen*

The p/T diagram for hydrogen absorbed on tungsten at $\sim$ 100 K (Fig. 9) reveals two interesting features. First, there are two distinct regions over which desorption occurs, which appears to indicate two different types of interaction. This by

*T. A. VANDERSLICE, working in this laboratory, has observed such uneven heating in nickel strips as well.

VOL. 5 195

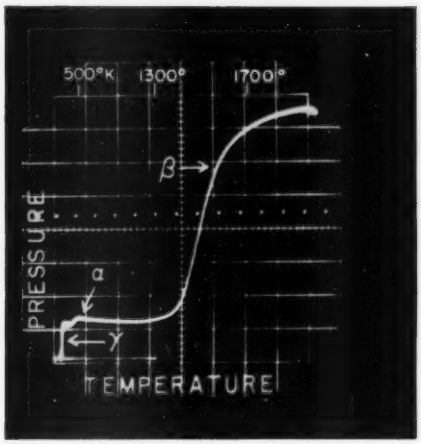

FIG. 6. Desorption of nitrogen from tungsten initially at ~ 100°K. Temperature range: ~ 100–2000°K.

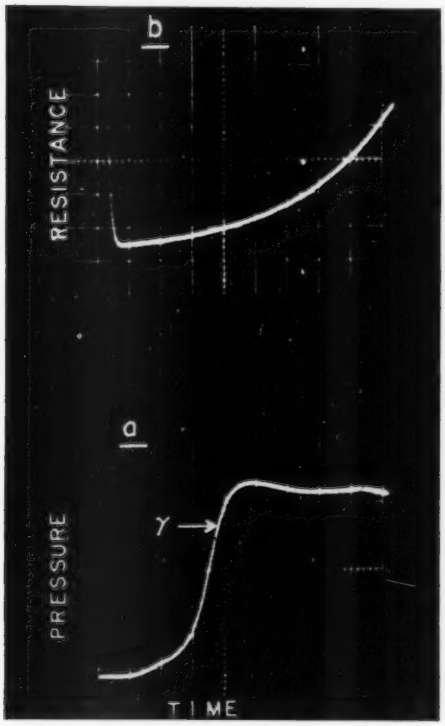

FIG. 7. Desorption of γ-nitrogen from tungsten initially at 100°K. (a) Pressure in flash-filament cell versus time. (b) Filament resistance versus time. Markers = 0·1 Ω. Oscilloscope sweep = 250 msec/cm. Desorption temperature range: ~ 115–180°K.

[*Facing page* 54

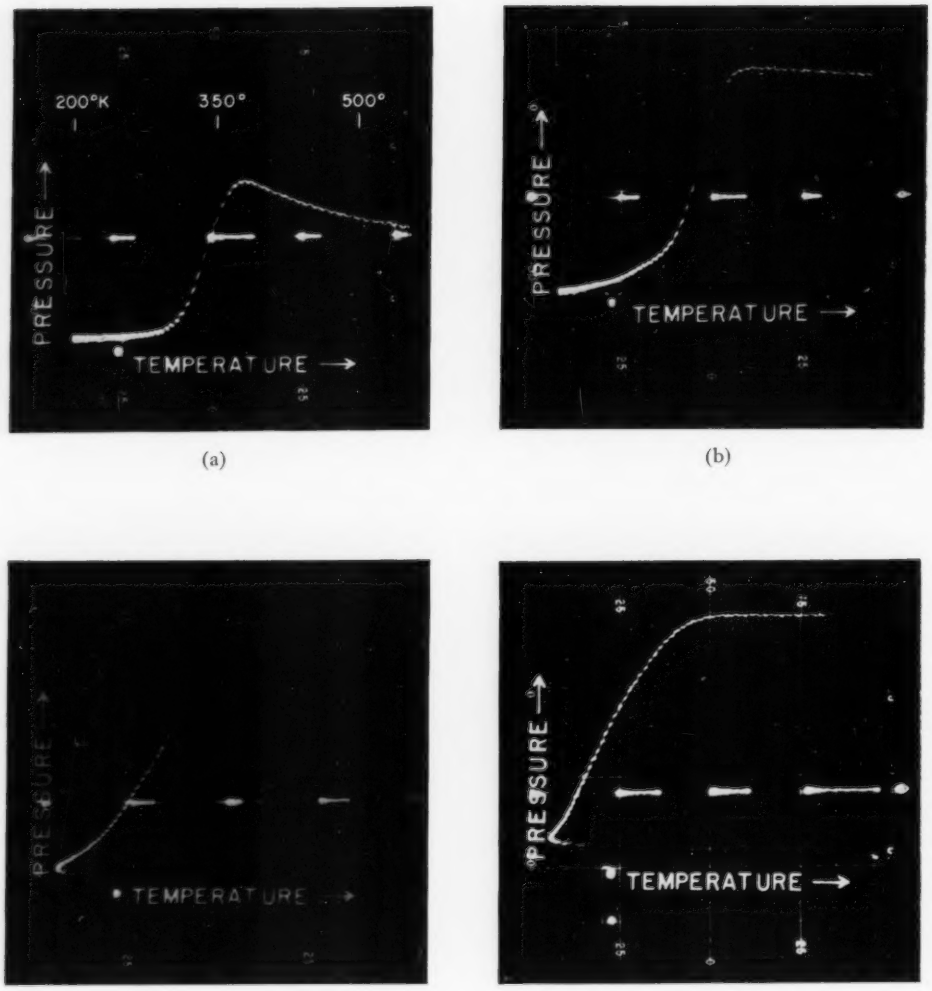

FIG. 8. Dependence of desorption of α-nitrogen from tungsten, initially at 200°K, on population of β-state. Temperature and pressure scales identical throughout sequence. Temperature range: 200–600°K.

(a) $n_\beta = [36 \times 10^{12}$ molecules/cm^2
(b) $n_\beta = 80 \times 10^{12}$ molecules/cm^2
(c) $n_\beta = 100 \times 10^{12}$ molecules/cm^2
(d) $n_\beta = 150 \times 10^{12}$ molecules/cm^2

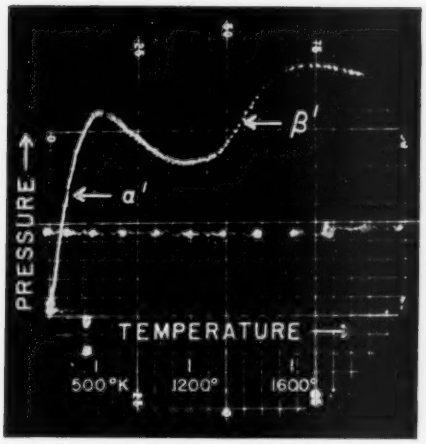

FIG. 9. Desorption of hydrogen from tungsten initially at ~ 100°K. Temperature region: ~ 100–2000°K.

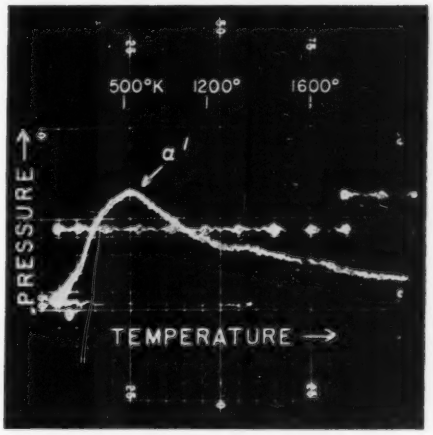

FIG. 13. Desorption of hydrogen from tungsten initially at ~ 100°K. Note absence of β'-peak. Temperature region: ~ 100–2000°K.

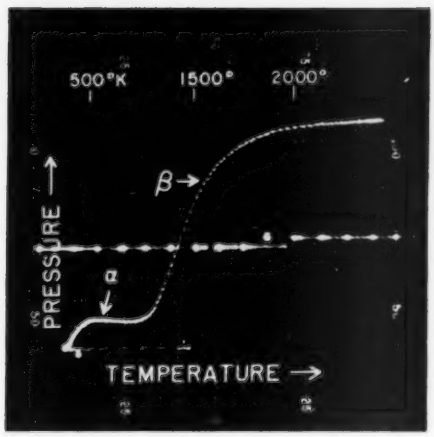

FIG. 14. Desorption of oxygen from tungsten initially at 200°K. Temperature region: 200–2300°K.

VOL.
5
1958

itself is not surprising, as such a possibility was already raised by BLODGETT and LANGMUIR[22] and has often been considered since then in the elucidation of surface catalytic reactions involving hydrogen. However, the more tightly bound state in our experiments appears to accumulate after the formation of the more weakly bound one is substantially

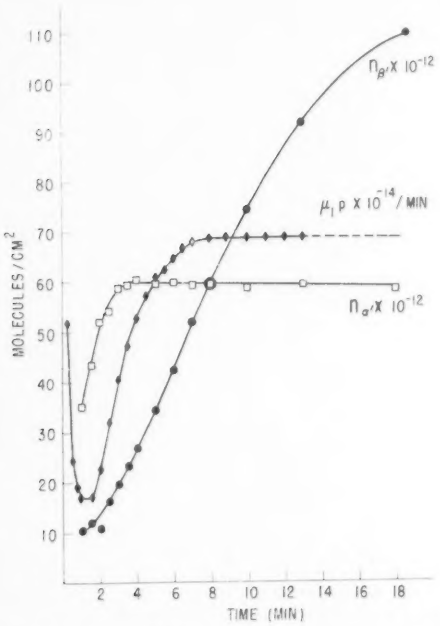

FIG. 10. Adsorption of hydrogen on tungsten at 298°K. $n_{\alpha'}$, $n_{\beta'}$ = number of molecules/cm² adsorbed in state α' and β' respectively. $\mu_1 p$ = number of molecules striking unit filament area per minute. Nominal initial pressure = $3{\cdot}9 \times 10^{-7}$ mm.

completed, as shown in Fig. 10. Second, the evolution of gas occurs as soon as the temperature of the filament is raised above that at which adsorption takes place, indicating that the adsorbed material is exchanging with the gas phase at $\sim$ 100°K. The region of gas evolution for α' extends from $\sim$ 100 to 540°K; that of β' from 1100 to 1700°K; both thus must be bound to the surface by other than van der Waals forces. Actually, it can be shown that the β'-peak is an artifact, which does not directly involve the interaction of molecular hydrogen in the gas phase with the sample surface, but arises as a result of the pressure-measuring device employed, which depends upon a hot tungsten filament as an electron source. Under the conditions of our experiments, this operates at $\sim$2100°K at which temperature molecular hydrogen is appreciably dissociated. That it is the action of this hot filament which is responsible for β' is indicated by the marked decrease in the magnitude of

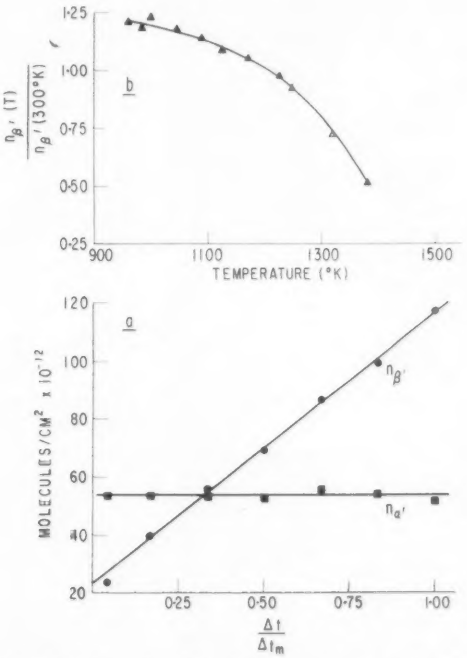

FIG. 11. Adsorption of hydrogen on tungsten. (a) Effect on $n_{\alpha'}$, and $n_{\beta'}$ of operating ionization gauge in cell during a fraction of total adsorption interval. Δt_m = 6 min. Adsorption temperature = 298°K. (b) Effect on $n_{\beta'}$ of increasing filament temperature during adsorption interval. $n_{\beta'}$ (300°K) = 92×10^{12} molecules/cm². Cell temperature = 300°K. Constant gas-flow conditions.

this pressure peak if operation of the ionization gauge is discontinued for part of the interval of adsorption. In Fig. 11(a) is recorded the number of molecules evolved in the high-temperature β'-peak for a fixed adsorption interval, Δt_m = 6 min, with the gauge filament at operating temperature only during the fraction of the total time indicated, and otherwise maintaining the flow of gas the same. The number of molecules adsorbed in state α' remains constant and is unaffected by this change; the number in the β'-peak increases

linearly with the time of operation of the ionization gauge. The intercept of this graph is not zero, since atomic hydrogen is also produced when the flash filament is kept hot during the establishment of the steady pressure prior to the adsorption interval, and can be adsorbed on cooling. This interpretation is buttressed by the data in Table 1, on the effect

Table 1. *Effect of filament equilibration temperature on chemisorption of hydrogen on tungsten*

Equilibration temperature (°K)	$n_{\alpha'} \times 10^{-12}$ (molecules/cm²)	$n_{\beta'} \times 10^{-12}$ (molecules/cm²)
1810	49	93
1880	49	94
1940	49	100
2000	50	110
2075	53	117
2160	52	128

of the equilibration temperature of the filament upon the population in the two states, under otherwise equivalent flashing conditions; the higher the equilibration temperature the higher the nominal initial pressure and the larger the population of β' is found to be, without affecting that in state α'. The production of atomic hydrogen during the establishment of the steady-state pressure with the adsorption sample hot makes the interpretation of the ion current in terms of pressure uncertain, since neither the ionization efficiency for atomic hydrogen nor the exact proportion of it in the gas are known.

The nature of the adsorbed entities in the two states of binding is far from clear at the moment, and on the basis of the data available one can only venture a *tentative* conclusion. The rate of formation of α', the low-temperature form which is characteristic of the interaction of molecular hydrogen with the tungsten surface, diminishes rapidly, and a steady state is reached at the low pressures of these experiments (10^{-7}mm) at a coverage of $\sim 100 \times 10^{12}$ molecules/cm². Measurements, at 298°K, of the steady-state population at different pressures, all taken with atomic hydrogen in the cell as well, seem to indicate, as shown in Fig. 12, that the cover increases linearly with the gas pressure, as would be expected for a molecularly adsorbed layer. For the higher temperature

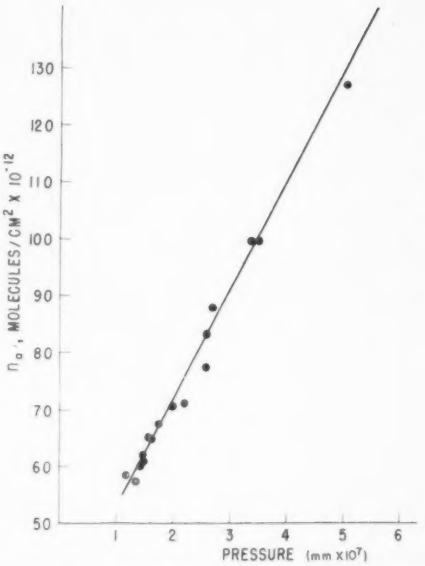

FIG. 12. Adsorption of hydrogen on tungsten initially at 298°K. Increase in $n_{\alpha'}$ with increased pressure in cell just prior to flashing filament.

β'-state, the rate of formation is appreciable over the adsorption intervals of our experiments ($\sim$ 50 min in some cases). Further, it is of interest that the rate of formation does not diminish with increasing filament temperature, as has been found for nitrogen and carbon monoxide on tungsten. As shown in Fig. 11(b) the amount adsorbed during a given time interval, under the same flow conditions actually appears to be higher at 900°K than at 300°K, presumably owing to the absence of competition with the α'-state. Only above 1000°K, just below the temperature range where evolution sets in, does the amount adsorbed diminish. This temperature-dependence of the rate is similar to that for cesium on tungsten observed by TAYLOR and LANGMUIR,[23] and is typical of that to be expected for free radicals. The interpretation closest at hand is that the α'-state exists on the surface in the form of molecules, and does not involve disruption of the bond between the hydrogen atoms. The β'-peak in the desorption, which arises as a result of the presence of atomic hydrogen, would appear to be made up of atomic hydrogen which, when the filament is brought to higher temperatures during flashing, recombines and is evolved

in molecular form. In the past it has generally been taken for granted, from the conversion of *ortho*- to *para*-hydrogen, the H_2–D_2 exchange on tungsten, from measurements of the total amounts adsorbed, and from the values of the heats of adsorption, that hydrogen is dissociated on the metal and exists in the form of adatoms. The interpretation of the data just presented is in conflict with this point of view. The evidence in favor of the dissociation of hydrogen is certainly not conclusive; for example, BLODGETT and LANGMUIR[22] already have pointed out that the surface reactions could be explained without invoking an ad-layer of dissociated hydrogen. The interpretation of α' as a molecularly bound entity does, however, require the existence of some barrier to conversion to the atomic form—without atomic hydrogen produced externally in the gas, the β'-form is not found.

An alternative interpretation of the data would identify the α'-state as typical of hydrogen, and the β'-state as being due to some contaminating impurity, formed by the interaction of atomic hydrogen in the system with the cell itself. BLODGETT and LANGMUIR, in studying the thermal accomodation coefficient of hydrogen on tungsten, report an adsorbed film brought about by the presence of atomic hydrogen, produced by a hot filament in the system. They attribute this to contamination by oxygen or water, resulting from a reaction of the atomic hydrogen with oxides present in the system. This point has not been fully explored as yet, but it has been observed that the rate of diminution of pressure in the cell after a flash is considerably greater with hydrogen than with the other gases, oxygen and nitrogen. Measurements yield a ratio of 3·4 for the pumping speed of hydrogen to that of nitrogen out of the cell under similar conditions. This compares favorably with the value of 3·7 which would be expected for this quantity for the rate of gas removal, if this is limited by collision of hydrogen molecules with the cell interior and if the material measured by the gauge actually were hydrogen. The evidence available seems to point to the first explanation as the more likely; a decision should, however, await further study.

One point that does emerge from these experiments is the ability of hydrogen in the α'-state—presumably formed merely by the interaction of molecular hydrogen with the tungsten surface—to exchange with the gas even at low temperature, $\sim 100°$K. This is quite clearly illustrated in Fig. 13, showing the desorption trace starting at $\sim 100°$K. Although atomic hydrogen is produced in the gas, the β'-state forms only slowly and is initially barely present, yet evolution of the α' occurs as soon as the sample temperature is raised. The presence of β' (that is, possibly contamination) cannot, under these circumstances, be held accountable for this evolution, and this ease of evaporation must be characteristic of hydrogen on tungsten. However, although we are able to detect only a smooth, continuous desorption curve for hydrogen over the low-temperature region and do *not* isolate any breaks, this does not necessarily imply that the α'-peak is characteristic of only a single type of interaction with the tungsten surface. If, during the heating of the filament, the conversion of one type of adsorbed material to another can occur rapidly, a continuous evolution of gas will result; thus, on the basis of the data available at the moment, we cannot establish the nature of the adsorbed species on the surface at 100°K, and it is this information which will be required for the elucidation of exchange reactions involving hydrogen on tungsten.

Although the nature of β' has not been settled, the fact that it is formed from atomic hydrogen only is of interest in connection with the evaluation of previous work on the effect of hydrogen upon the contact potential of metals; with tungsten in particular, the decrease in surface potential of the gas-covered metal below that of a clean surface has been found to be unusually large when determined in the presence of a hot filament.[24] This effect is presumably due to the presence of the β'-state, and not due to the interaction of molecular hydrogen with the surface under investigation.*

(iii) *Oxygen*

The interaction of molecular oxygen with tungsten, already extensively examined in the past, has

* *Note added in proof*: Examination of the nature of the α'- and β'-peaks with an omegatron has now shown that the β'-peak is *not* hydrogen, but appears to be composed chiefly of CO arising from the interaction of atomic hydrogen with the cell. The α' peak is entirely hydrogen during the initial stages of adsorption, thus confirming the second interpretation.

recently undergone closer study by means of the field emission microscope;[25,26] the results obtained by our essentially macroscopic technique appear to provide a very necessary complement to the latter. Though our data must still be considered as *preliminary*, they suffice to show some of the complexity of the system. Fig. 14, giving the desorption trace for oxygen adsorbed on tungsten at 200°K, reveals that for this system also there is a multiplicity of states involved in the binding of the gas, even in the vicinity of room temperature. A low-temperature α-peak is completely desorbed at 500°K; the β-peak, on the other hand, only begins to evaporate, for low coverages at least, at 1300°K. The change in the populations of these states, as well as that in the impingment rate as a function of the time of adsorption, at 298°K, is depicted in Fig. 15(a). For hydrogen, the technique of measuring the pressure has been found to affect the observed adsorption; a similar but more complicated effect appears in the measurements on oxygen, which must be elucidated before interpreting the nature of the states. The effect of varying the time during which the ionization gauge is in operation upon the total peak height of β, keeping the adsorption interval and the flow conditions constant, is shown in Fig. 15(b). The peak height diminishes when the gauge is not operated continuously; the peak does *not* disappear, however, when gauge operation is discontinued even during a long interval of adsorption, and moreover, in contrast to hydrogen, the apparent number chemisorbed is larger if the ionization gauge is operated at the end of an adsorption interval rather than an equal fraction of time at the beginning. Oxygen differs in one more respect from hydrogen; merely shutting off the electrode potentials results in a diminution of the β-peak, a further and more significant decrease resulting from discontinuation of the gauge operation entirely.

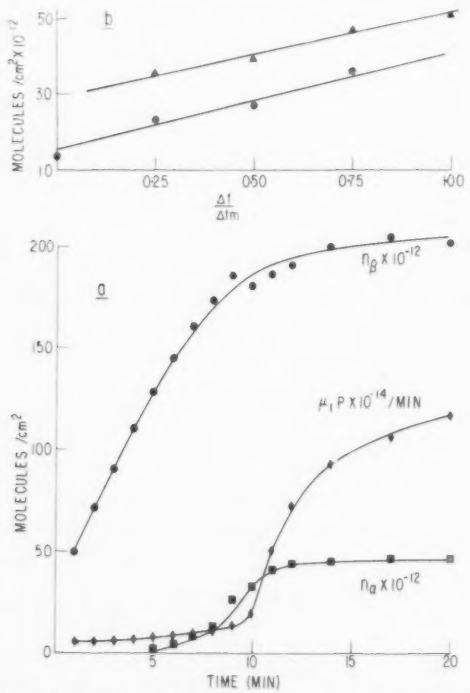

FIG. 15. Chemisorption of oxygen on tungsten at 298°K. (a) n_α, n_β = number of molecules adsorbed in state α and β respectively, $\mu_1 p$ = number of molecules striking unit filament area per minute. Initial pressure = 13×10^{-7} mm. (b) Effect on n_β of operating ionization gauge in cell during adsorption interval; ● = ionization gauge on for initial fraction of adsorption interval; ▲ = gauge on for final fraction of adsorption interval. Δt_m = 8 min.

We conclude from these experiments that although the β-peak is affected by the active species produced by the interaction of the hot ionization-gauge filament with molecular gas, it is characteristic also of the interaction of molecular oxygen itself with a tungsten surface. The α-peak is likewise found whether the ionization gauge is run or not. The exact nature of the active species is not known, but, according to LANGMUIR,[27] atomic oxygen is given off from a hot tungsten wire above 2300°K if it is kept in a dilute atmosphere ($< 10^{-4}$ mm) of oxygen. The material which is evolved in the β-peak when the tungsten wire is heated above 1800°K should, again on the basis of LANGMUIR's deduction, be atomic oxygen, and we must expect that the shape of this peak, i.e. the variation of the pressure in the cell with time during the desorption, should show a marked dependence upon the nature of the gas covering the glass surface of the flash-filament cell. The ionization gauge can follow the gas evolution from the filament only if the desorption from the intervening glass walls is rapid. Moreover, the response of the ionization gauge will depend upon the constitution of the gas evolved; it will differ according as oxygen is evolved as atoms, or molecules, or as a mixture of the two. On a bare Pyrex surface, atomic oxygen

VOL. 5 1958

would have an appreciable lifetime, and we would expect a very slow response of the ionization gauge to the flash. However, on a surface already largely covered with atomic oxygen, recombination, either by diffusion of one adatom toward another, or by impact of a gaseous atom with one adsorbed, would be rapid and so also would be the response of the gauge. Such a mechanism would explain the greater effect of gauge operation upon the β-peak toward the end of the adsorption interval, since the atomic oxygen so formed does not have an opportunity to recombine and therefore is present to effect the rapid recombination of the additional atoms evolved from the sample filament.

Though the interpretation of the gauge effects may be somewhat speculative, two conclusions can be reached from this experimental work. First, a quantitative interpretation of surface studies carried out with oxygen in the presence of hot tungsten electron sources may be deceptive, since the results may be influenced by the presence of atomic oxygen or excited molecular species. This appears to be a particularly serious objection to work carried out by the flash-filament technique, where there appears to be an additional complication introduced by the evolution of oxygen atoms from the sample on flashing. Second, despite this limitation, the technique does afford a qualitatively significant insight into the adsorption processes. Of particular interest is the isolation of the state of low binding energy, α. Such a state was first suggested by LANGMUIR[28] and has since then been detected by ROBERTS,[29] from the change in the thermal accommodation coefficient of neon, as well as in the field emission microscope, by BECKER[25] and MÜLLER.[26] In the past it has been assumed, however, that the formation of such a second layer commences only when the more stable first layer has been completed. Fig. 15a shows that this is not the case and that the α-state assumes a measurable extent even while β is still forming.*

* *Note added in proof*: Further experiments have not substantiated this interpretation of the data. Examination of the gas composition with an omegatron has revealed that both CO and CO_2 are formed by the action of the ionization gauge filament [in agreement with WAGENER J. S. and MARTH P. T. *J. Appl. Phys.* **28,** 1027 (1957)], and that CO is actually the main constituent of both peaks, even if the operation of the electron sources is discontinued.

(c) *Quantitative Determination of Desorption Kinetics*

In the investigation of the interaction between chemisorbed gas and a metal surface, study of the desorption kinetics appears as a powerful tool to elucidate the nature of the state of association of the gas on the surface and the strength of the interaction between gas and substrate, as well as of the interaction between the adsorbed species themselves. However, measurements of the rate of desorption of chemisorbed molecular gas from a metal surface are few, and in the past they have generally been carried out by indirect means. Oxygen has received most attention, the kinetics having been examined by LANGMUIR and VILLARS,[30] using cesium as an indicator in a measurement of thermionic electron emission. BOSWORTH and RIDEAL[31] later carried out a study, measuring the contact potential change during desorption, and JOHNSON and VICK[32] investigated the high-temperature kinetics, following the very fast reaction above 2000°K by the change in thermionic emission from the tungsten wire itself. These investigations all point to a desorption occurring initially at a rate proportional to the concentration of adsorbed oxygen and having an activation energy of approximately 150 kcal/mole. The nature of the desorbing units has not been re-examined in the later work, but LANGMUIR[27] very early reported evidence to show that these were oxygen atoms. BOSWORTH[33] also studied the desorption of nitrogen by the contact-potential method, but his work appears to conflict with later studies. Measurements of this type depend upon a correct evaluation of the effects of the adsorbed layer on the property used to follow desorption. When different states of binding must be taken into account, and one is not dealing with an ideal homogeneous surface, this can be achieved unequivocally only by a separate direct investigation of the adsorption of the gas. The only direct studies of desorption in which gas evolution has been measured, rather than the effect of this evolution on a surface property, are those of LEYPUNSKY,[34] who examined the desorption of hydrogen from various evaporated metal films on which atomic hydrogen had been deposited, and that of BECKER and HARTMAN[8] on the evolution of adsorbed nitrogen from a tungsten strip. Both suggest second-order kinetics, that is, a desorption of molecules by recombination of adatoms. Because of the multiplicity of binding levels involved

in the adsorption of nitrogen on tungsten, and also because of the possibility of a dependence of the kinetics on surface structure, we have carried out a detailed examination of the desorption of β-nitrogen from tungsten wires. The experimental justification for considering the β-state alone has already been presented. Here we shall devote ourselves to a discussion of the detailed interpretation of the pressure/temperature curves and of the procedures for obtaining quantitative data on binding energies and states of binding, as well as to a presentation of the information obtained by these techniques concerning the strongly bound chemisorbed nitrogen layer. Because of the anomalies reported in Section 3(b) (ii) and (iii), the results for oxygen and hydrogen are not yet susceptible to such an analysis.

(i) *Analysis of desorption curves*

At any moment the pressure p_c in a flash-filament cell of volume V and temperature T_c is dictated by the competition between the rate of supply of molecules, by flow from the reservoir, $\mathcal{F}_A$, by desorption from the sample, $\mathcal{F}_F$, and possibly also by desorption from the walls, and the rate at which gas is removed, by adsorption on the sample $(p_c/kT_c)S_F$, by flow out of the cell, by the action of the ionization gauge, and to some extent by adsorption on the cell interior. All these competitive effects must be included in the quantitative statement of the mass balance in the cell,

$$\frac{V}{kT_c}\frac{dp_c}{dt} = \left[\mathcal{F}_F - \frac{p_c}{kT_c}S_F\right] + \left[\mathcal{F}_A - \frac{p_c}{kT_c}S_{w'}\right] \quad (1)$$

in which the rate of loss by other than adsorption on the sample has been grouped together into the last term, $(p_c/kT_c)S_{w'}$.

The first expression in brackets establishes the contribution of the adsorption sample, the second one the contribution from various other extraneous processes; we shall assume that during the desorption, conditions have been adjusted to make the latter effects negligible, or, where this has not been feasible, that the contribution has been kept to a calculable minimum. The procedures for achieving this have already been indicated,[2] and we shall note here only that during the experiments described later $\mathcal{F}_A$ ranged from $1-5\times10^{11}$ molecules/sec, and at maximum, 3 per cent of the total number of molecules evolved was lost in pumping during a flash.

Three distinct situations may be profitably isolated: (1) The rate of desorption is negligible by comparison with that of adsorption. This is the condition under which the rate of chemisorption has been studied and has been reported on in detail elsewhere.[2] (2) The rate of adsorption on the sample at any instant is equal to the rate of desorption. The pressure rise in the system upon increasing the sample temperature is then indicative of the displacement of the steady-state condition; this situation will be important if the rate at which the filament is heated is slow compared with that at which the system can reach a new steady state, that is, essentially the rate at which desorption occurs. (3) The rate of desorption is large by comparison with that of adsorption. This will be the situation of importance if the filament is heated so rapidly that throughout the temperature range the rate of gas evolution is insufficient to restore the balance. The relations involved in analyzing the desorption curves for the two cases relevant to desorption processes, as well as the techniques for distinguishing between the two, are derived below.

(1) *Adsorption = evaporation.* The rate at which molecules are chemisorbed on unit surface (either in the form of undissociated entities or as adatoms) will be written as $v^F = dn/dt = \mu_1 ps$ where p is the pressure in millimeters, $\mu_1 p$ the arrival rate of molecules per unit geometrical area per unit time at the temperature T_c of the cell, and s the sticking coefficient which, for a given surface, is itself a function of the temperature and of the number of molecules already adsorbed. The rate at which the number of molecules per unit area, n, is depleted by desorption is given by

$$v^R = -\frac{dn}{dt} = n^x \nu_x \exp\left(\frac{-\Delta H}{RT}\right). \quad T = \text{constant.} \quad (2)$$

Here x designates the order of the reaction resulting in desorption, ν_x is the pre-exponential factor which includes an appropriate correction for roughness of the surface, and which as a first approximation we assume independent of T, and ΔH denotes the heat of activation for the desorption process, which, for the moment, we consider as independent of n and T. In the steady state, the rate of depletion is balanced by that of adsorption, $v^R = v^F$, and

$$n^x \nu_x \exp\left(\frac{-\Delta H}{RT}\right) = \mu_1 ps. \quad (3)$$

Provided that we confine ourselves to pressures such that p_c, the instantaneous pressure in the cell during a flash, is much larger than p_0, the pressure just prior to flashing, then

$$\frac{n_0-n}{n^x}=\frac{V}{AkT_c s\mu_1}\nu_x \exp\left(\frac{-\Delta H}{RT}\right), \qquad (4)$$

n_0 being the number of molecules per unit area of sample just prior to flashing and A the filament area. Under these conditions the instantaneous pressure in the cell is fixed by the initial concentration of adsorbed species and by the temperature of the filament; the course of the pressure in the cell as a function of the time after flashing is thus dictated solely by the course of the temperature, that is

$$\frac{V}{AkT_c}\frac{dp_c}{dt}=\frac{dn}{dT}\cdot\frac{dT}{dt}.$$

In order to derive a value for x and ΔH from the observed pressure rise, it would be required to have data on the dependence of s upon T and n, obtained from separate experiments. If we can represent s by a function of the form $s=f(n)\exp(-\Delta Ha/RT)$ then a plot of $\ln(n_0-n)f(n)/n^x$ against $1/RT$ should yield a curve with slope $RT/2-\Delta H_A$, where ΔH_A is the heat of adsorption per mole of chemisorbed material and thus permits determination of both parameters of interest.

(2) *Evaporation* $\gg$ *adsorption.* Again restricting ourselves to the pressure range $p_c \gg p_0$, we have, at any instant,

$$-\frac{dn}{dt}=n^x\nu_x \exp\left(\frac{-\Delta H}{RT}\right). \qquad (5)$$

During gas evolution, the temperature of the sample is continuously changing, so that the surface concentration at a time t after starting the heating cannot be obtained by the ordinary procedures of chemical kinetics. If, however, the reciprocal temperature can be adequately represented as a function of the time t by $1/T=a_0+b_0t$ then

$$-\int_{n_0}^{n}\frac{dn}{n^x}=\nu_x \exp\left(\frac{-\Delta Ha_0}{R}\right)\int_{t_0}^{t}\exp\left(\frac{-\Delta Hb_0t}{R}\right)dt$$
$$=\frac{\nu_x R}{(-\Delta Hb_0)}\epsilon \exp\left(\frac{-\Delta H}{RT}\right) \qquad (6)$$

where

$$\epsilon=\left[1-\exp\left\{\frac{\Delta H}{R}\left(\frac{1}{T}-\frac{1}{T_0}\right)\right\}\right]$$

and t_0 denotes the time necessary to reach the temperature T_0 at which desorption is first detected. Depending upon the order of the desorption reaction, the integral of the concentration-dependence becomes

$$-\int_{n_0}^{n}\frac{dn}{n^x}=\begin{cases}\ln\dfrac{n_0}{n} & x=1\\[2ex] \dfrac{n_0-n}{nn_0} & x=2.\end{cases} \qquad (7)$$

The pressure in the cell at any instant now depends upon the initial concentration, n_0, upon the temperature at the chosen instant, and upon the way in which the filament has been brought to this temperature. The surface concentration (in terms of molecules/cm^2), n, at a fixed temperature will be smaller the slower the rate of heating, that is, the smaller $(-b_0)$; conversely the number that have appeared in the gas, $A(n_0-n)$, will be the greater.

Under these conditions the order of the desorption reaction as well as its activation energy can be determined from a logarithmic plot of either $(n_0-n)/\epsilon nn_0$ or $1/\epsilon\ln n_0/n$ against $1/RT$. A straight line having the slope $-\Delta H$ will be obtained for the plot of the correct concentration-dependence. The correction factor, ϵ, itself depends upon ΔH but, for a temperature range from 1000 to 2000°K and a heat of the order of 50 kcal/mole, it is small and can be conveniently accounted for by successive approximation.

For a given desorption curve, a distinction between subsections (i)(1) and (i)(2) can be readily achieved byrepeating the desorption at a different heating rate. If a steady state is achieved in the gas evolution, that is if the situation described under subsection (i)(1) is applicable, the quantity $(n_0-n)/n^x$ is fixed for a fixed temperature and should be independent of the rate of heating of the filament. A dependence of $(n_0-n)/n^x$ upon the rate of heating does not, however, establish that desorption predominates to such an extent that the reverse process can be neglected; that is, it does not establish the validity of the assumptions entering into (i)(2). It follows from equation (6) that at a fixed temperature T,

$$x=2,\quad \frac{d\left[\dfrac{n_0-n}{nn_0}\right]_{T=\text{const.}}}{d(-1/b_0)}=\frac{\nu_x R}{\Delta H}\epsilon \exp\left(\frac{-\Delta H}{RT}\right),$$
$$x=1,\quad \frac{d\left[\ln\dfrac{n_0}{n}\right]_{T=\text{const.}}}{d(-1/b_0)} \qquad (8)$$

and that the concentration term at a given temperature should be linear in the time necessary to reach that temperature, or inversely proportional to the heating rate, $(-b_0)$, and it is this test which must be met to establish that the desorption does indeed follow the assumptions made under subsection (i)(2).

(3) *The effect of the temperature distribution along the filament*. The analysis of the pressure/temperature curves has so far been carried out on the assumption that the entire sample is at a uniform temperature during the desorption. That this is not the case, and that the leads cool the filament and therefore diminish the rate of evaporation in their vicinity is well known. We shall limit ourselves here to the effect of this temperature distribution upon the considerations of the preceding paragraph.

If the rearrangement of the adsorbed entities as a result of the temperature gradient can be neglected, then the rate of evaporation from such a filament, with the central portion at temperature T_m, will differ from that of an ideal filament, having the same specifications, but without any end-losses through the leads, being smaller by a factor ϕ. Instead of using equation (2) we must represent the instantaneous rate of desorption from the filament by

$$-\frac{dn}{n^x}=\phi\nu_x \exp\left(\frac{-\Delta H}{RT}\right)dt. \qquad (9)$$

If ϕ can be adequately represented as a linear function of the reciprocal temperature, i.e. if we are justified in writing

$$\phi=\phi_0+\frac{1}{T}\phi_1,$$

then equation (9) can be integrated on the same assumptions entering equation (6) to yield

$$-\int_{n_0}^{n}\frac{dn}{n^x}=\frac{\nu_x R\,\Sigma}{(-\Delta H b_0)}\exp\left(-\frac{\Delta H}{RT}\right) \qquad (10)$$

where

$$\Sigma=\epsilon\left(\phi+\phi_1\frac{R}{\Delta H}\right)+[\phi(T)-\phi(T_0)](1-\epsilon).$$

The kinetic parameters of interest can therefore be obtained by the procedures already outlined, with the substitution of the correction term Σ for the ϵ of equation (6). The factor ϕ depends upon the particular temperature distribution existing over the filament; for the steady-state distribution ϕ can be evaluated by standard procedures.[9] For the filament lengths involved in our experiments, and heats of desorption of the order of 70 kcal mole, the steady-state value of ϕ varies between one-half and four-fifths over the range $1300°<T<1900°$ K.

(ii) *The kinetics of the desorption of β-nitrogen*

(1) *The order of the desorption kinetics*. The nature of the processes which dictate the shape of the pressure/temperature diagrams for the β-state of nitrogen is immediately revealed by obtaining a family of curves at different heating rates. In Fig. 16 are shown the number of molecules per unit area evolved up to the temperature T, for different rates of heating the sample (filament number 3). It is apparent that fixing the temperature does *not*

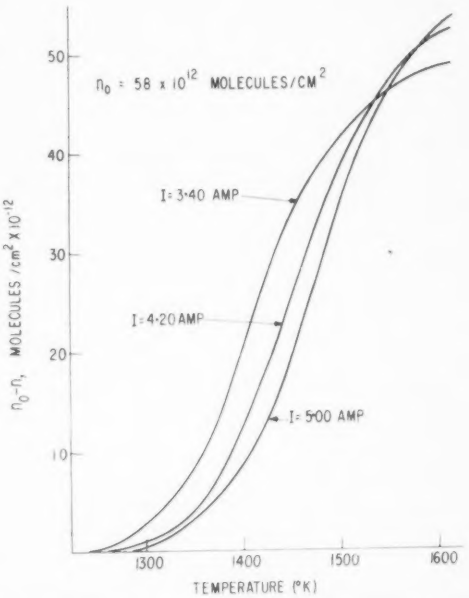

FIG. 16. Effect of rate of heating of filament on desorption of β-nitrogen from tungsten.

fix the population of adsorbed entities or the number already evolved; the smaller the rate of heating (that is the smaller the heating current), the greater the number of adsorbed entities given off at the lower temperatures. Clearly the steady-state approximation [subsection (i)(1)] does not apply to these systems, and for the elucidation of the kinetics the heating curve of the filament is required in order to accomplish the integration of the rate equations. As was shown in Fig. 4, the reciprocal of the absolute temperature [obtained from resistance measurements by the technique described in Section 2(b)(ii)] is linear in time over the temperature region of the desorption (1300–1750°K), and the technique of approximating the temperature integrals given above appears applicable. In Fig. 17 we have plotted the data from a typical desorption curve according to both a first- and a second-order law; we can tentatively conclude from the fact that only the latter gives a satisfactory straight line, that the desorption of chemisorbed

nitrogen involves the collision of two adatoms with one another and their desorption as a molecule. That this tentative conclusion is not obviated by the participation of the competing process, namely adsorption, is indicated by the linearity of the plot of $(n_0-n)/n\epsilon$ at various fixed temperatures, against the time of reaching these temperatures, shown in Fig. 18, following the argument leading to equation (8).

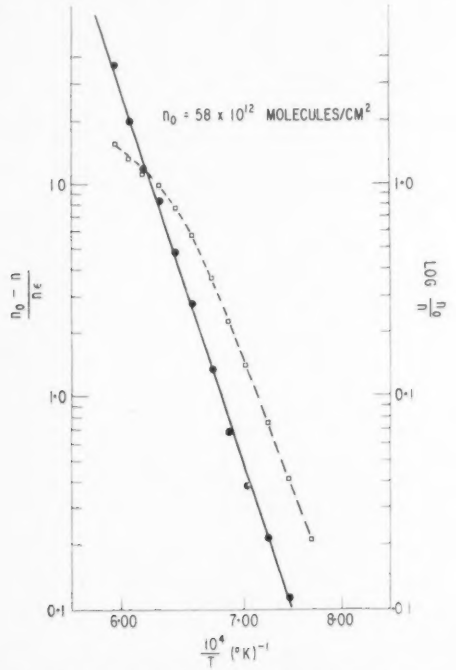

FIG. 17. Analysis of pressure/temperature curves for β-nitrogen according to first-order (□) and second-order (●) kinetics.

There remains still a question which has so far been ignored: is it conceivable that ΔH, the heat of desorption, depends upon the concentration of adsorbed nitrogen and that the method of analysis used here is inapplicable? In a plot of the type shown in Fig. 17, the concentration on the sample filament is continually decreasing as higher temperatures are reached. This would mean that if ΔH increased with decreasing concentration, as may be possible, the magnitude of the integral

$$\int_{t_0}^{t} \exp\left(\frac{-\Delta H}{RT}\right) dt$$

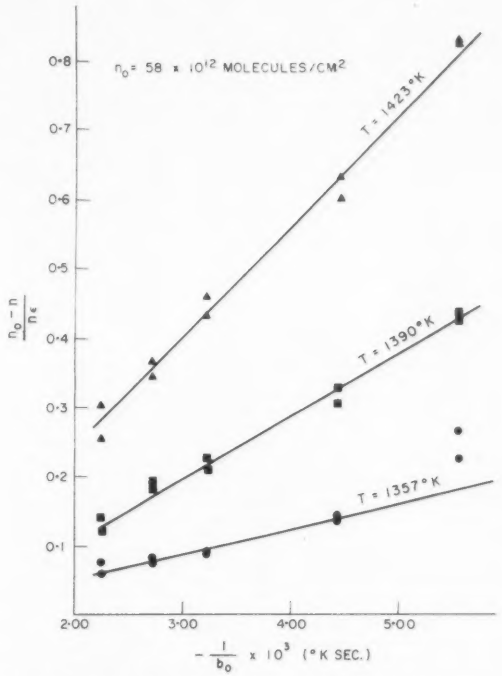

FIG. 18. Dependence of integrated expression for second-order desorption kinetics on the rate of heating of the filament, at constant temperature

$(-b_0) = [-0{\cdot}66\times10^{-4}+2{\cdot}06\times10^{-5}I^2\ (\mathrm{A})]\ (^\circ\mathrm{K\ sec})^{-1}$.

would be diminished below that indicated on the graph at low concentrations (that is, low values of $1/T$). The fact that a straight line would not obtain does not allow a decision here, inasmuch as this criterion was established on the assumption that $\Delta H \neq \Delta H(n)$. However, if the desorption is plotted for increasing initial concentrations of nitrogen, we find, as shown in Fig. 19, that straight lines are obtained for each value of n_0, and that these are parallel to each other if the data are represented as a second-order desorption. A given temperature now corresponds to quite a different value of n on different curves, and for a concentration-dependent heat of desorption, parallel lines could not be expected.

The criterion for the insignificance of the adsorption reaction given by equation (8) was also derived on the assumption of a constant ΔH. That there is no complication due to this follows

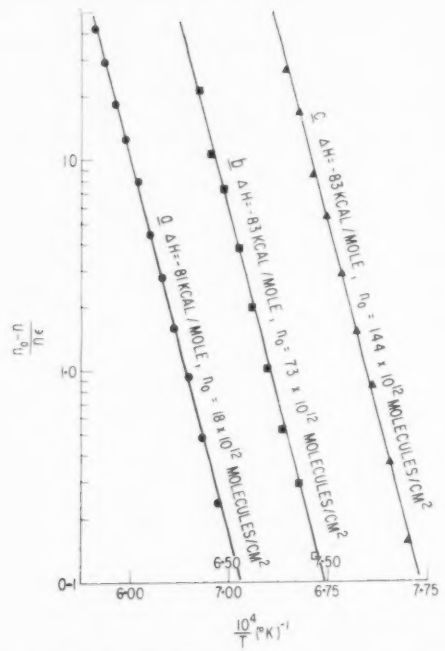

FIG. 19. The heat of desorption of nitrogen from tungsten at different initial coverages.

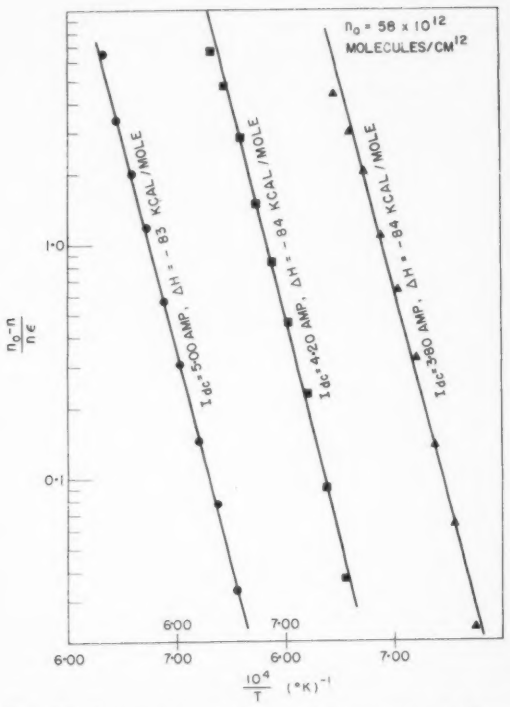

FIG. 20. Comparison of the heat of desorption of nitrogen from tungsten at different filament heating rates and identical coverage.

from the curves in Fig. 20, obtained at an intermediate coverage but over a range of heating rates, which should favor the reverse reaction. These curves still have the same slope as their counterparts at higher ($-b_0$) and indicate as good a fit to a second-order desorption. They also establish the justification for the temperature scale used here. As pointed out in Section 2(b)(ii), the instantaneous resistance values were converted to a temperature corresponding to that of the central portion of the filament, on the assumption that the temperature distribution over the filament during a flash can be approximated by that existing when the filament is in a steady state with respect to temperature. As shown in that section, there are discrepancies in these two distributions, but they diminish as the heating rate of the filament is lowered. The agreement of the two sets of curves, obtained at different heating rates, establishes that this error in determining the temperature has no significant effect on the evaluation of the desorption parameters. Moreover, if the instantaneous temperature distribution over the filament does approach the steady-state distribution, then it is possible to correct the desorption kinetics for the temperature variation as outlined in Section 2(b)(ii). When these corrections are made, however, the fit of the straight lines, and their slopes, are *not* affected. We conclude therefore that under the conditions of these experiments the evolution of β-nitrogen is dictated by the desorption reaction only, and that this can be satisfactorily represented by a second-order rate law with a constant heat of desorption.

(2) *The rate law and its dependence upon structure*. The variation of the slope of the desorption plot with the concentration of adsorbed nitrogen, n, is shown in Fig. 21a. The heat of desorption is seen to be essentially independent of cover within the limit of error of the measurements, ± 4 kcal/mole, having a value of 81 kcal/mole up to $n_\beta = 150 \times 10^{12}$ molecules/cm^2. The second-order

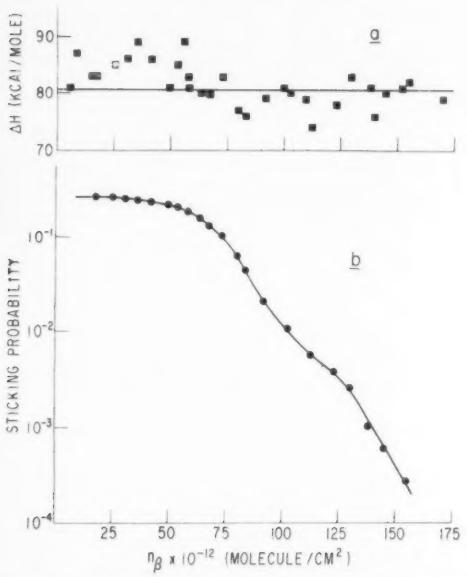

FIG. 21. (a) Dependence of heat of desorption of nitrogen from tungsten on coverage (n_β). (b) Dependence of sticking probability, s, of nitrogen in state β on coverage.

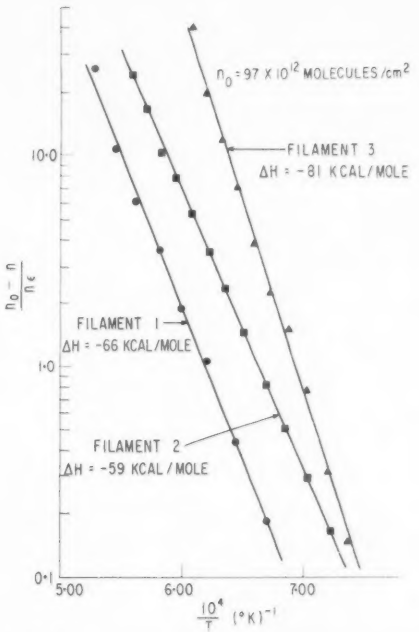

FIG. 22. Structure sensitivity of desorption. Comparison of second-order desorption plots for three different filaments.

rate constant, k_2, can be evaluated from equation (6) by substituting the experimentally determined heat of desorption ΔH and the heating rate, b_0, and is found to be $k_2 = 0{\cdot}2\ \exp(-81{\cdot}10^3/RT)$ molecules^{-1}cm^{2}sec^{-1}. This is appreciably different from the value $k_2 = 2{\cdot}4 \times 10^{-4}\ \exp(-71{\cdot}10^3/RT)$ molecules^{-1}cm^{2}sec^{-1} deduced by us[2] from the work of BECKER and HARTMAN[8] which was carried out on a rolled tungsten strip. The figure for the heat of desorption obtained from their variation in the isothermal rate of nitrogen evolution with temperature, 71 kcal/mole, in turn was markedly lower than the value of 95 kcal/mole for the calorimetrically determined differential heat of adsorption of nitrogen on a tungsten film as reported by BEECK,[16] and suggested a possible dependence of the heat term upon the particular surface under investigation. To establish whether these differences could be due entirely to differences in techniques and conditions, we have examined a number of tungsten samples, and in Fig. 22 are compared the desorption plots for the three wire specimens described above, taken at comparable coverages. Although the data points for the individual samples are well respresented by a second-order desorption curve, the slopes of these curves differ significantly. Only filament 2 has been examined in the rigorous detail described for 3, but the fit of the simple second-order desorption equation can be taken as an indication that desorption here is also overwhelmingly responsible for the shape of the pressure curves. The quantitative information obtained from these measurements on the kinetics of the desorption of the β-state of nitrogen is summarized in Table 2.

It is significant that we find here a striking variation both in the rate of chemisorption, that is in the sticking coefficient s, and in the kinetics of the desorption step, which can be ascribed to differences in the surface structure of the sample. It should be noted that an effect of the surface structure upon the heat of desorption of oxygen from tungsten somewhat similar to our findings for nitrogen, has already been reported by JOHNSON and VICK.[32] The details of this dependence upon structure and its implications will be discussed later. Our measurements completely confirm our

Table 2. Variation of rate constants for the desorption of nitrogen from tungsten

Filament number	Second-order rate constant, k_2 (molecules^{-1}cm^{2}sec^{-1})	Concentration range ($n \times 10^{-12}$)	Sticking coeff., s, for $T = 300°K$, $n = 0$
1	$8 \times 10^{-5} \exp\left(\frac{-67 \times 10^3}{RT}\right)$	40–120	0·12
2	$2 \times 10^{-5} \exp\left(\frac{-59 \times 10^3}{RT}\right)$	30–150	0·12
3	$2 \times 10^{-4} \exp\left(\frac{-81 \times 10^3}{RT}\right)$	10–150	0·26

earlier conclusion that nitrogen chemisorbed on tungsten in the β-state is dissociated into atoms and is evolved as molecules in a second-order reaction. They also confirm our suggestion that the break in the sticking coefficient (see Fig. 21b) is not to be associated with the filling up of all available binding sites on the bare metal, but rather is to be taken as a qualitative indication of the filling up of the more reactive ledge sites.[1] Confirmation of our conclusions on the dependence of heats of desorption upon surface structure through calorimetric measurements still appears desirable.

4. DISCUSSION

The studies on the evaporation of diatomic gases from a tungsten surface which have been presented above are of interest in that they reveal an unexpected complexity in the interaction between the absorbed gas and the metal interface, as well as a marked dependence upon the surface structure of the metal. Only for the desorption of nitrogen from tungsten are the data sufficiently detailed and the experiments decisive enough to warrant a detailed analysis, and it is this system that we shall consider, confining ourselves to a discussion of the strongly chemisorbed nitrogen, the β-state. The effects found here have a bearing, however, upon three interrelated problems that have been of concern in the past: (1) the action of surface structure upon adsorption, (2) the physical basis for the dependence of the heat of adsorption upon the amount adsorbed, and (3) the correlation between band structure of the adsorbent and surface properties. We shall examine these in relation to our own experimental findings. Fundamental to this is, of course, an understanding of the processes which lead to evaporation, and it is to a phenomenological discussion of these that we shall first address ourselves.

(a) *The Mechanism of Desorption*

(i) *Formulation of the rate law*

The desorption of nitrogen has been found to obey a rate law of the second order with respect to the amount of material adsorbed, indicating that in the β-state nitrogen is dissociated and exists as adatoms on the surface and that the limiting step in the evolution is the interaction of two such energetic adatoms with one another. The rate of production of molecules per unit area by such a second-order process can be formally related to the properties of the adsorbed entities in terms of the transition-state method through the expression

$$-\frac{dn}{dt} = N^2 \frac{kT}{h} \frac{F^*}{F^2} \qquad (11)$$

in which F and F^* are, respectively, the complete partition function per unit area of the adsorbed atoms, and the partition function of the activated complex with one degree of freedom factored out, both referred to the same energy zero. We have designated the concentration of adatoms by N. If, as is customary, we refer the energies to the zero

point level of the individual entities involved, this expression is modified by the introduction of a Boltzmann factor $\exp[-(2\chi-\chi^*)/kT]$, χ being the heat of desorption (at $T = 0°K$) of a single adatom and χ^* the corresponding quantity for the desorption of a "molecule" in the activated state to atoms at infinity. Three different modes by which desorption may occur by a second-order reaction in a very dilute adsorbed film can be conveniently classified by comparing χ and χ^* with the other relevant energy parameters of the adsorbed material, the activation energy for adsorption, E, for dissociation of the molecule in the gas phase, D, and for surface diffusion, E_s.

If the condition $2\chi < D$ is met, adsorption is endothermic, and the adsorbed material is unstable with respect to the molecular gas; the adatoms are then to be found on the surface only because they are essentially frozen in place and the activation energy for desorption as molecules, $(2\chi-\chi^*)$, should thus equal that for surface diffusion, E_s. This mechanism for the evolution of adsorbed atoms is, under some conditions, operative in the recombination of atoms and free radicals at metal surfaces[34] and will be discussed in detail with respect to this problem in a separate report. For exothermic adsorption, that is, if $2\chi > D$, we may have desorption occurring by collision of adjacent, essentially localized adatoms, if $2\chi-\chi^* < E_s$, and also through the interaction of atoms moving more or less freely over the surface if $2\chi-\chi^* > E_s$, that is, if the activation energy for the desorption as a molecule exceeds that for the migration of the adatoms. Limitation of the desorption step by the rate of surface diffusion can be easily recognized, since this situation will occur only if adatoms are unstable with respect to the gaseous molecules. It will thus not be important for a film of adatoms which has been formed by adsorption from the molecular gas. The extent to which diffusion of adatoms is significant in the desorption of a gas for which $2\chi > D$ is more difficult to discern; the limited experimental data on surface diffusion of adatoms over a metal surface does, however, point to an activation energy $E_s \ll \chi$. It should be observed that if the activation energy for surface diffusion exceeds that for the desorption of a pair of adjacent atoms in the form of a molecule, the latter process will presumably occur at lower temperatures and will result in the elimination of any such pairs from the surface. The rate of this elimination would be proportional to the number of pairs which, for a dilute layer formed from the molecular gas, implies a first-order desorption reaction rather than one of the second order. If the disparity between the barrier to diffusion and to evaporation (as molecules) is sufficiently large, then isolated atoms will be found only if they have been deposited from a beam of atoms, and not from a molecular gas. Moreover, for the former, after the removal of any pairs that *may* have resulted, the remaining isolated atoms will be frozen on the surface, and will be eliminated as molecules only at a higher temperature by a second-order reaction that is diffusion-controlled, just as for the endothermic adsorption considered already. For a dilute adsorbed layer formed on the metal from a molecular gas, for which the evolution follows a second-order rate law, we would thus expect the participating adatoms to have considerable mobility.

Although an exact evaluation of the partition functions which define these possible desorption mechanisms is quite beyond our scope at the moment, we can achieve considerable insight into the contribution of the processes described by considering an idealized model both for the surface and for the interactions with the adatoms and complexes. We assume that desorption occurs from a single perfect crystal plane and that the concentration of adsorbed species is small compared to the number of atom sites, N_s. In order to account for the possible localization of adatoms around sites of minimum potential energy, we assume that the surface is simple cubic with a lattice spacing equal to d, and that in the two principal directions parallel to the surface the binding energy varies sinusoidally with the distance between the potential minima, separated from one another by a barrier of height E_s. Furthermore, we represent the activated complex as a molecule having a single degree of rotation (with a moment I) around an axis perpendicular to the surface, whose translatory motion is inhibited in a manner similar to that of the adatoms by the periodic variation of the binding energy over the surface. The decomposition co-ordinate is assumed to be the internuclear distance between the two adatoms in the complex. Under these special assumptions, the partition function F can be written as:[35]

$$F = \frac{2\pi^2 N_s u \exp(-2u) I_0^2(u)}{[1-\exp(-\kappa u)]^2} j_n$$
$$u = E_s/2kT, \quad \kappa = \left(\frac{2h^2}{md^2 E_s}\right)^{\frac{1}{2}} \tag{12}$$

where $I_0(u)$ is a modified Bessel function of the first kind and j_n represents the contribution of internal degrees of freedom to the partition function. The partition function for the activated complex would differ from this both through a different potential, E_s^*, and mass, $2m$, as well as by the introduction of a multiplicative factor for the rotational contribution, $(\pi/h)(2\pi IkT)^{\frac{1}{2}}$. The form of the partition function F is such as to formally encompass both a mobile and a localized adsorbed state. If the barrier to surface diffusion, E_s, is large compared to $2kT$, we have

$$\lim_{u\to\infty} F = \frac{N_s}{[1-\exp(-\kappa u)]^2} j_n. \tag{13}$$

In the opposite situation of a small barrier

$$\lim_{u\to 0} F = \frac{1}{\Lambda^2} j_n \quad \Lambda = h(2\pi mkT)^{-\frac{1}{2}}. \tag{14}$$

For a second-order desorption reaction from a layer of completely mobile adatoms, which appears as a convenient model for the interpretation of the data on nitrogen, the rate expression becomes

$$-\frac{dn}{dt} = N^2 r_0 \left(\frac{\pi kT}{m}\right)^{\frac{1}{2}} \exp -\left(\frac{2\chi-\chi^*}{kT}\right) \tag{15}$$

in which r_0 denotes the internuclear distance of the activated complex. If we identify r_0 as a hard-sphere-collision diameter, this expression is identical to the one obtained by treating the adatoms as forming a simple two-dimensional gas, and assuming that the collision of two such atoms having a relative translation energy along the line of centers in excess of $2\chi-\chi^*$ results in the desorption of a molecule. On this model, and for a collision diameter $r_0 \sim 1$Å, the pre-exponential for the desorption of nitrogen has a value of 8×10^{-3} molecules^{-1}cm^{2}sec^{-1}.

So far, we have assumed that desorption occurs entirely through the evolution of molecules; actually there is a finite probability for the evolution of atoms as well. The ratio of the rate of desorption of molecules to that for atoms is given by $N_A(\nu_M/\nu_A)\exp[-(\chi-D)/kT]$, the subscripts M and A designating the quantities appropriate to molecules and atoms, respectively. The term $N_A(\nu_M/\nu_A)$ is of the order of unity, and thus the values of the dissociation energy and the binding energy suffice to establish that, for nitrogen, molecular evolution overwhelmingly predominates in the temperature range of interest to us. The most severe assumption entering into the quantitative discussion has been the idealization of our surface as a single perfect crystal plane. That this is not a justifiable assumption should be apparent from any number of facts at our disposal: from a microscopic examination of the surface, from the well-established variation of thermionic-emission properties, even of single-crystal specimens, with the crystal orientation, as well as from the differences in the rates of adsorption and desorption for different wire samples, reported above. It is thus desirable to examine how the presence of such heterogeneities can be accounted for in the formulation of the rate law.

(ii) *The effect of heterogeneities upon the desorption process*

We can describe an actual surface as consisting of i patches, each uniform throughout but differing in its properties from those of the other patches constituting the whole. If we designate the total partition function for the adatom, taken over the entire available area A_i of patch i by f_i, then the rate of desorption for unit area of a given patch i considered as isolated from all others, is given by

$$\nu^R{}_i = \frac{kT}{h}\frac{f_i^*}{A_i}\left(\frac{N_i}{f_i}\right)^2 \tag{16}$$

where N_i is the total number of adatoms in the area A_i of the patch. The total rate of desorption from unit area of the actual surface will be the sum of the rates from the individual patches, that is $\nu^R = \Sigma \nu^R{}_i A_i$ and substituting from equation (16) this becomes

$$\nu^R = \frac{kT}{h}\sum_i f_i^*\left(\frac{N_i}{f_i}\right)^2. \tag{17}$$

We now *further* assume that during the evaporation process equilibrium is maintained at all times between the adatoms on the various patches. The

chemical potential, μ, of the adatoms is given by $\mu_i/kT = \ln N_i - \ln f_i$ for a dilute film of N_i non-interacting atoms distributed over area A_i, and the equality of the chemical potentials of the adatoms on any two patches, i and j, establishes the condition $N_i/N_j = f_i/f_j$, which allows us to write equation (17) in the form

$$\nu^R = \frac{kT}{h}\frac{N_i^2}{f_i^2}\sum_i f_i^*. \tag{18}$$

Experimentally, we have at our disposal only the total number of atoms adsorbed per unit area, N, and not the number, N_i, on the given patch i. The equilibrium assumption allows us to write

$$N_i^2 = \frac{N^2 f_i^2}{(\sum_i f_i)^2} \tag{19}$$

and the total rate thus becomes

$$\nu^R = \frac{kT}{h}N^2\frac{\sum f_i^*}{(\sum_i f_i)^2} = \frac{kT}{h}N^2\frac{F^*}{F^2}. \tag{20}$$

The *form* of the rate law for a heterogeneous surface on which the adatoms are at equilibrium is thus precisely the same as that for a uniform surface; the heterogeneity of the surface manifests itself only in that the partition functions are now sums over the different patches. As we change the distribution of patches, we may change the rate constant for desorption; however, it is also apparent that as long as we are justified in assuming an equilibrium distribution of adatoms over the surface, as well as the lack of interactions between the adatoms, the rate constant does *not* in any way vary with the degree of cover. For a given surface with a fixed site distribution, the desorption can thus be described by an effective activation energy for the desorption and a suitable pre-exponential factor. The heat of desorption which is obtained from the temperature-dependence of the rate will, however, be an average quantity and if we can neglect the dependence of $(\partial \ln f_i^*)/(\partial 1/kT)$ upon the nature of the patch, a procedure justified by the small barrier to the adsorption step, we find upon making use of (20) that

$$-\partial \ln\left(\frac{\nu^R}{N^2}\right)\Big/\partial 1/kT = \frac{2\sum_i N_i H_i}{\sum_i N_i} - H^*:$$

$$H_i = \frac{\partial \ln f_i}{\partial 1/kT};\quad H^* = kT + \frac{\partial \ln f^*}{\partial 1/kT}. \tag{21}$$

That is, the heat of desorption is a *number* average obtained by weighting the heat of desorption for a given patch by the number of adatoms on this patch in equilibrium with the adatoms in all other patches. Two points are important. First, the heat term depends upon the way the sample is made up of patches, inasmuch as the number of adatoms on a given patch will be dictated by the properties of *all* the patches. Different samples of the same material may thus show diverse adsorption behavior if the properties of the adatoms vary with the structure of the substrate. Second, at lower temperatures the equilibrium occupation will be primarily dictated by the binding energies on the patches, and the average heat obtained will therefore be weighted in favor of those regions for which the heat of adsorption is high and will be insensitive to the temperature. If there are marked differences between patches, the use of the experimentally obtained average heat to deduce a pre-exponential factor from the experimental rate will lead to a value larger than that for a uniform surface having the same heat of desorption. This effect is apparent in Table 2: the pre-exponential factor increases with increasing values of the heat of desorption. The experimental values have not been corrected for the temperature distribution over the filament, and may thus be too small by a factor of two, partly compensating for an effect due to heterogeneity. It is of interest, however, that the values found for the three samples *bracket* that obtained for the collision frequency in a two-dimensional gas. The significantly lower pre-exponential found for filament 2 indicates that this idealization is *not* warranted, and that the activated complex is considerably more restricted; if, for example, we consider it as lacking all rotational freedom, good agreement with the experimental value for filament 1 is obtained. For a heterogeneous surface, a more detailed comparison would require knowledge of the details of the patch distribution but, as is apparent from the results for filament 3, even without this, comparison with a

simple model may at least provide a diagnostic for heterogeneity.

We have already pointed out that in order to observe a second-order desorption in a dilute layer, surface diffusion must be sufficiently rapid that collisions between adatoms localized around adjacent sites constitute only a negligible fraction of the total number of binaries. This would already be the case if the adatoms on a few patches only had lateral mobility. The requirement that equilibrium be maintained over the entire surface is considerably more severe, however; the mean time between the collisions of an adatom leading to evaporation from *any* given patch must be large compared with the mean time interval for the escape of the adatom across the boundary of the patch into another one. Almost as great a simplification of the desorption from a heterogeneous surface may arise, however, under quite the opposite conditions, if the properties of the patches are so different that evaporation may occur readily from some, but is completely negligible on others. It is then possible to have a step-wise evaporation with the various steps independent of one another. Material from the regions of low binding energies will evaporate at the lower temperatures with a second-order rate, while those from the remaining regions will be affected only at higher temperatures. Moreover, the redistribution of adatoms out of the low-binding regions will be negligible. The condition for the realization of such an evaporation process is that the rate of desorption from a patch of low-binding energy be far in excess of the rate at which atoms are exchanged by diffusion across the boundaries.

We can quantitatively formulate the relations between the rate of evaporation and diffusion as follows: the rate of evaporation of atoms per unit area is $2N^2k_2$; inasmuch as the concentration of adatoms is N, the number of collisions per atom resulting in evaporation is $2Nk_2$ and the mean time between such collisions, τ_E, merely the reciprocal of this. To estimate the time of escape from a patch by surface diffusion, we must assume some particular geometry. For simplicity we consider an infinitely long strip, a cm wide, the boundaries of which are formed by the co-ordinate lines $z = 0$ and $z = b$, where for convenience the unit of the co-ordinate system is the root mean square jump distance l_z of an adatom, parallel to the z co-ordinate, and $a = bl_z$. If the jump frequency is γ, then the mean time for the diffusion of an adatom located at z to one of the borders is $2z(b-z)/\gamma$, if we ignore the possibility of evaporation, and the *average* time for the escape of a particle

$$\tau_D = \frac{2}{\gamma b}\sum_1^b z(b-z) = \frac{1}{3\gamma}(b^2-1) \sim \frac{1}{3\gamma}b^2.$$

Making use of the relation $1/\gamma = l_z^2/2D_s$ between the jump frequency, the jump distance, l_z, and the diffusion constant, D_s, the escape time τ_D becomes $\tau_D = a^2/6D_s$. The condition for the maintenance of equilibrium over the surface, $\tau_E \gg \tau_D$ thus can be stated after some rearrangement as

$$\frac{N}{3}k_2^2 a \ll D_s. \tag{22}$$

To establish the conditions under which a step-wise desorption can go on independently on various patches, we must evaluate τ_D by a different procedure, since our previous assumption of no loss by evaporation is inapplicable. For unit length of strip the flux over the two borders, assuming a complete absence of the reverse flow, is $2D_sN/l_z$; the total evaporation rate is equal to $2N^2k_2a$ and the condition $\tau_E \ll \tau_D$ is therefore

$$Nk_2 a l_z \gg D_s. \tag{23}$$

Although the quantitative data on surface diffusion are sparse, at low temperatures at which E_s, the activation energy for diffusion is much larger than RT, we can approximate the surface diffusion coefficients by $D_s = l_z^2\nu_s \exp(-E_s/RT)$, assuming that ΔS, the entropy of activation, is negligible. ν_s is the vibrational frequency of an adatom in the potential well hindering migration in the direction of impending diffusion and for a sinusoidal barrier of the type introduced in Section 4 (a)(i) is given by $\nu_s = (E_s/2md^2)^{\frac{1}{2}}$. We make the additional assumption that the barrier to diffusion is approximately $0{\cdot}21\chi$ as found at low coverages for cesium,[23] oxygen,[36] and hydrogen[37] on tungsten, and that the jump distance l_z is of the order of a single lattice spacing. The latter will give us a minimum value of D_s which will, however, be in serious error only at high temperatures.

Under these assumptions we can attempt a

rough order-of-magnitude estimate of the patch size on our filaments for the two extreme conditions we have described above. We have found experimentally heats of desorption ranging from 59 to 81 kcal/mole. Since the samples are polycrystalline and prepared in the same way, we can assume that they are made up of different distributions of more or less the same types of patches or inhomogeneities, and that filament 2 for example has some patches with characteristics approximating those found for filament 3. For a filament with the high heat of desorption, we select for consideration a patch with a desorption energy of approximately 50 kcal/mole, and a concentration of adatoms of $10^{14}/cm^2$. In order for the adatom population of this patch at 1500°K to be in equilibrium with surroundings at higher binding energy, the requirement from equation (22) is that the characteristic patch dimension, a, be small compared with 1×10^{-5} cm. Similarly, for a patch with $\Delta H \sim 80$ kcal/mole, we must have $a \ll 1\times10^{-3}$ cm. For a patch with $\Delta H \sim 40$ kcal/mole, the size restriction is considerably more stringent, the condition for equilibrium being $a \ll 3\times10^{-6}$ cm; that is, the smaller the binding energy of the atoms on a patch, the smaller the patch dimension must be to preserve equilibrium. This is a simple consequence of the fact that on our model the activation energy for diffusion is directly related to that for the desorption of a single atom χ, whereas evaporation depends upon a quantity $(2\chi-D)$ and can thus, for small values of χ, become competitive with the diffusion processes. On the other hand, in order to have the material adsorbed on a 50 kcal/mole patch evaporate independently of the surrounding patches, we find from equation (23) that the smallest dimension of such a patch would have to be *large* compared with 10^{-3} cm.

(iii) *The physical nature of surface heterogeneities*

Although, in view of our lack of detailed knowledge of surface diffusion, these considerations have at best only semi-quantitative significance, they do elucidate the physical nature of the patches which we have so far not specified. It has been shown that desorption of β-nitrogen from the filaments examined here can be described by a single rate expression and occurs *without* any breaks, and we must therefore conclude that the adatoms *are* in equilibrium over the surface. That the surface is *not* homogeneous is revealed, however, by the differences in the desorption from different samples. Inasmuch as we have surface equilibrium, the considerations of the preceding paragraph indicate an upper limit for the patch dimension, which must be considerably less than 10^{-3} cm; this eliminates the grain structure of the wires as a source of the heterogeneity, since at least one dimension of these is generally comparable to the wire diameter, that is of the order of 10^{-2} cm. That the individual grains must have a non-uniform surface structure is apparent from the gross geometry of the sample. Drawing of the wire tends to bring about an orientation of the [110] axis in the direction of drawing, and a single grain extending over the entire diameter of a perfectly cylindrical specimen would thus have exposed all faces with Miller indices of the form (*hhk*); the marked variation of electron emission with surface orientation of such cylindrical wires is well known.[38] We can also eliminate small-scale surface defects, such as the grain boundaries themselves or the termini of dislocations, from the requirement that the number of such defects be of the same order of magnitude as the number of adatoms that can be adsorbed with a high heat. From the observed grain size of the specimens and from observations of the surface structure of tungsten with the field emission microscope,[39] it must be concluded that dislocations and grain boundaries fall short of this requirement by several orders of magnitude.

However, the filaments are aged and subsequently prepared for measurements at temperatures higher than 2200°K, at which rearrangement of the surface, both by volume and surface diffusion is possible. The operations are carried out under conditions of very large under-saturation, the tungsten vapor pressure in the system corresponding to a temperature no higher than 400°K, so that, for example, a lattice step, terminating at the point of emergence of a screw dislocation, should be formed into a tight spiral with a distance of only a few atom spacings between successive turns; steps should thus cover the entire surface, including the very stable low-index faces. In its effect upon the distribution of conduction electrons at the interfaces, such a step can be considered as an added line dipole, resulting in a lowering of the work function, and this perturbation could also be reflected in a difference of

interaction between adatom and substrate. Lattice steps appear to fulfill all the requirements for the heterogeneities that we have imposed: they can be expected to alter the binding of the adatoms, they present a number of binding sites comparable to the number of adsorbed atoms actually found, and they are spaced sufficiently close to one another that surface diffusion should be able to bring about equilibration over the entire sample. We have previously associated steps with sites of high reactivity toward the chemisorption process. It is therefore of interest that the sample having the highest heat of desorption also shows the highest rate of adsorption. These considerations do not, however, allow us to ascertain the importance of crystallographic orientation as a source of the heterogeneity of binding sites.

Thus far we have confined ourselves to a consideration of the desorption from tungsten filaments. As already mentioned, some rolled strips examined by us show anomalies which still remain to be clarified; however, on others, the desorption of the β-nitrogen occurs continuously, and we have been able to measure second-order kinetics, similar to those found for the filaments. This is of particular interest in elucidating the nature of the heterogeneities responsible for differences in the binding energies. Although rolling tends to orient the grains, so that they have a (100) plane in the plane of rolling, pole-figure determinations reveal variations from this, and grains with surface normals ranging from [100] to [112] have been found by us.* The average diameter of the grains is of the order of 5×10^{-2} cm, and according to our previous estimates, this is a size such that if only the *gross* surface orientation of the grains were to influence significantly the binding energies, then we could *not* expect to find a continuous second-order desorption process. We must therefore conclude that such gross crystallography does not necessarily exert a dominant effect, and that a finer-scale heterogeneity appears to be involved, in agreement with the deductions from the study of the filament samples. In these fine-scale heterogeneities, however, the orientation may, of course, still play an important role in determining the strength of binding.

* The variation in grain orientation was kindly brought to our attention by Dr. J. A. BECKER of the Bell Telephone Laboratories.

(b) *The Variation of Binding Energy with Cover*

We have shown above that for an adsorbed layer of *non-interacting* particles the heat of desorption, as well as that of adsorption, should be constant and independent of the state of occupation of the surface, even if the latter be heterogeneous, provided only that surface diffusion is extensive enough to establish equilibrium in the adsorbed layer over the entire sample. Our results indicate, moreover, that for nitrogen on tungsten the heat is initially constant and the adatoms are mobile over the surface. These findings are in contrast to measurements of the heat of adsorption reported in the literature for other systems, which even at low coverages generally show a significant decrease with increase of the amount of gas adsorbed. In the past this has been attributed either to possible interactions between adatoms or to variations in binding energy over the patches of which the surface may be composed. Our analysis of the previous paragraphs *appears* to support the first explanation, which in the immediate past has been in disfavor, and it is thus proper to examine more carefully both the measurements and the theories which suggest a dependence of binding energy upon the coverage.

(i) *The interpretation of heat-of-adsorption measurements**

An interpretation of desorption measurements carried out under conditions which ensure surface mobility has already been given above. Here we need point out only that our conclusions are equally applicable to equilibrium heat measurements from isotherms at different temperatures, and shall consider the meaning of those experiments in which surface diffusion in the chemisorbed layer does *not* suffice to establish equilibrium. Under these circumstances the integral heat of adsorption will be determined by the reactivity of the various surface sites for chemisorption, as well as by the binding energy characteristic of these sites. If, in a time interval dt, we allow dn molecules to adsorb on the surface under investigation, the heat of adsorption, as measured in a calorimeter, will be $\sum_i \overline{H}_i \rho_i \, dn$, where $\overline{H}_i$ is the differential heat characteristic of patch i, and ρ_i is the fraction of the total number of

* A qualitative discussion has already been presented by EHRLICH[2].

VOL. 5 1958

molecules that are adsorbed on this patch. If there is no appreciable evaporation, ρ_i is of course given by the ratio of the rate of adsorption on patch i to the total rate on the surface, and $\overline{H}_i$ as well as ρ_i may be a function of the surface concentration. The integral heat of adsorption is thus $\int_0^n \sum_i \overline{H}_i \rho_i \, dn / \int_0^n dn$, and explicitly depends upon the way in which the adsorption step occurs. In the adsorption of nitrogen on tungsten, for example, there appear to be significant differences in the reactivity of the various portions of the surface, and a heat measured in this way would weight most heavily these reactive sites. If a high binding energy is associated with high reactivity, then such a measurement could yield a heat decreasing with coverage, the most reactive sites filling up first and leaving only the less reactive and, on these assumptions, less favorable energetically. We wish to emphasize here that the correct interpretation of heat data obtained in this way demands an intimate knowledge of both the adsorption step and the relationship between reactivity and binding energy, which is, in general, lacking.

This is well illustrated by the system hydrogen on nickel, for which calorimetric measurements of the heat of adsorption reported by BEECK[16] indicated a decrease in the heat with increasing cover. MILLER[40] interpreted this to show an immobile layer with repulsive interactions between adatoms, on the assumption that the adsorption occurred randomly over the entire surface. BEECK,[16] in contrast, concluded that this indicated a mobile adsorbed layer. He argued that the surface was made up largely of pores in the evaporated film used as a sample, and that for an immobile layer a hydrogen molecule would penetrate such a pore just until it would come in contact with the first available site, on which it would chemisorb. On the average the interaction of the adatom with its surroundings would always be the same regardless of cover, that is ρ_i as well as $\overline{H}_i$ is independent of the amount adsorbed, and a constant heat should be found in contrast to the actual experimental results. Implicit in BEECK's argument is the very *specific* assumption about the way in which the adsorption occurs. If we accept that a hydrogen molecule may be weakly held to a metal surface prior to chemisorption, and that there are variations of reactivity over the metal surface, then BEECK's conclusions no longer follow. Actually, using our criterion for the activation energy for surface diffusion of adatoms, we can surmise that hydrogen on nickel is in equilibrium at room temperature, and that therefore the decrease in the heat of adsorption must be considered as indicative of the interactions of the adsorbed entities and not of the kinetics of the adsorption process. In what follows we shall limit ourselves to consideration of systems for which mobility of the adsorbed layer can be assumed and for which we are thus at least able to assign the cause of the variation of the heat to an equilibrium property.

(ii) *The mutual interactions of adatoms*

As already mentioned, in a surface layer in which the adatoms are in equilibrium with each other and do not interact, the heat of adsorption is constant and does not depend upon the cover, regardless of the dependence of adsorption properties on surface structure. Conversely, if one does observe a decrease in the heat for a system which can be considered to be in equilibrium, only interactions between adatoms can be held responsible. The values of the heats of desorption of cesium, oxygen, and nitrogen from tungsten and the heats of adsorption of hydrogen on several metals at room temperature have been obtained under conditions which appear to ensure the equilibrium requirement. Only the nitrogen data give a constant heat, however. All others have been reported as showing a marked diminution with cover which we would have to interpret as due to interactions. This does not mean that the variation of binding over the surface does not play an important role, but only that *without* interaction these variations would not cause such a diminution.

At low enough temperatures, it is the heat of adsorption which largely dictates the population of a patch. We can therefore have a high enough concentration of adatoms on tight binding patches that even short-range repulsive forces become important, while on other regions the concentration may be such that the perfect gas approximation is still valid. The net effect would be a diminution in the heat of adsorption at an (area) average surface concentration lower than could be expected from short-range forces only on a uniform surface. Such a diminution would arise because of an interplay of both surface heterogeneity and interaction of

adatoms. The question which has to be answered is, therefore: what is the nature of the interactions between adatoms? The results on the desorption of nitrogen from tungsten clearly reveal a dependence of binding energy on surface structure and a similar dependence is to be expected for other systems as well. They also show the absence of any long-range interactions between the adatoms. The latter is particularly interesting inasmuch as all attempts to introduce such effects for a dilute layer in other than completely ionized entities, such as cesium on tungsten, have so far appeared doubtful. BOUDART's[41] suggested relation between the change in the true work function $\Delta\Phi$ and that of the heat, as well as the more recent revival of this idea by HIGUCHI *et al.*[42] which predict $\delta\Delta H = 2\Delta\Phi$ rests upon the untenable assumption of a continuous, smeared-out charge distribution even at very low coverages. That this is not in accord with experience was already pointed out by DE BOER[43] in his discussion of cesium on tungsten. The most reliable measurements indicate a contact potential of $-0{\cdot}50$ V for a saturated nitrogen-covered tungsten surface (relative to bare tungsten), which should correspond to a decrease in the heat of desorption of 23 kcal/mole at full coverage. Under the conditions of our experiments, even at the highest coverage, achieved by saturation at 2×10^{-7} mm, the heat was found constant within the limit of error—approximately ±4 kcal/mole. The alternative suggestion[44,45] that the decrease is not due to a change of the average surface dipole, but rather to a change in the Fermi level of the conduction electrons of the metal fails, since for any sample of ordinary size the number of conduction electrons is infinite compared to the number that can be involved in a strictly surface effect. The recent proposal of TEMKIN[45] to consider the metal electrons which participate in bond formation at the surface as forming a two-dimensional gas remedies this difficulty; the number of electrons is now significantly affected by adsorption and the kinetic energy of the remaining ones is therefore also changed. For a metal, however, this model is untenable, since the electrons form a continuous equilibrium distribution which acts as an essentially infinite reservoir from which levels at the surface can be replenished.

The most extensive data on heats of adsorption involve hydrogen on metal films, and it is of interest that for hydrogen on tungsten MIGNOLET[24] reports a contact potential, at saturation, equal to that for nitrogen on tungsten ($-0{\cdot}48$ V), for which we do *not* find a dependence of heat on coverage. The work that must be done against the double layer at the surface in forming the ad-layer does not appear to be responsible for the observed changes in the heat. We are led to conclude that for adatoms which are not involved in the formation of a pronounced polar-link to the surface, such as judging from the changes in the work function may be expected for cesium and oxygen on tungsten, the diminution of the heat of adsorption with increasing cover should be ascribed to the variation in binding strength over the surface and to short-range interactions between adatoms. An important contribution to both these effects would, however, be expected from contamination of the surface which, as we have shown in Section 3(a), can be significant under the conditions under which much of the calorimetric work has been carried out. This would result in an actual coverage significantly higher than that estimated by the experimenter, and would therefore allow for important short-range interactions. The presence of impurities would of course also immediately establish a heterogeneity of binding, not however characteristic of the metal.

(c) *Band Structure and Chemisorption*

In our discussion of chemisorption we have so far limited ourselves to a phenomenological consideration of the kinetic processes and their relation to surface structure, without touching upon the interactions which are responsible for the strong bonding of adatoms to the surface. Attempts have been made in the past to relate chemisorption to the bulk electronic structure of the adsorbent. One of the more interesting generalizations, initiated by DOWDEN[46] and BEECK[47] and extended by TRAPNELL,[48] has considered the chemisorption bond, in gases other than oxygen, as a covalent link between the adatom and the partly filled *d*-band of the solid. A different point of view, advanced by ELEY,[49] considers the surface contribution to the bond between metal and adatoms as analogous to the bonding within the metal, without necessarily involving *d*-electrons; this permits the estimation of bond strengths from available thermochemical data, using Pauling's

VOL. 5 1958

empirical rule for covalent bonds. Data on the variation of the heat of chemisorption for a given gas with the nature of the metal substrate have frequently been invoked in attempts to discriminate between these two interpretations. However, these become less than convincing if one considers the possibility of a marked dependence of surface effects upon structure which is implied in our experimental results and it is thus of interest to examine the applicability of the two theories to the predictions of chemisorption behavior, in the light of other experimental information available.

According to the *d*-band theory of chemisorption, as formulated by TRAPNELL, chemisorption of gases other than oxygen involves the formation of a covalent bond with a *d*-electron of the substrate; this implies, as one of the requirements for bond formation, an incompletely filled *d*-band in the adsorbent, or else, if the *d*-band is full, the promotion of electrons out of the filled band during the chemisorption process. For nitrogen, with its possibility of multiple-bond formation, three holes in the *d*-band are held to be necessary for chemisorption. However, the experiments on which these deductions are based measured chemisorption on different metals as it occurred from the molecular gas, and thus it should be clear that they do not give a direct indication of the electronic requirements for the formation of a bond between adatom and surface. For the adsorption of a diatomic gas they are indicative, rather, of the stability of an atom interacting with the surface compared with the stability of an atom interacting with another one in the diatomic molecule. Chemisorption will occur only until the chemical potential per atom in the gas is equal to that of the adatoms on the surface. The electronic requirements for bond formation of an atom and a surface are more properly revealed by examining the adsorption from a beam of atoms. The data available here are sparse, but the *indications* are that chemisorption of atoms occurs on metals in general, regardless of the possible contribution of *d*-bands, as well as on semiconductors and ionic crystals. For example, at low temperatures, under conditions that will inhibit surface diffusion, and thus recombination [see Section 4(a)(i)] MIGNOLET[50] has observed a negative surface potential of a few tenths of a volt for mercury in the presence of atomic hydrogen; a similar effect has been reported for copper films,[51] where at 77°K in atomic hydrogen a surface potential of −0·325 V has been found. LEYPUNSKY[34] has actually been able to measure the retention of atomic hydrogen by copper and aluminum films at liquid-air temperatures, under conditions where *no* adsorption from the molecular gas was observed. That hydrogen atoms, at least, can be adsorbed on semiconductors such as silicon[52] and ZnO[53] appears well established; the adsorption on ionic CaF_2[54] is also well documented. Cadmium, zinc, and, to a smaller extent, tin are known to catalyze fairly efficiently the recombination of hydrogen atoms at room temperature[55] and thus presumably are also capable of chemisorbing hydrogen atoms. Experiments on the recombination of nitrogen on platinum and nickel have led SCHECHTER[56] to conclude that nitrogen atoms are chemisorbed on these metal surfaces with binding energies in excess of 50 kcal/atom,* and the effectiveness of copper and silver in catalyzing the recombination of nitrogen atoms[57] points to a formation of strong bonds on these surfaces as well.

For none of the metals listed here as active in the adsorption of atomic hydrogen has it been established that there are vacant levels in the *d*-bands; the semiconductors, by definition, have essentially filled bands at the temperature of the experiments. It is interesting to note that hydrogen atoms are adsorbed on those metals on which chemisorption of oxygen was observed from the molecular gas and from which it was deduced that oxygen chemisorption did *not* involve covalence with the *d*-band. Copper, silver, platinum, and nickel all have less than three *d*-band vacancies, yet all appear capable of forming an electron exchange bond with nitrogen atoms. It should be pointed out, however, that the band structure of metals is generally not well enough established to eliminate unequivocally the possible need for the participation of *d*-bands in chemisorption; the wave functions of the conduction electrons may well have some *d*-character, and we cannot readily eliminate

* Preliminary experiments carried out by us also indicate that a nickel strip, even at 800°K, does not chemisorb any appreciable amount of nitrogen from the *molecular gas* (at room temperature) and that the absence of chemisorption is thus *not* due to a high activation barrier separating a stable adsorbed state from the gas, but is the result of the unfavorable thermodynamics.

the possibility of promotion of electrons out of a band. To the extent that this theory *is* based upon a correlation between experimental data on adsorption with the band structure of the sorbent, however, it cannot be considered as proven until the latter is known. Moreover, the correlation, even if we were to accept it, would not be a particularly useful one, inasmuch as in our present state of knowledge it does not provide a basis for a reliable extrapolation from known data. That there should be a straightforward relation between the band structure of a solid and its ability to form a strong surface bond with an adatom is to be doubted, in any event, since it is well established that the presence of an interface may profoundly alter the electron distribution in its vicinity.

ELEY's approach to the problem of the interaction of an adatom with a metal surface has in the past been criticized because it predicts an incorrect order for the heats of adsorption of hydrogen on various metals. This objection loses much of its force if we take into account the possible effects brought about by differences in surface structure as well as the uncertainties in the experimental results which may be brought about by possible impurities. Although the calculation of the heat values is essentially empirical, it appears to be correct in emphasizing the high reactivity of metal surfaces, regarded as an array of dangling bonds, for the formation of linkages with adatoms, and also in emphasizing the necessity for considering the details of the surface structure itself, which is implicit in the electronegativity term for the substrate.

Acknowledgements—We are greatly indebted to our colleagues in the Research Laboratory for their many stimulating suggestions concerning techniques and interpretation. We are particularly grateful to D. S. RODBELL for his interest in our instrumentation problems. In much of the experimental work, we have had the welcome assistance of FRANK HUDDA.

REFERENCES

1. EHRLICH G. *J. Phys. Chem. Solids* **1,** 3 (1956).
2. EHRLICH G. *J. Phys. Chem.* **60,** 1388 (1956).
3. WAGENER S. and JOHNSON C. B. *J. Sci. Instrum.* **28,** 278 (1951).
4. JONES H. A. and LANGMUIR I. *Gen. Elect. Rev.* **30,** 310, 354, 408 (1927).
5. HAGSTRUM H. S. *Rev. Sci. Instrum.* **24,** 1122 (1953).
6. LANGMUIR I., MACLANE S. and BLODGETT K. B. *Phys. Rev.* **35,** 478 (1930).
7. COX M. *Phys. Rev.* **64,** 241 (1943).
8. BECKER J. A. and HARTMAN C. D. *J. Phys. Chem.* **57,** 157 (1953).
9. HICKMOTT T. W. and EHRLICH G. *J. Chem. Phys.* **24,** 1263 (1956).
10. GOOD R. H. and MÜLLER E. W. *Handbuch der Physik* Vol. 22, p. 176. Springer-Verlag, Berlin (1956).
11. WHEELER A. *Structure and Properties of Solid Surfaces* p. 439. University of Chicago Press, Chicago, Ill. (1953).
12. RIDEAL E. K. and TRAPNELL B. M. W. *J. Chim. Phys.* **47,** 126 (1950).
13. SINGLETON J. H., ROBERTS E. R. and WINTER E. R. S. *Trans. Faraday Soc.* **47,** 1318 (1951).
14. DUSHMAN S. *Scientific Foundations of Vacuum Technique* p. 656. John Wiley and Sons, Inc., New York (1949).
15. CARTWRIGHT *ibid.* p. 521.
16. BEECK O. *Advanc. Catalysis* **2,** 151 (1951).
17. RIDEAL E. K. and TRAPNELL B. M. W. *Proc. Roy. Soc.* A **205,** 409 (1951).
18. MÜLLER E. W. *Ergeb exakt. Naturwiss.* **27,** 290 (1953).
19. ANDERSON P. A. *Phys. Rev.* **59,** 1034 (1941).
20. EHRLICH G. and HICKMOTT T. W. *Nature, Lond.* **177,** 1045 (1956).
21. EHRLICH G. and HICKMOTT T. W. *J. Chem. Phys.* **26,** 219 (1957).
22. BLODGETT K. B. and LANGMUIR I. *Phys. Rev.* **40,** 78 (1932).
23. TAYLOR J. B. and LANGMUIR I. *Phys. Rev.* **44,** 423 (1933).
24. MIGNOLET J. C. P. *Rec. Trav. Chim. Pays-Bas* **74,** 685 (1955).
25. BECKER J. A. and BRANDES R. G. *J. Chem. Phys.* **23,** 1323 (1955).
26. MÜLLER E. W. *Z. Elektrochem.* **59,** 372 (1955).
27. LANGMUIR I. *J. Amer. Chem. Soc.* **37,** 1139 (1915).
28. LANGMUIR I. *Chem. Rev.* **6,** 451 (1929).
29. MORRISON J. L. and ROBERTS J. K. *Proc. Roy. Soc.* A **173,** 1 (1939).
30. LANGMUIR I. and VILLARS D. S. *J. Amer. Chem. Soc.* **53,** 486 (1931).
31. BOSWORTH R. C. L. and RIDEAL E. K. *Physica* **4,** 925 (1937).
32. JOHNSON M. C. and VICK F. A. *Proc. Roy. Soc.* A **151,** 308 (1935).
33. BOSWORTH R. C. L. *J. Roy. Soc. New S. Wales* **79,** 166 (1946).
34. LEPUNSKY O. I. *Acta Phys-chim. URSS* **5,** 271 (1936).
35. HILL T. L. *J. Chem. Phys.* **14,** 441 (1946).
36. GOMER R. and HULM J. K. *J. Amer. Chem. Soc.* **75,** 4114 (1953).
37. GOMER R. and WORTMAN R. *J. Chem. Phys.* **23,** 1741 (1955).
38. SMITH G. F. *Phys. Rev.* **94,** 295 (1954).

39. DRECHSLER M., PANKOW G. and VANSELOW R. *Z. phys. Chem.* (N.S.) **4,** 249 (1955).
40. MILLER A. R. *Disc. Faraday Soc.* **8,** 57 (1950).
41. BOUDART M. *J. Amer. Chem. Soc.* **74,** 3556 (1952).
42. HIGUCHI I., REE T. and EYRING H. *J. Amer. Chem. Soc.* **79,** 1330 (1957).
43. DE BOER J. H. and VEENEMANS C. F. *Physica* **1,** 960 (1934).
44. MIGNOLET J. C. P. *J. Chem. Phys.* **23,** 753 (1955).
45. TEMKIN M. I. *Voprosy Khim. Kinetiki. Kataliza i Reaktsionnoi Sposobnosti* p.484. Academy of Sciences of the U.S.S.R., Moscow (1956).
46. DOWDEN D. A. *J. Chem. Soc.* 242 (1950).
47. BEECK O. *Disc. Faraday Soc.* **8,** 118 (1950).
48. TRAPNELL B. M. W. *Proc. Roy. Soc.* A **218,** 566 (1953).
49. ELEY D. D. *Disc. Faraday Soc.* **8,** 34 (1950).
50. MIGNOLET J. C. P. *Rec. Trav. Chim. Pays-Bas* **74,** 701 (1955).
51. BLOYAERT F., D'OR L. and MIGNOLET J. 6e *Réunion de chimie Physique* (Paris) (1956).
52. LAW J. T. and FRANCOIS E. E. *J. Phys. Chem.* **60,** 353 (1956).
53. HEILAND G. *Z. Phys.* **148,** 15 (1957).
54. DE BOER J. H. and LEHR J. J. *Z. phys. Chem.* B **24,** 98 (1934).
55. KATZ S., KISTIAKOWSKY G. B. and STEINER R. F. *J. Amer. Chem. Soc.* **71,** 2258 (1949).
56. SCHECHTER A. *Acta phys.-chim. URSS* **10,** 379 (1939).
57. BUBEN N. and SCHECHTER A. *Acta phys.-chim. URSS* **10,** 371 (1939).

OL.
5
958

J. Phys. Chem. Solids Pergamon Press 1958. Vol. 5. pp. 78–84.

THE STICKING PROBABILITIES OF GASES CHEMISORBED ON THE SURFACES OF SOLIDS—II

P. KISLIUK

Bell Telephone Laboratories, Inc., Murray Hill, New Jersey

(*Received* 28 *August* 1957; *revised* 14 *October* 1957)

Abstract—An earlier treatment of the sticking probability for chemisorption is extended to include diatomic molecules which dissociate on chemisorption. It is shown that if it is assumed that all incoming molecules are physisorbed and come to thermal equilibrium with the adsorbent, the lack of dependence of the sticking probability on coverage found for nitrogen on tungsten can be reasonably explained only if the sticking probability on the clean metal is nearly unity. Experimentally, it is found to be in the range 0·1–0·5. It can be shown, however, both theoretically and experimentally, that this assumption is not valid, and that many of the molecules desorbed arise from the portion of the physisorbed molecules not yet in thermal equilibrium with the substrate. The discrepancy between the present theory and experiment is reduced if this fact is taken into account.

VOL.
5
1958

1. INTRODUCTION

If it is assumed that every gas molecule impinging on a solid surface is physically adsorbed, and if the sticking probability, S, for chemisorption is not too close to unity, there is an appreciable probability, $1-S$, that it will be desorbed. As the coverage is increased, a molecule has to visit a larger number of sites to achieve the same chance of chemisorption. If the probability of desorption while passing over a filled site is not negligible compared to the probability of chemisorption while over an empty site, the sticking probability is necessarily appreciably reduced by this increase in coverage.

Experimentally, the sticking probability of nitrogen on clean tungsten is of the order of 0·1–0·5[1–3] and is nearly independent of coverage up to a value of about one-quarter the number of tungsten atoms on the surface.

The treatment due to Becker[4–6] corresponds to a picture in which the mobility of molecules over filled sites is large and the time spent over a single site is so short that the probability of desorption while over such a site is negligible. Ehrlich's[7] treatment corresponds to a similar picture in which the surface is intrinsically patchy and some regions are unavailable for chemisorption even on the clean surface, but the probability of desorption while passing over these regions is negligible.

The present explanation of the experimental facts avoids the assumption that every impinging molecule is adsorbed in the "precursor" state (herein assumed to be the physisorbed state) and is in thermal equilibrium with the substrate. The excess kinetic energy derived from the attractive van der Waals forces is not instantaneously lost, and during the time required for thermalization most of the molecules observed to leave the surface may be desorbed from the precursor state. This leads to a smaller dependence of the sticking probability on coverage.

The remainder of this paper is devoted to a more formal development of these ideas, and to evidence favoring this suggestion.

2. THE STICKING PROBABILITY FOR DIATOMIC MOLECULES WHICH DISSOCIATE ON CHEMISORPTION

In an earlier paper,[8] a theory of the sticking probability for chemisorption on solids was developed (on the assumption of the existence and constancy of certain probabilities) for molecules which do not dissociate on chemisorption. The result was compared with experimental data from

the literature for the sticking probability of nitrogen on tungsten as a function of coverage. The objection might be raised that nitrogen (as well as oxygen and hydrogen) are believed to dissociate on adsorption.[5,9] An attempt will therefore be made to extend the treatment to include this case. This extension necessitates certain additional assumptions, but even if these assumptions are not justified for the experimental cases of interest, the effect on the earlier calculation of the requirement that two adjacent empty sites be available for chemisorption is clarified.

We again apply a model in which the chemisorption proceeds from a reservoir of molecules in the physisorbed state.[4,5,7] We consider a molecule small enough so that in its physisorbed state it is in contact with only one site for chemisorption (of an atom), but that the chemisorption can take place only if both this site and at least one nearest-neighbor site are unoccupied.[10]

Let us assume that:

(1) The probabilities of migration and desorption of a physisorbed molecule are dependent only on the state of occupation (for chemisorption) of the site over which the molecule is adsorbed, and not on that of neighboring sites.

(2) The probability of chemisorption when a physisorbed molecule is over an empty site for chemisorption is proportional to the number of unoccupied nearest-neighbor sites.

(3) The distribution of filled sites is random.*

Let the fraction of the sites for chemisorption (of an atom) which are filled be θ, and the number of nearest-neighbor sites be n. The probability that the site over which a molecule is physisorbed be empty is $(1-\theta)$ and the probability that all n nearest neighbors be empty is $(1-\theta)^n$, that all but one be empty is $n\theta(1-\theta)^{n-1}$, &c. If the probability that the molecule be chemisorbed at this site before being desorbed or migrating to another site is P_a when all relevant sites are unoccupied, this probability, according to assumption (2) above, becomes $(n-1/n)P_a$ if one nearest-neighbor site is filled, $(n-2/n)P_a$ if two are filled, etc. The probability of becoming chemisorbed on a randomly chosen site then becomes:

$$\left.\begin{aligned} P_{a1} &= P_a(1-\theta)\Big[(1-\theta)^n+\frac{(n-1)}{n}n\theta(1-\theta)^{n-1}+ \\ &\quad +\frac{n-2}{n}\frac{n(n-1)}{2}\theta^2(1-\theta)^{n-2}+ \\ &\quad +\ \ldots\ +\frac{1}{n}\frac{n!}{(n-1)!}\theta^{n-1}(1-\theta)\Big] \\ &= P_a(1-\theta)^2\Big[(1-\theta)^{n-1}+(n-1)\theta(1-\theta)^{n-2}+ \\ &\quad +\frac{(n-1)(n-2)}{2}\theta^2(1-\theta)^{n-3}+\ \ldots\ +\theta^{n-1}\Big] \\ &= P_a(1-\theta)^2[(1-\theta)+\theta]^{n-1} = P_a(1-\theta)^2 \end{aligned}\right\} \quad (1)$$

Proceeding as in Part I,[8] let the probability that a physisorbed molecule's sojourn above a given site be terminated by desorption be P_b if the site is unoccupied by a chemisorbed atom, and P_b' if it is occupied. The probabilities that a physisorbed molecule be chemisorbed, desorbed, or migrate on to another site at the first site visited are, respectively:

$$\left.\begin{aligned} P_{a1} &= P_a(1-\theta)^2 \\ P_{b1} &= (1-\theta)P_b+\theta P_b' \\ P_{c1} &= 1-P_{a1}-P_{b1} = 1-(P_a+P_b)+ \\ &\quad +\theta(2P_a+P_b-P_b')-\theta^2P_a. \end{aligned}\right\} \quad (2)$$

The corresponding probabilities for the second site visited are:

$$\left.\begin{aligned} P_{a2} &= P_{c1}P_{a1} \\ P_{b2} &= P_{c1}P_{b1} \\ P_{c2} &= P_{c1}^2,\ \text{\&c., for } P_{a3},\ P_{a4},\ \ldots \end{aligned}\right\} \quad (3)$$

The sticking probability is the sum of the probabilities of being chemisorbed on the first, second, third, etc., site visited. Therefore

$$\begin{aligned} S = P_{a1}+P_{a2}+\ \ldots\ &= P_a(1-\theta)^2[1+P_{c1}+P_{c1}^2+\ \ldots] \\ &= \frac{P_a(1-\theta)^2}{1-P_{c1}} \qquad (4) \\ &= \frac{P_a(1-\theta)^2}{P_a+P_b-\theta(2P_a+P_b-P_b')+\theta^2P_a}, \end{aligned}$$

* The validity of this assumption is discussed by KISLIUK[3].

and, defining $S_0 = S_{\theta\to 0} = \dfrac{P_a}{P_a+P_b'}$, we have:

$$S/S_0 = \frac{(1-\theta)^2}{1-\theta(1-K)+\theta^2 S_0} = \frac{1-\theta}{1+\dfrac{\theta}{1-\theta}K+\dfrac{\theta^2}{1-\theta}S_0}, \tag{5}$$

where

$$K = \frac{P_b'-P_a}{P_a+P_b}.$$

Equation (5) is to be compared with equation (6) of Part I,[8] namely

$$S/S_0 = \frac{1}{1+\dfrac{\theta}{1-\theta}K},$$

where

$$K = \frac{P_b'}{P_a+P_b}.$$

We note three essential differences:

(1) The presence of the factor $(1-\theta)$.

(2) The additional term in the denominator, $(\theta^2/1-\theta)S_0$. (Because of this there can be no unique plot of S/S_0 for a given value of K, since S_0 must be regarded as an additional adjustable parameter.)

(3) The altered definition of K, which permits negative values, although $K > -S_0 > -1$.

Equation (5) is plotted for various values of the parameters K and S_0 in Figs. 1–3.

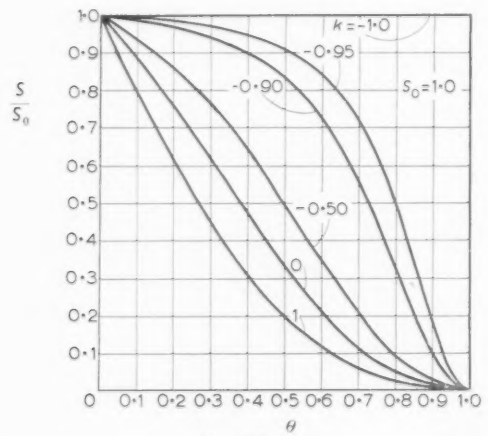

FIG. 1. $S/S_0 = \dfrac{(1-\theta)^2}{1-\theta(1-K)+\theta^2 S_0}$ (equation 5) for $S_0 = 1$ and various values of K.

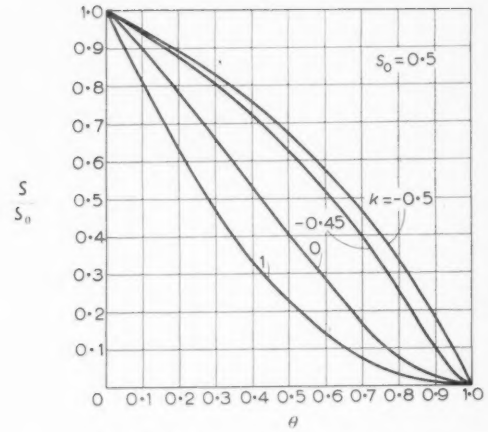

FIG. 2. As Fig. 1, for $S_0 = 0{\cdot}5$.

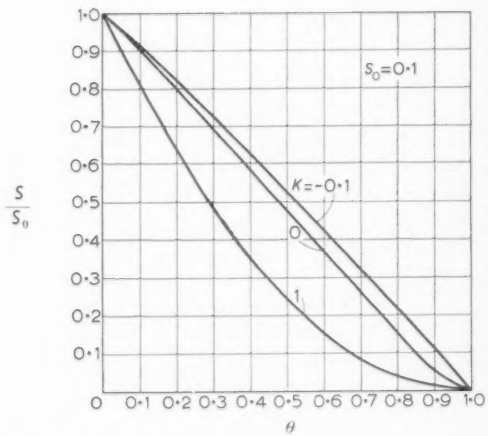

FIG. 3. As Fig. 1, for $S_0 = 0{\cdot}1$.

The case where further migration is the most probable event at a given site and where the rates of migration and desorption are independent of the state of occupation of the underlying site is

obtained by letting $P_b = P_b'$.[11] This corresponds to the model used by EHRLICH.[7,12] Then:

$$K = \frac{P_a - P_b}{P_a + P_b} = 1 - 2S_0, \tag{6}$$

and equation (5) becomes:

$$S = \frac{S_0(1-\theta)^2}{1+\theta S_0(\theta-2)}, \tag{7}$$

which does indeed, after some rearrangement, correspond to an equation given by EHRLICH.[12]

Just as in the simpler case of Part I[8], where the analog of equation 7 is

$$S = \frac{S_0(1-\theta)}{1-S_0\theta},$$

there is, under these assumptions, no adjustable parameter to fit the form of the curve. The value of S at zero coverage dictates the entire course of the curve.

Equation (7) is plotted in Fig. 4 for several values of S_0.

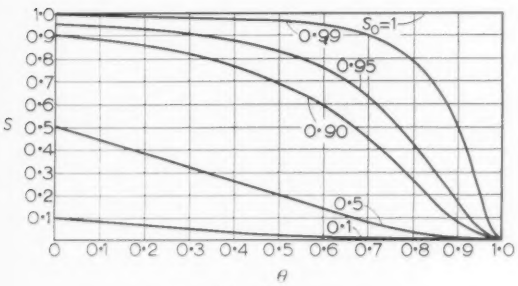

FIG. 4. $S = S_0\dfrac{(1-\theta)^2}{1+S_0\theta(\theta-2)}$ (equation 7), for various values of S_0.

3. COMPARISON WITH EXPERIMENT

It is apparent on comparing Figs. 1–4 with Fig. 2 of Part I[8] that the *form* of the experimental curves for nitrogen on tungsten can be approximated by equations (5) or (7) only if S_0 is nearly unity and K is roughly $-S_0$. Since experimentally S_0 is of order of 0·5 or less, there appears to be a discrepancy between the present theory and experiment. On the credit side, however, there is for $K \neq -S_0$, a region near $\theta = 1$ where the slope of S/S_0 versus θ decreases, a feature of the experimental curves which was unexplained by the simpler theory of Part I.

To account for the discrepancy mentioned above, let us assume, as will be justified in the next section, that newly physisorbed molecules have temporarily a kinetic energy in excess of that corresponding to thermal equilibrium with the adsorbent, and that those molecules desorbed arise predominantly from this group. To visualize the direction of the effect of this consideration on our calculation of sticking probability, let us take an extreme case where a fraction M of the incoming molecules are physisorbed in instantaneous thermal equilibrium with the lattice, while $1-M$ are reflected back into the gas phase on first impact. The theory presented above deals only with those molecules which are physisorbed, so we will define S (theor.) and S_0 (theor.) as the fractions of those molecules which are physisorbed which eventually become chemisorbed, these quantities obeying equation (5). Let S (expt.) and S_0 (expt.) be the sticking probabilities one would actually expect to observe in an experiment. Clearly:

$$\left.\begin{aligned} S_0\,(\text{expt.}) &= MS_0\,(\text{theor.}) \\ S\ (\text{expt.}) &= MS\ (\text{theor.}) \end{aligned}\right\}$$

By taking $M = S_0$ (expt.), it is possible to make S_0 (theor.) equal to unity, even though the experimental S_0 is considerably less than unity, and thus to preserve the required form of the curve. That is, the form of the curve can be made independent of the measured value of S_0 by the introduction of the parameter M. This assumption serves the same purpose in fitting theory to experiment as the introduction of regions of the surface with high and low sticking probability by EHRLICH.[7]

This model may appear rather artificial, but the approach to thermal equilibrium must somehow be taken into account, and the effect of this consideration is to lower the values of S at all coverages. The effect on the general shape of the curve of sticking probability versus coverage may be less drastic.

4. THE APPROACH TO THERMAL EQUILIBRIUM OF MOLECULES IMPINGING ON A SOLID

In references (5), (7) and (8) and in the derivation of equation (5) and (7), it has been assumed that every molecule impinging on the surface is

physisorbed. Furthermore, whenever a temperature-dependence has been considered in these references, expressions of the form $A \exp(-\epsilon/kT)$ have been introduced for the rates, where T is the temperature of the solid adsorbent. In Part I and in the present paper, P_b, P_b', P_c and P_c' have been taken as constants, i.e. they have not depended on whether the site under consideration is the first or the twentieth site visited by the molecule. Thus it is implicit in these treatments that even those molecules which are desorbed were in contact with the surface long enough to come to thermal equilibrium.

When a molecule approaches the surface, it is attracted by van der Waals forces, which may be represented by a potential energy such as that illustrated schematically in Fig. 5. The kinetic

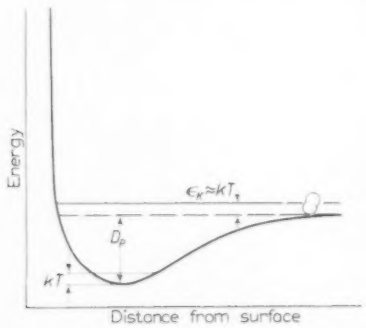

FIG. 5. Schematic representation of the interaction energy between a gas molecule and a solid surface due to van der Waals forces. ϵ_K, with an average value kT, is the normal kinetic energy of the incoming molecule when far from the surface. The average value of the vibrational energy when the molecule is in thermal equilibrium with the surface in the region near the potential minimum is also kT. D_p is the depth of the potential well.

energy due to the component of velocity toward the surface ϵ_K, (equal, on the average, to kT when the molecule is far from the surface) is increased by the depth of the potential well, D_p. If we ignore the possibility of chemisorption for the moment, the molecule will collide with the surface and be reversed in direction by the repulsive forces. If no normal kinetic energy is lost, it will be reflected back into the gas phase. If normal energy greater than ϵ_K is lost, the molecule will be trapped in the potential well and will most probably lose more of its excess kinetic energy on subsequent collisions, eventually coming to thermal equilibrium with an average vibrational energy kT above the bottom of the potential well. Of course, there is a certain small probability that at any time in this process the molecule will gain enough kinetic energy from the lattice vibrations to escape, but this probability becomes smaller as the molecule subsides to the bottom of the potential well.

To give some idea of the orders of magnitude involved, D_p for nitrogen or oxygen is typically between 0·1 and 0·2 eV,[13] while kT at room temperature is 0·025 eV. The molecule will therefore become physisorbed if about one-sixth of the maximum kinetic energy attained when over the potential minimum is lost to the lattice during the first reflection.

This problem, as well as the closely related problem of thermal accommodation coefficients to be considered shortly, has been treated quantum-mechanically by LENNARD–JONES and DEVONSHIRE.[14,15] They proceed by assuming the interaction potential to be a Morse function uniform over the surface of the solid. The validity of such a treatment may be questioned, because the potential function must vary over the surface plane, being periodic with a period equal to the distance between equivalent surface atoms. The forces in the surface plane will be largest when the molecule reaches its point of nearest approach to the surface, where the forces can be approximately represented as the interactions of hard spheres. Thus there are forces which may divert the incoming molecule, so that some of its normal kinetic energy might be converted into kinetic energy in the plane of the surface. The molecule may thus be trapped in the physisorbed state, even though an energy less than ϵ_K has been lost to the solid.* In the absence of an estimate of the importance of this effect, the theoretical calculation can only be regarded as a lower limit. DEVONSHIRE finds for hydrogen on clean tungsten that only about 15 per cent of the impinging molecules are physisorbed.[15]

In addition to the theoretical results, there is experimental evidence to invalidate the assumption that every molecule impinging on a metal surface is physisorbed and is in thermal equilibrium with the surface by the time it is desorbed.

* I am indebted to Dr. J. A. BECKER for pointing this out.

This comes from the measurement of thermal accommodation coefficients. This number may be defined as:

$$\alpha = \lim_{E_1 \to E_0} \frac{E' - E_0}{E_1 - E_0} \qquad (9)$$

where E_1 is the average energy of a gas molecule at the temperature of the solid, E_0 is the average thermal energy of the impinging gas molecules, and E' is the average energy of the gas molecules leaving the surface.*

The thermal accommodation coefficient is thus a measure of the degree to which the molecules approach thermal equilibrium during their interaction with the surface.

ROBERTS[16] found for helium and neon on tungsten that adsorbed gas films had a powerful influence on α, which was less than 0·1 in the clean state, but of order of 0·3 for helium and 0·6 for neon on a "completed monolayer" of oxygen. THOMAS and SCHOFIELD[17] found that by careful cleaning they could observe values of α for helium on tungsten as low as 0·016. They found only a very weak dependence on temperature.

For nitrogen on platinum THOMAS and BROWN[18] found $\alpha \approx 0{\cdot}7$, but it seems possible that adsorbed gases may have been present, in which case this value may be higher than that appropriate to the clean metal. On this same surface they found for argon $\alpha = 0{\cdot}8$–$0{\cdot}9$, for krypton $\alpha \approx 0{\cdot}9$, and for hydrogen $\alpha \approx 0{\cdot}25$.

For argon, which may have van der Waals forces of strength comparable to that of nitrogen, workers in THOMAS's laboratory have found α on clean tungsten to lie between 0·3 and 0·47.[19,20]

The experimental evidence thus seems quite clear that an appreciable fraction of the molecules impinging on a metal surface depart before they come to thermal equilibrium with the surface.

5. CONCLUSION

In the terms used in first section of this paper and in Part I,[8] the facts presented in the previous section suggest that the probabilities P_b and P_b' should not be regarded as constant, but are high for the first few vibrations on the surface, falling to lower values as the molecule comes to temperature equilibrium with the surface. In terms of the treatments of BECKER[5] and EHRLICH,[7] it is not justifiable to use the temperature of the substrate in rate expressions involving the desorption (or other processes) of the physisorbed molecule, or somewhat equivalently, to assume that every molecule is physisorbed.

Nevertheless, the present treatment provides a framework in which the variation of the sticking probability with coverage can be related to certain elementary probabilities, and the consequences of the model proposed by BECKER[4,5] examined in more detail. If we accept the crude approximation introduced in Section 3, the flatness of the experimental curves at low coverage requires that $S_0 \approx 1$ and $K \approx -1$, whence $P_a \gg P_b$ and $P_a \gg P_b'$. In other words, if θ is not too close to unity, almost all the physisorbed molecules which attain thermal equilibrium are eventually chemisorbed, and the molecules desorbed are predominantly those which have not yet lost the extra kinetic energy derived from the van der Waals forces.

The physisorbed molecule is pictured as wandering about overfilled sites until it reaches an eligible site for chemisorption. If the probability of chemisorption is high (i.e. $P_a \approx 1$) the adsorbed film will develop in patches, which would invalidate assumption (3) in Section 2, and therefore this development. If, however, $P_a \ll 1$, the film will develop in a nearly random manner, and the curves of Figs. 1–4 should be a fair approximation to the form of the experimental curves. A measurement of the patchiness of films of coverage $\theta < 1$ on a single crystal plane would therefore be of interest.

The absolute value of S and its variation with temperature[1,12] appear to require analyses of the type of that presented by DEVONSHIRE,[15] with the addition of a potential well for chemisorption (see, for example, LENNARD-JONES[21]) and perhaps also including the forces in the plane of the surface due to its atomic nature. This may be excessively difficult. On the other hand it is possible that the experimental values of S as a function of temperature may suggest a simplified model which will permit a reasonable interpretation of the data.

* The measuring technique presumes a steady state in which the rate of arrival is equal to that of departure of the gas molecules. Thus any chemisorbed films are assumed to be complete.

REFERENCES

1. BECKER J. A. and HARTMAN C. D. *J. Phys. Chem.* **57,** 157 (1953).
2. EHRLICH G. *J. Phys. Chem.* **60,** 1388 (1956).
3. EISINGER J. T. To be published.
4. BECKER J. A. *The Structure and Properties of Solid Surfaces* p. 459. University of Chicago Press (1952).
5. BECKER J. A. *Advances in Catalysis* Vol. VII. Academic Press, New York (1955).
6. BECKER J. A. Private discussion.
7. EHRLICH G. *J. Phys. Chem. Solids* **1,** 3 (1956).
8. KISLIUK P. *J. Phys. Chem. Solids* **3,** 95 (1957).
9. MILLER A. R. *The Adsorption of Gases on Solids.* Cambridge University Press (1949).
10. MILLER A. R. *Ibid.* Chap. IV.
11. KISLIUK P. *J. Phys. Chem. Solids* **3,** 98 (1957).
12. EHRLICH G. *J. Phys. Chem.* **59,** 473 (1955) (Equation 8).
13. TRAPNELL B. M. W. *Chemisorption* p. 144. Butterworth Scientific Publications, London (1955).
14. LENNARD-JONES J. E. and DEVONSHIRE A. F. *Proc. Roy. Soc.* **A156,** 6, 29 (1936).
15. DEVONSHIRE A. F. *Proc. Roy. Soc.* A **158,** 269 (1937).
16. ROBERTS J. K. *Proc. Roy. Soc.* A **135,** 192 (1932); also described in Ref. 9.
17. THOMAS L. B. and SCHOFIELD E. B. *J. Chem. Phys.* **23,** 861 (1955).
18. THOMAS L. B. and BROWN R. E. *J. Chem. Phys.* **18,** 1367 (1950).
19. FAUST J. W., JR. *Diss. Abs.* **15,** 49 (1955).
20. SILVERNAIL W. L. *Diss. Abs.* **15,** 50 (1955).
21. LENNARD-JONES J. E. *Trans. Faraday Soc.* **28,** 333 (1932).

VOL
5
195

J. Phys. Chem. Solids Pergamon Press 1958. Vol. 5. pp. 85–88.

NUCLEAR MAGNETIC RESONANCE IN LiF*

F. J. LOW and C. F. SQUIRE

The Rice Institute, Houston, Texas

(*Received* 18 *July* 1957; *revised* 23 *September* 1957)

Abstract—The line width of the nuclear magnetic resonance in a single crystal of LiF has been observed as 11 G for ^{7}Li and 12 G for ^{19}F; these values are constant with temperature between 1·4 and 80°K. The spin-lattice relaxation time, T_1, has been measured by observing the exponential growth of the absorption signal after saturation. The value of T_1 for ^{7}Li is $3{\cdot}6 \times 10^4$ sec at 1·4°K and is $7{\cdot}8 \times 10^2$ sec at 80°K; for ^{19}F the value of T_1 is $1{\cdot}8 \times 10^4$ sec at 1·4°K and is $3{\cdot}0 \times 10^2$ sec at 80°K. These values are for a steady field of 4 kG.

OL.
5
958

INTRODUCTION

THE experiments reported in this paper have been concerned with the line width, $\sim 1/T_2$, and the spin-lattice relaxation time, T_1, of the nuclear magnetic resonance in ^{7}Li and ^{19}F in a very pure single crystal of LiF from 290°K down to 1·4°K. BLOCH[1] has recently published a generalized theory of relaxation. KHUTSISHVILI[2] has discussed the theory of ionic crystals of the type we have studied, in which the existence of paramagnetic impurity must be inferred. Without making the list complete by any means, we would also indicate the recent theoretical studies on these matters by SEIDEN.[3]

Our own interest in this problem stems from our recent work[4] on the lattice vibration spectrum and elastic constants of single crystals of LiF. As a matter of fact, the vibration spectrum does not play an important role on line shape, according to present theoretical ideas,[5] and the present experiments support the theory. Spin-lattice relaxation is a different matter. BLOEMBERGEN[6] and ROLLIN and HATTON[7] have been among the early workers in the field of spin-lattice relaxation time in solids, and they concluded that small quantities of paramagnetic impurities are able greatly to speed up the transfer of energy from the spin system to the lattice. POUND[8] has likewise carried out some careful studies at room temperature on pure single crystals of LiF, and our crystals, supplied by Harshaw Chemical Company, are of similar high purity, optical quality. BLOEMBERGEN[6] argues that, even so, such crystals may have an Fe ion present to the amount one part in 10^6 and that this trace may explain his experiments on ionic crystals such as CaF_2 and presumably also the present results on LiF. Our results are in accord with BLOEMBERGEN's ideas, and we believe will add quantitative information for further theoretical calculations.

EXPERIMENTAL PROCEDURE

The apparatus needed to study the nuclear magnetic resonance in a single crystal of LiF is shown

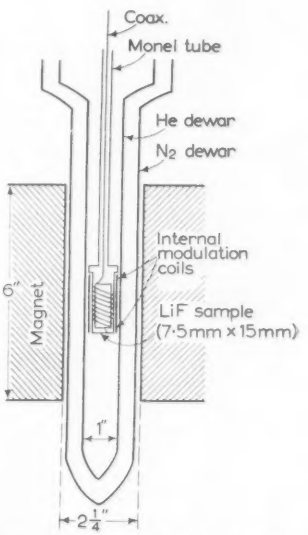

FIG. 1. Scheme of cryostat for N.M.R. at low temperatures.

* Supported by the Robert A. Welch Foundation.

schematically in Fig. 1. Two glass Dewars surround the N.M.R. probe when it is placed in the center of the magnet gap. The inner Dewar was used for liquid helium and for liquid hydrogen, while the outer Dewar contained liquid nitrogen. The vapor pressure of the liquid in the inner Dewar may be reduced by rapid pumping, so that bath temperatures of 1·5°K were easily obtained with liquid helium. Standard temperature-measuring methods were used. The magnet was made by Varian Associates and has 6 in. pole faces. The $2\frac{1}{4}$ in. gap required for the Dewar flasks necessitates a sacrifice of available field strength and field homogeniety, but in the broad line work reported here this was not a limitation.

The spectrometer used in observing resonance signals was developed by POUND[9] and WATKINS,[10] and was manufactured by the Nuclear Magnetics Corporation (Perkin Elmer). Fig. 2

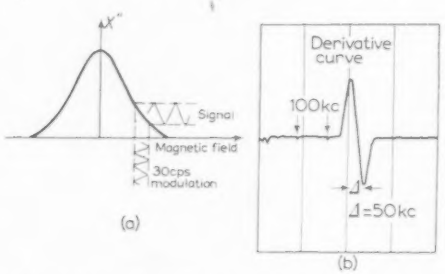

FIG. 2. (a) Typical absorption curve. (b) Reproduction of ^{19}F derivative curve at 300°K.

shows a typical absorption curve which is observed on the oscilloscope if the field is modulated at sufficient amplitude to traverse the entire resonance. If, however, the amplitude of the modulation is decreased to a fraction of the line width, as shown in the figure, the resulting signal is a sine wave whose amplitude, A, is proportional to the slope or derivative of the absorption curve at each point. If either the field or the frequency is slowly varied through resonance at a constant rate, the quantity A, considered as a function of time, becomes the derivative curve as shown in Fig. 2. We used a geared-down clock motor to drive the tuning capacitor and thus produced a constant rate of change in the frequency. The derivative curves were taken from the output of the lock-in amplifier and were all recorded by a Varian Graphic Recorder (an example is given in Fig. 2). By means of crystal markers, which are also shown, the linear time axis may be converted to a linear frequency axis for line-width determinations. The line widths Δ are taken to be the separation of the maximum and minimum of the derivative curve. There are well-known relations[11] between T_2 and Δ.

In making measurements of Δ by tracing out the derivative curve, it is necessary to use a modulation amplitude considerably less than the line width. Also, the rate of passage through resonance must be slow compared to the integrating time constant of the final d.c. amplifier output stage driving the recorder. The longer the time constant, the narrower the band width and the lower the noise level. For weak signals such as those at room temperature, time constants of 5–10 sec were employed with suitably slow passage through resonance. A difficulty encountered was the gradual saturation of the signal due to the heating up of the spin system. It was considered best to shorten the final output time constant to 1 sec for the stronger signals at lower temperature, where T_1 is very long, in order to allow faster passages through resonance.

Since T_1 is of the order of minutes to as much as hours for the sample of LiF used in this experiment, it was possible to apply the direct method of observing the exponential growth of the absorption signal after saturation. The absorption signal was obtained by using square-wave modulation in conjunction with a lock-in amplifier.[10] It was necessary to observe the signal with a very weak r.f. field and to do so intermittently for only very short periods of time. In this way the act of observing the signal height did not greatly warm up the spin system. T_1 is found by measuring the time required for the absorption signal to build up to 0·63 of its final value. At the lowest temperatures the value of T_1 became so great that the slope of the curve at the beginning was measured and the spin-lattice relaxation time computed from this slope. Fields of 4000 G for ^7Li and 2800 G for ^{19}F were used. In accord with POUND[12] and WATKINS,[10] it was found that both T_1 and T_2 display a dependence upon crystal orientation in the field. Our research involved the temperature-dependence only, so it was therefore necessary to maintain a given orientation of the sample throughout the measurements.

VOL. 5 1958

RESULTS

Table 1 gives the averaged values of the line widths and shows that both ^{7}Li and ^{19}F have nearly the same line width when expressed in gauss and that there is no measurable dependence on temperature over the range covered. The averaged values have an error of 3 per cent, and this is about the same at each temperature.

Table 1. Averaged line widths in LiF

Temperature (°K)	^{7}Li (G)	^{19}F (G)
80	11·35	11·90
4·2	11·15	12·05
1·4	11·00	12·10

Fig. 3 is a plot of the output signal versus time taken on ^{19}F at 4·2°K, and from the curve the value of T_1 is deduced to be 50 min. In Table 2 the data on T_1 are summarized. We get good agreement with POUND,[8] whose work was carried out at room temperature. Finally, we have plotted the results in Fig. 4 as log T_1 versus log temperature

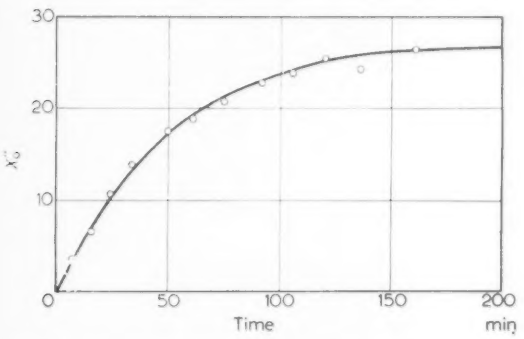

FIG. 3. Absorption peak signal output versus time (in min) for ^{19}F at 4·2°K. The solid line is the equation $\chi_0'' = 27{\cdot}5\,[1-\exp(-t/50)]$; the good agreement allows one to conclude $T_1 = 50$ min.

Table 2. Experimental values of T_1 in LiF

Temperature (°K)	^{7}Li (sec)	^{19}F (sec)	
300	720	120	
80	780	240	300
20	780	270	330
14	720		
4·2	8100	3000	
1·4	36,000	18,000	
H_0	4000 G	2800 G	4000 G

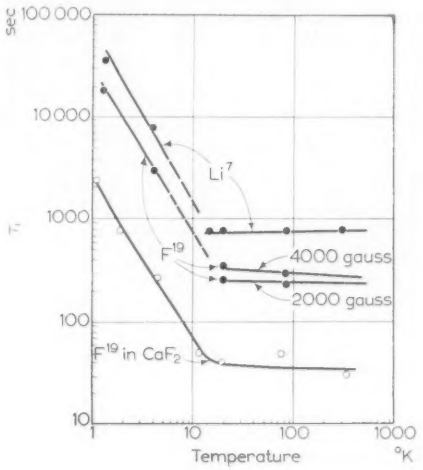

FIG. 4. Spin-lattice relaxation time, T_1, versus temperature in a single crystal of LiF of high purity. The field-dependence of the ^{19}F is illustrated. BLOEMBERGEN's values for ^{19}F in pure CaF_2 are also shown.[16]

for both ^{7}Li and ^{19}F. These curves may be compared to the lowest curve in Fig. 4, which represents the data published by BLOEMBERGEN[6] for ^{19}F in the pure crystal CaF_2. The accuracy of our measurements on T_1 is 10 per cent when based on data of the kind shown in Fig. 3, and we would say the error is twice as big at 1·5°K as well as at 80 and 300°K. At 20 and 80°K, T_1 was measured for ^{19}F, using fields of both 2800 and 4000 G. It is shown in Fig. 4 that T_1 increases slightly with H_0.

DISCUSSION AND CONCLUSIONS

The spin-lattice interaction for a really pure crystal arises from the fluctuations in the internal magnetic fields caused by one nuclear magnetic dipole on another. This mechanism was first suggested by WALLER,[13] and the value of T_1 at room temperature is expected to be of the order of 10^6 sec. Below room temperature the value of T_1 should vary as $1/T^7$, according to WALLER's theory. It is apparent that the relaxation process

observed in our crystal of LiF depends on some faster mechanism. As indicated in the introduction, both BLOEMBERGEN[6] and KHUTSISHVILI[2] base such a mechanism on traces of impurities of a paramagnetic ion such as the Fe ion.

Our results show that the ratio of the values of T_1 for Li and F is equal to their ratio of γ, the gyromagnetic ratio of each ion. Further work must be carried out on other crystals to determine whether this is an accidental relationship.

Acknowledgements—The authors are indebted to President W. V. HOUSTON and to Professor H. E. RORSCHACH, JR., for many discussions and helpful suggestions.

REFERENCES

1. BLOCH F. *Phys. Rev.* **105,** 1206 (1957).
2. KHUTSISHVILI G. R. *Soviet Physics JETP* **4,** 382 (1957).
3. SEIDEN J. *J. Phys. Radium* **18,** 173 (1957).
4. BRISCOE C. V. and SQUIRE C. F. *Phys. Rev.* **106,** 1175 (1957).
5. PURCELL E. *Physica* **17,** 282 (1951).
6. BLOEMBERGEN N. *Physica* **15,** 386 (1949).
7. ROLLIN B. V. and HATTON J. *Phys. Rev.* **74,** 346 (1948).
8. POUND R. V. *Phys. Rev.* **81,** 156 (1950).
9. POUND R. V. *Progr. Nuc. Phys.* **2,** 21 (1952).
10. WATKINS G. D. Thesis, Harvard University (1952).
11. ANDREW E. R. *Nuclear Magnetic Resonance* p. 105. Cambridge University Press (1956).
12. POUND R. V. *J. Phys. Chem.* **59,** 743 (1953).
13. WALLER I. *Z. Phys.* **79,** 370 (1932).

VOL.
5
1958

J. Phys. Chem. Solids Pergamon Press 1958. Vol. 5. pp. 89–101.

OPTICAL PROPERTIES OF SEMICONDUCTORS UNDER HYDROSTATIC PRESSURE—I. GERMANIUM*

WILLIAM PAUL and D. M. WARSCHAUER

Division of Engineering and Applied Physics, Harvard University, Cambridge, Mass.

Lincoln Laboratory, Massachusetts Institute of Technology, Lexington, Mass.

(*Received* 24 *June* 1957)

Abstract—The room-temperature absorption spectrum of high-purity single-crystal germanium has been measured between absorption coefficients of 1 and 100 at hydrostatic pressures up to 7000 kg/cm². The results have been interpreted to give a pressure coefficient for the optical energy gap in satisfactory agreement with the more precise value determined from measurement of the intrinsic resistivity as a function of pressure.

INTRODUCTION

MEASUREMENTS of the variation of the electrical resistivity of germanium with pressure[1] can be interpreted to show that, up to pressures of 10,000 kg/cm², the thermal energy gap between the valence and conduction bands of this element increases uniformly with pressure at a rate of approximately 5×10^{-12} eV/dyne cm^{-2}. Consideration of the band structure of germanium, as established by the theoretical calculations[2] of HERMAN and his co-workers, and by the cyclotron resonance experiments† shows that this increase is due to an increase in the separation of a conduction band minimum in the (111) direction in the Brillouin zone, and a valence-band maximum in the (000) position.‡ (See Fig. 1). Complicated behavior involving the electrons in the (100) conduction band minimum is suggested by the data at pressures greater than 10,000 kg/cm².[1] We shall not elaborate on this here, since the work to be reported is at pressures up to but not exceeding 10,000 kg/cm². No calculation of the effect of pressure on the band edges predicting the sign and size of the change to be expected has been reported to date. It might be expected that the change

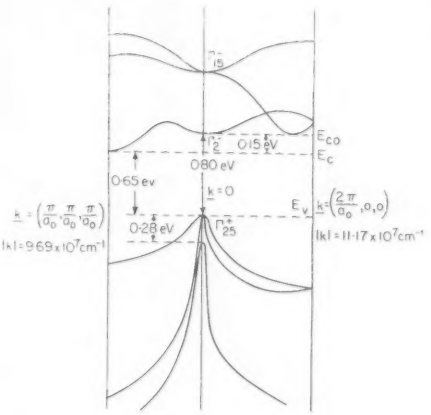

FIG. 1. Band structure of germanium.

in gap with pressure would be related to the electron and hole mobilities through a deformation potential theory.[3] An approximate attempt to derive such relations for germanium and silicon has been made by BROOKS[10] and the correlation found was fair. However, the complexity of the

* The research in this document was supported jointly by the O.N.R. under contract with Harvard University and by the Army, Navy and Air Force under contract with the Massachusetts Institute of Technology.

† References to the work of the groups at Berkeley and Lincoln Laboratory can be found under reference (2).

‡ The valence-band structure is described in reference (2). Its details will not concern us.

band edge structure and of the full mobility theory have, up to the present, prevented a really quantitative correlation being arrived at between theory and experiment. At the moment we can but try to fit the results of the measurement of resistivity and other parameters into one consistent pattern.* For this, the measurement of the effect of pressure on the infrared absorption spectrum is of considerable interest. This has been briefly reported before.[5]

Similar measurements on silicon and on alloys of silicon and germanium of varying composition will be reported in Parts II and III of this series.

METHOD

It is necessary to discuss the experimental apparatus and technique in order to understand the nature and magnitude of the errors in the measurements to be presented.

A hardened-steel pressure vessel having two sapphire windows on an axis transverse to the central bore was used to subject the sample to hydrostatic pressure during optical-transmission measurements. An optically-polished plane-parallel slab of 30 Ω cm *n*-type germanium, 0·030 in. thick, was mounted in a mask-and-holder arrangement parallel to the window surfaces and approximately 1 mm from the nearer surface. The holder used brass shim "fingers" to hold the sample in place gently; this design was used to minimize the possibility of non-hydrostatic stresses on the germanium due to the difference in compressibility between holder and sample. At the end of the experiment, a check was made that the sample was in the same position as at the start; it was, and the assumption was made that it had not shifted its position reversibly during the experiment. The sapphire windows were sealed by the POULTER technique.[6] High pressure was produced by a press kindly provided by Professor BRIDGMAN.[7] The pressure was measured with a manganin gauge calibrated against the freezing-point of mercury. A Perkin–Elmer monochromator with a glass prism provided chopped monochromatic radiation which was directed through the vessel and sample by an auxiliary optical system. The transmitted energy was detected by a cooled lead sulfide cell whose response was amplified and recorded by a 13 cycle Perkin–Elmer system. Carbon disulfide was used as the hydraulic fluid† in which the sample was immersed, because it was found to be the only common liquid meeting the requirements of transparency in the 1·5–2·5 micron infrared region and remaining liquid at room temperature up to 10,000 kg/cm².

The possible sources of error in the transmission measurements are:

(1) Source-intensity change with time.
(2) Source-spectral-dependence change with time.
(3) Detector-gain change with time.
(4) Detector-spectral-sensitivity change with time.
(5) Refractive-index changes with pressure:
  (a) Sample reflection correction.
  (b) Effect of sample-index change on beam geometry.
  (c) Change of index of refraction of fluid.
(6) Window distortion with pressure.
(7) Changes at reference wavelength (when used).
(8) Spectrometer resolution.

If a sample holder were available to move the sample in and out of the radiation beam during measurements at any given pressure, suitable and obvious procedures would allow for removal or minimization of error sources 1, 2, 3, 4, 6 and 7. Such a mechanism is now being built for use in this experiment, but it was not used in the present measurements. Another method of measuring the transmission was used for these data. A reference wavelength near the minimum of free carrier absorption was carefully chosen. Experimental runs of I (transmission with sample in vessel) were made at each pressure of interest, with the response always referred to the response at the reference wavelength. The sample was then removed and identical runs made of I_0 (vessel and fluid

* For Hall-effect and magnetoresistance measurements, see BENEDEK *et al.*;[4] for optical data, see WARSCHAUER *et al.*[5]

† There are very few liquids which show no selective absorption whatsoever between 1 and 2 microns. Of the common liquids, carbon tetrachloride and freon freeze at pressures below 4000 kg/cm². Carbon disulfide remains both liquid and transparent, but its toxicity and low flash point demand extra precautions. The density of CS_2 in the experimental area was kept as low as possible. Also, because of the possibility of a fast pressure leak or even of rapid vaporization of the CS_2 in a pressure explosion, and of its ignition by the hot tungsten bulb of the optical apparatus, the room was carefully ventilated, and fire-hazard precautions followed.

VOL. 5 1958

transmission), again referred to the reference wavelength. It can be shown that I/I_0 is then a measure of the relative transmission of the sample within the errors mentioned above. Errors 1, 2, 3 and 4 have been demonstrated by separate experiment to be small when appropriate experimental precautions are taken. Error 6 is partially corrected, although a spectral effect arising from the birefringence of the sapphire may exist. In considering error 8, we note that the spectral slit width used in the experiments was 9×10^{-3} microns. It can be shown, as will be discussed in more detail in a subsequent paper on silicon, that neither the shape nor the movement of the absorption edge is affected by large changes in resolution, at least up to the value mentioned here. Errors 5(b) and 5(c) remain uncorrected only if there is a strong spectral-dependence of the fluid or sample refractive-index variation. Error source 5(a) is treated as follows:

It is unlikely that the change of index of refraction of germanium with pressure is large and has a strong spectral-dependence. The change of the refractive index with pressure, calculated from a translation of the refractive index versus frequency curve of BRATTAIN and BRIGGS[8] along the frequency axis by the amount of the energy gap change with pressure, is of the order of 1 per cent in 8000 kg/cm². Considering this to be small, the procedure outlined above yields a satisfactory measure of the relative transmission both at any given pressure and also at all pressures relative to one another. *Experiments* on the change of transmission at the reference wavelength with pressure indicate that both the reference wavelength transmission and that of wavelengths nearer the edge increase by the same amount, approximately 4 per cent from 1 to 8000 kg/cm². It is as yet undetermined whether this change occurs because of fluid or sample changes of refractive index. However, since these changes are very slow functions of wavelength, the relative transmissions are not affected. In the data to be presented, these relative transmissions have been normalized to absolute transmission, in order to allow computation of absorption coefficients needed by theory.

In practice, the reference wavelength chosen was 2·26 microns. It was determined that this wavelength, although very close to the absorption edge, gave I/I_0 results negligibly different from the experimentally less-accessible, longer reference wavelengths. The values of I, including those at 2·26 microns, were measured at convenient pressure intervals. The sample was then removed and the values of I_0 measured, with a determination at the reference wavelength included. Relative transmission was obtained from the ratio of I to I_0. Curves of n and k for germanium were then prepared from the literature[8] with a reasonable averaging of the data. The formula quoted by BRATTAIN and BRIGGS[8] for transmission was modified for our particular sample arrangement, and the absolute transmission at the reference wavelength computed. The relative transmissions at this wavelength were then normalized to the computed value. The formula was then used, in conjunction with the n and k curves, to determine the absorption coefficient; the small correction for reflection at the sample faces is automatically taken into account.

Absorption coefficient curves were determined several times, with slightly different assumptions. An exact calculation was made, using a suitable extrapolation of the data of BRIGGS,[8] in accord with the curve of refractive index versus wavelength of BRATTAIN and BRIGGS.[8] Subsequent calculations, using constant indices of 4·1 and 4·2, showed no significant difference from the first calculation, when applied to the atmospheric pressure data. The high-pressure curves of absorption coefficient were therefore computed using a constant

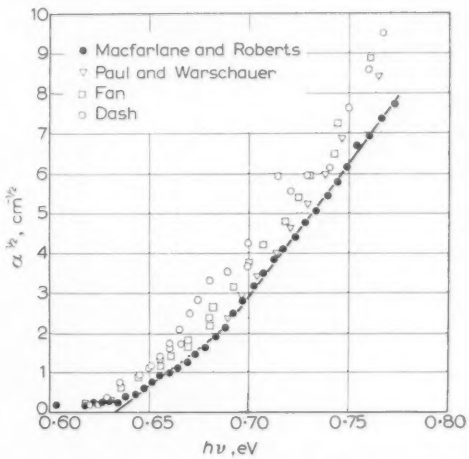

FIG. 2. Comparison of the germanium room-temperature low-absorption coefficients versus photon energy with the work of other investigators.

refractive index for germanium of 4·2. Fig. 2 compares our values of absorption coefficient at atmospheric pressure with those of other workers.

EXPERIMENTAL RESULTS

Fig. 3 shows the change in the absolute transmission as a function of wave-number, for several pressures between zero and 7000 kg/cm². The

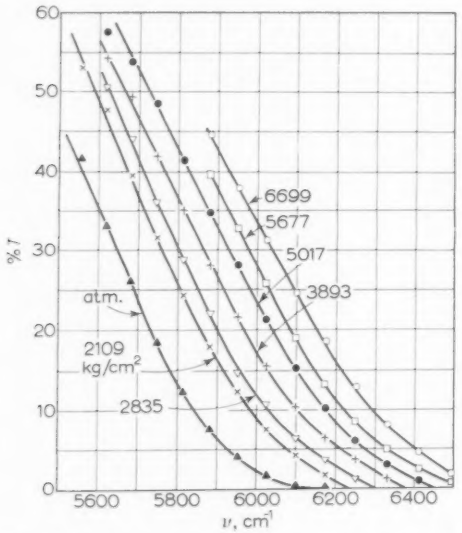

FIG. 3. Room-temperature transmissivity of a germanium sample versus wave-number at several pressures.

results clearly demonstrate a movement of the transmission edge toward higher wave number. The procedure outlined above is then applied to obtain Fig. 4, which shows the variation of absorption constant with the energy of the incident photon, for the chosen pressures.

Fig. 4 shows that there is a definite tendency for the shape of the curve of absorption coefficient α to change with pressure. This shape change will be more evident in later figures and will be interpreted in the next section.

Since some indication of the change in energy gap with pressure might be given by the horizontal shift of the absorption curves, Fig. 5 shows a set of isoabsorption curves. Pressure is plotted against photon energy, with α as a parameter. Apart from a slight scatter of the points, which is probably due to experimental error, the isoabsorption curves are straight lines. The slope of the isoabsorption lines varies from approximately 9×10^{-12} eV/dyne cm^{-2} to about 6×10^{-12} eV/dyne cm^{-2} at $\alpha = 3$.

It is to be noted that the interpretation of the low values of α is not obscured by the presence of appreciable free-carrier absorption, since this is considerably smaller at the frequencies of the measurement than the α values quoted.

Since the slope as $\alpha \to 0$ will correctly give the variation of the energy gap with pressure (apart from a possible correction for phonon energy changes discussed later), this variation must be

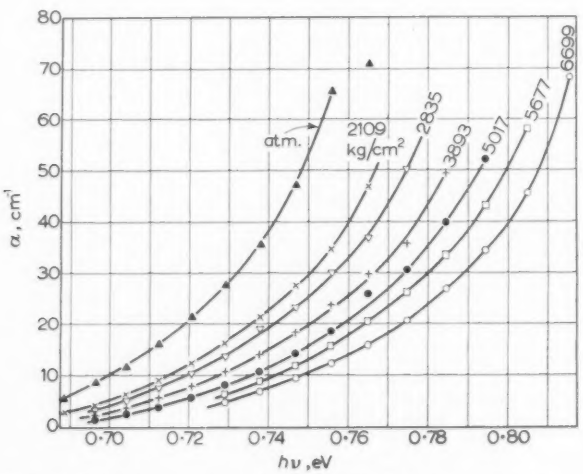

FIG. 4. Room-temperature absorption coefficient for germanium versus photon energy at several pressures.

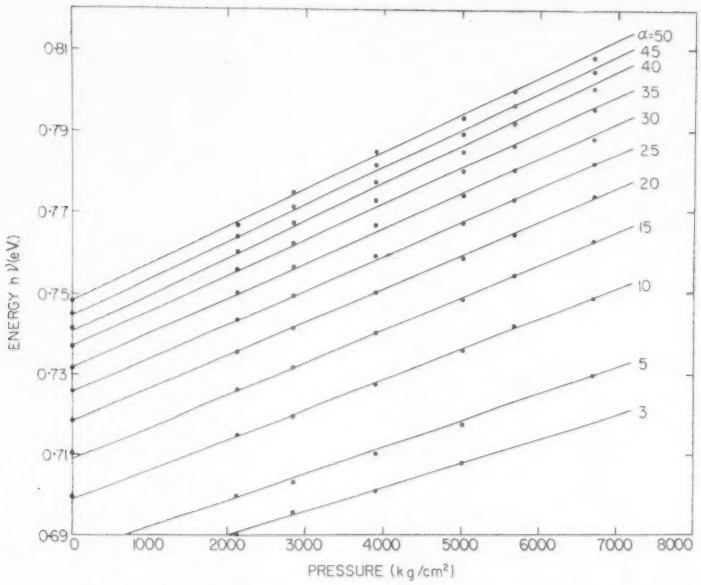

FIG. 5. Isoabsorption curves for germanium at room-temperature.

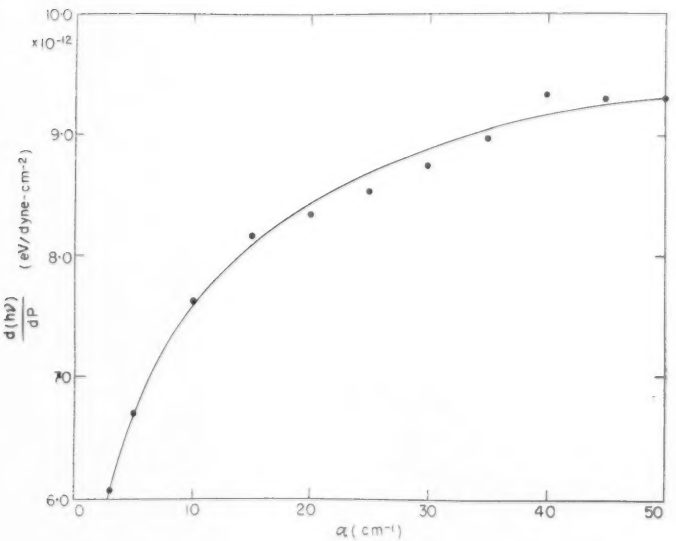

FIG. 6. Variation with absorption coefficient of the slope of the isoabsorption lines shown in Fig. 5.

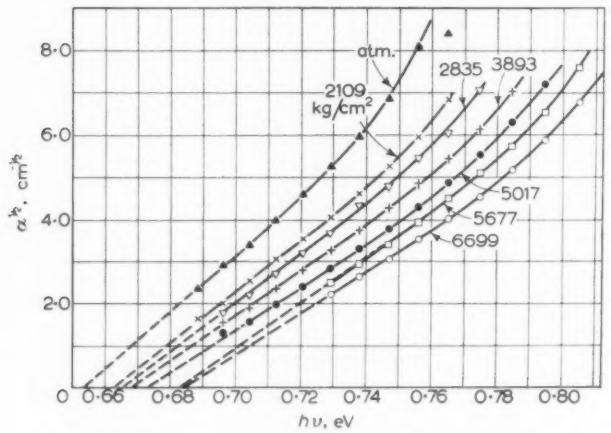

FIG. 7. Square root of absorption coefficient of germanium versus photon energy at several pressures.

less than 6×10^{-12} eV/dyne cm^{-2}. A more exact value requires a more reliable method of extrapolation than Fig. 6 would afford.

From the theoretical considerations of the next section, it appears that either $\alpha^{\frac{1}{2}}$ or $\alpha^{\frac{1}{3}}$ varies directly as $h\nu$ at low values of α. (Strictly speaking, $(\alpha\nu)^{\frac{1}{2}}$ or $(\alpha\nu)^{\frac{1}{3}}$ varies as $h\nu$, but for a limited range of ν our approximation will make little difference.) In Figs. 7 and 8 this is tested. From these figures alone it would appear that the $\alpha^{\frac{1}{2}}$ versus $h\nu$ curve is the better straight line. However, the apparent deduction from this must be qualified; this will be discussed in the following section.

The straight-line fits to the data in Figs. 7 and 8 have been extrapolated, and the $\alpha = 0$ intercepts on the $h\nu$-axis plotted against pressure in Figs. 9 and 10. The results were checked by the method of least squares. It is clear from Figs. 7–10 that the intercepts show a fair amount of scatter, although there is no recognizable curvature. Nevertheless, the limits of the energy-gap change from Fig. 9 are approximately 3·9 and 4·7

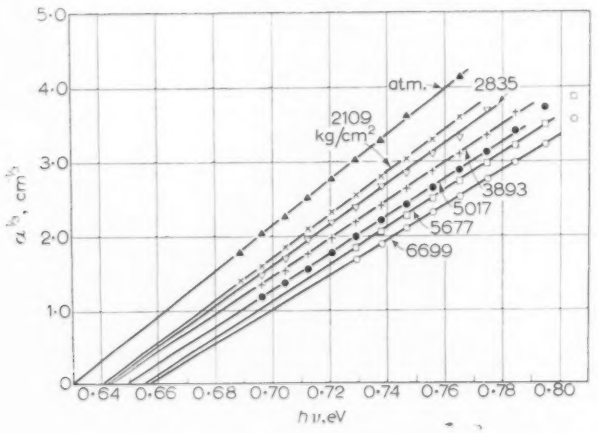

FIG. 8. Cube root of the absorption coefficient versus photon energy at several pressures.

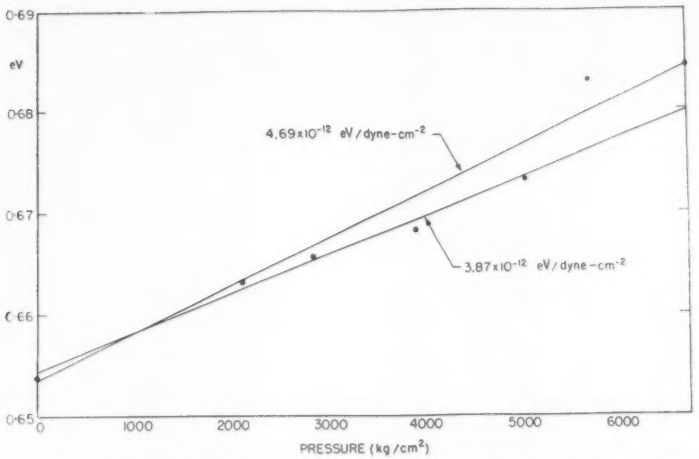

FIG. 9. Intercepts at $\alpha = 0$ from the $\alpha^{\frac{1}{2}}$ versus $h\nu$ curve of Fig. 7 plotted versus pressure.

eV/dyne cm^{-2}, and the change from Fig. 10 (where the line is straighter) is $4{\cdot}0\times10^{-12}$ eV/dyne cm^{-2}. This result is close to the value of $5{\cdot}0\times10^{-12}$ eV/dyne cm^{-2} found by PAUL and BROOKS.[1]

DISCUSSION

The general form of the absorption spectrum of germanium can be discussed in terms of the band-structure diagram of Fig. 1. The degeneracy of the valence band maxima E_v at the center of the Brillouin zone does not concern us. The conduction-band minimum at the center, E_{co}, is 0·80 eV above E_v.[9] The lowest conduction-band minimum E_c is in the (111) direction in the Brillouin zone, about 0·65 eV above E_v[10] at 294°K. There is also a conduction-band minimum in the (100) direction about 0·15 eV above E_c, which becomes important in germanium–silicon alloys,[11] and is supposed to become the lowest minimum in germanium at high pressures.[1,12]

The main absorption corresponds to electrons making the $E_v \rightarrow E_{co}$ transition; at lower frequencies, absorption takes place by the $E_v \rightarrow E_c$ transition, the momentum probably being conserved by the absorption or emission of phonons. We observe the second process in our experiments.

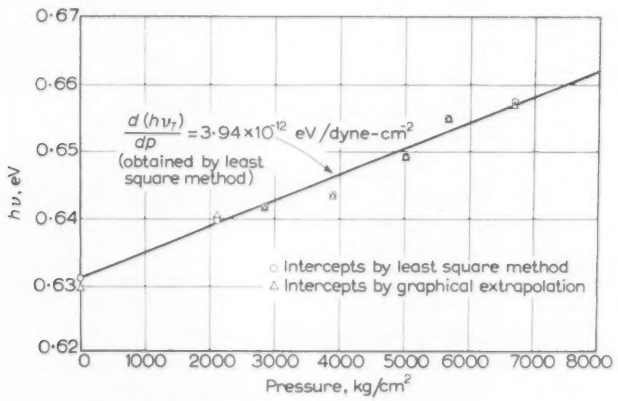

FIG. 10. Intercepts at $\alpha = 0$ from the $\alpha^{\frac{1}{2}}$ versus $h\nu$ curves of Fig. 8 plotted versus pressure.

BARDEEN *et al.*[13] obtain for this indirect or forbidden absorption the expression

$$\alpha = \frac{NM_s^2(2N_s+1)e^2(m_v m_c)^{3/2} f_{ia}(\Delta E)^2 \langle (E_a - E_i) \rangle_{av}}{4\pi^2 ncm\hbar^6 \nu \langle (E_a - E_f)^2 \rangle_{av}} \tag{1}$$

when the $E_v \rightarrow E_{co}$ transition is allowed parity-wise, and

$$\alpha = \frac{NM_s^2(2N_s+1)e^2 m_v (m_v m_c)^{3/2} (\Delta E)^3}{12\pi^2 ncm_T^2 \hbar^6 \nu \langle (E_a - E_f)^2 \rangle_{av}} \tag{2}$$

when the $E_v \rightarrow E_{co}$ transition is forbidden.

In these expressions N is the number of conduction-band minima, M_s is a matrix element describing the electron-phonon interaction, N_s the number of the appropriate phonons in the Bose–Einstein distribution at the temperature of the crystal, m_v the valence band density-of-states effective mass, m_c the same mass for a conduction-band minimum, f_{ia} an oscillator strength for vertical transitions, n the refractive index, m the free electron mass, and ν the frequency of the incident radiation. m_T is an effective mass defined by BARDEEN *et al.*[13] as a convenience in describing parity-disallowed transitions. ΔE equals $h\nu - E_g$, where E_g is the forbidden-energy gap between E_c and E_v in Fig. 1. E_i is the initial state of the electron in the valence band, E_a the intermediate state in the conduction band, and E_f the final state. For the energy-band structure of Fig. 1,

$$\langle (E_a - E_i) \rangle_{av} \sim E_{co} - E_v$$

and

$$\langle (E_a - E_f)^2 \rangle_{av} \sim (E_{co} - E_c)^2.$$

MACFARLANE and ROBERTS[14] have used a modified form of (1),

$$\alpha = A\left\{\frac{(h\nu - E_g + k\theta)^2}{e^{\theta/T} - 1} + \frac{(h\nu - E_g - k\theta)^2}{1 - e^{-\theta/T}}\right\}, \tag{3}$$

in fitting experimental results on germanium and silicon. They include the phonon energies $k\theta$ in their expression whereas BARDEEN *et al.*[13] ignore them. Coefficient A includes the constants and energy numerator and denominator of BARDEEN *et al.* Evidently it is assumed that the $E_v \rightarrow E_{co}$ transition is parity-allowed. It is not clear, from evidence on the indirect transitions alone, that this is so.[15] Plots of ln α versus ln $(\nu - \nu_t)$ where ν_t is the threshold frequency for absorption, might be expected to resolve this point. Such plots involve an initial choice of ν_t, which is subject to critical errors, especially since it is complicated by phonon absorption. FAN *et al.*[15] have tried this, and found $n = 2{\cdot}5$ in $\alpha \sim (\nu - \nu_t)^n$. Since the index is very sensitive to this choice, the deduced index is not too reliable.

It is clear that E_g can be obtained from equations (1) and (2) by plotting $\alpha^{\frac{1}{2}}$ or $\alpha^{\frac{1}{3}}$ against $h\nu$, and finding the intercept on the $h\nu$-axis at $\alpha = 0$. If equation (3) is adhered to, the deduction is not as straightforward. When $E_g + k\theta > h\nu > E_g - k\theta$, absorption of radiation can take place only by the simultaneous absorption of a phonon of momentum sufficient to carry the electron from the center of the Brillouin zone to the position of the conduction-band minima. Then only the first term of equation (3) is operative, and the $\alpha = 0$ intercept occurs when $h\nu = E_g - k\theta$. Since $k\theta$ is undetermined, this gives only an approximate value of E_g. When $h\nu > E_g + k\theta$, both terms in equation (3) are operative, and are of the same order of magnitude at room temperature. θ and A may be found from fitting complete absorption curves over a range of temperatures in a consistent fashion, assuming they are not functions of temperature. This is not really allowable, especially in the case of A, but there is no clear correction to apply. With θ known, E_g is determined.

MACFARLANE and ROBERTS[14] plot a curve of $\alpha^{\frac{1}{2}}$ versus $h\nu$ for $h\nu > E_g + k\theta$ and obtain a straight line. An analysis of this situation shows that the intercept of this line on the $h\nu$-axis at $\alpha = 0$ is not simply E_g, but contains a second term in $k\theta$ and kT. The exact value of the intercept depends on how the straight line is fitted to the data. According to MACFARLANE and ROBERTS, $\theta = 260°\text{K}$, which they deduced corresponds to the existence of eight minima in the conduction band about two-thirds of the way along the (111) axes to the

VOL. 5 1958

Brillouin zone boundary. Other evidence favors the location of the minima at the zone boundary.

If we assume that θ does not change with pressure* (which is not warranted *a priori*), and if we assume that we fit straight lines consistently to $\alpha^{\frac{1}{2}}$ versus $h\nu$ data, then the change with pressure of the $h\nu$ intercept at $\alpha = 0$ gives the pressure shift of the energy gap. If the correct law is not a law with squared terms on the right-hand side, but cubed terms, similar considerations apply.

It is straightforward to show that any one curve of $\alpha^{\frac{1}{2}}$ or $\alpha^{\frac{1}{3}}$ versus $h\nu$ where $h\nu > E_g + k\theta$ can be fitted equally well for $\theta = 260°$ or $\theta =$ (say) $360°$, by changing the coefficient A slightly. We know of no good way of estimating A independently. BARDEEN *et al.*[13] tried to do this from the experimental value of the mobility, but this is a questionable procedure, since other phonons are involved. Certainly A is not known well enough to allow a distinction to be made between $\theta = 260°$ and $\theta = 360°$ on the basis of one experimental curve.

If data involving low values of α are available, information may be obtained, as indicated above, from extrapolation to $\alpha = 0$ and also by demanding a consistent fit of the slopes above and below the "knee" of MACFARLANE and ROBERTS' data.[14] However, we tend to think that the experimental accuracy demanded in this region is considerable and that the possible sources of error in the pressure measurements would preclude the obtaining of useful information. Reflection corrections are of prime importance in this region, and the variation in refractive index of both germanium and CS_2 with pressure is unknown. It also appears that interpretation of *reliable* α versus $h\nu$ curves may be troublesome. For example, in the measurements of MACFARLANE and ROBERTS, one curve of which is included in Fig. 2, the fit of the line in the region $0 < \alpha < 1$ is not particularly good.

Our data scan only a small range of α (1–100 cm^{-1}), at one temperature, where phonon emission and absorption take place simultaneously. It was not possible to measure higher values of α with the sample we used; at high values of α, however, direct transition absorption is taking over, and the deductions made concern other inter-extrema transitions. Fig. 2 shows our data for α versus $h\nu$ at atmospheric pressure, plotted with those of other investigators. The general form of the curves is the same, but it is quite clear that quantitative information derived from the shape would not be consistent. Although our data are in reasonable agreement with those of the other investigators, we have not pressed for a determination of the absolute value of E_g (or $k\theta$), nor have we attempted to use the published values of A or θ in our interpretation, since we do not consider these sufficiently reliable at present. Instead, we have concentrated on the pressure coefficient of E_g and on changes in the coefficient A of equation (3). Fortunately, conclusions of value about these coefficients can be reached while uncertainty about the exact functional dependence of α still remains.

The isoabsorption curves of Fig. 5 and their slopes, as plotted in Fig. 6, indicate a shift of the absorption edge with pressure combined with a change in the shape of the edge. The value of the isoabsorption line slope at high values of α, about $8-9\times10^{-12}$ eV/dyne cm^{-2}, has been reported by us in a preliminary publication,[5] and is the value quoted for the change of the optical energy gap with pressure found by FAN *et al.*[15] and by NEURINGER.[16] The latter two investigations were carried out at pressures up to 1000 kg/cm^{-2}, and no change in the shape of the edge was mentioned, possibly because any change could not be positively identified in the small pressure range. We believe that the high value thus obtained is not to be interpreted as the gap change, and that from Fig. 6 alone this coefficient is less than 6×10^{-12} eV/dyne cm^{-2}. Since the pressure coefficient of the energy gap from measurements of the change of the intrinsic resistance is found to be about $5{\cdot}0\times10^{-12}$ eV/dyne cm^{-2}, the lower values are more plausible still.

Bearing in mind that the theoretical law for the absorption coefficient is not substantiated because there are uncertainties in the size of the phonons involved and in the application of $\alpha^{\frac{1}{2}}$ and $\alpha^{\frac{1}{3}}$ curves, and that possible changes of $k\theta$ with pressure must be ignored, we examine Figs. 7 and 8. It appears that the $\alpha^{\frac{1}{3}}$ versus $h\nu$ curve is the better straight line. We do not believe, however, that this warrants the conclusion that the appropriate law for α

* We have estimated the change in Θ from the compressibility of germanium and data on the change in ultrasonic wave velocity with pressure given us by Dr. MARTIN BAILYN of Northwestern University. The change is about an increase of 3 per cent in 10,000 kg/cm^2 and is considered small enough to neglect here.

contains cubed terms such as $(h\nu - E_g \pm k\theta)^3$. In the first place, very small changes in α, in the form of additive corrections due to errors in normalization, can alter the fit of the points to a straight line very considerably. This is true even though our absolute values for α are close to those of other investigators. In the second place, the assumption of a single interacting phonon for momentum conservation, and of one set of selection rules for vertical transitions, to explain absorption coefficients ranging over approximately 0·1 eV in photon energies, is probably an oversimplification. Nevertheless, if the laws have approximate validity, the pressure coefficient of the energy gap as deduced from the $h\nu$ intercepts at $\alpha = 0$ has equal validity. The intercepts, as seen from Fig. 7 and 8, give a value for the gap change of 4×10^{-12} eV/dyne cm^{-2} which is in not unsatisfactory agreement with the electrical value. Interestingly enough, roughly the same value is obtained from either law.

A slightly different method of finding the energy-gap change has been tried by us. Suppose the law $\alpha = B(\nu - \nu_t)^n$ holds, with n assumed unknown. First, we can plot ln α versus ln$(\nu - \nu_t)$ with ν_t as parameter, at each pressure. The resultant curves are nearly straight lines whose slopes give values for n. It is not in practice easy to say what n should be from these graphs, since equally good straight lines are found for n ranging from, say, $n = 1{\cdot}5$ to $n = 3{\cdot}5$. However, having obtained a set of corresponding n and ν_t for each pressure, ν_t can be plotted against pressure for any chosen n. The results show that the pressure coefficient, which is not too sensitive to the choice of n between 2 and 3, is about the same as that determined from the $\alpha^{\frac{1}{2}}$ or $\alpha^{\frac{1}{3}}$ curve intercepts. This method of determination is not a sensitive one, and is not recommended. We quote it only to illustrate that all these methods of analyzing the results give pressure coefficients near 5×10^{-12} eV/dyne cm^{-2}, in agreement with the electrical value.

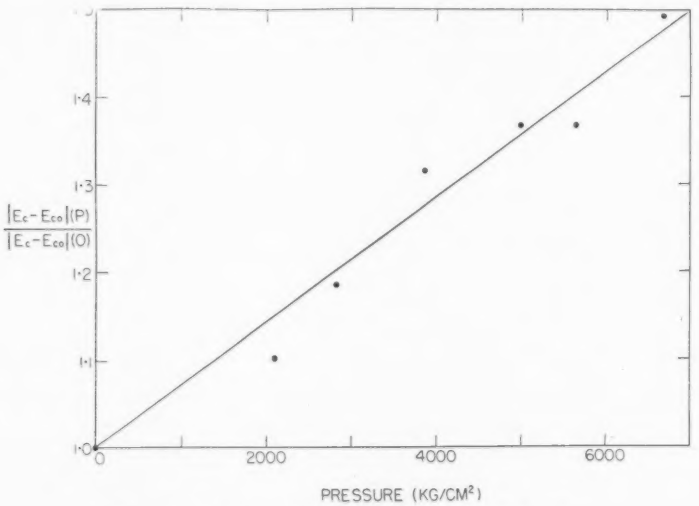

FIG. 11. Variation of the energy gap $(E_c - E_{co})$ with pressure.

The method of interpretation above would indicate that the coefficient A of equation (3), which is given by the expressions of equation (1) or (2), is changing with pressure. This is clearly reasonable from an examination of the parameters in the coefficient.

The phonon matrix element M_S^2 may be changing with pressure, but we have no way of predicting its behavior. The phonon density N_S may change because of a change of the vibrational spectrum of germanium, or because of an alteration in the position of the (111) minimum, but again we have no way of predicting the effect. The effective masses can also change, but this change we know to be small from pressure experiments on the

mobility of electrons and holes. Any change in refractive index near the edge has not been investigated experimentally yet. However, all the above changes, if they occur, are expected to be smaller than the changes in the values of $E_{co}-E_c$ and $E_{co}-E_v$. The change of E_c-E_v is given by the gap change deduced from electrical-resistivity measurements, or less certainly by the interpretation of the optical results presented above. The change in $E_{co}-E_v$ can be found approximately from the experimental work of FAN *et al.*[15] or of NEURINGER,[16] which would give

$$d(E_{co}-E_v)/dp = 1{\cdot}2\times10^{-11}\ \text{eV/dyne-cm}^{-2}.$$

This would make $d(E_{co}-E_c)/dp \approx 7\text{–}8\times10^{-12}$ eV/dyne cm^{-2}. We can now show that the present work gives indirect confirmation of this picture.

If we can assume a law of the form of equation (2), then we can write

$$\alpha = A(P)(h\nu-h\nu_t)^3 \qquad (4)$$

so that the slopes of curves of $\alpha^{\frac{1}{3}}$ versus $h\nu$ at several pressures give the variation of $A(P)^{\frac{1}{3}}$ with P. If we then assume $A(P)\propto 1/(E_{co}-E_c)^2$, we can find the variation of $E_{co}-E_c$ with P. This is presented in Fig. 11. There is considerable scatter to the points; however, the change is nearly 50 per cent in $E_{co}-E_c$ (atmospheric pressure) in 7000 kg/cm^2. Since the atmospheric pressure separation of E_{co} and E_c is about 0·15 eV, the pressure coefficient of $E_{co}-E_c$ is then approximately 1×10^{-11} eV/dyne cm^{-2}. Considering the assumptions involved, this is satisfactory agreement.

If we assume instead of equation (4) a law of the form

$$\alpha = A(P)(h\nu-h\nu_t)^2, \qquad (5)$$

where $A(P)\propto(E_{co}-E_v)/(E_{co}-E_c)^2$, we can again find $d(E_{co}-E_c)/dp$ by using the slopes of $\alpha^{\frac{1}{2}}$ versus $h\nu$ curves. As we saw, our data do not fit equation (5) very well. However, we do obtain order-of-magnitude agreement with 1×10^{-11} eV/dyne cm^{-2}.

CONCLUSIONS

Despite the fact that our determination of the absorption coefficients at atmospheric pressure is less direct than is usual because the sample has to be inside a pressure vessel, our curve of absorption coefficient versus photon energy is very similar to that published by other workers. It is apparent, however, that all the published curves of absorption coefficient are in qualitative but not quantitative agreement. The deduced energy gap will be approximately the same for each of these curves, but the phonon energy involved in the indirect transition process will not. In view of the importance attached to the deduction of the location of the conduction-band minima in establishing correct statistics for the carrier distributions, and in setting up a mobility theory for the germanium conduction band, it seems that the absorption curve found by MACFARLANE and ROBERTS[14] should be verified. This should be done preferably with high-purity single-crystal material to avoid the possibility of indirect transitions induced by imperfections and to reduce the free-carrier absorption background. MACFARLANE and ROBERTS' crystals were polycrystalline.

It may be difficult to obtain precise information from a *correct* absorption coefficient curve by the method used by MACFARLANE and ROBERTS. The theory assumes a single interacting acoustical phonon, whereas it is clear that beyond the foot of the absorption edge, lower-energy acoustical phonons can participate. It is not clear why transverse acoustical phonons and optical phonons are excluded at room temperature.

The law assumed by MACFARLANE and ROBERTS gives $E_g-k\theta$ as an intercept on the $h\nu$ axis at $\alpha = 0$ when the lower points on an experimental curve are extrapolated. These points are subject to considerable experimental error and, moreover, sometimes do not give a good straight line on which to perform the extrapolation. As is evident from an examination of Fig. 2, E_g cannot be assumed from electrical data in order to determine $k\theta$, since the value of E_g found from such data depends on a decision regarding four or eight minima in the conduction band. If eight minima are assumed, the thermal-energy gap is close to 0·673 eV. This would make the value of $k\theta$, required from MACFARLANE and ROBERTS' curves, about 0·040 eV, which is appreciably higher than the present estimate of $k\theta$ (Debye) = 360°K. If four minima are assumed, the thermal-energy gap is about 0·655 eV, making $k\theta = 0{\cdot}022$ eV, or $\theta \approx 260$°K. This is smaller than $k\theta$ (Debye). It is not impossible that $\theta = 260$°K represents a fair average value for the energy of the interacting phonon, but that a better

knowledge of the vibrational spectrum for germanium will show that this phonon energy is consistent with the existence of minima at the Brillouin-zone boundary. The higher absorption coefficients (above the knee in MACFARLANE and ROBERTS' curve) cannot be extrapolated to give an intercept at $\alpha = 0$ independent of $k\theta$ and kT. An attempted fit of the absorption curve, above and below the "knee" may yield all the unknown parameters, but with doubtful correctness. If absorption curves at different temperatures are used, as by MACFARLANE and ROBERTS, then either the individual temperature curves must be analyzed separately or together. If done separately, the above remarks apply to each. If considered together, there is a net simplification only if: (1) $k\theta$ is assumed independent of temperature, which is probably reasonable; (2) the coefficients in equation (3) are assumed independent of temperature, which is not strictly correct. The coefficient A may depend on temperature through N_s, n, m, $E_{co}-E_c$, and $E_{co}-E_v$.

Because of the uncertainties in the exact expression for the absorption coefficient, the lack of quantitative agreement in the published absorption coefficient results, and the difficulty of a really reliable deduction of E_g and $k\theta$ from the experimental curves, we concentrated on finding the pressure coefficients of the different energy gaps independent of the gaps themselves.

From the change of the slope of the isoabsorption plots alone, we deduce that the variation of the energy gap E_c-E_v with pressure is less than 6×10^{-12} eV/dyne cm^{-2}, which in itself can be compared with the pressure coefficient found from measurements of the intrinsic resistivity of $5{\cdot}0\times10^{-12}$ eV/dyne cm^{-2}. This agreement is not found by other workers. FAN *et al.*,[15] for example, find 8×10^{-12} eV/dyne cm^{-2} for this gap change. Since this agrees with the slope of our isoabsorption curves at high absorption coefficient and the range of pressure in FAN's experiment was so small (900 kg/cm^2) that a change in shape of the absorption edge might not be identifiable, we believe FAN's result and ours can be easily reconciled. NEURINGER[16] has recently reported a change of 8×10^{-12} eV/dyne cm^{-2}, at pressures, up to 1000 kg/cm^2, but he also finds no shape change, possibly for the same reason that FAN found none. He deduces, on the basis of the same type of analysis as we perform, that this value represents the true energy-gap coefficient. It is hard to see what physical mechanism would give a pressure coefficient for an optical energy gap different from that for a thermal one. On this basis alone, a lower value is more plausible.

A more exact deduction of the energy gaps can be made by applying the correct theory for the absorption coefficient. We have tried to show above the difficulties inherent in this procedure at the moment. Nevertheless, we have analyzed our data after the fashion dictated by equations (1)–(3), in the hope that useful qualitative information can be found, from the general pattern of the deductions. In doing this, we realize that we add several dubious assumptions to those already made. We have to assume pressure independence of θ. Furthermore, if equation (3) is followed, various straight lines can be fitted to $\alpha^{\frac{1}{2}}$ versus $h\nu$ or $\alpha^{\frac{1}{3}}$ versus $h\nu$ curves, depending on the part of the curve being fitted, and these will give different intercepts on the $h\nu$-axis at $\alpha = 0$. We know, since the shape of the absorption curve is changing with pressure, that we are probably fitting different parts of the curve at different pressures, and that the intercepts will not be the same combination of E_g, θ, and T. This is accepted as contributing to the spread of the points in Figs. 9 and 10, for example. For the energy gap E_c-E_v, the pressure coefficient is about 4×10^{-12} eV/dyne cm^{-2}; this is in fair agreement with the thermal value. It is probable that the pressure coefficients of the optical and thermal energy gaps will be brought into exact agreement by the application of more correct expressions for the absorption coefficient. In this connection we note that the coefficient found by PAUL and BROOKS[1] may be reduced if the electron mobility pressure coefficient is temperature-dependent.

Still more assumptions have to be made when the pressure coefficients of $E_{co}-E_c$ and $E_{co}-E_v$ are deduced. However, the order-of-magnitude agreement with direct measurements of the shift of the absorption edge for direct transitions is to be noted.

Acknowledgements—It is a pleasure to acknowledge the considerable help and guidance given us by Professor HARVEY BROOKS in this research. We would like to thank also Professor P. W. BRIDGMAN for the extended use of

VOL. 5 195

some of his high-pressure equipment, the Bell Telephone Laboratories and Mr. G. L. PEARSON for giving samples of germanium, and MELVIN G. HOLLAND, MARSHALL I. NATHAN and ARTHUR C. SMITH for advice and discussion.

REFERENCES

1. See PAUL W. and BROOKS H. *Phys. Rev.* **94,** 1128 (1954) for a review to June 1954 of these measurements.
2. See HERMAN F. *Proc. Inst. Radio Engrs.* **43,** 1703 (1955) for references to this work.
   See also GLICKSMAN M. and CHRISTIAN S. M. *Phys. Rev.* **104,** 1278 (1956).
3. BARDEEN J. and SHOCKLEY W. *Phys. Rev.* **80,** 72 (1950).
4. BENEDEK G. B., PAUL W. and BROOKS H. *Phys. Rev.* **100,** 1129 (1955).
5. WARSCHAUER D. M., PAUL W. and BROOKS H. *Phys. Rev.* **98,** 1193 (1955).
   WARSCHAUER D. M. and PAUL W. *Photoconductivity Conference* (Edited by R. G. BRECKENRIDGE, B. R. RUSSELL and E. E. HAHN). Wiley, New York (1956).
   PAUL W. and WARSCHAUER D. M. *Bull. Amer. Phys. Soc.* **1,** 226 (1956).
6. POULTER T. C. *Phys. Rev.* **35,** 297 (1930).
7. BRIDGMAN P. W. *The Physics of High Pressures.* Bell, London (1949).
8. BRATTAIN W. H. and BRIGGS H. B. *Phys. Rev.* **75,** 1705 (1949).
   BRIGGS H. B. and FLETCHER R. C. *Phys. Rev.* **87,** 1130 (1952).
   AVERY D. G. and CLEGG P. L. *Proc. Phys. Soc.* B **66,** 512 (1953).
9. ZWERDLING S. and LAX B. *Bull. Amer. Phys. Soc.* **2,** 141 (1957).
10. BROOKS H. *Advances in Electronics and Electron Physics* Vol. 7. Academic Press, New York (1955).
11. HERMAN F. *Phys. Rev.* **95,** 847 (1954).
    PAUL W. and WARSCHAUER D. M. *Bull. Amer. Phys. Soc.* **1,** 226 (1956).
12. BROOKS H. and PAUL W. *Bull. Amer. Phys. Soc.* **1,** 48 (1956).
13. BARDEEN J., BLATT F. J. and HALL L. H. *Photoconductivity Conference* (Edited by R. G. BRECKENRIDGE, B. R. RUSSELL and E. E. HAHN). Wiley, New York (1956).
14. MACFARLANE G. G. and ROBERTS V. *Phys. Rev.* **97,** 1714 (1955).
15. FAN H. Y., SHEPHERD M. L. and SPITZER W. *Photoconductivity Conference* (Edited by R. G. BRECKENRIDGE, B. R. RUSSELL and E. E. HAHN). Wiley, New York (1956).
16. NEURINGER L. *Bull. Amer. Phys. Soc.* **2,** 134 (1957).

J. Phys. Chem. Solids Pergamon Press 1958. Vol. 5. pp. 102–106.

OPTICAL PROPERTIES OF SEMICONDUCTORS UNDER HYDROSTATIC PRESSURE—II. SILICON*

WILLIAM PAUL and D. M. WARSCHAUER

Division of Engineering and Applied Physics, Harvard University, Cambridge, Mass.
Lincoln Laboratory, Massachusetts Institute of Technology, Lexington, Mass.

(*Received* 2 *August* 1957)

Abstract—The pressure coefficient of the optical absorption edge due to indirect transitions has been measured in silicon over a pressure range of 1–8000 kg/cm². A value of $(dE/dP)_T = -1{\cdot}3 \times 10^{-12}$ eV/dyne cm^{-2} was obtained, in agreement with other optical and resistivity measurements. The lack of an observable change of shape of the edge with pressure implies that a simple displacement of the (100) conduction-band minima relative to the (000) valence-band maximum takes place with change of pressure.

VOL. 5 195

INTRODUCTION

THE variation of the optical energy gap in germanium with hydrostatic pressure has been discussed by us in a preceding paper.[1] In this paper we shall present similar results for silicon, but since much of the technique of measurement and interpretation is common to both experiments, we refer the reader to the germanium discussion for many of the details.

The band structure of silicon is shown schematically in Fig. 1. Our primary concern in this paper will be with the pressure shift of the fundamental absorption edge at low absorption coefficients, i.e. with the absorption edge caused by indirect optical transitions from the top of the valence band (E_v) to the conduction-band minima (E_c) in the (100) direction, where the (000) minimum in the conduction band (E_{co}) is a possible intermediate state. Other details of the band structure, discussed elsewhere,[2] will not concern us here.

As we discussed in the introduction to our paper on germanium, it is not feasible at present to compare experimental measurements of the energy-gap change with pressure with a theoretical coefficient deduced from a deformation potential analysis. We can only try to fit our results on the measurement of resistivity and other parameters into a consistent pattern. Several estimates for

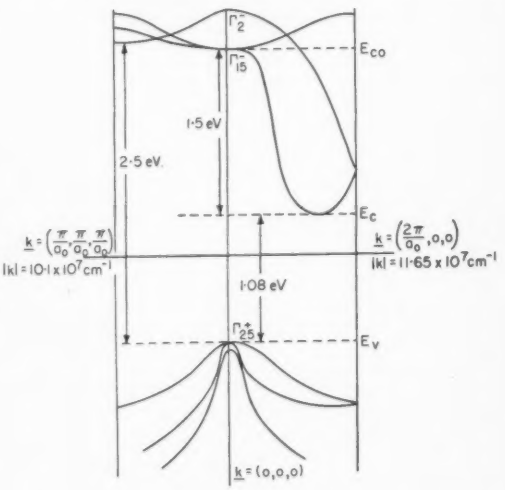

FIG. 1. Band structure of silicon in the (111) and (100) directions.

the pressure variation of the energy gap have already been reported. PAUL and PEARSON[3] cite a value $(dE/dP)_T = -1{\cdot}5 \times 10^{-12}$ eV/dyne cm^{-2} derived from resistivity measurements under the

* The research in this document was supported jointly by the Army, Navy, and Air Force under contract with the Massachusetts Institute of Technology and by the O.N.R. under contract with Harvard University.

assumption of no mobility changes. This value is in agreement with our optical value, previously reported briefly,[4] and with the value obtained optically by NEURINGER[5] over a smaller pressure range. NATHAN and PAUL[6] arrived at a value of -2×10^{-12} eV/dyne cm^{-2} from pressure measurements on a gold level in silicon. However, FAN *et al.*[7] observed an increase rather than a decrease in the optical energy gap with pressure.

METHOD

The discussion of the apparatus, experimental techniques, and treatment of sources of errors in the previous paper[1] is also pertinent here. The sample was an optically polished plane-parallel slab of 25–35 Ω cm *p*-type silicon, 0·0109 in. thick. Carbon disulfide was again used as hydraulic fluid because of its transparency in the near infrared. The pressure range in these experiments was from 1 to 8000 kg/cm^2.

Since some question seems to exist concerning the direction of the edge variation with pressure, and since the direction deduced may depend on the manner of reduction of results, we present in Fig. 2 tracings of the original recordings of the unnormalized transmitted energy of a sample as measured, with pressure as a parameter. No spectrum was taken at 3000 kg/cm^2. The vertical lines represent specific wavelengths on the spectra which have been matched on the combined tracing.

Because the edge shift is small over the available pressure range, further experiments were done, using the second and third order of a 300 lines/mm blazed grating mounted in a Perkin–Elmer spectrometer in order to obtain sufficient resolution and angular dispersion. Suitable filters were used to eliminate overlapping orders.

The smallness of the shifts dictates that we examine carefully the following possible sources of error in the measurement.

(1) Source-intensity change with time.
(2) Source-spectral-dependence change with time.
(3) Detector-gain change with time.
(4) Detector-spectral-sensitivity change with time.
(5) Refractive-index changes with pressure:
  (a) Sample-reflection correction.
  (b) Effect of sample-index change on beam geometry.
  (c) Change of index of refraction of fluid.

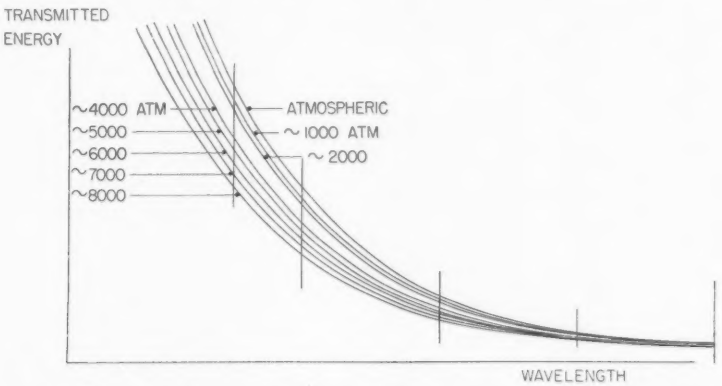

FIG. 2. Transmitted energy versus wavelength at several pressures for a silicon sample.

(6) Window distortion with pressure.
(7) Changes at reference wavelength (when used).
(8) Spectrometer resolution.

These are reproduced from the paper on germanium. From the discussion there, we have to examine most carefully sources 5 and 8. We consider error source 8 first.

Transmissivity as a function of pressure at a 500 micron slit width is shown in Fig. 3. The second order resolution at 1 micron for this slit width is 6×10^{-3} microns. In Fig. 4 transmissivities are shown for 2000 micron slit widths, i.e. at 3×10^{-2} micron resolution. This resolution is comparable to that of Fig. 2, where a glass prism was used. The two sets of curves are identical to

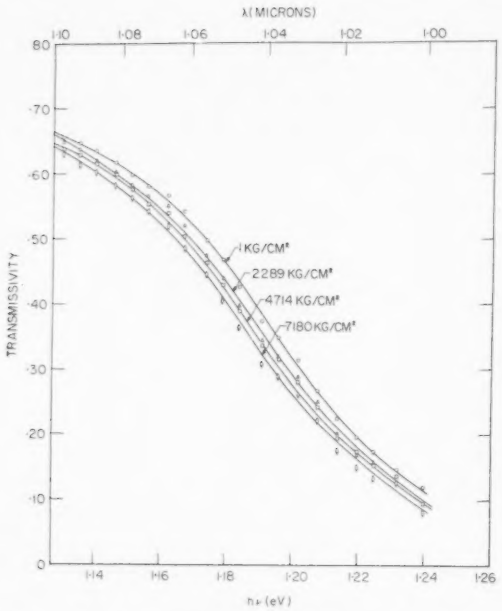

FIG. 3. Room-temperature transmissivity of a silicon sample versus photon energy at several pressures. Spectral slit-width of 6×10^{-3} microns used in measurement.

within other experimental errors, such as the detector sensitivity variation. Thus, for resolution of 3×10^{-2} microns or better, the same, presumably correct, shape and movement of the absorption edge is observed.

We consider error source 5 next. Errors 5(b) and 5(c) remain uncorrected only if there is a strong spectral-dependence of the fluid or sample-index variation. The change of the refractive index of silicon with pressure, calculated from a translation of the index-versus-frequency curve along the frequency axis by the amount of the energy-gap change with pressure,[3–6] is of the order of 0·1 per cent in 5000 kg/cm². Experimentally, a 5 per cent increase in unnormalized transmission at long wavelengths over a pressure range of 5000 kg/cm² was observed. It is not yet determined whether this change occurs because of fluid- or sample-index variation, but, in any case, the change is probably a slow function of wavelength. Since only a small wavelength interval is of interest in this experiment, it is unlikely the index of refraction changes of either the sample or the CS_2 are large enough to invalidate the normalization process for obtaining the absolute transmission. This normalization procedure was described in

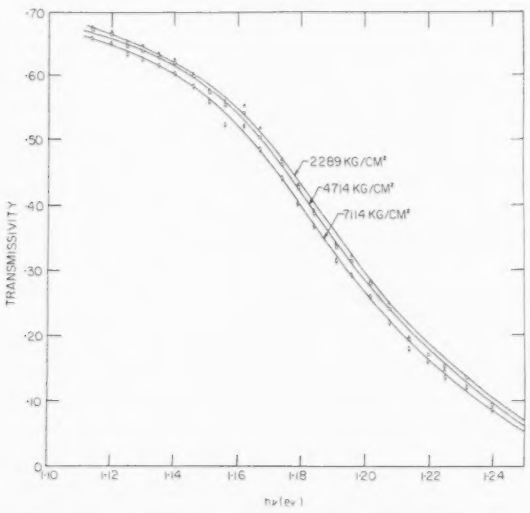

FIG. 4. Room-temperature transmissivity of a silicon sample versus photon energy at several pressures. Spectral slit-width of 3×10^{-2} microns used in measurement.

the paper on germanium. The absorption coefficients were similarly determined using values of the refractive index and extinction coefficient averaged from several sources.[8] Fig. 5 shows our atmospheric data compared to that of other workers.[7,9]

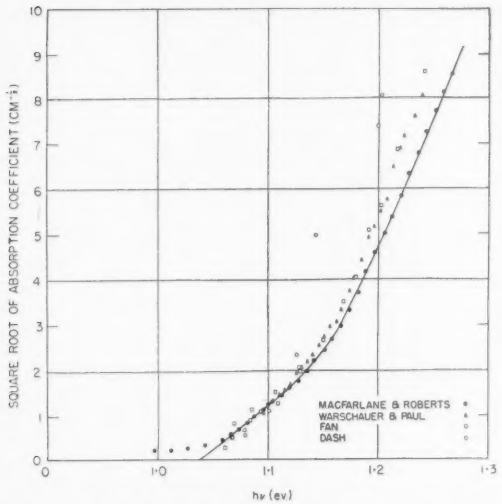

FIG. 5. Comparison of silicon room-temperature low-absorption coefficients versus photon energy with the work of other investigators.

RESULTS

As can be seen from either Fig. 3 or 4, the shift of the edge wavelength at any value of transmissivity is small as a function of pressure, and careful examination reveals no detectable change in the shape of the edge over this range of absorption constant and pressure. Thus, the pressure coefficient of the energy gap can equally well be found from isoabsorption or isotransmission curves, or from an extrapolation of the absorption coefficient curves to zero absorption coefficient. Although we have chosen to use curves of transmissivity to obtain the pressure coefficient of the energy gap, the corresponding absorption coefficients can easily be found by using Fig. 5. Fig. 6 shows an isotransmission plot derived from the curves of Fig. 3. The average pressure coefficient obtained from these curves, which were taken at room temperature, is $(dE/dP)_T = -1{\cdot}3\times10^{-12}$ eV/dyne cm^{-2}. This is seen to be in agreement with the values obtained by other workers cited earlier,[3–6] but not with that of FAN *et al.*[7] The fact that the isotransmission lines are approximately parallel to within the experimental accuracy verifies the lack of observable shape change in the absorption edge.

From the comparison of our absorption-coefficient range with that obtained by other

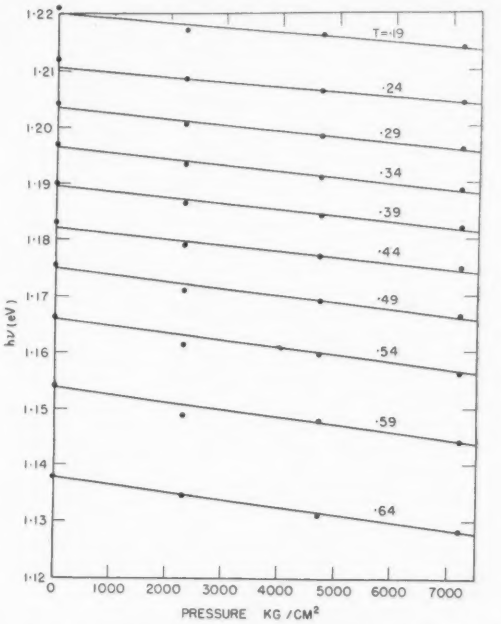

FIG. 6. Isotransmission curves for silicon at room temperature.

workers, as shown in Fig. 5, we interpret our measurements as pertaining to indirect optical transitions between E_v and E_c of Fig. 1. E_{co} may play a role as a virtual state in this process, but since its height above E_c and E_v is large, any movement of this minimum should have only a very small effect* on the value of $[d(E_c-E_v)/dP]_T$ as determined from the experiment. The good agreement between the above optical coefficient and the resistivity-derived values[3,6] indicates the extent of validity of this view. The more elaborate examination of the effects of pressure carried out on the germanium data has not been attempted here because of the lack of indication of any change in the shape of the absorption edge with pressure.

* See the discussion of the effect of energy denominator on absorption coefficient given in reference (1).

CONCLUSIONS

Our earlier measurements of the pressure coefficient of the optical energy gap $(dE/dP)_T = -1{\cdot}3\times10^{-12}$ eV/dyne cm^{-2} have been confirmed, in agreement with resistivity measurements[3,6] and with the value of NEURINGER.[5] The lack of change of shape of the absorption edge with pressure and the agreement of the coefficient with that derived from resistivity measurements indicate that the shift in the range of absorption measured can be attributed primarily to a simple displacement of the (100) conduction-band minima relative to the (000) maximum in the valence band.

Acknowledgements—We wish to thank several people for help in this work. Professor HARVEY BROOKS gave invaluable aid and guidance. Professor P. W. BRIDGMAN provided much pressure equipment and the benefit of his long experience. Bell Telephone Laboratories and Mr. G. L. PEARSON generously supplied the samples. ARTHUR C. SMITH, MARSHALL I. NATHAN and MELVIN G. HOLLAND were available for advice, discussion, and encouragement whenever needed.

REFERENCES

1. PAUL W. and WARSCHAUER D. M. *J. Phys. Chem. Solids* **5,** 99 (1958).
2. BROOKS H. *Advances in Electronics and Electron Physics* Vol. 7. Academic Press, New York (1955).
3. PAUL W. and PEARSON G. L. *Phys. Rev.* **98,** 1755 (1955).
4. WARSCHAUER D. M., PAUL W. and BROOKS H. *Phys. Rev.* **98,** 1193 (1955).
5. NEURINGER L. J. *Bull. Amer. Phys. Soc.* **2,** 134 (1957)
6. NATHAN M. and PAUL W. *Bull. Amer. Phys. Soc.* **2,** 134 (1957).
7. FAN H. Y., SHEPHERD M. L. and SPITZER W. *Photoconductivity Conference* (Edited by R. G. BRECKENRIDGE, B. R. RUSSELL, and E. E. HAHN). Wiley, New York (1956). Note comments regarding silicon at end of paper.
8. PFESTORF G. *Ann. Phys. Lpz.* **81,** 906 (1926).
   BRATTAIN W. H. and BRIGGS H. B. *Phys. Rev.* **75,** 1705 (1949).
   BRIGGS H. B. *Phys. Rev.* **77,** 727 (1950).
   MOSS T. S. *Photoconductivity in the Elements.* Academic Press, New York (1952).
9. DASH W. C. and NEWMAN R. *Phys. Rev.* **99,** 1151 (1955).
   MACFARLANE G. G. and ROBERTS V. *Phys. Rev.* **98,** 1865 (1955).

VOL. 5 1958

J. Phys. Chem. Solids Pergamon Press 1958. Vol. 5. pp. 107–116.

SOME MAGNETIC AND CRYSTALLOGRAPHIC PROPERTIES OF THE SYSTEM $Li_x^+Ni_{1-2x}^{++}Ni_x^{+++}O$*

J. B. GOODENOUGH, D. G. WICKHAM and W. J. CROFT†

Staff Members, Lincoln Laboratory, Massachusetts Institute of Technology, Lexington, Mass.

(*Received* 29 *August* 1957; *in revised form* 26 *September* 1957)

Abstract—Crystallographic and magnetic measurements of the system $Li_x^+Ni_{1-2x}^{++}Ni_x^{+++}O$ for the entire range $0 \leqslant x \leqslant 0{\cdot}5$ are reported. For values of $x \leqslant 0{\cdot}3$, the lattice appears to be antiferromagnetic and is cubic above the Curie temperature. For the range of compositions $0{\cdot}3 < x < 0{\cdot}5$, the lattice is rhombohedral and ferrimagnetic, a maximum magnetic moment per gram of 31 c.g.s. cm^3/g being observed at $x = 0{\cdot}46$. A maximum ferrimagnetic Curie temperature of 241°K was observed for the composition $x = 0{\cdot}41$. These properties are interpreted in terms of a partial ordering of lithium and nickel ions into alternate sets of (111) planes which couple antiparallel to one another, the moments within any set being either ferromagnetically coupled or paramagnetic, depending upon the number of non-magnetic near neighbors in the neighboring planes. This system is compared to the ordered rock-salt-type compound $Cu_{0{\cdot}25}Co_{0{\cdot}75}O$. The lack of ferrimagnetism and the tetragonal distortion to $c/a < 1$ in $Cu_{0{\cdot}25}Co_{0{\cdot}75}O$ are explained.

1. INTRODUCTION

THE electrical, magnetic, and crystallographic properties of the system of oxides represented by the formula $Li_x^+Ni_{1-2x}^{++}Ni_x^{+++}O$ have been the subject of several investigations. VERWEY and his co-workers[1] observed that when NiO and Li_2O are heated together at 1200°C in air, the following reaction takes place:

$$(\tfrac{1}{2})x\mathrm{Li_2O}+(1-x)\mathrm{NiO}+(\tfrac{1}{4})x\mathrm{O_2}\rightarrow \mathrm{Li}_x^{+}\mathrm{Ni}_{1-2x}^{++}\mathrm{Ni}_x^{+++}\mathrm{O}.$$

VERWEY prepared compositions for values of $x < 0{\cdot}3$ and studied the electrical conductivity and lattice parameter of these materials as a function of composition. These materials crystallized with the cubic rock-salt structure of NiO, the length of the unit-cell edge decreasing slightly with increasing concentration of Ni^{+++} ions. BROWNLEE and MITCHELL[2] have also observed this contraction of the lattice parameter with Ni^{+++} concentration and have used this fact as evidence that NiO is rarely stoichiometric, some Ni^{+++} usually being present. Actually NiO is not cubic below its antiferromagnetic Curie temperature; ROOKSBY[3] has shown that below 250°C the lattice is slightly distorted to give a rhombohedral cell of 60°6′ at room temperature.

The electrical resistivity of the system was found[1] to fall from 10^7 Ω-cm to about 1 Ω-cm as the concentration of Ni^{+++} increased to $Li_{0{\cdot}1}Ni_{0{\cdot}8}^{++}Ni_{0{\cdot}1}^{+++}O$. This decrease in resistivity is in accord with the atomic model of electronic conductivity in oxides which was developed by DE BOER and VERWEY.[4] The mechanism of electrical conductivity has also been discussed by HAUFFE and VIERK[5] and HAUFFE and BLOCK.[6]

The possible importance of the electrical conductivity for the magnetic properties of an oxide system containing magnetic cations was postulated by ZENER[7] in an attempt to explain the ferromagnetism observed by JONKER and VAN SANTEN[8] in the perovskite-type system (La, Ca)MnO_3. Since there was a strong correlation between ferromagnetism and low electrical resistivity, the indirect ferromagnetic interaction was ascribed to the coupling between the bound *d* electrons and

* The research in this document was supported by the Army, Navy, and Air Force under contract with the Massachusetts Institute of Technology.

† Now with R.C.A. Laboratories, Needham, Mass.

the migrant conducting electrons of a disordered array of Mn^{3+}, Mn^{4+} ions. If such a magnetic interaction is responsible for the ferromagnetism in the (La, Ca)MnO_3 system, it is reasonable to assume that similar indirect, ferromagnetic interactions should take place in other oxides containing two valence states of the same magnetic cation in a disordered array. JOHNSTON and HEIKES[9] have examined lithium-substituted systems of MnO, CoO, NiO and CuO and found no such magnetic interaction. FENSHAM,[10] in a study of the system $Li_x^{+}Ni_{1-2x}^{++}Ni_x^{+++}O$, observed a ferromagnetism with Curie temperature at 360°C which was definitely attributable to impurities of metallic nickel. Recently PERAKIS *et al.*[11] have reported the observation of an "induced ferromagnetism" in compositions of NiO containing small amounts of lithium (e.g. $Li_{0.02}Ni_{0.98}O$), but this weak magnetism was probably also due to a magnetic impurity. JANUSZ *et al.*[9] concluded that the lack of magnetism in the system $Li_xNi_{1-x}O$ ($x < 0.3$), where the resistivity showed a semiconductor type of behavior throughout the temperature range investigated, precludes the possibility in this system of any ferromagnetic double-exchange coupling according to the ZENER mechanism.

An investigation of the magnetic interactions in the system $Li_xNi_{1-x}O$ was initiated at this laboratory to see, first, whether there was any evidence of ferromagnetism and, second, whether there was any evidence of ferrimagnetism due to an ordering between the lithium and nickel ions. The possibility of preparing a complete range of solid solutions over the entire compositional range $0 \leqslant x \leqslant 0.5$ was suggested by the preparation of an almost pure $Li_{0.5}^{+}Ni_{0.5}^{+++}O$ by DYER *et al.*[12] who passed an oxygen stream through molten LiOH contained in a metallic nickel tube heated at a temperature of 800°C. The compound was found to have a layer-type structure ($CsCl_2I$ type) which is closely related to the rock-salt structure, the nickel and lithium ions preferentially occupying alternate (111) layers of octahedral positions within a slightly distorted cubic-close-packed oxygen lattice. Such a series of single-phase compositions was successfully prepared, and the layer-type structure was observed for compositions in the range $0.3 < x < 0.5$.

A significant saturation magnetization was observed at low temperatures through this same range of composition. Some crystallographic and magnetic evidence that this is a ferrimagnetic moment associated with an ordering of the lithium and nickel ions in a lattice of antiferromagnetically coupled nickel ions is given below. This system is contrasted with the ordered compound $Cu_{0.25}Co_{0.75}O$ in which there is no ferrimagnetism.

2. PREPARATION AND ANALYSIS OF SAMPLES

When Li_2CO_3 and NiO in the proper proportions are ground together and heated at 800°C, the Li_2O resulting from the decomposition of Li_2CO_3 combines with NiO, while a portion of the nickel equivalent to the amount of lithium present is simultaneously oxidized by the air to the trivalent state. Compositions $Li_x^{+}Ni_{1-2x}^{++}Ni_x^{+++}O$ in which x varied from 0 to 0·3 were prepared by this method. To obtain the compositions with the higher values of x in this range, frequent regrinding and several days' heating were required. More drastic methods were required in order to obtain values of x between 0·3 and 0·5. A mixture of lithium and nickel carbonates heated at 800°C under pure oxygen gave a maximum value of x equal to 0·325. Values for x in the vicinity of 0·4 were found by heating NiO with molten LiOH at 600°C. The presence of an oxidizing agent in the reaction mixture was necessary for values of x exceeding 0·4. The most useful one found was Li_2O_2, the mixture (contained in a silver crucible) slowly heated to 800–840°C. Excess lithium oxides were extracted with cold water from the insoluble, finely crystalline, black product. The product was then similarly retreated a second time with Li_2O_2.

The samples for analysis were reacted with a hydrochloric acid solution of potassium iodide under an inert atmosphere; the iodine liberated by the oxidizing action of the Ni^{+++} was titrated with standard sodium thiosulfate solution. Total nickel was determined as the dimethylglyoxime complex. On the basis of these two determinations, a representative series of compositions, correctly formulated as $Li_xNi_{1-2x}^{++}Ni_x^{+++}O$, was chosen for X-ray-diffraction and magnetic measurements. A number of samples were annealed at 650°C for 110 hr. Annealing at higher temperatures was impracticable because small changes in composition resulted from a loss of lithium as the volatile Li_2O.

VOL. 5 1958

3. CRYSTALLOGRAPHY OF $Li_x^+Ni_{1-2x}^{++}Ni_x^{+++}O$

The compound studied crystallographically by DYER *et al.*[12] may be represented by the formula $Li_{0.487}^+Ni_{0.026}^{++}Ni_{0.487}^{+++}O$. Analysis of the X-ray diffraction patterns indicated a structure analogous to that of cesium dichloro-iodide, $CsCl_2I$, which is rhombohedral with space-group D_{3d}^5—$R\bar{3}m$. The cell dimensions referred to hexagonal axes are $a = 2{\cdot}878$, $c = 14{\cdot}19$ Å. The oxygen anions form an approximately cubic-close-packed array with, presumably, lithium and nickel ions preferentially occupying alternate layers of octahedral interstices perpendicular to the threefold axis. A portion of the idealized, completely ordered structure is shown in Fig. 1. The unit cell of the rock-salt

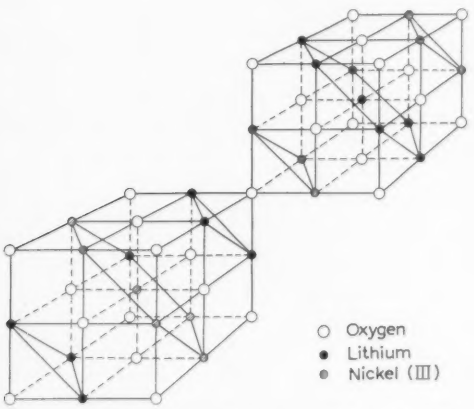

FIG. 1. Idealized crystal structure of $Li_{0.5}Ni_{0.5}O$.

structure of NiO may be visualized by considering either of the cubes in the figure and imagining all of the cations to be identical Ni^{++} ions.

In the present investigation the lattice parameters for $Li_x^+Ni_{1-2x}^{++}Ni_x^{+++}O$ were calculated from spectrometer traces taken with a Philips Norelco Diffractometer, using Fe$K\alpha$ radiation. It was found that as the value of x is increased from 0 to $\sim 0{\cdot}3$, the rock-salt structure is preserved, while the length of the unit-cell edge decreases slightly, in agreement with the reports of previous investigators.[1,2]

In the powder pattern for $Li_{0.325}^+Ni_{0.35}^{++}Ni_{0.325}^{+++}O$, however, an additional set of X-ray diffraction lines was present, indicating a doubling of the unit-cell edge or an eightfold increase in cell volume. The two cubes shown in Fig. 1 with a common corner now represent two octants whose threefold axes are coincident with the threefold axis of a new, larger unit cube, or pseudo-cube. Such a configuration can be seen to result from the appearance of two kinds of cation layers alternating on (111) planes. Whereas the constituency of the two kinds of layers is idealized in Fig. 1 to the extreme case of complete ordering between Li^+ and Ni^{+++} ions, the effect appears wherever the cation population of the two layers differs because of a partial ordering of the cations.

As the value of x is further increased, many of the X-ray diffraction lines in the powder pattern split in such a manner as to indicate a rhombohedral distortion of the original cubic lattice. The magnitude of the distortion increases as the composition $Li_{0.5}^+Ni_{0.5}^{+++}O$ is approached: however, the total distortion is very small. The rhombohedral angle varies from 33°28′ at $x = 0{\cdot}388$, where the distortion is first observed, to 33°22′ at $x = 0{\cdot}483$, where x has the maximum value obtained. The lattice parameters for this latter substance are identical to those given by DYER *et al.*[12] for the nearly identical composition $x = 0{\cdot}487$. The measured lattice parameters are summarized in Table 1.

An observable measure of the distortion can also be made by calculating the variation from 90° of the angle at one corner of a "cube" face of the "double" nickel-oxide unit cell. The deviation of the corner angle from 90° is calculated by using the approximation $\cos\gamma = 3\Delta/a$, where γ is the corner angle, a the unit-cell edge of the pseudo-cube, and Δ the difference between the cube diagonal and the rhombohedral c axis. As the value of x in $Li_x^+Ni_{1-2x}^{++}Ni_x^{+++}O$ changes from 0·325 to 0·483, the corner angle which meets the threefold axis of the unit rhombohedron varies from 90° to 88°54′.

The volumes of the unit cells corresponding to the various compositions are also listed in Table 1. For compositions 5 and 6, in which the layer-type structure has appeared and the length of the unit-cell edge has apparently doubled, one-eighth the unit-cell volume has been indicated. For the rhombohedral samples, twice the volume of the true rhombohedral cell is shown in order to compare volumes of equivalent size. The continuity of the solid-solution series is indicated in Fig. 2 by

Table 1. *Lattice parameters for* $Li_x^+Ni_{1-2x}^{++}Ni_x^{+++}O$

Composition	Rhombohedral unit cell		Hexagonal transform		Hexagonal c/a	Volume of cubic unit cell	$2\times$Volume of rhombohedral unit cell
	a (Å)	α	c (Å)	a (Å)		(Å^3)	(Å^3)
NiO						72·877	—
(1) $Li_{0\cdot052}^+Ni_{0\cdot896}^{++}Ni_{0\cdot052}^{+++}O$						72·512	—
(2) $Li_{0\cdot10}^+Ni_{0\cdot80}^{++}Ni_{0\cdot10}^{+++}O$						71·939	—
(3) $Li_{0\cdot20}^+Ni_{0\cdot60}^{++}Ni_{0\cdot20}^{+++}O$						70·907	—
(4) $Li_{0\cdot30}^+Ni_{0\cdot40}^{++}Ni_{0\cdot30}^{+++}O$					(4·900)	69·731	—
(5) $Li_{0\cdot325}^+Ni_{0\cdot350}^{++}Ni_{0\cdot325}^{+++}O$						69·528*	—
(6) $Li_{0\cdot370}^+Ni_{0\cdot260}^{++}Ni_{0\cdot370}^{+++}O$						69·072*	—
(7) $Li_{0\cdot388}^+Ni_{0\cdot224}^{++}Ni_{0\cdot388}^{+++}O$	5·032	33°28′	14·240	2·897	4·915	—	69·006
(8) $Li_{0\cdot41}^+Ni_{0\cdot18}^{++}Ni_{0\cdot41}^{+++}O$	5·023	33°28′	14·212	2·894	4·911	—	68·677
(9) $Li_{0\cdot46}^+Ni_{0\cdot08}^{++}Ni_{0\cdot46}^{+++}O$	5·018	33°25′	14·205	2·885	4·924	—	68·250
(10) $Li_{0\cdot475}^+Ni_{0\cdot05}^{++}Ni_{0\cdot475}^{+++}O$	5·016	33°24′	14·199	2·882	4·927	—	68·014
(11) $Li_{0\cdot483}^+Ni_{0\cdot034}^{++}Ni_{0\cdot483}^{+++}O$	5·013	33°22′	14·190	2·878	4·930	—	67·866

* One-eighth volume calculated for a cubic unit cell (see text).

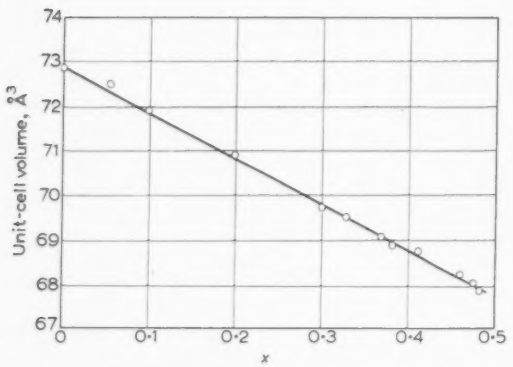

FIG. 2. Composition versus unit-cell volume of $Li_x^+Ni_{1-2x}^{++}Ni_x^{+++}O$.

the almost linear relationship of these volumes to the composition.

4. MAGNETIC MEASUREMENTS

The instrument used to determine the magnetic properties of the samples is an improved version of the vibrating-coil magnetometer first described by SMITH.[13] Details of the instrument will be given in a forthcoming publication.[14] Briefly, the sample is held in a uniform magnetic field, and the dipole field resulting from its magnetic moment is detected by a symmetric pair of vibrating coils. The powdered materials were weighed and packed in a teflon capsule: teflon caused no detectable signal at any temperature. The samples were then immersed in liquid helium (4·2°K) in a magnetic field of 10,000 Oe, and the resulting induced voltages were compared with those from a pure nickel standard of known mass. The measurements are accurate within 5 per cent.

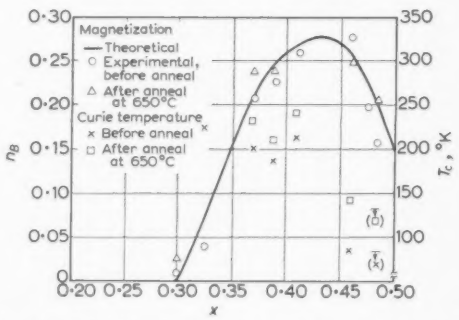

FIG. 3. Curie temperature, T_c, and magnetization, n_B, in Bohr magnetons per molecule as a function of x for the system $Li_x^+Ni_{1-2x}^{++}Ni_x^{+++}O$. (Theory assumes high-spin-state Ni^{+++} ions.)

To determine the Curie temperatures, the powdered samples were placed in copper holders placed in thermal contact with a thermocouple and heating coils within a liquid-nitrogen bath. The whole system was placed in a field of 3000 Oe, and the output voltages were automatically plotted as a function of the thermocouple voltage on an X–Y recorder. The Curie temperatures could be read off those graphs to within the calibration accuracy of the thermocouple.

The results of these measurements are summarized in Fig. 3. The authors are deeply indebted to K. DWIGHT and N. MENYUK, who made these measurements.

5. DISCUSSION

In order to interpret the observed magnetic moments in the system $Li_x^+Ni_{1-2x}^{++}Ni_x^{+++}O$, it is reasonable to start with the current knowledge of the magnetic properties of NiO. From neutron-diffraction experiments,[15,16] it is known that the Ni^{++} ions, which form a cubic-close-packed array in the octahedral interstices of the oxygen lattice, may be thought of as consisting of four interpenetrating simple-cubic sublattices, the magnetic moments on each sublattice coupling antiparallel to their near neighbors below the antiferromagnetic Curie temperature at 250°C. The principal magnetic-exchange interactions are within a given sublattice. Although the exchange interactions between sublattices are probably extremely weak, there is a significant dipole–dipole interaction which must influence the total configuration of the atomic moments both with respect to the lattice symmetry and the mutual configurations of the four sublattices. A general expression for this dipole–dipole interaction energy has been worked out for the rock-salt-type lattice;[17] a low-energy configuration which agrees with the neutron-diffraction data is one in which the atomic moments in a set of alternate (111) planes are parallel, but antiparallel to those in the neighboring (111) planes, the moment directions being directed along a [110] direction within these (111) planes. In zero external field, a similar low-energy configuration could be one in which the moments belonging to different sublattices might be oriented along different [110] directions in these (111) planes. Here too, however, there would be an antiferromagnetic coupling between neighboring (111) planes, so that if a ferrimagnetism occurred as a result of preferential ordering of cations on alternate (111) planes, there would be a single axis along which the atomic moments are aligned in the presence of an external field strong enough to saturate the material. It is therefore assumed that for all compositions at saturation the magnetic moments in alternate (111) planes are parallel, and antiparallel to those in the neighboring (111) planes.

From the crystallographic data, it is suggested that there is an ordering of the cations in alternate (111) planes. The general compositional formula is therefore better written as

$$(\underset{x-y}{Li^+}\ \underset{0.5-x-\xi}{Ni^{++}}\ \underset{\xi+y}{Ni^{+++}})_A(\underset{y}{Li^+}\ \underset{0.5-x+\xi}{Ni^{++}}\ \underset{x-y-\xi}{Ni^{+++}})_B O;$$

$$2y \leqslant x,\ 2\xi \leqslant (1-2x);$$

where the brackets represent sets of alternate (111) planes which couple antiferromagnetically and are designated sublattice A and sublattice B, respectively. Since the parameters y and ξ indicate, respectively, the degree of ordering of the Li^+ and the Ni^{++} ions, it is convenient to define two ordering parameters:

$$z \equiv 1-(2y/x) \text{ with } 0 \leqslant z \leqslant 1,$$

$$\zeta \equiv 2\xi/(1-2x) \text{ with } 0 \leqslant \zeta \leqslant 1.$$

If z and ζ are both zero, there is no ordering of the lattice, and the net magnetic moment is zero; in this case the material is antiferromagnetic. If, however, z and/or ζ are not zero, the net magnetic moments on the sublattices A and B are not equal, and a net ferrimagnetic moment may become manifest.

In order to calculate the ferrimagnetic moment for given values of z and ζ, it is necessary to know the net magnetic moment per ion for Ni^{++} and Ni^{+++}. As a first approximation it will be assumed that the angular momenta of these ions are quenched so that the spectroscopic splitting factor for each is $g = 2$. For Ni^{++} the spin-only value for the ionic magnetic moment is unambiguously $2\mu_B$: the magnetic moment of the Ni^{+++} ion, however, may be either $3\mu_B$ (high-spin state) or $1\mu_B$ (low-spin state). In an octahedral interstice, the degenerate d energy levels for the ion are split into

an upper, doubly degenerate level and a lower, triply degenerate level by the crystalline electric fields.[18] If the magnitude of this splitting is larger than the exchange splitting between the levels of different electronic spin, Hund's rule is not obeyed in Ni^{+++} as the triply degenerate level is completely filled with electrons of each spin, only one electron being left over to occupy a doubly degenerate level and contribute a magnetic moment. The large crystalline field associated with a Ni^{+++} ion makes the condition for this low-spin state highly probable.

Since only one of the doubly degenerate levels is occupied in the low-spin-state Ni^{+++}, it is anticipated that at low temperature the oxygen octahedron around low-spin-state Ni^{+++} may become distorted to tetragonal symmetry[19] with $c/a > 1$.

Besides the degree of order and the ionic magnetic moments, it is necessary to know the type and magnitude of the magnetic coupling which occurs between the various cations. If the Ni^{+++} ions are in a high-spin state, the Ni–Ni neighbors on opposite sides of an oxygen ion should be antiferromagnetic, and if the Ni^{+++} ions are in a low-spin state with ordered distortions of the oxygen octahedron to $c/a > 1$, the Ni–O–Ni interactions may be both ferro- and antiferromagnetic, depending upon direction.[20] If, however, the Ni^{+++} ions are in a low-spin state, but with no lattice distortion, the magnitude and sign of the Ni^{++}–O–Ni^{+++} and Ni^{+++}–O–Ni^{+++} interactions are not predictable from qualitative considerations alone. The recent report[21] that $LaNiO_3$ is paramagnetic down to liquid-helium temperatures, while the lattice structure remains, apparently, rhombohedral rather than distorting to the orthorhombic phase of pure $LaMnO_3$, does not relieve this ambiguity.

However, in order to make a calculation of the ferrimagnetic moments of the $Li_xNi_{1-x}O$ system which can be checked against the experimental points, it is assumed that all Ni–O–Ni interactions are antiferromagnetic. Two situations are considered: one with Ni^{+++} in the high-spin state, the other with Ni^{+++} in the low-spin state. With these assumptions and the experimental data, it is possible to determine the type and degree of ordering which take place in the lattice as well as the number of near neighbors to a given nickel ion in a simple-cubic sublattice which must also be nickel ions if the given nickel ion is to be coupled magnetically to the lattice.

If the origin of the ordering forces in $Li_xNi_{1-x}O$ is predominantly electrostatic, it is reasonable to assume that $\xi = \zeta = 0$; and if their origin is ionic-size differences, the ratio of Ni^{++} to total nickel should be the same on both sublattices, or $\zeta/z = x/(1-x)$.

(a) *High-Spin-State* Ni^{+++}

For high-spin-state Ni^{+++} ($3\mu_B$ per ion) and an electrostatic origin for the ionic ordering ($\xi = 0$), the magnetic moment per oxygen ion in $Li_xNi_{1-x}O$ is given by

$$\begin{aligned} m &= m_B - m_A, \\ m_B &= (1-W')(1-2x+3x-3y) \\ &= (1-W')(1+x-3y) \qquad (1) \\ m_A &= (1-W'')(1-2x+3y), \end{aligned}$$

where $(1-W')$, $(1-W'')$ are, respectively, the probabilities that the nickel ions in plane B, or A, have such an environment that they couple magnetically to the lattice. (If a nickel atom does not couple magnetically to the lattice, its contribution to the net ferrimagnetic moment is negligible; it does, of course, contribute to the paramagnetic susceptibility.)

The probability function W depends upon the number of nickel-ion neighbors in a simple-cubic sublattice which are required to couple a given nickel magnetically. If all the near-neighbor ions are Li^+, the nickel ion will not couple magnetically to the lattice since the exchange interactions between simple-cubic sublattices are extremely weak. The probability that all six near-neighbor cations on the simple-cubic array are Li^+ is given by

$$\frac{n}{N}\left(\frac{n-1}{N-1}\right)\left(\frac{n-2}{N-2}\right)\left(\frac{n-3}{N-3}\right)\left(\frac{n-4}{N-4}\right)$$

$$\times\left(\frac{n-5}{N-5}\right) \approx \left(\frac{n}{N}\right)^6 \text{ for } 6 \ll N.$$

Here n is the number of Li^+ ions in a pair of similar (111) planes and N is the total number of ions in those planes. If $f_0 = (n/N)$ is the fraction of cations which are Li^+ in a given set of alternate (111)

VOL. 5 1958

planes, then the probability that a nickel ion is paramagnetic is

$$W' = f_{0A}^6,\ W'' = f_{0B}^6 \tag{2}$$

if only one near-neighbor nickel is required to couple a given nickel magnetically to the lattice.

If a nickel ion is paramagnetic when there is either one or no near-neighbor nickel ion in its simple-cubic sublattice, it is necessary to further determine the probability that a nickel ion have five Li^+ near neighbors. For $6 \ll N$, this is given by

$$f_0 \cdot f_0 \cdot f_0 \cdot f_0 \cdot f_0 \cdot (1-f_0) + f_0 \cdot f_0 \cdot f_0 \cdot f_0 \cdot (1-f_0) \cdot f_0 + \ldots = 6f_0^5(1-f_0),$$

and the probability that a nickel ion is paramagnetic is

$$W = f_0 + 6f_0^5(1-f_0) = (6-5f_0)f_0^5.$$

So far this derivation does not take account of the fact that a paramagnetic nickel neighbor cannot be counted as a neighbor which contributes to the magnetic coupling. For the case that only one near-neighbor nickel is sufficient to cause magnetic coupling, this problem does not arise; but if two or more near-neighbor nickel ions are required, the fraction f must be appropriately corrected. For the case that at least two near-neighbor nickels are required for magnetic coupling within a simple-cubic sublattice, the correction is

$$f_A = f_{0A} + (1-f_{0A})6f_{0B}^5(1-f_{0B});$$

$$f_B = f_{0B} + (1-f_{0B})6f_{0A}^5(1-f_{0A}),$$

and

$$W' = (6-5f_A)f_A^5;\ W'' = (6-5f_B)f_B^5. \tag{3}$$

Similarly if a nickel ion is paramagnetic when there are two, or fewer, near-neighbor nickel ions in its simple-cubic sublattice, the probability that the nickel ion is paramagnetic is

$$W = f^4(15-24f+10f^2), \tag{4}$$

where f has been appropriately modified to account for the paramagnetic nickel neighbors.

Further, if N is the total number of cations present, $(x-y)N$ is the number of Li^+ ions in A planes, yN is the number of Li^+ in B planes, and $N/2$ is the number of cations in A or B planes. Therefore the fraction of Li^+ ions in A or B planes, respectively, is $f_{0A} = 2(x-y)$, $f_{0B} = 2y$. In terms of the ordering parameter z, these fractions can be expressed as

$$f_{0A} = x(1+z),\ f_{0B} = x(1-z). \tag{5}$$

The mathematical problem, then, is simply to determine what values of z and what formulas for W provide the observed magnetic moments. From equation (1), the number of Bohr magnetons per oxygen atom is given by

$$n_B = 3xz + (W''-W') - (W'+2W'')x + \tfrac{3}{2}f_{0B}(W'+W'') \tag{6}$$

where W is given by either (2), (3), or (4).

To determine the feasibility of expression (2), consider the magnetic moment for the composition corresponding to $x = 0{\cdot}48$. The minimum value for n_B should, for this value of x, coincide either with perfect ordering, or with very little ordering. Since the magnetic moments go through a maximum with increasing x, whereas the lattice distortion continuously increases with x, a large degree of ordering is indicated. For perfect ordering, $z = 1$ and $f_{0A} = 0{\cdot}96$, $f_{0B} = 0$, $W' = 0{\cdot}783$, $W'' = 0$, $n_B = 0{\cdot}28$. Since the measured values are considerably smaller than this minimum value, it is concluded that if the original assumptions are correct, more than one near-neighbor nickel cation in the simple-cubic sublattice is required to couple a nickel ion magnetically to the lattice.

Similarly it can be shown that expression (4) gives too low a value for the magnetic moment. It is therefore concluded that under the stated conditions, expression (3) gives the correct relation for W and that two or more near-neighbor nickel cations on the simple-cubic sublattice magnetically couple a nickel ion. From equations (3), (5), and (6), values for $z = z(x)$ were chosen to give a best fit with the experimental data. This curve is shown in Fig. 3; the corresponding values for $z = z(x)$ are given in Fig. 4.

A fit with the experimental points could also have been obtained by lowering z and giving ζ a finite value. Since the degree of order indicated by

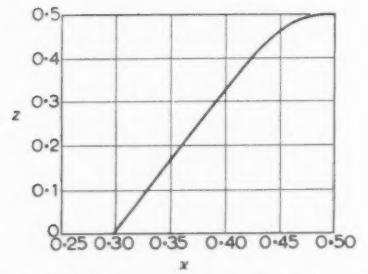

FIG. 4. Ordering parameter $z = 1-(2y/x)$ as a function of x for the system $(Li^{+}_{x-y}Ni^{++}_{0\cdot5-x}Ni^{+++}_{y})(Li^{+}_{y}Ni^{++}_{0\cdot5-x}Ni^{+++}_{x-y})O$, $x \geqslant 2y$, given high-spin-state Ni^{+++} ions.

Fig. 4 is already lower than might be expected for $Li_{0\cdot5}Ni_{0\cdot5}O$, this is not a reasonable alternative. Therefore it is concluded that if Ni^{+++} is in a high-spin state, it requires two or more Ni–O–Ni interactions to couple a nickel atom magnetically to the lattice, the origin of the ordering forces for Li^{+} is electrostatic, and the degree of ordering is as given in Fig. 4.

(b) *Low-Spin-State* Ni^{+++}

For low-spin-state Ni^{+++}, but all Ni–O–Ni interactions antiferromagnetic, the magnetic moment per oxygen ion in $Li_zNi_{1-z}O$ is given by

$$n_B = \tfrac{1}{2}[2+\zeta-x(3-z+2\zeta)](1-W') - \tfrac{1}{2}[2-\zeta-x(3+z-2\zeta)](1-W''). \quad (7)$$

If $\xi = 0$, it is not possible to account for the experimental data from equation (7). If, however, it is assumed that the origin of the ordering forces for lithium is the differences in ionic size, then $\zeta/z = x(1-x)$ and, given that only one Ni–O–Ni interaction is required to couple a nickel ion magnetically to the lattice, the theoretical curve for n_B is that shown in Fig. 5, where the values of $z = z(x)$ shown in that same figure were used to give a best fit with the experimental data.

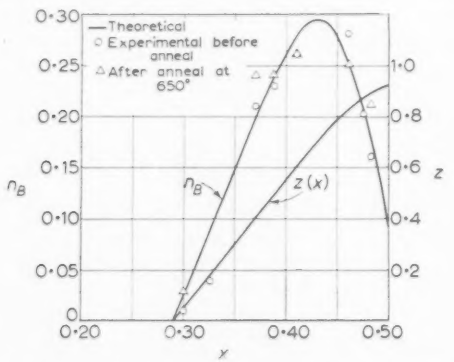

FIG. 5. Magnetization n_B in Bohr magnetons per molecule and ordering parameter z as a function of composition for the system $Li^{+}_{z}Ni^{++}_{1-2z}Ni^{+++}_{z}O$. (Theory assumes Ni^{+++} in low-spin state.)

It is concluded that if Ni^{+++} is in a low-spin state, only one Ni–O–Ni interaction is required to couple a nickel ion magnetically to the lattice, the origin of the Li^{+} ordering is predominantly elastic, and the degree of ordering is given by the curve $z(x)$ in Fig. 5.

(c) *Sensitivity to Heat Treatment*

Since, as shown in Figs. 3 and 5, the observed magnetic moment can be satisfactorily interpreted in terms of a ferrimagnetism associated with an ordering of the lithium and nickel ions into different (111) planes, it was decided to anneal the samples at 650°C for 110 hr to see whether the degree of order could be influenced by the heat treatment. The X-ray patterns showed no change; however, the magnetic properties changed as indicated in Fig. 3. There is no evident pattern to the changes in the value of the saturation magnetization, so that no conclusion can be drawn apart from the fact that the value of the saturation moment is sensitive to heat treatment as was suspected.

The Curie temperature should depend upon the number of nickel–nickel magnetic interactions. It can be expected to decrease monotonically with increasing lithium content, as indicated in Fig. 3. (The sample with $x = 0\cdot41$ was much more crystalline in appearance and gave a slightly different line profile in the spectrometer trace. This sample is slightly anomalous in all of its properties. This indicates that the parameters quoted are dependent upon preparation, as would be expected for properties which depend upon the degree of cation ordering.) It is interesting that for every sample annealed at 650°C, the Curie temperature was increased by the anneal. If the anneal had merely caused more complete ordering of the lithium and nickel ions in alternate (111) planes, the number of nickel–nickel bonds would have decreased, and the Curie temperature should have fallen. If, however, the anneal caused ordering to

VOL. 5 1958

take place within the (111) planes such that the Ni^{+++} ions tended to be surrounded, within the simple-cubic sublattice, by Li^+ ions, then the Curie temperature could be expected to rise, especially if the Ni^{++}–Ni^{++} magnetic interactions are stronger than the Ni^{++}–Ni^{+++} or Ni^{+++}–Ni^{+++} interactions. Such an ordering is likely, as it would further reduce the electrostatic energy of the crystal without appreciably affecting the elastic energy.

(d) *Comparison with Ordered* $Cu_{0.25}Co_{0.75}O$

BERTAUT and DELORME[22] have reported an ordered structure for the compound $Cu_{0.25}Co_{0.75}O$. This compound has a tetragonally distorted rock-salt-type lattice with $c/a < 1$, in which the Cu^{++} ions are ordered in alternate (001) planes. The compound is not ferrimagnetic. BERTAUT and DELORME noted that the tetragonal distortion was in an opposite sense to that usually found in compounds containing Cu^{++}.

If one assumes that the Cu^{++} order within the copper-containing (001) planes in such a way that one of the four simple-cubic, interpenetrating cation sublattices is all Cu^{++}, the other three are all Co^{++}, then it is possible to interpret both the tetragonal distortion and the lack of ferrimagnetism. The ordered structure is illustrated in Fig. 6.

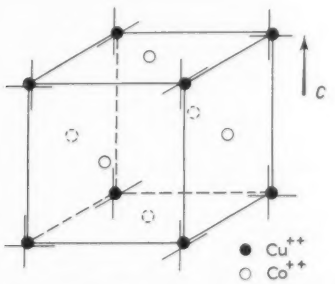

FIG. 6. Cation lattice for ordered $Cu_{0.25}^{++}Co_{0.75}^{++}O$.

The lattice distortion to tetragonal symmetry with $c/a < 1$ can be understood by analogy with the compound $LaMnO_3$.[20,23] Cu^{++} (d^9), like Mn^{+++} (d^4), has one electron missing from a completely filled half d shell. In an octahedral site of a cubic lattice, the lowest-energy configuration for such ions is that with an unfilled, or empty, $d_{x^2-y^2}$ orbital; this reduces the electrostatic repulsion between the cation and the four near-neighbor anions in the x–y plane; it also provides an empty orbital with large overlap of the filled p orbitals of these four anions in the x–y plane, so that electron sharing, or covalent bonding, is optimized in this plane. These effects cause the octahedron around the Cu^{++} or Mn^{+++} ion to become distorted to tetragonal symmetry[19] with $c/a > 1$. This is the distortion which is commonly found associated with Cu^{++} in octahedral interstices. In a lattice, the distorted octahedra couple together in a co-operative way so as to minimize the elastic energy of the crystal. In a simple-cubic array of such octahedra, such as is found in the copper sublattice of $Cu_{0.25}Co_{0.75}O$ or the manganese sublattice of the perovskite-type compound $LaMnO_3$, the configuration which minimizes the elastic energy is that shown in Fig. 6, where the crossed lines indicate the orientation of the plane about each cation which contains the shorter cation-anion bonds.[20] It is at once apparent that such a configuration would produce a lattice distortion to tetragonal symmetry with $c/a < 1$, even though the octahedra surrounding the individual Cu^{++} ions have a distortion with $c/a > 1$.

Since the magnetic interactions are antiferromagnetic within any simple-cubic cation sublattice, the compound will be antiferromagnetic rather than ferrimagnetic, as each sublattice is occupied by only one type of ion. Whereas the Co^{++} ions should be coupled antiferromagnetically to each of their near-neighbors on the simple-cubic sublattice, the Cu^{++} should, again by analogy with $LaMnO_3$, be coupled weakly within a (001) plane, antiferromagnetically between (001) planes.[20,23] Thus it is seen that an ordered rock-salt structure is not a sufficient condition for ferrimagnetism.

6. CONCLUSIONS

From the crystallographic, magnetic, and electric properties of the system $Li_x^+Ni_{1-2x}^{++}Ni_x^{+++}O$, it is possible to draw the following self-consistent conclusions:

(1) Double exchange is, in this system, a higher-energy mechanism than super- or semi-covalent exchange, these latter indirect-exchange mechanisms providing an antiferromagnetic interaction between near-neighbor nickel ions on the same simple-cubic sublattice.[19,20,24] This must be true, since the presence of both Ni^{++} and Ni^{+++} on the

same type of lattice sites does not introduce ferromagnetism even though their coexistence reduces the electrical resistivity by a factor of 10^7.

(2) In the samples measured, the ordering of lithium and nickel ions on alternate sets of (111) planes is not complete, the ordering parameter $z(x)$ varying as shown in Fig. 4 or 5. In this system, the appearance of ferrimagnetism depends upon preferential ordering in alternate (111) planes.

(3) Of the two possibilities considered, Ni^{+++} in a high-spin state or in a low-spin state, the conclusions for the low-spin case appear to be the most reasonable, provided that it is correct to assume that all Ni–O–Ni interactions are antiferromagnetic.*

(4) Ordered $Cu_{0.25}Co_{0.75}O$ is not ferrimagnetic because the population of (111) planes is not changed by the ordering. Its distortion to tetragonal symmetry with $c/a < 1$ is consistent with the behavior of Cu^{++} in other compounds.

---

* *Note added in proof*: Recent paramagnetic-susceptibility measurements by BONGERS[25] on $NaNiO_2$ and $(Li_{0.95}Ni_{0.05})NiO_2$ indicate that Ni^{+++} is in a low-spin state in these compounds. Also, although at room temperature BONGERS finds no evidence of octahedral-site distortion about low-spin-state Ni^{+++} in the $(Li_{0.95}Ni_{0.05}NiO_2$ specimen, he shows that such distortions are compatible with his room-temperature X-ray data for $NaNiO_2$.

REFERENCES

1. VERWEY E. J. W., HAAYMAN P. W., ROMEYN F. C. and VAN OOSTERHAUT G. W. *Chem. Weekblad* **44,** 705 (1948); *Philips Res. Rep.* **5,** 173 (1950).
2. BROWNLEE L. D. and MITCHELL E. W. J. *Proc. Phys. Soc.* B **65,** 710 (1952).
3. ROOKSBY H. P. *Nature, Lond.* **152,** 304 (1943); *Acta Cryst.* **1,** 226 (1948).
4. DE BOER J. H. and VERWEY E. J. W. *Proc. Phys. Soc.* **49,** 59 (1937).
5. HAUFFE K. and VIERK A. L. *Z. Phys. Chem.* **196,** 160 (1950).
6. HAUFFE K. and BLOCK J. *Z. Phys. Chem.* **196,** 438 (1951).
7. ZENER C. *Phys. Rev.* **82,** 403 (1951).
8. JONKER G. H. and VAN SANTEN J. H. *Physica* **16,** 337 (1950).
9. JOHNSTON W. D. and HEIKES R. R. *J. Amer. Chem. Soc.* **78,** 3255 (1956).
   JANUSZ T. P., HEIKES R. R. and JOHNSTON W. D. *J. Chem. Phys.* **26,** 973 (1957).
10. FENSHAM P. J. *J. Amer. Chem. Soc.* **76,** 969 (1954).
11. PERAKIS N., SERRES A., PARRAVANO G. and WUCHER J. *C.R. Acad. Sci., Paris* **242,** 1275 (1956).
12. DYER L. D., BORIE B. S., JR. and SMITH G. P. *J. Amer. Chem. Soc.* **76,** 1499 (1954).
13. SMITH D. O. *Phys. Rev.* **102,** 959 (1956); *Rev. Sci. Instrum.* **27,** 261 (1956).
14. DWIGHT K., MENYUK N. and SMITH D. O. *Conference on Magnetism and Magnetic Materials.* Sponsored by A.I.E.E., A.I.M.M.E., I.R.E., and Amer. Phys. Soc., Washington, D.C. (18–20 November, 1957), to be published in *J. Appl. Phys.*
15. SHULL C. G., STRAUSER W. A. and WOLLAN E. O. *Phys. Rev.* **83,** 333 (1951).
16. ROTH W. L. *American Crystallographic Association Annual Meeting Program and Abstracts* (11–15 June, 1956); *Bull. Amer. Phys. Soc.* **2,** 119 (1957).
17. LOEB A. L. and GOODENOUGH J. B. *Conference on Magnetism and Magnetic Materials* (16–18 October, 1956) p.55. A.I.E.E., New York (1957).
18. BETHE H. A. *Ann. Phys. Lpz.* **3,** 133 (1929).
19. GOODENOUGH J. B. and LOEB A. L. *Phys. Rev.* **98,** 391 (1955).
20. GOODENOUGH J. B. *Phys. Rev.* **100,** 564 (1955).
21. KOEHLER W. C. and WOLLAN E. O. *J. Phys. Chem. Solids* **2,** 100 (1957).
22. BERTAUT F. and DELORME C. *C.R. Acad. Sci., Paris* **238,** 1829 (1954).
23. WOLLAN E. O. and KOEHLER W. C. *Phys. Rev.* **100,** 545 (1955).
24. KRAMERS H. A. *Physica* **1,** 182 (1934); ANDERSON P. W. *Phys. Rev.* **79,** 350 (1950); VAN VLECK J. H. *J. Phys. Radium* **12,** 262 (1951); ANDERSON P. W. and HASEGAWA H. quoted in *Advanc. Phys.* **4,** 65 (1955).
25. BONGERS P. F. *Structure and Magnetic Properties of Several Complex Oxides of the Transition Elements.* Thesis, Univ. of Leyden (1957).

J. Phys. Chem. Solids Pergamon Press 1958. Vol. 5. pp. 117–128.

RADIAL ATOMIC DISTRIBUTION IN LIQUID HELIUM—4 BY X-RAY SCATTERING*†

W. L. GORDON,‡ C. H. SHAW and J. G. DAUNT

Department of Physics, Ohio State University, Columbus, Ohio

(*Received* 27 *July* 1957)

Abstract—Measurements have been made of the scattering of Cu$K\alpha$ X-rays ($\lambda = 1{\cdot}54$ Å) from liquid helium at several temperatures between 1·4 and 4·2°K, and from gaseous helium at 4·2°K in the same apparatus. The measurements were made with a low-background proportional counter over a range of scattering angles from 1·5° to 90° at 1·4 and 4·2°K, and for lesser angular ranges at other temperatures. The gas scattering gives a new comparison with theory for the total differential scattering cross-section of the helium atom. The liquid structure factor is found to be unity within the experimental error in the angular range from 65° to 90°, and it seems reasonable to assume that it remains unity for larger angles. On this assumption the radial atomic distribution for the liquid is computed by using the standard Fourier inversion procedure. Estimates are made of the mean separation of nearest neighbors in the liquid, as well as the co-ordination number at the various temperatures.

1. INTRODUCTION

SEVERAL studies have been made of the atomic order in liquid helium and its change with temperature, both by X-ray and by neutron scattering. No appreciable change in ordering is reported as the liquid temperature is brought below the lambda point, either in the X-ray results (large angle,[1,2,3] small angle,[4] or a combination of both[5]) or in the neutron studies.[6,7] Nor does theory indicate that significant changes are to be expected.[8] But because liquid helium shows some properties in sharp contrast with those of ordinary liquids, while it is an unusually "simple" liquid in several respects, a knowledge of its structure is particularly desirable.

If one examines the process of analysis which must be applied to the experimental curve of scattered intensity versus scattering angle to obtain the radial distribution of atomic density from an arbitrary origin atom in the liquid, he is impressed with the necessity of considerable accuracy in the experimental data. Without such accuracy the final result is likely to be highly ambiguous. For this reason, changes were made in the apparatus previously used in obtaining preliminary results[5] over the angular range 1·5°–90° scattering angle, and more accurate intensity measurements were completed at the several liquid temperatures of 1·4, 2·4 and 4·2°K.

One of the most important sources of uncertainty in the interpretation of X-ray diffraction patterns from liquids is the adjustment of the differential scattering cross-section per isolated atom to the observed intensities from the liquid in order to determine the interference effects due to the liquid state. This correction is a critical one in helium, because of the large Compton scattering at large angles. The difficulty is overcome in the experiment reported here by comparing directly the scattering from liquid helium to that from gaseous helium, thereby normalizing the

* This investigation was assisted by a grant-in-aid from the Research Corporation of New York, and by the Office of Naval Research through a contract with the Ohio State University Research Foundation.

† Grateful acknowledgement is made of financial assistance from the Ohio State University Development Fund for equipment.

‡ This work was submitted as a dissertation in partial fulfillment of the requirements for the Doctor of Philosophy degree at the Ohio State University. Now at Department of Physics, Case Institute of Technology, Cleveland, Ohio.

liquid scattering to the atomic scattering. The comparison was made possible by suitable design of the scattering apparatus and by the use of a very stable X-ray detector of low natural background count.

Analyses of the results were made by the usual technique of the Fourier integral transformation to obtain the radial distribution of atomic density in the liquid at the three temperatures. Since the average number density in the liquid is the same at 1·4 and 2·4°K, any difference in the resulting atomic arrangements aside from the temperature-dependence must arise from inherent differences in He I and He II.

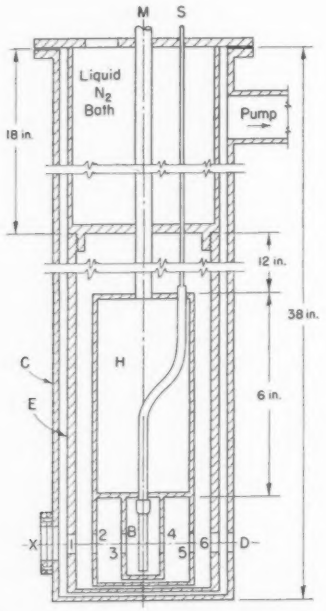

FIG. 1. The cryostat. The heavy copper cylinder E was kept at liquid-nitrogen temperature by the upper bath and acted as the main radiation shield. The liquid-helium bath H was supported by the filler tubes S, M and centered by fiber spacers in the shield E. The sample gas was admitted through the filler tube S and condensed in the beryllium sample tube B by thermal contact with the coolant in H. The X-ray beam entered the cryostat through a thin beryllium window at X and proceeded through windows 1, 2, 3, covered with thin beryllium in the various shields, to the scattering sample. The exit windows, 4, 5, 6, and D were horizontal slots, again covered with beryllium, to allow observation of the scattered beam throughout the range of scattering angles from 0° to 90°.

2. APPARATUS

The cryostat

Both the cryostat and the X-ray spectrometer were especially designed for the experiment. A schematic cross-section of the former appears in Fig. 1. The main body, 5 in. in diameter and 38 in. long, is made of brass $\frac{1}{8}$ in. thick, copper plated and polished inside, and is represented by C in the figure. The main body was fixed permanently in place relative to the X-ray spectrometer, to be described later, by suitable clamps. The inside parts of the cryostat could be removed as a unit from the top. The helium bath, H, of capacity 980 cm³, served to adjust the temperature of the liquid helium sample, which was contained in a beryllium metal tube, B, 0·25 in. in diameter, and having a wall thickness of 0·010 in. Reference to the figure will show that, though the helium sample system was separate from the reservoir system, the sample itself was in intimate thermal contact with the reservoir. The helium sample system, then, was a static one, while the reservoir system was, of course, dynamic. This arrangement has the obvious advantages over the dynamic sample system that: (1) the possibility of nitrogen or oxygen contamination of the sample is eliminated, (2) the sample vapor pressure is easily measured, (3) bubbles in the liquid do not form, and (4) helium gas at low temperature and at any pressure up to atmospheric can be used as the sample. The helium sample could be formed by introducing purified helium gas from a 50 l. storage tank under such conditions that approximately 2 cm³ of liquid would be condensed.

The evaporation rate of helium from the reservoir during the experiment was approximately 45 cm³ of liquid per hour. Experience during the course of the experiment showed that the most important single factor in keeping the evaporation rate low was the excellence of vacuum in the cryostat. The pressure was no higher than 1×10^{-7} mm Hg as shown by the ion gauge.

Suitable windows, covered with thin beryllium, were provided in the cryostat for the entry of the incident X-ray beam and the exit of the scattered beam. Radiation scattered at angles from 0° to 90° from the main beam could be observed.

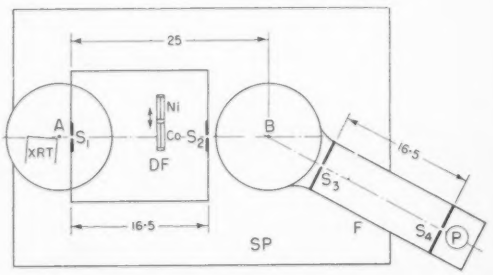

FIG. 2. The spectrometer. SP = surface plate; A, B = rotating tables; S_1, S_2, S_3, S_4 = slits; F = rotating arm; P = proportional counter; DF = differential X-ray filter; XRT = target of X-ray tube. Distances are in cm.

The spectrometer

Fig. 2 is a schematic plan of the spectrometer. Two accurately constructed rotating tables A and B were permanently mounted on a surface plate, which formed the base of the instrument. Narrow slits ($< 0{\cdot}001$ in. wide) were mounted accurately on and parallel to the axes of A and B to provide a fine sheet of X-rays. With the aid of the X-rays, the permanent slits $S_{1,2,3,4}$, each 0·50 mm wide, were positioned so that the incident and scattered beams would be aligned with the axis B within 0·001 in. After removal of the fine slits, the Machlett A-2 copper-anode X-ray tube used in the experiment was mounted on table A as near S_1 as possible.

An estimate of the angular resolution is given by the shape and width of the intensity curve as the arm F is swept through the direct beam. The curve had a somewhat Gaussian shape above one-tenth the maximum intensity with a width at half maximum of approximately 0·3°. The angular resolution, then, might be said to be roughly $\frac{1}{2}°$.

The spaces between S_1, S_2, and between S_3, S_4 could be flooded with helium gas to reduce absorption in the path. The detector arm F could be positioned manually or motor driven at a constant rate of 0·304°/min. Its angular position was read on a suitable scale. The nickel–cobalt foil differential filter, used to monochromatize the X-ray beam,[9] was mounted between S_1 and S_2 and was positioned by a two-phase reversible motor.

The cryostat was located over the table B in such a way that the sample tube was accurately on the axis of rotation. The effective height of the sample was determined by the vertical divergence of the slits S_3 and S_4.

At scattering angles greater than 20°, the scattering volume, defined by the slits $S_{1,2,3,4}$, was entirely in the helium. At lesser angles the beryllium scattering was measured at 4·2°K and subtracted from the observed intensities to give the scattering from the helium sample. The smallest practicable scattering angle, defined by the increasing background intensity with decreasing angle, was 1·5°.

The X-ray power supply

The high potential was rectified, condenser filtered, and stabilized.[10,11] Typical operating parameters were 40 kV and 17 mA. The X-ray intensity could generally be trusted to remain constant to 0·2 per cent for periods of an hour or so, though periodic checks were always made at least each half hour during an experiment.

The detecting system

The detector was a side-window proportional counter with a beryllium window 0·002 in. thick, filled with xenon to a partial pressure of 66 cm Hg and with methane to a partial pressure of 4 cm Hg. The pulse height distribution for Cu$K\alpha$ X-rays was nearly Gaussian, with a width at half maximum of 4·5 V at a median pulse height from the amplifier of 23 V. Pulses from the amplifier were led into a single-channel differential pulse height discriminator and thence to a scaler. Precautions were taken during the measurements that the pulse distribution remained centered in the 20–27 V "window" range of the pulse-height analyzer.

A cam driven by a synchronous motor actuated the scaler and the differential X-ray filter, so that measurements of 0·95-min duration could be made alternately through the nickel and cobalt filters with ease and convenience.[12] The interval of 0·05 min between the end of one reading interval and the beginning of the next was sufficient to read the scaler. This arrangement turned out to be a great boon in the thousands of readings made during the experiment.

The natural background of the counter without the channel discriminator was approximately 35 counts/min, while that with the discriminator was 3·5 counts/min. The operating potential and sensitivity of the counter have remained sensibly constant over a period of three years of use. The low background and excellent stability proved to be of great value in measuring the scattering from gaseous helium, where the intensity at 90° scattering angle was about 20 counts/min. This intensity was measured to 3 per cent standard deviation.

3. PROCEDURE AND RESULTS

Data of three kinds were required: (a) blank runs for the beryllium scattering at angles less than 20°, (b) scattered intensity from helium gas at 4·2°K over the entire angular range, and (c) diffraction patterns from liquid helium at the various temperatures. No dependence of the scattering from beryllium on temperature below that of liquid nitrogen (77°K) is expected because of the high Debye temperature of this metal, nor was any such dependence found.

Table 1 compares the observed scattering from the helium gas with that predicted by theory. Because the results of the calculations of the total scattering cross-section from HARTREE functions[13] by JAMES and BRINDLEY[14] differ from those by HERZOG,[15] the calculations were repeated. The new results are shown in the third, fourth, and fifth columns. These results are in somewhat better agreement with HERZOG than with JAMES and BRINDLEY.

Observed scattering cross-sections σ_{exp} are given in the sixth column. These were obtained from the measured intensities after correction for polarization of the scattered beam and the variation of scattering volume with angle, as determined geometrically. The scattering cross-sections σ_{total} and σ_{exp} were matched at 20°, where the statistical accuracy is greatest, by multiplication of the observed intensities by the appropriate factor. The curve-fit was within experimental error, though the latter is uncomfortably large at the smaller angles. This

Table 1. *Helium gas scattering*

Scattering angle (degrees)	$\sin\theta/\lambda$ (A^{-1})	$\sigma_{theor.}$*			$\sigma_{exp.}$*	Statistical accuracy (per cent)
		σ_e	σ_i	σ_{total}		
2	0·011	3·994	0·002	3·996	4·08	±6
5	0·028	3·96	0·02	3·98	4·14	±3
10	0·057	3·81	0·10	3·91	3·65	±3
15	0·085	3·56	0·22	3·78	3·73	±2
20	0·113	3·22	0·38	3·60	3·60	±1
30	0·168	2·54	0·72	3·26	3·30	±2·5
50	0·274	1·34	1·30	2·64	2·69	±3
70	0·373	0·68	1·62	2·30	2·24	±3
90	0·459	0·36	1·74	2·10	2·06	±3·5

* To obtain the total differential cross-section for the helium atom σ_{total} should be multiplied by the Thomson scattering per electron. σ_e and σ_i represent the elastic and inelastic contributions, respectively.

is brought about by the feebleness of the gas scattering in this angular range, as compared to that of the beryllium container, so that the former scattering is obtained as the (relatively) small difference between two large numbers of counts.

The last column of Table 1 shows the statistical accuracy of the observed intensities. At large scattering angles this may likewise be taken as the precision, for there should be no other experimental uncertainties sufficiently large to influence this estimate. Agreement of theoretical and observed scattering cross-sections over the range 20°–90° scattering angle verifies this. However, at smaller scattering angles, another important source of uncertainty enters, namely, the presence of iron K fluorescence radiation from the minute impurities in the beryllium sample tube. This source of error was eliminated by shifting the X-ray differential filters from the position shown in Fig. 2 to a new position between S_3 and S_4 for all small-angle data.

During the gas-scattering measurements, the intensities at the various angles were referred to the intensity at 20° scattering angle, where the beryllium scattering had fallen to a negligible level, but where the gas scattering was still satisfactorily intense to give good statistics in a reasonable time. It was the intensity at this position, then, which was used to determine the scale between the gas scattering and the liquid scattering, as described below.

Scattered intensities from the liquid were observed by two techniques. In the early work the detector arm was driven at the constant angular rate of 0·304°/min. When enough data had been

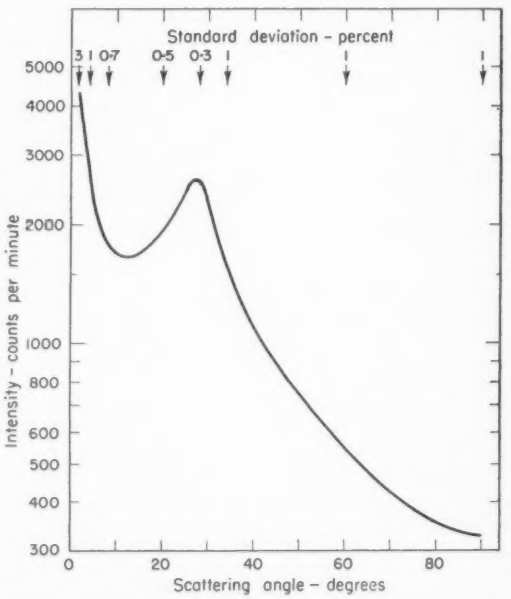

FIG. 3. Observed scattering curve on a logarithmic scale from liquid helium at 4·2°K. Only one correction, that for scattering from the beryllium container, has been applied. Accuracy of the data is indicated by the standard deviations given at the top.

accumulated to indicate the general form of the intensity curve, selected points were chosen and the intensities were measured accurately at these points. The reference angle, to which all liquid intensities were referred, was 28°, the position of maximum intensity for radiation scattered by the liquid. During the course of the work, seventeen determinations of the ratio of liquid to gas scattering were made at the reference angles mentioned above. The standard deviation of this ratio was 1 per cent.

Fig. 3 is an illustration of the type of liquid diffraction pattern observed over the full scattering angle range 1·5°–90°. It shows the smoothed composite curve from all the data obtained at 4·2°K by both sweep and point techniques, corrected only for background scattering obtained with the sample tube evacuated. The statistical standard deviations in several angular regions are given for the corrected curve to illustrate the accuracy of the experiment. At angles greater than 20° the background intensities are quite small, ranging from 4 counts/min at 90° to 9 counts/min at 20°. Inside of 20° the beryllium scattering rises rapidly, until, for angles less than 5°, the statistical accuracy for the liquid scattering is quite noticeably impaired.

With the liquid held at 1·4°K, scattering data were obtained over the same angular range as at 4·2°K and to approximately the same statistical accuracy except at small angles where the lower intensities led to increased statistical error. At both 1·4 and 4·2°K, the scattered intensities over the angular range 65°–90° agree within the statistical error with the scattering from the same number of gas atoms; that is, no interference effects are found in the scattered beam for angles greater than 65° (see Fig. 6).

In order to compare the diffraction patterns from the liquid in the helium I and helium II regions, but at a constant number density, data were obtained in the angular range 1·5°–60° with the liquid at 2·4°K, where the number density is identical to that at 1·4°K. Because the low intensities at large angles would have required an impractically large time for measurement, it was assumed that the curve for 2·4°K would follow exactly that at 1·4° for angles greater than 60°. Accuracy comparable to that at 1·4°K was obtained over the angular range studied.

To give a more complete picture of the scattering at angles less than 28°, data were also taken at the intermediate temperatures of 3·0 and 3·5°K. These results are shown in Fig. 4, together with the 1·4, 2·4 and 4·2°K data in this angular range. All observed points are shown and error bars give an indication of the statistical accuracy at the smallest angles. Again, the beryllium background has been subtracted.

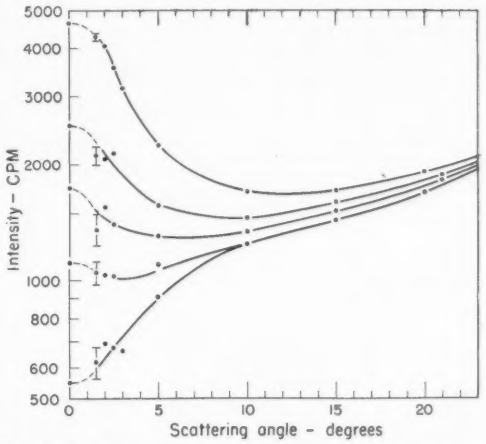

FIG. 4. Small-angle scattering from liquid helium on a logarithmic scale. The curves are, from bottom to top, for 1·4, 2·4, 3·0, 3·5 and 4·2°K. Error bars give standard deviations in the intensities at the smallest angle for which measurements could be made; accuracy improves with increasing scattering angle. Intensities predicted from statistical theory[8] for forward scattering are indicated.

Fig. 5 displays reduced scattering curves for the liquid temperatures of 1·4, 2·4 and 4·2°K. To obtain these curves, the observed intensities have

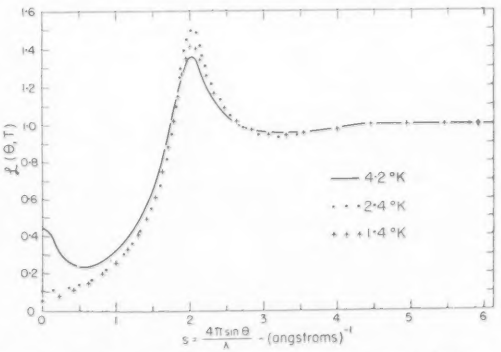

FIG. 5. Reduced scattering curves for liquid helium.

Table 2. Reduced scattered intensity I_R (counts/min) *and liquid structure factor for liquid helium of atomic weight 4 as a function of scattering angle 2θ and of $s = 4\pi \sin\theta/\lambda$*

s (A^{-1})	2θ (degrees)	4·2°K		2·4°K		1·4°K	
		$\mathcal{L}$	I_R	$\mathcal{L}$	I_R	$\mathcal{L}$	I_R
0·1	1·4	0·420	524	0·103	129	0·058	72
0·2	2·8	0·345	432	0·105	133	0·070	89
0·3	4·2	0·277	349	0·114	146	0·087	113
0·4	5·6	0·250	316	0·124	161	0·104	136
0·5	7·0	0·239	304	0·137	179	0·125	164
0·75	10·5	0·251	329	0·180	246	0·180	246
1·00	14·1	0·325	426	0·258	351	0·258	351
1·25	17·6	0·446	565	0·370	484	0·376	490
1·50	21·2	0·654	775	0·561	683	0·573	695
1·70	24·0	0·929	1013	0·837	933	0·860	954
1·80	25·4	1·094	1152	1·056	1118	1·070	1130
1·90	26·9	1·247	1264	1·305	1315	1·255	1273
2·00	28·4	1·349	1326	1·485	1439	1·417	1380
2·10	29·8	1·330	1285	1·476	1400	1·374	1319
2·20	31·2	1·224	1177	1·319	1250	1·268	1210
2·30	32·7	1·143	1097	1·214	1149	1·190	1131
2·50	35·6	1·044	989	1·068	1004	1·072	1008
2·75	39·4	0·986	910	0·974	902	0·990	912
3·00	43·1	0·962	862	0·937	849	0·952	857
3·25	46·9	0·955	829	0·932	819	0·948	826
3·50	50·8	0·957	803	0·943	797	0·945	798
3·75	54·7	0·964	780	0·959	779	0·960	778
4·00	58·7	0·975	762	0·975	762	0·975	762
4·25	62·8	0·988	747	0·988	747	0·988	747
4·50	67·0	0·997	730	0·997	730	0·997	730
4·75	71·2	1	712	1	712	1	712
5·00	75·5	1	695	1	695	1	695
5·25	80·0	1	682	1	682	1	682
5·50	84·8	1	668	1	668	1	668
5·75	89·6	1	656	1	656	1	656

been corrected for polarization of the scattered radiation and for variation of scattering volume with angle to yield results corresponding to a constant number of atoms, invariant with scattering angle. For ease in comparison of the three reduced scattering curves, they have been corrected for liquid transmission and for the change in number density with temperature[16] to refer all number densities to that of liquid helium at 4·2°K. Table 2 lists the actual values for these reduced scattering curves (I_R). Values are given for the scattering variable $s = (4\pi \sin\theta)/\lambda$, where θ is half the scattering angle and λ is the wavelength, as the primary independent variable; but the corresponding θ values are also given.

4. ANALYSIS OF RESULTS

The details of the theory relating the form of the X-ray diffraction pattern from a liquid element to the arrangement of atoms in the liquid have been clearly discussed in a review article by GINGRICH,[17] so that a brief description of terms and notation used here should be sufficient.

If $I_G(\theta)$ represents the scattered intensity at the scattering angle (2θ) from N_G independent atoms, when irradiated by monochromatic X-rays of wavelength λ (a fixed parameter in these experiments),

$$I_G(\theta) = BP(\theta)Y_G N_G[\sigma_e(\theta)+\sigma_i(\theta)], \qquad (1)$$

where N_G is invariant with the scattering angle. Here, B includes all the Thomson scattering terms except the

polarization factor $P(\theta) = [1/2](1+\cos^2 2\theta)$, Y_G is the transmission factor for the gas, and σ_e and σ_i are the elastic and inelastic differential scattering cross-sections per gas atom.* It is this quantity $(\sigma_e+\sigma_i)$, the total differential cross-section, which is given in Table 1.

In the liquid state interference occurs in the elastically scattered radiation, since the atoms are not located in a perfectly random spatial array. The resulting elastic scattering per atom may be written in a product form as $\sigma_e \mathcal{L}(\theta, T)$, giving the scattered intensity from the liquid as

$$I_L(\theta, T) = BP(\theta) Y_L N_L [\sigma_e(\theta) \mathcal{L}(\theta, T) + \sigma_i(\theta)], \quad (2)$$

where Y_L and N_L are defined in an obvious way and $\mathcal{L}$ is the liquid structure factor. The interference terms are related to the atomic arrangement by

$$\mathcal{L}(\theta, T) = 1 + \int_0^R 4\pi r^2 [\rho(r, T) - \rho_0(T)] \frac{\sin sr}{sr}\, dr, \quad (3)$$

where $s = (4\pi \sin\theta)/\lambda$, $\rho(r, T)$ is the radial distribution function or atomic number density at a distance r from an arbitrary origin atom and $\rho_0(T)$ is its mean value in the liquid. The integration is carried to the boundary, R, of the container (essentially infinite compared with atomic dimensions). A Fourier integral transformation then yields the variation in number density,

$$4\pi r^2(\rho - \rho_0) = \frac{2r}{\pi} \int_0^\infty s(\mathcal{L} - 1) \sin sr\, ds. \quad (4)$$

Strictly speaking, the term "structure factor" refers to an *amplitude* in electron units. However, in accordance with common usage as established in preceding papers in the field,[1,8] we define the intensity liquid structure factor as the ratio of the intensity of the radiation scattered elastically per atom of liquid to that per independent atom, and call this simply the "liquid structure factor".

To obtain the value of $\mathcal{L}$ from any one of the data curves in Fig. 5, one may use equation (1) and (2) in combination with the gas data† of Table 1 for I_G with the result

$$\mathcal{L}(\theta, T) = \frac{Y_G N_G I_L}{Y_L N_L I_G} \left[1 + \frac{\sigma_i}{\sigma_e}\right] - \frac{\sigma_i}{\sigma_e}. \quad (5)$$

The gas transmission Y_G is sensibly unity. The transmission of the liquid was determined from the liquid density at the temperature of interest, the specimen dimensions, and the mass absorption coefficient of 0·39 cm²/g from VICTOREEN.[19] The result agrees with an approximate transmission measurement made during the course of the experiment more closely than does the value as determined from tables in COMPTON and ALLISON.[20] The ratio N_G/N_L is given by $\rho_G/\rho_0(T)$, since both gas and liquid scattered intensities were measured from identical volumes of material. Liquid helium densities as given by KEESOM[16] were used to find the number density $\rho_0(T)$. The number density ρ_G in the gas at 4·2°K and 40·8 cm Hg pressure, where the measurements were made, was calculated from the virial equation, using first and second virial coefficients from KELLER's recent work.[21]

In addition to this direct method for determination of $\mathcal{L}$, one may use equation (2) alone if BN_L is evaluated. As defined previously, the reduced scattering, I_R, given in Table 2 and pictured in Fig. 5 is

$$I_R(\theta, T) = I_L(\theta, T)/P(\theta) Y_L = BN_L(\sigma_e \mathcal{L} + \sigma_i). \quad (2a)$$

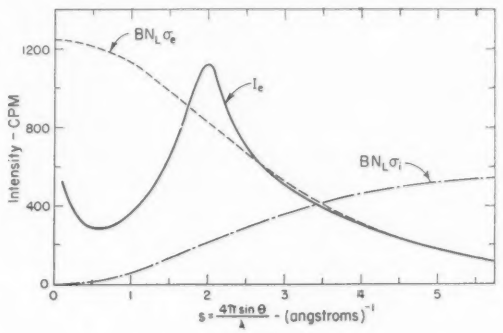

FIG. 6.
– – – – – elastic scattering from N_L independent atoms;
— · — inelastic scattering from N_L atoms;
——— elastic scattering from N_L atoms in the liquid at 4·2° K. For $s > 4$, the liquid and gas elastic scattering curves are indistinguishable.

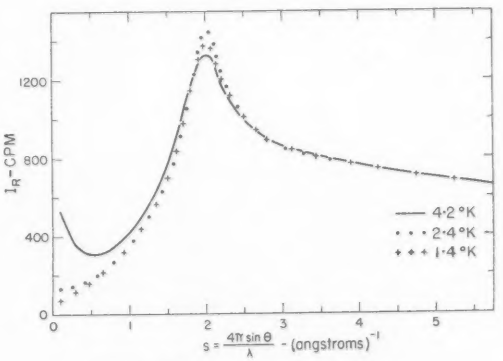

FIG. 7. The liquid structure factor.

* σ_e and σ_i are the coherent scattering and the incoherent (Compton) scattering per atom of the GINGRICH paper.[17] These terms are avoided here because of ambiguities which arise in considerations of scattering by liquids and solids.[18]

† The gas intensities corresponding to the I_R values in Table 2 will be given by multiplying column 5 of Table 1 by the factor 18·4.

At large scattering angles $\mathcal{L} = 1$, so that BN_L is easily evaluated. Fig. 6 displays the elastic ($BN_L\sigma_e$) and inelastic ($BN_L\sigma_i$) scattering from N_L independent atoms and the elastic scattering I_e from N_L atoms in the liquid.

The liquid structure factor $\mathcal{L}$ shown in Fig. 7 is given by the quotient of the corresponding ordinates of the two curves (Fig. 6), I_e and $BN_L\sigma_e$. Comparison of the $\mathcal{L}$ values obtained by this method and by the first method at several check points verified the BN_L value most satisfactorily.*

One test to which the liquid structure factors at each temperature can be subjected follows from equation (4). In the limit as $r \to 0$, $\rho(r) \to 0$, since $\rho(r)$ excludes the arbitrary origin atom. Equation (4) then becomes

$$-2\pi^2\rho_0 = \int_0^\infty s^2(\mathcal{L}-1)\,ds. \qquad (6)$$

At large s values, corresponding to large scattering angles where high accuracy in measured intensities is difficult to attain, the sensitivity of this test increases rapidly. Consequently more confidence might be placed in the $\mathcal{L}$ values at large s if this equation is satisfied. The application of this test is considered later.

Small angles

Liquid-structure-factor values obtained from the observed intensities extend from $s = 0{\cdot}1$ A^{-1} to $s = 5{\cdot}77$ A^{-1}, so that an extrapolation to $s = 0$, based on smoothed intensity curves from the data at 1·5°, 2°, and 2·5° scattering angles, had to be made to complete the $\mathcal{L}$ curves. It was found that the small-angle $\mathcal{L}$ value at 4·2°K followed the expected[8] parabolic dependence on s and extrapolated to 0·455. The data at lower temperatures are not inconsistent with the parabolic dependence and extrapolate to 0·225 at 3·5°K, 0·15 at 3·0°K, 0·102 at 2·4°K, and 0·052 at 1·4°K.

Statistical theory[8,23] has shown that as the scattering angle approaches zero, the liquid structure factor approaches $nkT\chi_T$, where n is the number of atoms per unit volume in the liquid, k is the Boltzmann constant, and χ_T is the isothermal compressibility. TWEET,[4] GOLDSTEIN,[24] and later EGELSTAFF[25] have computed from first-sound velocities and the ratio of specific heats for helium that the $nkT\chi_T$ values at the above temperatures are 0·66 at 4·16°K,[4] (0·45–0·47)[24] or 0·44[25] at 4·2°K, 0·24 at 3·5°K, 0·165 at 3°K, 0·105 at 2·4°K, and 0·052 at 1·4°K. Zero-angle intensities corresponding to these predicted $nkT\chi_T$ values (using 0·44 at 4·2°K) are indicated in Fig. 4. TWEET's value appears to be inconsistent with the results given in Fig. 4 on the basis of the parabolic extrapolation.

Radial distribution

The radial variations of atomic density from the mean value at each temperature, $4\pi r^2[\rho(r)-\rho_0]$, can be calculated by the evaluation of the integral in equation (4), using $\mathcal{L}$ values from Table 2. The results, obtained on the IBM 650 electronic calculator at Case Institute of Technology, are displayed in Fig. 8, carried out to a distance of 12·5 Å

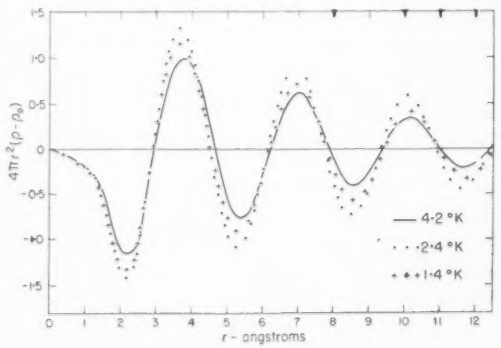

FIG. 8. Deviation of the number of atoms in the liquid in the spherical shell from r to $(r+dr)$, as a function of the distance r from an arbitrary atom, from the number curve for a homogeneous liquid of density ρ_0. $\rho_0(4{\cdot}2°\text{K}) = 0{\cdot}0189$ atoms/Å^3; $\rho_0(1{\cdot}4°\text{K}) = \rho_0(2{\cdot}4°\text{K}) = 0{\cdot}0218$ atoms/Å^3.

* Another method for evaluating BN_L has been suggested,[22] which employs intensities obtained over the entire range of scattering angles. Using the elastically scattered intensity of Fig. 6, I_e, one can show from equations (2) and (3) that

$$\int_0^S I_e\,s\,ds - BN_L\int_0^S \sigma_e\,s\,ds$$

$$= 4\pi BN_L\int_0^S\int_0^R \sigma_e(\rho-\rho_0)r\sin sr\,dr\,ds = K,$$

where the first and second integrals are proportional, respectively, to the total elastic scattering cross-section for the liquid and for N_L independent atoms. The difference, K, between these two integrals depends on the amount of ordering in the liquid, vanishing for the case of complete randomness, to be sure, but probably not vanishing for liquid helium. A rough estimate indicates that K is negative and equal to about 10 per cent of the total elastic cross-section for the liquid. This does not seem to be an acceptable method.

from the arbitrary origin atom. In spite of the identical values of the liquid density at 1·4 and 2·4°K, there was a definite difference in the scattered intensities at these two temperatures, particularly in the neighborhood of the diffraction peak. This difference is reflected in the transforms of the two scattering patterns as illustrated in Fig. 8.

As expected, order is lost more rapidly with increasing r in the liquid at 4·2 than at 2·4°K, as shown by the greater relative decrease in amplitude of the 4·2°K curve in Fig. 8. It is, however, interesting that the 1·4°K curve shows less ordering with increasing r than does the 2·4°K curve, rather than greater, as one might expect.

From equation (3) and the results of statistical theory[8,23] mentioned earlier we have

$$1+\int_0^R 4\pi r^2[\rho(r,T)-\rho_0(T)]\,dr = nkT\chi_T. \quad (7)$$

Applying this test to the curves of Fig. 8, we find that at 4·2°K the integral appears, by extrapolation, to converge to a value of −0·58, at 2·4°K to −0·90, and at 1·4°K to −0·97, in satisfactory agreement with the expectations. Whether evaluation of the curves of Fig. 8 to larger radii would improve these results by reducing the required amount of extrapolation is uncertain, but agreement appears to be adequate at present. Unfortunately this test is not sensitive to many of the uncertainties inherent in the transformation of diffraction patterns. The most serious of these is the occurrence in the transforms of spurious maxima and minima on either side of true maxima and minima. Anomalies of this kind are attributed to a lack of knowledge of the diffraction pattern at large scattering angles, i.e. to insufficient accuracy because of relatively small intensities and early termination of the diffraction pattern.[26,27,28] FINBAK,[27] in particular, has discussed other sources of spurious variations in the transforms such as those causing unreal liquid density fluctuation inside the radius of the origin atom. Spurious peaks of the former type are not observed in the transforms (Fig. 8), implying that the liquid structure factors (Fig. 7) correctly vanish with increasing scattering angle. However, spurious structure of the latter type does exist at small r, but because of its obvious nature and relatively small amplitude, it can be ignored in the radial-distribution curves described later.

The liquid "structure" as depicted in the curves of Fig. 8, showing fluctuations about the average number density with distance from an arbitrary origin atom, can be ascribed to the overlapping of spherical shells of atoms containing nearest neighbors, next-nearest neighbors, and so on, arranged loosely in a sort of packing of spherical atoms. The width of each shell is associated with the motion of atom centers from their mean spacing about the origin atom. The usual convention is to obtain the approximate occupancy of such shells by a replot of the data as $4\pi r^2\rho(r)$ against r and by the resolution of these curves into series of symmetric peaks whose areas give the numbers of

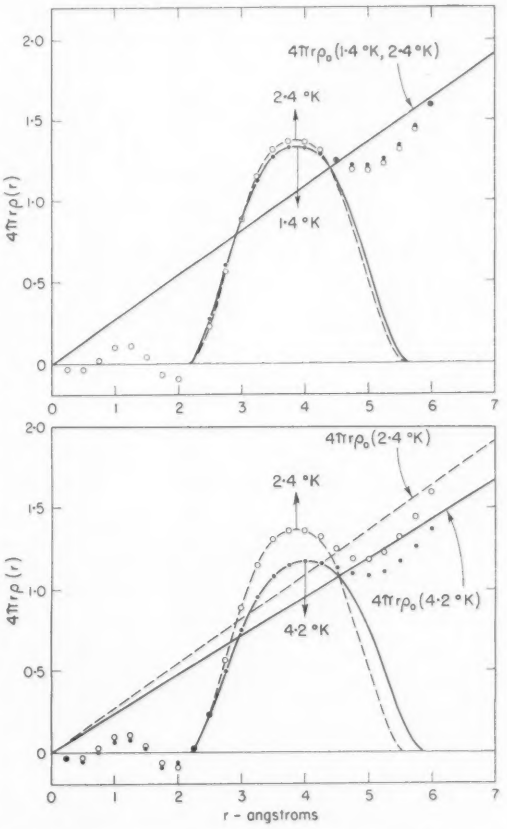

FIG. 9. The functions $4\pi r\rho(r,T)$ and $4\pi r\rho_0(T)$. The symmetrical peaks are obtained by reflection of the initial rise about the ordinate indicated.

atoms in the respective shells. However, COULSON and RUSHBROOKE[29] have shown that for an Einstein model liquid, the distribution of atoms in each shell should be symmetrical about the mean radius of that shell in an $r\rho(r)$ plot rather than the $r^2\rho(r)$ plot. They do not estimate the loss of symmetry of these distributions in the $r\rho(r)$ representation for liquids in which the Einstein approximation is inadequate.

To obtain the number of nearest neighbors of any given atom in the liquid at the three temperatures studied, the curves of Fig. 8 were first plotted in the form of $4\pi r\rho(r)$ versus r and symmetrical nearest-neighbor peaks constructed. Fig. 9 illustrates this procedure, where a reflection has been performed about the radius appearing to correspond to the first maximum in $4\pi r\rho(r)$. While the procedure is somewhat uncertain because of the choice permitted in the mean radius about which reflection occurs, construction of distributions corresponding to second and third shells of atoms is made still less trustworthy by the overlap. For this reason only nearest neighbors have been considered here. The results are shown in Table 3, where the width was found at $1/e$ of the maximum peak height. The co-ordination number was evaluated by numerical integration under the peaks on a $4\pi r^2\rho(r)$ curve such as shown in Fig. 10 for the three temperatures. The nearest-neighbor peak in Fig. 10 is related to that in Fig. 9 by a factor of r. The asymmetry of the peak and its shift in position are obvious.

Table 3. Atomic distribution in liquid helium—4.

Temperature (°K)	Distribution of nearest neighbors		
	Peak location (Å)	Peak width (Å)	Co-ordination number
4·2	4·00	2·6	10·4
2·4	3·85	2·3	10·5
1·4	3·87	2·4	10·6

If one assumes that the $4\pi r^2\rho(r)$ curve should be symmetrical, the problem of choosing the position of the peak is much more difficult than for the $4\pi r\rho(r)$ plot, since the latter gives a clear maximum while the former has only a point of inflection.

Because the liquid-structure-factor curves of Fig. 7 did not satisfy the test of equation (6) adequately, yielding a value of nearly $-4\pi^2\rho_0$ instead of $-2\pi^2\rho_0$, a modification of the 4·2°K curve was tried. By introduction of a small positive maximum in the region of $s = 4{\cdot}5$ A^{-1} in the $\mathcal{L}$ curve for 4·2°K, corresponding to $\frac{1}{2}$ per cent increase in observed scattering data in that range, equation (6) was exactly satisfied for this temperature. The transform of this modified $\mathcal{L}$ curve exhibited only slight changes from that shown in Fig. 8, the largest change occurring in the first valley and peak. When referred to the 4·2°K curve in Fig. 9, these changes amount to less than 2 per cent of the ordinates shown in the first peak and suggest a slightly broader peak. While this trial modification is instructive as an indication of the sensitivity of transforms to data accuracy, it does not appear to be justified as a general procedure. There are too many possible modifications of the observed data, all within experimental error, which would each satisfy equation (6).

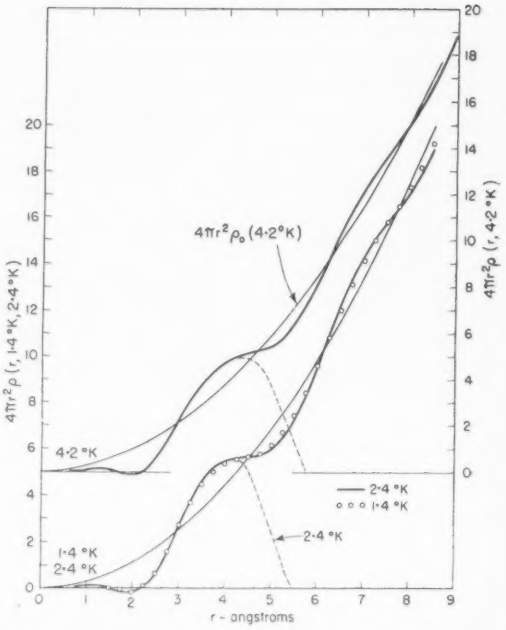

FIG. 10. The functions $4\pi r^2\rho(r,T)$ and $4\pi r^2\rho_0(T)$. The peaks corresponding to those in Fig. 9 are now noticeably asymmetric. Co-ordination numbers for nearest neighbors were determined from the areas under these peaks.

Qualifications in the transforms and in methods of interpreting them introduce uncertainties in Table 3. There is every indication that the differences observed in the curves of scattered intensity for the various temperatures are outside the experimental error. It is difficult to generalize, however, on the effects of slight changes in the scattering curves on the transforms. It is, for example, not easy to distinguish uniquely the effect of the small-angle scattering upon the radial-distribution function for the various temperatures. Such considerations become of importance in the curves of Fig. 9, where a rather minor variation in a given transform can produce an appreciable effect in the form of the nearest neighbor peak and hence in the corresponding co-ordination number. We must conclude that, while the change in peak location in Table 3 with temperature from 4·2 to 2·4°K appears to be real enough, hardly any significance can be attached to the differences in co-ordination number.

Both the amount of the shift in the nearest-neighbor peak position with decreasing temperature and the number of nearest neighbors at all temperatures are in disagreement with the neutron-scattering results of HURST and HENSHAW.[7] They observed a negligible shift between 4·24 and 2·25°K, while their number of nearest neighbors at 4·2°K was some 23 per cent smaller than the present value. The present results do not indicate much closer packing than did the neutron work, since the mean spacing for the work reported here is about 8 per cent greater, compensating for the larger group of neighbors.

The observed shift of nearest-neighbor peak position with increasing temperature (Fig. 9) from 2·4 to 4·2°K is nearly that expected to account for the 15 per cent liquid-density change, on the assumption of uniform dilatation. However, the zeros of the density fluctuations (Fig. 8) do not exhibit the 5 per cent shift with increasing r also expected with uniform dilatation.* This behavior is consistent with the vacancy picture in the cellular model of a liquid where the number of vacancies increases with increasing temperature along the vapor/liquid equilibrium curve, leading to a looser, less-dense structure. No significant change in cell size is to be expected on the average, i.e. no uniform dilatation throughout the liquid. On this model one might expect in addition that local disorder would be enhanced in the vicinity of a vacancy, as evidenced by the observed nearest-neighbor-peak shift of some 4 per cent toward larger values between 2·4 and 4·2°K.

The slight shift of peak location and width and the change of co-ordination number between 1·4 and 2·4°K offer no conclusive evidence for or against a vacancy model below the lambda point, but, since the number densities are identical at these temperatures, no significant change would be expected.

Evidence of a pressure-dependent dilatation effect in the liquid in passing isothermally from liquid at 1 atm pressure and 1·95°K to liquid at 27·5 atm has been obtained recently by HENSHAW.[30] The 20 per cent density increase is accompanied by a clear shift of peaks and crossovers in the $r^2(\rho-\rho_0)$ plot, indicating a pressure-dependent density change, which appears to be an

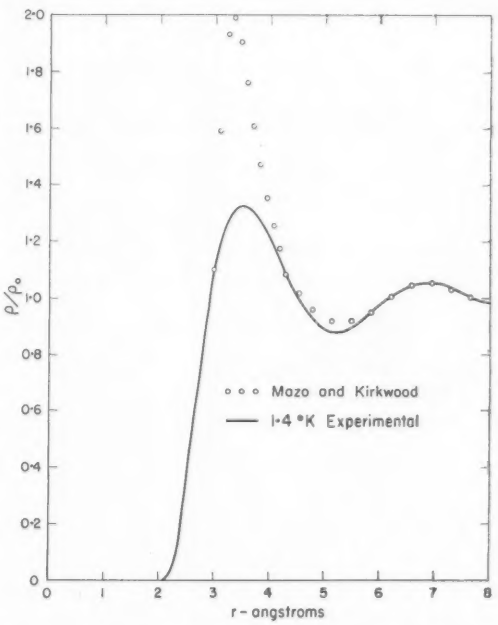

FIG. 11. The ratio of ρ, the number density in the liquid, to ρ_0, the average number density, as a function of r, according to MAZO and KIRKWOOD[31] and as found in the experiment for 1·4°K.

* This is in agreement with neutron-scattering measurements.[7]

entirely different process from the temperature-dependent change along the liquid/vapor equilibrium curve. In the cellular model, interatomic spacings decrease with pressure, with only a small accompanying change in the number of vacancies.

One final point of interest is the comparison of the radial-distribution function at 1·4°K, the lowest temperature studied here, to distributions obtained theoretically to apply in the ground state of the liquid. MAZO and KIRKWOOD[31] have derived a pair-distribution function shown in Fig. 11. Their suggested scale factor of 2·99 was used to convert to a radial scale in ångströms. No values for r less than 2·99 were given. The extreme sharpness of the first peak should correspond to a more pronounced diffraction peak than has yet been observed in the liquid. It is possible that at temperatures nearer 0°K, this might be found.

Acknowledgements—The authors make grateful acknowledgement as follows: to Dr. T. H. BLEWITT, of the Oak Ridge National Laboratory, for his assistance in obtaining the beryllium sample tube; to the General Electric Company for a Coffin Fellowship for one of us (W.L.G.); to the Ohio State University Research Foundation and the Case Institute of Technology Computer Laboratory for computer time; and to the National Carbon Company Research Laboratory for contributing their harmonic analysis program for the IBM 650 computer. We are much indebted to Dr. LOUIS GOLDSTEIN and to Professor JAN KORRINGA for helpful discussions and suggestions, and to Dr. D. G. HENSHAW for permission to mention his recent work on liquid helium under pressure.

REFERENCES

1. KEESOM W. H. and TACONIS K. W. *Physica* **5,** 270 (1938).
2. REEKIE J. *Proc. Camb. Phil. Soc.* **36,** 236 (1940); **43,** 262 (1947).
3. BEAUMONT C. F. A. and REEKIE J. *Proc. Roy. Soc.* A **228,** 363 (1955).
4. TWEET A. G. *Phys. Rev.* **93,** 15 (1954).
5. GORDON W. L., SHAW C. H. and DAUNT J. G. *Phys. Rev.* **96,** 1444 (1954).
6. SOMMERS H. S., DASH J. G. and GOLDSTEIN L. *Phys. Rev.* **97,** 855 (1955).
7. HURST D. G. and HENSHAW D. G. *Phys. Rev.* **100,** 994 (1955).
8. GOLDSTEIN L. *Phys. Rev.* **84,** 466 (1951).
9. SOULES J. A., GORDON W. L. and SHAW C. H. *Rev. Sci. Instrum* **27,** 12 (1956).
10. PEPINSKY R. and JARMOTZ P. *Rev. Sci. Instrum.* **19,** 247 (1948).
11. LEMIEUX A. F. and BEEMAN W. W. *Rev. Sci. Instrum.* **17,** 130 (1946).
12. WILSON E. B. *An Introduction to Scientific Research* p. 75. McGraw-Hill, New York (1952).
13. HARTREE D. R. *Proc. Camb. Phil. Soc.* **24,** 89, 111 (1928).
14. JAMES R. W. and BRINDLEY G. W. *Phil. Mag.* **12,** 81 (1931).
15. HERZOG G. *Z. Phys.* **70,** 583, 590 (1931).
16. KEESOM W. H. *Helium* p. 207. Elsevier, Amsterdam (1942).
17. GINGRICH N. S. *Rev. Mod. Phys.* **15,** 90 (1943).
18. LAX M. *Rev. Mod. Phys.* **23,** 287 (1951).
19. VICTOREEN J. A. *J. Appl. Phys.* **20,** 1141 (1949).
20. COMPTON A. H. and ALLISON S. K. *X-Rays in Theory and Experiment* p. 802. Van Nostrand, New York (1935).
21. KELLER W. E. *Phys. Rev.* **97,** 1 (1955); **98,** 1571 (1955).
22. HULTGREN R., GINGRICH N. S. and WARREN B. E. *J. Chem. Phys.* **3,** 351 (1935).
23. ZERNIKE F. and PRINS J. A. *Z. Phys.* **41,** 184 (1927).
24. GOLDSTEIN L. Private communication.
25. EGELSTAFF P. A. *Proc. Roy. Soc.* A **242,** 374 (1957).
26. SUGAWARA T. *Sci. Rep. Res. Inst. Tôhoku Univ.* **A3,** 39 (1951).
27. FINBAK C. *Acta Chem. Scand.* **3,** 1279, 1293 (1949).
28. WASSER J. and SCHOMAKER V. *Rev. Mod. Phys.* **25,** 671 (1953).
29. COULSON C. A. and RUSHBROOKE G. S. *Phys. Rev.* **56,** 1216 (1939).
30. HENSHAW D. G. Private communication (to be published).
31. MAZO R. M. and KIRKWOOD J. G. *Proc. Nat. Acad. Sci.* **41,** 204 (1955).

VOL. 5 1958

J. Phys. Chem. Solids Pergamon Press 1958. Vol. 5. pp. 129–141.

DISLOCATIONS IN THE DIAMOND LATTICE

J. HORNSTRA

Philips Research Laboratories, N.V. Philips' Gloeilampenfabrieken, Eindhoven-Netherlands

(*Received* 20 *August* 1957)

Abstract—In this paper several possible structures of dislocations in the diamond lattice are discussed. Special attention is paid to the occurrence of broken bonds in the core of the dislocations and in jogs; for instance, edge-type dislocations can occur in configurations without broken bonds. Jogs can act as a source or sink of interstitials and vacancies; in the diamond lattice this is complicated by the existence of two kinds of atom sites.

The most probable types of partial dislocations and the mechanism of their formation from simple dislocations are discussed. In the last section something is said about the occurrence of partial dislocations at twin boundaries and about a line imperfection with zero Burgers vector which may occur at the end of a twin lamella.

1. INTRODUCTION

Recently the study of dislocations in germanium and silicon has become of great importance. Their rôle in plastic deformation[1] and their electrical properties[2] are being studied intensively. Most authors restrict themselves to two types of dislocations: the screw dislocation and the 60° dislocation. However, it appears that in small-angle grain boundaries a different type is found, viz: an edge dislocation in a ⟨100⟩ direction.[3] Therefore it seemed desirable to investigate, what types of dislocations are possible at all and what may be the detailed structure of the core and of jogs.

Furthermore investigation has been carried out into the possible occurrence of partial dislocations, the existence of which has been questioned by SEITZ[4] and by SHOCKLEY.[5]

2. THE DIAMOND LATTICE

Before discussing the details of the structure of dislocations, it is appropriate to look more closely at the undisturbed diamond lattice (Figs. 1 and 2). In Fig. 1a the spatial arrangement of the atoms in the cubic unit cell (broken lines) is shown. In Fig. 1b a projection of the cubic unit cell (full lines) on the (001) plane is given. The height of the atoms above this plane is denoted in fractions of the cell dimension. In Fig. 1c is shown what might be called the tetragonal unit cell; its projection on the (001) plane is denoted by broken lines in Fig. 1b. In Fig. 1d its projection on the $(1\bar{1}0)$ plane can be seen; here the height of the atoms is expressed in fractions of the dimension of this cell normal to the plane of projection. Parts of neighbouring cells have been added to show the hexagonal channels in the $[1\bar{1}0]$ direction.

Three possible slip planes, the (001), the (110) and the (111) plane, are normal to this plane of projection; their traces are shown in Fig. 1d. It may be seen that {111} will be the most important slip plane; and indeed, only this slip plane is found experimentally.[1,6] The Figs. 2a and 2b are obtained by turning the Figs. 1a and 1d to the right until one bond direction becomes vertical. From Fig. 2 all further figures have been derived.

In Fig. 1a the configuration of the staggered hexagon is seen, one of them being drawn with heavy lines. In organic chemistry this configuration is called the chair form to distinguish it from the boat form, which, as will be shown, may occur in screw dislocations and at twin boundaries.

3. SIMPLE DISLOCATIONS

The shortest lattice vectors that are allowed as Burgers vectors are $\frac{1}{2}\langle 110\rangle$ or $\langle \frac{1}{2}\ \frac{1}{2}\ 0\rangle$ i.e. half the diagonal of a cube face or one of the short edges of the tetragonal cell. These vectors are equal to the shortest distance between two equivalent atoms.

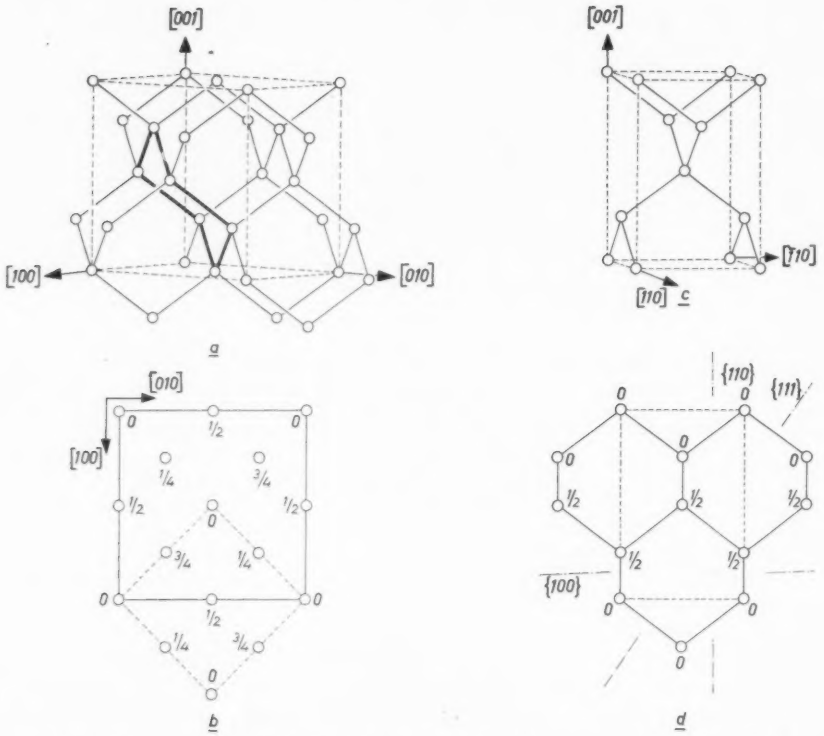

FIG. 1. The diamond lattice; the height above the plane of projection is denoted in fractions of the cell dimension normal to that plane. (a) The cubic unit cell, (b) its projection on (001), (c) the "tetragonal" unit cell, (d) its projection on $(1\bar{1}0)$. The "tetragonal" unit cell is indicated by broken lines in (b).

Dislocations with larger Burgers vectors will not be discussed in this paper, because they are of less importance, as may be seen from stability considerations.[7,8] The major part of the free energy E of a dislocation is the elastic energy E_{el} of the strain field around the dislocation as may be seen from the following estimation. The energy of one broken bond per atomic plane is of the same order or less than the band gap, about 1 eV in Si and Ge. The elastic energy is about $\frac{1}{4} G b^3$ per atomic plane, where G is the shear modulus 7×10^{11} dn/cm^2 in Ge, and b is the Burgers vector 4×10^{-8} cm in Ge. Thus the elastic energy is about 7 eV. This elastic energy is proportional to the square of the Burgers vector. When two dislocations with Burgers vectors b_1 and b_2 may be combined to form one dislocation with Burgers vector b_3, the increase of free energy $\Delta E \approx \Delta E_{el}$ is proportional to $(b_3^2-b_1^2-b_2^2)$. When ΔE_{el} is positive, the combined dislocation will be unstable and the dislocations 1 and 2 will repel each other; when ΔE_{el} is negative, the reverse will be true. If ΔE_{el} is zero, the stability will be determined by other factors, e.g. the number of distorted and broken bonds.

As may be seen on close inspection, an arbitrary direction in the crystal may be considered as the sum of steps in $\langle 110 \rangle$ directions. Thus, for instance, a dislocation in the [111] direction consists of steps in the [110], the [101] and the [011] direction. This may be written in the form of a vector equation $[111] = \frac{1}{2}[110]+\frac{1}{2}[101]+\frac{1}{2}[011]$. Therefore the only simple dislocations that need to be studied are those along $\langle 110 \rangle$ directions. The direction of the dislocation will be called its axis.

Now, as the axis and the Burgers vector are

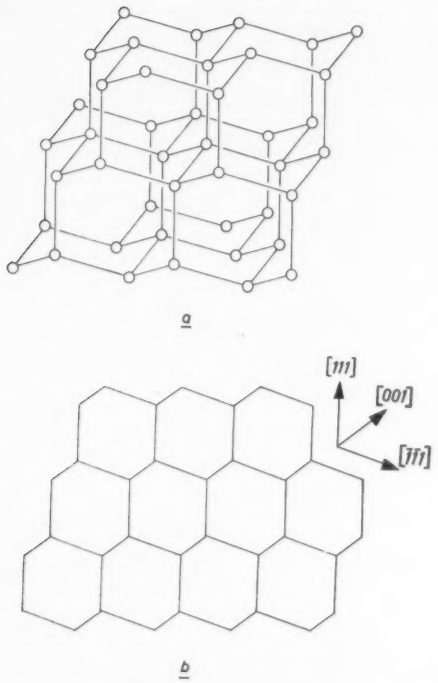

FIG. 2. (a) The diamond lattice with [111] vertical, (b) projection of (a) on the (1$\bar{1}$0) plane. From these two projections all further drawings have been derived.

both in ⟨110⟩ directions, there are only three types of dislocation to be considered here: a screw-type, an edge-type and a so-called 60° dislocation. Fig. 3a shows the narrowest form of a screw dislocation. The screw character may be seen by comparing the normal hexagon 7–8–9–10–11–12–7 with the structure 13–2–3–14–15–16–17. In the first case atom 7 is the beginning and end of the loop, in the latter case there is a gap between 13 and 17; the vector 13–17 is equal to the Burgers vector.

Hexagons around the axis have a distorted boat form, one of them has been drawn with heavy lines: 3–14–15–16–17–4–3.

The configuration of Fig. 3a is perhaps not the only one; Fig. 3b shows another possibility. It can be derived from Fig. 3a by breaking the bonds 2–3, 4–5 etc. and forming double bonds between the atoms 1–2, 3–4, 5–6 etc. By so doing, the dislocation is split into two components, occupying neighbouring channels. These two component dislocations are indicated by their axes, passing

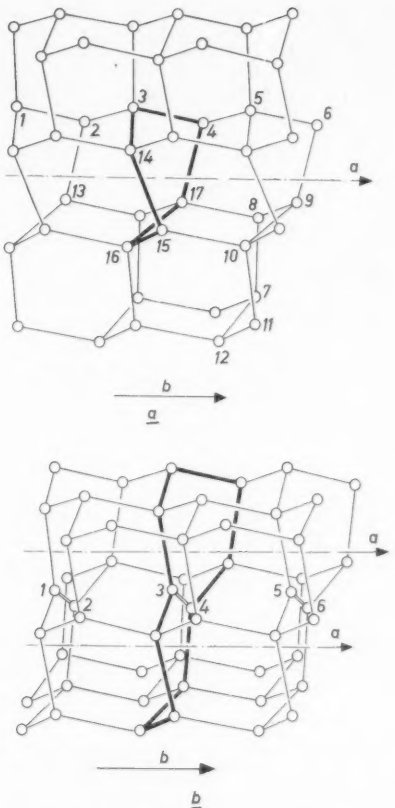

FIG. 3. Screw dislocation in the diamond lattice, (a) its simplest form, (b) alternative form with double bonds; corresponding atoms have the same number. a = axis, b = Burgers vector.

through the hexagons drawn with heavy lines. Attention is drawn to the fact that this splitting is entirely different from the splitting into partial dislocations, which is to be discussed in Section 7, because these components cannot be separated by a stacking fault.

The occurrence of the configuration of Fig. 3(b) in Si and Ge is rather doubtful, as it is uncertain whether these elements form double bonds like carbon does. However, even when double bonds do not exist, there may be a configuration like Fig. 3(b) with broken bonds at the atoms 1, 2, 3, 4, 5, 6 etc. This configuration may be considered as one with the smallest number of broken bonds, apart from that of Fig. 3(a). The same number is formed

by splitting into partial dislocations (Section 7). In both cases the distortion of bonds is considerably less than in Fig. 3(a), but, in our opinion, this does not outweigh the large number of broken bonds.

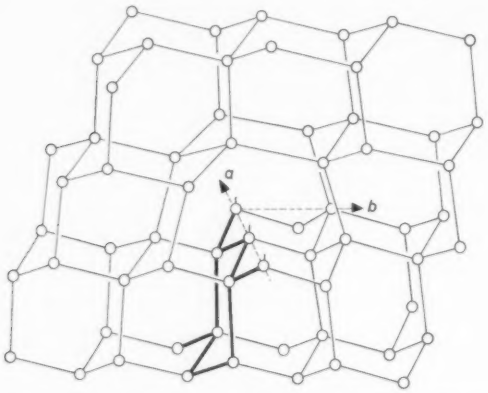

FIG. 4. 60° dislocation in the diamond lattice; heavy lines denote extra half plane. a = axis, b = Burgers vector.

In Fig. 4 the well-known[2] 60° dislocation is presented; its screw-type component is only small, and almost invisible in the figure. The edge-type component is more pronounced, for a (double) extra half plane can easily be assigned to the dislocation. A possible choice of this extra plane, {111}, has been indicated by heavy lines. This plane ends in free, or "dangling" bonds, drawn as short vertical lines at tetrahedral angles to the other bonds. However, a planar rearrangement of the latter three bonds is more likely, unless the atoms have accepted an electron. The glide plane of this dislocation is a {111} plane. The two types discussed so far are certainly the most important dislocations formed by plastic deformation.[9]

The edge dislocation is pictured in two forms in Fig. 5, the axis is $[1\bar{1}0]$, the Burgers vector is [110] and the glide plane is (001). In Fig. 5a a possible choice of the (double) extra half plane has been drawn with heavy lines. The two configurations given cannot simply be transformed into each other; that of Fig. 5(b) has been derived from Fig. 5(a) by omitting the atoms with two free bonds and connecting the originating free bonds. This transformation can only take place at a sufficiently high temperature by diffusion of vacancies or interstitials. In that case the configuration of 5(b), having no broken bonds, will certainly be more stable. Here rings of five and seven atoms are present instead of those of six. Similar configurations may occur in partial dislocations, as will be

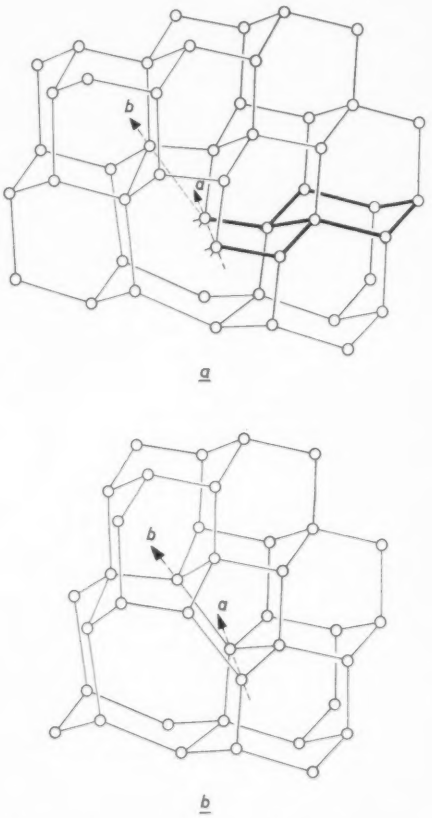

FIG. 5. Two forms of the edge dislocation with glide plane {100}. a = axis, b = Burgers vector, heavy lines denote extra half plane.

shown in Section 7. The point to be stressed here is, that in the diamond lattice a type of edge dislocation can exist that has no broken bonds at all.

4. OTHER DISLOCATIONS AND JOGS

Every dislocation can be resolved into steps of the simple dislocations, discussed in the previous section. The alternation of different orientations of the axis offers the same problem as a jog does, where a dislocation is interrupted by a short piece having a different orientation. This problem is

mainly, what is the structure of the core at the point where a dislocation changes the direction of its axis? To solve it, all types of dislocations have been studied that can be considered as being built up from only two simple dislocations. An example is shown in Fig. 6a. Steps of the simple dislocations alternate in such a way that these dislocations may be said to consist entirely of jogs.

Looking at the tetrahedron ABCD (Fig. 6b), of which the edges are along ⟨110⟩ directions, it may be seen that a combination of dislocations with axes CD [101] and BD [011] gives a dislocation with axis PD [112]. This may be written as $[101]+[011]=[112]$. Combination of BD [011] and CA $[0\bar{1}1]$ or of BA $[\bar{1}01]$ and CD [101] gives a dislocation along PQ [001], which may be written as $[011]+[0\bar{1}1]=[\bar{1}01]+[101]=2[001]$.

The ⟨211⟩ directions (like PD) are the bisectors of the angle between edges of the same face of the tetrahedron, the ⟨100⟩ directions (like PQ) are the bisectors of the angle between edges not belonging to the same face.

Because of the high symmetry several combinations are equivalent. To find all non-equivalent combinations, the Burgers vector is kept along BC (Fig. 6b). Now any edge represents a simple dislocation and the sum of two edges an alternating combination of two simple dislocations; e.g. BC is a screw dislocation and AD an edge dislocation. The result is summarized in the table below, together with the three types discussed already. The crystallographic direction of the axis, the angle between axis and Burgers vector, the glide plane and the number of broken bonds are also given.

The dislocations number IV and V have the same glide plane as the original dislocations, therefore they correspond to non-essential jogs or kinks. They may occur in loops generated by Frank–Read sources and in curved dislocations.

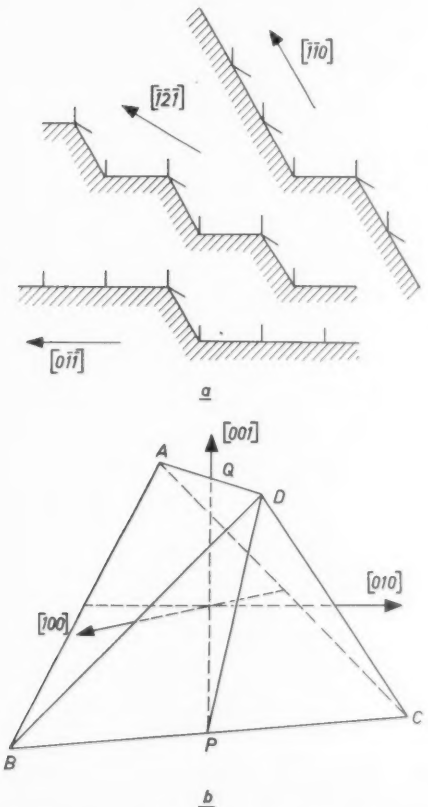

FIG. 6. (a) Schematic drawing of the edge of the extra half plane $(1\bar{1}1)$ of three dislocations with the same Burgers vector $[\bar{1}10]$. The short lines represent broken bonds. The three dislocations with axes $[0\bar{1}\bar{1}]$, $[\bar{1}\bar{1}0]$ and $[\bar{1}\bar{2}\bar{1}]$ may be seen in detail in the Figs. 4, 5a and 9 respectively. The structure of the last one is similar to that of the jogs in the other two. (b) Regular tetrahedron with edges along ⟨110⟩ shown in its position with respect to the cubic axes. AB = $[10\bar{1}]$, AC = $[01\bar{1}]$, AD = [110], BC = $[\bar{1}10]$, BD = [011] and CD = [101].

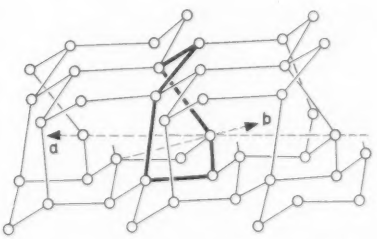

FIG. 7. 30° dislocation (nr. IV in the table). a = axis, b = Burgers vector.

Dislocation IV is presented in Fig. 7, it has a large screw-type component, as can be seen from the distorted boat form of the hexagon drawn with heavy lines. Number V is an edge dislocation (Fig. 8), it has twice as many atoms with free bonds as number IV. For these dislocations and the 60° dislocation the number of free bonds per unit length is proportional to the sine of the angle between axis and Burgers vector.[2] This relation

Table of dislocations having Burgers vector $BC = \frac{1}{2}\langle 110\rangle$

Nr.	Axis of the dislocation	Symbol of axis	Angle between axis and Burgers vector	Glide plane	Number of broken bonds per a cm
I	BC	⟨110⟩	0°	—	0
II	AB, AC, DB and DC	⟨110⟩	60°	{111}	1·41
III	AD	⟨110⟩	90°	{100}	2·83 or 0
IV	BC+AC, BC+BA, BD+BC and DC+BC	⟨211⟩	30°	{111}	0·82
V	AC+AB and DC+DB	⟨211⟩	90°	{111}	1·63
VI	AD+BD, DA+BA, AD+CD and DA+CA	⟨211⟩	73°13′	{311}	2·45 or 0·82
VII	AB+DB and AC+DC	⟨211⟩	54°44′	{110}	1·63 or 0
VIII	AC+DB and AB+DC	⟨100⟩	90°	{110}	2·0 or 0
IXa	AD+BC and AD+CB	⟨100⟩	45°	{100}	2·0 or 0
IXb	AC+BD and AB+CD	⟨100⟩	45°	{100}	2·0 or 0

a is the lattice constant

does not hold for dislocations with different glide planes.

A possible structure of number VI, the 73° dislocation, is shown in Fig. 9. Beside atoms with one broken bond (4), there are atoms (1 and 5) with two broken bonds as in Fig. 5(a). When these atoms with two free bonds are removed, a structure corresponding to Fig. 5(b) is obtained. The structure of Fig. 9 will probably be unstable, as an atom with two broken bonds (1) may easily diffuse away and become interstitial. As a new bond will be formed between 2 and 3, the number of broken bonds is reduced. But such an interstitial atom is easily captured between the atoms 4, 5, 6 and 7, still more reducing the number of broken bonds, as the atoms 6 and 7 are no longer bound to each other but to the captured atom. The result of this migration is that only atoms with one free bond are left. The interaction of these atoms with vacancies and interstitials will be comparable to that of a 60° dislocation. Thus jogs of this kind are not a more important source or sink of interstitials and vacancies than dislocations; only when they are in the unstable form can they easily capture or emit

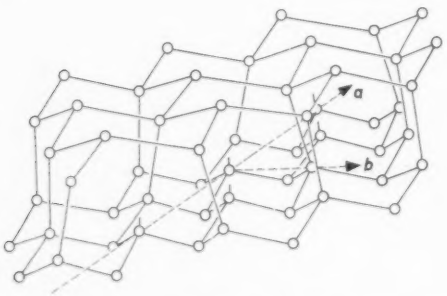

FIG. 8. Edge dislocation (nr. V) with glide plane {111}.

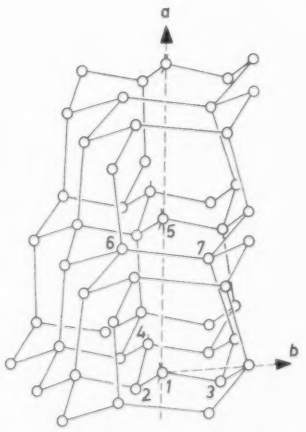

FIG. 9. 73° dislocation (nr. VI). a = axis, b = Burgers vector.

one atom. It may be shown that the same holds for other types of jogs. These rearrangements and the capture or loss of atoms will impede the mobility of the dislocations, so that jogs may act as pinning points not only in screw dislocations but in all types of dislocations.

Dislocations VII and VIII have the same glide plane and therefore show much the same pattern.

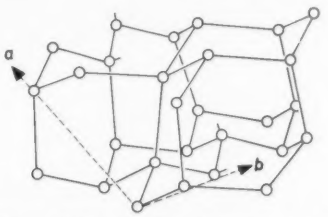

FIG. 10. Edge dislocation (nr. VIII) with glide plane {110} and axis along ⟨001⟩.

Only a drawing of VIII is shown (Fig. 10), because it is this dislocation that is found in small-angle grain boundaries.[3] In this dislocation the broken bonds occur at atoms immediately bound to each other, whereas in the Figs. 4, 5, 8 and 9 there always is an atom in-between. These atoms form pairs, bound to the lattice by four bonds; when one of the atoms diffuses away, the other can form four bonds, which gives a structure without broken bonds.

The Figs. 11(a) and (b) show the dislocations IXa and IXb. As these dislocations have the same glide plane, axis and Burgers vector, they are identical. The transition of IXa into IXb takes place by opening of the bond 1–2 and formation of the bond 1–3. The screw character of this 45° dislocation is shown by the boat-shaped hexagon in Fig. 11(a) (heavy lines). In Fig. 11(b) it is not easily visible just like in the 60° dislocation (Fig. 4). By removal of the atoms with two broken bonds from Fig. 11(a), a dislocation without broken bonds is formed, corresponding to Fig. 5(b); now the transition of IXa into IXb has become impossible.

5. STACKING FAULTS IN THE DIAMOND LATTICE

It is well known (see e.g. SEEGER[7]), that stacking faults in the diamond lattice resemble those in the face-centered cubic (f.c.c.) lattice. Partial dislocations and stacking faults in the f.c.c. lattice have been extensively treated by FRANK and NICHOLAS,[10]

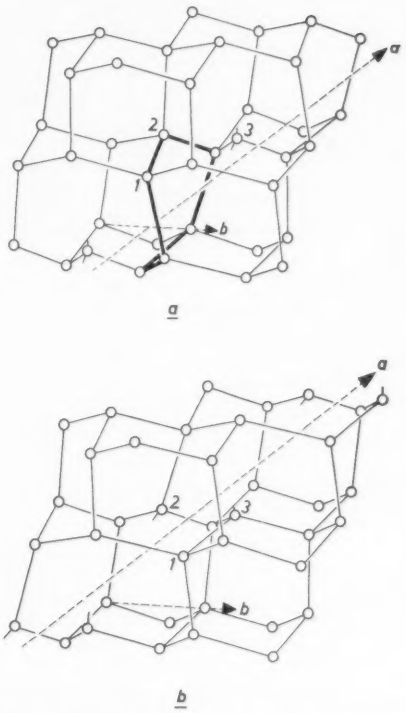

FIG. 11. Two forms of a 45° dislocation (nr. IXa and IXb). a = axis, b = Burgers vector.

so we can use their results. However, as will be shown in section 7, to one type of partial dislocation in the f.c.c. lattice often correspond two types in the diamond lattice.

In the f.c.c. lattice the position of successive layers parallel to (111) can be denoted by *abcabc*. In the diamond lattice pairs of atoms connected by a bond in the [111] direction may be distinguished. It is these pairs that follow the same pattern as the single atoms in the f.c.c. lattice. To put it differently, there are always two successive layers at the same position, so their position may be indicated by *aabbccaabbcc*. Because, even in twins and stacking faults, all letters appear in pairs, one of each pair may be omitted. Therefore in Fig. 12 the letters have been put between two layers in the same position. Between two letters two layers in different position are seen lying very close together; during the formation of stacking faults there are transitions of atoms from one of these layers to the other, as will be shown below.

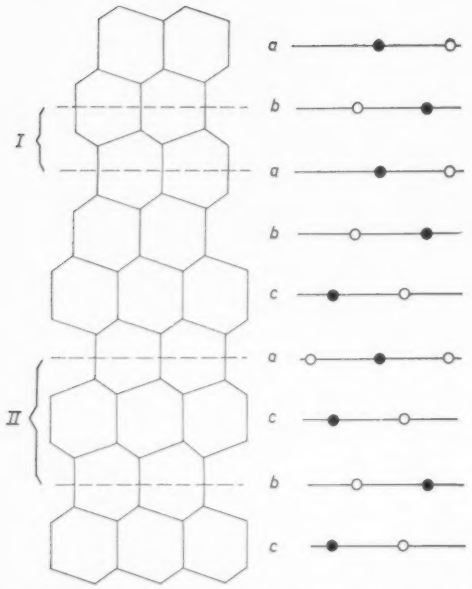

FIG. 12. Stacking faults in the diamond lattice (left) and the f.c.c. lattice (right) of type I (top) and type II (bottom); the broken lines denote twin surfaces; filled and open circles denote atoms at different height.

The left part of Fig. 12 shows a projection on a {110} plane of the diamond lattice with two stacking faults. At the right side the f.c.c. lattice with corresponding stacking faults is seen. Type I is an intrinsic stacking fault,[11] such as is formed by the removal of two layers of the same position (one in the f.c.c. lattice), here denoted by *c*. Type II is an extrinsic stacking fault, as is formed by insertion of two such layers. This removal or insertion changes the directions of the bonds between the atomic layers coming close together, in such a way that twin planes are formed (broken lines).

These stacking faults may be described in another way, viz. as the insertion of twin lamellae of different width. This demonstrates the relationship between stacking faults and twins. As twins are easily formed during growth in silicon and germanium, they have presumably a low surface energy and the surface energy of stacking faults will also be low. Thus, energetically, there will be no serious difficulty in the formation of partial dislocations with stacking faults.

These stacking faults are two-dimensional imperfections and thence have to be bounded by a one-dimensional imperfection: a dislocation. In the next section it will be shown that the Burgers vector of this dislocation is not a lattice vector; it has been called a partial dislocation[12] because two of these can combine to form one perfect dislocation (Section 7).

6. THE BURGERS VECTOR OF PARTIAL DISLOCATIONS

For the construction of the Burgers vector of a partial dislocation the Burgers circuit is used. This is a closed circuit around the dislocation. When this circuit is transferred to the normal lattice it shows a gap equal to the Burgers vector. With partial

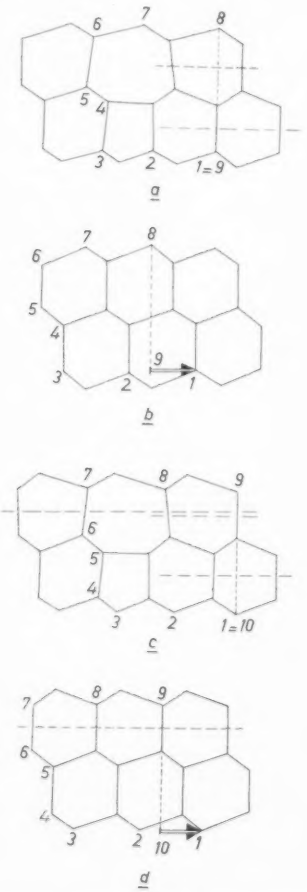

FIG. 13. The construction of the Burgers vector of partial dislocations, (b) and (d) reference structure, (c) and (d) a partial dislocation forming a step in a twin boundary.

disclocations this procedure has to be modified because of the stacking fault,[7,8,11] as will be explained with the aid of Fig. 13. The partial dislocation used here, will be discussed in the next section (Fig. 15). One begins the Burgers circuit at one side of the stacking fault and goes clockwise around the dislocation (1 to 8 in Fig. 13a). The atoms 1 and 8 are chosen in such a way that the line connecting them is perpendicular to the plane of the stacking fault; this line completes the Burgers circuit. This circuit is transferred to the normal lattice (Fig. 13b), and the line 8–9 is made equal and parallel to the line 8–9 in Fig. 13(a). The vector 9–1 is then the Burgers vector of the partial dislocation.

When a partial dislocation occurs at a twin boundary and one of the twin planes of the stacking fault coincides with the twin boundary, the result is a jump of the twin boundary to the next lattice plane (Section 8); for the two coinciding twin planes have no meaning (double broken line in Fig. 13c). The Burgers circuit is illustrated in Fig. 13(c) with the same partial dislocation as in Fig. 13(a). Now the loop is transferred to an ideal twin (Fig. 13d), in which the twin plane has the same position with respect to the Burgers circuit, viz. between the atoms 6 and 7. The Burgers vector 10–1 is the same as in Fig. 13(b).

The lower twin boundary of the stacking fault may also be considered as the original twin boundary; then the stacking fault is at the left side of the partial dislocation and a similar construction will give the same Burgers vector. This Burgers vector is parallel to the plane of projection, as may be seen from a model or a projection on the (111) plane.

To show some of the possible Burgers vectors of partial dislocations, Fig. 14 has been drawn. In Fig. 14(a) the tetrahedron of Fig. 6(b) is shown in another position. Its position with respect to the atoms is indicated in Figs. 14(b) and (c); Figs. 14(d) and (e) are projections hereof on the (110) plane.

The direction and length of several vectors are represented in the following way: the symbol between brackets is the crystallographic symbol of the direction; the length of $\frac{1}{2}[h\,k\,l]$ is $\frac{1}{2}a\sqrt{h^2+k^2+l^2}$, where a is the cube edge. Now we can see that the Burgers vector of the dislocation of Fig. 13 is $AE = \frac{1}{6}[11\bar{2}]$.

FRANK and NICHOLAS[10] distinguish between

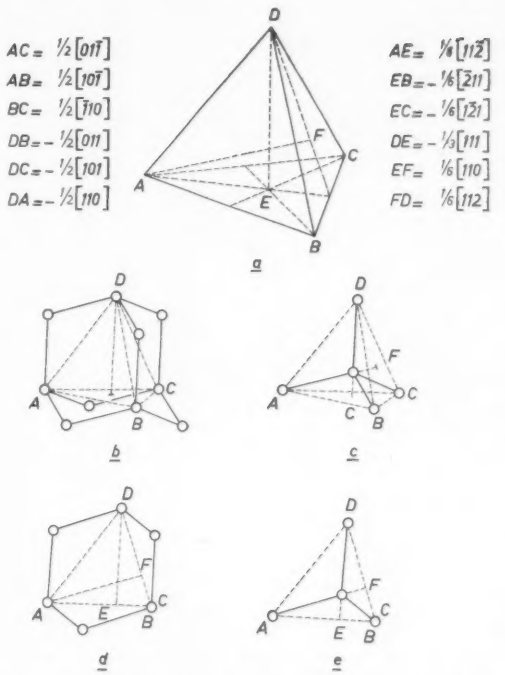

FIG. 14. (a) Tetrahedron showing the orientations and crystallographic symbols of several Burgers vectors. (b) and (c) Its position among the atoms, (d) and (e) projections of (b) and (c).

right and left partials, i.e. dislocations at the right or at the left side of the stacking fault (Fig. 13(a) is a left one). The difference is not fundamental, in the case of Fig. 13(c), where we can choose the stacking fault at the left or right side, the difference is even meaningless.

We shall denote partial dislocations by I or II, according to the two types of stacking fault (Fig. 12), and add a small letter to distinguish different types. Partial dislocations that can be transformed into one another by rotation or reflection are considered as of one type.

Any stacking fault is bounded by two partials: one at the left side and one at the right side. The Burgers vectors of these two dislocations add up to zero or to the Burgers vector of a perfect dislocation. This may be proved by considering a loop encircling the stacking fault and both partials. When the Burgers vector of the partial dislocation at one side is AE, that of the partial at the other side is EB, EC, ED or EA. When the sum of the

Burgers vectors is not zero, one may speak of an extended dislocation, formed by the splitting up of a perfect dislocation.

7. PARTIAL DISLOCATIONS

The different types of partial dislocations that can be derived by splitting up perfect dislocations will be discussed now simultaneous with the mechanism of formation. In Fig. 15 two ways are shown

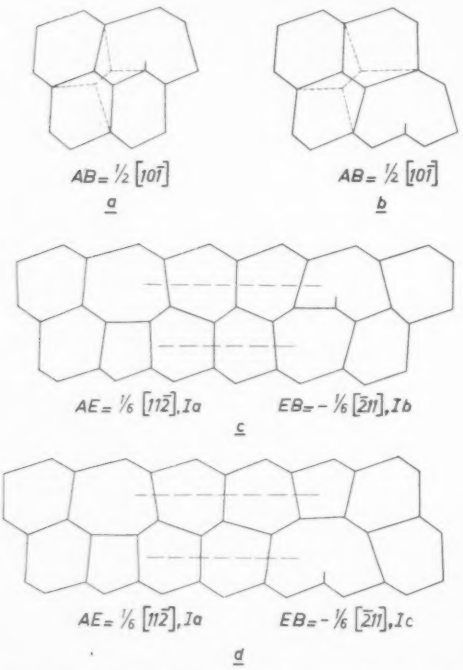

FIG. 15. Two ways of splitting up a 60° dislocation into partial dislocations, (a) and (b) first step, (c) and (d) result of three steps. Below each dislocation the Burgers vector and type notation are given.

in which a 60° dislocation may be split up, each time with a stacking fault of type I parallel to the glide plane. In this way three types of partials are obtained, which will be denoted by I*a*, I*b* and I*c* respectively. All partials are of the so-called Shockley-type.[12] At the top the first step is shown: a ribbon of atoms is rotated over about 90° and bonds are interchanged. At the same time the ribbon is displaced over a short distance normal to the plane of projection, but this can only be seen in a model or in another projection. After three of those steps have been performed, Fig. 15(a) is transformed into 15(c) and Fig. 15(b) into 15(d). It may be noticed that this splitting is stable, as $AE^2 + EB^2 < AB^2$. Type I*b* and I*c* are clearly different, although they have the same Burgers vector. When a screw dislocation is split up, one partial of the type I*c* and one of the type I*b* are obtained, with Burgers vectors EB and CE or EC and BE.

We have found only these three types of Shockley-partials with a stacking fault of type I. The detailed structure of type I*b* is shown in Fig. 16; there is some uncertainty in the position of the

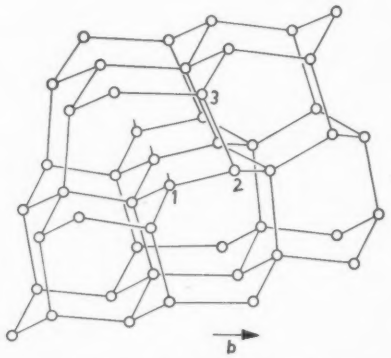

FIG. 16. The partial dislocation of type I*b*.

free bond, it may be shifted from atom 1 to atom 2. When a double bond is possible between atom 1 and 2, the free bond may be even at atom 3 of the adjacent layer. In cases like this, where different electronic structures are possible, one might speculate that the free energy may be lowered by resonance, as in aromatic ring systems.

All simple dislocations have their axes, ⟨110⟩ directions, along the intersecting line of two {111} planes. A stacking fault may be parallel to either of these two planes. Fig. 15 has shown the case of stacking faults parallel to the glide plane, the other possibility is illustrated in Fig. 17 for a 60° dislocation (top left and centre) and an edge dislocation of Fig. 5(b) (top right and bottom). The edge dislocation cannot be split with a stacking fault parallel to the glide plane, as its glide plane is {100}. In both cases a partial dislocation I*d* of the Frank-type[13] is formed, which is sessile; its Burgers vector is ED. At the end of this section it

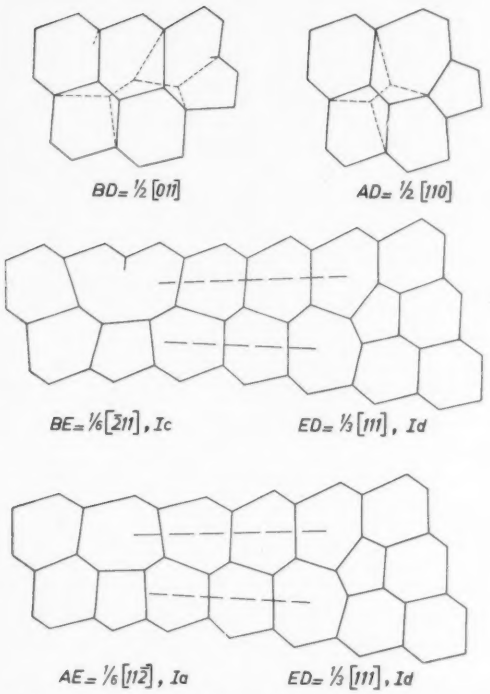

FIG. 17. Splitting up of 60° and edge dislocation with a stacking fault not parallel to the glide plane. Top: first step; bottom: result of three steps.

will be shown that this partial is not stable (section 3) and may split up into two partial dislocations with Burgers vectors EF and FD. This instability has not been mentioned* by FRANK and NICHOLAS.[10]

Partial dislocations with type II stacking faults are highly improbable, as during their formation two ribbons of atoms have to rotate simultaneously. Although the partial dislocations formed have the same Burgers vectors as those of type I, they contain more distorted and broken bonds and are therefore energetically less favourable. It is for these two reasons that we will not discuss them in detail.

Two partial dislocations with stacking faults parallel to different {111} planes may be combined to form a new type of partial dislocation at the line where these two planes intersect. These dislocations, which can neither glide nor climb, are the so-called Cottrell-type[14] or stair-rod dislocations. FRANK and NICHOLAS[10] have discussed different types of this kind; we shall only discuss one with Burgers vector EF (Fig. 18), which may be formed by combination of two

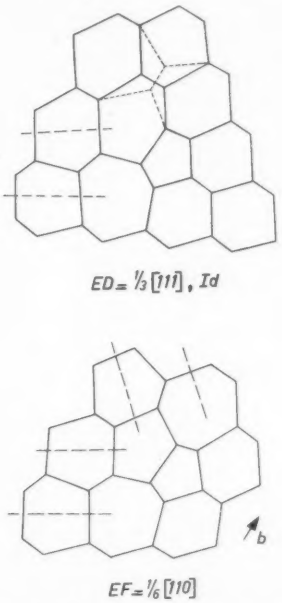

FIG. 18. Splitting of a Frank-type partial dislocation into one of Shockley-type and one of Cottrell-type. Top: first step; bottom: Cottrell-type or stair-rod dislocation. The stacking faults are found between the broken lines.

partials with Burgers vector EB and BF. It can also be formed by splitting type Id with Burgers vector ED into two partials with Burgers vectors EF and FD. As $EF^2+FD^2 < ED^2$ (Fig. 14), it is clear that type Id is unstable.

The combined result of the splitting of Fig. 17 centre and Fig. 18 is that a 60° dislocation is split into three partial dislocations with Burgers vectors BE, EF and FD. Combination of the partials with Burgers vector BE and EF to one with Burgers vector BF gives the same situation as splitting the original dislocation with a stacking fault parallel to the glide plane (Fig. 15). As $BF^2 < BE^2+EF^2$,

* *Note added in proof*: It has been omitted as this splitting will occur only if the partial dislocation is perfectly straight along ⟨110⟩ (private communication by Prof. F. C. FRANK). To my opinion, straight segments of sufficient length along ⟨110⟩ may well occur (see e.g. DASH).[9]

this combination will lower the free energy (section 3) and these two dislocations will attract each other. In this way the splitting of a 60° dislocation not parallel to the glide plane can easily change into an extended dislocation with the stacking fault parallel to the glide plane, which is energetically more favourable. The most stable configuration of the edge dislocation (b = AD) is one with three partials with Burgers vectors AE, EF and FD.

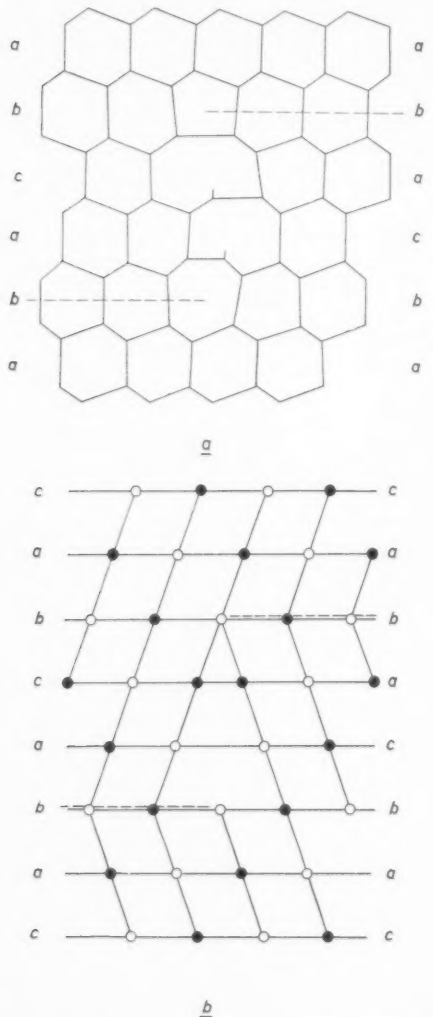

FIG. 19. Partial dislocation of type III with $b = 0$ at a twin boundary, (a) in the diamond lattice, (b) in the f.c.c. lattice. Filled and open circles denote atoms at different height.

8. DISLOCATIONS AND TWIN BOUNDARIES

As has been shown in Fig. 13(c), a shift of the twin boundary involves a partial dislocation. A shift of one (double) atomic plane involves a partial of type I, a shift of two planes one of type II, a shift of three planes, however, involves a lattice defect of a different kind. The possible structure of it is shown in Fig. 19(a) for the diamond lattice and in Fig. 19(b) for the f.c.c. lattice. It is no dislocation as its Burgers vector is zero. This fact may be explained by noting that at both sides of the boundary every third plane has the same position: we have abcaba opposite *abacba*. In Fig. 19(b) one can see that it may be considered as a combination of a row of partial vacancies and a row of partial interstitials. This defect might play an important rôle at the end of twin lamellae.

When the sets of allowed Burgers vectors belonging to the structures at opposite sides of a twin boundary are compared, it may be seen that the three Burgers vectors parallel to the twin plane are common to both structures but that the other three differ from those at the opposite side by an amount equal to the Burgers vector of a partial dislocation. Only dislocations with a Burgers vector parallel to the twin plane can extend across the twin boundary or pass the twin boundary during plastic deformation without change of Burgers vector; only the glide plane may be changed. The other dislocations must have a node at the twin boundary, where a partial dislocation begins or ends[15,16] or, in plastic deformation, leave a partial behind at the twin boundary.

9. CONCLUSIONS

In this paper it has been shown that all types of dislocations may occur in less mobile forms. Screw dislocations may form double bonds, 60° dislocations may very easily form extended dislocations and other types may lose atoms with two broken bonds. Screw dislocations will not readily form extended dislocations, as this involves the formation of broken bonds.

Of the partial dislocations only three types (Ia, Ib and Ic) are important; the other types are kinetically or energetically unfavourable. Whether partial dislocations do exist is difficult to prove experimentally; it is rather probable, however, as the surface energy of stacking faults must be low.

VOL. 5 195

Acknowledgements—The author wishes to express his thanks to Dr. H. G. VAN BUEREN, Dr. H. J. VINK, and Messrs. F. H. STIELTJES, P. PENNING and D. POLDER for valuable discussions and instructive criticism.

REFERENCES

1. VOGEL F. L., JR. *F. Metals* **8**, 946 (1956).
   BILLIG E. *Proc. Roy. Soc.* A **235,** 37 (1956), and several other papers.
2. READ W. T., JR. *Phil. Mag.* **45,** 775 (1954).
   READ W. T., JR. *Phil. Mag.* **46,** 111 (1955).
3. VOGEL F. L., JR. *Acta Met.* **3,** 245 (1955).
4. SEITZ F. *Phys. Rev.* **88,** 722 (1952).
5. SHOCKLEY W. *Phys. Rev.* **91,** 228 (1953).
6. GREINER E. S. *J. Metals*, N.Y. **7,** 203 (1955).
7. SEEGER A. *Handbuch der Physik VII Kristallphysik I.* Springer Verlag, Berlin, p. 383–663 (1955).
8. READ W. T., JR. *Dislocations in Crystals*, McGraw-Hill, New York (1953).
9. DASH W. C. *J. Appl. Phys.* **27,** 1193 (1956).
10. FRANK F. C. and NICHOLAS J. F. *Phil. Mag.* **44,** 1213 (1953).
11. FRANK F. C. *Phil. Mag.* **42,** 809 (1951).
12. HEIDENREICH R. D. and SHOCKLEY W. *Report on Strength of Solids* p. 57. Bristol (1948).
13. FRANK F. C. *Proc. Phys. Soc.* A **62,** 202 (1949).
14. COTTRELL A. H. *Phil. Mag.* **43,** 645 (1952).
15. COTTRELL A. H. and BILBY B. A. *Phil. Mag.* **42,** 573 (1951).
16. HALL H. O. *Twinning* Chap. VI. Butterworths Scientific Publications, London (1954)

OL.
5
958

J. Phys. Chem. Solids Pergamon Press 1958. Vol. 5. pp. 142–144.

CHEMICAL BONDING IN BISMUTH TELLURIDE

J. R. DRABBLE, and C. H. L. GOODMAN

Research Laboratories of The General Electric Co. Ltd.
Wembley, England

(*Received* 16 *September*, 1957)

Abstract—A model for the chemical bonding in bismuth telluride is proposed which appears to dispose of some of the difficulties involved in earlier models. The new model is used to explain some of the properties of bismuth telluride and of its alloys with bismuth selenide.

VOL.
5
195

THE nature of the chemical bonding in bismuth telluride and its relation to the electrical and optical properties have been discussed by LAGRENAUDIE[1] and by MOOSER and PEARSON.[2] Both of the suggested schemes seem unsatisfactory for reasons discussed below, and we wish to propose an alternative scheme which appears to remove some of the difficulties.

The atomic arrangement in bismuth telluride is most simply visualized in terms of the layer structure. Essentially, this consists of a stacking of "quintuple layer" leaves, where, in each leaf the layers occur in the order $Te^{(1)}$–Bi–$Te^{(2)}$–Bi–$Te^{(1)}$. The superscripts are used to distinguish two types of differently bonded tellurium atoms. From the crystal structure given by LANGE[3] it is found that the $Te^{(2)}$ atoms are surrounded almost octahedrally by six bismuth atoms, the bond length $Te^{(2)}$–Bi being 3·22 Å and the bond angles departing from true octahedral symmetry by about $4\frac{1}{2}°$. The bismuth atoms are bonded to three $Te^{(2)}$ atoms on one side and to three $Te^{(1)}$ atoms with a bond length of 3·12 Å on the other side. Again, the symmetry of the bonding of the bismuth atoms is nearly octahedral, the angle between the Bi–$Te^{(1)}$ bonds being about 89° 20′. The $Te^{(1)}$ atoms have three nearest-neighbour bismuth atoms in the same leaf and the next nearest atoms are three $Te^{(1)}$ atoms in the adjacent leaf. The latter bonds have a length of 3·57 Å, and the angle between the bonds is about 75° 42′.

MOOSER and PEARSON[2] have assumed that the $Te^{(1)}$ atoms are co-ordinated in a similar way to the atoms in the tellurium crystal. Their concept requires the presence of resonating bonds to satisfy the co-ordination, with the consequence that an empty orbital is present in the valence shell of some of the atoms because of the electron promotion necessary to give rise to the resonance. This empty orbital is responsible for metallic behaviour in other crystals, and to retain consistency with their theory, MOOSER and PEARSON claim that bismuth telluride and the isomorphous bismuth selenide show metallic behaviour. However, it seems to be firmly established, from experiments in this laboratory,[4] that bismuth telluride behaves in all respects like a typical small-energy-gap semiconductor and, in particular, sufficiently pure samples show a negative temperature-dependence of the resistivity from 200°K upwards. Thus, apart from the difficulty of correlating the assumed resonance with the widely differing bond lengths surrounding the $Te^{(1)}$ atoms, the experimental evidence in support of the ideas of MOOSER and PEARSON is very doubtful.

LAGRENAUDIE[1] attempts to apply to bismuth telluride the model proposed by KREBS[5] for lead sulphide. This requires that the bismuth atoms are trivalent, the two 6*s* electrons forming a lone pair, while the three 6*p* electrons are used to form six *p*-type bonds to the surrounding tellurium atoms. However, this scheme does not appear to be self-consistent if the contribution of the tellurium atoms is considered. In extending the KREBS model to bismuth telluride, the $Te^{(2)}$ atoms presumably have the same type of bond as the bismuth atoms, giving rise to octahedral co-ordination, the bonds being effectively one-electron bonds. However, the

$Te^{(1)}$ atoms are considered by LAGRENAUDIE as forming pyramidally directed *p*-orbitals (presumably as in ammonia). The two types of bonding orbitals do not seem compatible with the resonance conditions necessary to explain the semiconducting properties on the basis of KREB's theory. Furthermore, this scheme does not account for all eighteen of the available valence electrons.

An alternative scheme which appears to remove the difficulties discussed above is as follows. The bond length between $Te^{(1)}$ atoms in adjacent leaves is of the same order as the bond length between tellurium atoms in adjacent chains of the tellurium structure (3·74 Å) and these are usually assumed to be of the Van der Waals type. If we assume that the same is true in bismuth telluride, then this explains the observed easy cleavage and implies that the electron density in these bonds is effectively zero. Thus the valence electrons in $Te^{(1)}$ atoms are used only in bonding to the three nearest-neighbour bismuth atoms, i.e. in three nearly perpendicular bonds. This co-ordination is consistent with the behaviour of the $Te^{(1)}$ atoms assumed by LAGRENAUDIE, viz. that these atoms use only *p*-orbitals in bonding, and that only the *p*-electrons are used, the two 5*s* electrons forming a lone pair.

However, the $Te^{(2)}$ atoms and the bismuth atoms have nearly octahedral co-ordination. This is consistent with the assumption that the bonding orbitals on these atoms are sp^3d^2 hybrids, and that both *s* and *p* electrons are used in the bonding of these atoms. Assuming this to be the case and also that the $Te^{(1)}$ atoms behave as discussed in the preceding paragraph, then a fully saturated bonding structure with two electrons per bond is obtained. The total number of valence electrons per unit cell is twenty-four (four from each of the two $Te^{(1)}$ atoms, five from each of the two Bi, and six from the $Te^{(2)}$ atom) and these are shared between the twelve bonds per unit cell. This model would suggest that the Bi–$Te^{(2)}$ bond length would differ from the Bi–$Te^{(1)}$ bond length, since a different kind of overlap is involved. This is in fact observed, although the difference is not large, and the shorter Bi–$Te^{(1)}$ distance suggests that this bond is stronger than the other type. This conclusion is strengthened by considering the formal covalent formula for the suggested scheme, viz. $Te\ Bi_2^{1-}\ Te_2^{1+}$, which emphasizes the difference in nature between the two types of tellurium atom and suggests that there will be an ionic component along the Bi–$Te^{(1)}$ bonds leading to an increase of bond strength above the normal covalent value.[6]

Some further tentative conclusions may be drawn relating to the observations of AUSTIN and SHEARD[7] on the variation of the optical energy gap of alloys of composition $Bi_2Te_{3-x}\ Se_x$ with increasing selenium content. On the above model, the most energetically favoured sites for Group VI atoms are the $Te^{(2)}$ sites, since these involve six bonds to nearest neighbours as opposed to the three bonds associated with $Te^{(1)}$ sites. If selenium or sulphur is substituted for tellurium, then because of the increased electronegativity, a lower energy will be obtained if the substituted atoms rather than tellurium atoms go into the $Te^{(2)}$ sites. Thus, in $Bi_2\ Te_{3-x}\ Se_x$, it is to be expected that as *x* increases from zero, the selenium atoms will at first go into the $Te^{(2)}$ sites.*

In these substituted alloys, the selenium atoms in $Te^{(2)}$ sites, being more electronegative, will increase the ionic component of the bonding between bismuth and the atoms in these sites. The previous discussion has indicated that this bonding is the weaker type in the structure and hence probably determines the energy gap of the solid. Thus it is concluded that in an alloy $Bi_2Te_{3-x}\ Se_x$, as *x* first increases from zero, the bond strength and hence energy gap,[6] will increase with increasing *x*, until *x* reaches one, when all the $Te^{(2)}$ sites will be occupied. Thereafter, the trend will be reversed to some extent, i.e. the energy gap will tend to decrease with increasing *x*, since now the selenium atoms will go into $Te^{(1)}$ sites and tend to attract charge along the Bi–$Te^{(1)}$ site bonds, making the bismuth atoms more electronegative, which in turn causes charge to move towards the bismuth along the Bi–$Te^{(2)}$ site bonds. These predictions are in very good

* LANGE[3] found that in tetradymite (Bi_2Te_2S), the sulphur atoms occupy the sites corresponding to $Te^{(2)}$ atoms in Bi_2Te_3. His additional observation that Bi_2Te_3 and Bi_2Te_2S do not form a range of solid solutions is in contrast to results which have been obtained in this laboratory.

The alloys used by AUSTIN and SHEARD[7] were single-phase solid solutions. Further work is now in progress to determine the position of the selenium atoms in these alloys.

agreement with the observations of AUSTIN and SHEARD,[7] who find a maximum energy gap at a composition close to Bi_2Te_2Se.

REFERENCES

1. LAGRENAUDIE, J. *J. Phys. Radium* **18,** 39 (suppt.) (1957).
2. MOOSER, E. and PEARSON W. B. *Canad. J. Phys.* **34,** 1369 (1956).
3. LANGE P. W. *Naturwissenschaften* **27,** 133 (1939).
4. WRIGHT D. A. *Halbleiterprobleme* **4**. In press.
5. KREBS H. *Physica* **20,** 1125 (1954).
6. GOODMAN C. H. L. *J. Electronics* **1,** 115 (1955).
7. AUSTIN I. G. and SHEARD A. *J. Electronics* **3,** (1957).

VOL.
5
195

Note on: "The band structure of aluminum: a self-consistent calculation"*

(*Received* 30 *September* 1957)

IN paragraph 4 of the paper by HEINE[1] (Hereafter referred to as I) published under the above title, a systematic numerical error has been discovered which appreciably alters the values presented in Tables 3 and 4 of I and subsequent results. The error lies in the calculation of $U_2(\mathbf{r})$, the potential in a face-centered-cubic lattice of protons in a uniform background of negative charge with a density of one electron per proton. This potential $U_2(\mathbf{r})$ is of importance in calculating the potential in any f.c.c. lattice, so that we present here a more complete and correct set of values. We also estimate the effect of this error on the results of I.

Table 3 of I presents the results for $U_2(\mathbf{r})$ at five important points in the lattice, along with the quantity $U_4(\mathbf{r})$, which is defined by

$$U_4(\mathbf{r}) = U_2(\mathbf{r}) - U_3(\mathbf{r})$$

where

$$U_3(\mathbf{r}) = -\sum_j V_3(|\mathbf{r}-\mathbf{r}_j|)$$

the summation extending over all lattice sites, and

$$V_3(r) = \frac{2}{r} - \frac{3}{r_0} + \frac{r^2}{r_0^3} \quad \text{for } r \leqslant r_0,$$

$$V_3(r) = 0 \qquad \text{for } r > r_0,$$

that is, $U_3(\mathbf{r})$ is the "atomic spheres" potential. Here r_0 is the radius of the Wigner sphere. These values should be replaced by those given in Table 1.

The values of $V_4(r)$ are determined at intermediate points in the manner of I, and are listed in Table 2 (replacing Table 4 of I). The charge density corresponding to V_3+V_4 was obtained using Poisson's equation, and is also given. Here r is measured in units of the Bohr radius, V is in rydbergs, and the charge density is in electrons per atom.

From Table 2 it is seen that at $r = 0$, V_4 is about twice the value calculated in I and drops off more rapidly. This difference in behavior is reflected in the associated charge density. The charge density presented in Table 2 is better behaved than that given in I, although it still varies abruptly at $r = r_0$(2·9765 a.u.). This behavior is partly a consequence of the sharp cut-off at $r = r_0$ of the charge density associated with V_3 and partly tying V_4 to the values calculated at the points P_i. No attempt has been made to smooth the charge density near $r = r_0$, since neglecting the θ and ϕ dependence of V_4 makes the significance of the charge density in this region quite dubious. The results in Table 2 may be applied to a face-centred-cubic lattice of lattice constant a' by multiplying the values of r by a'/a and the corresponding potential by a/a', with $a = 7{\cdot}6163$ a.u.

In order to get an estimate of the θ and ϕ dependence which has been neglected in $V_4(\mathbf{r})$, two additional points in the [111] and [100] directions were calculated. The results are presented in Table 3. We thus see that the maximum deviation (called

* Supported in part by the Office of Naval Research, the Signal Corps, the Air Force Office of Scientific Research, and the National Security Agency.

Table 1. *Potentials in a proton lattice*

Point	$U_2(P_i)$	$U_3(P_i)$	$U_4(P_i)$	$V_4(R_i)$
Near P_0	0·917804*	1·00790	—0·09010	0·09010
P_1	—0·133190	—0·01964	—0·11355	0·05678
P_3	—0·083164	0	—0·08316	0·02772
P_4	—0·075569	0	—0·07557	0·01889
P_2	0	0	0	0

* Plus $-2/r+0(r)$.

Table 2. Correction to "uniform spheres" potential

r	$V_4(r)$	Charge density	r	$V_4(r)$	Charge density
0	0·0901	1·000	2·4	0·0759	0·2
0·5	0·0900	1·0	2·5	0·0711	0·0
0·9	0·0899	1·0	2·6	0·0647	0·0
1·1	0·0898	1·0	2·7	0·0560	0·6
1·2	0·0897	0·9	2·8	0·0471	1·2
1·3	0·0895	0·9	2·9	0·0402	1·2
1·4	0·0892	0·9	3·0	0·0336	1·2
1·5	0·0888	0·9	3·1	0·0282	0·1
1·6	0·0883	0·9	3·2	0·0231	0·1
1·7	0·0877	0·9	3·3	0·0188	0·0
1·8	0·0870	0·9	3·4	0·0144	0·0
1·9	0·0861	0·8	3·5	0·0105	0·0
2·0	0·0849	0·8	3·6	0·0068	0·0
2·1	0·0834	0·7	3·7	0·0033	0·0
2·2	0·0815	0·7	3·8	0·0002	0·0
2·3	0·0790	0·5	$>3·808$	0	0

Table 3. Potentials in a proton lattice

Point	$U_2(P_i)$	$U_3(P_i)$	$U_4(P_i)$	$V_4(R_i)$
$(\frac{1}{16}, \frac{1}{16}, \frac{1}{16})a$	—1·533883	—1·443604	—0·09028	0·09028
$(\frac{1}{8}, \frac{1}{8}, \frac{1}{8})a$	—0·399835	—0·308072	—0·09176	0·09176
$(\frac{1}{4}, 0, 0)a$	—0·260965	—0·179951	—0·08101	0·08101
$(\frac{1}{3}, 0, 0)a$	—0·083609	—0·024296	—0·05931	0·05931

$V_5(r, \theta, \phi)$ in I) from the smoothed potential $V_4(r)$ is $\pm 0·009$ rydberg. $V_5(r, \theta, \phi)$ is essentially zero for $r < 0·9$ a.u. and $r > 2·7$ a.u. Neglecting V_5 can certainly lead to no more than an error of 0·005 rydberg in the energy levels, as was anticipated in I.

The new values of $V_4(r)$ given in Table 2 above must be used to determine $2Z_p(r, k_M)$ shown in Table 1 of I. Columns VII, IX, and X must be corrected. It has been estimated that the effect of this correction is to raise all energy levels in I by about 0·1 rydberg, but to shift them relative to one another by only about 0·03 rydberg. In I, HEINE estimates the error in the energy levels relative to one another as a result of various numerical approximations to be about 0·03 rydberg; hence the above correction approximately doubles the stated error. While the correction is quantitatively quite important, it does not change qualitatively the results obtained in I.

Acknowledgement—It is a pleasure to thank Dr. HEINE for helpful discussions during the course of this calculation.

Department of Physics ROBERT E. BEHRINGER
University of California
Berkeley, Calif.

REFERENCE

1. HEINE V. *Proc. Roy. Soc.* A **240**, 361 (1957).

Defense of the strain-energy approach for small solute atoms

(*Received* 13 *September* 1957)

In a recent issue of this journal, Oriani[1] discussed the use of an elastic model which evaluates the energy of formation of primary metallic solid solutions as a strain energy. He concluded that not only are the experimental data on the heats of formation of solid and liquid solutions inconsistent with such a model, but also that the model itself is not self-consistent for the case of solute atoms that are smaller than the solvent atoms. The writer is in agreement with the difficulties pointed out by Oriani in the interpretation of experimental heats of solution in terms of strain-energy concepts, but finds the argument concerning the internal inconsistency of these concepts very misleading. Strain-energy calculations have been used widely, not only to interpret heats of solution but also in other connections, e.g. in the interpretation of entropies of solution.[2,3] It therefore seems desirable to correct the erroneous impression conveyed by Oriani's paper.

The claim made by Oriani (at the suggestion of Hart) is that, because of the absence of repulsive forces, the "misfit energy" for a smaller solute atom is necessarily negative when the small foreign atom is placed into the larger-sized hole created by the removal of a solvent atom. If then the relaxation of atoms adjacent to the foreign atom takes place, this relaxation can only produce a further negative contribution. The total contribution is then negative, in contradiction to the strain-energy calculation. What this argument fails to take into account is that a macroscopic theory such as the elastic model must, to be complete, recognize the existence of some kind of surface-energy term. Thus, for example, without including surface energy, the formation energy of a vacancy involving no nearest-neighbor relaxation would be zero, and with relaxation it would be negative. Brooks[4] has shown that macroscopic concepts can be useful in the calculation of the energy of formation of a vacancy, if one obtains the result by minimizing the combined surface and strain energy associated with a vacancy. The result obtained is then positive and reasonable in magnitude. The surface energy on an atomic scale need not be the same as that of the macroscopic free surface, and for the case of a vacancy the problem of how to calculate this surface energy becomes important. When one applies the same considerations to an undersized solute atom, however, the actual surface energy does not enter into the calculation. One simply notes that placing the solute into the unrelaxed vacancy produces no strain energy, but involves a surface energy equal to that associated with the free surfaces of the solute atom plus the vacancy. Thus the energy of the unrelaxed state is indeed positive relative to the pure solvent and solute. If one now relaxes the solvent atoms into the vacancy to the point where continuity with the solute atom is achieved, the surface energy term disappears but is replaced by strain energy calculated in the usual way.[2,5] This strain energy will be less than the surface energy of the unrelaxed state, unless the solute atom is very much smaller than the solvent atom, in which case it may be anticipated that a substitutional solid solution would not form. Thus, the magnitude of the surface energy on an atomic scale does not actually enter into the calculation; the mere fact that such a term exists eliminates the objection to the strain-energy calculation raised by Oriani and Hart.

Acknowledgements—The writer is indebted to D. P. Seraphim, J. F. Freedman, and several other of his former students at Yale University for a stimulating discussion of this subject.

IBM Watson Laboratory A. S. Nowick
Columbia University
New York City

REFERENCES

1. Oriani R. A. *J. Phys. Chem. Solids* **2,** 327 (1957).
2. Zener C. *Acta Cryst.* **2,** 163 (1949); *Thermodynamics in Physical Metallurgy* p. 16. American Society for Metals, Cleveland (1950).
3. Freedman J. F. and Nowick A. S. *Acta Met.* In the press.
4. Brooks H. *Impurities and Imperfections* p. 1. American Society for Metals, Cleveland (1955).
5. Lawson A. W. *J. Chem. Phys.* **15,** 831 (1947).

BOOK REVIEW

D. McLEAN: **Grain Boundaries in Metals.** Clarendon Press, Oxford, 1957. 346 pp., 50s.

WHEN a liquid solidifies the process is governed by the kinetics of the so-called "nucleation and growth" phenomena. Since there are usually many nuclei, generally in a random orientation, the result is an assembly of variously oriented grains. These grains are joined along grain boundaries which thus play a fundamental role in affecting the properties of the polycrystalline solid and have also characteristic properties of their own. Although the presence and general nature of grain boundaries were known for a long time, a better insight into their structure and into their characteristic properties was not obtained until quite recently. Actually grain boundaries were for long mentioned only as *malum necessarium* of the structure of polycrystalline materials and as a probable and unknown location of most of the impurities. With the advent of interest in crystalline defects, this point of view has now been replaced by a feeling that a precise knowledge of grain boundaries is of paramount importance for various practical problems and of great fundamental interest as well. There is a host of fascinating topological, structural, electronic, and chemical problems associated with grain boundaries, and many of them are only now beginning to be unravelled.

The book here reviewed is the first survey ever published of the immense field of grain-boundary phenomena in metals, both as far as properties and structure of the boundaries, as well as their influence on the bulk properties of solids, are concerned. While the appearance of such a book has been long awaited, one has a feeling that only within the last few years has the subject matter reached a state of sufficient understanding and clarity for a specialized monograph to be written. This impression is justified by a quick glance at the references in the book. Nearly one quarter of all pertinent publications appeared in the years 1952–53, with a steadily decreasing flux ever since. No doubt the main spur to this interest in the physics and chemistry of grain boundaries came from the successful application of the dislocation theory to low-angle boundaries. Although the theory of high-angle boundaries is still in a quite unsatisfactory state, most of the observed phenomena find at least a qualitative, if not a quantitative, interpretation.

The most striking aspect of the present book is its apparent completeness. All the various theories which have been proposed are at least mentioned, and the huge mass of experimental material, whether concerning directly properties of grain boundaries or the influence of the presence of grain boundaries on bulk properties, is carefully reviewed. About the only omission—which by the way the author acknowledges in his preface—is the chemical effects at grain boundaries, in particular, corrosion. This is too bad, since this field is now extremely active and even an incomplete survey would have been useful. The author chose to deal only with metals, and thus grain-boundary phenomena in such interesting and vital fields as semiconductors and dielectrics are left out.

The book is directed essentially at a metallurgical audience and therefore the theoretical derivations are usually only sketched. On the other hand, such a variety of topics as the influence of temperature and impurities on interfacial energies, topological relations for the analysis of microstructures, solute concentration and its influence on grain boundaries all the various mechanical phenomena, diffusion, sub-boundaries, grain mobility, and viscosity are treated in considerable detail. The presentation is clear and well arranged. On the whole, an extremely worth-while book.

R. SMOLUCHOWSKI

VOL.
5
195

CONTENTS LISTS OF VOLUME 3, NOS. 1–4

Volume 3 Nos. 1/2

page

E. A. Taft et H. R. Philipp:
Emission photoélectrique à partir de la bande de valence de quelques halogénures alcalins . 1

Jean François Laurent et Jacques Bénard:
Autodiffusion des ions dans les cristaux uniques des halogénures de potassium et des chlorures alcalins 7

J. D. Dunitz et L. E. Orgel:
Propriétés electroniques des oxydes des metaux de transition—I. Distorsions de la symétrie cubique 20

S. Geller et M. A. Gilleo:
La structure cristalline et le ferrimagnetisme du grenat de fer–yttrium $Y_3Fe_2(FeO_4)_3$. . 30

M. H. Francombe:
Changements de structure dans les chromites de fer du type spinelle 37

Edgar F. Westrum, Jr. et D. M. Grines:
Chaleur specifique à basse température et propriétés thermodynamiques du ferrite de zinc 44

L. E. Orgel:
Les structures cristallines du manganèse et des actinides 50

S. Triebwasser:
Energie libre, champs internes et polarisabilites ioniques dans $BaTiO_3$ 53

R. N. Hall:
Variation du coefficient de distribution et de la solubilité solide avec la température . . 63

E. M. Pell:
Solubilité du lithium dans le germanium 74

E. M. Pell:
Solubilité du lithium dans le silicium 77

C. J. Gallagher:
Electrolyse du cuivre dans le silicium solide 82

J. J. Lander:
Concentration en hydrogène et semi-conductibilité de ZnO bombardé par de l'hydrogène ionisé 87

P. Kisliuk:
Les probabilités de pénétration des gaz adsorbés chimiquement à la surface des solides . 95

Robert W. Keyes:
Effets d'élasto-résistance dans un alliage germanium–silicium 102

F. G. Allen et A. B. Fowler:
Variation de la différence de potentiel de contact avec la face cristalline pour le germanium . 107

Henry J. Bolden:
Microréversibilité dans les transitions non-verticales 115

Walter Baltensperger:
Correlations entre les fluctuations thermiques de tension dans un circuit 118

George H. Vineyard:
Facteurs de fréquence et effets isotopiques dans les processus de taux de l'état solide . 121

J. E. Aubrey et R. G. Chambers:
Resonance cyclotron dans le bismuth 128

I. T. Steinberger, E. A. Braun et E. Alexander:
Effets de memoire et Gudden–Pohl dans compose phosphorescent stimule par l'infra-rouge 133

D. M. Grimes:
Propriétés réversibles des corps ferromagnétiques polycristallins 141

Lettres aux redacteurs 153

Revue de livre 161

Volume 3 Nos. 3/4

page

E. A. Lynton, B. Serin et M. Zucker:
La température critique de supraconductibilité et la chaleur spécifique électronique de l'étain impur 165

A. B. Pippard:
L'effet d'alliage sur la température de transition de supraconductibilité de l'étain . . 175

Théodore G. Castner et Werner Känzig:
La structure électronique des centres V 178

F. J. Morin et Howard Reiss:
Précipitation du lithium dans le germanium 196

George L. Hall:
Distorsion autour d'imperfections ponctuelles dans des cristaux simples 210

Roy F. Potter:
Le caractère ionique et les modules d'élasticité des réseaux du type de la blende . . 223

D. G. Thomas:
Le zinc intersticiel dans l'oxyde de zinc 229

F. K. Lotgering et E. W. Gorter:
Solutions solides entre des composés antiferromagnétiques et ferromagnétiques avec la structure de NiAs 238

A. W. Lawson:
Corrélation de ΔS et ΔV dans les réactions à activation simple dans les solides . . . 250

R. R. Haering et P. R. Wallace:
Les propriétés électriques et magnétiques du graphite 253

A. M. Garofalo et J. S. Plaskett:
Energie d'interaction due aux électrons libres d'imperfections ponctuelles dans les métaux. 275

D. H. Tomboulian, D. E. Bedo et W. M. Neupert:
Spectre d'absorption $M_{2,3}$ des éléments solides Cr à Ge 282

J. E. Worsham, Jr., M. K. Wilkinson et C. G. Shull:
Observations de diffraction des neutrons sur les systèmes palladium–hydrogène et palladium–deutérium 303

Donald S. McClure:
La distribution des cations des métaux de transition dans les spinelles 311

J. D. Dumitz et L. E. Orgel:
Propriétés électroniques des oxydes de métaux de transition—II. Distribution du cation parmi les emplacements octaédriques et tétraédriques 318

R. W. Schmitt et J. S. Jacobs:
Comportement magnétique et électrique à basse température des alliages dilués de Mn dans Cu 324

Revue de livre 338

Volume 3 Nos. 1/2

Е. А. Тафт и Г. Р. Филипп:
Фотоэлектрическая эмиссия из валентной полосы некоторых галоидных солей щелочных металлов 1

Ж. Ф. Лоран и Ж. Бенар:
Автодиффузия ионов в кристаллах галоидных солей щелочных металлов . . 7

Дж. Д. Дуниц и Л. Е. Оргель:
Электронные свойства окислов переходных металлов—I. Отклонения от кубической симметрии 20

VOL. 5 1958

page

С. Геллер и М. А. Гиллео:
Кристаллическая структура и ферримагнетизм $Y_2Fe_2(FeO_4)_3$ 30

М. Франкомб:
Изменения решетки в хромитах железа шпинелевого типа 37

Э. Ф. Веструм мл. Д. М. Граймс:
Теплоемкость и термодинамические свойства феррита цинка при низких температурах 44

Л. Е. Оргель:
Кристаллическая структура марганца и актинидных элементов 50

С. Трибвассер:
Свободная энергия, внутренние поля и ионные поляризуемости в $BaTiO_3$ . . 53

Р. Н. Холл:
Изменение коэффициента распределения и растворимости в твердой фазе с температурой 63

Е. М. Пелл:
Растворимость лития в германии 74

Е. М. Пелл:
Растворимость лития в кремнии 77

К. Галлахер:
Электролиз меди в твердом кремнии 82

Дж. Ландер:
Концентрация водорода и полупроводимость ZnO при бомбардировке ионами водорода 87

П. Кислюк:
Вероятности прилипания для газов при хемисорбции на твердой поверхности . 95

Р. В. Кейс:
Эффекты эластосопротивления в сплаве германия с кремнием 102

Ф. Аллен и А. Б. Фоулер:
Изменение контактного потенциала в зависимости от кристаллографической грани у германия 107

Г. Боулден:
Детальное равновесие при невертикальных переходах 115

В. Бальтеншпергер:
Корреляции во флуктуациях напряжения в цепях 118

Дж. Вайн'ярд:
Частотная зависимость и изотопические эффекты в движении дефектор в твердых телах 121

Дж. Е. Обри и Р. Чемберс:
Циклотронный резонанс в висмуте 128

И. Т. Штейнбергер, Е. А. Браун и Е. Александер:
Эффекты Гуддена-Поля и запоминания в инфракрасных стимулированных фосфорах 133

Д. М. Гаймс:
Обратимые свойства в поликристаллических ферромагнетиках—I. Теория ожидаемых измеений в обратимых свойствах при намагничении 141

Письма к редактору 153

Рецензия: 161

OL.
5
958

Volume 3 Nos. 3/4

page

Е. А. Линтон, Б. Серин и М. Цуккер:
Сверхпроводящая критическая температура и электронная теплоемкость загрязненного олова 165

А. Б. Пиппард:
Влияние примесей на сверхпроводящую точку перехода в олове . . . 175

Т. Кастнер и В. Кенциг:
Электронная структура V-центров 178

Ф. Морин и Г. Рейсс:
Осаждение лития в германии 196

Дж. Л. Холл:
Деформация вокруг точечных нарушений в монокристаллах . . . 210

Р. Ф. Поттер:
Ионный характер и упругие модули решеток типа цинковой обманки . . 223

Д. Поттер:
Интерстициальный цинк в окиси цинка 229

Ф. К. Лотгеринг и Е. В. Гортер:
Твердые растворы ферромагнитных и антиферромагнитных соединений со структурной типа NiAs 238

А. В. Лоусон:
Корреляция между ΔS и ΔV в простых активированных процессах в твердых телах 250

Р. Р. Херринг и П. Р. Уоллес:
Электрические и магнитные свойства графита 253

А. М. Гарофало и Дж. С. Пласкетт:
Энергия взаимодействие точечных нарушений в металлах, обусловленная свободными электронами 275

Д. Томбульян, Д. Е. Бедо и В. М. Нейперт:
$M_{2,3}$ спектры поглощения твердых элементов от Cr до Ge 282

Дж. Е. Воршам мл., М. К. Вилькинсон и Шелл:
Нейтроно-диффракционные наблюдения на системах палладий–водород и палладий–дейтерий 303

Д. С. МакКлюр:
Распределение катионов переходных металлов в шпинелях 311

Дж. Д. Дуниц и Л. Е. Оргель:
Электронные свойства окислов переходных металлов—II. Распределение катионов между октаэдрическими и тетраэдрическими узлами 318

Р. В. Шмитт и И. С. Джекобс:
Низкотемпературные электрическое и магнитное поведения разбавленных растворов Mn в Cu 324

Рецензия: 338

Volume 3 Nos. 1/2

E. A. Taft und H. R. Philipp:
Photoelektrische Emission aus dem Valenzband einiger Alkalihalogenide . . . 1

Jean-François Laurent und Jacques Bénard:
Die Selbstdiffusion der Ionen in Einkristallen der Kaliumhalogenide und Alkalichloride . 7

J. D. Dunitz und L. E. Orgel:
Die Eigenschaften der Oxyde der Übergangsmetalle—I. Abweichungen von der kubischen Symmetrie 20

VOL.
5
1958

page

S. GELLER und M. A. GILLEO:
Die Kristallstruktur und Ferrimagnetismus von Yttrium–Eisengranat, $Y_3Fe_2(FeO_4)_3$. . 30

M. H. FRANCOMBE:
Gitteränderungen bei Eisenchromiten vom Spinelltyp 37

EDGAR F. WESTRUM, JR. und D. M. GRIMES:
Wärmekapazität und thermodynamische Eigenschaften des Zinkferrits bei tiefen Temperaturen 44

L. E. ORGEL:
Die Kristallstrukturen des Mangans und der Aktiniden 50

S. TRIEBWASSER:
Freie Energie, innere Felder und Ionenpolarisierbarkeit bei $BaTiO_3$ 53

R. N. HALL:
Die Änderung des Verteilungskoeffizienten und der festen Löslichkeit mit der Temperatur 63

E. M. PELL:
Die Löslichkeit des Lithiums in Germanium 74

E. M. PELL:
Die Löslichkeit des Lithiums in Silizium 77

C. J. GALLAGHER:
Kupferelektrolyse bei festem Silizium 82

J. J. LANDER:
Wasserstoffkonzentration und Leitfähigkeit in ZnO beim Beschiessen mit den Wasserstoff-Ionen H_1^+, H_2^+ und H_3^+ 87

P. KISLIUK:
Die Haftwahrscheinlichkeiten von Gasen, die an der Oberfläche von Festkörpern chemiesorbiert werden 95

ROBERT W. KEYES:
Die Änderung des elektrischen Widerstandes bei elastischer Verformung einer Germanium-Silizium Legierung 102

F. G. ALLAN und A. B. FOWLER:
Die Änderung des Kontaktpotentials mit der Kristalloberfläche bei Germanium . . . 107

HENRY J. BOWLDEN:
Das detaillierte Gleichgewicht bei indirekten Übergängen 115

WALTER BALTENSPERGER:
Die Beziehungen zwischen thermischen Schwankungen der Spannung in einem Stromkreis 118

GEORGE H. VINEYARD:
Frequenzfaktoren und Isotopeneffekt bei Reaktionsabläufen in festen Körpern . . . 121

J. E. AUBREY und R. G. CHAMBERS:
Zyklotronresonanzen in Wismut 128

I. T. STEINBERGER, E. A. BRAUN und E. ALEXANDER:
Gudden-Pohl Effekt und Erinnerungsvermögen bei einem infrarot angeregten Phosphor . 133

D. M. GRIMES:
Reversible Eigenschaften von polykristallinen Ferromagnetikas—I. Die Theorie der Änderung reversibler Eigenschaften mit der Magnetisierung 141

Briefe an die Herausgeber 153

Besprechung 161

Volume 3 Nos. 3/4

E. A. LYNTON, B. SERIN und M. ZUCKER:
Die kritische Temperatur der Supraleitung und die spezifische Elektronenwärme von verunreinigtem Zinn 165

page

A. B. PIPPARD:
Die Wirkung der Legierungsbildung bei Zinn auf die Sprungtemperatur der Supraleitung 175

THÉODORE G. CASTNER und WERNER KÄNZIG:
Die Elektronenstruktur von V-zentren 178

F. J. MORIN und HOWARD REISS:
Die Ausscheidung von Lithium in Germanium 196

GEORGE L. HALL:
Die Verzerrungen in der Nähe von Punktförmigen Fehlstellen in einfachen Kristallen . 210

ROY F. POTTER:
Der Ionencharakter und die Elastizitäts-Moduli bei Gittern vom Zinkblendetyp . . 223

D. G. THOMAS:
Zwischengitteratome des Zinks in Zinkoxyd 229

F. K. LOTGERING und E. W. GORTER:
Feste Lösungen zwischen ferromagnetischen und antiferromagnetischen Verbindungen mit NiAs-Struktur 238

A. W. LAWSON:
Der Zusammenhang Zwischen ΔS und ΔV bei einfachen, aktivierten Prozessen in Festkörpern 250

R. R. HAERING und P. R. WALLACE:
Die elektrischen und magnetischen Eigenschaften von Graphit 253

A. M. GAROFALO und J. S. PLASKETT:
Die von den freien Elektronen herrührende Wechselwirkungsenergie von punktförmigen Fehstellen in Metallen 275

D. H. TOMBOULIAN, D. E. BEDO und W. M. NEUPERT:
$M_{2,3}$-Absorptionsspektren der Elemente von Cr bis Ge 282

J. E. WORSHAM, JR., M. K. WILKINSON und C. G. SHULL:
Beobachtungen der Neutronenbeugung an Palladium–Wasserstoff und Palladium–Deuterium Systemen. 303

DONALD S. MCCLURE:
Die Verteilung von Kationen der Übergangsmetalle in Spinellen 311

J. D. DUNITZ und L. E. ORGEL:
Die Eigenschaften der Elektronen bei Oxyden der Übergangsmetalle—II. Die Kationenverteilung zwischen Oktaeder- und Tetraederseiten 318

R. W. SCHMITT und I. S. JACOBS:
Das elektrische und magnetische Verhalten verdünnter Legierungen von Mn in Cu bei tiefen Temperaturen 324

Besprechung 338

VOL. 5 1958

PAPERS TO BE PUBLISHED IN FUTURE ISSUES

V. L. GINZBURG and A. P. LEVANIUK: Light scattering near second-order phase transition and Curie points.

D. F. C. MORRIS: The lattice energy and heat of formation of lithium monosulphide.

J. C. PHILLIPS and H. B. ROSENSTOCK: Topological methods of locating critical points.

F. A. KRÖGER and H. J. VINK: Relations between the concentrations of imperfections in solids.

J. W. NIELSEN and E. F. DEARBORN: Growth of single crystals of magnetic garnets.

R. W. KEYES: Effects of electron–electron scattering on the electrical properties of semiconductors.

D. S. TANNHAUSER: Self-diffusion of bromine in silver bromide.

G. B. BENEDEK and T. KUSHIDA: Pressure dependence of the Knight shift in the alkali metals and copper.

H. A. GERSCH and W. C. KOEHLER: Types of magnetically ordered configurations on simple lattices.

R. J. SLADEK: Magnetically induced impurity banding in *n*-InSb.

H. M. BATH and M. CUTLER: Measurement of surface recombination velocity in silicon by steady-state photoconductance.

O. FLINT and J. H. O. VARLEY: On the mechanism of oxide film formation on zirconium.

T. O. WOODRUFF and W. KÄNZIG: Paramagnetic resonance absorption of a *V*-center in LiF.

M. YA. AZBEL' and E. A. KANER: Cyclotron resonance in metals.

A. ASCOLI, M. ASDENTE, E. GERMAGNOLI and A. MANARA: Activation energies for production and migration of vacancies in platinum.

G. BOGNER and E. MOLLWO: Über die Herstellung von Zinkoxydeinkristallen mit definierten Zusätzen.

H. RUPPRECHT: Über Konzentration und Beweglichkeit von Elektronen in Zinkoxydeinkristallen mit definierten Zusätzen.

A. D. PEARSON: Studies on the lower oxides of titanium.

R. M. BOZORTH and D. E. WALSH: Ferromagnetic moment of $CoMnO_3$.

J. M. WHELAN and G. H. WHEATLEY: The preparation and properties of gallium arsenide single crystals.

T. S. SWOBADA, R. C. TOOLE and J. D. VAUGHAN: New magnetic compounds of the ilmenite type structure.

H. KAWAMURA: The deformation potential of potassium chloride.

D. B. FISCHBACH and A. S. NOWICK: Some transient electrical effects of plastic deformation in NaCl crystals.

W. G. MAISCH and H. G. DRICKAMER: The effect of pressure on color centers in alkali halide crystals.

G. HEILAND: Feldeffekt und Photoleitung an ZnO-Einkristallen.

A. SMAKULA and J. KALNAJS: Oxygen impurity in silicon single crystals.

R. E. SCHLIER and H. E. FARNSWORTH: Structure of epitaxed copper deposited by evaporation onto a clean (00·1) face of a titanium crystal.

J. L. BIRMAN: Calculation of coulomb crystal potentials.

D. SAINT-JAMES: Détermination des lois de force dans les cristaux du type du diamant.

J. I. PANKOVE: Radiative surface effect in germanium.

H. FRITZSCHE: Resistivity and Hall coefficient of Sb-doped germanium at low temperatures.

D. G. WORDEN and G. C. DANIELSON: Electrical resistivity of thin films of potassium at 100°K.

D. H. ROBERTS and J. E. BAINES: Photoconductivity in chemically deposited films of lead selenide.

J. B. GOODENOUGH: An interpretation of the magnetic properties of the Perovskite-type mixed crystals $La_{1-x}Sr_xCoO_{3-\lambda}$.

P. G. DE GENNES: Neutron scattering by antiferromagnets above the Néel-point.

B. K. AGARWAL and M. P. GIVENS: Soft X-ray absorption by manganese and manganese oxide.

T. A. SANDENAW and R. A. GIGNEY: The electrical resistivity and thermal conductivity of plutonium metal.

C. S. FULLER and J. M. WHELAN: Diffusion, solubility and electrical behavior of copper in gallium arsenide.

W. PAUL and D. M. WARSCHAUER: Optical properties of semiconductors under hydrostatic pressure—III. Silicon–germanium alloys.

L. P. KAO and E. KATZ: Phenomenological theory of anisotropic isothermal galvanomagnetic effects.

G. LEIBFRIED and CHR. LEHMANN: Gittertheoretische Behandlung einer Schraubenversetzung in Alkalimetallen.

E. DANIEL: Influence du potentiel du reseau et contribution des couches a l'annihalation du positon dans le cuivre.

R. A. ORIANI and W. K. MURPHY: Thermodynamics of ordering alloys—III. Energies of transformation of the $Au_{1/2}Cu_{1/2}$ phases.

A. TAYLOR and JONES: Constitution and magnetic properties of iron-rich iron–aluminum alloys.

W. LOW and D. SHALTIEL: Paramagnetic resonance spectrum of gadolinium in single crystals of thorium oxide.

A. H. MONES and E. BANKS: Ferrimagnetism in the system Na_2O–ZnO–Fe_2O_3.

R. NATHANS, M. T. PIGOTT and C. G. SHULL: The magnetic structure of Fe_3Al.

C. H. L. GOODMAN: The prediction of semiconducting properties in inorganic compounds.

U. GONSER and B. OKKERSE: The question of radiation induced phase changes.

R. A. EPPLER and H. G. DRICKAMER: The effect of pressure on the spectra of the Te^+ ion alkali halide lattices.

D. F. C. MORRIS: The instability of some dihalides of copper and silver.

E. SCHLÖMANN: Ferromagnetic resonance in polycrystalline ferrites with large anisotropy.

E. MOOSER and W. B. PEARSON: The crystal structure and properties of the group VB to VIIB elements and of compounds formed between them.

A. B. LIDIARD: Anion diffusion in alkali halide crystals.

E. SCHLÖMANN: Spin wave analysis of ferromagnetic resonance in polycrystalline ferrites.

E. O. KANE: The influence of exchange on the effective mass formation.

ERRATUM

LIFSHITZ I. M. and KOSEVICH A. M. Theory of the Shubnikov–de Haas Effect. *J. Phys. Chem. Solids* **4**, 1 (1958).

LIFSHITZ I. M. Quantum theory of the electrical conductivity of metals in a magnetic field. *J. Phys. Chem. Solids* **4**, 11 (1958).

The publishers regret that the initials of I. M. LIFSHITZ were inadvertently given as E. M. throughout the above two papers.

VOL. 5 1958

J. Phys. Chem. Solids Pergamon Press 1958. Vol. 5. pp. 157–170.

MAGNETICALLY INDUCED IMPURITY BANDING IN *n*-InSb

R. J. SLADEK

Westinghouse Research Laboratories, Pittsburgh 35, Pennsylvania

(*Received* 16 *September* 1957)

Abstract—A detailed study of the effect of a strong magnetic field on donor levels in *n*-InSb has been made by means of Hall-effect and resistivity measurements down to 1·5°K, using field strengths up to 28,000 G.

The results of these measurements indicate that donor levels which are split off from the conduction band under the influence of the magnetic field form a narrow impurity band with finite mobility.

The position of the impurity band (i.e. donor ionization energy) and the mobility of electrons in the impurity band have been determined as a function of magnetic field strength.

The impurity band mobility can be understood in terms of quantum-mechanical resonance jumping of electrons between donors by taking into account the dependence of the donor wave function on magnetic field strength, although there are some quantitative difficulties when the magnetic field is parallel to the current.

Experimental confirmation of our impurity banding model is provided by non-ohmic effects which indicate the occurrence of impact ionization of donors in electric fields of the order of 1 V/cm.

1. INTRODUCTION

In even the purest *n*-type InSb available, donor energy levels are merged with the conduction band under ordinary circumstances. However, these levels may lie below the conduction band when a strong magnetic field is present.[1,2] Such behavior is a consequence of the small effective electron mass,[3] which causes electronic wave functions centered on different donor atoms to overlap at a small enough impurity concentration so that experimentally available magnetic fields can shrink the donor wave functions sufficiently to remove the overlap.[4]

With the disappearance of overlap, electronic orbitals due to donors become more or less localized in the vicinity of donor ions. This effect depends on electron motion being quantized by the magnetic field in the plane perpendicular to the direction of the field. An estimate of the field strength required may be obtained by noting when the radius of the cyclotron motion of conduction-band electrons ($r_c = m^*v/eB$, where v is the electron velocity, e the electronic charge, and B the magnetic field) becomes as small as the distance between neighboring donors. Thus, the smaller the effective mass, the smaller the magnetic field needed for the disappearance of overlap.

Due to its influence on the conduction-band orbitals, a quantizing magnetic field causes the lowest state in the conduction band to be raised by an energy of $\frac{1}{2}\hbar\omega$ (where $\hbar$ is Planck's constant divided by 2π and ω is the cyclotron angular frequency eB/m^*). In addition, due to its influence on the donor wave functions, the field narrows the previously spread-out donor levels into an impurity band and raises them by an amount less than $\frac{1}{2}\hbar\omega$. Thus, when the field is strong enough, some donor levels lie below the conduction band, and a non-zero donor ionization energy exists.

The ionization energy increases as the magnetic field is increased and may exceed 1 Ry (the ionization energy given by the hydrogen atom model of an impurity in a semiconductor, which for *n*-InSb is 0·00069 eV) considerably when the overlap between electronic wave functions centered on adjacent donors is small.[5] The existing theory of these states is not applicable to available *n*-InSb in weak magnetic fields. However, for strong enough fields the theory should at least indicate the qualitative behavior of the donor ionization

energy in n-InSb as a function of magnetic field strength.

The initial purpose of the present work was to deduce from experimental measurements the donor ionization energy in n-InSb due to the presence of a quantizing magnetic field. Accordingly, we measured the Hall coefficient as a function of temperature and magnetic field strength at low temperatures for several n-InSb samples. Analysis of the Hall data permits a determination of the concentrations of electrons in the conduction band and in donor levels and thereby the donor ionization energy.

Of course, in the event that electrons in donor levels are completely immobile, the Hall coefficient is simply inversely proportional to the concentration of electrons in the conduction band. The first experiments performed, involving the "freeze-out" of electrons into donor levels in the presence of a strong magnetic field, were in fact analyzed on such a basis.[1]

Subsequent Hall-effect data showed that electrons localized around donor ions have non-zero mobility, and hence the donor levels must form a band of finite width. Thus we extended our investigation to study the mobility of electrons in this impurity band as a function of magnetic field strength.

To test the two-band-model interpretation of our Hall data, we have also made Hall-effect and resistivity measurements as a function of *electric* field strength above the Ohm's law region. Under proper conditions we expected that the electric field would accelerate conduction-band electrons enough to ionize donors by impact, thus raising electrons from the donor impurity band into the conduction band. This effect would presumably be reflected as a decrease in the Hall coefficient as the electric field is increased until the exhaustion value was reached. Further increases in electric field strength should produce no further change in Hall coefficient. Our experiments confirm these expectations in detail.

Our method of presentation will be as follows. First, we shall describe the two-band model and the theory used to analyze our Hall data in Section 2(a). Next, the method used to determine the impurity band mobility from resistivity measurements is indicated in Section 2(b). Then, following a short description of experimental details in Section 3, the results of our experiments will be presented and discussed in Section 4. Finally, the most important conclusions will be summarized in Section 5.

2. THEORY AND METHOD OF ANALYSIS OF DATA

(a) *Donor Ionization Energy and Number of Impurity-Band Levels*

Our method for determining the donor ionization energy in a high magnetic field involves measuring the Hall coefficient over a range of temperatures including those at which the maximum and exhaustion values of R_H occur. To determine the influence of the magnetic field strength on this energy, the Hall coefficient versus temperature measurements are made at a number of different magnetic field strengths.

For analyzing our Hall data, we employed a model in which conduction takes place in a high-mobility conduction band and a low-mobility impurity band, the latter having been split off from the conduction band by a quantizing magnetic field. In its simplest form a two-band model applied to electrons in such bands gives the following expression for the Hall coefficient[6]

$$R_H = \frac{xb^2+(1-x)}{n_0 e[xb+(1-x)]^2}, \qquad (1)$$

where b is the ratio of the mobility of electrons in the conduction band (μ_e) to the mobility of electrons in the donor impurity band (μ_i), x and $(1-x)$ are the fractional concentrations of electrons in the conduction band and in the impurity band, respectively, and n_0 is the total electron concentration, which equals the excess in the concentration of donors over that of acceptors.

Strictly speaking, equations (1) and (2), below, are valid as written only for magnetic field strengths such that $\omega\tau \ll 1$, where τ is the relaxation time of the charge carrier in question, and when, in addition, the ratio of Hall mobility to drift mobility for each type of carrier $= 1$. In our samples the latter condition is true for impurity-band electrons, and should be at least approximately true for conduction-band electrons, which incidentally are no longer in a degenerate distribution when high fields are present. However, since in our samples $\omega\tau$ for conduction-band electrons becomes of the order of

VOL. 5 1958

unity at the largest fields employed, we derived a simple formula for R_H which takes this fact into account by assuming τ to be independent of energy. Applying this formula to analyze our data on one sample, we obtained values for x and b which were not sufficiently different from those obtained using equations (1) and (2) to affect the value of the donor ionization energy. Hence equations (1) and (2) are adequate as written for analyzing our Hall data.

When the Hall coefficient (for a fixed magnetic field) goes through a reasonably large maximum as a function of temperature, the mobility ratio, b, can be calculated by means of equation (1), using the values of R_H at maximum and at exhaustion, i.e. when all electrons are in the conduction band, provided that b is independent of temperature,[7] or at least only slightly temperature-dependent compared to x. Specifically, for a fixed magnetic field,

$$\frac{(R_H)_{\max}}{(R_H)_{\text{exh}}} = \frac{(b+1)^2}{4b}. \tag{2}$$

Using the value of b obtained from equation (2), the exhaustion electron concentration, n_0, and the measured Hall coefficient at a given temperature, we can calculate x and hence the conduction electron concentration $n_c = xn_0$ for that temperature from equation (1).

Having determined n_c by using equations (1) and (2), we can obtain the Fermi energy, ζ, from the relation

$$n_c = 2\sqrt{2m^*kT}\frac{eB}{h^2}F_{-\frac{1}{2}}(\zeta/kT), \tag{3}$$

where, in addition to the already defined symbols, T is the absolute temperature; h is Planck's constant; k is Boltzmann's constant; and $F_{-\frac{1}{2}}(\zeta/kT)$ is a Fermi–Dirac integral.[8] The $-\frac{1}{2}$ order of this integral results because of the one-dimensional nature of the conduction band in the direction parallel to the magnetic field. The zero of energy has been taken to be the lowest state in the conduction band in the presence of the magnetic field.

As written, equation (3) applies only when all conduction-band electrons are in the lowest oscillator state. For this to occur two conditions must be met. First, there must be a sufficient number of conduction-band energy states, N_c, associated with the lowest oscillator level to accommodate the electrons which are not bound to donors. Integration of the density of conduction-band energy states in the presence of a quantizing magnetic field up to $\hbar\omega_0$ reveals that $N_c \approx 10^{10}B^{\frac{3}{2}}\text{cm}^{-3}$, where B is in gauss. Since all our samples have total electron concentrations less that 10^{15}cm^{-3} (see Table 1), there are indeed enough states associated with the lowest oscillator level to accommodate all electrons which do not "freeze out".

Second, thermal energy must be too small to cause electrons to occupy higher oscillator states. This requires that $kT \ll \hbar\omega$. For n-InSb we note that at $B = 1600$ G, $\hbar\omega/k$ is already equal to 16°K. Since the pertinent measurements are made at liquid-helium temperature and higher field strengths, this second condition is also met.

The concentration of electrons in the donor impurity band, n_d, is related to ζ by the relation

$$n_d = \frac{N_B}{\frac{1}{2}\exp[(\epsilon_B-\zeta)/kT]+1} = n_0-n_c, \tag{4}$$

where N_B is the number of impurity-band (bound) states per cm^3 and ϵ_B is the energy at which all these states are assumed to lie. Referred to the same zero of energy as that used in equation (3), ϵ_B is negative and equal to minus the donor ionization energy. For N_B and ϵ_B independent of temperature, we can calculate ϵ_B from equation (4) by using the values of n_d and ζ for two different temperatures, since

$$\frac{n_d(T_1)}{n_d(T_2)} = \frac{n_0-n_c(T_1)}{n_0-n_c(T_2)} = \frac{\frac{1}{2}\exp[(\epsilon_B-\zeta_2)/kT_2]+1}{\frac{1}{2}\exp[(\epsilon_B-\zeta_1)/kT]+1}. \tag{5}$$

Although equation (5) has two solutions, only the larger value for $|\epsilon_B|$, or ionization energy, is consistent with a number of bound donor levels which is independent of temperature and is also of reasonable magnitude. The smaller value of $|\epsilon_B|$ would require a number of bound states over ten times the excess donor concentration. Indeed such a value would be greater than what we believe the total donor concentration to be. (For a discussion of various impurity concentrations see Section 4(d).)

To check the accuracy of the values of the ionization energy and N_B obtained for a given sample,

data for several pairs of temperatures were used to calculate these quantities for a given magnetic field strength.

(b) *Impurity-Band Mobility*

In order to determine the mobility of electrons in the impurity band as a function of magnetic field strength, we measured the resistivity at a temperature far enough below the temperatures of the maxima in the Hall coefficient so that most of the conduction is due to the impurity-band electrons. Then we calculated the mobility from the data, using the relation

$$\mu_i = \frac{1}{\rho e n_0} \tag{6}$$

where ρ is the measured resistivity and n_0 is the total electron concentration arising from excess donors. Using n_0 to calculate μ_i means, of course, that we assume that all electrons from excess donors are in the impurity band.

3. EXPERIMENTAL DETAILS

(a) *Specimens*

The specimens were cut and lapped to size (approximately $10 \times 2{\cdot}5 \times 1$ mm) from single-crystal n-type indium antimonide provided through the courtesy of Dr. A. C. BEER of the Battelle Memorial Institute and Dr. H. P. R. FREDERIKSE of the National Bureau of Standards, and from polycrystalline n-type indium antimonide made by the Ohio Semiconductor Company, which was supplied to us by Mr. O. LINDBERG of the Materials Engineering Department, Westinghouse Electric Corporation.

Two current and four potential leads of No. 40 copper wire were attached to each specimen with tin solder. While most measurements were made on samples with lapped surfaces, some measurements were also made on samples with etched surfaces. No differences in electrical properties due to these two different types of surfaces were observed.

The specimens are identified in Table 1.

Table 1. *Concentrations of electrons and impurities and donor spacing obtained from Hall and resistivity measurements*

n_0 is the concentration of electrons in the conduction band when all excess donors are ionized and is equal to the excess-donor concentration. N_I is the total concentration of ionized impurities. r_s/a_0 is one-half the separation between, and N_D the concentration of, donors important for conduction by impurity-band electrons when a transverse magnetic field is present.

The sample letters stand for the source of the material as follows: N—National Bureau of Standards, Washington, D.C.; O—Ohio Semiconductor Company, Columbus, Ohio; and B—Battelle Memorial Institute, Columbus, Ohio.

n-InSb sample	n_0 (cm^{-3})	N_I (cm^{-3})	r_s/a_0	N_D (cm^{-3})
	$\times 10^{14}$	$\times 10^{15}$		$\times 10^{14}$
N-4	0·30	2·2	1·33	3·5
O-1*	1·04	1·8	1·37	3·1
O-2*	0·99	1·8	1·35	3·3
B-1	1·4	3·0	1·15	5·3
N-3	3·3	1·4	1·14	5·5

* These samples were cut from the same slice of the same ingot and had very similar electrical properties.

(b) *Apparatus and technique*

The specimens were immersed directly in liquid helium, hydrogen, or nitrogen contained in a metal Dewar flask of the type described by other investigators.[9]

The temperature was controlled by keeping the vapor pressure of the refrigerant constant, using a large vacuum pump appropriately throttled. Mercury or Octoil-S manometers were used to measure the vapor pressure of the bath and thereby determine the temperature.

An Arthur D. Little electromagnet provided magnetic fields up to 28,000 G. The field was measured with the Rawson rotating coil fluxmeter supplied with the magnet. Control of the field to within ± 2 per cent or better was provided manually by adjusting the excitation to the generator supplying the magnet current, while using the fluxmeter to monitor the field.

Specimen current and potentials were measured by means of a conventional d.c. potentiometer-galvanometer arrangement.

(c) *Experimental uncertainties*

At all but the lowest temperatures, our Hall and resistivity measurements have a precision of a few per cent, which is limited principally by how well the magnetic field is controlled. At the lowest temperatures and large magnetic fields, the resistance of some samples became large enough to seriously limit galvanometer sensitivity and hence the precision of our Hall-effect data. Such data are not reported here.

Our data indicate the presence of slight inhomogeneities in the impurity concentrations of the samples. We deduce the presence of such inhomogeneities from slight disagreements ($\leqslant 20$ per cent) between the values of the Hall coefficient determined from two different sets of leads on the same sample. Samples showing greater inhomogeneity were not measured in detail and are not reported here. Considering the high degree of compensation which occurs in samples having the small excess

donor content needed for our experiments,* we regard the inhomogeneities in the specimens reported on here as quite small.

4. RESULTS AND DISCUSSION

(a) *Hall Effect*

Hall-coefficient versus reciprocal-temperature data for three different *n*-InSb samples are presented in Figs. 1–3, respectively. Note that

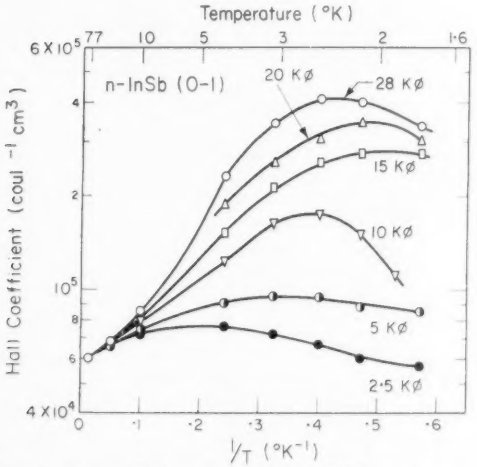

FIG. 1. Hall coefficient at a number of different magnetic field strengths as a function of reciprocal absolute temperature for *n*-type InSb (sample O-1).

logarithmic scales are used for the Hall coefficient.

If we first turn our attention to Hall data for a given temperature in the liquid-helium range, we see that the Hall coefficient increases markedly with magnetic field strength at high fields. Such large increases in R_H with increases in field strength can be explained only by decreases in the number of electrons in the conduction band.[1] The electrons which have left this band presumably fall into donor impurity-band levels which have been split off from the conduction band as a result of the strong magnetic field. The depth of these levels, i.e. the donor ionization energy, increases with field strength.

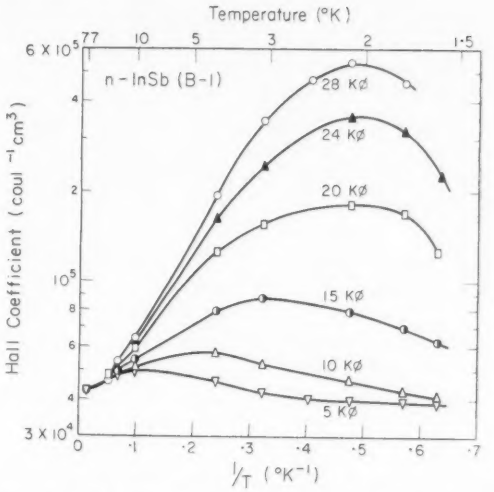

FIG. 2. Hall coefficient at a number of different magnetic field strengths as a function of reciprocal absolute temperature for *n*-type InSb (sample B-1).

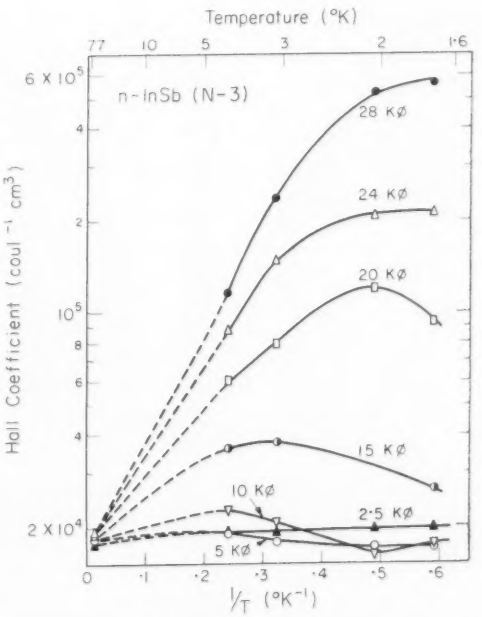

FIG. 3. Hall coefficient at a number of different magnetic field strengths as a function of reciprocal absolute temperature for *n*-type InSb (sample N-3).

* Exploratory measurements on additional samples (from Dr. S. KURNICK of Chicago Midway Laboratories) having excess donor content of somewhat greater than 10^{15} cm^{-3} and total impurity content of about 10^{16} cm^{-3} indicated no freeze-out.

If electrons in the donor levels had zero mobility, the Hall coefficient for a given field would keep increasing as the temperature decreased. Such is not the case, however. Instead, R_H passes through a maximum at some temperature, if the magnetic field is strong enough (see Figs. 1–3), indicating that electrons in localized donor levels have non-zero mobility. The Hall maximum phenomenon has also been observed in studies of impurity banding in germanium.[10] Unlike the case of germanium, however, a sufficiently strong magnetic field is necessary before any maximum appears, and the height of the maximum increases as the field is increased. This latter can be interpreted as due to an increase in the mobility ratio ($b = \mu_c/\mu_i$) with increasing field strength. Now in view of the large magnetoresistance exhibited by n-InSb even when no freeze-out occurs,[1] we expect the conduction electron mobility (μ_c) to decrease as the magnetic field is increased. Hence, for b to increase with field strength, the mobility of electrons in donor levels (μ_i) must decrease more sharply than μ_c does as the field is increased. Such behavior for μ_i has indeed been observed and will be discussed below.

It may be noted in Figs. 1–3 that at the lowest temperatures the Hall coefficient at low magnetic field strengths sometimes falls somewhat below the exhaustion values. This may indicate that a more sophisticated treatment of the Hall coefficient for electrons in the impurity band is needed than is involved in equation (1).

Comparison of Figs. 1–3 shows that sample N-3, which has the largest concentration of excess donors requires a larger magnetic field to initiate freeze-out of electrons than samples O-1 and B-1. In view of the approximate nature of our knowledge of the total donor concentrations in these samples (see Section 4(d)), this observation is not amenable to a clear-cut interpretation. It may indicate that the spacing between excess donors determines how much the electronic wave functions must be shrunk to produce bound levels.

(b) *Donor Ionization Energy and Number of Impurity-Band (Bound) Levels*

The donor ionization energies for three samples were calculated by the method described in Section 2(a). The results are plotted as a function of magnetic field strength in Fig. 4. The limits of error indicated are taken as the spread in the values obtained for the ionization energy at a particular magnetic field strength, using data for different pairs of temperatures.

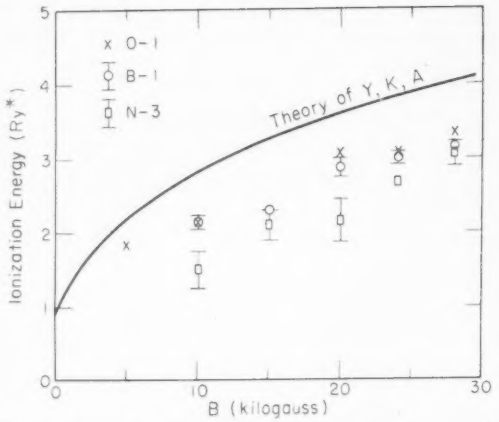

FIG. 4. Donor ionization energy as a function of magnetic field strength. The points were calculated from Hall-effect data on n-InSb samples O-1, B-1, and N-3. The curve is that given by the theory of YAFET *et al.*[6] for an isolated donor.

The ionization energies for samples B-1 and O-1 are equal within the uncertainty of our determinations. The ionization energies for sample N-3 seem to be smaller than for the other two samples, at least at the lower field strengths. However, the difference is not much greater than the uncertainty

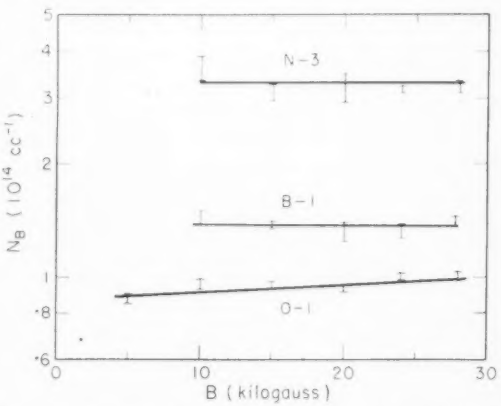

FIG. 5. Number of impurity-band (bound) levels in n-InSb samples O-1, B-1, and N-3 as a function of magnetic field strength. The points were calculated from our Hall data.

VOL. 5 1958

in the energies. If real, it is in accord with the fact that the concentration of excess donors is largest in sample N-3, since this implies the greatest overlap between wave functions centered on adjacent excess donors and hence the smallest ionization energy.

For comparison, the theoretical curve for donor ionization energy given by YAFET *et al.*[5] is also included in Fig. 4. Since their theory is for widely separated donors, it may not be quite applicable to our results. It is interesting to note, however, that the field-dependence we find for the binding energy is similar to that predicted by the theory. Our ionization energies are all about 1 Ry less than the theoretical ones at the same magnetic fields.*

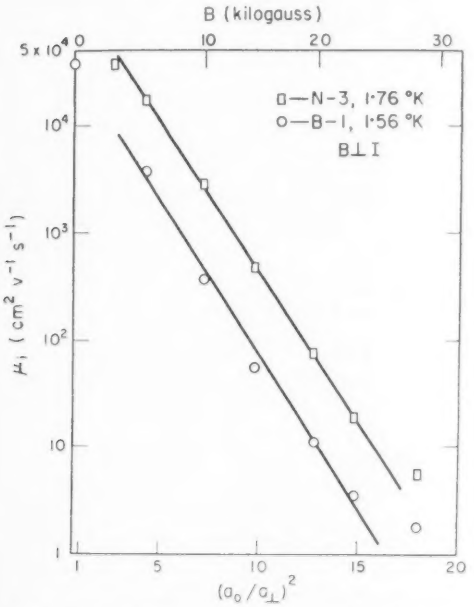

FIG. 6. Effect of a magnetic field transverse to the current direction upon the mobility of electrons in the impurity band in *n*-type InSb samples B-1 and N-3. The logarithm of the mobility is plotted against the square of the reciprocal of the reduced radius of a donor wave function in a direction perpendicular to the magnetic field.

* *Note added in proof:* Our experimental values for the donor binding energy agree with the separation between the theoretical ground state donor level and an excited *p*-like donor level recently obtained theoretically by E. N. ADAMS [private communication] and by H. WALLIS and H. J. BOWLDEN [*J. Phys. Chem. Solids*, to be published].

Fig. 5 shows the number of donor energy levels per cm³ in the impurity band which we obtain for samples B-1, O-1, and N-3 as a function of magnetic field strength. Note that the number of levels per cm³ is independent of field strength, at fields where we can determine this number, at any rate, and is about equal to the concentration of excess donors. This latter fact is *a posteriori* justification of the validity of the method we have used to analyze our Hall data to obtain donor ionization energy. In addition, it may indicate that since the total concentration of ionized impurities always seems to be quite large compared to the concentration of excess donors in all of these samples (see Table 1), only the more widely spaced uncompensated (excess) donor ions provide sites for localization of electrons.

(b) *Impurity-Band Mobility*

The effect of magnetic field strength on the mobility of electrons in the impurity band in

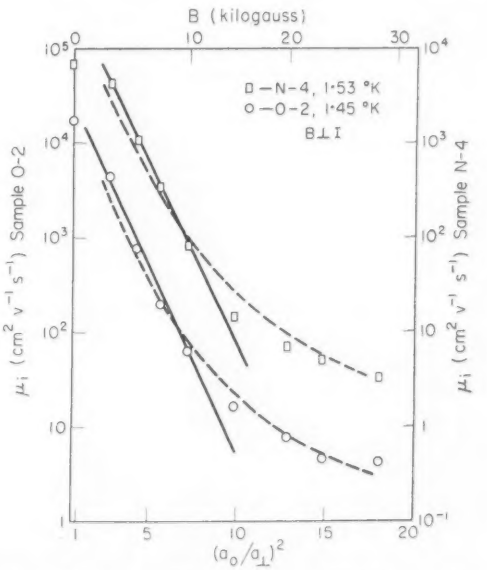

FIG. 7. Effect of a magnetic field transverse to the current direction upon the mobility of electrons in the impurity band in *n*-type InSb, samples N-4 and O-2. The logarithm of the mobility is plotted against the square of the reciprocal of the reduced radius of a donor wave function in a direction perpendicular to the magnetic field. Note that different ordinate scales are used for the two samples. The dashed curves are calculated using equation (9) and made to fit the data near 10,000 G.

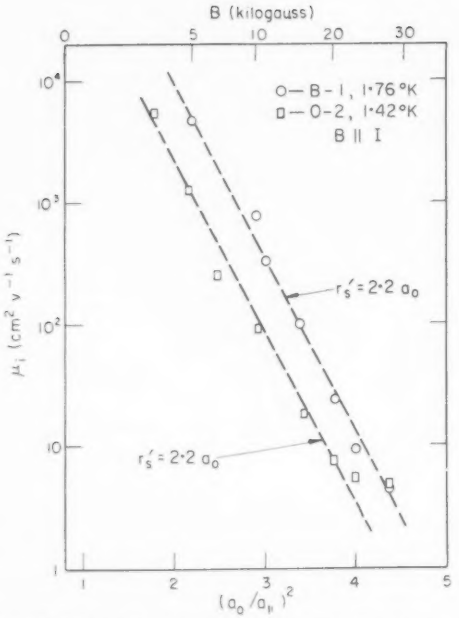

FIG. 8. Effect of a magnetic field parallel to the current direction upon the mobility of electrons in the impurity band in *n*-type InSb, samples B-1 and O-2. The logarithm of the mobility is plotted against the square of the reciprocal of the reduced radius of the donor wave function in a direction parallel to the magnetic field. The dashed curves are calculated using equation (10) and made to fit the data at one field. Under certain conditions r_s' would equal one-half the spacing between donors important for exchange jumping of electrons (see text).

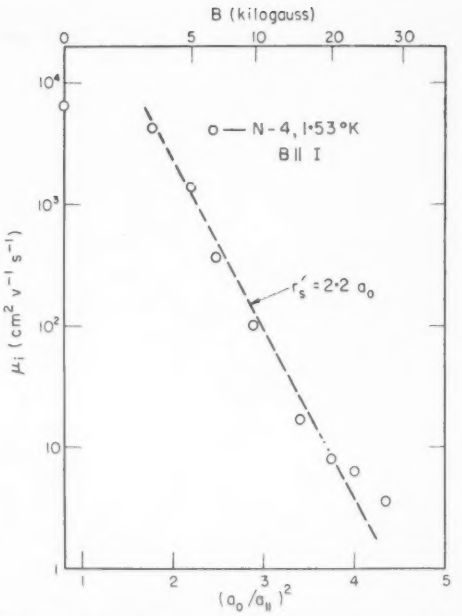

FIG. 9. Effect of a magnetic field parallel to the current direction upon the mobility of electrons in the impurity band in *n*-type InSb, sample N-4. The logarithm of the mobility is plotted against the square of the reciprocal of the reduced radius of the donor wave function in a direction parallel to the magnetic field. The dashed curves are calculated using equation (10) and made to fit the data at one field. Under certain conditions r_s' would equal one-half the spacing between donors important for exchange jumping of electrons (see text).

various *n*-type indium antimonide samples is presented in Figs. 6–9. The magnetic fields used are either perpendicular to, or parallel to, the long sample dimension (and current direction), as indicated in the figures. In each case the logarithm of the mobility, obtained from resistivity data by using equation (6), is plotted against the inverse square of the appropriate radius of the donor wave function taken from the theory of YAFET *et al.*[5] Theory suggests the use of such a plot. The actual magnetic field strengths used are also indicated in these figures.

We were not able to determine the temperature-dependence of μ_i because of the limited temperature range experimentally available, in which most conduction seems to be due to electrons in the impurity band. However our results indicate that μ_i is not strongly temperature-dependent.

To interpret the impurity-band mobility, we consider a conduction mechanism which consists essentially of quantum-mechanical resonance jumps by electrons between donor ions, with the net jumping being non-zero along the direction of the applied electric field due to the presence of this field. The mobility is taken to be proportional to a diffusion constant which is given by the product of the jump frequency times the square of the component of the jump distance along the electric field direction integrated over all possible angles between the jump direction and the electric field direction.

In order to obtain the jump frequency, we calculate the exchange integral, K, since for large enough donor separation $\nu_{\text{jump}} = 2K/h$. According to the theory of YAFET *et al.*,[5] in the presence of a strong magnetic field in the z direction, an

electron wave function centered on a donor at x_D, y_D, z_D has the form

$$\psi(x_D, y_D, z_D) = [(2\pi)^{\frac{3}{2}} a_\perp^2 a_\parallel]^{-\frac{1}{2}} \times \times \exp[-\{(x-x_D)^2+(y-y_D)^2\}/4a_\perp^2 - -(z-z_D)^2/4a_\parallel^2]. \quad (7)$$

Using this wave function for donors at x_0, y_0, z_0 and $-x_0, -y_0, -z_0$, the exchange integral, K, is given by

$$K = \exp\left[-\frac{1}{8}R^2\left(\frac{\sin^2\theta}{a_\perp^2}+\frac{\cos^2\theta}{a_\parallel^2}\right)\right] \int_{\substack{\text{electron}\\ \text{coördinates}}} \psi^2(0,0,0)\frac{e^2}{\sqrt{(x+x_0)^2+(y+y_0)^2+(z+z_0)^2}}\,dxdydz \quad (8)$$

where outside the integral x_0, y_0, z_0 have been expressed in polar coördinates with z_0 being the polar axis, e.g. $x_0 = \frac{1}{2}R\sin\theta\cos\phi$, and R is the separation between the donors. If, inside the integral, we let $a_\perp = a = a_\parallel$ and $y_0 = 0 = z_0$, then for $R > 2a$, the integral in equation (8) is almost independent of a and in fact is within 30 per cent of the asymptotic value, $2e^2/R$, which it approaches at very large R. Hence the field-dependence of the exchange integral in this case is contained in the exponential factor before the integral in equation (8).

Using the exchange integral obtained from equation (8) in the limit of large R, we obtain for the diffusion constants

$$D_{\text{trans}} = \frac{4\pi e^2}{h}R\left\{\left(1+\frac{1}{2A}\right)\exp(-R^2/8a_\perp^2)\times \times \int_0^1 \exp(A\gamma^2)\,d\gamma - \frac{1}{2A}\exp(-R^2/8a_\parallel^2)\right\} \quad (9)$$

when the magnetic field is perpendicular to the applied electric field, and

$$D_{\text{long}} = \frac{32\pi e^2}{hR}\frac{1}{1/a_\perp^2-1/a_\parallel^2}\times \times \left\{\exp(-R^2/8a_\parallel^2) - -\exp(-R^2/8a_\perp^2)\int_0^1 \exp(A\gamma^2)\,d\gamma\right\} \quad (10)$$

when the magnetic field is parallel to the applied electric field. In both equations (9) and (10), the quantity $A = \frac{1}{8}R^2(1/a_\perp^2 - 1/a_\parallel^2)$.

In order to determine the field-dependence predicted by equation (9) for the mobility in a transverse magnetic field, we insert trial values of R into equation (9). Upon doing so we find that for values of R important for explaining our measured mobilities, equation (9) predicts that at low enough field strengths μ_i^{trans} varies essentially like $\exp(-R^2/8a_\perp^2)$. However, at higher fields it predicts that μ_i^{trans} decreases less strongly than $\exp(-R^2/8a_\perp^2)$, the departure from this exponential being greatest for large R and highest fields.

Looking now at Figs. 6 and 7, we see that the transverse field mobility data do follow these predictions, at least qualitatively, the slopes of the straight lines drawn through the data, and hence the values of R, being greater in samples O-2 and N-4 than in samples B-1 and N-3.

To test just how well the observed field-dependence of the mobility can be fitted by using equation (9) when the data depart from a simple exponential behavior, we have included the dashed curves in Fig. 7. These dashed curves are calculated from equation (9), using the values of R obtained from the slopes of the straight lines drawn through the data points as discussed in the next paragraph, and are made to agree with the observed mobilities near 10,000 G.

When the observed impurity-band mobility, in the presence of a transverse magnetic field, is simply proportional to $\exp(-\text{constant}/a_\perp^2)$, we identify the constant with $\frac{1}{2}r_s^2$, where r_s is equal to one-half the donor spacing, R. The value of this constant for each sample is obtained from the slope of the pertinent straight line in Figs. 6 and 7, and the values of r_s are tabulated in Table 1. By assuming that donors important for the electron-jump process are uniformly distributed, each occupying a spherical volume equal to $(4\pi/3)r_s^3$, we can calculate a donor concentration, N_D, for each sample. These values of N_D are given in Table 1.

From Table 1 it can be seen that the value of N_D for a given sample is always greater than the exhaustion electron concentration, n_0 (and thus the concentration of excess donors) and is less than the total concentration of ionized impurities, N_I. For all samples, N_D is between about one-sixth and one-third the total concentration of ionized impurities. Thus the values we obtain for N_D from the dependence of the impurity-band mobility upon transverse magnetic field strength are quite reasonable. (See Section 4(d) for a further discussion of the various impurity concentrations.)

Leaving now the field-dependence of the impurity-band mobility, we should like to consider the magnitude of this mobility in the presence of a transverse magnetic field. In order to calculate its magnitude, we need to relate the mobility to the diffusion constant given by equation (9). Employing the Einstein relation

$$\mu = \frac{eD}{kT}, \tag{11}$$

where the symbols have their usual meanings, we obtain values for μ_i which are about a factor of ten higher than the corresponding measured mobilities. This may be a consequence of the fact that equation (11) is for non-interacting particles in a Boltzmann distribution. In our samples the occupation of the bound donor levels due to excess donors is almost complete, thus electrons occupy these levels in accordance with equation (4). If we use the distribution given by equation (4), thus permitting electron jumps only to empty bound donor levels, in the exact form of the Einstein relation for a system of interacting particles, i.e. $\mu = eD/(d\zeta/d\log n)$,[11] we obtain

$$\mu_i = \frac{eD}{kT}\cdot\frac{1}{2}\exp\{(\epsilon_B-\zeta)/kT\}. \tag{12}$$

This expression yields values for μ_i which agree in order of magnitude with measured mobilities at low magnetic field strengths. However, at high field strengths it yields values of μ_i which are as much as an order of magnitude smaller than the mobilities measured at these fields. These discrepancies may indicate that some of the compensated donors provide sites for electrons to jump into. These extra sites are of importance only at the highest fields, where the occupation of bound levels is most complete.

Since the magnitudes predicted for the mobility by equations (11) and (12) seem to bracket the observed values, we believe that a satisfactory explanation of the magnitudes of the measured mobilities requires taking into account both the unavailability of neutral donors as jump sites and the presence of compensated donors, the role played by the latter being complicated by the presence of compensated acceptors.

Turning now to the case of a longitudinal magnetic field, we find that, upon inserting various values of R in equation (10), both the factor in braces and the $1/a_\perp{}^2-1/a_\parallel{}^2$ factor contribute to the field-dependence of D_{long}, the relative contributions depending on the particular value of R. For $R \approx 2a_0$ most of the field-dependence of D_{long} is contained in the $1/a_\perp{}^2-1/a_\parallel{}^2$ factor, but for somewhat larger values of R the field-dependence of D_{long} is sensitive to the value of R. If R is large enough,

$$D_{\text{long}} \sim [1/a_\perp{}^2-1/a_\parallel{}^2]^{-1}\exp(-R^2/8a_\parallel{}^2).$$

Now for each of our samples the value of R seems to be intermediate between the extremes mentioned above (as indicated by the values of R which fit the dependence of the mobility upon transverse magnetic field strength). Thus, in each of our samples, the variation of the mobility with longitudinal magnetic field strength should depend on the value of R characteristic of the sample and in fact at high field strengths should become proportional to $[1/a_\perp{}^2-1/a_\parallel{}^2]^{-1}\exp(-R^2/8a_\parallel{}^2)$ according to equation (10).

Looking now at the data for a longitudinal magnetic field (see Figs. 8 and 9), we see that the mobility is almost as strongly dependent on field strength as when a transverse field is present. The presence of the $[1/a_\perp{}^2-1/a_\parallel{}^2]^{-1}$ factor in equation (10) does account for part of this strong dependence on field strength when we use the same value for R as in the transverse-field case.

However, if we try to fit the shape of the (longitudinal field) mobility data accurately by calculating curves, using equation (10) and making them agree in magnitude with the data at one field (see Figs. 8 and 9), we find that equation (10) cannot reproduce the tailing off of the observed mobilities at high fields. In addition, a larger value

of $R(=2r_s')$ is needed to fit the overall field-dependence of the mobility than was needed in the case of a transverse field. The quantity r_s' seems to be the same for all samples, i.e. $r_s' = 2{\cdot}2\ a_0$. Since such a large value of r_s' would yield a value for N_D less than the concentration of excess donors, we reject it as unrealistic. Furthermore the observed field-dependence of the mobility in a longitudinal magnetic field also fits the function $\exp(-r_s^2/2a_\perp^2)$ with r_s very close to that obtained from the mobility when a transverse magnetic field is present (see Fig. 10).

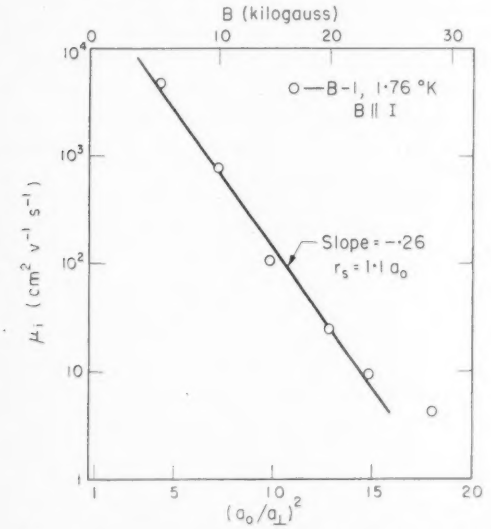

FIG. 10. Logarithm of the mobility of electrons in the impurity band in *n*-type InSb, sample B-1, in the presence of a *longitudinal* magnetic field plotted against the reciprocal squared of the reduced radius of a donor wave function in a direction *perpendicular* to the magnetic field. Under certain conditions r_s is equal to one-half the spacing between donors important for exchange jumping of electrons (see text).

The above difficulties in interpreting the impurity-band mobility in the case of a longitudinal magnetic field may arise because representing the wave function of a bound state around a donor as a gaussian in the direction parallel to the magnetic field is not adequate for treating the longitudinal-field-mobility results,[12] although such a form is adequate for a variational calculation of donor ionization energy.[5]

We have used a gaussian form for the donor wave function in the direction parallel to the magnetic field because it allows the exchange integral to be calculated in a straightforward manner. In addition, it yields a more reasonable interpretation of the mobility than another tractable wave function, namely an exponential of the first power of $R/a_\parallel$.

In ending the discussion of the impurity-band mobility, we should like to point out that thus far we have neglected another factor which should influence the mobility (when either a transverse or a longitudinal magnetic field is present). This factor is the non-uniform spacing between donors due to the latter not being distributed uniformly in the crystal. Rough estimates we have made indicate that the effect of such non-uniformity would be to reduce the overall field-dependence of μ_i. These estimates also indicate that μ_i should be most field-dependent at highest fields. Thus we do not believe non-uniform donor spacing is the reason for the deviations in observed mobilities from that expected on the basis of the simple conduction model we have used.

(d) *Impurity Concentrations*

We should like to review in this section just what information we have about the concentrations and types of impurities present in our samples and how this information was obtained. Consideration of the latter allows assessment of the degree of accuracy of this information.

First of all, the sign of the Hall coefficient and high mobilities of charge carriers at 77°K indicate that our samples are *n*-type, i.e. there is an excess in the concentration of donors over that of acceptors. This excess-donor concentration is directly determinable from the Hall coefficient when all electrons from excess donors are in the conduction band (exhaustion) and there are no intrinsic carriers. We have used Hall measurements at 77°K at fields sufficiently large so that the Hall coefficient is independent of field strength in order to determine the exhaustion electron concentration, n_0, and thus the excess-donor concentration. Values which we obtain for n_0 (listed in Table 1) are about as accurate as our Hall measurements (provided, of course, that the conduction band is spherical, as has been reported).[2]

Since ionized impurity scattering seems to be the important scattering mechanism in *n*-InSb at low temperatures,[13] we have attempted to estimate total impurity concentration, N_I, from the

conduction-electron mobility at such temperatures. Unfortunately, the relationship between N_I and the mobility given by theory is simple and unambiguous only when the Born approximation is valid.* In addition, the theory applies only if the impurities scatter independently, and this may not be the case in our samples because the wavelengths of conduction electrons are comparable to the spacing between impurities. Nevertheless, we shall use a theoretical Born approximation formula for the mobility because such a formula does yield correct values for N_I† in uncompensated samples of n-type InAs in which the electron wavelengths are comparable to impurity spacing.[15]

Since the range of the scattering potential of an individual ion is also involved in the theoretical formulae for the mobility, we need to know it in order to be able to determine N_I. Fortunately, the mobility is much less sensitive to this range than it is to N_I. This range has been taken by some authors[16] to be just half the mean distance between impurity ions. However, theoretical calculations have also been made in which the screening effect of conduction-band electrons determines the range of the potential.[17,19] When only donor impurities are present, and they are all ionized, both the above methods of estimating the range of potential yield the same results. However, this may not be the case when there are appreciably more scattering ions than electrons, for example, when the acceptor concentration is not small compared to the donor concentration. SCLAR[18] points out that the range of the potential should be taken as the smaller of the two values obtained from the mean impurity spacing and the screening length due to the electron cloud.

When we apply this prescription to our samples, we obtain values for N_I from the mobility of conduction-band electrons at 77 and 1·5°K which agree very well (within about 30 per cent for all but one sample). This is satisfying, since at 77°K the screening length is much larger than one-half the mean impurity spacing, whereas at 1·5°K the two are comparable. Thus we were encouraged to obtain estimates of N_I from the conduction-band mobility.

The values of N_I listed in Table 1 were obtained by using as the mobility the product of the conductivity measured at 1·5°K in zero applied magnetic field and the exhaustion Hall coefficient (determined at 77°K). The particular theoretical formula for the mobility which we used was that appropriate to a degenerate electron distribution (in the conduction band) as given by DINGLE.[19] In view of the above discussion, the values thus obtained for N_I should not be in error by as much as an order of magnitude. It is interesting to note that the value we obtain for N_I in a given sample is always greater than our estimates of N_D and n_0 in that sample, as we would expect if all these quantities were known accurately.

The other impurity concentration involved in this work is the quantity N_D, estimated from the dependence of the impurity-band mobility on transverse magnetic field strength. According to our interpretation of this impurity-band mobility, N_D should be the concentration of donors involved in the electron-jump process. In the case of no compensation, N_D would presumably be the total ionized donor concentration and be equal to both n_0 and N_I. Since we find N_I always appreciably greater than n_0 (or the excess donor concentration), the question arises as to just what effect acceptor ions have on the jump process. It is reassuring that (in a transverse magnetic field at any rate) N_D turns out to be between the excess-donor concentration ($= n_0$) and the total concentration of donors given by $\frac{1}{2}(N_I+n_0)$; see Table 1.

(e) *Non-ohmic Behavior*

Experimental confirmation of the model used in interpreting our Hall data above is provided by measurements of the Hall coefficient at a fixed low temperature and high magnetic field as a function of electric field strength. Representative Hall-coefficient data are presented in Figs. 11 and 12. At fields $\gtrsim 0{\cdot}5$ V/cm, R_H decreases as the electric field is increased until it reaches its exhaustion value. Further increases in electric field strength cause no further change in R_H. Such behavior is readily interpreted in terms of the above model as follows.

* Recent discussions of ionized impurity scattering, which also review previous work, have been given by BLATT[14] and SCLAR.[18]

† By correct N_I values we mean that for a given sample the value of N_I determined from the mobility agreed with the concentration of extrinsic electrons, and thus the concentration of donor ions, obtained from the Hall coefficient.

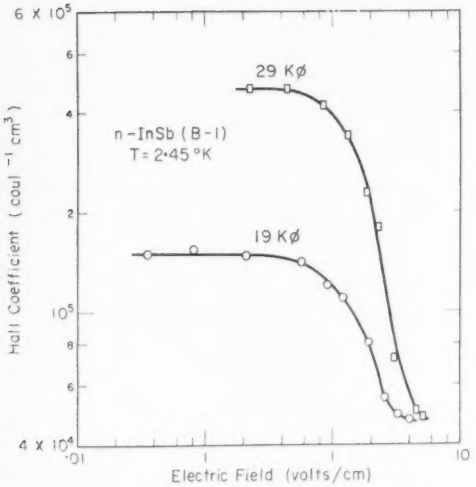

FIG. 11. The Hall coefficient as a function of electric field strength for *n*-type InSb, sample B-1, at two different magnetic field strengths.

Electrons which had fallen into localized donor levels in the presence of the magnetic field are freed from the donor ions by conduction-band electrons which have been accelerated sufficiently by the electric field to cause impact ionization of the donors similar to that occurring in germanium.[20] When all electrons have been raised from the impurity-band levels into the conduction band, the Hall coefficient becomes saturated. That energetic or "hot" electrons are available is indicated by the fact that the electrical conductivity starts to increase with electric field before R_H begins to decrease (see Fig. 12), and field-enhanced mobility for "hot" conduction-band electrons is to be expected when scattering by ionized impurities is dominant.[21]

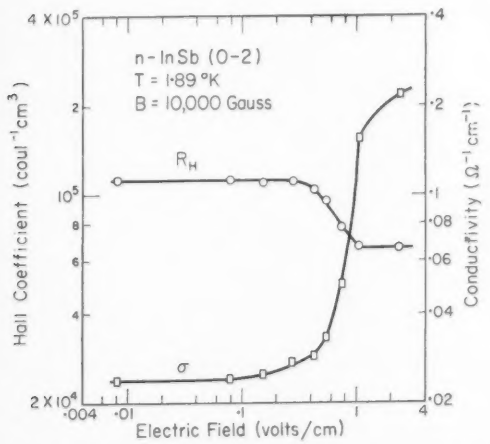

FIG. 12. The Hall coefficient and electrical conductivity as a function of electric field strength for *n*-type InSb, sample O-2.

There is no theory available for deducing the donor ionization energy from the electric field strengths required to cause the above effects. However, our results are in qualitative agreement with what is known about the dependence of donor ionization energy and electron mobilities upon magnetic field strength. For example, it can be seen in Figs. 11 and 12 that the Hall coefficient saturates sooner, the smaller the magnetic field. This is to be expected, since donor ionization energy decreases and conduction-electron mobility increases with a decrease in magnetic field strength.

One might expect R_H to begin decreasing at lower electric field strengths for successively weaker magnetic fields. Our measurements indicate no appreciable dependence of the onset of the decrease in R_H upon magnetic field strength, at least between 10,000 and 29,000 G. However, this onset is so gradual that it is difficult to define.

The complication introduced by the non-zero mobility of electrons in donor levels prevents quantitative analysis of the Hall-coefficient and conductivity versus electric-field data over most of the range of electric fields in the non-ohmic range on the basis of present data.

5. CONCLUSIONS

A unique opportunity for investigating impurity banding occurs in *n*-type indium antimonide. Both the position of the impurity-band levels and the mobility of electrons in these levels can be studied for varying amounts of overlap between donor wave functions in one and the same sample, since this overlap depends on the strength and direction of the applied magnetic field.

Acknowledgements.—It is a pleasure to acknowledge the cooperation and advice afforded by my colleagues at this laboratory and elsewhere. Particular gratitude is due to R. W. KEYES for many stimulating discussions and ideas; to A. C. BEER, of the Batelle Memorial Institute, H. P. R. FREDERIKSE, of the National Bureau of Standards, and

O. LINDBERG of Westinghouse Materials Engineering, for sample material; to R. BOWERS for the loan of the Dewar flask; and to E. N. ADAMS for helpful criticism of the manuscript.

REFERENCES

1. KEYES R. W. and SLADEK R. J. *J. Phys. Chem. Solids* **1,** 143 (1956).
2. FREDERIKSE H. P. R. and HOSLER W. R. *Bull. Amer. Phys. Soc.* **1,** 298, U2 (1956).
3. DRESSELHAUS G., KIP A. F., KITTEL C. and WAGONER G. *Phys. Rev.* **98,** 556 (1955).
4. ADAMS E. N. Private communication.
5. YAFET Y., KEYES R. W. and ADAMS E. N. *J. Phys. Chem. Solids* **1,**, 137 (1956).
6. HUNG C. S. *Phys. Rev.* **79,** 727 (1950).
7. CONWELL E. M. *Phys. Rev.* **103,** 51 (1956).
8. MCDOUGALL J. and STONER E. C. *Phil. Trans.* **A237,** 67 (1938).
   BEER A. C., CHASE M. N. and CHOQUARD P. F. *Helv. Phys. Acta* **28,** 529 (1955).
9. HENRY W. E. and DOLECEK R. L. *Rev. Sci. Instrum.* **21,** 496 (1950).
10. See, for example, FRITZSCHE H. *Phys. Rev.* **99,** 406 (1955).
11. KUBO R. *J. Phys. Soc. Japan* **12,** 570 (1957). A less general derivation is also given by ALLEN J. W. and MACKINTOSH I. M. *J. Electronics* **1,** 138 (1955).
12. KEYES R. W. Private communication.
13. SLADEK R. J. *Phys. Rev.* **105,** 460 (1957).
14. BLATT F. *J. Phys. Chem. Solids* **1,** 262 (1957).
15. HARMAN T. C., GOERING H. L. and BEER A. C. *Phys. Rev.* **104,** 1562 (1956).
16. CONWELL E. and WEISSKOPF V. F. *Phys. Rev.* **69,** 258 (1946); **77,** 388 (1950).
    JOHNSON V. A. and LARK-HOROVITZ K. *Phys. Rev.* **71,** 374 (1947).
17. HERRING C. Unpublished results.
    BROOKS H. *Advances in Electronics and Electron Physics* Vol. 7. Academic Press, Inc., New York (1956).
18. SCLAR N. *Phys. Rev.* **104,** 1548 (1956).
19. DINGLE R. B. *Phil. Mag.* **46,** 831 (1955).
20. See, for example, SCLAR N. and BURSTEIN E. *J. Phys. Chem. Solids*, **2,** 1 (1957).
21. CONWELL E. M. *Phys. Rev.* **90,** 769 (1953).

VOL.
5
1958

J. Phys. Chem. Solids Pergamon Press 1958. Vol. 5. pp. 171–179.

MEASUREMENT OF SURFACE RECOMBINATION VELOCITY IN SILICON BY STEADY-STATE PHOTOCONDUCTANCE*

H. M. BATH and M. CUTLER

Semiconductor Laboratory, Hughes Products, Los Angeles, Calif.

(*Received* 8 *April* 1957; *revised* 16 *September* 1957)

Abstract—A method of minority-carrier lifetime measurement is presented which uses the steady-state enhancement of conductivity produced by optical excitation. The illumination may be of two types, bulk-generating and surface-generating, which produce excess minority-carrier distributions dependent primarily on the bulk and surface properties, respectively, of the sample filament. In applying the method to silicon, it was found that the surface velocity behaves in a manner different from that of germanium. The value of s is dependent on the concentration of added minority carriers, even though the fractional change in conductivity is small. In the sample studied, the surface velocity had the form $s = kC$ for values of C larger than approximately 10^{11} cm^{-3}, where C is the concentration of added minority carriers near the surface.

1. INTRODUCTION

STEADY-STATE photoconductance (SSP) has long been known and used as a means for studying recombination rates. Recently, there has been renewed emphasis on the study of surface recombination velocity from the standpoint of information pertinent both to device fabrication and theoretical understanding of the surface barrier. The purpose of this paper is to present some further refinements of the SSP method which are aimed particularly at the study of the surface recombination velocity. The method has been used, in particular, in a study of surface recombination in silicon, where a non-linear recombination behavior has been observed and measured.

We shall first present the theory of the measurement in some detail, and then outline the nature of our experimental apparatus and the measures used to check the validity of the theory. The final sections will be devoted to the results of the application of the method to the study of surface recombination velocity on silicon, which we find to be qualitatively different from that observed on germanium.

2. THEORY

WHEN a filament of semiconductor is exposed to illumination, additional hole–electron pairs will be created and the conductivity will be increased above that at equilibrium. If, through a filament of rectangular cross-section, a current is maintained constant by a large series resistor, the potential drop across the filament will vary between light and dark conditions. It is easy to show that for small changes in sample conductivity

$$\Delta V = i\rho^2 dA^{-1} e\mu_p (b+1)\bar{p} = i\Delta R_s, \qquad (1)$$

where ΔV is the change in potential drop between illuminated and non-illuminated conditions, i is the (constant) sample current, ρ the resistivity, d the length of the illuminated portion of the sample, A the cross-sectional area of the filament ($= t \times w$), e the electronic charge, μ_p the hole mobility, b the ratio of electron to hole mobility, R_s the resistance of sample, and $\bar{p}$ the excess minority-carrier

* The contents of this paper are based on material presented originally at the November, 1955, meeting of the American Physical Society in Chicago, Ill. The section concerning the surface velocity on silicon was first presented at the May, 1956, meeting of the Electrochemical Society, in San Francisco.

concentration in the illuminated portion averaged over the thickness of the sample:

$$\bar{p} = t^{-1} \int_0^t p(x)\, dx. \tag{2}$$

Thus the problem of calculating ΔV is the problem of finding $\bar{p}$, which will depend ultimately on the bulk and surface lifetime parameters of the filament, the geometry, and the character of the illumination. One may calculate $\bar{p}$ by solving the steady-state diffusion equation under the customary boundary conditions for recombination at the surface.[1] As outlined in the Appendix, the equation is solved separately for each wavelength, λ, of incident radiation with its particular intensity, $\mathcal{I}_\lambda$, and absorption constant in the semiconductor. Finally, the separate solutions are summed over all wavelengths. The general solution may be written in the form

$$\bar{p} = \Sigma_\lambda \mathcal{I}_\lambda F(\lambda, r, k), \tag{3}$$

where F is a function which depends on λ, the particular wavelength of incident light, and r and k, which are dimensionless parameters that depend on the electrical and geometrical properties of the sample:

$$r = t/L, \quad k = sL/D, \quad L^2 = D\tau \tag{4}$$

D is the diffusion constant for the minority carrier, and τ the bulk lifetime of minority carriers.

The expression for F is complicated for an arbitrary spectral distribution of λ, but considerable simplification occurs in two extremes: where the incident light is absorbed entirely at the surface of the sample, or where the light is absorbed uniformly throughout the thickness of the sample. If the incident light is composed entirely of wavelengths which satisfy one of these two conditions, the dependence of F on λ can be factored out, giving

$$\bar{p}_A = \mathcal{I}_A \tau f_A(r, k) \tag{5}$$

$$\bar{p}_B = \mathcal{I}_B \tau f_B(r, k). \tag{6}$$

The subscript A refers to the non-penetrating or surface-generating light, and B to the penetrating or bulk-generating radiation. $\mathcal{I}_A$ and $\mathcal{I}_B$ are the total effective non-penetrating and penetrating, respectively, light intensities. It may be necessary, in some cases, to correct the incident light intensities for varying amounts of reflection at the sample surface. We discuss the forms of f_A and f_B in the Appendix. Equation (1) may be combined with (5) or (6) to yield

$$\Delta V_v = i\rho^2 d A^{-1} e \mu_p (b+1) \mathcal{I}_v \tau f_v(r, k) \tag{7}$$

where the subscript v refers to either case A or B.

f_A and f_B can themselves be simplified if their arguments, r and k, become large or small with respect to unity. If, for example, $k \gg 1$, f_A will approach the form $f_A(r, k) = 1/k \sim 1/s$. Simplified forms for f_A and f_B are given in Tables 1 and 2. For a particular experimental problem, it will usually be possible to obtain the desired information quite directly. A judicious choice of illumination and sample geometry may permit a form of $f_v(r, k)$ from which the value of the unknown parameter can be calculated with a minimum of difficulty.

3. EXPERIMENTAL

(a) *Apparatus*

The steady-state quantity ΔV may be measured quite simply by chopping the light and using a.c.

Table 1. *Limiting values of* $tf_A(r, k)$ *for extreme values of* r *and* k

	$k \gg 1$	any k	$k \ll 1$
$r \gg 1$	$1/k$	$1/(1+k)$	1
any r	$\dfrac{\cosh r - 1}{k \sinh r}$	$\dfrac{\sinh r + k(\cosh r - 1)}{(1+k^2)\sinh r + 2k \cosh r}$	$\dfrac{\sinh r + k(\cosh r - 1)}{\sinh r + 2k \cosh r}$
$r \ll 1$	$r/2k$	$r/(r+2k)$	$r/(r+2k)$

VOL. 5 1958

Table 2. Limiting values of $f_B(r, k)$ for extreme values of r and k

	$k \gg 1$	any k	$k \ll 1$
$r \gg 1$	$1 - \frac{2}{r} \cdot \frac{k}{k+1}$	$1 - \frac{2}{r}\left[\frac{k}{k+1} + \left(\frac{k}{k+1}\right)^2 e^{-r}\right]$	$1 - \frac{2k}{r}$
any r	$1 - \frac{2}{r} \cdot \frac{\sinh r + k(\cosh r - 1)}{k \sinh r + 2k \cosh r}$	$1 - \frac{2k}{r} \cdot \frac{\sinh r + k(\cosh r - 1)}{(1+k^2)\sinh r + 2k \cosh r}$	$1 - \frac{2k}{r} \cdot \frac{\sinh r + k(\cosh r - 1)}{\sinh r + 2k \cosh r}$
$r \ll 1$	$\frac{r}{k(kr+2)}$	$\frac{r}{r(k^2+1)+2k}$	$\frac{r}{r+2k}$

techniques of amplification. Because one is interested only in the amplitude of ΔV and not its transient when the light intensity is changed, narrow-band techniques may be used to secure increased gain and improved signal-to-noise ratio. The chopping rate (240 c/s in our equipment) must be low enough to assure that steady-state conditions are in effect during the major portion of either half-cycle.

We have used filters to secure illumination of the two suitable types. Wavelengths which will generate carriers only at the surface of germanium will result if the white light from an incandescent source is passed through a few centimeters of water. Such a filter will effectively remove wavelengths longer than $1{\cdot}3\mu$.[2] For silicon, with its larger energy gap, a cupric salt may be added to the water, reducing the cut-off wavelength to $0{\cdot}8\mu$.[3] Penetrating light, on the other hand, will result from passing the white light through a filter made of the same semiconductor as the one under examination. If the filter is several times as thick as the experimental filament, it will at the same time absorb those wavelengths which would be attenuated appreciably as they pass through the filament, and transmit enough penetrating radiation to cause appreciable excitation of carriers. The greater the ratio of filter thickness to sample thickness, the more uniformly will the carriers be generated throughout the thickness of the sample. On the other hand, the number of photons incident on the sample which will be capable of creating a hole–electron pair will also be smaller, resulting in less sensitivity. Our filters have been $0{\cdot}4$ cm thick, with both surfaces optically polished to minimize scattering.

In a decay-type measurement, one measures the lifetime directly, by determining a decay time in a transient situation. Here, on the other hand, the quantity measured—ΔV_v in equation (7)—depends not only on τ, but on the light intensity and other factors. For this reason, one must obtain a calibration of the light intensity. The simplest procedure is to compare the values of ΔV_v from two samples, one of which is a standard that has completely known characteristics, and the other is the sample under investigation. The expression for ΔV given in equation (7) may be said to consist of three types of factors: $i\rho^2 de\mu_p(b+1)/A$, which can be computed readily from the known bulk properties; $\mathcal{I}_v$, which is unknown, but a constant of the system; and $\tau f_v(r, k)$ which is known for the standard and unknown in whole or in part for the sample under investigation. When we solve for $\tau f_v(r, k)$ of the unknown sample in terms of the known, the factor $\mathcal{I}_v$ will cancel, and therefore need not be known explicitly. Furthermore, if ΔV_v is known not in volts, but in terms of some arbitrary unit, the proportionality factor between volts and these units will also cancel.

In some cases, however, this calibration procedure is inadequate. For example, the determination of C, the surface concentration, requires that $\mathcal{I}_v$ be known in absolute value (photons $\text{cm}^{-2}\ \text{sec}^{-1}$). As will be shown in Section 5, s may be dependent on the value of C, and hence on the light intensity. Under these circumstances, the value of f_v which describes a standard will vary

with $\mathcal{J}_v$; any calibration procedure which depends on knowing the value of s will be invalid. This difficulty is most important in calibrating non-penetrating light. If, however, a grown p–n junction bar is illuminated with a line of light parallel to the back-biased junction and narrow with respect to the diffusion distance, a fraction of the pairs generated in the sample will diffuse to the junction and be collected. One may thus use the calculations of VAN ROOSBROECK[4] to determine the light intensity from the measured values of the photocurrent and distance between the junction and the illumination. In our experiments, we happened to obtain a sample with an appreciable "channel".[5] In this case, it was possible to collect all of the surface generated carriers and thus obtain a convenient calibration of the light source.

(b) *Confirmation of the Method*

The method used to establish the validity of this method as a whole was to check the theory for both penetrating and non-penetrating light with germanium. HENISCH[6] has described briefly a check of the theory using non-penetrating light only. Germanium was used at this time for, as will be shown later, agreement between theory and experiment will not occur with silicon if one assumes a value of the surface recombination velocity which is independent of light intensity. From equation (7) it is apparent that the quantity $B = e\mu_p(b+1)\mathcal{J}_v$ should be the same when different samples are measured, assuming, of course, that the light intensity remains constant for all these measurements. The theory was regarded as adequately verified and the technique satisfactory when consistent results were obtained from samples with widely varying values of resistivity, lifetime, and geometry. Bulk lifetimes and surface velocities were determined by either the pulse-delay,[7] or optical-decay methods. In Table 3 are given the results of measurements on a typical group of samples. The value of B varies somewhat within the group; however, the variation may be accounted for by experimental errors. A principal source of error is the resistivity: an error of only 5 per cent in the measurement of resistivity will result in a 10 per cent error in the value of B. The samples used were cut from ingots selected for uniformity in their bulk properties—resistivity and bulk lifetime. In all cases the thickness of the samples was much less than the width. This geometry is necessary to satisfy the requirements of the theory, which takes into account recombination only at the illuminated surface and the one opposite. Surfaces were lapped, etched, and rinsed with distilled water. The appearance of the surfaces was uniformly specular. Any possible differences in response due to differing reflectance from sample to sample were disregarded.

4. DISCUSSION

(a) *General*

It might be well to point out briefly the relationship between the method of lifetime measurement which we present here, and other means which are in use.

Table 3. Typical results obtained using germanium

The four samples, all n-type, had similar bulk properties but represent a considerable range in s. Values of $f_A(r, k)$ and $f_B(r, k)$ were calculated from equations (10) and (11), using lifetime parameters s and τ obtained from decay measurements. ΔV was measured in arbitrary units. The average values of B_A and B_B are, respectively, $6{\cdot}86\times10^{-4}$ and $2{\cdot}05\times10^{-3}$. The maximum deviation of any value of B_A or B_B from the average is 23 per cent, which occurred with the value of B_A on sample 1.

Sample	ρ (Ω-cm)	s (cm/sec)	$A = t\times w$ (cm²)	τ (μsec)	r	k	$f_A(r, k)$	$f_B(r, k)$	$\Delta V_A/i$	$\Delta V_B/i$	B_A	B_B
1	5·0	630	$0{\cdot}105\times0{\cdot}424$	290	0·86	1·48	0·22	0·275	181·7	109	$5{\cdot}3\times10^{-4}$	$2{\cdot}4\times10^{-3}$
2	5·0	1330	$0{\cdot}089\times0{\cdot}413$	290	0·73	3·12	0·11	0·15	188	65·6	7·7	2·2
3	5·3	165	$0{\cdot}115\times0{\cdot}421$	360	0·84	0·44	0·47	0·51	628	194	7·4	1·8
4	5·3	140	$0{\cdot}159\times0{\cdot}419$	360	1·16	0·38	0·57	0·62	381	162	7·0	1·7

In both the steady-state photoconductivity (SSP) method and the photomagnetoelectric (PME) and photodiffusion (PD) effects,[8] one creates a steady-state distribution of excess carriers, the magnitude of which depends on the lifetime parameters and the geometry. In the PME and PD effects, one determines this magnitude by measuring a voltage which depends on the difference in the excess-carrier distribution between the two surfaces. Since it is the net gradient which is the cause of the effects, either the excitation or the recombination parameters must be asymmetrical. The SSP method uses the change in conductivity of the sample as a measure of the excess-carrier concentration; the measurement is therefore independent of the existence of a net gradient. It is for this reason that either asymmetrical or symmetrical distributions of added carriers can be used. With excitation from both penetrating and non-penetrating light available, one may emphasize the components of lifetime which depend, respectively on the bulk, and on the surface. In many cases, it may be possible to measure both s and τ on the same sample. At the same time, it is possible to calculate C, the non-equilibrium concentration of minority carriers added at the surface of the sample. (This should also be possible in other steady-state methods.) Measurements of the surface recombination velocity as a function of C are therefore possible.

(b) *Experimental Problems*

To achieve the satisfactory degree of accuracy in the use of the method, which is reflected by the consistency in the value of B, it was necessary to observe several precautions. Large currents passing through the sample can, of course, result in heating effects. Much smaller currents and resultant electric fields along the length of the sample may cause appreciable sweeping of carriers. Since some sweeping must occur, any gradient in the lifetime and resistivity will manifest themselves as a difference in the values of ΔV_v obtained for the two possible directions of i through the sample. By measuring ΔV_v for both current directions, and averaging the two values, one makes a first-order correction to changes in response caused by the sweeping, and furthermore balances out the photovoltages arising from the resistivity gradient.

A lower limit to the amount of light which could be used in the measurements of s versus C described in Section 5 was set by the level of noise present in the filament. Early work on n-type silicon filaments with rhodium-plated end contacts indicated that the contacts, though ohmic, were acting as noise generators which appear in series with the desired signal. The component of the noise at 240 c/s would mask the signal at low light intensities. In order to carry out the measurements over a large range of intensities, it was necessary to make special provision for a low-noise end contact. The method used was a modification of a fusion technique developed for fabrication of silicon transistors. The resulting n–n^+ junctions were ohmic and produced noise voltages lower by an order of magnitude, at constant current, than the previous plated contacts. The technique was not applied to p-type material, on which plated contacts seem more satisfactory.

5. APPLICATION TO SILICON

(a) *Experimental*

It proved impossible to get consistent values of B when SSP was applied to silicon rather than germanium. However, during the course of the work with silicon, it was observed that its behavior was in one respect qualitatively different from that of germanium. The response to non-penetrating radiation was very sensitive to the amount of stray ambient light falling on the sample in addition to the chopped measuring radiation. This suggested the possibility that the surface velocity is affected by the stray light.*

If the measuring illumination is of the penetrating variety, the response should depend weakly on s in a thick sample as compared to a thin one. With non-penetrating light, on the other hand, changes in surface recombination should have a strong effect regardless of thickness. Experimentally, it was found that if, during measurement by means of

* If s is a constant, the diffusion equation governing the carrier distribution is linear. Under these circumstances, non-equilibrium carrier concentrations arising from various means of injection remain independent of one another. Flooding, although it produces a change in the carrier concentration in the sample, cannot change ΔV_v, which is caused by a different source of excitation. In the small signal case, interaction between the flooding and ΔV can occur only through the effect of the former on the value of s.

chopped penetrating radiation, the samples were illuminated by a second unfiltered light source which was not modulated (flooding), the response remained unaffected if the sample was "thick", but would decrease markedly if the sample was "thin". On the other hand, during measurement with non-penetrating radiation, flooding resulted in drastic decreases in response, for both thick and thin samples. These effects were too large to be ascribed to changes in the bulk conductivity caused by the flooding. From these results it was possible to conclude that the flooding was producing a negligible effect in the bulk of the material, but was affecting recombination at the surface. The behavior of these samples was consistent with a model in which the value of the surface recombination velocity increases with additional illumination.

It was possible to perform an experiment which confirmed the hypothesis that the surface recombination velocity changes with illumination. ΔV_A was measured as a function of the intensity of the chopped non-penetrating radiation, in the absence of any flooding. As shown in Fig. 1, it was

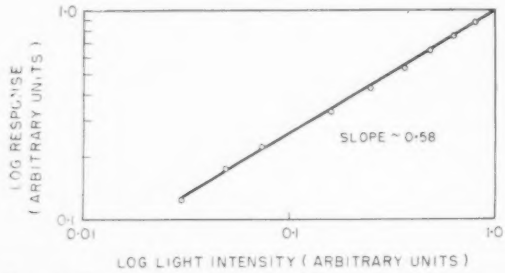

FIG. 1. Typical photoconductive response (ΔV_A) as a function of intensity of non-penetrating light ($\mathcal{J}_A$). The light intensities were such as to produce values of C such that $s \propto C$.

found that ΔV_A, instead of being proportional to the first power of the intensity, was approximately proportional to its square root. From equation (7) it is clear that since $\Delta V_A/\mathcal{J}_A i$ is not a constant, f_A, and hence s, must be changing with light intensity.

Using the procedure described in the Appendix, detailed measurements of s versus C were made on three samples, two n-type and one p-type. The n-type samples were equipped with fused contacts, and all were thin ($\sim$ 0·025 cm) to maximize the useful response. Measurements were carried out at room temperature in laboratory air, after an acid etch. In Fig. 2 we have plotted s against C for one of the n-type samples. For the larger values of C which we were able to produce with the available

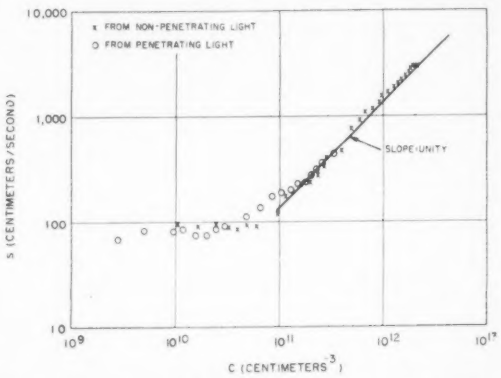

FIG. 2. Surface recombination velocity, s, versus surface minority-carrier concentration, C, for an n-type sample etched 2 days prior to measurement. $\rho = 7{\cdot}1\ \Omega$-cm, $\tau = 130\ \mu$sec. The data for penetrating and non-penetrating light were pieced together as described in the text.

illumination, s was not a constant but was found to be proportional to C; the slope of the log–log plot was 1·0 within the experimental error. At smaller light intensities and correspondingly smaller values of C (less than $\sim 5\times10^{10}$ cm^{-3}), s ceases to be a function of C, but remains constant at a value of about 80 cm/sec. The increasing scatter of points at low values of C is due to deteriorating signal-to-noise ratio with decreasing light intensity. The maximum value of C which could be obtained with this surface and the available light intensity was 2×10^{12}/cm^3, two orders of magnitude less than the majority-carrier concentration as calculated from the resistivity of the bulk material.

The second n-type sample, which was measured using only non-penetrating light, behaved very similarly to the first. The only difference between the two was that the second sample exhibited twice the value of s for a given value of C. The leveling-off of s at low C was again present. This time at a value of $s \sim 150$ cm-sec^{-1}. The p-type sample, shown in Fig. 3, again exhibited the slope of unity, but the plateau in s for low values of C was absent. The measurements were not continued in this case to values of s and C as low as were

possible for the n-type samples, where leveling-off occurred.

The differences among the samples studied may be attributed to some extent to the different intervals between etching and measurement. It was

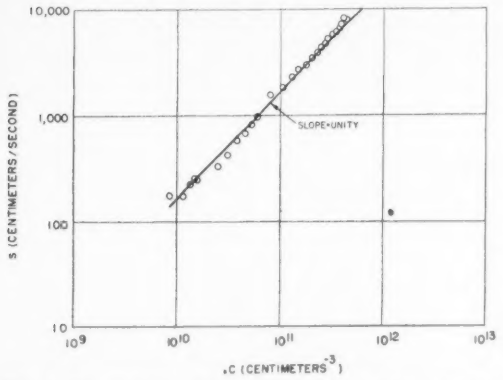

FIG. 3. Curve of s versus C for a 16-Ω-cm p-type sample. $\tau = 60$ μsec. Etching was performed 2 hr prior to measurement.

observed qualitatively that after etching, the surface initially exhibits a rather high value of s, which, with ageing in laboratory air, decreases, passes through a minimum, and increases again after a period of a few days.

(b) *Discussion*

The data obtained from penetrating and non-penetrating light agree very well. It is only in the transition range, between $s = \text{const.}$ and $s \propto C$, that the two curves fail to coincide. Such behavior is to be expected for the following reason. For non-penetrating illumination, recombination will take place primarily at the illuminated surface in the range where s is high; recombination at the back surface will be relatively unimportant. For low C, (C refers to the concentration at the illuminated surface) significant recombination will occur at both the front and back surfaces, and the theory will correctly give the carrier distribution. In the intermediate range, however, the recombination at the back surface is neither insignificant nor equal to that at the front. Being lower than at the front surface, it will tend to cause an excessively low value of s to be computed for the front.

All of the three experimental samples which we studied in detail exhibited similar functional dependences of s on C. These, in themselves, do not represent a large domain of study. However there is, in our experience, reason to believe that the observed dependence of s on C may be a fairly general phenomenon, for we have observed in many other samples that the ΔV_A produced by the non-penetrating radiation is invariably sensitive to the amount of background light present. This behavior is in contrast to that of germanium, which does not show this sensitivity to flooding.

The leveling-off of s at low values of C appears to be a real effect. Such a behavior could have been the result of a small amount of stray light falling on the sample during measurement, which would have set a lower limit on the value of C, and hence of s, which could have been obtained. The measurements made at low values of light intensity were repeated, making certain that only chopped measuring radiation reached the sample. ΔV_A was found to be proportional to the first power of $\mathcal{I}_A$, confirming the constancy of s in this range of C. The penetrating light data also contributes evidence that s becomes constant for small C.

The fact that this similarity in behavior in s is observed for two quite different means of carrier excitation argues strongly against any photochemical reaction taking part in the effect. It is hardly conceivable that measurements of s as a function of C by two modes of excitation as different as penetrating and non-penetrating light should result in such similar results if such a reaction were involved. The agreement between results for the two kinds of light, as well as the flooding experiments, also eliminate the possibility that it is the bulk lifetime and not the surface velocity which varies with excitation.

Some comment seems desirable about the meaning of $s(C)$ for the case of non-penetrating light, where most of the carriers may be generated in the space-charge region. C refers to the concentration of minority carriers in the bulk at the boundary of the space-charge region; this boundary is defined as $x = 0$. However, the solution of the diffusion equations for the case A, where $\alpha^{-1} \ll t$, $\alpha^{-1} \ll D/s$ is equivalent to the case where carriers are being generated at $x = 0^-$. It makes no difference exactly where they are being generated, provided only that the distance from the surface is small compared to t and D/s. One may raise the question whether generation in the space-charge region will

cause an effect peculiarly different from generation in the bulk. Theoretical discussions[8] of steady-state surface recombination show that excess minority carriers cause changes in the surface barrier, and in the concentration (C_s) of the carriers at the surface proper. However, it is always assumed that the quasi-Fermi level is constant throughout the barrier and the region adjacent to it. This is a good approximation as long as s is small compared to the thermal velocity $(kT/2\pi m^*)^{\frac{1}{2}}$. Therefore, the definition of s as the ratio between J and C relates to a set of changes, as the result of $C \neq 0$, in C_s, the surface barrier, the population of surface states and the ensuing recombination current. The fact that carriers are generated in the space-charge region rather than outside of it should cause no difference in the value of C and in the resulting J. The generated carriers in a steady-state situation will distribute themselves in the same manner between the bulk and the surface in either case.

It was only at the higher light intensities that it was possible to observe the waveform of ΔV on the oscilloscope. Within the range in which such examination was possible, there were no evidences of trapping; the waveform was quite accurately a square wave, as would befit a filament of low lifetime being illuminated by light chopped at a slow rate. As the light intensity was decreased, the waveform became obscured by noise long before the response from the tuned amplifier became unusable. Extremely long time-constant traps may have been present, but would have remained filled and ineffective during the measurement. Since the non-linear response was observed in the high excitation range where oscilloscope observations were possible, surface trapping is excluded as an explanation *per se* of the dependence of s on C.

An error in the measurement of the light intensity, or of any other factor in the expression for one of the f_v's would not be expected to have a qualitative effect on the conclusions made here. The measurements with non-penetrating light result in the determination of f_A which, if $k \gg 1$, is inversely proportional to s. Hence an error in f_A would result in only a multiplicative error in s, which would alter neither the slope nor the existence of the plateau in the plot of s against C. For values of k not so extreme, the effect of an incorrect value of $\mathcal{I}_A$, &c., would be more complicated, and the shape of the curve in the transition between high and low values of C might be distorted. For penetrating light, the same considerations hold. In the present measurements, errors in the constants for the standard sample for the determination of $\mathcal{I}_B$ were sufficient to cause an impossible value for f_B. (It led to values of f_B somewhat greater than unity in the low s range.) The value of $\mathcal{I}_B$ was adjusted so that the constant value of s which was obtained at low values of C agreed with that obtained from the non-penetrating light data. When this was done, very good agreement was found over the rest of the curve as shown in Fig. 2.

6. CONCLUSIONS

We have described a means of measuring lifetime by steady-state photoconductance which differs from previous methods in that excitation can be accomplished by penetrating as well as non-penetrating light. By use of penetrating light, the response may be made to depend strongly on the bulk properties and with non-penetrating light, on the surface. The method as a whole is particularly valuable for studying surface recombination velocities, for one may calculate the excess minority-carrier concentrations at the surfaces where recombination is taking place. The ability to calculate C should be valuable in investigations other than of surface velocity, for it is possible to produce known and hence controlled values of C.

The application of this method to silicon indicates that its surface may behave in recombination processes in a manner quite different from that of germanium. The concept of surface recombination velocity as a proportionality "constant" between C and the surface recombination current density, J, should be broadened to allow s to be a variable function of C. Since over a considerable range of C, s is of the form $s = \text{const} \cdot C$, we have $J/q = sC = \text{const} \cdot C^2$. This is a second-order reaction in C. Such an expression could be expected if C were at least of the same order of magnitude as the majority-carrier concentration. But in the present case, C is always at least two orders of magnitude smaller. Our attempts to find a simple model to explain this type of recombination have been unsuccessful.

In addition to the theoretical consequences, the variation of s with C makes meaningless a description of a surface by a single value of s, unless it is

VOL. 5 1958

accompanied by a specification of the value of C at which s was measured. Thus, in an experiment of the decay-type, C and s will be changing in the course of the experiment, and one would expect to observe non-exponential behavior in any decay process in which s enters strongly. In these cases, the decay behavior must be described in terms other than lifetime.

APPENDIX

The problem of finding $\bar{p}$ has been treated by Moss *et al.*[9] in their discussion of the PME effect and, more recently, by DE VORE,[10] and RITTNER.[11] If we let $\alpha =$ the absorption constant for wavelength λ, the light will be surface-generating (case A) if $\alpha^{-1} \ll t$, $\alpha^{-1} \ll D/s$ and bulk generating (case B) if $\alpha^{-1} \gg t$, $\alpha^{-1} \gg D/s$. In these two limits, the expressions for $\bar{p}$ becomes:

$$\bar{p} = \tau f_A(r,k)\mathcal{J}_A \tag{8}$$

$$\bar{p} = \tau f_B(r,k)\mathcal{J}_B \tag{9}$$

$$f_A(r,k) = [\sinh r + k(\cosh r - 1)]/t\Delta \tag{10}$$

$$f_B(r,k) = 1 - 2ktf_A/r \tag{11}$$

$$\Delta = (1+k^2)\sinh r + 2k\cosh r. \tag{12}$$

In Tables 1 and 2 are contained simplified expressions for f_A and f_B which hold if r and or k approach limiting values.

The expressions for $\bar{p}$ are the results of integrating $p(x)$ over the thickness of the sample. If, instead of integrating, we evaluate $p(x)$ at $x = 0$ and $x = t$, we can find the surface carrier concentrations. For case B, $C_B \equiv C_B(0) = C_B(t)$, since the carrier distribution is symmetrical in the mid-plane of the sample. However, $C_A \equiv C_A(0) \neq C_A(t)$, if it is the surface of the sample at $x = 0$ that is illuminated. The expressions for the surface concentrations are as follows:

$$C_A = \mathcal{J}_A \tau f_{AS}(r,k) \tag{13}$$

$$C_B = \mathcal{J}_B \tau f_{BS}(r,k) \tag{14}$$

$$f_{AS}(r,k) = [\cosh r + k\sinh r]/\Delta \tag{15}$$

$$f_{BS}(r,k) = [\sinh r + k(\cosh r - 1)]/\Delta. \tag{16}$$

To measure $s = s(C)$, as was done with silicon, the following procedure was followed. ΔV_A in volts was measured as a function of $\mathcal{J}_A$ in photons cm^{-2} sec^{-1}, using a sample with known r. ($\mathcal{J}_A$ was determined with a p–n junction, since it was assumed that s cannot be determined uniquely on silicon.) Calculate $f_A[r, k(\mathcal{J}_A)]$ from equations (7) and (8), using the known bulk properties of the material. Since the values of r are known for the experimental sample, it will now be possible to calculate the value of $k(\mathcal{J}_A)$ from equation (10), and finally $s(\mathcal{J}_A)$ from equation (4). With both k and r known, one may compute $f_{AS}(r, k)$, and get $C_A(\mathcal{J}_A)$ from equation (13). The procedure is similar for the penetrating light case.

REFERENCES

1. SHOCKLEY W. *Electrons and Holes in Semiconductors* pp. 318 ff. D. Van Nostrand Co., Inc., New York (1950).
2. STRONG J. *Procedures in Experimental Physics* p. 369 Prentice-Hall, Inc., New York (1938).
3. *Ibid*, p. 369 and p. 402.
4. VAN ROOSBROECK W. *J. Appl. Phys.* **26,** 380 (1955).
5. For example BROWN W. L. *Phys. Rev.* **91,** 518 (1953).
6. HENISCH H. K., REYNOLDS W. N. and TIPPLE P. M. *Physica* **20,** 1033 (1954).
7. SPITZER W. G., FIRLE T. W., CUTLER M., SHULMAN R. G. and BECKER M. *J. Appl. Phys.* **26,** 414 (1955).
8. BRATTAIN W. H. and BARDEEN J. *Bell System Tech. J.* **32,** 1 (1955).
9. MOSS T. S., PINCHERLE L. and WOODWARD A. M. *Proc. Phys. Soc.* B **66,** 743 (1953).
10. DE VORE H. B. *Phys. Rev.* **102,** 86 (1956).
11. RITTNER E. S. *Photoconductivity Conference* p. 224 John Wiley and Sons, Inc., New York (1956).

J. Phys. Chem. Solids Pergamon Press 1958. Vol. 5. pp. 180–201.

TYPES OF MAGNETICALLY ORDERED CONFIGURATIONS ON SIMPLE LATTICES

H. A. GERSCH* and W. C. KOEHLER

Oak Ridge National Laboratory, Oak Ridge, Tennessee

(*Received* 17 *May* 1957; *revised* 16 *September* 1957)

Abstract—A scheme for enumerating possible magnetically ordered configurations on simple lattices is described, and a system of nomenclature descriptive of the arrangement is proposed. Examples of the method as applied to simple cubic, face-centered cubic, body-centered cubic, and hexagonal layer lattices are given. Magnetic structure amplitudes for configurations based on the above lattices are tabulated.

VOL. 5 1958

1. INTRODUCTION

In crystals which contain magnetically active ions or atoms, various ordered arrangements of the moments may exist, depending upon the details of the interactions between the spins and upon the space lattice appropriate for the crystal. Ordered configurations corresponding to energy minima under simplifying assumptions concerning the interactions (isotropic with specified interactions between nearest and next-nearest neighbors) have been predicted for a number of simple lattices[1–4] and have been found experimentally by neutron-diffraction experiments. These latter investigations have also uncovered other types of ordered configurations.

At the present time neutron-magnetic scattering data are analyzed to a great extent by trial-and-error methods. It is therefore of some interest to investigate systematically the diffraction effects to be expected from ordered configurations on a number of simple lattices. To this end a consistent scheme for enumerating structure types possible for a given lattice without regard to energy considerations but subject to a geometrical constraint has been developed, and a system of nomenclature, descriptive of the moment arrangement, is proposed.

2. THE CATALOGUING SCHEME

The model on which the cataloguing scheme is based assumes scalar spins so that at each lattice point there is either a "spin up" (+) or a "spin down" (−), and the ordered configurations are obtained by the imposition of an equivalence condition which is defined precisely below. Once a configuration has been found, its energy, in the same approximation as in references (1–4), may readily be computed.

Within the above-mentioned approximation, the Hamiltonian for the spin system may be written in the form

$$\mathscr{H} = \tfrac{1}{2} \sum_{ij} A_{ij} S_i S_j \qquad (1)$$

where A_{ij} represents the interaction between the i-th and the j-th spins, and the double sum is over all spins in the lattice. Usually the A_{ij} are assumed non-zero between nearest and next-nearest neighbors.

The energy of the spin system is a quadratic form in the spin variables S_i, each of which can take on only discrete values which for simplicity are taken as ± 1. Without this restriction to discrete values, the Hamiltonian would be analogous to the potential energy of a crystal lattice expanded about its energy minimum. (Then S_i would refer to the continuous displacement of the i-th atom from its equilibrium position and A_{ij} would represent the force on the j-th atom for a unit displacement of the i-th atom.) This similarity between spin configurations and atomic vibrations forms the basis for the scheme of cataloguing the

* Permanent Address: School of Physics, Georgia Institute of Technology, Atlanta, Georgia.

possible ordered spin arrangements. The spin variables S_i are supposed to be continuous; they can then be represented in terms of normal coördinates. Each normal mode describes a spin configuration with definite phase relations between neighboring spins. The ordered spin states which are sought correspond to those normal modes for which neighboring spins are in phase (spins parallel) or 180° out of phase (spins antiparallel). If cyclic boundary conditions are imposed on the S_j, then the requirement of equivalence of spins at different lattice sites can be satisfied for all sites, since the effect of this condition is to remove the surface.

The one-dimensional crystal

The details for the simplest case of a one-dimensional chain of N spins will be given by way of illustration. The cyclic boundary condition bends the chain into a circle so that

$$S_j = S_{N+j}, j = 1, \ldots, N. \tag{2}$$

Let the normal coördinate amplitudes be designated by q_k, $k = 1, \ldots, N$. Then the unitary transformation from the S_i to the q_k is expressed by

$$S_i = \sum_{k=1}^{N} t_{ik} q_k \tag{3}$$

where the transformation coefficients t_{ik}, $i, k = 1, \ldots, N$ must be chosen to satisfy the cyclic condition (2) and to diagonalize the Hamiltonian (1) so that

$$\mathcal{H} = \tfrac{1}{2} \sum_{i,k=1}^{N} A_{ik} S_i S_k = \tfrac{1}{2} \sum_{k=1}^{N} \nu_k^2 q_k^2. \tag{4}$$

The cyclic condition (2) requires that

$$t_{ik} = t_{N+i,k}, \tag{5}$$

while (4) requires

$$\sum_{i,k=1}^{N} A_{ik} S_i S_k = \sum_{i,k=1}^{N} A_{ik} \sum_{l=1}^{N} t_{il} q_l \sum_{m=1}^{N} t_{km} q_m$$

$$= \sum_{l,m=1}^{N} q_l q_m \sum_{i,k=1}^{N} A_{ik} t_{il} t_{km} \tag{6}$$

$$= \sum_{k=1}^{N} \nu_k^2 q_k^2.$$

Since the transformation is unitary,

$$\sum_{k=1}^{N} t_{kl} t_{km} = \delta_{lm} \tag{7}$$

and the desired result is obtained if

$$\sum_{i=1}^{N} A_{ik} t_{il} = \nu_l^2 t_{kl}. \tag{8}$$

Equation (8) is the familiar *eigen*-value equation for the "frequencies" ν_l of the normal modes.

The real transformation coefficients which satisfy equations (5), (7), and (8) are

$$t_{ik} = \frac{1}{\sqrt{N}} \left(\cos \frac{2\pi}{N} ik + \sin \frac{2\pi}{N} ik \right) \tag{9}$$

and the spin configurations expressed in terms of normal modes may be written as

$$S_i = \frac{1}{(N)^{\frac{1}{2}}} \sum_{k=1}^{N} \left(\cos \frac{2\pi}{N} ik + \sin \frac{2\pi}{N} ik \right) q_k. \tag{10}$$

It is now required that the following constraint be satisfied:

$$S_{j+1}[S_{j+1+m} + S_{j+1-m}] = S_j[S_{j+m} + S_{j-m}] \tag{11}$$

for all j, m, $= 1, \ldots, N$. In this the left side is the correlation between spins at the $(j+1)$st lattice point and its m-th neighbors, and the right side is the corresponding correlation between the j-th site and its m-th neighbors. The condition expressed by (11) is required to hold for all j and m from 1 to N, and this is possible only because of the imposition of the cyclic boundary conditions. With these, as given by equation (2) and for $m = N$, condition (11) reduces to

$$S_{j+1}^2 = S_j^2 \text{ or } S_{j+1} = \pm S_j, \tag{12}$$

so that the constraint has the effect of extracting from the continuous spin configuration only those with discrete spins. It may be noted that condition

(11) is equivalent to the requirement that the number of like and unlike m-th neighbors ($m = 1, \ldots, N$) be the same for all spins.

It is shown in the Appendix that there are only four distinct possibilities for normal modes which satisfy the constraint, and these correspond to the values

$$\omega = \frac{2\pi k}{N} = 0, \frac{\pi}{2}, \pi, \frac{3\pi}{2}. \tag{13}$$

Since, in any one of these modes, the relative phases between the spins are given by

$$S_i \sim (\cos \omega i + \sin \omega i), \tag{14}$$

one obtains the four possible ordered configurations shown in Fig. 1. There are no others

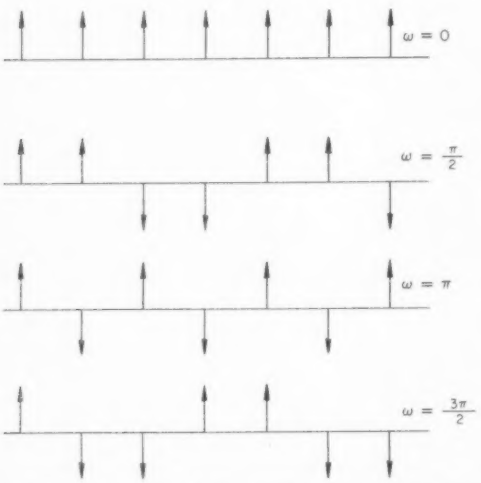

FIG. 1. Possible ordered spin configurations for a one-dimensional chain.

which satisfy the constraint, and hence fulfill the condition that every spin shall have the same number of like and unlike neighbors as any other spin.

Since the "wavelength" for a normal mode is, in units of the lattice spacing, $\lambda = N/k$, it follows that $\omega = 2\pi/\lambda$ is the propagation vector measured in the same units.

3. GENERALIZATION TO THREE DIMENSIONS

The foregoing discussion is directly applicable to an arbitrary three-dimensional lattice. Positions are described by lattice vectors so that instead of S_i one writes $S_{\boldsymbol{R}}$, where

$$\boldsymbol{R} = l_1\boldsymbol{a}_1 + l_2\boldsymbol{a}_2 + l_3\boldsymbol{a}_3, \tag{15}$$

in which l_1, l_2, l_3 are integers and $\boldsymbol{a}_1$, $\boldsymbol{a}_2$, $\boldsymbol{a}_3$ are basis vectors for the lattice. The transformation coefficients are:

$$t_{ik} = \frac{1}{N^{3/2}}(\cos \boldsymbol{k}\cdot\boldsymbol{R} + \sin \boldsymbol{k}\cdot\boldsymbol{R}) \tag{16}$$

with $\boldsymbol{k} = \omega_1\boldsymbol{b}_1 + \omega_2\boldsymbol{b}_2 + \omega_3\boldsymbol{b}_3$ in which $\boldsymbol{b}_1$, $\boldsymbol{b}_2$, $\boldsymbol{b}_3$ is the vector set reciprocal to $\boldsymbol{a}_1$, $\boldsymbol{a}_2$, $\boldsymbol{a}_3$ and $-\pi \leqslant \omega_i \leqslant \pi$ for $i = 1, 2, 3$.

The constraint which extracts the ordered configurations is written in direct analogy to equation (11):

$$S_{\boldsymbol{R}}[S_{\boldsymbol{R}+\boldsymbol{A}_L} + S_{\boldsymbol{R}-\boldsymbol{A}_L}] = S_{\boldsymbol{R}+\boldsymbol{a}_i}[S_{\boldsymbol{R}+\boldsymbol{a}_i+\boldsymbol{A}_L} + S_{\boldsymbol{R}+\boldsymbol{a}_i-\boldsymbol{A}_L}] \tag{17}$$

in which $\boldsymbol{R}$, and $\boldsymbol{a}_i$ are defined above and $\boldsymbol{A}_L$ is any lattice vector. Although equation (17) is the obvious generalization of the one-dimensional constraint, there is the following important difference in the two cases. The constraint for the one-dimensional case is equivalent to requiring the number of like and unlike m-th neighbors to be the same for all spins and for all m. The corresponding statement is not true in the three-dimensional case. The condition expressed by equation (17) is more restrictive than demanding equal numbers of like and unlike neighbors. Clearly equation (17) demands equivalence of spins with respect to any lattice vector $\boldsymbol{A}_L$, so that a configuration which satisfies the condition will automatically satisfy the requirement of equal numbers of like and unlike neighbors. This may be seen, from equation (17), by summing the $\boldsymbol{A}_L$ over fixed magnitudes. The converse is not true, for configurations can be found which satisfy an equivalence condition with respect to neighbor relations, but which do not satisfy the more restrictive condition above.

It may be pointed out, however, that once the configurations have been enumerated which satisfy condition (17), it is a relatively easy matter to obtain from them others which satisfy the less restrictive requirement.

In the Appendix it is shown that the constraint (17) restricts each of the ω_i to the values

VOL. 5 1958

$$\omega_i = 0, \pm\pi/2, \pi \quad i = 1, 2, 3. \tag{18}$$

The range $-\pi$ to $+\pi$ for each ω_i rather than the range 0 to 2π is used to allow propagation vectors in all directions. Thus the previous value $\omega=(3\pi/2)$ now becomes $-(\pi/2)$. Since there are four possible values for each of the three ω_i, there are in all sixty-four possible ordered arrangements. To each choice of the ω_i there corresponds a spin configuration which is described by:

$$S_{l_1 l_2 l_3} \sim \cos(\omega_1 l_1 + \omega_2 l_2 + \omega_3 l_3) + \\ + \sin(\omega_1 l_1 + \omega_2 l_2 + \omega_3 l_3). \tag{19}$$

The spin configuration may be constructed by choosing the spin at the origin as either up (+) or down (−) and then finding all others according to equation (19). Alternatively, one observes that the propagation vector $\boldsymbol{k} = \omega_1 \boldsymbol{b}_1 + \omega_2 \boldsymbol{b}_2 + \omega_3 \boldsymbol{b}_3$ is normal to planes of like spin. The manner in which these planes alternate in sign is determined from the wavelength $\lambda = (2\pi/|k|)$, which gives the distance along $\boldsymbol{k}$ for one complete cycle of (+) or (−) planes. For example, the configurations $[(\pi/2)(\pi/2)(\pi/2)]$ and $(\pi\,\pi\,\pi)$ for a simple cubic lattice both describe (111) planes of parallel spins. For $[(\pi/2)(\pi/2)(\pi/2)]$ these planes occur in the order $+\,+\,-\,-\,+\,+\,-\,-$, while for $(\pi\,\pi\,\pi)$ they occur as $+\,-\,+\,-\,+\,-$. The wavelength λ for $[(\pi/2)(\pi/2)(\pi/2)]$ is four units of the distance between planes, but only two units of this distance for the $(\pi\,\pi\,\pi)$ configuration.

If isotropic first- and second-nearest-neighbor interactions are assumed, the energy of a configuration may be obtained from equation (4) by setting $q_k{}^2 = N$ for the particular configuration, yielding the energy per spin E:

$$E = \tfrac{1}{2}\nu^2 \omega_1 \omega_2 \omega_3 \tag{20}$$

with $\nu_{\omega_1\omega_2\omega_3}$ obtained from equation (8). This procedure is equivalent to writing the energy in the form:

$$E = \tfrac{1}{2}\alpha \sum_{l_1 l_2 l_3} S_{l_1 l_2 l_3} \sum_{NN} S_{l_1' l_2' l_3'} + \\ + \tfrac{1}{2}\beta \sum_{l_1 l_2 l_3} S_{l_1 l_2 l_3} \sum_{NNN} S_{l_1' l_2' l_3'} \tag{21}$$

where α and β are nearest- and next-nearest-neighbor interaction energies, positive if antiferromagnetic (AF) and negative if ferromagnetic (F), $S_{l_1 l_2 l_3}$ is (± 1) as above, and the sums are taken over the first- and second-nearest-neighbor configuration for each spin. Since, for all our configurations, the environment with respect to like and unlike neighbors is identical for each spin, the average energy per spin may also be expressed in the convenient form

$$E/|\alpha| = \tfrac{1}{2}\{\pm 1(n_l - n_u)_{NN} \pm \rho(n_l - n_u)_{NNN}\} \tag{22}$$

where ρ is $|\beta|/|\alpha|$ and the plus sign is to be taken for AF interactions, the minus sign for F interactions, and n_l and n_u are the numbers of like and

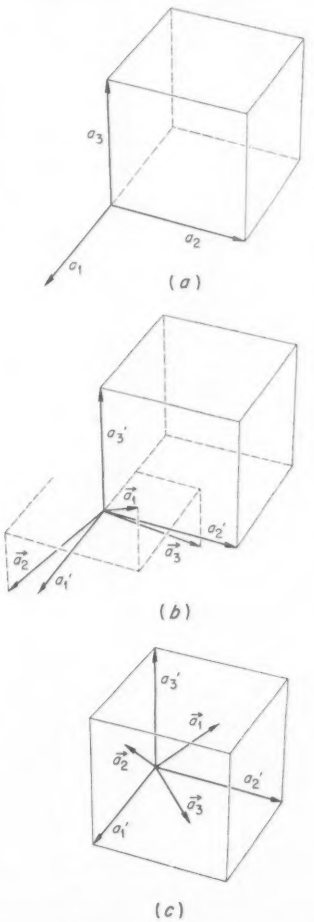

FIG. 2. Choice of lattice vectors: (*a*) simple cubic lattice, (*b*) body-centered cubic lattice, (*c*) face-centered cubic lattice.

Table 1. Ordered spin configurations on a simple cubic lattice

Type	$\omega_1\omega_2\omega_3$	Number of configurations	Neighbors				$E/\|\alpha\|$
			NN		*NNN*		
			Like	Unlike	Like	Unlike	
1	$0\,0\,0$	1	6	0	12	0	$3+6\rho$
2	$\frac{\pi}{2}\,0\,0$	6	5	1	8	4	$2+2\rho$
3	$0\,0\,\pi$	3	4	2	4	8	$1-2\rho$
4	$\frac{\pi}{2}\,\frac{\pi}{2}\,0$	12	4	2	6	6	1
5	$\frac{\pi}{2}\,\frac{\pi}{2}\,\frac{\pi}{2}$	8	3	3	6	6	0
6	$\frac{\pi}{2}\,0\,\pi$	12	3	3	4	8	-2ρ
7	$0\,\pi\,\pi$	3	2	4	4	8	$-1-2\rho$
8	$\frac{\pi}{2}\,\frac{\pi}{2}\,\pi$	12	2	4	6	6	-1
9	$\frac{\pi}{2}\,\pi\,\pi$	6	1	5	8	4	$-2+2\rho$
10	$\pi\,\pi\,\pi$	1	0	6	12	0	$-3+6\rho$

unlike spins around a given one at the distances indicated.

4. APPLICATIONS TO SIMPLE LATTICES

(a) *Simple cubic lattice*

To illustrate the variety of types of ordered spin configurations, we first give results for the simple cubic lattice in Table 1. The choice of lattice vectors is illustrated in Fig. 2a. Of the sixty-four configurations which result from all possible choices of ω_i, only ten are distinctly different. (The remaining fifty-four can be derived from these by cyclic permutation of the basis vectors, by shift in origin, or by rotation.)

The quantity $E/|\alpha|$ for the case that both interactions are AF as calculated from equation (20) is:

$$E/|\alpha| = \cos\omega_1+\cos\omega_2+\cos\omega_3+ \\ +2\rho[\cos\omega_1\cos\omega_2+\cos\omega_1\cos\omega_3+ \\ +\cos\omega_2\cos\omega_3]. \qquad (23)$$

In Table 1, values of $E/|\alpha|$ are given for this case, and the three cases $\alpha>0, \beta>0$; $\alpha<0, \beta>0$; and $\alpha>0, \beta<0$ are illustrated in Fig. 3, where $E/|\alpha|$ is plotted as a function of $\rho = |\beta|/|\alpha|$ for the ten configurations.

The results of considerations contained in references (1–4) are that two types of ordering are

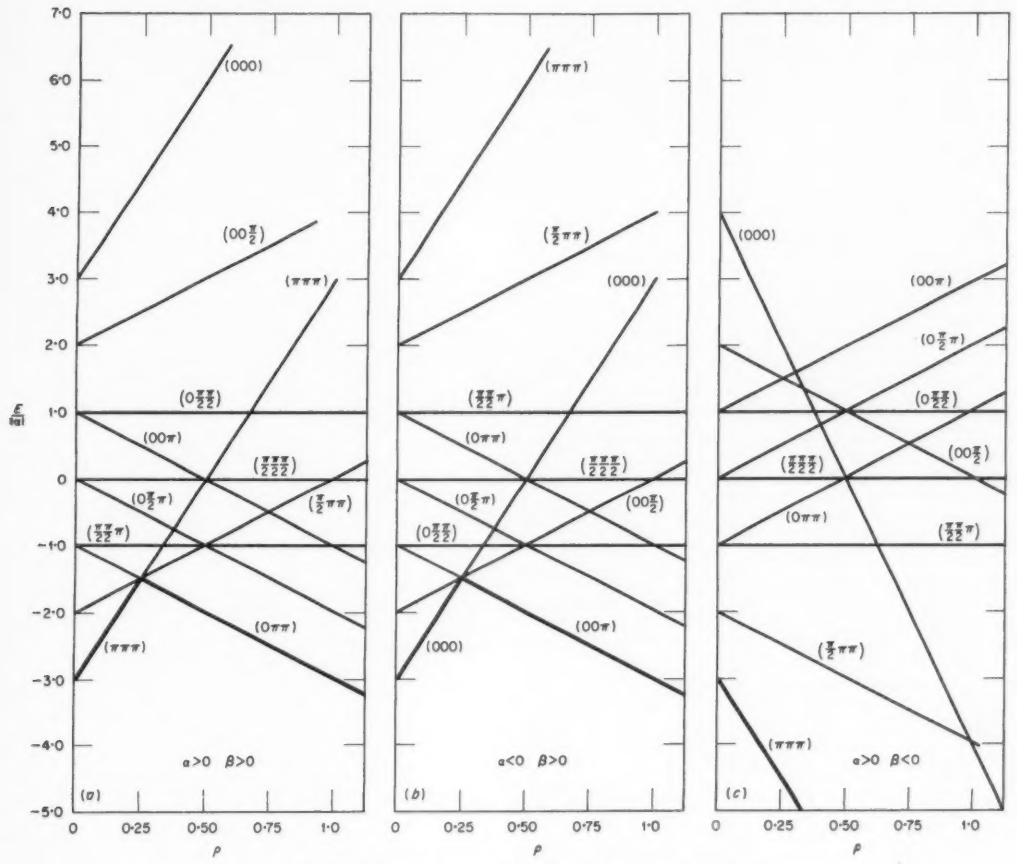

FIG. 3. $E/|\alpha|$ versus $\rho = |\beta|/|\alpha|$ for simple cubic lattice.

(*a*) Both interactions antiferromagnetic $\alpha > 0$, $\beta > 0$.
(*b*) $\alpha < 0$, $\beta > 0$.
(*c*) $\alpha > 0$, $\beta < 0$.

Favored configurations:
(*a*) $\rho < 0{\cdot}25$ $(\pi\,\pi\,\pi)$, $\rho > 0{\cdot}25$ $(0\,\pi\,\pi)$.
(*b*) $\rho < 0{\cdot}25$ $(0\,0\,0)$, $\rho > 0{\cdot}25$ $(0\,0\,\pi)$.
(*c*) $(\pi\,\pi\,\pi)$.

energetically possible if isotropic nearest- and next-nearest-neighbor AF interactions are assumed. These are illustrated in Fig. 3a, where for $\rho < 0{\cdot}25$, the $(\pi\,\pi\,\pi)$ configuration is favored, and for $\rho > 0{\cdot}25$, the $(0\,\pi\,\pi)$ configuration is predicted. These correspond respectively to configurations (a), in which each spin has six antiferromagnetically aligned nearest neighbors, and (b), in which chains of like spin are surrounded by four oppositely oriented chains of like spin. In Fig. 3b ($\alpha < 0$, $\beta > 0$) the ferromagnetic $(0\,0\,0)$ configuration is favored if $\rho < 0{\cdot}25$ and the alternating ferromagnetic sheet configuration $(0\,0\,\pi)$ for $\rho > 0{\cdot}25$. In the final case only the $(\pi\,\pi\,\pi)$ configuration is stable.

Experimentally the perovskite-like compounds ABO_3 which contain magnetically active A or B site cations provide examples of magnetic ions on a simple cubic lattice. To a fair approximation the A and B site cations in the manganese perovskites, for example $(La, Ca)(Mn^{+3}, Mn^{+4})O_3$, in the rare-earth orthoferrites, and rare-earth orthochromites form simple cubic lattices, and magnetic ordering configurations for a number of these compounds have now been reported.[5,6] Of the configurations listed in Table 1, four have been observed: in the

Table 2. Ordered spin configurations on a face-centered cubic lattice

Equivalent configurations are given in parenthesis. The four-sublattice designation is given in square brackets where the origins are taken at 000, $(a_1'+a_2')/2$, $(a_2'+a_3')/2$, and $(a_1'+a_3')/2$, respectively.

No.	$\omega_1\omega_2\omega_3$	Number of configurations	Neighbors				$E/\lvert\alpha\rvert$
			NN		*NNN*		
			Like	Unlike	Like	Unlike	
1	$0\,0\,0$ $[0\,0\,0;\ 0\,0\,0;\ 0\,0\,0;\ 0\,0\,0]$	1	12	0	6	0	$6+3\rho$
2	$0\,\pi\,\pi$ $[0\,0\,0;\ -(0\,0\,0);\ 0\,0\,0;\ -(0\,0\,0)]$	3	4	8	6	0	$-2+3\rho$
3	$\frac{\pi}{2}\frac{\pi}{2}0\text{--}\left(\frac{\bar\pi}{2}\frac{\bar\pi}{2}0\text{--}\right)$ $[\pi\,0\,0;\ \pi\,0\,0;\ \pi\,0\,0;\ \pi\,0\,0]$	6	8	4	4	2	$2+\rho$
4	$\frac{\pi}{2}\frac{\bar\pi}{2}\pi\text{--}\left(\frac{\bar\pi}{2}\frac{\bar\pi}{2}\pi\text{--}\right)$ $[\pi\,0\,0;\ -(\pi\,0\,0);\ -(\pi\,0\,0);\ \pi\,0\,0]$	6	4	8	4	2	$-2+\rho$
5	$\frac{\pi}{2}\frac{\bar\pi}{2}0\text{--}\left(\frac{\bar\pi}{2}\frac{\pi}{2}0\text{--};\ \frac{\pi}{2}\frac{\pi}{2}\text{--}\pi;\ \frac{\bar\pi}{2}\frac{\bar\pi}{2}\text{--}\pi\right)$ $[0\,\pi\,\pi;\ -(0\,\pi\,\pi);\ 0\,\pi\,\pi;\ 0\,\pi\,\pi]$	12	6	6	2	4	$-\rho$
6	$0\,0\,\pi(\pi\,\pi\,\pi)$ $[\pi\,\pi\,\pi;\ \pi\,\pi\,\pi;\ -(\pi\,\pi\,\pi);\ \pi\,\pi\,\pi]$	4	6	6	0	6	-3ρ
7	$\frac{\pi}{2}\frac{\pi}{2}\frac{\pi}{2}\text{---}\left(\frac{\bar\pi}{2}\frac{\bar\pi}{2}\frac{\bar\pi}{2}\text{---};\ 0\,0\text{--}\frac{\pi}{2};\ 0\,0\text{--}\frac{\bar\pi}{2}\right)$ $\left[\frac{\pi}{2}\frac{\pi}{2}\frac{\pi}{2}\text{---};\ \frac{\bar\pi}{2}\frac{\bar\pi}{2}\frac{\bar\pi}{2}\text{---};\ \frac{\bar\pi}{2}\frac{\bar\pi}{2}\frac{\bar\pi}{2}\text{---};\ \frac{\bar\pi}{2}\frac{\bar\pi}{2}\frac{\bar\pi}{2}\text{---}\right]$	8	9	3	3	3	3
8	$\frac{\bar\pi}{2}\frac{\bar\pi}{2}\frac{\pi}{2}\text{---}\left(\frac{\pi}{2}\frac{\pi}{2}\frac{\bar\pi}{2}\text{---};\ 0\,\frac{\pi}{2}\text{--};\ 0\,\frac{\bar\pi}{2}\text{--};\ 0\frac{\bar\pi}{2}\frac{\pi}{2}\text{--};\ 0\frac{\bar\pi}{2}\frac{\bar\pi}{2}\text{--};\ \frac{\pi}{2}\frac{\pi}{2}\text{--};\ \frac{\pi}{2}\frac{\bar\pi}{2}\text{--}\right)$ $\left[\frac{\pi}{2}\frac{\pi}{2}\frac{\pi}{2}\text{---};\ \frac{\bar\pi}{2}\frac{\bar\pi}{2}\frac{\bar\pi}{2}\text{---};\ -\left(\frac{\bar\pi}{2}\frac{\bar\pi}{2}\frac{\bar\pi}{2}\text{---}\right);\ -\left(\frac{\bar\pi}{2}\frac{\bar\pi}{2}\frac{\bar\pi}{2}\text{---}\right)\right]$	24	5	7	3	3	-1

mixed oxides series the pure compounds $LaMnO_3$ and $CaMnO_3$ exhibit ordering of the types $(0\,0\,\pi)$ and $(\pi\,\pi\,\pi)$ respectively, and for certain concentrations of Mn^{+4} the $(0\,0\,0)$ and $(0\,\pi\,\pi)$ configurations are also found. In the rare-earth orthoferrites $AFeO_3$[7] (A = La, Nd, Er, or Ho) and in $LaCrO_3$, the Fe^{+3} and Cr^{+3} order at high temperatures in the $(\pi\,\pi\,\pi)$ arrangement and Er^{+3} and Ho^{+3} appear to order at very low temperatures in the $(0\,\pi\,\pi)$ configuration. These four structure types were originally designated as Types A, B, C, G; in the present notation they are respectively $(0\,0\,\pi)$, $(0\,0\,0)$, $(0\,\pi\,\pi)$, and $(\pi\,\pi\,\pi)$. This latter notation will be adopted for the balance of this

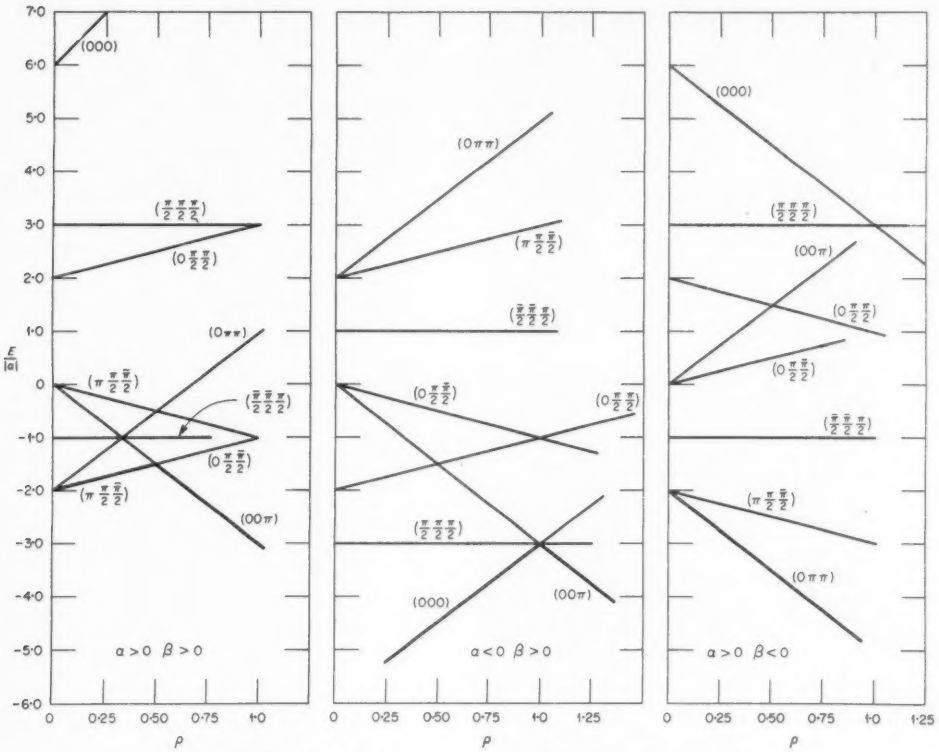

FIG. 4. $E/|\alpha|$ versus $\rho = |\beta|/|\alpha|$ for face-centered cubic lattice.

(*a*) Both configurations antiferromagnetic $\alpha>0$, $\beta>0$.
(*b*) $\alpha < 0$, $\beta > 0$.
(*c*) $\alpha > 0$, $\beta < 0$.

Favored configurations:
(*a*) $\rho < 0{\cdot}50$ $[\pi(\pi/2)(\bar{\pi}/2)]$ $\rho > 0{\cdot}50$ $(0\,0\,\pi)$.
(*b*) $\rho < 1{\cdot}00$ $(0\,0\,0)$ $\rho > 1{\cdot}00$ $(0\,0\,\pi)$.
(*c*) $(0\,\pi\,\pi)$.

discussion as being more descriptive of the spin arrangement in the several structures.

(b) *The face-centered cubic lattice*

The basis vectors for the face-centered cubic lattice and their relationship to a convenient orthogonal coördinate system are illustrated in Fig. 2c. As in the previous case, there are a total of sixty-four possible configurations, corresponding to the sixty-four possible combinations of ω_1, ω_2, ω_3. Of these, again, forty may be excluded as arising from cyclic permutations of existing combinations, and of the remaining twenty-four, eight may be considered as distinct. The eight configurations listed in Table 2 may be more graphically described by giving the configurations of the simple cubic sublattices into which the face-centered cubic lattice naturally divides. The notation adopted is the following: the origins of the four sublattices are taken at 0 0 0; $(\boldsymbol{a}'_1+\boldsymbol{a}'_2)/2$; $(\boldsymbol{a}'_2+\boldsymbol{a}'_3)/2$; and $(\boldsymbol{a}'_1+\boldsymbol{a}'_3)/2$ as indicated in Fig. 2c, and the sublattice is designated as positive or negative as the spin at its origin is up (+) or down (−). In accordance with the requirement of equivalence, each sublattice configuration must be the same one of the ten simple cubic configurations described above. In Table 2 the sublattice configurations are given in the above-mentioned sequence.

For each configuration the number of like and unlike nearest and next-nearest neighbors is tabulated. The energy $E/|\alpha|$ for isotropic AF interactions expressed in terms of the ω_i is

Table 3. Ordered spin configurations on a body-centered cubic lattice

Equivalent configurations are given in parentheses. The two-sublattice description gives the configurations of the (000) and $(\frac{1}{2}\frac{1}{2}\frac{1}{2})$ sublattices in that order.

No.	Oblique coördinates	Orthogonal coördinates	Number of configurations	Neighbors				$E/\lvert\alpha\rvert$
				NN		*NNN*		
				Like	Unlike	Like	Unlike	
1	$0\,0\,0$	$0\,0\,0;\ 0\,0\,0$	1	8	0	6	0	$4+3\rho$
2	$\pi\,\pi\,\pi$	$0\,0\,0;\ -(0\,0\,0)$	1	0	8	6	0	$-4+3\rho$
3	$\underset{2}{\pi}\ \underset{2}{\bar{\pi}}\ \underset{2}{\bar{\pi}}\ \left(\underset{2}{\bar{\pi}}\ \underset{2}{\pi}\ \underset{2}{\pi}\right)$	$0\,0\,\pi;\ 0\,0\,\pi$	6	4	4	4	2	ρ
4	$0\,0\,\pi(\pi\,\pi\,0)$	$0\,\pi\,\pi;\ 0\,\pi\,\pi$	6	4	4	2	4	$-\rho$
5	$\underset{2}{\pi}\ \underset{2}{\pi}\ \underset{2}{\pi}\ \left(\underset{2}{\bar{\pi}}\ \underset{2}{\bar{\pi}}\ \underset{2}{\bar{\pi}}\right)$	$\pi\,\pi\,\pi;\ \pi\,\pi\,\pi$	2	4	4	0	6	-3ρ
6	$\underset{2}{\pi}\ \underset{2}{\bar{\pi}}\ -0\left(\underset{2}{\bar{\pi}}\ \underset{2}{\pi}\ -0;\ 0\,0\underset{2}{-};\ 0\,0\underset{2}{-}\right)$	$\underset{2}{\pi}\ \underset{2}{\pi}\ 0\underset{2}{-};\ \underset{2}{\bar{\pi}}\ \underset{2}{\bar{\pi}}\ 0\underset{2}{-}$	12	6	2	4	2	$2+\rho$
7	$\underset{2}{\bar{\pi}}\ \underset{2}{\pi}\ -\pi\left(\underset{2}{\pi}\ \underset{2}{\bar{\pi}}\ -\pi;\ \pi\,\underset{2}{\pi-};\ \pi\,\underset{2}{\pi-}\right)$	$\underset{2}{\pi}\ \underset{2}{\pi}\ 0\underset{2}{-};\ -\left(\underset{2}{\bar{\pi}}\ \underset{2}{\bar{\pi}}\ 0\underset{2}{-}\right)$	12	2	6	4	2	$-2+\rho$
8	$0\,\underset{2}{\pi}\,\pi-\left(0\,\underset{2}{\bar{\pi}}\,\pi-;\ \underset{2}{\pi}\ \underset{2}{\pi}\ -;\ \underset{2}{\bar{\pi}}\ \underset{2}{\bar{\pi}}\ -;\right.$ $\left.\underset{2}{\pi}\ 0\underset{2}{-}\pi;\ \underset{2}{\bar{\pi}}\ 0\underset{2}{-}\pi;\ \underset{2}{\pi}\ \underset{2}{\pi}\ -0;\ \underset{2}{\bar{\pi}}\ \underset{2}{\bar{\pi}}\ -0\right)$	$\underset{2}{\pi}\ \underset{2}{\pi}\ \pi-;\ \underset{2}{\pi}\ \underset{2}{\pi}\ \pi-$	24	4	4	2	4	$-\rho$

$$E/|\alpha| = \cos\omega_1+\cos\omega_2+\cos\omega_3+\cos(\omega_1-\omega_3)+ +\cos(\omega_1-\omega_2)+\cos(\omega_2-\omega_3)+ +\rho(\cos(\omega_1+\omega_2-\omega_3)+\cos(\omega_1-\omega_2+\omega_3)+ +\cos(-\omega_1+\omega_2+\omega_3). \quad (24)$$

These values are given in the table and displayed graphically in Fig. 4(a). The other two cases of interest are also plotted in the figure.

When α and β are both positive, the $[\pi(\pi/2)(\bar{\pi}/2)]$ configuration is favored if $\rho < 0{\cdot}5$ and the $(0\,0\,\pi)$ configuration if $\rho > 0{\cdot}5$. The $(0\,0\,\pi)$ arrangement may be alternatively viewed as consisting of four interpenetrating $(\pi\,\pi\,\pi)$ simple cubic configurations so oriented that the propagation vector $\boldsymbol{k}$ is normal to (111) planes of the face-centered cubic lattice. Ordering of this type has previously been designated as "ordering of the second kind", and it is this configuration which is apparently found for Mn^{+2} in MnO and α-MnS according to recent measurements of CORLISS *et al.* and of ROTH.[8] The $[\pi(\pi/2)(\bar{\pi}/2)]$ configuration consists of $(\pi\,0\,0)$ configurations such that the planes of like spin are (120) planes. Measurements by CORLISS *et al.*[8] have shown that this configuration is adopted by Mn^{+2} in the zinc blend modification of MnS. This configuration has been variously described as "improved ordering of the first kind" or "ordering of the third kind".

VOL. 5 1958

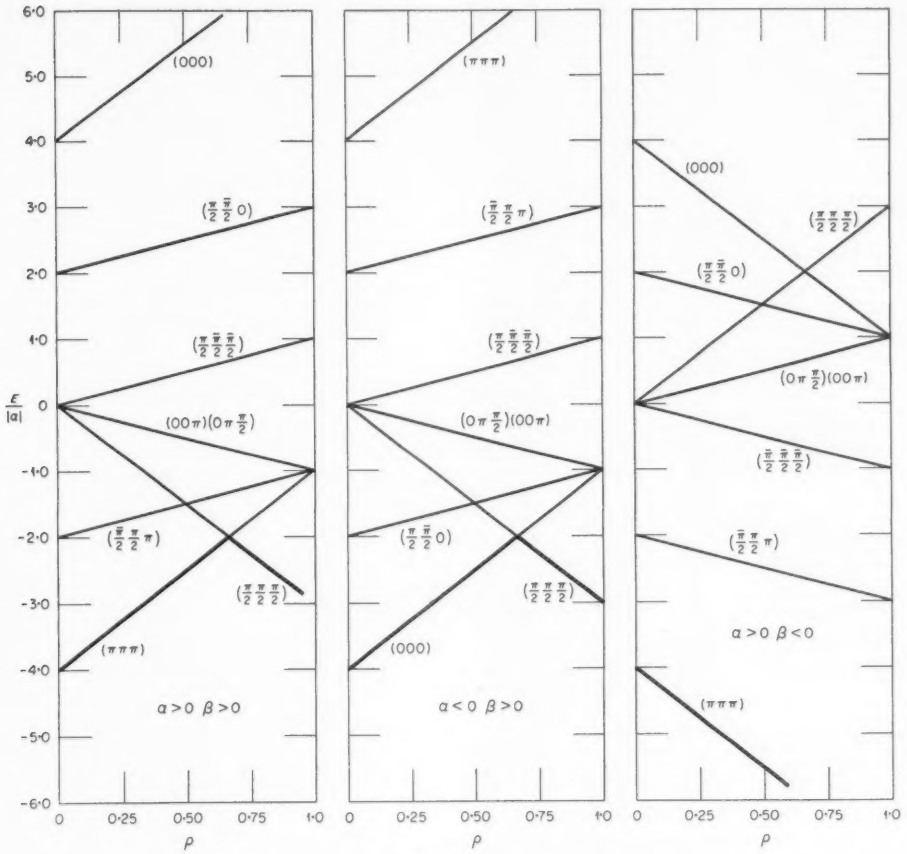

FIG. 5. $E/|\alpha|$ versus $\rho = |\beta|/|\alpha|$ for body-centered cubic lattice.

(*a*) Both interactions antiferromagnetic $\alpha >$, $\beta > 0$.
(*b*) $\alpha < 0$, $\beta > 0$.
(*c*) $\alpha > 0$, $\beta < 0$.

Favored configurations:
(*a*) $\rho < \frac{2}{3}(\pi\,\pi\,\pi)$, $\rho > \frac{2}{3}[(\pi/2)(\pi/2)(\pi/2)]$.
(*b*) $\rho < \frac{2}{3}(0\,0\,0)$, $\rho > \frac{2}{3}[(\pi/2)(\pi/2)(\pi/2)]$.
(*c*) $(\pi\,\pi\,\pi)$.

We note that $(\pi\,0\,0)$ configurations may also be arranged to form a configuration in which each spin has eight like and four unlike nearest neighbors $[0(\pi/2)(\pi/2)]$ in distinction to the case above. Energetically this case is not favored for any combination of F and AF first- and second-neighbor interactions, nor has an experimental example been found as far as we know.

As illustrated in Fig. 4 for first-neighbor F and second-neighbor AF interactions, the ferromagnetic $(0\,0\,0)$ configuration is stable for $\rho < 1{\cdot}0$ and the $(0\,0\,\pi)$ for $\rho > 1{\cdot}0$. The $[(\pi/2)(\pi/2)(\pi/2)]$ arrangement has the same energy as the other two for $\rho = 1{\cdot}0$. This also appears not to be found experimentally.

For the case of AF first- and F second-neighbor interactions, only the $(0\,\pi\,\pi)$ configuration is energetically favored. This is an antiferromagnetic structure composed of ferromagnetic simple cubic configurations and is a layer structure; the propagation vector for $(0\,\pi\,\pi)$ is perpendicular to (100) planes. The $(0\,\pi\,\pi)$ configuration has been called "ordering of the first kind" and seems to be the ordering arrangement of U^{+4} in fluorite type UO_2.[9]

It is interesting to point out that the configuration

$[0(\pi/2)(\bar{\pi}/2)]$, which is made up of $(0\,\pi\,\pi)$ configurations, is possibly represented in nature by the AF structure of Er_2O_3.[10] This configuration is, however, not energetically favored for isotropic first- and second-neighbor interactions.

(c) *The body-centered cubic lattice*

In a manner similar to that described above, the various ordered configurations for the body-centered cubic lattice are listed in Table 3. As before we give the alternative description for each of the two sublattices. The choice of lattice vectors is illustrated in Fig. 2b. There are eight different configurations, only three of which are energetically favored for isotropic nearest- and next-nearest-neighbor interactions. The energies of the several configurations expressed in terms of the ω_i are given by:

$$E/|\alpha| = \cos\omega_1+\cos\omega_2+\cos\omega_3+ +\cos(\omega_1+\omega_2+\omega_3)+\rho[\cos(\omega_1+\omega_2)+ +\cos(\omega_1+\omega_3)+\cos(\omega_2+\omega_3)] \qquad (25)$$

and are listed in the table for the case that both interactions are AF. This and the other two cases are illustrated in Fig. 5.

When both interactions are AF, the $(\pi\,\pi\,\pi)$ configuration is stable for $\rho < \frac{2}{3}$; for $\rho > \frac{2}{3}$, the favored configuration is the $[(\pi/2)(\pi/2)(\pi/2)]$. These have been termed ordering of the first and second kind, respectively. The $(\pi\,\pi\,\pi)$ configuration, as one sees from the table, consists of two oppositely oriented ferromagnetic configurations. In the $[(\pi/2)(\pi/2)(\pi/2)]$ configuration, there is a simple cubic $(\pi\,\pi\,\pi)$ configuration on each sublattice.

If α is < 0 and $\beta > 0$, the ferromagnetic $(0\,0\,0)$ configuration exists for $\rho < \frac{2}{3}$ and for $\rho > \frac{2}{3}$ the $[(\pi/2)(\pi/2)(\pi/2)]$ configuration is again favored. In the last instance ($a > 0$, $\beta < 0$), only the $(\pi\,\pi\,\pi)$ arrangement is stable.

Relatively few examples of magnetically ordered configurations on a body-centered cubic lattice are known. An approximation to this case exists, however, in the tetragonal difluorides of manganese, iron, cobalt, and nickel, in which the cation spins order in the $(\pi\,\pi\,\pi)$ configuration.[11] A structure tentatively proposed for tetragonal MnO_2 is the $[(\pi/2)(\pi/2)(\pi/2)]$ arrangement.[12]

(d) *The hexagonal layer lattice*

As a final example we consider briefly the hexagonal layer structures. We first tabulate the number of ordered structures that satisfy our criterion which may be constructed for a two-dimensional lattice. If the basis vectors are the usual ones for hexagonal systems ($a_1 = a_2 \neq a_3$), the four possible configurations are those listed in Table 4. For the three-dimensional lattice, each of these may be combined with $(0\,0\,0)$, $(0\,0\,\pi)$, or $[0\,0\,(\pi/2)]$ to

Table 4. Ordered spin configurations on a two-dimensional hexagonal lattice

Equivalent configurations are given in parentheses.

Type	$\omega_1\omega_2$	Number of configurations	Neighbors			
			NN		*NNN*	
			Like	Unlike	Like	Unlike
1	$0\,0$	1	6	0	6	0
2	$\pi\,\pi(0\,\pi;\ \pi\,0)$	3	2	4	2	4
3	$\frac{\pi}{2}\frac{\pi}{2}\left(\frac{\bar{\pi}}{2}\frac{\pi}{2};\ \frac{-\pi}{2}\frac{\pi}{2};\ \frac{\bar{\pi}}{2}\frac{\bar{\pi}}{2};\ \frac{-}{2}\frac{\pi}{2};\ \frac{\bar{\pi}}{2}\frac{-\pi}{2}\right)$	6	2	4	4	2
4	$\frac{\pi}{2}\frac{\bar{\pi}}{2}\left(\frac{\bar{\pi}}{2}\frac{0}{2};\ \frac{-0}{2}\frac{\pi}{2};\ \frac{\bar{\pi}}{2}\frac{\pi}{2};\ \frac{-}{2}\frac{0}{2};\ \frac{\pi}{2}\frac{-0}{2}\right)$	6	4	2	2	4

Table 5. Ordered spin configurations on an hexagonal layer lattice

Type	$\omega_1\omega_2\omega_3$	Number of configurations	Neighbors				$E/\lvert\alpha\rvert$
			NN (parallel to layer)		*NNN* (normal to layer)		
			Like	Unlike	Like	Unlike	
1	$0\,0\,0$	1	6	0	2	0	$3+\rho$
2	$0\,0\,\pi$	1	6	0	0	2	$3-\rho$
3	$0\,0\,\frac{\pi}{2}$	2	6	0	1	1	3
4	$\pi\,\pi\,0$	3	2	4	2	0	$-1+\rho$
5	$\pi\,\pi\,\pi$	3	2	4	0	2	$-1-\rho$
6	$\pi\,\pi\,\frac{\pi}{2}$	6	2	4	1	1	-1
7	$\frac{\pi}{2}\,\frac{\pi}{2}\,0$	6	2	4	2	0	$-1+\rho$
8	$\frac{\pi}{2}\,\frac{\pi}{2}\,\pi$	6	2	4	0	2	$-1-\rho$
9	$\frac{\pi}{2}\,\frac{\pi}{2}\,\frac{\pi}{2}$	12	2	4	1	1	-1
10	$\frac{\pi}{2}\,\frac{\bar{\pi}}{2}\,0$	6	4	2	2	0	$1+\rho$
11	$\frac{\pi}{2}\,\frac{\bar{\pi}}{2}\,\pi$	6	4	2	0	2	$1-\rho$
12	$\frac{\pi}{2}\,\frac{\bar{\pi}}{2}\,\frac{\pi}{2}$	12	4	2	1	1	1

give twelve distinct configurations, ($[\omega_1\omega_2\pm(\pi/2)]$, differ only in choice of origin), and these are tabulated along with their first- and second-nearest-neighbor relationships in Table 5. Here also we calculate the energy of the several configurations for isotropic AF nearest- and next-nearest-neighbor interactions, given by

$$E/|\alpha| = \cos\omega_1+\cos\omega_2+ \\ +\cos(\omega_1+\omega_2)+\rho\cos\omega_3). \tag{25}$$

The stable configurations, illustrated in Fig. 6, are $(0\,0\,\pi)$, $(\pi\,\pi\,0)$ or $[(\pi/2)(\pi/2)]\,0$, and $(\pi\,\pi\,\pi)$ or $[(\pi/2)(\pi/2)\,\pi]$. Of these $(0\,0\,\pi)$, $(\pi\,\pi\,0)$, and $(\pi\,\pi\,\pi)$

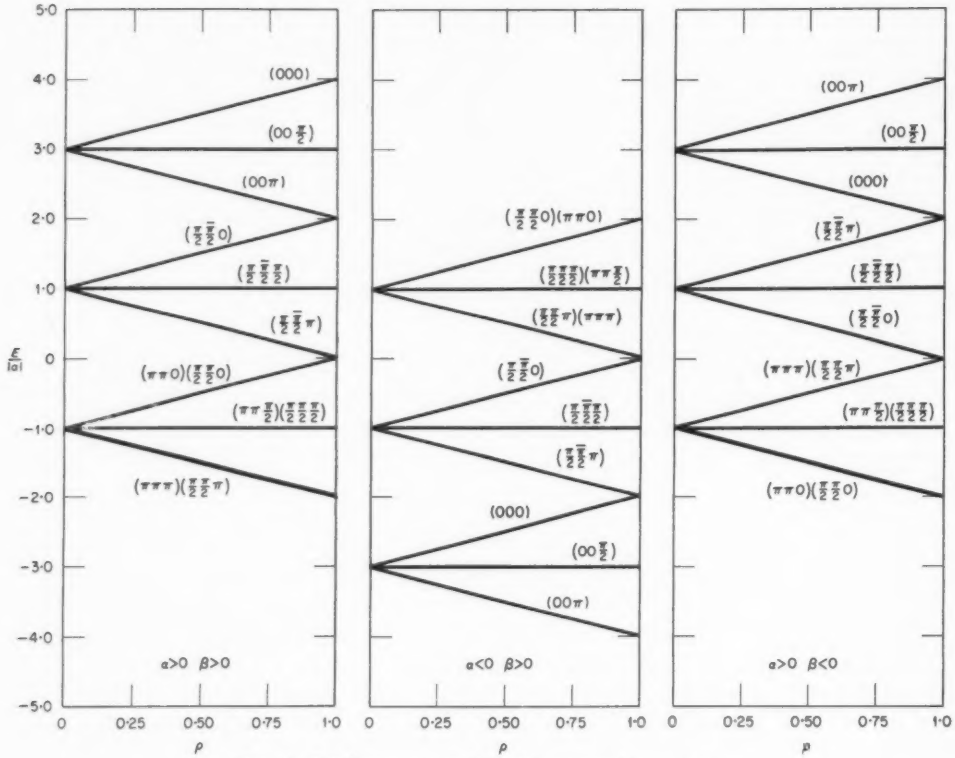

FIG. 6. $E/|\alpha|$ versus $\rho = |\beta|/|\alpha|$ hexagonal layer lattice.

(*a*) Both interactions antiferromagnetic $\alpha > 0$, $\beta > 0$.
(*b*) $\alpha < 0$, $\beta > 0$.
(*c*) $\alpha > 0$, $\beta < 0$.

Favored configurations:
(*a*) $(\pi\ \pi\ \pi)$ or $[(\pi/2)(\pi/2)\pi]$.
(*b*) $(0\ 0\ \pi)$.
(*c*) $(\pi\ \pi\ 0)$ or $[(\pi/2)(\pi/2)\ 0]$.

have previously been designated as first, second, and third kind, respectively.

This classification of spin arrangements on hexagonal layer lattices may be used as a basis for classifying ordered structures corresponding to various stackings of hexagonal layers. Obviously, if the stacking approximates cubic close packing, the results described above for the face-centered cubic lattice are immediately applicable. For simple hexagonal close-packed structures, the two layer lattices are translated with respect to each other by a vector $\frac{2}{3}\boldsymbol{a}_1+\frac{1}{3}\boldsymbol{a}_2+\frac{1}{2}\boldsymbol{a}_3$. If we denote the translated lattice as positive or negative as the spin at its origin is (+) or (−), we may combine configurations on the two lattices in a variety of ways. By way of example we classify the structures considered by CORLISS *et al.*[8] in their work on hexagonal MnS. These are given for the case considered by these authors in Table 6. The extension to larger magnetic unit cells is obvious.

5. DISCUSSION: LIMITATIONS OF THE CATALOGUING SCHEME

It is to be emphasized that we have constructed a method for the enumeration only of certain ordered spin configurations. The method gives all possible ordered configurations corresponding to a single normal mode, or equivalently, to a single propagation vector. It is implicit in our method that there be a single axis of magnetization and a single type of magnetic ion. All of the configurations tabulated have the property that all spins have the same numbers of like and unlike neighbors at all distances, but as we have mentioned above,

Table 6. Classification of hexagonal close-packed structures when $\omega_3 = 0$

The designations given by CORLISS, ELLIOT, and HASTINGS[8] are catalogued for layer lattices with origin at 000 and $\frac{2}{3}a_1+\frac{1}{3}a_2+\frac{1}{2}a_3$, respectively. In computing distances of various neighbors, the ideal c/a ratio has been assumed.

No.	C.E.H.	$\omega_1\omega_2\omega_3$	1st Neighbors		2nd Neighbors		3rd Neighbors		4th Neighbors	
			Like	Unlike	Like	Unlike	Like	Unlike	Like	Unlike
1		0 0 0; 0 0 0	12	0	6	0	2	0	18	0
2	2nd kind	0 0 0; $-$(0 0 0)	6	6	0	6	2	0	6	12
3	2nd kind	$\pi\,\pi\,0$; $\pi\,\pi\,0$	6	6	0	6	2	0	10	8
4	1st kind	$\pi\,\pi\,0$; $-(\pi\,\pi\,0)$	4	8	6	0	2	0	6	12
5	4th kind	$\frac{\pi\,\pi}{2\,2}\,0$; $\frac{\bar\pi\,\bar\pi}{2\,2}\,0$	6	6	2	4	2	0	8	10
6	3rd kind	$\frac{\pi\,\pi}{2\,2}\,0$; $-\left(\frac{\bar\pi\,\bar\pi}{2\,2}\,0\right)$	4	8	4	2	2	0	12	6

not all such arrangements are counted by our method. There are therefore a large number of possible ordered spin configurations, some of them experimentally observed, which are not contained in our cataloguing scheme. However, as we shall illustrate, such configurations may be considered as superpositions of configurations which are contained in our enumeration.

For example, we may cite the C-E structure described by WOLLAN and KOEHLER in their study of manganese perovskites.[5] The simple cubic point lattice is subdivided into two tetragonal lattices, as illustrated in Fig. 7, and on these the Mn^{+3} ions have a $(\pi\,0\,\pi)$ configuration; the Mn^{+4} a $(\pi\,\pi\,\pi)$ configuration. The Mn^{+3} ions and Mn^{+4} ions separately are represented by single-mode configurations, but the overall arrangement is a superposition of the two. If one disregards the difference in ion type, the arrangement may still be described as a superposition of $(\pi\,0\,\pi)$ and $(\pi\,\pi\,\pi)$ configurations, and it will be noted that while the neighbor relation condition is satisfied for first neighbors, it fails for second neighbors.

As a second example, consider the face-centered cubic $(0\,0\,\pi)$ configuration (No. 6, Table 2) which is alternatively described as $[\pi\,\pi\,\pi;\ \pi\,\pi\,\pi;\ -(\pi\,\pi\,\pi);\ \pi\,\pi\,\pi]$. A second configuration may be obtained from this by changing the sign of one of the constituent configurations: thus $[\pi\,\pi\,\pi;\ -(\pi\,\pi\,\pi);\ -(\pi\,\pi\,\pi);\ \pi\,\pi\,\pi]$. These two spin arrangements, disregarding moment orientation, have been proposed for Mn^{+2} in MnO and α-MnS; the first by SHULL *et al.*[13] and the second by Li.[14] Both spin arrangements have equal numbers of like and unlike neighbors for all spins at all distances, and they are energetically degenerate for isotropic first- and second-neighbor interactions. This degeneracy has already been noted by ANDERSON[1] and LUTTINGER.[2] In the first-mentioned case the orientations of the four $(\pi\,\pi\,\pi)$ configurations are such that there exists a single propagation vector; e.g. the arrangement is characterized by sheets of like spin alternating in sign along a [111] direction. The second configuration does not correspond to a single mode, but must be considered as a superposition of modes. The two types may in general, be distinguished by single-crystal neutron-diffraction data and in favorable cases by powder data. For MnO and α-MnS, a better explanation of the data is obtained with the first-mentioned configuration.[8]

It is of interest to point out also that no other distinct configuration having the same neighbor relations as the two given above can be found, for

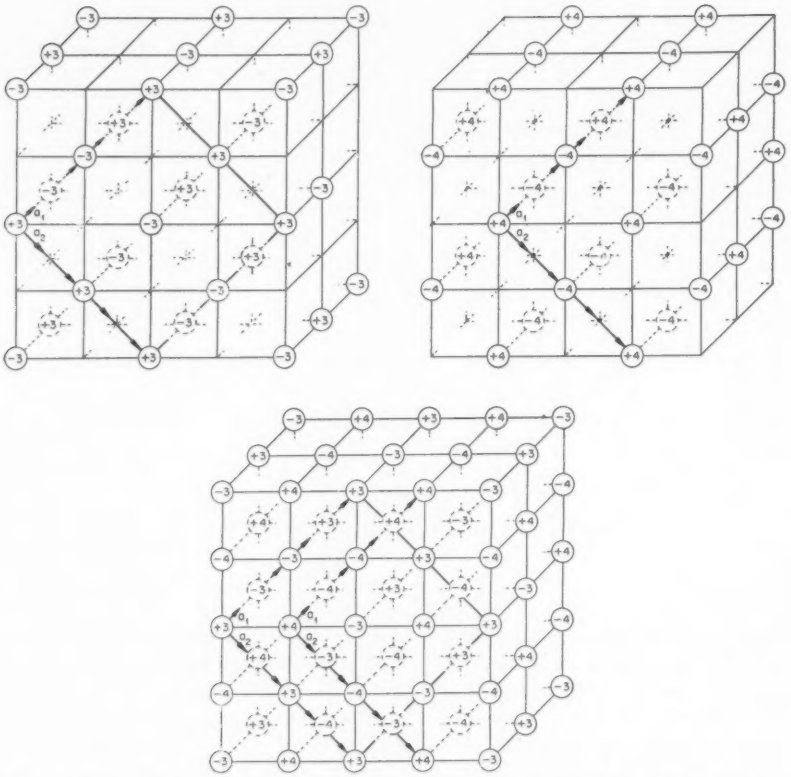

FIG. 7. Type-CE structure. If tetragonal sublattices are chosen, the configuration is Mn^{+3} $(\pi\, 0\, \pi)$; Mn^{+4} $(\pi\, \pi\, \pi)$.

all other sign permutations lead to equivalent configurations.

The derivation of other configurations based on the lattices considered here and for other point lattices may be carried out systematically in the manner illustrated above by considering various superpositions. Clearly, if the number of superpositions becomes large, the method loses its simplicity.

6. DIFFRACTION EFFECTS

Once a configuration of spins has been given, it is a straightforward matter to calculate the geometrical part of the structure amplitude. The results of such calculations are collected in Tables 7–10. Obviously the effect of moment direction on the intensity must be accounted for separately.

The magnetic unit cell for a given configuration may be chosen in general in a variety of ways. We have given two convenient alternative choices for configurations based on the simple cubic lattice. It is of interest to note that in no case does the unit cell required exceed $4a_0 \times 4a_0 \times 4a_0$, where a_0 is the magnitude of the lattice period.

Results for the face-centered and body-centered cubic cases are expressed in terms of the orthogonal rather than oblique coördinate system for convenience. Also, for convenience of intercomparison, we have not always chosen the smallest unit cell possible for each of the configurations.

Structure amplitudes for the configurations based on an hexagonal layer lattice are referred to orthohexagonal unit cells, examples of which are shown in Fig. 8.

Each configuration has a set of characteristic absences, so that even with powder data one or

VOL. 5 1958

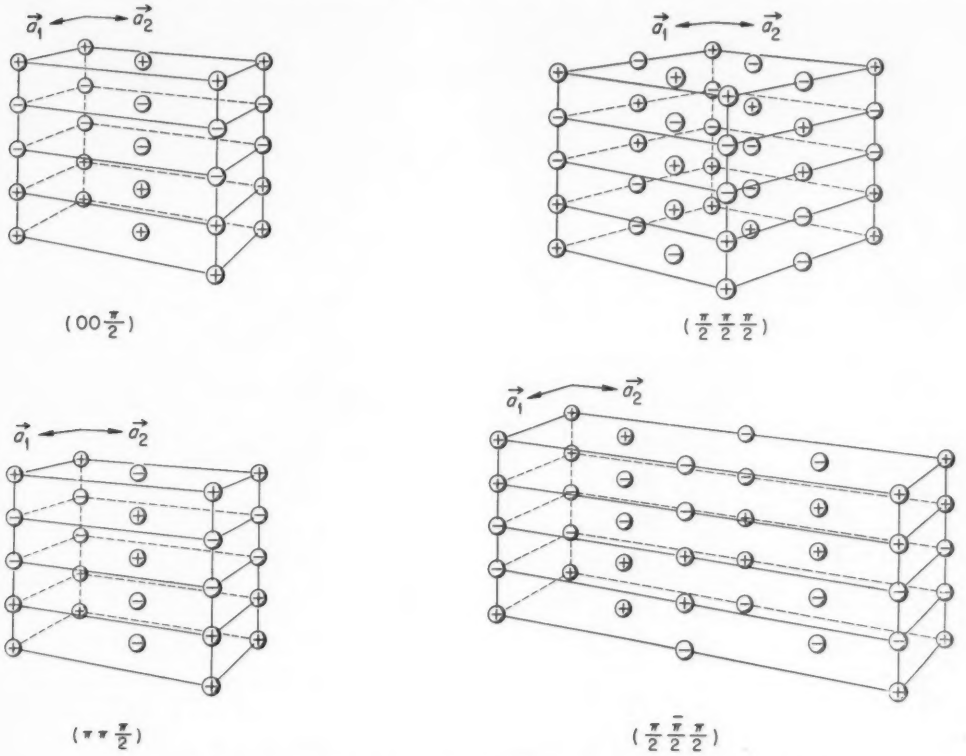

FIG. 8. Orthohexagonal unit cells for configurations on an hexagonal layer lattice.

more of the arrangements tabulated may be eliminated from consideration in a given experimental case simply by inspection.

Acknowledgements—We wish to express our appreciation to Dr. E. O. WOLLAN and Dr. M. K. WILKINSON for helpful conversations. One of us (H.A.G.) wishes to express his appreciation to the Physics Division of the Oak Ridge National Laboratory for its hospitality during the summer of 1956.

APPENDIX:

Formal derivation of possible ordered configurations

(a) *One dimensional chain*

We give a proof that our enumeration of spin configurations for a one-dimensional chain given by equation (13) exhausts all possibilities for ordered arrangements fulfilling the requirement that every spin has the same environment of like and unlike neighbors as every other spin.

We start from equation (10), which is

$$S_i = N^{-\frac{1}{2}} \sum_{k=1}^{N} q_k \left(\cos\frac{2\pi}{N} ik + \sin\frac{2\pi}{N} ik \right).$$

This is a completely general expression for the spins S_j—every possible configuration of spins can be described by assigning different values to the continuous variables q_k. The only restriction we have used is the cyclic boundary condition, which is clearly essential if the environment of each spin is to be identical, i.e. if surface effects are to be removed.

We also rewrite the constraint of equation (11), using the fact that it requires $S_{j+1} = \pm S_j$,

$$S_j(S_{j+m} + S_{j-m} \mp S_{j+1+m} \mp S_{j+1-m}] = 0. \tag{A1}$$

Expressing the spins S_j in terms of normal coördinates, q_k from equation (10) brings this into the form

Table 7. Structure amplitudes for configurations on a simple cubic lattice

Indices of allowed reflections are given for unit cells of the indicated size based on the cubic lattice periods and on the tetragonal lattice periods. In the latter case the sublattices given are those with origin at 000 and $(a_1' + a_2')/2$, respectively.

Cubic $2a_0 \times 2a_0 \times 2a_0$		Tetragonal			
		$\sqrt{2}a_0 \times \sqrt{2}a_0 \times 2a_0$		$2\sqrt{2}a_0 \times 2\sqrt{2}a_0 \times 2a_0$	
1	$0\,0\,0$ $H_1 = 2n$ $H_2 = 2n$ $H_3 = 2n$ $R = 8$	1	$0\,0\,0$; $0\,0\,0$ $H_1+H_2 = 2n$ $H_3 = 2n$ $R = 4$	1	
2	$0\,0\,\pi$ $H_1 = 2n$ $H_2 = 2n$ $H_3 = 2n+1$ $R = 8$	2	$0\,0\,\pi$; $0\,0\,\pi$ $H_1+H_2 = 2n$ $H_3 = 2n+1$ $R = 4$	2	$\pi\,\pi\,0$; $\pi\,\pi\,0$ $H_1 = 2n+1$ $H_2 = 2n+1$ $H_1+H_2 = 4n$ $H_3 = 2n$ $R = 16$
3	$\pi\,\pi\,0$ $H_1 = 2n+1$ $H_2 = 2n+1$ $H_3 = 2n$ $R = 8$	3	$0\,0\,0$; $-(0\,0\,0)$ $H_1+H_2 = 2n+1$ $H_3 = 2n$ $R = 4$	3	$\pi\,\pi\,\pi$; $\pi\,\pi\,\pi$ $H_1 = 2n+1$ $H_2 = 2n+1$ $H_1+H_2 = 4n$ $H_3 = 2n+1$ $R = 16$
4	$\pi\,\pi\,\pi$ $H_1 = 2n+1$ $H_2 = 2n+1$ $H_3 = 2n+1$ $R = 8$	4	$0\,0\,\pi$; $-(0\,0\,\pi)$ $H_1+H_2 = 2n+1$ $H_3 = 2n+1$ $R = 4$	4	

VOL. 5 1959

	$4a_0 \times 4a_0 \times 4a_0$		$2\sqrt{2}a_0 \times 2\sqrt{2}a_0 \times 4a_0$
5	$0\,0\,\frac{\pi}{2}\; H_1 = 4n\; H_2 = 4n\; H_3 = 4n \pm 1$ $R = 32(1 \pm i)$	5	$0\,0\,\frac{\pi}{2};\; 0\,0\,\frac{\pi}{2}\; H_1 = 2n\; H_2 = 2n\; H_1 + H_2 = 4n\; H_3 = 4n \pm 1$ $R = 16(1 \pm i)$
6	$\pi\,\pi\,\frac{\pi}{2}\; H_1 = 4n+2\; H_2 = 4n+2\; H_3 = 4n \pm 1$ $R = 32(1 \pm i)$	6	$0\,0\,\frac{\pi}{2};\; -\left(0\,0\,\frac{\pi}{2}\right) H_1 = 2n\; H_2 = 2n\; H_1 + H_2 = 4n+2\; H_3 = 4n \pm 1$ $R = 16(1 \pm i)$
7	$\frac{\pi}{2}\,\frac{\pi}{2}\,0\; H_1 = 4n \pm 1\; H_2 = 4n \pm 1\; H_3 = 4n$ $R = 32(1 \pm i)$	7	$0\,\pi\,0;\; 0\,\pi\,0\; H_1 = 2n\; H_2 = 2n+1\; H_3 = 4n\; H_1 + H_2 = 4n \pm 1$ $R = 16(1 \pm i)$
8	$\frac{\pi}{2}\,\frac{\pi}{2}\,\pi\; H_1 = 4n \pm 1\; H_2 = 4n \pm 1\; H_3 = 4n+2$ $R = 32(1 \pm i)$	8	$0\,\pi\,\pi;\; 0\,\pi\,\pi\; H_1 = 2n\; H_2 = 2n+1\; H_3 = 4n+2$ $R = 16(1 \pm i)$
9	$0\,\pi\,\frac{\pi}{2}\; H_1 = 4n\; H_2 = 4n+2\; H_3 = 4n \pm 1$ $R = 32(1 \pm i)$	9	$\pi\,\pi\,\frac{\pi}{2};\; \pi\,\pi\,\frac{\pi}{2}\; H_1 = 2n+1\; H_2 = 2n+1\; H_1 + H_2 = 4n\; H_3 = 4n \pm 1$ $R = 16(1 \pm i)$
10	$\frac{\pi}{2}\,\frac{\pi}{2}\,\frac{\pi}{2}\; H_1 = 4n \pm 1\; H_2 = 4n \pm 1\; H_3 = 4n \pm 1$ $R = 32(1 \pm i)$	10	$0\,\pi\,\frac{\pi}{2};\; 0\,\pi\,\frac{\pi}{2}\; H_1 = 2n\; H_2 = 2n+1\; H_1 + H_2 = 4n \pm 1\; H_3 = 4n \pm 1$ $R = 16(1 \pm i)$

Table 8. Structure amplitudes for configurations on a face-centered cubic lattice

The unit cells are given in terms of the orthogonal coördinate system. The sublattices are those with origin at 000; $(a_1'+a_2')/2$; $(a_2'+a_3')/2$; and $(a_1'+a_3')/2$, respectively.

	$\omega_1\omega_2\omega_3$		$2a_0'\times 2a_0'\times 2a_0'$
1	0 0 0	0 0 0; 0 0 0; 0 0 0; 0 0 0	$H_1=2n\ H_2=2n\ H_3=2n\ H_1+H_2=4n\ H_2+H_3=4n\ H_1+H_3=4n$ $R=32$
2	$0\ \pi\ \pi$	0 0 0; $-(0\,0\,0)$; $(0\,0\,0)$; $-(0\,0\,0)$	$H_1=2n\ H_2=2n\ H_3=2n\ H_1+H_2=4n+2\ H_2+H_3=4n$ $H_1+H_3=4n+2$ $R=32$
3	$\begin{matrix}\pi & \pi\\ 0 & -\\ 2 & 2\end{matrix}$	$\pi\,0\,0$; $\pi\,0\,0$; $\pi\,0\,0$; $\pi\,0\,0$	$H_1=2n+1\ H_2=2n\ H_3=2n\ H_2+H_3=4n$ $R=16(1\pm i)$
4	$\begin{matrix}\pi & \bar\pi\\ \pi & -\\ 2 & 2\end{matrix}$	$\pi\,0\,0$; $-(\pi\,0\,0)$; $-(\pi\,0\,0)$; $\pi\,0\,0$	$H_1=2n+1\ H_2=2n\ H_3=2n\ H_2+H_3=4n+2$ $R=16(1\pm i)$
5	$\begin{matrix}\pi & \bar\pi\\ 0 & -\\ 2 & 2\end{matrix}$	$0\,\pi\,\pi$; $-(0\,\pi\,\pi)$; $0\,\pi\,\pi$; $0\,\pi\,\pi$	$H_1=2n\ H_2=2n+1\ H_3=2n+1\ H_2+H_3=4n$ $R=16(1\pm i)$
6	$0\ 0\ \pi$	$\pi\,\pi\,\pi$; $\pi\,\pi\,\pi$; $-(\pi\,\pi\,\pi)$; $\pi\,\pi\,\pi$	$H_1=2n+1\ H_2=2n+1\ H_3=2n+1\ H_1+H_2=4n\ H_2+H_3=4n+2$ $H_1+H_3=4n$ $R=32$
			$4a_0'\times 4a_0'\times 4a_0'$
7	$\begin{matrix}\pi & \pi & \pi\\ - & - & -\\ 2 & 2 & 2\end{matrix}$	$\begin{matrix}\pi&\pi&\pi\\-&-&-\\2&2&2\end{matrix}$ $\begin{matrix}\bar\pi&\bar\pi&\bar\pi\\-&-&-\\2&2&2\end{matrix}$ $\begin{matrix}\bar\pi&\bar\pi&\bar\pi\\-&-&-\\2&2&2\end{matrix}$ $\begin{matrix}\bar\pi&\bar\pi&\bar\pi\\-&-&-\\2&2&2\end{matrix}$	$H_1,\ H_2,\ H_3=4n\pm 1\cdot H_i+H_j=8n\pm 2$ $R=128(1\pm i)$
8	$\begin{matrix}\bar\pi & \bar\pi & \pi\\ - & - & -\\ 2 & 2 & 2\end{matrix}$	$\begin{matrix}\pi&\pi&\pi\\-&-&-\\2&2&2\end{matrix}$; $\begin{matrix}\bar\pi&\bar\pi&\bar\pi\\-&-&-\\2&2&2\end{matrix}$; $-\left(\begin{matrix}\bar\pi&\bar\pi&\bar\pi\\-&-&-\\2&2&2\end{matrix}\right)$; $-\left(\begin{matrix}\bar\pi&\bar\pi&\bar\pi\\-&-&-\\2&2&2\end{matrix}\right)$	$H_1,\ H_2,\ H_3=4n\pm 1\ H_1+H_2=8n\pm 2\ H_2+H_3=8n\pm 6$ $H_1+H_3=8n\pm 6$ $R=128(1\pm i)$

VOL. 5 1958

Table 9. Structure amplitudes for configurations on a body-centered cubic lattice

The unit cells are given in terms of the orthogonal coördinate system. The sublattices have origin at 000 and $(\boldsymbol{a}_1' + \boldsymbol{a}_2' + \boldsymbol{a}_3')/2$, respectively.

	$\omega_1\omega_2\omega_3$		$2a_0' \times 2a_0' \times 2a_0'$	
1	0 0 0	0 0 0; 0 0 0	$H_1 = 2n\ H_2 = 2n\ H_3 = 2n\ \Sigma H_i = 4n$	$R = 16$
2	$\pi\ \pi\ \pi$	0 0 0; $-(0\ 0\ 0)$	$H_1 = 2n\ H_2 = 2n\ H_3 = 2n\ \Sigma H_i = 4n+2$	$R = 16$
3	$\pi\ \bar{\pi}\ \bar{\pi}$ $-\ -\ -$ 2 2 2	0 0 π; 0 0 π	$H_1 = 2n\ H_2 = 2n\ H_3 = 2n+1$	$R = 8(1 \pm i)$
4	0 0 π	0 π π; 0 π π	$H_1 = 2n\ H_2 = 2n+1\ H_3 = 2n+1\ \Sigma H_i = 4n$	$R = 16$
5	$\pi\ \pi\ \pi$ $-\ -\ -$ 2 2 2	$\pi\ \pi\ \pi$; $\pi\ \pi\ \pi$	$H_1 = 2n+1\ H_2 = 2n+1\ H_3 = 2n+1$	$R = 8(1 \pm i)$
			$4a_0' \times 4a_0' \times 4a_0'$	
6	$\pi\ \bar{\pi}$ $-\ -0$ 2 2	$\pi\ \pi$ $\quad \bar{\pi}\ \bar{\pi}$ 0 $-$ $-$; 0 $-$ $-$ 2 2 $\quad$ 2 2	$H_1 = 4n\ H_2,\ H_3 = 4n \pm 1\ \Sigma H_i = 8n \pm 2$	$R = 64(1 \pm i)$
7	$\bar{\pi}\ \pi$ $-\ -\pi$ 2 2	$\pi\ \pi$ $\quad -\left(\bar{\pi}\ \bar{\pi}\right)$ 0 $-$ $-$; $\left(0 - -\right)$ 2 2 $\quad$ 2 2	$H_1 = 4n\ H_2,\ H_3 = 4n \pm 1\ \Sigma H_i = 8n \mp 2$	$R = 64(1 \mp i)$
8	π 0 $\pi-$ 2	$\pi\ \pi$ $\quad \pi\ \pi$ $\pi-\ -$; $\pi-\ -$ 2 2 $\quad$ 2 2	$H_1 = 4n+2\ H_2,\ H_3 = 4n \pm 1\ \Sigma H_i = 8n$	$R = 64(1 \pm i)$

$$0 = \sum_{k=1}^{N} q_k \cos\frac{2\pi}{N}mk\left[\cos\frac{2\pi}{N}jk \times \right.$$
$$\times\left(1 \mp \cos\frac{2\pi}{N}k \mp \sin\frac{2\pi}{N}k\right) +$$
$$\left. + \sin\frac{2\pi}{N}jk\left(1 \mp \cos\frac{2\pi}{N}k \pm \sin\frac{2\pi}{N}k\right)\right] \quad \text{(A2)}$$

Multiplying by $\cos 2\pi mk/N$, and summing m from 1 to N, there results

$$\begin{aligned} 0 = {} & q_\omega[\cos\omega j(1 \mp \cos\omega \mp \sin\omega) + \\ & + \sin\omega j(1 \mp \cos\omega \pm \sin\omega)] + \\ & + q_{2\pi-\omega}[\cos\omega j(1 \mp \cos\omega \pm \sin\omega) - \\ & - \sin\omega j(1 \mp \cos\omega \mp \sin\omega)] \end{aligned} \quad \text{(A3)}$$

where $\omega = 2\pi k/N$ ranges from 0 to 2π as $N \to \infty$. This equation is to hold for all values of j from 1 to N, and the choice of plus or minus signs can change arbitrarily with j. Clearly the values $\omega = \pi,\ 2\pi$ are solutions of equation (A3), since for these values every term in round brackets can be made zero. For $\omega = 2\pi$, we must choose the upper signs for all j, corresponding to the ferromagnetic ordering $S_{j+1} = S_j$ for all values of j. (As the number of spins $N \to \infty$, the lowest value of $\omega \to 0$, and gives the same configuration as $\omega = 2\pi$. We have preferred to use $\omega = 0$ in the text.) For $\omega = \pi$, the lower signs must be chosen for all j corresponding to the pure antiferromagnetic ordering $S_{j+1} = -S_j$ for all j.

In addition to $\omega = \pi,\ 2\pi$, there are the solutions $\omega = \pi/2$ or $3\pi/2$, for which we can still make the terms in the round brackets equal to zero. To see this, we write out equation (A3) for $\omega = \pi/2$,

$$0 = q_{\pi/2}\left[\cos\frac{\pi}{2}j(1 \mp 1) + \sin\frac{\pi}{2}j(1 \pm 1)\right] +$$
$$+ q_{3\pi/2}\left[\cos\frac{\pi}{2}j(1 \pm 1) - \sin\frac{\pi}{2}j(1 \mp 1)\right]. \quad \text{(A4)}$$

This can be satisfied by putting $q_{3\pi/2} = 0$, and choosing

Table 10. *Structure amplitudes for ordered configurations on an hexagonal layer lattice*

Allowed reflections are indexed on orthohexagonal unit cells of the indicated size.

	*Ortho*hexagonal indexing $a_1 = a_0$ $a_2 = \sqrt{3}a_0$ $a_3 = 4c_0$	
$0\,0\,0$	$H_1+H_2 = 2n$ $H_3 = 4n$	$R = 8$
$0\,0\,\pi$	$H_1+H_2 = 2n$ $H_3 = 4n+2$	$R = 8$
$0\,0\,\frac{\pi}{2}$	$H_1+H_2 = 2n$ $H_3 = 4n\pm1$	$R = 4(1\pm i)$
$\pi\,\pi\,0$	$H_1+H_2 = 2n+1$ $H_3 = 4n$	$R = 8$
$\pi\,\pi\,\pi$	$H_1+H_2 = 2n+1$ $H_3 = 4n+2$	$R = 8$
$\pi\,\pi\,\frac{\pi}{2}$	$H_1+H_2 = 2n+1$ $H_3 = 4n\pm1$	$R = 4(1\pm i)$
	*Ortho*hexagonal indexing $a_1 = 2a_0$ $a_2 = \sqrt{3}a_0$ $a_3 = 4c_0$	
$\frac{\pi}{2}\,\frac{\pi}{2}\,0$	$H_1 = 2n+1$ $H_1+2H_2 = 4n\pm1$ $H_3 = 4n$	$R = 8(1\pm i)$
$\frac{\pi}{2}\,\frac{\pi}{2}\,\pi$	$H_1 = 2n+1$ $H_1+2H_2 = 4n\pm1$ $H_3 = 4n+2$	$R = 8(1\pm i)$
$\frac{\pi}{2}\,\frac{\pi}{2}\,\frac{\pi}{2}$	$H_1 = 2n+1$ $H_1+2H_2 = 4n\pm1$ $H_3 = 4n\pm1$	$R = 8(1\pm i)$
	*Ortho*hexagonal indexing $a_1 = a_0$ $a_2 = 2\sqrt{3}a_0$ $a_3 = 4c_0$	
$\frac{\pi}{2}\,\frac{\bar{\pi}}{2}\,0$	$H_2 = 2n+1$ $2H_1+H_2 = 4n\pm1$ $H_3 = 4n$	$R = 8(1\pm i)$
$\frac{\pi}{2}\,\frac{\bar{\pi}}{2}\,\pi$	$H_2 = 2n+1$ $2H_1+H_2 = 4n\pm1$ $H_3 = 4n+2$	$R = 8(1\pm i)$
$\frac{\pi}{2}\,\frac{\bar{\pi}}{2}\,\frac{\pi}{2}$	$H_2 = 2n+1$ $2H_1+H_2 = 4n\pm1$ $H_3 = 4n\mp1$	$R = 8(1\pm i)$

the upper sign for even j, and the lower sign for odd j. Alternatively, $q_{\pi/2}$ can be put equal to zero, and the equation satisfied by the reverse choice of signs. These sign choices generate the two configurations $\omega = \pi/2,\ 3\pi/2$, respectively, which are shown in Fig. 1. They differ only by a translation along the chain by one lattice spacing.

Equation (A3) is identical if written for $\omega = 3\pi/2$, and leads to the same configurations as just obtained.

No other values of ω are possible, because the terms in round brackets in equation (A3) are not zero for any value of ω other than $0,\ \pi/2,\ \pi,\ 3\pi/2$. For, if we satisfy the equation for some particular value of j by choosing some

other ω, say ω_i, it clearly cannot be satisfied with this ω_i for all values of j from 1 to N.

(b) *Three-dimensional lattice*

The proof that the configurations given by equation (18) are the only ones satisfying our equivalence requirement as expressed by equation (17) exactly parallels the steps used for the one-dimensional chain. Since again our constraint requires $S^2_{\boldsymbol{R}+\boldsymbol{a}_i} = S^2_{\boldsymbol{R}}$, we write it in the form

$$S_{\boldsymbol{R}}[S_{\boldsymbol{R}+\boldsymbol{A}_L}+S_{\boldsymbol{R}-\boldsymbol{A}_L}\mp S_{\boldsymbol{R}+\boldsymbol{a}_i+\boldsymbol{A}_L}\mp S_{\boldsymbol{R}+\boldsymbol{a}_i-\boldsymbol{A}_L}] = 0 \tag{A5}$$

Expressing the spins appearing here in terms of normal coördinates gives

$$\begin{aligned} 0 = \sum_{\boldsymbol{k}} q_{\boldsymbol{k}} \cos \boldsymbol{k}\cdot\boldsymbol{A}_L[&\cos \boldsymbol{k}\cdot\boldsymbol{R}(1\mp\cos \boldsymbol{k}\cdot\boldsymbol{a}_i\mp \\ &\mp\sin \boldsymbol{k}\cdot\boldsymbol{a}_i)+\sin \boldsymbol{k}\cdot\boldsymbol{R}(1\mp\cos \boldsymbol{k}\cdot\boldsymbol{a}_i\pm \\ &\pm\sin \boldsymbol{k}\cdot\boldsymbol{a}_i)] \end{aligned} \tag{A6}$$

where $\boldsymbol{k} = 2\pi(k_1\boldsymbol{b}_1+k_2\boldsymbol{b}_2+k_3\boldsymbol{b}_3)/N^{\frac{1}{3}}$, the $\boldsymbol{b}_i$ are basis vectors of the reciprocal lattice and the triple sum is over $1 \leqslant k_i \leqslant N^{\frac{1}{3}} i = 1, 2, 3$. Multiplying by $\cos \boldsymbol{k}'\cdot\boldsymbol{A}_L$ and summing over all lattice vectors $\boldsymbol{A}_L$ results in the equation

$$\begin{aligned} 0 = q_{\boldsymbol{k}}[&\cos \boldsymbol{k}'\cdot\boldsymbol{R}(1\mp\cos \boldsymbol{k}'\cdot\boldsymbol{a}_i\mp\sin \boldsymbol{k}'\cdot\boldsymbol{a}_i)+ \\ &+\sin \boldsymbol{k}'\cdot\boldsymbol{R}(1\mp\cos \boldsymbol{k}'\cdot\boldsymbol{a}_i\pm\sin \boldsymbol{k}'\cdot\boldsymbol{a}_i)]+ \\ &+q_{\boldsymbol{K}-\boldsymbol{k}}[\cos \boldsymbol{k}'\cdot\boldsymbol{R}(1\mp\cos \boldsymbol{k}'\cdot\boldsymbol{a}_i\pm\sin \boldsymbol{k}'\cdot\boldsymbol{a}_i)- \\ &-\sin \boldsymbol{k}'\cdot\boldsymbol{R}(1\mp\cos \boldsymbol{k}'\cdot\boldsymbol{a}_i\mp\sin \boldsymbol{k}'\cdot\boldsymbol{a}_i)] \end{aligned} \tag{A7}$$

with $\boldsymbol{K} = 2\pi(\boldsymbol{b}_1+\boldsymbol{b}_2+\boldsymbol{b}_3)$. There are three such equations, one for each of the basis vectors of the real lattice, $\boldsymbol{a}_1, \boldsymbol{a}_2, \boldsymbol{a}_3$, and again each equation must be satisfied for all lattice positions $\boldsymbol{R}$. By exactly the same reasoning as for the one-dimensional chain, their solution is the set

$$\omega_i = \frac{2\pi k_i}{N^{\frac{1}{3}}} = 0, \pm\frac{\pi}{2}, \pi \qquad i = 1, 2, 3 \tag{A8}$$

as given in the text. Again these are the only values for ω_i for which equation (A7) can be satisfied for all lattice positions $\boldsymbol{R}$ because the terms in the round brackets in (A7) cannot be made zero for any other choice of ω_i.

REFERENCES

1. Anderson P. W. *Phys. Rev.* **79,** 705 (1950).
2. Luttinger J. M. *Phys. Rev.* **81,** 1015 (1951).
3. Smart J. S. *Phys. Rev.* **86,** 968 (1952); **90,** 55 (1953).
4. Van Vleck J. H. *J. Phys. Radium* **12,** 262 (1951).
5. Wollan E. O. and Koehler W. C. *Phys. Rev.* **100,** 545 (1955).
6. Koehler W. C. and Wollan E. O. *J. Phys. Chem. Solids* **2,** 100 (1957).
7. Koehler W. C., Wollan, E. O., Wilkinson, M. K. and Cable J. W. to be published.
8. Corliss L., Elliot N., and Hastings J. *Phys. Rev.* **104,** 924 (1956).
9. Henshaw D. G. and Brockhouse B. N. *Bull. Amer. Phys. Soc.* **2,** 9 (1957).
10. Wilkinson M. K., Koehler W. C., Wollan E. O., and Cable J. W. *Bull. Amer. Phys. Soc.* **2,** 129 (1957).
11. Erickson R. A. *Phys. Rev.* **90,** 779 (1953).
12. Erickson R. A. *Thesis, Texas A and M College* (1952).
13. Shull C. G., Strauser W. A., and Wollan E. O. *Phys. Rev.* **83,** 333 (1951).
14. Li Y. Y. *Phys. Rev.* **100,** 627 (1955).

J. Phys. Chem. Solids Pergamon Press 1958. Vol. 5. pp. 202–207.

THE GROWTH OF SINGLE CRYSTALS OF MAGNETIC GARNETS

J. W. NIELSEN and E. F. DEARBORN

Bell Telephone Laboratories, Inc.,

Murray Hill, New Jersey

(*Received* 29 *August* 1957)

Abstract—Crystals of magnetic garnets, $Y_3Fe_5O_{12}$, $Sm_3Fe_5O_{12}$, $Er_3Fe_5O_{12}$, and $Gd_3Fe_5O_{12}$, suitable for many research purposes have been grown from iron-rich melts of lead oxide. A satisfactory composition is PbO 52·5, Fe_2O_3 44, and M_2O_3 3·5 mole per cent, where M is Y, Sm, Er, or Gd. Portions of the phase equilibrium diagrams for the systems Fe_2O_3–$YFeO_3$ and PbO–Y_2O_3–Fe_2O_3 have been approximately determined. All the data obtained concerning the growth of magnetic garnets are consistent with these diagrams.

1. INTRODUCTION

THE recent discovery[1,2] of a new series of magnetic compounds which has the formula $M_3Fe_5O_{12}$, where M is yttrium or certain rare-earth ions, and which exhibits the garnet structure, suggested the desirability of obtaining single crystals of these new materials for use in fundamental experimentation.[2–5] REMEIKA[6] has demonstrated that single crystals of many of the perovskite-like orthoferrites can be grown from molten lead oxide. Because several of these—$YFeO_3$, $SmFeO_3$, $GdFeO_3$, etc.—contain the same components as the magnetic garnets, it was thought that the garnets might also be crystallized from molten lead oxide under the proper conditions. Yttrium–iron garnet (Y.I.G.) was selected for the first attempts.

Because the phase equilibrium diagrams required for selection of the suitable compositions for the growth of garnet crystals were not known, the compositions and conditions for garnet crystallization were found at first empirically. After the first traces of Y.I.G. crystals had been obtained, the solutions to two problems were undertaken: (1) the approximate determination of that part of the phase equilibrium diagram of the system Fe_2O_3–Y_2O_3–PbO in which Y.I.G. is the stable solid phase; and (2) the search for the best conditions for the growth of Y.I.G. crystals. The partial solution of these problems has resulted in the growth of single crystals of $Y_3Fe_5O_{12}$ (Y.I.G.), $Gd_3Fe_5O_{12}$ (Gd.I.G.), $Sm_3Fe_5O_{12}$ (Sm.I.G.), $Er_3Fe_5O_{12}$ (Er.I.G.), and Y.I.G. with part of the iron replaced by gallium.

2. EXPERIMENTAL METHOD

(a) *Crystal growth*

Reagent-grade oxides were used in all experiments. The oxides were placed in 100-ml platinum crucibles which were fitted with tightly crimped lids to minimize loss by evaporation. The amount of sample was such that the dry oxides just filled the crucible. The filled crucibles were placed in a furnace equipped with a silicon carbide muffle heated by silicon carbide resistance heaters. Zirconium oxide setter batts were used to prevent attack on the platinum by silicon carbide. The crucibles were placed in the furnace at temperatures of 1300–1370°C, held at constant temperature a few hours, and then cooled slowly at a rate of 1–5°C/hr to the desired withdrawal temperature, after which they were withdrawn and either cooled in air or quenched in water. For example, to obtain Er.I.G. crystals, a mixture of 100 g PbO, 60 g Fe_2O_3, and 11·5 g Er_2O_3, was heated at 1350°C for 5 hr, cooled at 1°C/hr to 930°C, and then withdrawn and quenched.

In each run the crucible and contents were weighted to determine evaporation losses. The solidified melt was separated from the crystals by heating the entire mass in dilute nitric acid. The crystals of the four solid phases which one may observe in these melts—Fe_2O_3, magnetoplumbite ($PbFe_{12}O_{19}$), orthoferrite ($MFeO_3$), and garnet—are all insoluble in hot dilute nitric acid.

The solid phases were separated from each other by utilizing the differences in their Curie temperatures, T_c. In a typical run three solid phases would usually be found: Fe_2O_3, $Y_3Fe_5O_{12}$ (T_c 275°C), and $PbFe_{12}O_{19}$ (T_c 360°C). By heating the mixture to 350°C and passing a small magnet over it repeatedly, then repeating the procedure below 275°C, the crystalline mixture could be separated into $PbFe_{12}O_{19}$, Y.I.G., and Fe_2O_3. To obtain good separation, it was necessary to repeat the procedure on the three fractions several times, with some crushing of the samples between passes. The crushing reduced the error resulting from epitaxial growth.

(b) The phase diagram for the system Fe_2O_3–$YFeO_3$

The samples used for the phase diagram Fe_2O_3–$YFeO_3$ were prepared by carefully mixing the desired amounts of the oxides in a mortar, pressing the powders into pills, and firing the pills for 2 hr at 1300°C. The pills were then crushed until very finely divided, pressed into shape again, and fired for 16 hr at 1300°C. The pellets were crushed, small samples placed in a platinum strip furnace, and the point of complete melting observed with an optical pyrometer.* The observed melting points from three to five separate portions of the same pellet agreed to within ±10°C.

Quenched melts prepared from single crystals of Y.I.G. and $YFeO_3$ were examined by X-ray diffraction; it was established that Y.I.G. melts incongruently and $YFeO_3$ congruently. The melting points of the single crystals were measured by the method outlined above, except that Y.I.G. was carefully observed for the onset of melting rather than for complete melting.

3. DISCUSSION OF EXPERIMENTAL RESULTS

(a) Procedure

Early attempts to grow crystals of Y.I.G. were made, using PbO concentrations near those used by REMEIKA.[6] It was soon discovered that the primary phase was $YFeO_3$ for compositions above about 70 mole per cent PbO and from 2 to about 10 mol. per cent Y_2O_3 (see Fig. 1). After a number of unsuccessful runs, it was suspected that Y.I.G. might be an incongruently melting compound. This would put the liquidus region to the left of the composition of Y.I.G. on the phase equilibrium diagram for Y_2O_3 and Fe_2O_3† and usually suggests a narrow liquidus range. This would further suggest that the field in the ternary diagram for PbO–Y_2O_3–Fe_2O_3 from which Y.I.G. crystallizes may be narrow and may perhaps terminate before high PbO concentrations are reached. Therefore, runs were made with high iron and low yttrium contents so that, as crystallization proceeded, the composition of the melt would drift toward the garnet field which was assumed to be present. These runs were successful and their compositions are shown in Fig. 1.

(b) Binary phase equilibrium diagrams

Evidence for the validity of the assumptions on

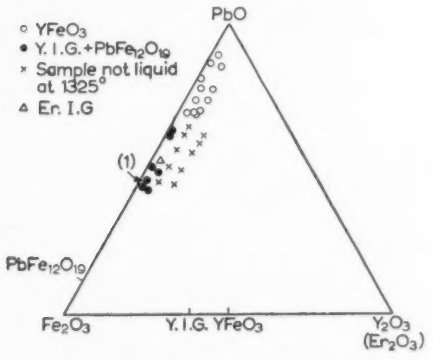

FIG. 1. Initial compositions of trial-and-error runs.

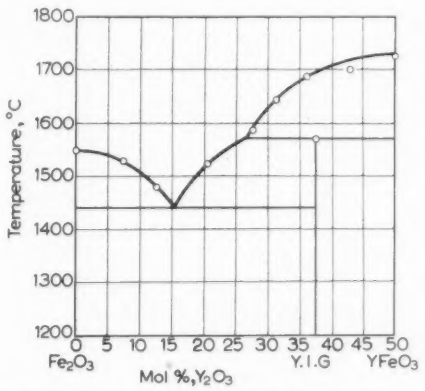

FIG. 2. Proposed phase diagram for Fe_2O_3 and $YFeO_3$.

* The melting point of barium titanate was measured as a check on the accuracy with which the pyrometer could be used to measure these melting points and was found to be 1625°C. RASE and ROY[7] report 1618°C as the melting point of $BaTiO_3$. This is excellent agreement for this technique.

† The system Fe_2O_3–Y_2O_3 is not, strictly speaking, a two-component system if kept in contact with air. At the temperatures and compositions of interest here, this pseudo-binary system behaves as a true binary system. Similarly, the pseudo-ternary system PbO–Fe_2O_3–Y_2O is conveniently considered a true ternary system in this work.

which the successful runs were made is shown by the phase diagram in Fig. 2. The liquidus curve for Y.I.G. is roughly 15–27 mole per cent Y_2O_3. Y.I.G. melts incongruently at about 1580°C.

In spite of the high precision of the data and the check with the reported melting point of $BaTiO_3$, the temperatures shown on the phase diagram must be accepted with reservation. The authors consider this binary diagram to be semi-quantitative only, for errors of 20–50°C are not uncommon in phase diagrams determined in a similar way.

Further assumptions had to be made about the binary diagram for the system PbO–Fe_2O_3. Some work up to 1000°C has been done on this system by Cocco.[8] Although his diagram is not correct in detail, it indicates that the only compound formed by PbO and Fe_2O_3 which is stable above 1000°C is $PbFe_{12}O_{19}$, magneto-plumbite (mistakenly labelled $PbFe_{10}O_{16}$ by Cocco). This compound was found by the authors to melt incongruently at 1540±30°C. With this information it was predicted that both Fe_2O_3 and $PbFe_{12}O_{19}$ might be found in the melts prepared for the trial runs from which Y.I.G. was first precipitated. As indicated earlier, both compounds were indeed found in the melts; in fact, $PbFe_{12}O_{19}$ was by far the most prevalent phase.

The presence of Fe_2O_3, $PbFe_{12}O_{19}$, and Y.I.G. simultaneously is a violation of the phase rule and establishes that the system is not at equilibrium during the growth cycle. It was decided that more information was needed about the yield of the three solid phases present as a function of growth rate and temperature in order to establish which phase was in an unstable state.

(*c*) *Discussion of the crystal yields*

The many runs made to determine the relative amounts of the solid phases, Y.I.G., Fe_2O_3, and $PbFe_{12}O_{19}$, at different temperatures were carried out under conditions which were identical except for the rate of cooling. These runs were all begun at 1325±5°C and had the initial composition PbO 45, Fe_2O_3 53, and Y_2O_3 2 mole per cent, which is designated (1) in Fig. 1 and will be so designated in what follows. The runs were withdrawn at different temperatures, quenched, and the crystal yields determined as previously described.

The crystal yields of Fe_2O_3, Y.I.G., and $PbFe_{12}O_{19}$ are shown plotted against temperature of withdrawal in Figs. 3 and 4. From Fig. 3 it is clear that the yield of Fe_2O_3 depends on the cooling rate and that Fe_2O_3 apparently begins to dissolve somewhere below 1260°C. At 1260°C neither Y.I.G. nor $PbFe_{12}O_{19}$ is observed, and at 1325°C

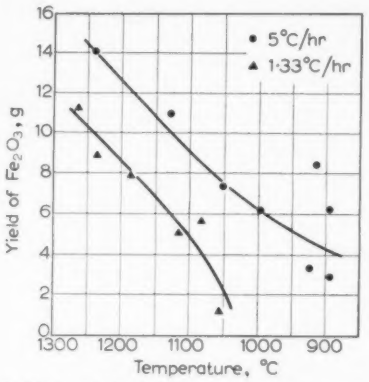

FIG. 3. Yield of Fe_2O_3 as a function of temperature and growth rate for identical initial conditions.

composition (1) is entirely liquid. Both Y.I.G. and $PbFe_{12}O_{19}$ appear at a temperature somewhat above 1235°C and crystallize together rapidly below that point.

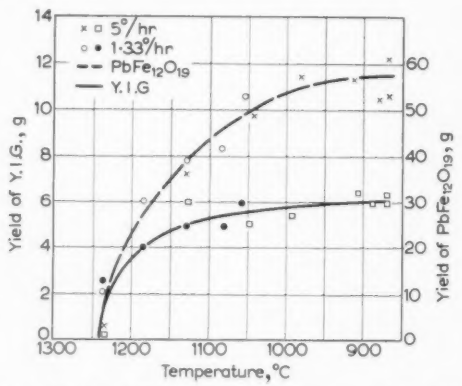

FIG. 4. Yields of $PbFe_{12}O_{19}$ and Y.I.G. as a function of temperature for identical initial conditions.

It is apparent from Figs. 3 and 4 that although the data scatter somewhat because of difficulties in separating the phases and exactly duplicating conditions, the primary phase crystallizing from composition (1) is Fe_2O_3. At a temperature somewhat above 1235°C, the liquidus composition

reaches the boundary line between either Fe_2O_3 and $PbFe_{12}O_{19}$, or Fe_2O_3 and Y.I.G. In any case the point of intersection is very near the quadruple point resulting from the intersection of the boundary lines between Fe_2O_3 and Y.I.G., Fe_2O_3 and $PbFe_{12}O_{19}$, and Y.I.G. and $PbFe_{12}O_{19}$ (see Fig. 5).

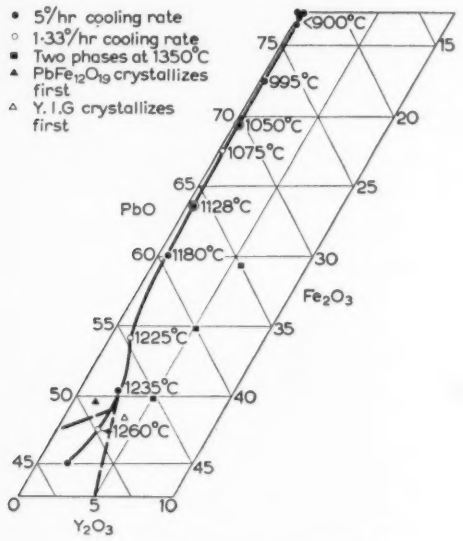

FIG. 5. The crystallization path.

At this point, upon further decrease of temperature Fe_2O_3 should dissolve and the crystallization path should follow the boundary between Y.I.G. and $PbFe_{12}O_{19}$ to give large crystals of both phases. Lead oxide systems are sluggish, however, and apparently the solution of Fe_2O_3 does not occur rapidly. Since all the solid phases are less dense than PbO, they float on the surface of the melt, and the new phases, Y.I.G. and $PbFe_{12}O_{19}$, thus lift the Fe_2O_3 partly off the melt in many cases. This contributes to the scatter in the Fe_2O_3 yield, particularly at high growth rates. In a later run cooled to 1200°C and held there for 4 days before further cooling, no Fe_2O_3 was found.

(d) Melt compositions on the crystallization path

The results of chemical analyses of quenched melts prepared by interrupting crystal-growth runs at different temperatures are shown in Fig. 5, which is a section of the ternary diagram for the system Fe_2O_3–Y_2O_3–PbO. The initial melt composition was (1), shown at the start of the crystallization curve. It will be noted immediately that the melts cooled at two different rates have compositions which fall on the same smooth curve within the limits of experimental error. Although it has been established that the melts were not in equilibrium with the crystalline phases, since Fe_2O_3 was present in all runs, the presence of Fe_2O_3 has little effect on the melt compositions. This may be explained as follows: If the Fe_2O_3 had all dissolved, it would necessarily be distributed among the three phases present. Since almost all the system is melt and $PbFe_{12}O_{19}$, and since the undissolved Fe_2O_3 represents less than 5 per cent of the system by weight, the melt composition is quite insensitive to changes in the small amount of Fe_2O_3 present. In other words, since $PbFe_{12}O_{19}$ is 85 mole per cent Fe_2O_3, crystals which are all $PbFe_{12}O_{19}$ and crystals which are mostly $PbFe_{12}O_{19}$ and partly Fe_2O_3 are in contact with melts of very nearly the same composition. This suggests that although the crystal-growth runs cannot be at equilibrium, the melt compositions observed are very close to the equilibrium compositions, and for most purposes the melt composition curve shown in Fig. 5 may be considered a true liquidus curve.

Fig. 5 also indicates the region in which the quadruple point, Fe_2O_3–Y.I.G.–$PbFe_{12}O_{19}$–liquid, must be located. Only Fe_2O_3 is present as a solid phase in the run interrupted at 1260°C. Two runs of slightly different compositions, shown by the triangular points, yielded $PbFe_{12}O_{19}$ and Y.I.G. as primary phases. These three points, together with the point at 1235°C in which run Fe_2O_3 and small amounts of Y.I.G. and $PbFe_{12}O_{19}$ were observed, surround the quadruple point. An estimate of its true location is sketched in Fig. 5. The temperature at the quadruple point is believed to be between 1235 and 1250°C.

(e) The magnetic garnet crystals

The following magnetic garnets have been grown by the method described above: $Y_3Fe_5O_{12}$, $Er_3Fe_5O_{12}$, $Sm_3Fe_5O_{12}$, $Gd_3Fe_5O_{12}$, and $Y_3Ga_xFe_{5-x}O_{12}$. The rare-earth garnets were all grown from the composition designated by the triangular point in Fig. 1. The presence of gallium in the three-component garnet was established by X-ray diffraction.

All the magnetic garnets crystallize with a habit

similar to that often observed in natural garnets, i.e. dodecahedra showing (110) faces. In the cases of Y.I.G. and Er.I.G., a second habit is noted and becomes dominant at faster growth rates (~ 5°C/hr). This habit is shown in Fig. 6; note that the faces are now (211) planes.

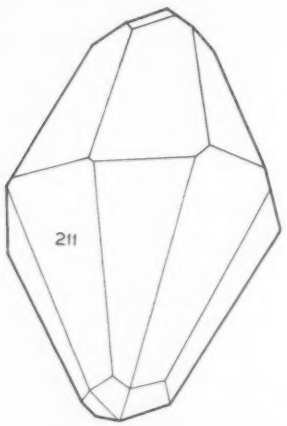

FIG. 6. Habit of Y.I.G. grown at high cooling rates.

The crystal size obtained in the runs depends on growth rate and the particular type of garnet being grown. At 1°C/hr crystals weighing 2g are quite common. The largest grown to date in a 100-ml crucible was a $Gd_3Fe_5O_{12}$ crystal weighing 6g.

As is often the case with crystals grown from molten salts, the magnetic garnet crystals may contain included melt. Usually, however, when the crystals grow to a fairly large size, that portion of the crystal near a well-developed face will be quite sound. The growth behaves normally in that a slow growth rate improves the overall quality of the crystals. Except for included melt in some portions, spectrochemical analyses indicate that the crystals are quite pure. The lattice constants agree very well with those obtained by GELLER and GILLEO[5] on very pure ceramic samples.

4. DISCUSSION OF THE GROWTH PROCEDURE

Fig. 7 shows the area in the ternary system, Y_2O_3–Fe_2O_3–PbO, in which magnetic garnets can be grown. Although the diagram is drawn for the yttrium–iron garnets, experience indicates that the phase equilibrium diagrams of all the rare-earth oxide–iron oxide–lead oxide systems studied so far are similar in the regions of interest to garnet growth. The diagram shown is believed to approximate the same portions of the true equilibrium diagram. (The cross-hatched section indicates the uncertainty of the location of the Fe_2O_3–$PbFe_{12}O_{19}$ boundary.)

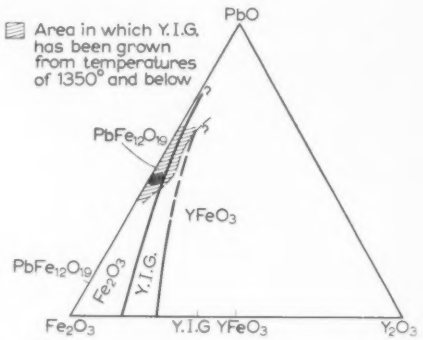

FIG. 7. A partial phase diagram suggested for the system PbO–Y_2O_3–Fe_2O_3.

The composition PbO 52·5, Fe_2O_3 44, and M_2O_3 3·5 mol. per cent, where M is Y, Gd, Er, or Sm has been found to yield crystals of magnetic garnets suitable for many research purposes. This composition was the most convenient for the apparatus used, since it is molten below 1350°C. It is difficult to use platinum crucibles to contain lead oxide melts above 1380°C; the melts contain some platinum when carried through the crystallization path from above 1350°C. This limitation prevents the growth of crystals from melts with high yttrium contents whose compositions lie farther into the garnet field and whose melting points rise steeply in the direction of increasing yttrium content.

In the case of Y.I.G., there is evidence that it may not be very desirable to use a starting composition within the Y.I.G. field. The largest and soundest Y.I.G. crystals have been grown when the first phase to precipitate was either Fe_2O_3 or $PbFe_{12}O_{19}$. This apparently results from the lower rate of nucleation of Y.I.G. beneath the surface layer of the other crystals which crystallize first for initial compositions outside of the Y.I.G. field. Nucleation is often enhanced at the melt surface and multiple nucleation is not desirable. Thus runs originating in the Y.I.G. field will

yield a larger mass of crystals but few large individuals.

Although it was convenient to keep the cooling rate constant during individual runs, this is not necessary early in the run. Once it is certain that the starting mixture is entirely molten and uniform, the temperature can be lowered quickly to the crystallization point of the primary phase. The initial temperature should be substantially higher than the crystallization temperature, since the rate of solution is quite slow. The cooling rate should be slow, 1°C/hr or less, and controlled as carefully as possible. Temperature fluctuations should be kept to a minimum. The fluctuations in the furnaces used by the authors were ± 3°C, i.e. greater in magnitude than the cooling rate, and this probably caused much of the faulty growth observed in some runs.

Finally, the phase diagrams presented here should serve as a guide for further work. Because of the small amount of data and other uncertainties in their determination, however, they should be considered only semi-quantitative. The results of this work have proved to be of great aid in growing crystals of rare-earth magnetic garnets other than Y.I.G.

Acknowledgements—The authors are grateful for the excellent analytical work of Mr. J. F. JENSEN who determined the melt compositions.

The authors would like to thank M. A. GILLEO and S. GELLER for the help they received through their suggestions and discussions.

REFERENCES

1. BERTAUT F. and FORRAT F. *C.R. Acad. Sci. (Paris)* **242,** 382 (1956).
2. GELLER S. and GILLEO M. A. *Acta Cryst.* **10,** 239 (1957).
3. DILLON J. F. Jr. *Phys. Rev.* **105,** 759 (1957).
4. DILLON J. F. Jr. *Bull. Amer. Phys. Soc.* **2,** 22, 128, 238 (1957).
5. GELLER S. and GILLEO M. A. *J. Phys. Chem. Solids* (in the Press).
6. REMEIKA J. P. *J. Amer. Chem. Soc.* **78,** 4259 (1956).
7. RASE D. E. and ROY R. *J. Amer. Ceram. Soc.* **38,** 111 (1955).
8. COCCO A. *Ann. Chimica* **45,** 737 (1955).

J. Phys. Chem. Solids Pergamon Press 1958. Vol. 5. pp. 208–223.

RELATIONS BETWEEN THE CONCENTRATIONS OF IMPERFECTIONS IN SOLIDS*

F. A. KRÖGER and H. J. VINK

Philips Research Laboratories, N.V. Philips' Gloeilampenfabrieken, Eindhoven, Netherlands

(*Received* 25 *July* 1957)

Abstract—Imperfect crystals behave statistically like liquid solutions, the crystal being the solvent and the imperfections the solutes. Application of the law of mass action to atomic and electronic reactions taking place in the crystal and between the crystal and the other phases leads to the notion that the concentrations of the various imperfections are interdependent as a result of reactions having partners in common.

The consequences of this interdependence are demonstrated by means of a graphical method. Imperfections having opposite effective charges tend to increase each other's concentrations.

Foreign atoms are incorporated in a manner dependent both on the energy levels caused by them and on the type of imperfection prevailing in the crystal in the absence of these foreign atoms. In monatomic solids the mechanism of incorporation can be influenced only through the temperature; in compounds it can also be influenced through the partial pressures of the components of the basis crystal.

It is shown that these arguments given are valid irrespective of the type of bonding.

1. INTRODUCTION

In many cases the physical properties of crystalline solids depend to a large extent on the presence of imperfections. Thus the conductivity of semiconductors depends on the presence of centers, able to give off electrons (donors), or holes (acceptors). Diffusion of atoms and ionic conductivity requires the presence of either vacancies or interstitials. The colour of crystals is often influenced by absorption processes involving imperfections (e.g. *F* centers in the alkali halides). Similarly, the luminescence properties of the phosphors or the photoconductive properties of photoconductors are often due to the presence of particular foreign atoms (activators), other centers (traps) causing a slow, temperature-dependent decay (phosphorescence). The magnetic properties of a solid, finally, may be due to misplaced atoms, vacancies, or foreign atoms (e.g. Al_2O_3-Mn).

The imperfections concerned are:† (1) electrons and holes, (2) vacancies, (3) interstitials, (4) misplaced atoms (in compounds), and (5) foreign atoms.

Once a certain property has been correlated with a particular imperfection, one can hope to be able to prepare crystals showing that property with a definite intensity, by controlling the concentration of the imperfection responsible for it. Both the identification of the imperfection responsible for a certain property and the control of its concentration may be seriously hindered by the fact that: (1) in most cases not one, but several different types of imperfections are present, and (2) the concentrations of the various imperfections are not independent; thus by changing the concentration of one imperfection one may change the concentrations of others at the same time.

In the present paper we will be mainly concerned with these points. The problem in hand has both chemical and physical aspects, though it is inadvisable to treat these separately. The two aspects are interwoven so intimately that separation would result in losing the chance of gaining an insight into the most fundamental points.

A method of approach to these problems was given a long time ago by Wagner and Schottky.[1]

* Paper presented at a Symposium on the Inorganic Chemistry of Electronically Active Solids, Miami, April 10, 1957.

† Excitons are left out of account. There are also more macroscopic imperfections, viz. dislocations, but these too will not be considered in the present paper.

It is based on the concept that crystals containing small concentrations of imperfections behave like dilute solutions, the crystal acting as solvent and the imperfections as solutes. The problem can be treated by statistical methods, either in the general form or in the deduced form known as the law of mass action. In this paper the latter will be used. A graphical method of presentation will be employed which greatly facilitates the discussion.[2,3]

In treating such problems one has to distinguish between: (*a*) crystals in a state in which they are in complete equilibrium, both internally and in relation to their surroundings, and (*b*) crystals in a state of partial equilibrium. As an example let us consider a crystal prepared at a high temperature in contact with a vapor of well-defined composition. In many such cases complete equilibrium will be established. During cooling to room temperature, some of the internal or external reactions required to establish equilibrium may be frozen in, and as a consequence a crystal in a state of partial equilibrium is obtained. Often an estimate of the situation under partial equilibrium can be made if we have sufficient knowledge of the state of complete equilibrium preceding it. Therefore we shall be mainly concerned with the state of complete equilibrium.

In the following we shall restrict ourselves to crystals in equilibrium with a gaseous phase. The arguments can be easily extended to other equilibria, e.g. liquid–gas or solid–liquid. The treatment to be presented has first been proposed for compounds.[1–3] Recently it has been recognized that it may also be applied fruitfully to the chemically much simpler monatomic solids such as germanium, silicon, and tellurium.[4,18] First monatomic, non-metallic solids, pure or with addition of foreign atoms, are considered, and then the arguments are extended to simple compounds.

2. COMPLETE EQUILIBRIUM CRYSTAL $\rightleftarrows$ VAPOR FOR PURE MONATOMIC CRYSTALS

If a monatomic solid consisting of atoms A is heated under its own pressure under conditions under which it may reach complete equilibrium, the reactions given on the left-hand side of equations (1)–(4) take place:

$$A_{\text{surface}} \rightleftarrows A_{\text{vapor}} \qquad p_A = K_p \qquad (1)$$

$$A_{\text{crystal}} \rightleftarrows A_{\text{vapor}} + V \qquad [V] = K_v' p_A^{-1} = K_v \qquad (2)$$

$$V \rightleftarrows V^- + \oplus \qquad p[V^-]/[V] = K_a' \qquad (3)$$

$$\text{and hence} \qquad p[V^-] = K_a' K_v = K_a \qquad (3a)$$

$$\text{Ground state} \rightleftarrows \ominus + \oplus \qquad np = K_i \qquad (4)$$

These reactions are also shown in Fig. 1. The first two reactions take place between the crystal

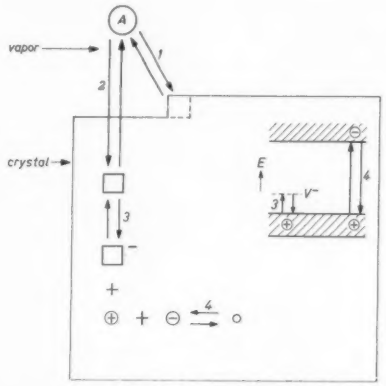

FIG. 1. Reactions taking place within a monatomic crystal and between the crystal and the vapor. Inset: Electronic energy scheme showing the valence band and the conduction band of the crystal and a localized acceptor level due to a vacancy.

and the gas phase. Reaction (1) describes the evaporation and condensation of atoms A from or at the surface of the crystal. This reaction builds up a certain partial pressure p_A of atoms A in the vapor. Reaction (2) describes the formation of unoccupied sites in the crystal (vacancies, V). Two other reactions take place within the crystal. Reaction (3) describes the ionization of the vacancies, V. It is based on the assumption that vacancies have a tendency to bind electrons, i.e. to act as electron acceptors. In this process free holes ($\oplus$) are formed. Free holes, together with free electrons ($\ominus$) are also formed by the intrinsic excitation process (4). It is customary to discuss such electronic reactions in relation to the electronic energy-band scheme. Therefore the place of the reactions (3) and (4) in such a picture is depicted in the inset to Fig. 1.

Application of the law of mass action to these reactions leads to relations between the concentrations of the various imperfections obtaining under

equilibrium conditions. These relations are indicated at the right-hand side of reactions (1)–(4). The concentrations of electrons and holes are indicated by n and p, and the other concentrations are indicated by the symbol of the imperfection enclosed by brackets. The relations are arrived at on the assumption that the concentrations of the imperfections are small, so that concentrations may be used instead of activities, and furthermore that the concentration of normal constituents of the crystal is effectively constant.

Since the crystal as a whole must be neutral, the sum of all the charges is zero; hence

$$n+[V^-]=p. \tag{5}$$

From equations (2)–(5), the concentrations of electrons, holes, and neutral and ionized vacancies can be calculated if the values of the constants are known:

$$p=(K_i+K_a)^{\frac{1}{2}} \qquad n=K_i(K_i+K_a)^{-\frac{1}{2}}$$
$$[V^-]=K_a(K_i+K_a)^{-\frac{1}{2}} \qquad [V]=K_v.$$

In general $K_i \neq K_a$.

If $K_i \gg K_a$ $\quad n \cong p \cong K_i^{\frac{1}{2}}$ $\quad [V^-] \cong K_aK_i^{-\frac{1}{2}}$;

if $K_i \ll K_a$ $\quad p \cong [V^-] \cong K_a^{\frac{1}{2}}$ $\quad n \cong K_iK_a^{\frac{1}{2}}$.

These approximate solutions are obtained directly if we approximate the neutrality condition (5) by an equality of the two dominating terms, neglecting the smaller term, i.e. either

$$n \cong p \text{ (corresponding to } K_i \gg K_a)$$

or

$$p \cong [V^-] \text{ (corresponding to } K_i \ll K_a).$$

It may seem superfluous to introduce an approximate solution for a problem for which the exact solution is so easily obtained. The point is, however, that if the problem becomes slightly more complicated, the exact solution is no longer easily obtained, whereas the approximate solution can always easily be found. Moreover, there is the following advantage. With the use of the approximate form of the neutrality condition, the set of equations (2)–(5) can be transformed into linear relations between the logarithms of the concentrations of the unknowns and the logarithms of the constants. Thus, in a logarithmic plot, relations between the various concentrations are represented by straight lines. This fact may be used to obtain the solutions by a graphical method, which greatly aids in obtaining an insight into the matters in hand.[3] This will be demonstrated now for the temperature-dependence of the concentrations in the case under discussion.

In general the constants appearing in the law of mass action have the form

$$K=K_0\exp(-E/kT)$$

in which K_0 is a constant related to the entropy involved in the reaction and E is the energy involved in the reaction.* Hence

$$\log K=\log K_0-E/kT.$$

Taking the logarithms of the left- and right-hand sides of the equations (2)–(4) and of one of the approximate forms of (5), and inserting for log K expressions of the form given above, it is found that we get linear equations in the logarithms of the concentrations and in E/kT.

For the approximation $n \cong p$, one obtains:

$$\log n=\log p=\tfrac{1}{2}\log K_i=\tfrac{1}{2}\log(K_i)_0-\frac{E_i}{2kT}.$$

$$\log[V^-]=\log K_a-\tfrac{1}{2}\log K_i$$

$$=\log(K_a)_0-\tfrac{1}{2}\log(K_i)_0-\frac{(E_a-\frac{1}{2}E_i)}{kT}.$$

* In semiconductor physics the constants K related to the excitation and trapping of electrons according to the reactions (3) and (4) are usually written in the form

$$K=f(T)\exp(-E_x/kT).$$

The reason is that the energies of electrons or holes have not one sharp value, but lie in bands. E_x in the formula represents the smallest excitation energy, and $K_0=f(T)$ results from a summation including the higher states. It is possible, however, to represent the variation of K with temperature over not too wide a temperature range with a pre-exponential K_0 which is independent of T, provided one inserts for E an average excitation energy which is of the order of

$$E=E_x+\tfrac{3}{2}akT$$

with $a=1$ for reaction (3) and $a=2$ for reaction (4).

Hence a plot of the logarithms of the concentrations against $1/T$ gives straight lines with slopes which are simple functions of the energies involved in the various reactions.

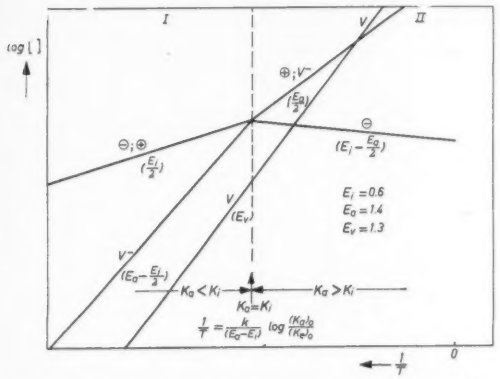

FIG. 2. Variation with temperature of the concentrations of the imperfections for a monatomic solid with vacancies having acceptor properties (see Fig. 1) for the case $E_a > E_i$.

Fig. 2 (range I) shows such a plot for the case in which $E_a > E_i$. The combinations of E's determining the various slopes are indicated in parentheses. The slope of $\log n = \log p$ is smaller than that of $\log [V^-]$:

$$E_a - \tfrac{1}{2}E_i > \tfrac{1}{2}E_i.$$

Therefore $[V^-]$, small at low temperatures, increases with temperature more rapidly than n and p; it may become greater than these quantities if the $[V^-]$ line intersects the $n = p$ line before the point $1/T = 0 (T = \infty)$ is reached. This will be the case if $(K_a)_0 > (K_i)_0$—the intersection taking place at the point where $K_a = K_i$, i.e. at

$$\frac{1}{T} = \frac{k}{E_a - E_i} \log \frac{(K_a)_0}{(K_i)_0}.$$

In range II, above the point of intersection, the electrical neutrality condition must be approximated by $p \cong [V^-]$ and the solution becomes

$$\log p = \log [V^-] = \tfrac{1}{2} \log [K_a)_0 - \frac{E_a}{2kT}$$

$$\log n = (K_i)_0 - \tfrac{1}{2} \log (K_a)_0 - \frac{E_i - E_a/2}{kT}.$$

In this range n may increase or decrease with temperature depending on whether $E_i > < E_{a/2}$. The situation in Fig. 2 corresponds to $E_i < E_{a/2}$. Indications of a range II, with $p = [V^-]$, as shown in Fig. 2, have been observed with Te[5].* In both ranges the concentration of V is a simple temperature function, given by

$$\log [V] = \log (K_v)_0 - \frac{E_v}{kT}.$$

The total concentration of vacancies $[V]_{\text{total}} = [V] + [V^-]$ thus increases irregularly with temperature.

A solution for the case in which

$$E_a < \frac{E_i}{2} < E_i$$

is shown in Fig. 3. The neutrality condition is governed by holes and V^- at low temperatures,

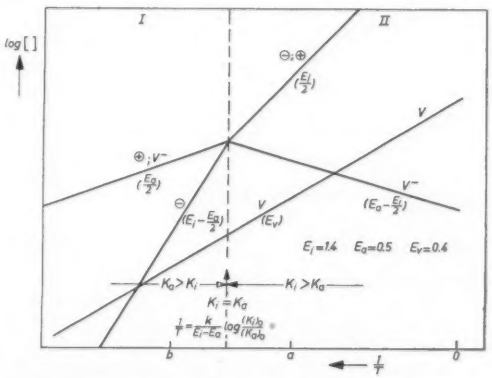

FIG. 3. Same as Fig. 2, but for $E_a < E_i$.

and by electrons and holes at high temperatures. The total concentration of vacancies first increases with increasing temperature then decreases, and finally increases again.

The case of monatomic solids containing interstitial atoms (which acts as donors) can be treated in the same way. Interesting effects may occur if the crystals can form both the donating interstitials and the accepting vacancies (Fig. 4). In

* Recent optical work by H. Y. FAN *et al.* indicates, however, that the effects observed must be explained in a different way, by assuming complex conduction bands.

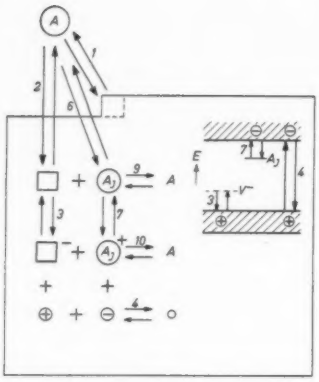

FIG. 4. Internal and external reactions for a monatomic crystal containing vacancies and interstitials. Inset: Electronic energy scheme.

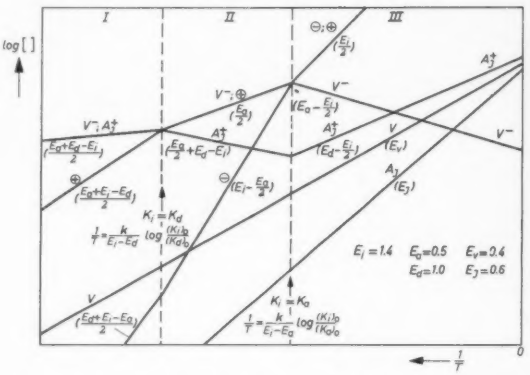

FIG. 5. Variation with temperature of the concentrations of the imperfections in a monatomic crystal to which Fig. 4 applies.

addition to the reactions and equations (1)–(4), we now also have

$$A_{\text{vapor}} \rightleftarrows A_I \qquad [A_I] = K_I \tag{6}$$

whereas the activity of interstitial A as a donor is described by:

$$A_I \rightleftarrows A_I^+ + \ominus \qquad \frac{n[A_I^+]}{[A_I]} = K_d'. \tag{7}$$

Combination of equations (6) and (7) leads to

$$n[A_I^+] = K_d' K_I \equiv K_d. \tag{7a}$$

The neutrality condition is now

$$n + [V^-] = p + [A_I^+]. \tag{8}$$

In addition to the possibilities for the simplified neutrality condition met in the case in which vacancies or interstitials are present alone, viz.

$$n = p \text{ and } p = [V^-] \text{ or } n = [A_I^+],$$

we now also have the possibility

$$[V^-] = [A_I^+].$$

Fig. 5 shows an example of a case in which a range governed by this simplified form of the neutrality condition occurs at low temperatures.

From equations (2)–(4) and (6)–(8) and Fig. 5, it is seen that although the concentrations of the uncharged vacancies and interstitials are independent of one another, and are in general unequal, the concentrations of the ionized imperfections are interdependent, and may become equal to one another. In the latter case we usually speak of Frenkel disorder.

The formation of vacancies and interstitials has been formulated in terms of the reactions (2) and (6) (followed by (3) and (7)) in Fig. 4. The formation of pairs of vacancies and interstitials can also be formulated more directly as is customary for Frenkel disorder (Fig. 4, reactions (9) and (10)). Application of the law of mass action to these reactions leads to

$$[A_I]\,[V] = K_I K_v \tag{9}$$

$$[A_I^+][V^-] = \frac{K_a K_d}{K_i}. \tag{10}$$

However, owing to the reactions (2) and (6), the concentrations of A_I and V_A actually formed will not be equal. Further, as we have no means (apart from the temperature) of varying either concentration, little use can be made of the product relationship (9); it simply states that the product of two constants is again a constant. For the charged imperfections the situation is different; the concentrations of these can be influenced through the ionization reactions (3) and (7), and this offers the opportunity of changing the ratio of the concentrations, equation (10) remaining valid. Examples of variations of the concentration of these imperfections by way of the electronic reactions will be given in the next section, where the influence of foreign atoms is considered.

3. MONATOMIC CRYSTALS CONTAINING FOREIGN ATOMS

If foreign atoms (F) are introduced into the system, two problems arise:

(1) what is the influence of the foreign atoms on the concentration of vacancies, interstitials, electrons and holes (the inherent imperfections of the crystal)?

(2) what is the influence of the inherent imperfections on the mechanism of incorporation and on the solubility of the foreign atoms?

In treating these problems it is necessary to know whether F acts as a donor or as an acceptor; in other words, what are the energy levels caused by F? In general it can be said that, if F is incorporated at a normal lattice position, replacing the normal lattice constituent, it causes an occupied level close to the conduction band (and thus acts as a donor) if F has more valence electrons than the atom which it replaces. It causes an unoccupied level close to the valence band (and acts as an acceptor) if it has less valence electrons.

There are, however, exceptions to this rule (e.g. zinc, gold and transition elements in germanium). Therefore in practice it is best to deduce from experiment the position and the nature of energy levels caused by a particular foreign atom we are interested in.

(a) *Influence of foreign atoms on the concentrations of native imperfections; the mechanism of incorporation of F*

Let us consider a crystal with vacancies acting as acceptors (i.e. a crystal to which Fig. 3 applies) and having a fixed concentration of foreign atoms F incorporated at normal lattice sites, these atoms acting as donors. The reactions taking place are shown in Fig. 6.* Application of the law of mass action to the equations leads to the relations (2)–(4):

$$[V] = K_v; \quad p[V^-] = K_a; \quad np = K_i.$$

In addition there is ionization of F according to:

$$F \rightleftarrows F^+ + \ominus \quad \frac{n[F^+]}{[F]} = K_f \qquad (11)$$

with

$$[F]_{\text{total}} = [F] + [F^+], \qquad (12)$$

* The assumption of a constant concentration of F corresponds to the neglect of the transfer of atoms F between the crystal and the gas phase. Thus we are actually considering a state of partial equilibrium (reaction (14) of Fig. 6 being frozen in).

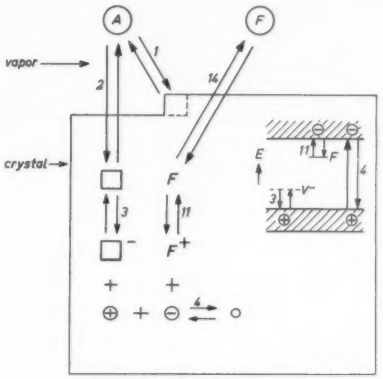

FIG. 6. Internal and external reactions for a monatomic crystal with vacancies (acceptors) in the presence of foreign atoms having donor properties. Inset: Electronic energy scheme.

whereas the neutrality condition takes the form

$$n + [V^-] = p + [F^+]. \qquad (13)$$

From these equations the problem of the variation with temperature of the concentration of impurities can be solved in a manner similar to that employed for the pure system. In this case linear equations in the logarithms of the concentrations and the constants are obtained if we approximate not only the neutrality condition (13), but also the relation (12) referring to the concentration of F in its various forms.[3] Expression (12) is approximated by either $[F]_{\text{total}} = [F]$ or by $[F]_{\text{total}} = [F^+]$. Expression (13) is approximated by one of the equations $n = p$; $n = [F^+]$; $[V^-] = [F^+]$.

Combinations of two such approximations define particular ranges. One of the many possible variations with temperature of the concentrations is shown in Fig. 7. Dotted lines give the concentrations of holes and V^- for the corresponding pure crystal (see Fig. 3).

It is seen that five different ranges appear, characterized by

$$[F]_{\text{total}} = [F^+] = [V^-] \qquad \text{(I)}$$

$$[F]_{\text{total}} = [F]; \quad [F^+] = [V^-] \qquad \text{(II)}$$

$$[F]_{\text{total}} = [F]; \quad [F^+] = n \qquad \text{(III)}$$

$$[F]_{\text{total}} = [F^+] = n \qquad \text{(IV)}$$

$$[F]_{\text{total}} = [F^+]; \quad n = p. \qquad \text{(V)}$$

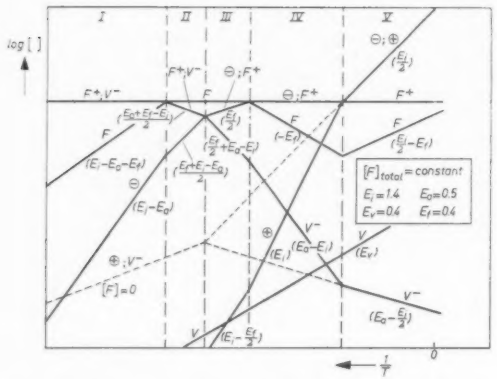

FIG. 7. Variation with temperature of the imperfections in a monatomic crystal with a fixed concentration of foreign donors F (see Fig. 6). The concentrations in the absence of F are indicated by broken lines.

Of these, (I) and (IV) are particularly noteworthy, because they indicate a special mode of incorporation of the foreign atom. In (I) F is incorporated with an equal concentration of vacancies; this corresponds to the replacement of two A atoms by one F atom. In (IV) F is incorporated as F^+ with an equal concentration of free electrons. Chemically speaking this corresponds to the substitution of one A atom by one F atom. Range (IV) corresponds to the situation obtaining in germanium and silicon containing arsenic, antimony or phosphorus in the extrinsic range. In the next section we shall see what factors determine the mechanism of incorporation.

If we compare the concentrations of the imperfections in the crystal containing F with that in the pure crystal, it is seen that F increases both the concentrations of vacancies (V^-) and of electrons as long as F plays a part in the neutrality condition (ranges (I)–(IV)). When F no longer appears in the simplified neutrality condition (range (V)), the concentrations of the inherent imperfections are independent of F. If F were an acceptor instead of a donor, it could be incorporated only as F^- plus an equal concentration of holes (such as aluminum or boron in germanium or silicon). In this case the concentration of V^- would be lowered below the concentration of these centres in the pure crystal. In general it can be said that the concentrations of imperfections having charges opposite to those that may be assumed by the foreign atoms tend to increase and those having the same charge as the foreign atoms tend to decrease.

(b) *Influence of inherent imperfections on the solubility of foreign atoms*

The complete equilibrium crystal $\rightleftharpoons$ vapour for a case in which atoms F are present should include the equilibrium between F in the crystal and in the vapour (Fig. 6, reaction (14)). This leads to an equation

$$[F] = K_F p_F \qquad (14)$$

in which p_F is the partial pressure of F in the vapour. The concentrations of all the imperfections (including F) can be obtained from the equations (2), (3a), (4), (11), (13) together with (14), the last taking the place of (12) in the problem with

$$[F]_{\text{total}} = \text{constant}.$$

The solution for the concentrations as a function of $1/T$ for a given value of p_F is similar to that shown in Fig. 4 if we replace A_I by F.

It is also possible to see how the concentrations vary with p_F at a given temperature. As far as F is concerned, this gives information concerning both its solubility and the mechanism of incorporation. The mechanism of incorporation depends on the simplified neutrality condition holding in the pure crystal at that temperature. Let us consider the crystal to be in a range governed by the condition

$$n = p$$

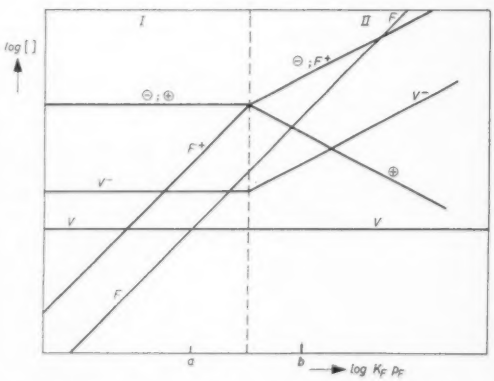

FIG. 8. Variation with p_F of the concentration of the imperfections in a monatomic crystal under conditions in which in the pure crystal $n \simeq p$.

(range II of Fig. 3; $K_a < K_i$); then the solution is as shown in Fig. 8. As long as $[F^+] < n$, p, the simplified neutrality condition remains unchanged (Fig. 8, range I; this range corresponds to a point within range V of Fig. 7). In this range the concentration of F^+ increases linearly with $K_F p_F$, and $[V^-]$ is constant. At the point where $[F^+]$ becomes greater than p, we get a new range (II) governed by the simplified neutrality condition

$$n = [F^+].$$

This range corresponds to range IV of Fig. 7. In this range n, $[F^+]$, and $[V^-]$ increase with $(K_F p_F)^{\frac{1}{2}}$ and p decreases

$$\sim (K_F p_F)^{-\frac{1}{2}}.$$

The uncharged imperfections show the same variation over both ranges, $[V]$ remaining constant, and $[F]$ increasing with $K_F p_F$. $[F]$ finally supersedes $[F^+]$ (corresponding to range III of Fig. 7).

The total concentration of the foreign atom

$$[F]_{\text{total}} = [F] + [F^+]$$

thus shows an intricate variation with $K_F p_F$.

If, on the other hand, the pure crystal is in a range governed by $p = [V^-]$ (range I of Fig. 3, $K_a > K_i$; e.g. point *b*), the solution is as shown in Fig. 9. Also in this case F starts to influence the concentration of the inherent imperfections (and these conversely the solubility of F) when the concentration of the ionized foreign atoms becomes greater than the concentrations of the

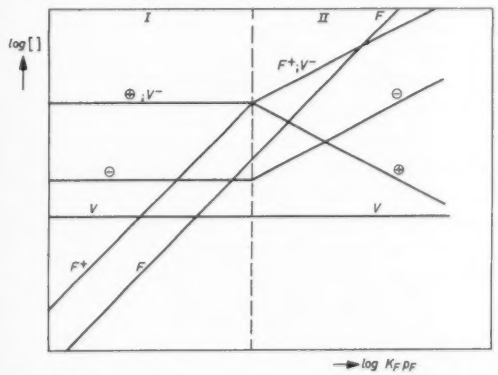

FIG. 9. As Fig. 8, but under conditions in which $p = [V^-]$ in the pure crystal.

charged imperfections governing the neutrality condition. In the new range (Fig. 9, range II, corresponding to Fig. 7, range I), F is incorporated mainly as F^+ with an equal concentration of vacancies (V^-) and the concentration varies with $(K_F p_F)^{\frac{1}{2}}$. The concentration of electrons increases with the same slope. The concentration of electrons is thus proportional to $[F^+]$, but unlike what was found in Fig. 8, now $n < [F^+]$. This means, that a small fraction of F is incorporated as $F^+ + \ominus$. If F were an acceptor instead of a donor, it would give rise to a range II governed by the simplified neutrality condition

$$[F^-] = \oplus$$

and would cause the concentration of V^- to decrease instead of increase. Thus it is seen again that the concentration of imperfections having a charge opposite to that of the foreign constituent is increased, but the concentration of imperfections having a charge of the same sign is decreased.

A variation of the concentration of vacancies caused by the presence of donor or acceptor atoms is indicated by recent measurements of the self-diffusion in heavily doped germanium.[6]

(c) *Monatomic solids containing two types of foreign atoms*

The same concepts can also be applied if more than one type of foreign atom is present. Let us consider the case of a crystal containing two types of foreign atom, one acting as a donor (F_d), the other as an acceptor (F_a). Let F_a be present in a constant concentration (i.e. the transfer of atoms F_a between the crystal and the vapor is supposed to be negligible), whereas the concentration of F_d in the crystal is variable, depending on the vapor pressure of F_d. For the sake of simplicity we shall neglect the presence of vacancies or interstitials. The equations applying to this case are

$$np = K_i \frac{p[F_a^-]}{[F_a]} = K_{fa} \quad \frac{n[F_d^+]}{[F_d]} = K_{fd}$$

$$[F_a]_{\text{total}} = [F_a] + [F_a^-] \, [F_d] = K_{Fd} p_{Fd}$$

$$n + [F_a^-] = p + [F_d^+],$$

the constants having the activation energies E_i, E_{fa}, E_{fd}, and E_{Fd}. Fig. 10 gives a solution of these equations as a function of p_{Fd} for the case in which

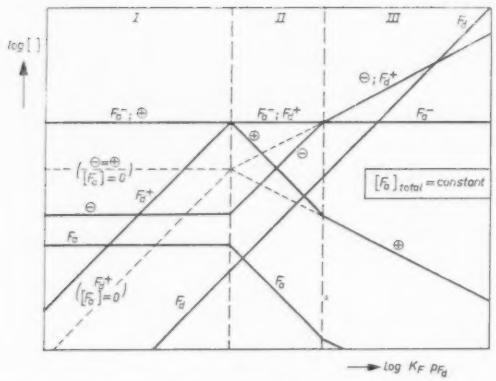

FIG. 10. Variation with p_{F_d} of the concentrations of the imperfections in a monatomic crystal with a fixed concentration of foreign acceptors (F_a) and a variable concentration of foreign donors (F_d).

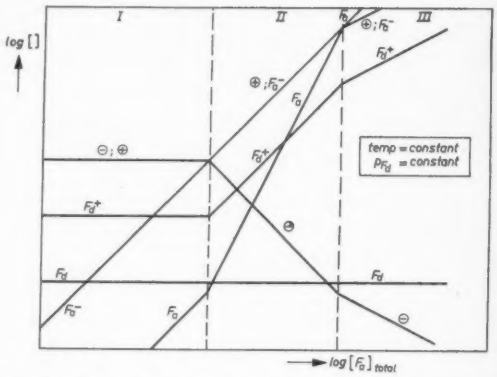

FIG. 11. Variation with $[F_a]_{total}$ for a monatomic crystal containing foreign acceptors (F_a) and donors (F_d) for p_{F_d} = constant. The figure applies to a case in which $n \cong [F_d^+]$ in the absence of F_a.

the conditions are such that in the crystal without F_d (i.e. at $p_{F_d} = 0$) the simplified neutrality condition is

$$[F_a^-] = p.$$

It is seen that there is a range II in which the concentrations of F_a^- and F_d^+ are equal and independent of p_{F_d}. In this range the crystal is "buffered" as far as its F_d content is concerned. The concentration of electrons and holes changes with p_{F_d}, however, and a new range III with

$$[F_d^+] = n$$

occurs when n has become greater than $[F_a^-]$.

The figure shows also the variation of n, p, and $[F_d^+]$ in the absence of F_a (dotted lines). It is seen that F_a causes a marked increase in the solubility of F_d in the ranges I and II, but not in range III (see also Figs. 11 and 12); the effects occur only when F_a (or rather F_a^-) plays a dominant rôle in the neutrality condition.

For a crystal which at $p_{F_d} = 0$ would be intrinsic (corresponding to a low concentration of F_a), the dependence of the concentrations on $K_{F_d} p_{F_d}$ would be similar to that shown in Fig. 8. The dependence of the various concentrations on the concentration of F_a for p_{F_d} = constant and T = constant is shown in Figs. 11 and 12. Fig. 11 applies to a case in which the crystal without F_a is intrinsic (corresponding to point a of Fig. 8); Fig. 12 applies to an extrinsic crystal (similar to point

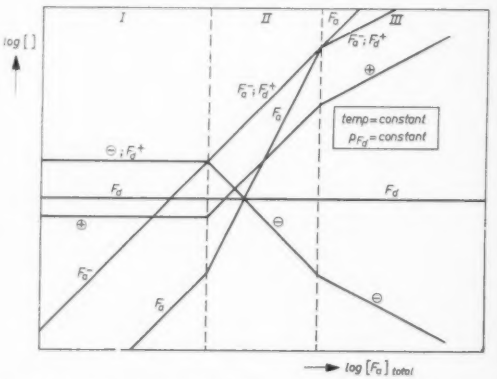

FIG. 12. As FIG. 11, but for the case in which $n \cong p$ in the absence of F_a.

b of Fig. 8). In both cases the concentration of F_d^+ is constant at low concentrations of F_a (range I); it increases proportional to $[F_a^-]$ when $[F_a^-]$ plays a rôle in the simplified neutrality condition (range II) and increases $\sim [F_a^-]^{\frac{1}{2}}$ when most of the acceptor atoms are present in the non-ionized form (range III). Effects corresponding to the ranges I and II have been observed by REISS *et al.*[4] with silicon + boron, lithium.

Fig. 13 shows a possible temperature-dependence of the concentrations for $[F_a]_{total}$ = constant and p_{F_d} = constant. At low temperatures the concentration of F_d^+ is equal to that of F_a^- (range I; this corresponds to range II of Figs. 10 and 12). At

VOL. 5 1958

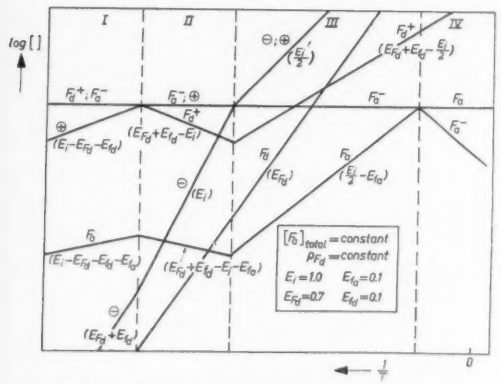

FIG. 13. Variation with temperature of the concentrations of the imperfections in a monatomic crystal containing foreign donors (F_d) and acceptors (F_a) for the case in which $[F_a]_{\text{total}}$ = constant and p_{F_d} = constant.

a higher temperature the concentration of F_d^+ decreases with increasing temperature (this range corresponds to range II of Fig. 11). At still higher temperatures (ranges III and IV), the concentration of F_d^+ increases again. Such effects have also been observed with silicon+boron, lithium.[4]*

It would be easy to give many more examples of this kind. It seems more profitable, however, to extend the discussion to compounds which, as we shall see, show some characteristic new features.

4. EQUILIBRIA CRYSTAL ⇄ VAPOR FOR SIMPLE COMPOUNDS†

In compounds also, considerations similar to those applied above hold. Let us first consider a pure compound AB in equilibrium with its vapor. It will be assumed that vacancies on both the A and B sites are possible, which will be called respectively V_A and V_B. If A is a more electropositive, B a more electronegative component, a vacancy V_A will act as an acceptor, V_B as a donor.[7]

The various reactions that occur in the system are shown in Fig. 14 and also in the text below

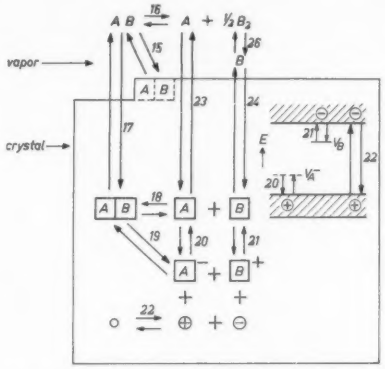

FIG. 14. Internal and external reactions for a simple compound AB with SCHOTTKY–WAGNER disorder. Inset: Electronic energy scheme.

(left-hand side). The reactions (16) and (26) take place in the gas phase and maintain equilibrium in that phase. The reactions (18)–(22) take place in the solid and maintain equilibrium there. The reactions (15), (17), (23), and (24) finally maintain the equilibrium between the crystal and the vapor.

For the vapor it will be assumed that A is present predominantly in the form of isolated atoms, whereas B is assumed to be present predominantly as B_2 molecules (equilibrium of reaction (26) shifted to the B_2 side).

Application of the law of mass action leads in the customary way to relations between the concentrations which are given at the right-hand side of the reaction equations:

$$AB_{\text{surface}} \rightleftarrows AB_{\text{vapor}} \quad p_{AB} = K_{15} \tag{15}$$

$$AB_{\text{vapor}} \rightleftarrows A_{\text{vapor}} + \tfrac{1}{2}(B_2)_{\text{vapor}} \quad \frac{p_A p_{B_2}^{\frac{1}{2}}}{p_{AB}} = K_{16} \tag{16}$$

which combined give

$$p_A p_{B2}^{\frac{1}{2}} = K_{15}K_{16} = K_{AB} \tag{16a}$$

$$AB_{\text{crystal}} \rightleftarrows AB_{\text{vapor}} + V_{AB} \quad [V_{AB}] = \frac{K_{17}}{p_{AB}} = \frac{K_{17}}{K_{15}} = K_V \tag{17}$$

* These experiments were carried out with a liquid phase as a source of the lithium (the donor) instead of with a vapor, as assumed in our example. The results are the same as long as the concentration of lithium in the liquid (and thus its thermodynamic potential) remains constant, which is the case at low and medium temperatures. At higher temperatures, the concentration of lithium in the liquid phase decreases, however, and this results in a decrease of the lithium concentration in the solid, which, as we see in Fig. 13, would not occur if the thermodynamic potential of lithium were maintained constant.

† For a more extensive discussion see ref. (7).

$$V_{AB} \rightleftarrows V_A + V_B \qquad \frac{[V_A][V_B]}{[V_{AB}]} = K_{18} \quad (18)$$

Combination of (17) and (18) gives:

$$[V_A][V_B] = K_{17}K_{18} = K_S \quad (18a)$$

$$V_{AB} \rightleftarrows V_A^- + V_B^+ \qquad \frac{[V_A^-][V_B^+]}{(V_{AB})} = K_{19}, \quad (19)$$

which, combined with (17) gives

$$[V_A^-][V_B^+] = K_{17}K_{19} = K_S' \quad (19a)$$

$$V_A \rightleftarrows V_A^- + \oplus \qquad \frac{p[V_A^-]}{[V_A]} = K_h \quad (20)$$

$$V_B \rightleftarrows V_B^+ + \ominus \qquad \frac{n[V_B^+]}{[V_B]} = K_e \quad (21)$$

$$\text{ground state} \rightleftarrows \ominus + \oplus \qquad np = K_i \quad (22)$$

$$A_{\text{crystal}} \rightleftarrows A_{\text{vapor}} + V_A \qquad p_A(V_A] = K_{23} \quad (23)$$

$$B_{\text{crystal}} \rightleftarrows B_{\text{vapor}} + V_B \rightleftarrows \tfrac{1}{2}(B_2)_{\text{vapor}} + V_B \qquad p_{B_2}^{\frac{1}{2}}(V_B] = K_{24} \quad (24)$$

Combination of (23) and (24) with (16a) leads to

$$[V_A] = \frac{K_{23}}{K_{AB}} p_{B_2}^{\frac{1}{2}} = K_{\text{ox}} p_{B_2}^{\frac{1}{2}} \quad (23a)$$

and

$$V[B] = \frac{K_{24}}{K_{AB}} p_A = K_{\text{red}} p_A. \quad (24a)$$

Finally the requirement of electrical neutrality in the crystal leads to

$$n + [V_A^-] = p + [V_B^+]. \quad (25)$$

As $[V_A]$ and $[V_B]$ are related by (18a) and p_A and p_{B_2} by (16a) there is a relation between the constants:

$$K_{\text{ox}} \cdot K_{\text{red}} = K_S \cdot K_{AB}^{-1}.$$

Similarly from (18a), (19a), (20), (21) and (22) it follows that there is also a relation between the constants of these relations:

$$K_i K_S' K_S^{-1} = K_h K_e.$$

Because of these relations only one of each of the relations (18a) and (19a) and (23a) and (24a) need be used to solve our problem. A solution for all the seven unknowns can be obtained for instance by using the seven equations (17), (19a), (20), (21), (22), (23a) and (25).

From equation (17) it is seen that the partial pressure of molecules AB is equal to K_V, i.e. it is a function of temperature only. This is the analogue of the corresponding behavior of the partial pressure p_A in the monatomic case (equation (1)). For compounds, however, the partial pressures of the separate lattice components p_A and p_B or p_{B_2} are not constant at a given temperature. They may be varied, though not independently of one another (see equation (16a)).

Because of the reactions (23) and (24), the concentrations of V_A and V_B must also vary when p_A and p_{B_2} are varied, a high pressure of p_{B_2} giving a small concentration of V_B and—owing to equation (18a)—a large concentration of V_A. A similar dependence holds also for the ionized vacancies. This is demonstrated in Fig. 15, which shows a possible

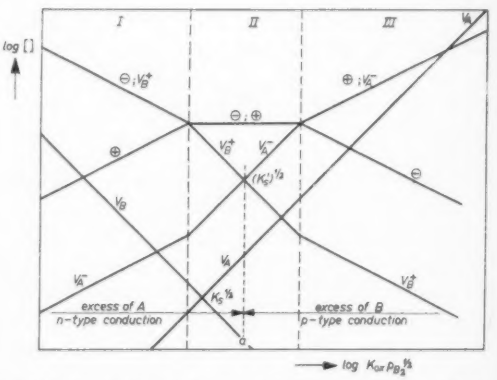

FIG. 15. Variation with p_{B_2} of the concentrations of the imperfections in a compound AB with SCHOTTKY–WAGNER disorder.

solution for the concentrations of the imperfections in the crystal as a function of p_{B_2} at constant temperature.

At large values of p_{B_2},

$$[V_A] + [V_A^-] > [V_B] + [V_B^+].$$

This means that the crystal contains an excess of B. In this range the crystal shows p-type conduction.

At low values of p_{B_2}, the crystal contains an excess of A and shows n-type conduction. Such a dependence has been observed with PbS.[8] The transition from excess B to excess A is a very sharp one; the system jumps from a marked excess of B to a marked excess of A at the value of p_{B_2} where the lines of V_A^- and V_B^+ cross. In the exact solution this jump is a little less pronounced, but it remains very steep. This has the consequence that it is practically impossible to prepare crystals having exactly stoichiometric composition. The value of the smallest deviation from stoichiometry that can be attained reproducibly is $(K_S')^{\frac{1}{4}}$. As K_S' increases with temperature, this indicates that the lower the temperature of preparation, the closer the stoichiometric composition can be approached. A solution for the concentrations of the imperfections as a function of temperature for p_{B_2} = constant is shown in Fig. 16; this figure corresponds

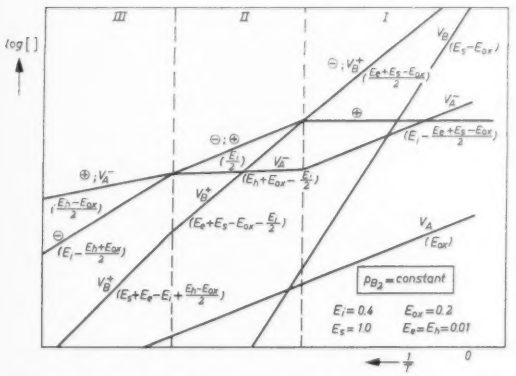

FIG. 16. Variation with temperature of the concentrations of the imperfections in a compound AB with SCHOTTKY–WAGNER disorder (p_{B_2} = constant).

more or less with what has been observed with PbS[8]. The ranges I, II, and III formed in Fig. 15 appear also in Fig. 16; this indicates that the oxidizing power of the atmosphere depends not only on p_{B_2} but also on the temperature.

5. EQUILIBRIA CRYSTAL — VAPOR FOR COMPOUNDS CONTAINING FOREIGN ATOMS[7]

Just as in the case of the monatomic crystals, foreign atoms have an effect on the inherent imperfections. These, in turn, have an influence on the foreign atoms.

Let us first consider the former effect. If a crystal like that treated in Section 4 contains foreign atoms F at A sites (F_A), and these atoms have donor properties, then the set of equations belonging to the pure crystal is modified by the relations

$$\frac{n[F_A^+]}{[F_A]} = K_f \quad [F_A]_{\text{total}} = [F_A]+[F_A^+]$$

and the neutrality condition (25) is changed to

$$n+[V_A^-] = p+[V_B^+]+[F_A^+].$$

A possible solution is shown in Fig. 17. At extremely high and extremely low values of p_{B_2},

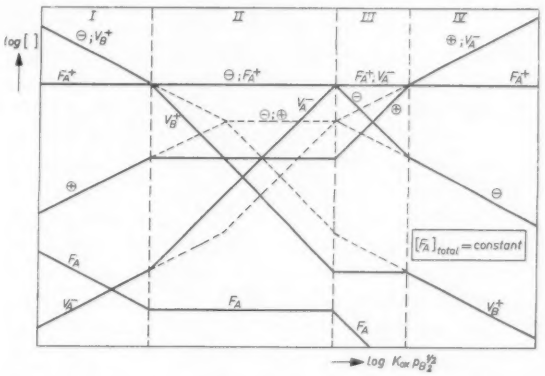

FIG. 17. Variation with p_{B_2} of the concentrations of the imperfections in a compound AB with a fixed concentration of foreign atoms F at A sites, F_A having donor properties. The concentrations in the absence of F are indicated by broken lines.

the concentration of the inherent imperfections is greater than that of the foreign atoms; here F_A does not affect the concentrations of the imperfections (ranges I and IV). At intermediate values of p_{B_2}, however, F_A has a marked effect provided that $[F_A]_{\text{total}} > K_i^{\frac{1}{2}}$. In range II, F_A is incorporated as F_A^+, together with an equal concentration of electrons; in range III it is incorporated with an equal concentration of V_A^-. In both cases the concentration of the native imperfections (electrons, V_A^-) is increased markedly above the level at which they are present in the absence of F_A (dotted lines). Such a dependence has been observed with PbS–Bi.[8] The system in the ranges II and III can also be written as a solid solution of two compounds. Range II corresponds to a solid

solution AB–F_AB (or, for the example mentioned, PbS–BiS). In this range the foreign atom has assumed the valence of the constituent which it replaces. It corresponds to what SELWOOD[9] has called "induced valence" and to what VERWEY *et al.*[10] have called "controlled valence".*

Range III corresponds to a solid solution AB–F_AB_2 (e.g. PbS–BiS_2 and also AgCl–$CdCl_2$[11]). These examples demonstrate that the compound of the foreign atom which is incorporated may correspond to one of the compounds of F normally known ($CdCl_2$) but need not necessarily do so (BiS_2).

Just as for the monatomic solids, the mechanism of incorporation of F is determined by the state prevailing in the crystals in the absence of F, characterized in particular by the simplified neutrality condition. If the neutrality condition is governed by electrons or holes, or by one of these in combination with an atomic imperfection that may assume a charge equal in sign to the charge of the foreign atom, F is incorporated as $F^+ + \ominus$ if F is a donor, and as $F^- + \oplus$ if F is an acceptor. If, among the imperfections governing the neutrality condition, there are atomic imperfections with a charge opposite to that which may be assumed by the foreign atom, the foreign atom is incorporated with the formation of those atomic imperfections.†

When we are interested in the same system under a condition such that not $[F_A]_{\text{total}} = \text{constant}$, but $p_{f_e} = \text{constant}$, i.e. taking into account the possibility of transfer of F from the crystal to the vapor and vice versa, the transfer reaction

$$(F)_{\text{vapor}} + V_A \rightleftarrows F_A$$

leads to

$$[F_A] = K_F p_F [V_A]$$

which takes the place of the relation $[F_A]_{\text{total}} =$ the concentrations as a function of $p_{B_2}^{\frac{1}{2}}$ is shown in Fig. 18. It is seen that the concentration of F_A in the crystal increases when p_{B_2} increases. The increase of the concentration of these donor centres prevents the occurrence of p-type conductivity at

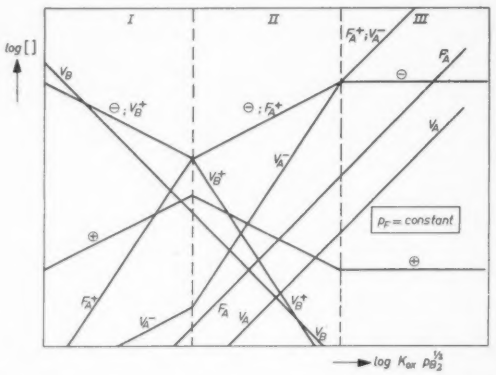

FIG. 18. As Fig. 17, but for p_F = constant instead of $[F_a]_{\text{total}}$ = constant.

$[F_A] + [F_A^+]$ of the previous case. A solution for large values of p_{B_2} If F were an acceptor, its concentration would vary in the opposite direction, and the occurrence of n-type conductivity at low values of p_{B_2} would be prevented.

In a similar way we can study the equilibrium vapor $\rightleftharpoons$ solid as a function of p_F at a given value of p_A (or p_{B_2}). All the effects are essentially the same as with the monatomic compounds (Figs. 8 and 9). The difference lies only in the fact that now, depending on the value chosen for p_A (or p_{B_2}), we can change from one case (e.g $n = p$, Fig. 8) to another ($p = [V_A^-]$, Fig. 9) (see Fig. 15). With the monatomic solids such a change could be brought about only by a change in temperature.

Further, it can easily be shown that, if two types of foreign atoms are present, one acting as a donor and the other as an acceptor, these may mutually increase each other's solubility; their concentrations tend to become equal and both types at centers are ionized, exactly as was found with the monatomic solids (Figs 10, 11, and 12). For ionic solids, this effect is known under the name of "charge compensation". It governs the composition of many minerals and has also been applied in synthesizing crystals with particular properties, e.g. phosphors.[12]

* For a more detailed discussion of this point, see ref. (7), section 26, and ref. (16).

† The situation becomes more complicated if the native atomic imperfections and/or the foreign atoms give rise to more than one level within the forbidden gap. In this case the mechanism of incorporation may become dependent on the concentration of F. The conclusion formulated above then still holds for the concentrations of F at which F starts to play a role in the neutrality condition.

6. PARTIAL EQUILIBRIA IN COMPOUNDS

In discussing monatomic solids containing foreign atoms (Section 3c), the possibility of partial equilibrium has been mentioned Similar possibilities exist also for compounds. Thus it may occur that internal atomic reactions describing the formation or annihilation of vacancies are frozen in, but that atoms may still enter the crystal through interstitial sites. This means that the composition and the properties of the basis crystal are fixed; the compound behaves to a certain extent as a monatomic crystal.

Such effects have been observed with PbS+Cu or Ni at temperatures between 100 and 500°C,[13] with ZnO+H_2[14] and with ZnO+Zn at temperatures between 500 and 1000°C.[15] The last example shows that the possibility of incorporating interstitial atoms under such conditions is not restricted to foreign atoms, but may exist also for the constituents of the matrix crystal.

7. CONCLUSIONS

The arguments of the present paper can easily be extended to more complicated systems (further types of defects; association effects;[16,17] compounds A_nB_m with $n - m$). Moreover, they can be applied to other equilibria such as liquid $\rightleftharpoons$ vapor, liquid $\rightleftharpoons$ solid and solid $\rightleftharpoons$ solid equilibria.[7,18]

The examples given may suffice, however, to show the effects we wanted to demonstrate. These effects may be summarized as follows:

(1) By using the law of mass action in combination with a simple graphical method of representation, it is easy to see that imperfections inside a solid are interdependent through reactions having partners in common.

(2) Imperfections having opposite effective charges tend to increase each other's concentrations; on the other hand imperfections having effective charges of the same sign tend to decrease each other's concentration.

(3) The mechanism of incorporation of foreign atoms depends on the energy levels caused by the foreign atoms in combination with the type of disorder prevailing in the crystal under the same condition in the absence of the foreign atoms.

(4) In monatomic solids the mechanism of incorporation of foreign atoms can only be influenced via the temperature: in compounds it can also be influenced via the partial pressures of the components of the base crystal or by any other way in which the thermodynamic potential of the crystal constituents may be altered.

8. THE APPLICATION OF THE THEORY IN PRACTICE

The various interrelations between the concentrations of imperfections have been demonstrated for models and equilibrium constants which were chosen quite arbitrarily. If one wants to apply the theory in practice, one usually has only a limited knowledge of these quantities and therefore it may seem a problem to know how to start. The following line may be followed in such cases:

(1) On the basis of provisional experimental results, a tentative correlation is arrived at between certain measured quantities (e.g. absorption, conductivity, magnetism) and certain imperfections (vacancies, interstitials, foreign atoms). This leads to the provisional choice of a model.

(2) A rough guess is made about the values of reaction constants K, as discussed in this paper. If possible, here too it is best to be guided by experiment. For electronic reactions, for instance, ionization energies may often be obtained from measurements of the Hall effect as a function of temperature.

(3) Using the provisionally chosen model in combination with the assumed constants, a graph is drawn of the concentrations of the various imperfections present in the model as a function of the parameter that has been varied in the experiment (partial pressure, temperature).

(4) The model can be checked and the constants adjusted by comparing the theoretical figure with a similar graph of the experimental data. This comparison can be made directly when the measurements have been carried out at a temperature at which the state of complete equilibrium is reached (e.g. at the temperature of preparation). Often the temperature of preparation is high, however, and the measurements are carried out at a lower temperature. In that case the experimental data have to be compared with the theoretical results for a cooled crystal, which can be deduced from the high-temperature equilibrium data. For particular assumptions that have to be made, see ref. (7). If there is agreement along general lines between theory and experiment (e.g. the slopes of log concentration against log partial pressure or $1/T$ have

the proper values), this indicates that the model chosen is correct. If not, changes have to be applied to the model until agreement is obtained. Now the proper values of the constants still have to be found. As the plots are on a logarithmic basis and all the equations are linear, variations in the constants result in a parallel shift of the lines. Therefore, from the shift of the lines required to make the theoretical and experimental curves coincide, the values of the constants can be obtained.

Such an analysis can often be carried out on the basis of physical experiments in one or two fields only (e.g. conductivity as a function of temperature and partial pressure). Once the proper model and the equilibrium constants have been determined, the theory predicts the variation of the concentrations of all the imperfections assumed in the model and thus predicts also the variation of all the properties of the system, including the ones that have not yet been measured. In such cases the theory is of great value in suggesting new experiments. In this way one also gets additional possible ways of checking the correctness of the assumptions made. Obviously the greater the diversity of experiments with which agreement is obtained, the surer one can be that the model and the constants arrived at are correct.

9. THE ABSENCE OF AN INFLUENCE OF THE TYPE OF BONDING

So far in this paper the interaction between imperfections has been discussed without any attention being paid to the type of bonding. Variations in the chemical composition were brought about by the addition or removal of atoms, and the formation of vacancies or interstitials was also discussed in terms of atoms. Charged imperfections appeared only as a consequence of ionization reactions. Charges built up in this way are charges relative to the normal crystal, i.e. they are *effective* charges. It is these effective charges which largely determine the statistical interaction between the various imperfections.

In compounds the actual state of the crystal will generally be one in which the constituents of the undisturbed crystal bear a charge. This is obviously so in ionic crystals, but in covalent crystals also there will normally be some accumulation of charge near constituents of one type. In discussing the properties of imperfections in such crystals, models are often used in which the charge distribution in the undisturbed crystal is taken into account and a corresponding notation is used. For instance, the properties of many compounds have been discussed in terms of ionic models (alkali halides, ZnS). Evidently in such cases more information is contained in the model and the symbols than is contained in the atomic representation as used in this paper. It may be asked whether this leads to different results. This is not the case. As long as we know that a substance is an insulator when pure and unperturbed, knowledge about the type of bonding is not required; conclusions concerning the interrelation between the concentrations of imperfections are independent of the model used. The reason for this is that in cases in which the actual charges are taken into account, the interaction between imperfections depends only on their effective charges, and these are the same in each type of representation, provided one compares centers that are chemically equivalent.[7]

As precise information concerning the type of bonding is often not available, it is advisable not to commit oneself but to use the general, atomic type of description. As has been shown in this paper, this has the additional advantage that one can use one type of description for monatomic solids and compounds, and this enables us to demonstrate similarities in the behavior of these crystals which would otherwise remain obscure.

VOL. 5 1958

REFERENCES

1. WAGNER C. and SCHOTTKY W. *Z. phys. Chem.* **B11,** 163 (1931).
   WAGNER C. *Z. phys. Chem.* (*Bodenstein Festband*) p. 177 (1931).
   WAGNER C. *Z. phys. Chem.* **B22,** 181 (1933); *Z. Elektrochem.* **39,** 543 (1933).
   SCHOTTKY W. *Z. phys. Chem.* **B29,** 335 (1935); *Z. Elektrochem.* **45,** 33 (1939).
   SCHOTTKY W. *Halbleiterprobleme* (Ed. W. SCHOTTKY) Vol 1, p. 139. F. Vieweg, Braunschweig (1954).
2. KRÖGER F. A. and VINK H. J. *Z. phys. Chem.* **203,** 1 (1954); *Physica* **20,** 950 (1954).
3. BROUWER G. *Philips Res. Rep.* **9,** 366 (1954).
4. REISS H., FULLER C. S., and MORIN F. J. *Bell Syst. Tech. J.* **35,** 535 (1956).
   REISS H., FULLER C. S., and PIETRUSZKIEWICZ A. J. *J. Chem. Phys.* **25,** 650 (1956).
5. FRITSCHE H. *Science* **115,** 571 (1952).
6. VALENTA M. W., and RAMASASTRY C. *Phys. Rev.* **106,** 73 (1957).

7. KRÖGER F. A., VINK H. J. *Solid-State Physics* (Ed. F. SEITZ and D. TURNBULL) Vol. 3, p. 307 Academic Press Inc., New York (1956).
8. BLOEM J. *Philips Res. Rep.* **11,** 273 (1956).
9. SELWOOD P. W. *J. Amer. Chem. Soc.* **70,** 883 (1948).
10. VERWEY E. J. W., HAAYMAN P. W., and ROMEIJN F. C. *Chem. Weekbl.* **44,** 705 (1948).
VERWEY E. J. W., HAAYMAN P. W., ROMEIJN F. C., and VAN OOSTERHOUT G. W. *Philips Res. Rep.* **5,** 173 (1950).
11. KOCH E. and WAGNER C. *Z. phys. Chem.* **B38,** 295 (1937).
12. KRÖGER F. A. and DIKHOFF J. A. M. *Physica* **16,** 297 (1950).
13. BLOEM J. and KRÖGER F. A. *Philips Res. Rep.* **12,** 281, 303 (1957).
14. THOMAS D. G. and LANDER J. J. *J. Chem. Phys.* **25,** 1136 (1956).
15. THOMAS D. G. *Bull. Amer. Phys. Soc.* (*II*) **1,** 348 (1956); HUTSON A. R. *Phys. Rev.* **108,** 222 (1957).
16. KRÖGER F. A. and VINK H. J. Report of the Conference on Semiconductors and Phosphors, Garmisch—Partenkirchen, 1956.
17. TELTOW J. *Halbleiterprobleme* (Ed. W. SCHOTTKY) Vol. 3, p. 26 F. Vieweg, Braunschweig (1956).
18. LONGINI R. L. and GREENE R. F. *Phys. Rev.* **102,** 992 (1956).

DL.
5
958

J. Phys. Chem. Solids Pergamon Press 1958. Vol. 5. pp. 224–235.

SELF-DIFFUSION OF BROMINE IN SILVER BROMIDE*

D. S. TANNHAUSER†

Department of Physics and Institute for the Study of Metals, University of Chicago, Chicago 37, Ill.

(*Received* 11 *September* 1957)

Abstract—The self-diffusion constant of bromine in AgBr has been measured in the temperature range 332–415°C, where D_{Br} varies from $2{\cdot}6\times10^{-12}$ to $4{\cdot}5\times10^{-10}$ cm²/sec. A plot of D_{Br} versus $1/T$ shows a definite curvature; $-Rd\ln D/d(1/T)$ increases from 45,000 cal/mole at the lower end to 60,000 cal/mole at the upper end of this range. D_{Br} has also been measured in 1·27 per cent cadmium-doped AgBr and found to be smaller by 15–30 per cent, the effect of cadmium being smaller at the lower temperature. These results do not fit into a simple theory of chemical equilibrium, and two alternative mechanisms of association between defects are invoked for an explanation. A number of experiments carried out under hydrostatic pressure give an activation volume for diffusion of ~ 44 cm³/mole, which supports the assumption that bromine diffuses by a vacancy mechanism.

VOL. 5 195

1. INTRODUCTION

THE defect structure of AgBr has received considerable attention, one of the reasons being the high concentration of defects near the melting point. These defects contribute measurably to the thermodynamic properties of the lattice, as well as to the more directly "defect-oriented" properties, such as electrical conductivity, diffusion, and magnetic resonance.

A simple model consisting of Ag^+ Frenkel defects (interstitials and vacancies in equal numbers) fits most of the experimental data below 300°C. TELTOW[1] measured the conductivity of pure and cadmium-doped AgBr, with Cd^{++} concentrations up to 22 per cent. KURNICK[2] extended these measurements to high pressures. These authors' interpretation of their data in the temperature range 150–300°C in terms of Frenkel defects is also in semiquantitative agreement with JUNG *et al.*'s[3] analysis of their tarnishing experiments as well as with a recent determination by LUCKEY and WEST[4] of the effect of bromine pressure on the dark conductivity of AgBr.

It should be mentioned that no discrimination is possible between a pure Frenkel defect structure on the one hand and a mixed Frenkel–Schottky defect structure on the other (a Schottky defect consists of a silver and bromine vacancy) on the basis of conductivity versus impurity-concentration isotherms. This fact, which has been stressed by TELTOW,[1] has frequently been overlooked. It is true both for his and for KURNICK's work.

The defect structure between 300°C and the melting point at 420°C is less clear. A predominantly Frenkel-defect structure in this temperature range has been proposed by CHRISTY and LAWSON[5] on the basis of heat-capacity and thermal-expansion data, by PATRICK and LAWSON[6] to explain thermoelectric measurements, and by FRIAUF,[7] who measured the deviation from the Nernst–Einstein relation.

On the other hand, the conductivity experiments indicate the appearance of Schottky defects above 300°C. KURNICK's experiments show an anomalously large pressure-dependence of the electrical conductivity at 406°C. Furthermore, an anomalous rise of the electrical conductivity above 350°C has been observed by both TELTOW and KURNICK. KURNICK tentatively interprets these indications to mean that at 406°C the concentration of Br^- vacancies is about 2·4 per cent, of Ag^+ vacancies about 2·6 per cent, and of Ag^+ interstitials about 0·15 per cent, and that the energy of formation of Schottky defects is about 50,000 cal/mole. In Fig.

* Based on a thesis submitted in partial fulfilment of the requirements for the Ph.D. to the University of Chicago.

† Present address: Laboratory for Insulation Research, Massachusetts Institute of Technology, Cambridge 39, Mass.

1 the temperature-dependence of the defect concentrations is plotted on this basis; the origin of the various slopes is explained in Section 4.

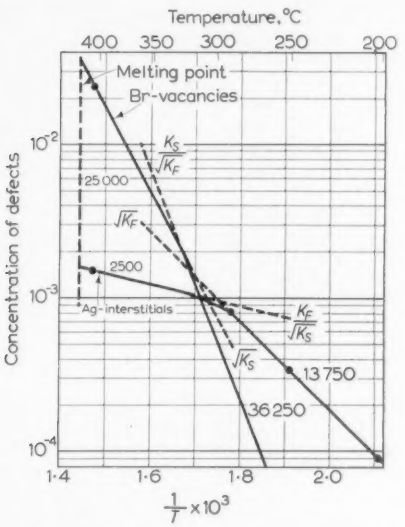

FIG. 1. Temperature-variation of the concentration of Ag^+ interstitials and Br^- vacancies in AgBr analyzed from KURNICK's[2] results (indicated by ●) on the basis of the chemical equilibrium equations (5), (6) and (7). Because of the interdependence of the two kinds of defects through the Ag^+ vacancies, the slopes change at the point $K_S = K_F$. The concentrations in the various regions are given by the symbols near the broken extension lines; the numbers are the values of $-R d\ln$ [concentration]$/d(1/T)$ in cal/mole.

CHRISTY's[8] creep experiments point to the diffusion of Schottky defects as being the rate-determining mechanism for creep. ZIETEN[9] even deduced from thermal-expansion measurements that Schottky defects predominate between room temperature and 280°C or higher.

Efforts have been made to determine the nature and concentration of defects by comparing the X-ray and macroscopic densities, but the results so far seem to be inconclusive (see TELTOW[10]).

We see that the temperature range 150–300°C can be fairly well analyzed in terms of Frenkel defects alone, even though no definite proof of their predominance exists, but less is known about the defect structure of AgBr above 300°C. Some experiments indicate that Schottky defects play a role near the melting point, but their number and temperature-dependence is very uncertain at best.

One phenomenon which is directly proportional to the number of Schottky defects present is the rate of self-diffusion of Br^- ions in AgBr. Here it is of course assumed that vacancy diffusion is the predominant mechanism. We have verified this by measuring the pressure-variation of the diffusion.

The rate of diffusion of Br^- ions in pure AgBr is not by itself a measure of the concentration of Schottky defects, since the mobility of the defects is not known. As shown later, the concentration can in principle be deduced from a combination of diffusion experiments on pure and impurity-doped material, provided that no association between defects exists.

The present paper reports diffusion experiments of this type. Cd^{++} ions were chosen as the impurity because the most lucid electrical-conductivity experiments[1,2] have been made on cadmium doped samples and because the ionic radius of Cd^{++} is only about 10 per cent smaller than that of Ag^+, so that Cd^{++} can be expected to introduce a minimum of strain in the lattice.

2. EXPERIMENTAL TECHNIQUE

The technique used is fairly standard today; a detailed description can be found, for instance, in the paper by COMPTON and MAURER.[11] Only a brief general account will be given here and points peculiar to the present experiment described in detail.

A thin layer of AgBr containing some radioactive Br^{82} (half-life = 35·8 hr) was evaporated on a circular masked portion of the base plane of a cylindrical sample of AgBr. During the run the tracer diffused into the sample, its total amount K per unit distance from the base plane obeying the equation (see JOST[12])

$$K = \frac{K_0}{(\pi D t)^{\frac{1}{2}}} \exp\left(-\frac{z^2}{4Dt}\right), \qquad (1)$$

where K_0 is the total amount of tracer, D the diffusion constant, t the total diffusion time, and z the distance from the base plane. After the run the sample was cut into thin slices parallel to the base plane. The radioactivity plotted logarithmically against z^2 resulted in a straight line with slope $1/4Dt$, from which D was calculated. "Thin" in this paragraph means $\ll (Dt)^{\frac{1}{2}}$. A proof that the essentially one-dimensional equation (1) applies

also to the present case, where the tracer does not cover the base plane of the sample completely, has been given elsewhere.[13]

The crystals were grown from the melt by the Czochralski method, and machined to cylindrical samples of about 8 mm diameter and 8–12 mm height. One surface was cut flat on a microtome, and the samples were annealed at 400°C for 24 hr, as was also done prior to each diffusion run. The samples were mostly single crystals, though a few broke up after annealing into a small number of grains with presumably low-angle grain boundaries.

The AgBr had been prepared in this laboratory from c.p. reagents and contained a few parts in 10^5 of metallic impurities (spectroscopically detected) and possibly 0·3 per cent chlorine.

No attempt was made to handle the crystals under red light. Some darkening was observed, but seemed to be confined to the outer fraction of a micron. A few experiments relevant to the darkening effect are discussed in Section 6.

One crystal (H) was grown from a melt to which 1·5 per cent $CdBr_2$ had been added. Since the amount of $CdBr_2$ in the crystal was above the limit of solid solubility at room temperature, it precipitated out on cooling. The resulting cloudiness disappeared on heating the crystal for a few minutes to 150°C. Sample H contained one large-angle grain boundary. Prior to the diffusion runs, this sample was annealed for 48 hr at 400°C. It was hoped that the diffusion value $D_{Cd} \geqslant 10^{-7}$ cm²/sec reported by SCHÖNE *et al.*[14] for Cd^{++} in AgBr would smooth out the inhomogeneities caused by the growth from the melt. The Cd^{++} content of the slices from this sample was analyzed polarographically after each run. 10 mg was dissolved in 10 ml NH_4OH (5 per cent) and the Ag^+ precipitated with HCl. About 10 per cent of the Cd^{++} coprecipitated with the Ag^+. This percentage was fairly reproducible and was taken into account. The method can be considered accurate to within ±10 per cent.

The radioactive AgBr was precipitated from HBr which had been irradiated in the Argonne National Laboratory reactor. A layer about 1 μ thick was evaporated in vacuum on to the samples and also onto a glass plate where its thickness was determined by weighing.

For the diffusion runs at atmospheric pressure, the samples were placed for 12–120 hr in a horizontal furnace in a region over which the temperature was uniform to within ½°C. The heating time of the furnace was about 1 hr; after the run the samples were quenched in air. The temperature was regulated by a proportional controller with a long-time stability of ±0·5°C. Frequent temperature readings were taken during the run with a platinum/platinum–10 per cent rhodium thermocouple calibrated by the Bureau of Standards and checked at the freezing points of lead, tin, and zinc. The accuracy of each reading was probably better than ±0·5°C.

For the high-pressure experiments, a conventional apparatus described by BRIDGMAN[15] was used. The high-pressure bomb was heated by a snug-fitting furnace. The heating time was about 5 hr and the runs all lasted 100–120 hr. DC–200 silicone oil transmitted the pressure, which was measured by a Manganin gauge with a probable accuracy of ±30 kg/cm². A Chromel/Alumel thermocouple, placed about 5 mm from the sample and calibrated against a Bureau of Standards platinum/platinum–rhodium couple, measured the temperature, which was kept constant by a proportional controller. Because of a noticeable temperature gradient in the bomb, the accuracy of each reading was probably not better than ±1°C.

Slices 2–10 μ thick were cut from the samples on an American-Optical microtome. The samples were aligned parallel to the cutting plane with a dummy sample and an optical beam system. In most cases the alignment was within 4 μ over the diameter of the sample.

During the first few runs, the thickness of the slices was determined by an interferometer, which measured the displacement of the sample holder. More accurate results were obtained in later runs from the weights of the slices and the known density of AgBr (6·473 g/cm³). In all the runs, the total thickness of the slices was also determined by the loss of weight of the sample.

The activity of the slices was in most cases determined in a scintillation counter, though for a few runs a G.M. flow counter was used. The scintillation counter usually gave better profiles. About 10^4 counts were accumulated from each slice, and appropriate corrections made for background and decay of activity. A diffusion profile of average quality is shown in Fig. 2.

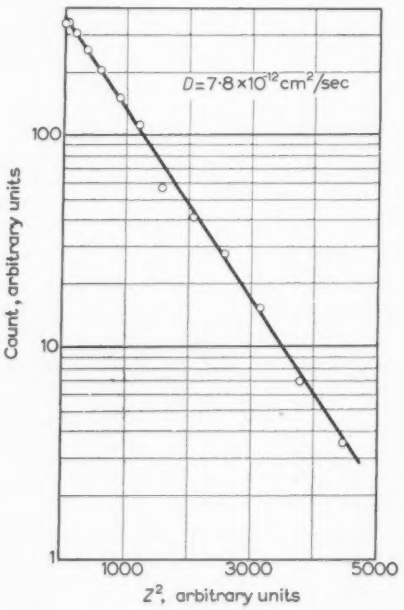

FIG. 2. A diffusion profile of average quality.

3. ERRORS AND CORRECTIONS

A correction formula for the finite thickness and the misorientation of the slices has been calculated by SHIRN *et al.*[16] An equivalent calculation for the finite thickness h of the applied layer leads to a correction factor of $[1-h^2/6Dt]$. The thicknesses were kept negligible (correction factor < 1 per cent); the misalignment correction amounted occasionally to 5 per cent.

The effects of the heating time and fluctuations about the equilibrium temperature were corrected by a procedure similar to the one used by SCHAMP and KATZ.[17]

The mean temperature was considered accurate to within $\pm 0{\cdot}5$°C in the atmospheric-pressure experiments and ± 1°C in the high-pressure experiments, which corresponds to an error of ± 4 and ± 8 per cent respectively in the diffusion constants.

The scatter of the points on the profile was usually very small, so that the slope $d\ln K/dz^2$ could be measured within ± 2 per cent. The determination of z^2 had some error involved in it, the sum of the weights of the slices tended to differ slightly from the loss of weight of the sample. This caused an uncertainty of up to ± 5 per cent in D.

The total estimated error varies from 5 to 10 per cent, and is indicated in the tables and figures.

4. THEORY

The diffusion will in general represent a superposition of several different diffusion mechanisms, each with its defect concentration n_i/N and defect jump frequency ν_i,

$$D = \frac{a^2}{N}\sum \nu_i n_i, \tag{2}$$

where a is the lattice constant and N the number of lattice sites per unit volume (see KITTEL[18]).

ν varies with temperature according to the formula

$$\nu = \nu_0 \exp\left(-\frac{\Delta G_\nu}{RT}\right) = \nu_0 \exp\left(\frac{\Delta S_\nu}{R}\right)\times \times \exp\left(-\frac{\Delta H_\nu}{RT}\right), \tag{3}$$

where ν_0 is an atomic vibration frequency, usually assumed to be temperature-independent, and ΔG_ν, ΔS_ν, and ΔH_ν are the Gibbs free energy, the entropy, and the enthalpy associated with raising one mole of defects isothermally from its equilibrium position to the top of the barrier between two such positions (WERT and ZENER[19]). n_i/N is governed for low concentrations by chemical equilibrium relations between the various kinds of defects.[20] The chemical equilibrium constants will also obey an activation-energy formula

$$K = K^0 \exp\left(-\frac{\Delta G_n}{RT}\right) = K^0 \exp\left(\frac{\Delta S_n}{R}\right)\times \times \exp\left(-\frac{\Delta H_n}{RT}\right), \tag{4}$$

where the thermodynamic quantities are associated with the "reaction" (formation, association, etc.) of one mole of defects. It has been proved[19] that the measured slope of an activated process will always be equal to ΔH. If ΔH varies with temperature, so will ΔS.

Thus the temperature-variation of the diffusion constant will only give some combination of activation enthalpies for the jump frequency and concentration of defects, and a pre-exponential D_0 containing the entropies of activation. Measurement of the diffusion as a function of impurity concentration will sometimes permit us to find the actual concentration and jump frequency of the defects. This will be discussed below. Information about the type of defects present can be deduced from the pressure-dependence of the diffusion constant. Since $\Delta H = \Delta E + p\Delta V$, ΔV being the activation volume for one mole of defects, both the jump frequencies and the concentrations of defects will decrease under a pressure p by factors of the form $\exp(p\Delta V/RT)$. Again we shall in general measure a combination of activation volumes, and theoretical assumptions will be necessary to sort out the various contributions.

We shall now outline the defect structure of AgBr as deduced from KURNICK's[2] conductivity measurements.

We assume with KURNICK that only Frenkel defects consisting of Ag^+ vacancies (Ag_v) and Ag^+ interstitials (Ag_i) and Schottky defects consisting of Ag^+ and Br^- vacancies (Br_v) exist in the lattice and that no association takes place.

The following equations govern the equilibrium between the defects:

$$[Ag_v]\cdot[Ag_i] = K_F(T) = K_F{}^0 \exp\left(-\frac{H_F}{RT}\right) \tag{5}$$

$$[Ag_v]\cdot[Br_v] = K_S(T) = K_S{}^0 \exp\left(-\frac{H_S}{RT}\right) \tag{6}$$

$$[Ag_i]+[Br_v] = [Ag_v], \tag{7}$$

where [ ] denotes concentration, and the entropy factors of equation (4) have been incorporated in $K^0_{F,S}$. It follows that

$$[Br_v] = \frac{K_S}{(K_S+K_F)^{\frac{1}{2}}} \tag{8}$$

$$[Ag_i] = \frac{K_F}{(K_S+K_F)^{\frac{1}{2}}} \tag{9}$$

so that the slopes of the defect concentrations change on passing through the point $[Br_v]=[Ag_i]$. The measured activation enthalpy of the diffusion of bromine by a vacancy mechanism should then be $(H_S/2)+H_v$ for $[Br_v] \gg [Ag_i]$ and $H_S-(H_F/2)+H_v$ for $[Br_v] \ll [Ag_i]$. In Fig. 1 the defect concentration in AgBr is plotted on the basis of KURNICK's[2] measurements (see Section 1) and the above equations.

To calculate the effect of unassociated divalent impurities on D_{Br}, we assume that:

(*a*) D_{Br} is proportional to $[Br_v]$.

(*b*) A divalent impurity of the form $CdBr_2$ goes into substitution in the lattice and changes the concentration of defects according to equations (5) and (6) and the following generalization of equation (7):

$$[Cd]+[Ag_i]+[Br_v] = [Ag_v], \tag{10}$$

where [Cd] denotes concentration of Cd^{++} ions.

(*c*) No association of defects takes place.

It follows that

$$Z = \frac{D_{Br}(\text{doped})}{D_{Br}(\text{pure})} = \frac{[Br_v](\text{doped})}{[Br_v](\text{pure})} = \frac{-\dfrac{[Cd]}{(K_F)^{\frac{1}{2}}} + \left\{\dfrac{[Cd]^2}{K_F} + 4\left(1+\dfrac{K_S}{K_F}\right)\right\}^{\frac{1}{2}}}{2\left(1+\dfrac{K_S}{K_F}\right)^{\frac{1}{2}}} \tag{11}$$

which measures the change of D_{Br} on doping. Equation (11) applies to any XBr_2 and with a change of sign to any Ag_2X. In Fig. 3 this equation is plotted on a semi-logarithmic scale for various ratios K_S/K_F. Since $K_F(T)$ is known,[1,2] a measurement of Z at a certain $[Cd]/(K_F)^{\frac{1}{2}}$ will measure K_S and therefore the concentration of Schottky defects. It is of interest that a given amount of divalent positive and negative impurities will decrease (or increase) D_{Br} by the same ratio.

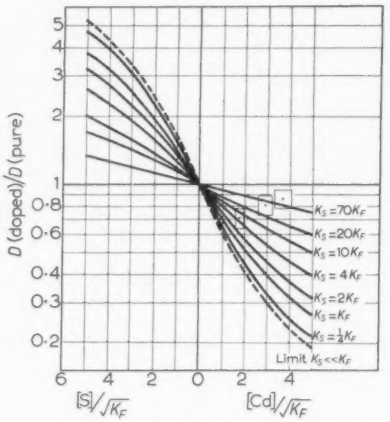

FIG. 3. The theoretical dependence of the diffusion constant of bromine on the divalent-impurity concentration and the equilibrium constants for Schottky and Frenkel defects in AgBr. ⊡ are measured points with their limits of error. (Section 7.)

If this model is correct, Z has to fall between the lower limit given by $K_S \ll K_F$ and the upper limit for which $[Br_v]$ is still a reasonable number, probably at most a few per cent near the melting point.

Two different association mechanisms can affect the diffusion:

(*a*) Association between Ag_v and Br_v. The number of complexes formed will obey the equation:

$$\frac{[Ag_v, Br_v]}{[Ag_v]\cdot[Br_v]} = K_a = K_a{}^0 \exp\left(\frac{H_a}{RT}\right), \tag{12}$$

where H_a is the enthalpy of association. By combining equation (12) with equation (6), the number $K_a \cdot K_S$ of these complexes is seen to be independent of all other defects in the lattice and not to be influenced by divalent impurities. Since they will contribute to diffusion, their number adds an unknown parameter which complicates the analysis.

(*b*) Association between Cd^{++} and Ag_v. The corresponding equation is:

$$\frac{[Cd, Ag_v]}{[Cd]\cdot[Ag_v]} = K_{a'} = K_{a'}{}^0 \exp\left(\frac{H_{a'}}{RT}\right). \tag{13}$$

VOL. 5 1958

Table 1. *The results of the diffusion experiments*

Run No.	Sample	Temperature (°C)	D_{Br}(cm²/sec)	l/l_0*	Type of experiment
4	B	332·2	$2{\cdot}57\pm0{\cdot}15\times10^{-12}$	1·014	Pure sample, standard procedure
4	E	332·2	$2{\cdot}63\pm0{\cdot}15\times10^{-12}$	1·014	Pure sample, standard procedure
5	B	349·6	$7{\cdot}7\ \pm0{\cdot}4\ \times10^{-12}$	1·015	Pure sample, standard procedure
3	B	350·6	$8{\cdot}2\ \pm0{\cdot}5\ \times10^{-12}$	1·015	Pure sample, standard procedure
3	E	350·6	$7{\cdot}9\ \pm0{\cdot}5\ \times10^{-12}$	1·015	Pure sample, standard procedure
6	B	361·5	$1{\cdot}46\pm0{\cdot}15\times10^{-11}$	1·016	Pure sample, standard procedure
9	E	380·2	$4{\cdot}73\pm0{\cdot}30\times10^{-11}$	1·018	Pure sample, standard procedure
2	E	403·7	$2{\cdot}19\pm0{\cdot}15\times10^{-10}$	1·021	Pure sample, standard procedure
7	E	415·0	$4{\cdot}55\pm0{\cdot}25\times10^{-10}$	1·023	Pure sample, standard procedure
6	H	361·5	$1{\cdot}27\pm0{\cdot}10\times10^{-11}$	1·016	Cd-doped sample
9	H	380·2	$3{\cdot}85\pm0{\cdot}25\times10^{-11}$	1·018	Cd-doped sample
7	H	415·0	$3{\cdot}24\pm0{\cdot}20\times10^{-10}$	1·023	Cd-doped sample
11	C	349·8	$2{\cdot}0\ \pm0{\cdot}20\times10^{-12}$	1·010	1,700 kg/cm² pressure
10	C	396·5	$3{\cdot}15\pm0{\cdot}3\ \times10^{-11}$	1·011	1,800 kg/cm² pressure
8	C	396·5	$4{\cdot}06\pm0{\cdot}4\ \times10^{-12}$	0·995	5,000 kg/cm² pressure
			Control Experiments		
2	F	403·7	$2{\cdot}2\pm0{\cdot}2\times10^{-10}$	1·021	Polycrystalline sample
2	B	403·7	$2{\cdot}2\pm0{\cdot}2\times10^{-10}$	1·021	Sample handled under red light
12	E	350·8	$7{\cdot}6\pm0{\cdot}5\times10^{-12}$	1·015	Diffusion run under bromine vapor

* Length of sample under the conditions of the experiment relative to length at r.t.p.

This again adds an unknown parameter to the analysis. The scheme of Fig. 3 cannot be used any more, since an unknown fraction of the Cd^{++} is associated and does not enter into equations (5), (6) and (10).

When discussing the results we shall consider both of these association mechanisms.

5. RESULTS

All the diffusion constants in this paper are corrected for thermal expansion and compressibility to give the actual diffusion values at the temperature and pressure of the experiment. The thermal-expansion values of ZIETEN[9] and the isothermal-compressibility values indirectly measured by TANNHAUSER *et al.*[21] were used to calculate the change in length relative to the length at room temperature and pressure. The ratios used are listed in Table 1.

It has been pointed out[22] that for the calculation of activation enthalpies of jump frequency and defect concentration the uncorrected values of the diffusion constants should be used because $D \propto a^2$ (see equation (2)). Presumably this argument holds only if most of the thermal expansion is caused by a change in lattice parameter and not by the creation of vacancies. Since in AgBr the latter might be true to a certain extent,[23] we have decided to use the corrected values of D. The correction for D is at most 5 per cent and the effect on the activation enthalpies is negligible.

The results of the diffusion runs on pure AgBr are shown in Table 1 and Fig. 4. The deviation of the diffusion values from a simple activation-energy curve is believed to be real and not due to experimental error.

The diffusion in the doped sample H was measured at three different temperatures; the results are shown in Table 1. Fig. 5 shows that the deviation from the pure material value decreases with decreasing temperature. In sample H some grain-boundary diffusion was detected autoradiographically, but most of the tracer diffused through the bulk of the material. No systematic deviation from an $\exp(-z^2)$ was detected. It is concluded that grain-boundary diffusion did not falsify the measured values.

By polarographic analysis sample H was found

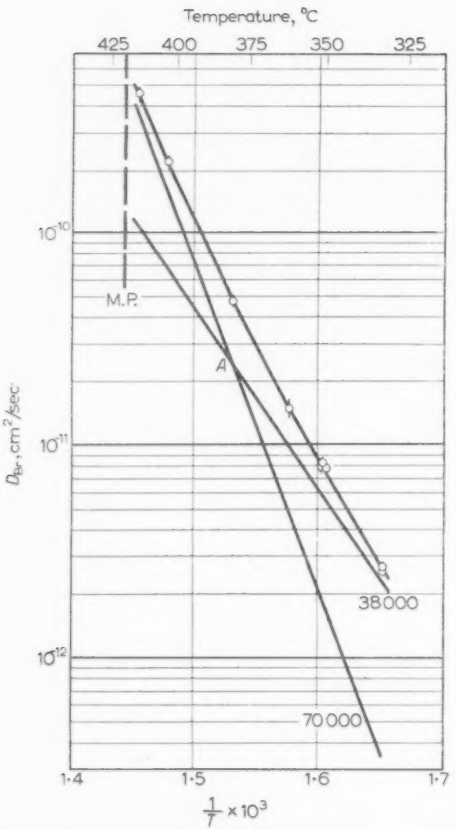

FIG. 4. Results of the diffusion experiments on pure AgBr. The sum of the two straight lines is equal to the measured curve. The numbers are the slopes of the lines in cal/mole.

to contain $1{\cdot}27 \pm 0{\cdot}13$ mole per cent Cd^{++}, without a discernible concentration gradient. Another sample showed a marked concentration gradient (0·6–1·8 mole per cent over a distance of 0·1 mm) after annealing for 48 hr at 400°C, which throws some doubt on SCHÖNE *et al.*'s[14] value of $D_{Cd} \geqslant 10^{-7}$ cm²/sec at 400°C.

Three experiments on pure AgBr were made at high pressure. The results are shown in Table 1 and plotted in Fig. 6 as a function of p/RT, together with the corresponding interpolated diffusion values at zero pressure. The slope of the isotherms determines an activation volume which will be discussed below.

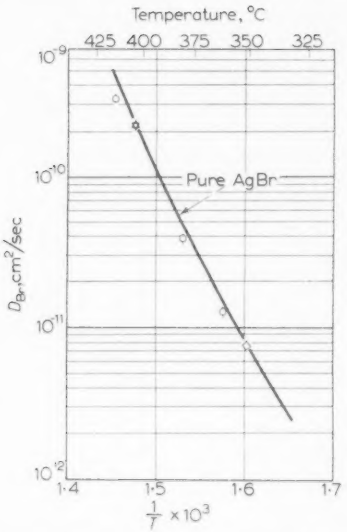

FIG. 5. Results of diffusion experiments on the Cd^{++}-doped sample H ⊙, on a polycrystalline sample △, a sample handled under red light ▽, and a sample diffused under bromine gas ◇.

6. CONTROL EXPERIMENTS

To judge whether grain-boundary and surface diffusion and photolytic loss of bromine from the crystals (see LUCKEY[24]) affected the measured diffusion constants, the following experiments and observations are pertinent.

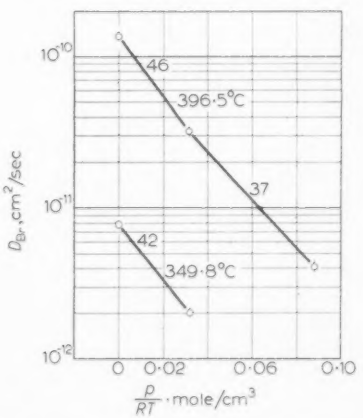

FIG. 6. Results of the high-pressure experiments plotted against p/RT. The numbers near the curves are the activation volumes in cm³/mole.

(*a*) A polycrystalline sample with a grain size ~ 2 mm gave at 403·7°C the same diffusion constant as the single crystals.

(*b*) Autoradiographs did not detect any surface diffusion or grain-boundary diffusion in the pure samples (for the cadmium-doped sample, see above).

(*c*) No systematic deviation from a $K \propto \exp(-z^2)$ relation was ever detected in the diffusion profiles.

(*d*) One sample was handled under red light from the time a fresh surface was cut on the microtome until after the end of the diffusion run. It was hoped that any effect of previous illumination would be confined to the outer few microns and that the diffusion value measured would be representative of the undisturbed crystal. The value measured was the same as in the usual run at the same temperature (403·7°C).

(*e*) One diffusion run was made at 350·8°C under bromine vapor. The partial pressure of bromine was about 60 mm, with some air present in the system. In this experiment the radioactive material which had been applied to one face of the sample distributed itself apparently uniformly around the sample, presumably by exchange with the bromine gas. This was detected autoradiographically and caused the activity of the slices to deviate upwards from the straight line at low activities. Nevertheless a fairly accurate diffusion rate could be determined from the first few slices. It was the same as in the usual runs, within the limit of error. This experiment was based on LUCKEY and WEST's[1] observation that bromine vapor brings crystals which are deficient in bromine back to the stoichiometric ratio in a few minutes. It shows that the bromine deficiency in our samples was much less than the intrinsic defect concentration at and above 351°C.

It is concluded that the diffusion values reported here are representative of the undisturbed crystals.

7. DISCUSSION

The objective of this work had been to determine the number of Schottky defects in AgBr from the values of $D_{Br}(\text{doped})/D_{Br}(\text{pure})$ and the known values of K_F. We found, however, that the diffusion constants measured do not lend themselves to an interpretation with a small enough number of parameters to permit this. After

*Table 2. Analysis of experiments on the Cd^{++}-doped sample H**

(a)		(b)			(c)
T(°C)	$\frac{D(\text{doped})}{D(\text{pure})}$	$\frac{[\text{Cd}]}{(K_F)^{\frac{1}{2}}}$	$[\text{Br}_v]$	$[\text{Ag}_i]$	$\frac{[\text{Cd, Ag}_v]}{[\text{Cd}] \cdot [\text{Ag}_v]} = K_{a'}$
361·5	0·87	3·7	$4{\cdot}5\times10^{-2}(0{\cdot}7\times10^{-2})$	$0{\cdot}03\times10^{-2}(0{\cdot}13\times10^{-2})$	$5{\cdot}6\times10^{2}$
380·2	0·81	2·9	$3{\cdot}1\times10^{-2}(1{\cdot}2\times10^{-2})$	$0{\cdot}06\times10^{-2}(0{\cdot}14\times10^{-2})$	$0{\cdot}84\times10^{2}$
415·0	0·71	1·8	$1{\cdot}8\times10^{-2}(3{\cdot}1\times10^{-2})$	$0{\cdot}3\times10^{-2}(0{\cdot}15\times10^{-2})$	$0{\cdot}033\times10^{2}$†

	(d)	(e)	
T(°C)	$\frac{D(\text{Ag}_v, \text{Br}_v)}{D(\text{Br}_v)}$	$\frac{D(\text{Ag}_v, \text{Br}_v)}{D(\text{Br}_v)}$	$\frac{D(\text{doped})}{D(\text{pure})}$
361·5	3/1	2/1	0·83
380·2	1/1	1/1	0·81
415·0	0·15/1†	0·28/1	0·86

Remarks:

Part (a). Measured values.

Part (b). Analysis with KURNICK's K_F on the basis of no association. KURNICK's values of $[\text{Br}_v]$ and $[\text{Ag}_i]$ are given in parentheses.

Part (c). Analysis with KURNICK's K_F and K_S and (Cd, Ag_v) complexes present.

Part (d). Analysis with KURNICK's K_F and K_S and (Ag_v, Br_v) complexes present.

Part (e). Values calculated from the analysis of D_{Br} (pure) (see equations (15)–(17)).

* Cd^{++} concentration = 1·27 mol. per cent.

† These values are extrapolated assuming a simple activated behavior for $K_{a'}$, and $D(\text{Ag}_v, \text{Br}_v)/D(\text{Br}_v)$, respectively.

demonstrating this, we shall interpret our results on the basis of KURNICK's[2] estimate of the defect concentration and the two alternative association mechanisms mentioned in Section 4.

We note that the large activation volume given in Fig. 6 supports the contention that a vacancy mechanism operates for Br^- diffusion; this will be taken up in detail later.

To analyze the values of D_{Br}(doped)/D_{Br}(pure) on the basis of equations (5), (6), and (10) (no association), we have plotted them in Fig. 3, using KURNICK's K_F and a mean value of 1·27 per cent for [Cd]. In Table 2, part (b), the values of $[Br_v]$ and $[Ag_i]$ so deduced are listed. Only at 415°C do the concentrations agree reasonably well with KURNICK's values; at lower temperatures $[Br_v]$ is much too large by any estimate. In other words, the effect of doping is too small to agree with this model, except near the melting point.

We shall therefore generalize our model and assume that at the lower temperatures part of the Cd^{++} is complexed with Ag_i and does not influence the Br_v concentration. Association constants $K_{a'}$ (see equation (13)) that would fit KURNICK's defect concentrations and our results are shown in Table 2, part (c). The enthalpy of association estimated from these values is $H_{a'} \sim 84{,}000$ cal/mole, which is much larger than the theoretical value $\epsilon^2/\epsilon r_0 = 6{,}200$ cal/mole ($\epsilon = 13{\cdot}1$, $r_0 = \sqrt{2}\times 2{\cdot}88$ Å) and the experimental value of 3,600 cal/mole estimated by EBERT and TELTOW[25] from conductivity measurements. It is just outside the conceivable upper limit of 82,000 cal/mole which results by setting $\epsilon = 1$. However, the uncertainties in the values of D_{Br}(doped)/D_{Br}(pure) are such that the large value of $H_{a'}$ calculated is extremely uncertain and does not necessarily invalidate the physical picture.

The above model does not explain the observed curvature in D_{Br}(pure) versus $1/T$. The activation enthalpy varies from $\sim 60{,}000$ cal/mole at the upper end to $\sim 45{,}000$ cal/mole at the lower end of our range. A curvature in the same direction is observed in the conductivity of AgBr[1,2] and to a lesser degree in the conductivity of AgCl.[11,25] It has not been observed in the diffusion of chlorine in AgCl,[11] but the measurements there are not as detailed as the present work. The curvature observed in the conductivity has found no satisfactory explanation, and whatever is causing it might also cause the one observed here. A loosening of the lattice, as proposed by EBERT and TELTOW,[25] would presumably cause opposite curvatures from the ones observed. A transition from a predominantly Frenkel to a predominantly Schottky defect structure would also cause the opposite effect for D_{Br}, as seen from Fig. 1, though it would qualitatively explain the conductivity results, as proposed by KURNICK. Experiment (e) of Section 6 rules out the possibility that a deficiency of bromine is the cause. Possibly at the high concentration of defects near the melting point, there is an interaction more complicated than the chemical equilibrium theory, which might give rise to all the observed curvatures. A detailed theory of such an interaction is lacking.

We can compare the average measured activation enthalpy $\bar{H} = 52{,}000$ cal/mole, which we assume here to be the enthalpy of creation and motion of unassociated Br_v, with other experiments. The corresponding enthalpy of activation for D_{Cl} in AgCl measured by COMPTON and MAURER[11] is 37,000 cal/mole. It is reasonable that the smaller Cl^- (1·81 Å according to PAULING[26] as compared with 1·95 Å for Br^-) has the smaller enthalpy. Using KURNICK's[2] estimate of $H_S \sim 50{,}000$ cal/mole for the enthalpy of formation of Schottky defects (see Fig. 1), we get the activation enthalpy of motion $H_v(Br_v) = \bar{H} - H_S/2 \cong$ $\cong 26{,}000$ cal/mole, which is about three times larger than $H_v(Ag_i)$, a reasonable result considering the much smaller size of Ag^+ (1·26 Å according to PAULING). Further, it is of interest that WEERTMAN[27] has recalculated CHRISTY's[8] data for creep of AgBr on the basis of his theory and an activation enthalpy of 51,000 cal/mole for D_{Br} and has found good agreement between theory and experiment.

As a second possible model to explain the ratios D_{Br}(doped)/D_{Br}(pure), we assume that at the lower temperatures part of the Schottky defects is in the associated state. The concentration of this part is not influenced by the Cd^{++} concentration (see equation (12)). The ratios of the contributions to diffusion that would fit roughly into KURNICK's defect concentrations and our measurements are listed in Table 2 part (d). Since the total activation enthalpy for diffusion of unassociated Br_v is $H_S/2 + H_v$ (assuming that the concentration of Frenkel defects is negligible) and for associated

Br_v is $H_S - H_a + H_{v'}$ (H_v and $H_{v'}$ are the activation enthalpies of motion of Br_v in the two states), the above ratios give

$$H_a - \frac{H_S}{2} + H_v - H_{v'} \cong 47{,}000 \text{ cal/mole.} \quad (14)$$

Before discussing equation (14), we shall deduce a number of other relations between the activation enthalpies from the plot of D_{Br}(pure) versus $1/T$. The curvature in this plot (Fig. 4) can also be explained by a transition from associated to dissociated Schottky defects, as invoked above. The curve should be the sum of the contributions of the two kinds of defects to diffusion and, since their concentrations are independent, it should be a sum of two exponentials. Because of the slight curvature, the choice of the cross-over point (A) is somewhat arbitrary, and we have chosen it at 380·2°C to correspond with the result from D_{Br}(doped)/D_{Br}(pure) at the same temperature. The exponents are affected by the choice of the cross-over point, but their difference is affected much less. From Fig. 4 follow the relations:

$$\frac{H_S}{2} + H_v = 70{,}000 \text{ cal/mole} \quad (15)$$

$$H_S - H_a + H_{v'} = 38{,}000 \text{ cal/mole} \quad (16)$$

so that

$$H_a - \frac{H_S}{2} + H_v - H_{v'} = 32{,}000 \text{ cal/mole.} \quad (17)$$

Equation (17) is probably better established than the equivalent equation (14) because of the uncertainties in D_{Br}(doped)/D_{Br}(pure). Using KURNICK's value of $H_S \sim 50{,}000$, we get from equations (15)–(17) $H_v = 45{,}000$ and $H_a - H_{v'} = 12{,}000$. Further, since the enthalpy to create an associated pair has to be positive, $H_a < H_S$, and since the surrounding of the Br_v is disturbed by the Ag_v in the associated state, which will presumably lower the enthalpy of activation for jumping, $H_{v'} < H_v$. $0 < H_{v'} < 38{,}000$ and $12{,}000 < H_a < 50{,}000$ satisfy all the above relations. H_a is within the theoretical limits $e^2/r = 115{,}000$ and $e^2/\epsilon r = 8{,}800$.

Going back and calculating from the two straight lines in Fig. 4 what the ratio D_{Br}(doped)/D_{Br}(pure) should be, we get the values given in Table 2, part (e). The lines have been chosen to agree with the experimental value of D_{Br}(doped)/D_{Br}(pure) at 380·2°C; at 361·5°C the agreement is still good, at 415°C the deviation between experiment and theory is appreciable, but even a completely dissociated Schottky defect structure would give 0·82 at this temperature instead of the measured 0·71; in other words the effect of Cd^{++} is larger at this temperature than would be expected on the basis of KURNICK's concentrations and completely dissociated defects.

Thus the second model explains semi-quantitatively both the curvature in D_{Br}(pure) versus $1/T$ and the ratios D_{Br}(doped)/D_{Br}(pure).

Up to this point ν_0 in equation (3) was assumed to be independent of temperature. Actually ν_0 will probably vary as $\sqrt{c_{ij}}$, where c_{ij} is an appropriate elastic constant near the defect. For a consistent analysis on this basis, all the data involving mobility of ions would have to be recalculated. However, the curvature in a plot of $D/\sqrt{c_{11}}$ against $1/T$ (where c_{11} is the elastic constant which shows the strongest temperature-dependence[21]) is scarcely different from the one in Fig. 4. It seems therefore that the curvature cannot be explained by the temperature-variation of ν_0.

A few remarks about the activation volumes follow. Fig. 6 shows that ΔV is 42–46 cm³/mole at low pressure and decreases slightly at higher pressure. The measurements are not extensive enough to consider the observed temperature- and pressure-variation significant (though the temperature-variation is in line with the observed variation of the activation enthalpy) and no conclusions will be drawn from this variation. CHRISTY's[8] value of 38·3 cm³/mole for the activation volume of creep, measured in the pressure range 3,000–6,000 kg/cm², is probably the same as ours within the limits of error. This supports CHRISTY's contention that diffusion of bromine is the rate-limiting mechanism for creep.

Since the activation volume contains an unknown fraction arising from the mobility, we cannot tell from it whether associated or unassociated Schottky defects play the main role and whether there is a transition between the two kinds. KURNICK's[2] work indicates that ΔV_S for formation

of unassociated Schottky defects (see equation (6)) is 43 ± 5 cm^3/mole; combining this with our measurements we find

$$\Delta V_v = 44 - \frac{43}{2} = 22{\cdot}5 \text{ cm}^3/\text{mole}$$

for the activation volume of jump frequency of unassociated Br_v. (Here we have assumed that $K_S \gg K_F$ in the range of our work.) If, on the other hand, associated Schottky defects operate, and we assume an activation volume of formation slightly smaller than the molar volume of AgBr, say 25 cm^3/mole, we get

$$\Delta V_{v'} = 44 - 25 = 19 \text{ cm}^3/\text{mole}$$

for the activation volume of motion of Br_v in the associated state. Both of these activation volumes are much larger than those deduced by KURNICK for the motion of Ag^+ defects, a reasonable result considering the relative size of the ions.

It is appropriate to discuss here MURIN *et al.*'s[28] measurements of the diffusion of bromine in AgBr. They report

$$D_{Br} = 0{\cdot}50 \times \exp(-24{,}000/RT) \text{ cm}^2/\text{sec}$$

in the temperature range 250–350°C. Their values for D_{Br} are larger than ours by one to two factors of ten, while the activation enthalpy is much smaller than ours. Since they worked with pressed powder samples and used an absorption method for measuring D_{Br}, it is hard to estimate the reliability of their data. JOHNSTON's[29] measurements of the conductivity in plastically deformed AgBr, which indicate an activation enthalpy of 26,000 cal/mole for the diffusion of bromine in such crystals, make it seem likely that MURIN *et al.* measured mainly grain-boundary and not volume diffusion.

8. CONCLUSIONS

The important results of the present work are:

(*a*) The curvature in the log D versus $1/T$ plot in pure AgBr.

(*b*) The deviation of the results on doped material from a simple chemical equilibrium theory.

(*c*) The large activation volume (~ 44 cm^3/mole) of diffusion.

Point (*c*) seems to establish definitely that a vacancy mechanism operates for diffusion, but no decision is possible from the magnitude of the activation volume whether the Br^- vacancies are free or associated with Ag^+ vacancies. A mixture of these two kinds of defects would explain (*a*) and (*b*). Another model consisting of unassociated Br^- vacancies together with association of Cd^{++} ions and Ag^+ vacancies would explain (*b*) but not (*a*); the enthalpy of association would be unreasonably high, but since its value depends very strongly on inaccuracies in the measurements the model is not necessarily ruled out.

It seems that accurate measurements of the diffusion of cadmium in AgBr, as proposed by LIDIARD,[30] would shed much light on the picture by giving independent estimates of the association constants of Cd^{++} ions and Ag^+ vacancies.

Acknowledgements—The author wishes to express his particular gratitude to Professor A. W. LAWSON for suggesting this problem and for his constant interest and encouragement. He is also indebted to Professor N. H. NACHTRIEB for frequent advice on the experimental aspects of this work and for the use of his laboratory and to Professor M. H. COHEN for many enlightening discussions. It is a pleasure to acknowledge the expert help of Mr. R. LOWELL in running the high-pressure system, and the kindness of Professors A. TURKEVITCH and C. T. TOMIZUKA in permitting the use of their scintillation counters.

This work was supported in part by the Office of Naval Research and by the Atomic Energy Commission.

REFERENCES

1. TELTOW J. *Ann. Phys.* (*Leipzig*) **5,** 63 (1950).
2. KURNICK S. *J. Chem. Phys.* **20,** 218 (1952).
3. JUNG L., STASIW O., and TELTOW J. *Z. phys. Chem.* **198,** 186 (1951).
4. LUCKEY G. W. and WEST W. *J. Chem. Phys.* **24,** 879 (1956).
5. CHRISTY R. W. and LAWSON A. W. *J. Chem. Phys.* **19,** 517 (1951).
6. PATRICK L. and LAWSON A. W. *J. Chem. Phys.* **22,** 1492 (1954).
7. FRIAUF R. J. *Phys. Rev.* **105,** 843 (1957).
8. CHRISTY R. W. *Acta Met.* **2,** 284 (1954).
9. ZIETEN W. *Z. Phys.* **145,** 125 (1956).
10. TELTOW J. *Ann. Phys.* (*Leipzig*) **12,** 111 (1953).
11. COMPTON W. D. and MAURER R. J. *J. Phys. Chem. Solids* **1,** 191 (1956).

12. JOST W. *Diffusion* p. 19 Academic Press, Inc., New York (1952).
13. TANNHAUSER D. S. *J. Appl. Phys.* **27,** 662 (1956).
14. SCHÖNE E., STASIW O., and TELTOW J. *Z. phys. Chem.* **197,** 145 (1951).
15. BRIDGMAN P. *Physics of Solids* G. Bell and Sons, London (1949).
16. SHIRN G. A., WAJDA E. S., and HUNTINGTON H. B. *Acta Met.* **1,** 513 (1953).
17. SCHAMP H. W. and KATZ E. *Phys. Rev.* **94,** 828 (1954).
18. KITTEL C. *Introduction to Solid-State Physics* p. 310 John Wiley and Sons, Inc., New York (1953).
19. WERT C. and ZENER C. *Phys. Rev.* **76,** 1169 (1949).
20. KRÖGER F. A. and VINK H. J. *Solid-State Physics* Vol. 3, p. 307 (Ed. F. SEITZ and D. TURNBULL) Academic Press, Inc., New York (1956).
21. TANNHAUSER D. S., BRUNER L. J., and LAWSON A. W. *Phys. Rev.* **102,** 1276 (1956).
22. TOMIZUKA C. T. Private communication.
23. LAWSON A. W. *Phys. Rev.* **78,** 185 (1950).
24. LUCKEY G. W. *J. Chem. Phys.* **23,** 882 (1955).
25. EBERT I. and TELTOW J. *Ann. Phys.* (*Leipzig*) **15,** 268 (1955).
26. PAULING L. *J. Amer. Chem. Soc.* **49,** 765 (1927).
27. WEERTMAN J. Private communication; theory in *J. Appl. Phys.* **28,** 362 (1957).
28. MURIN A. N., KAZAKOVA G. N., and LURIE B. G. *Dokl. Akad. Nauk SSSR* **99,** 529 (1954).
29. JOHNSTON W. G. *Phys. Rev.* **98,** 1777 (1955).
30. LIDIARD A. B. *Phil. Mag.* **46,** 815 (1955).

OL.
5
958

JEAN-MARIE MOULON: **Les Transistrons dans les Amplificateurs.** Gauthier-Villars, Paris, 1956. 316 pp.

M. MOULON's book is an exhaustive account of the application of transistors to amplifier circuits. The book is written from the viewpoint of the electrical engineer rather than from that of the scientist, and from that viewpoint it covers the subject matter thoroughly and, for the most part, clearly and accurately. The author limits himself quite strictly to amplifier circuits, no mention of oscillators and only the briefest passing references to counting and switching circuits being made.

After a brief introduction in which a very short and rather sketchy account of fundamental semiconductor physics and the principles of transistor operation is presented and after a brief review of the properties of linear passive four-terminal electrical networks, the author considers the applications of both junction and point-contact transistors at low frequencies. All possible aspects of transistors as linear circuit elements are discussed in terms of the equivalent circuits which are developed at the outset. A chapter is devoted to a discussion of the selection of the load impedance and operating point, and another to problems of biasing and power supply. Inverse feedback circuits, power amplifiers, and direct-coupled amplifiers are all considered in some detail in separate chapters.

The author presents a rather complete discussion of the behavior of transistors at high frequencies, and follows this material with a chapter about tuned amplifiers and another concerning wide-band amplifiers. A brief description of noise sources in transistors and of some modern developments such as unipolar transistors, surface barrier transistors, and NPIN and PNIP units concludes the book.

The material set forth is well organized and clearly presented, with very liberal use of diagrams and illustrations. Numerical examples are worked out in detail throughout the text, but no exercises are given. There is a table of contents, but no author or subject index. References to the literature are made at appropriate points in the text, though rather more sparsely than one might desire in a work on this subject. While the circuitry aspects of the material are very complete and suitably presented, the reader is not furnished with a very good introduction to semiconductor physics, the principles underlying the operation and fabrication of the devices under consideration being treated very briefly and at one point at least (where the physics of the alloying process used for making diodes and transistors is discussed) not very accurately. Nevertheless, the book treats those phases of the subject to which it is mainly directed very well, and should prove quite valuable to workers whose interests lie in the applications of transistors as linear circuit elements.

J. P. MCKELVEY

Solid State Physics. Volumes 4 and 5. Edited by F. SEITZ and D. TURNBULL. Academic Press, Inc., New York, 1957. Vol. 4: 540 pp., $12.00. Vol. 5: 455 pp., $11.00.

THESE two volumes, recently published, are of the same high standard as the preceding ones. They present, on the whole, advanced rather than introductory treatments, but most of the papers cover a large enough field to be of interest to non-specialist readers. The balance between theoretical and experimental material is well kept.

Titles in Volume 4 are: "Ferroelectrics and antiferroelectrics" by W. KÄNZIG; "Theory of mobility of electrons in solids" by F. J. BLATT; "The orthogonalized plane wave method" by T. O. WOODRUFF; "Bibliography of atomic wave functions" by R. S. KNOX; and "Techniques of zone melting and crystal growing" by W. G. PFANN.

The papers by KÄNZIG and BLATT are both more than 150 pages long, and cover their fields admirably and exhaustively. KÄNZIG presents very clearly the truly complex experimental situation in ferroelectricity. He rightly insists on the difficulties related to ionic polarization. BLATT's subject has often been treated, but never so simply, completely, and in such an up-to-date way. Emphasis is placed on semiconductors and metals; thermal and magnetic effects are discussed at length, and "new" subjects, such as phonon drag, hot electrons, scattering by stacking faults and dislocations, are presented. WOODRUFF's paper is a report of work on silicon. It is rather a pity that HEINE's extensive work on aluminium, using the

VOL. 5 1958

same method, appeared too late to be discussed here. KNOX's table of functions and PFANN's paper will no doubt be of great help to specialists.

Titles in Volume 5 are as follows: "Galvanometric and thermomagnetic effects in metals" by J. P. JAN; "Luminescence in solids" by C. C. KLICK and J. H. SCHULMAN; "Space groups and their representations" by G. F. KOSTER; "Shallow impurity states in silicon and germanium" by W. KOHN; and "Quadrupole effects in nuclear magnetic resonance studies of solids" by M. H. COHEN and F. REIF.

JAN's paper presents a very thorough picture of the experimental situation in his field, with emphasis on magnetoresistance and the Hall effect. It overlaps somewhat BLATT's paper in the previous volume, but the aims of the two papers are clearly different. KLICK and SCHULMAN's paper is a somewhat simplified account of luminescence. KOSTER's paper will be of great practical help in the computation of energy band structures in solids, including spin-orbit coupling. It is presented in a very systematic way. KOHN's paper deals with isolated impurities of a simple type in semiconductors. This rather restricted field is of primary importance for the comprehension of solid-state physics both from a theoretical point of view, and also from a utilitarian, technological point of view. KOHN presents an extremely clear, complete and interesting picture, which owes much to his own personal work. Finally, COHEN and REIF's paper outlines the theory of quadrupole nuclear resonance effects, and the data it has been possible to obtain from them on the electronic structure of solids.

J. FRIEDEL

H. K. HENISCH. **Rectifying Semiconductor Contacts.** Clarendon Press, Oxford, 1957. 372 pp., 70*s*.

THIS volume is announced as being intended primarily for those who wish to make a specialized study of rectifying contacts between metals and semiconductors. Being written by one of the best-known workers in the field, it is an extremely thorough review of the subject.

The introduction contains a very complete historical survey which can be criticized only on the ground that it is so thorough that some theories which are not nowadays of much interest, even historically, are included. The next two chapters are devoted to an exposition of the basic problems of semiconductor physics and the bulk properties of important semiconductors, which are used as a background in the rest of the book. There follow two chapters on phenomenological descriptions of the properties of plate and point-contact metal/semiconductor rectifiers. Theory is then dealt with in three chapters entitled respectively 'Unipolar rectification theories', 'Theory of injecting contacts', and some special contact theories. The last two chapters describe some recent and in some cases as-yet-unpublished experiments on point-contact and plate rectifiers.

On reading the book one may wonder why, after giving such a good and thorough-going description of the basic properties of semiconductors and explaining clearly concepts such as quasi-Fermi levels, etc., the author did not take advantage of them to include, besides the metal/semiconductor theories, some description of *p–n* junction behaviour. Indeed, one feels that the book would not have had to be much thicker in order to include internal rectification in semiconductor compositional structure besides the much more specialized and less well understood subject of metal/semiconductor contacts. Some of the now discarded theories and the less important experiments could have been omitted in order to eliminate enough pages to be able to include this treatment of *p–n* junctions. Nevertheless, in the opinion of the reviewer this is a rather minor drawback, inasmuch as the book is obviously intended more as a source of reference for workers in the field than as a textbook. References to work in the field of *p–n* junctions and transistors are available elsewhere, and there was undoubtedly a definite need for such a review as this in the field of metal/semiconductor contacts.

The author and the publisher are to be congratulated on the precise definition of symbols used consistently throughout the volume, with a table of symbols included at the end. A well-selected, though not exhaustive bibliography is appended, covering the period from 1874 to the first few months of 1955. As it stands this book will certainly be extremely useful to workers in the field of rectification in semiconductor devices.

P. AIGRAIN

PAPERS TO BE PUBLISHED IN FUTURE ISSUES

V. L. GINZBURG and A. P. LEVANIUK: Light scattering near second-order phase transition and Curie points.

D. F. C. MORRIS: The lattice energy and heat of formation of lithium monosulphide.

J. C. PHILLIPS and H. B. ROSENSTOCK: Topological methods of locating critical points.

R. W. KEYES: Effects of electron–electron scattering on the electrical properties of semiconductors.

G. B. BENEDEK and T. KUSHIDA: Pressure dependence of the Knight shift in the alkali metals and copper.

O. FLINT and J. H. O. VARLEY: On the mechanism of oxide film formation on zirconium.

T. O. WOODRUFF and W. KÄNZIG: Paramagnetic resonance absorption of a *V*-center in LiF.

M. YA. AZBEL' and E. A. KANER: Cyclotron resonance in metals.

A. ASCOLI, M. ASDENTE, E. GERMAGNOLI and A. MANARA: Activation energies for production and migration of vacancies in platinum.

G. BOGNER und E. MOLLWO: Über die Herstellung von Zinkoxydeinkristallen mit definierten Zusätzen.

H. RUPPRECHT: Über Konzentration und Beweglichkeit von Elektronen in Zinkoxydeinkristallen mit definierten Zusätzen.

A. D. PEARSON: Studies on the lower oxides of titanium.

R. M. BOZORTH und D. E. WALSH: Ferromagnetic moment of $CoMnO_3$.

J. M. WHELAN and G. H. WHEATLEY: The preparation and properties of gallium arsenide single crystals.

T. S. SWOBADA, R. C. TOOLE and J. D. VAUGHAN: New magnetic compounds of the ilmenite type structure.

H. KAWAMURA: The deformation potential of potassium chloride.

D. B. FISCHBACH and A. S. NOWICK: Some transient electrical effects of plastic deformation in NaCl crystals.

W. G. MAISCH and H. G. DRICKAMER: The effect of pressure on color centers in alkali halide crystals.

G. HEILAND: Feldeffekt und Photoleitung an ZnO-Einkristallen.

A. SMAKULA and J. KALNAJS: Oxygen impurity in silicon single crystals.

R. E. SCHLIER and H. E. FARNSWORTH: Structure of epitaxed copper deposited by evaporation onto a clean (00·1) face of a titanium crystal.

J. L. BIRMAN: Calculation of coulomb crystal potentials.

D. SAINT-JAMES: Détermination des lois de force dans les cristaux du type du diamant.

J. I. PANKOVE: Radiative surface effect in germanium.

H. FRITZSCHE: Resistivity and Hall coefficient of Sb-doped germanium at low temperatures.

D. G. WORDEN and G. C. DANIELSON: Electrical resistivity of thin films of potassium at 100 K.

D. H. ROBERTS and J. E. BAINES: Photoconductivity in chemically deposited films of lead selenide.

J. B. GOODENOUGH: An interpretation of the magnetic properties of the Perovskite-type mixed crystals $La_{1-x}Sr_xCoO_{3-\lambda}$.

P. G. DE GENNES: Neutron scattering by antiferromagnets above the Néel-point.

B. K. AGARWAL and M. P. GIVENS: Soft X-ray absorption by manganese and manganese oxide.

T. A. SANDENAW and R. A. GIGNEY: The electrical resistivity and thermal conductivity of plutonium metal.

C. S. FULLER and J. M. WHELAN: Diffusion, solubility and electrical behavior of copper in gallium arsenide.

W. PAUL and D. M. WARSCHAUER: Optical properties of semiconductors under hydrostatic pressure—III. Silicon–germanium alloys.

L. P. KAO and E. KATZ: Phenomenological theory of anisotropic isothermal galvanomagnetic effects.

G. LEIBFRIED und CHR. LEHMANN: Gittertheoretische Behandlung einer Schraubenversetzung in Alkalimetallen.

E. DANIEL: Influence du potentiel du reseau et contribution des couches a l'annihalation du positon dans le cuivre.

R. A. ORIANI and W. K. MURPHY: Thermodynamics of ordering alloys—III. Energies of transformation of the $Au_{1/2}Cu_{1/2}$ phases.

A. TAYLOR and JONES: Constitution and magnetic properties of iron-rich iron–aluminum alloys.

W. LOW and D. SHALTIEL: Paramagnetic resonance spectrum of gadolinium in single crystals of thorium oxide.

A. H. MONES and E. BANKS: Ferrimagnetism in the system Na_2O–ZnO–Fe_2O_3.

R. NATHANS, M. T. PIGOTT and C. G. SHULL: The magnetic structure of Fe_3Al.

C. H. L. GOODMAN: The prediction of semiconducting properties in inorganic compounds.

U. GONSER and B. OKKERSE: The question of radiation induced phase changes.

R. A. EPPLER and H. G. DRICKAMER: The effect of pressure on the spectra of the Te^+ ion alkali halide lattices.

D. F. C. MORRIS: The instability of some dihalides of copper and silver.

E. SCHLÖMANN: Ferromagnetic resonance in polycrystalline ferrites with large anisotropy.

E. MOOSER and W. B. PEARSON: The crystal structure and properties of the group VB to VIIB elements and of compounds formed between them.

A. B. LIDIARD: Anion diffusion in alkali halide crystals.

E. SCHLÖMANN: Spin wave analysis of ferromagnetic resonance in polycrystalline ferrites.

E. O. KANE: The influence of exchange on the effective mass formation.

R. T. BATE and C. V. HEER: Some optical and magnetic properties of irradiated LiF.

R. F. WALLIS and H. J. BOWLDEN: Theory of impurity photo-ionization spectrum of semiconductors in magnetic fields.

F. S. HAM: Theory of diffusion-limited precipitation.

C. R. VASSEL: L'effet des elements de la première longue période sur la résistivité du cuivre et de l'aluminium.

G. A. ALERS and J. R. NEIGHBORS: The elastic constants of zinc between 4·2° and 670°K.

W. DESORBO and G. E. NICHOLS: A calorimeter for the temperature region 1° to 20°K—The specific heat of some graphite specimens.

J. C. BOWMAN and J. A. KRUMHANSL: The low temperature specific heat of graphite.

K. KOMATSU: Particle size effect of the specific heat of graphite at low temperatures.

PIERRE BRISSONNEAU: Contribution a l'etude quantitative du trainage magnetique de diffusion du carbone dans le fer α.

W. D. JOHNSTON, R. R. HEIKES and D. SESTRICH: The preparation, crystallography and magnetic properties of the $Li_xCo_{(1-x)}$ system.

HELMUT BROSS und ALFRED SEEGER: Elektronentheoretische Untersuchungen uber Fehlstellen in Metallen—VI. Der elektrische Widerstand Doppelleerstellen in ein wertigen Metallen.

G. F. NEWELL: Extreme frequencies of lattice vibrations for disordered binary alloys.

I. BROSER und R. BROSER-WARMINSKY: Uber den Mechismus der Energiewanderung in Kadmiumsulfid-Kristallen.

E. F. WESTRUM and D. M. GRIMES: Low temperature heat capacities and thermodynamic properties of zinc ferrites—II. Effect of thermal history and metallic additives.

W. MARSHALL: The antiferromagnetism of $CuCl_2 2H_2 0$.

G. J. DIENES: The temperature dependence of the elastic moduli of vitreous silica.

GERALD W. SEARS: Strength of lithium fluoride whiskers.

NILS BÄCKLUND: Electrical resistance of some noble metals alloys at the temperatures of liquid helium.

VOL
5
195

J. Phys. Chem. Solids Pergamon Press 1958. Vol. 5. pp. 241–255.

THE PRESSURE DEPENDENCE OF THE KNIGHT SHIFT IN THE ALKALI METALS AND COPPER*

G. B. BENEDEK and T. KUSHIDA†

Division of Engineering and Applied Physics, Harvard University, Cambridge, Mass.

(*Received* 16 *September* 1957)

Abstract—Measurements of the pressure-dependence of the Knight shift in lithium, sodium, rubidium, cesium, copper, and aluminum have been made at room temperature in the pressure range 1–10,000 kg/cm². The volume-dependence of $\langle|\psi_F(0)|^2\rangle \equiv P_F$ has been deduced from these data, using PINES' collective electron picture for the paramagnetic susceptibility of the conduction electrons. The results of recent calculations of the volume-dependence of P_F are presented and compared with the experimentally deduced results. The Knight shift is shown experimentally to be an explicit function of the temperature at constant volume. A theory, which takes into account semiquantitatively the effect of the lattice vibrations on P_F, is proposed. Comparison is made between this theory and the experimental observations.

1. INTRODUCTION

SOON after the discovery[1] of the Knight shift (K), it was realized[2,3] that K is a measure of the product of the paramagnetic susceptibility (χ_P) of the conduction electrons and $P_F \equiv \langle|\psi_F(0)|^2\rangle$, which is the probability density that a conduction electron, with an energy equal to the Fermi energy, can be found at the nucleus. Since χ_P and P_F reflect rather directly the electronic structure of the metal, it is clear that measurements of K as a function of volume are of considerable theoretical interest. Calculations of the volume-dependence of P_F for sodium have been made[4] using a variational method.[5] More recently, developments in the theoretical calculation of the cohesive energy[6,7] of the alkali metals have enabled the evaluation of P_F as a function of the interatomic distances for all the alkali metals.[8] Furthermore, a recent treatment of the problem of electron–electron interactions[9] has produced a theory for the volume-dependence of χ_P for the alkali metals which is in good agreement with direct determinations[10] of χ_P in lithium and sodium at atmospheric pressure.

Clearly, the availability of these theoretical results suggests experiments which would measure independently K and χ_P as a function of pressure, thereby permitting the separate determination of the volume-dependence of χ_P and P_F. Unfortunately, the accuracy of present experimental methods is not high enough to permit measurements of χ_P as a function of pressure. However, rather accurate measurements of the pressure-dependence of K are possible. We have measured the pressure-dependence of K in the range 1–10,000 kg/cm² for lithium, sodium, rubidium, cesium, copper and aluminum. The alkali metals are particularly suitable from an experimental point of view because of the narrowness of the nuclear resonance line width,[11] and because of their large compressibility.[12] For example, lithium and cesium change volume by about 7 and 25 per cent, respectively, on the application of 10,000 kg/cm². Analysis of the data is carried out under the presumption that the PINES' collective electron picture gives a close approximation to the correct volume-dependence of χ_P. The deduced volume-dependence of P_F can then be compared with the theoretical calculations.

* This research was supported by the Office of Naval Research, the Signal Corps of the U.S. Army, and the U.S. Air Force.

† On leave of absence from the Department of Physics, Hiroshima University, Hiroshima, Japan.

Measurements[13] of the temperature-dependence of the Knight shift at atmospheric pressure can be compared with the present results on the volume-dependence of K to determine if the Knight shift is an explicit function of the temperature at constant volume. An explicit temperature-dependence is found, and its magnitude can be accounted for satisfactorily by means of a theory that includes the effect of the lattice vibrations on the time average value of P_F.

2. EXPERIMENTAL METHOD

The measurement of the pressure-dependence of the Knight shift consists in an observation of the change in the nuclear magnetic resonance frequency of a metal sample, as the hydrostatic pressure on the sample is increased.

In order to observe the nuclear resonance, it is necessary that the oscillating rf field H_1 penetrate the sample. To achieve this the samples are prepared in the form of a dense dispersion in a suitable dispersing medium. We have found that at room temperature particle sizes in the range 15–30 microns permitted rf penetration sufficient to produce symmetrical resonance lines. The dispersions were prepared by stirring at high speed, in an inert atmosphere, a mixture of the molten metal and the dispersing medium. The head of the stirrer consists essentially of a cylinder with numerous vertical slots in the curved surface. The bottom of the cylinder tapers to an opening and the top is closed. When the stirrer is spun on its axis at high speed, material is sucked up at the bottom and projected at high speed out of the slots. The shearing action of the turbulent dispersing liquid shreds the molten metal into small spherical particles. Stirring was carried out for 15–20 min using stirrer speeds of 10,000–12,000 rev/min. Coagulation of the metal particles during and after cooling was inhibited by including into the dispersing medium about 0·001 cc of oleic acid/cc of metal. The oleic acid reacts mildly with the alkali metals, forming a jelly-like protective coating on the surface of each particle.

Because of the widely differing reactivities of each of the alkali metals, somewhat different techniques were necessary in the preparation of each of the dispersions. In the case of lithium the dispersion was made in a stainless-steel dispersator under a helium atmosphere to avoid the formation of lithium nitride. Glass could not be used in the dispersator because of the reaction of lithium and glass at high temperatures. The dispersing medium was a purified commercial kerosene with the trade name "Deobase".

The preparation of the rubidium dispersion was carried out in a specially constructed box in which the air was replaced by dry nitrogen. Because of its boiling point (98·5 °C) and easily attainable purity, heptane was used in preparing the dispersion of rubidium, whose melting point is 38·5 °C. The amount of water and oxygen dissolved in the heptane was reduced considerably by washing with sodium–potassium alloy. This alloy, which is a liquid at room temperature, and can therefore be easily broken up into the form of pellets with a large surface area, is a rather effective purifying agent. After preparation of the dispersion, the heptane, which freezes at 7,000 atm at room temperature, was washed out and replaced by high-purity pentane (boiling point 36·2 °C), whose freezing point is above 10,000 atm at room temperature.

The extreme reactivity of cesium made it necessary to purify very carefully the pentane which was used as a dispersing medium. It was necessary to remove not only traces of water and dissolved oxygen but also any impurities in the form of unsaturated hydrocarbons. This was accomplished by several successive distillations of pentane in the presence of cesium. As to containing the dispersions, glass and polyethylene were found to be rather inert to attack by either cesium or rubidium.

In the case of copper and aluminum, the samples were purchased in the form of a fine powder. The small-diameter particles were separated from the larger ones by dispersing the powder in a liquid. The slower settling times of the smaller particles enables one to scoop the desired small sizes from the upper part of the dispersion. Using this "Stokes' law technique", it was possible to obtain particles in the 10- to 40-micron range.

After preparation, the dispersion was placed in a small polyethylene vial whose cap contained a small hole designed to permit passage of the pressure-transmitting fluid into the dispersion. As a result of measurements of the pure quadrupole resonance in non-metallic crystals,[14] it is believed that the pressure on the metal particles is hydrostatic to at least 1 part in 1,000. This vial was then placed inside an rf coil which was connected in turn to a high-pressure rf electrical plug. This assembly was screwed into a beryllium-copper high-pressure cylinder capable of containing pressures at least as high as 10,000 atm. A detailed description of the bomb and plug assembly can be found in reference (14). The pressure is generated by compressing the transmitting fluid, using one of Professor BRIDGMAN's presses.[12] The hydrostatic compression is transmitted from the press to the beryllium-copper bomb by means of flexible stainless-steel tubing.[15] The pressure was measured with an accuracy of about ± 3 kg/cm^2 at each pressure by observing the change in resistance of a coil of Manganin wire[12] with a Wheatstone bridge.

Fig. 1 shows a block diagram of the electronic system for the measurement of the line shift under pressure. This system can be divided into two parts. The first is the stabilization of the magnetic field. This field is produced by a 6-in. Varian magnet whose faces were shimmed for maximum homogeneity at a gap spacing of 2 in. In the present experiments the requirements on field stabilization are stringent. Consider, for example, the case of lithium. On increasing the pressure to 10,000

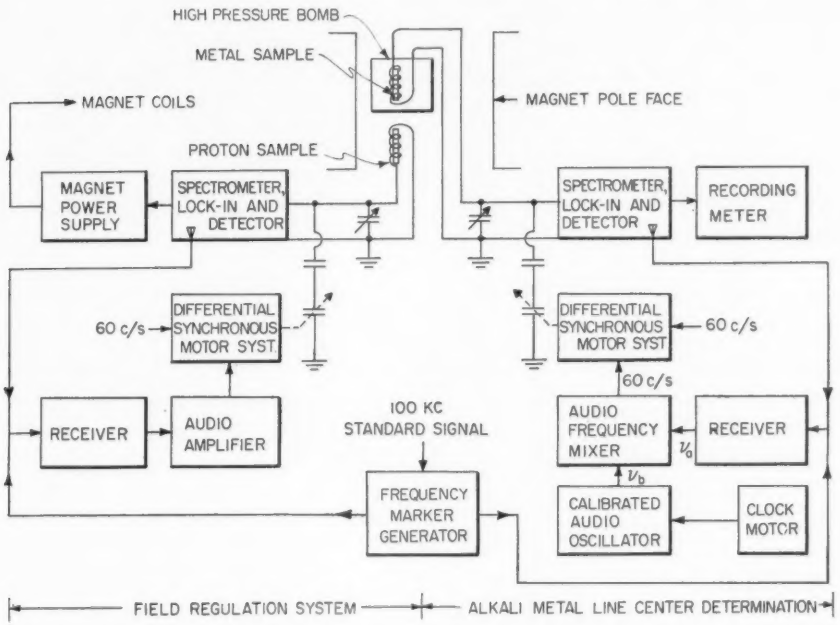

FIG. 1. Block diagram of the electronic system for the stabilization of the magnetic field and determination of center frequency of the nuclear resonance line.

atm, the line center shifts only 27 c/s relative to its value at atmospheric pressure. In order to ascertain this shift accurately as a function of pressure, one should measure the line center to about ± 3 c/s at each pressure. Since the lithium resonance frequency in the field used is about 10 Mc, it is seen that the field stabilization required is of the order of 3 parts in 10 million. Furthermore, this degree of field constancy must be maintained over the entire run, a period of 10–15 hr. The nuclear resonance of the proton is used as the basis of the stabilization system. A Pound–Knight–Watkins spectrometer is used to obtain the error signal which controls the magnetic field. This spectrometer has the advantage that it responds only to the absorption mode of the nuclear signal. However, the natural frequency stability of the spectrometer oscillator is usually not better than a few parts in 10^6 even for short time periods, unless elaborate stabilization techniques are employed. Any drift in the frequency (ω) of the spectrometer oscillator produces a corresponding change in the magnetic field, because the stabilization system acts so as to keep the resonance relation $\omega = \gamma H_0$ satisfied. In order to overcome this difficulty, an electromechanical servo-system was developed which stabilized the spectrometer frequency to about 1 part in 10^7 by comparing it continually with a standard frequency produced by the frequency-marker generator. The frequency-marker generator makes use of an extremely stable (1 part in 10^9) 100-kc frequency standard signal kindly supplied us by Dr. J. A. PIERCE. This 100-kc signal is multiplied and divided in the marker signal generator in such a way that the output of the generator supplies frequency markers 10 kc apart, ranging all the way from 1 to 30 Mc. The servo-system operates in conjunction with these frequency-markers as follows. The frequency of the spectrometer is chosen so that it falls about 60 c/s away from one of the 10 kc markers produced by the marker signal generator. These two radio frequencies are mixed in a communications receiver and the difference frequency appears at the audio output, which is fed in turn into an audio power amplifier. The output of the audio amplifier is applied then to the servo-motor system. The servo-system consists of two one-turn-

per-minute synchronous motors (A) and (B). A is driven by the 60 c/s line voltage and B is driven by the output of the audio amplifier. The two motors are coupled to the shaft of a variable air capacitor in such a way that this shaft turns with an angular velocity $\Delta\omega$ which is always equal to the difference between the angular velocities of the two motor shafts. The motors thus act as a mechanical frequency subtraction system. When the frequencies of the voltages feeding both motors are the same, the variable condenser does not rotate. However, if the frequencies differ by an amount $\Delta\omega$ then in a time Δt, the capacity of the condenser changes by an amount Δc which is proportional to $\int_t^{t+\Delta t} \Delta\omega\, dt$. The capacitor is coupled in parallel with the main tuning capacity of the spectrometer through a coupling condenser C'. The connections are arranged so that a change in the radio frequency of the spectrometer results in a change in the tuning capacity which acts to return the spectrometer frequency to its original value. The over-all response time for this process is of the order of several tenths of a second. The response time of the servo-system is shorter than the time constant of the lock-in amplifier, so that fluctuations in the spectrometer frequency are corrected before they can appear as line distortions in the output of the lock-in amplifier. The appropriate coupling between the servo-system and spectrometer is found by increasing the coupling (C') so that "hunting" of the spectrometer frequency begins. The coupling (C') is then reduced just below this critical value. In summary, the servo-system is essentially a mechanical counter which counts the number of cycles $\pm\int\Delta\omega\, dt$ that the spectrometer drifts relative to the standard. The servo-mechanism then feeds back to the spectrometer-tuning condenser a change in capacity ΔC proportional to $\int\Delta\omega\, dt$. The proportionality constant is determined by the coupling condenser. By this feedback action the servo-system considerably inhibits the fluctuation of the spectrometer frequency and automatically ensures that the average value of the spectrometer frequency is kept precisely 60 c/s away from the 10 kc frequency marker.

The size and line width of the proton samples used are determined by the following considerations: (*a*) stability of the controlling system, (*b*) line width of the alkali metal studied, and (*c*) "the wiggle effect". In connection with (*a*) it is obvious on the one hand that intensity of the signal must be large enough to control the field to the desired degree of accuracy. On the other hand, if the nuclear resonance signal is too large, the frequency control of the spectrometer by the servomotor system will fail. This effect occurs as follows. If the depth of modulation of the spectrometer frequency produced by the nuclear resonance is larger than $\pm$40 c/s, the motor system will simply fail to control, because the operating frequency range of the synchronous motor used was 60$\pm$40 c/s. The superposition of signals outside this range will inhibit or stop the counting action of the motors. Therefore, care was taken that the nuclear resonance modulation of the spectrometer frequency was less than 20 c/s. Regarding (*b*), the line width of the proton sample had to be chosen roughly equal to that of the alkali metal studied, because the same modulating field was used to sweep both the metal and the proton line. Consideration (*c*) refers to the fact that we must choose the modulation amplitude and frequency to be small enough relative to the line width so that transient distortions of the nuclear signal are not encountered. These transient distortions have been called "wiggles",[16,17] because of their appearance on a direct oscilloscope trace of the resonance. They must be avoided in the present case, because they affect the apparent center of the error signal. In satisfying the criteria implied in considerations (*a*), (*b*), and (*c*), it is most convenient to alter the line widths. This may be done either by adjusting the field homogeneity over the sample, or by doping water with paramagnetic ions. If the second alternative is adopted, as was the case in our experiments, it should be remembered that heavily doped water solutions show[18] a temperature-dependence of their resonance frequency. This can amount to several cycles per °C at 30 Mc. Thus, care had to be taken that the temperature of the proton sample was kept sufficiently constant.

In practice, it was found necessary to allow the magnet to operate for about 5 hr in order to reach thermal equilibrium. After this warm-up period the stabilization system operated rather successfully in providing field stability generally of the order of $\pm$3 parts in 10^7. If special care was exercised, stabilization to $\pm$1 part in 10^7 could be achieved over long periods of time.

VOL. 5 1958

The second part of the electronic system for the measurement of the line shift consists in the accurate determination of the spectrometer frequency at the line center for each pressure. The derivative of the absorption is displayed on a recording meter as the spectrometer frequency is swept slowly through the resonance. As the line is swept out, frequency markers indicating the spectrometer frequency are placed on the recording chart. The horizontal line which crosses the center of the derivative signal is found either by taking the mean between maximum and minimum in the recorded derivative, or by taking the zero line swept out when the frequency of the spectrometer is far from the line center. Both criteria will yield the same position for the line center, if the line is symmetrical. The line shapes were therefore checked to insure symmetry. The frequency corresponding to the center was determined by executing at least four passages through the line, alternately increasing and decreasing the spectrometer frequency. By averaging the line-center frequencies for each pair of "increase-decrease" passages, the time lag between the frequency-markers and the recording of the line can be removed. The major problem which had to be overcome in order to carry out this procedure was the elimination of the random fluctuations in the spectrometer frequency, while at the same time this frequency is being regularly varied. This is necessary for those lines whose width is narrow enough so that the random fluctuations of the spectrometer frequency are greater than a few per cent of the line width.

Stabilization is achieved as follows. The spectrometer frequency can be regulated at any desired frequency from 100 to 5,000 c/s away from one of the frequency-markers by the scheme shown in the block diagram Fig. 1. The spectrometer signal and the marker signal are mixed in a receiver. The difference frequency, ν_a, is then applied to an audio-frequency mixer which takes the difference between ν_a and the output of a calibrated audio oscillator ν_b. The difference frequency $\nu_a - \nu_b$ is adjusted to be nearly 60 c/s. This 60 c/s output of the audio mixer is then fed into a servomotor system of the same type as has been described above. The action of the servomotor system coupled to the spectrometer insures that $\nu_a - \nu_b$ is kept at 60 c/s. The spectrometer frequency is swept simply by sweeping the frequency of the calibrated audio oscillator with a clock motor and gear arrangement. Since the servo-system assures that $\nu_a - \nu_b = 60$ c/s, the spectrometer frequency changes at exactly the same rate as the audio oscillator. The frequency-markers placed on the recording chart were the frequencies of the audio oscillator. As an example of the accuracy attainable in the over-all system, Fig. 2 shows the sodium line at room temperature with 10 c/s markers placed on the horizontal axis. In all the measurements here reported, it was found possible to determine the line center to about 1 per cent of the line width, provided that the signal-to-noise ratio was reasonable.

3. EXPERIMENTAL RESULTS

Measurements of the pressure-dependence of the nuclear magnetic resonance frequency have been made for the alkali metals lithium, sodium, rubidium, and cesium. We have also studied copper

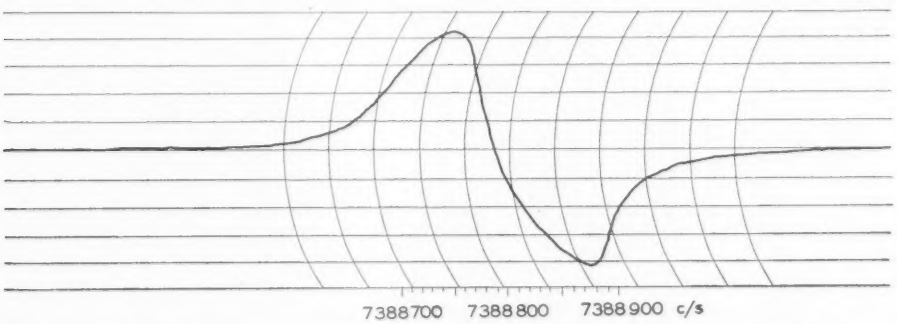

FIG. 2. The derivative of the ^{23}Na nuclear resonance absorption in a dispersion of metallic sodium at 24°C. The frequency markers on the horizontal axis are 10 c/s apart.

and aluminum. Potassium was not investigated because of the very poor signal-to-noise ratio of the metal line.

The lithium was provided by the Maywood Chemical Works. The minimum purity was 99·8 per cent. The impurities were silicon 0·015, iron and aluminum 0·03, calcium 0·03, sodium 0·02, heavy metals 0·07, nitrogen 0·03, chlorine 0·003

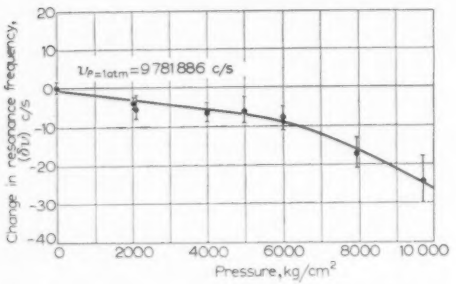

FIG. 3. The change in the ^{7}Li resonance frequency with pressure at $T = 18°$C.

per cent. In Fig. 3 is shown the decrease in the lithium resonance frequency as the pressure is increased from 1 to 10,000 atm at $T = 18°$C. At atmospheric pressure the line center was 9,781,886 c/s. The increase in error in the points at the higher pressures is a result of a decrease in signal strength. The pressure variation of the line width was not measured because the line was swept only near the line center in order to attain the best possible accuracy for the pressure shift. The accuracy in the determination of the line center corresponds to 1·5 parts in 10^7 at atmospheric pressure, and falls with increasing pressure to 6 parts in 10^7 at 10,000 kg/cm².

A sodium dispersion in toluene was obtained through the kindness of Dr. J. F. NOBIS of the Research Division of National Distillers Products Corporation. Its purity was about 99·95 per cent. In Fig. 4 is shown the decrease in the ^{23}Na resonance frequency with pressure at 24°C. At $P = 1$ atm the sodium resonance frequency was 7,388,542 c/s. Because the sodium line width is $\sim$ 100 c/s, a modulation of 13 c/s was used. The error in the determination of the resonance frequency is ± 1 c/s at each pressure. Actually, successive passages through the line at each pressure permitted a determination of the line center to about $\pm 0{\cdot}6$ c/s. The ± 1 c/s shown in Fig. 4 is presented as a conservative estimate of the long-term accuracy in center determination. It will be noted that ± 1 c/s corresponds to an over-all long-time stability, for the entire system, of $\pm 1{\cdot}5$ parts in 10^7. The line width was found to be independent of pressure up to 10,000 kg/cm². However, this may be due to the fact that the observed sodium line

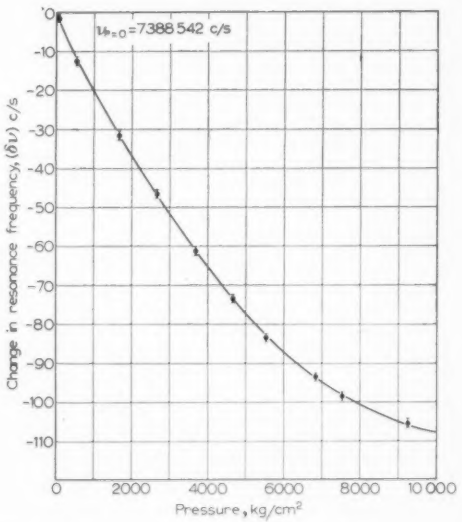

FIG. 4. The change in the ^{23}Na resonance frequency with pressure at 24·4° C. The accuracy of the determination of the Na frequency is ± 1 c/s at each pressure.

width was determined by the magnet inhomogeneity.

Rubidium was obtained from the A.D. Mackay Company. Its purity was 99·8 per cent. A trace of cesium metal was present. In Fig. 5 is shown the increase in the resonance frequency for rubidium at 20°C as a function of pressure from 1 to 10,000 kg/cm². The points designated with a triangle were taken during a different run from those designated with a circle. At $P = 1$ atm the ^{87}Rb resonance frequency was 9,159,670 c/s. The line width increased considerably on increasing the pressure. Because of this broadening the signal-to-noise ratio at the higher pressures did not make possible accurate determinations of the line width. However, it may be said that the line width increased by roughly a factor of four in going from atmospheric pressure to 10,000 kg/cm².

VOL.
5
195

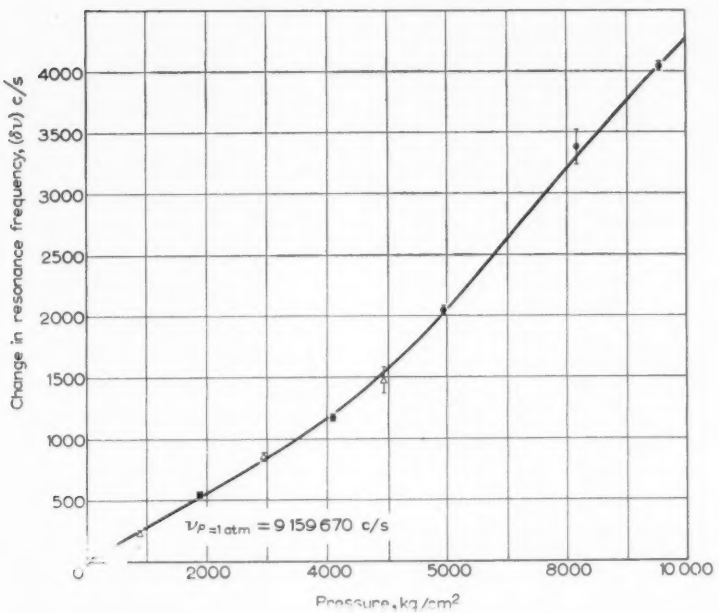

FIG. 5. The change in the ^{87}Rb resonance frequency with pressure at 20°C.

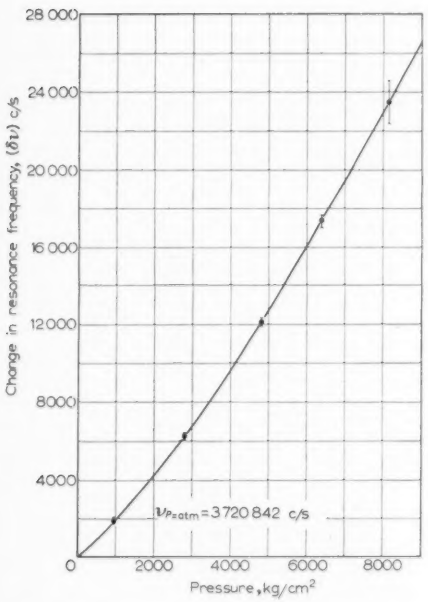

FIG. 6. The change in the ^{133}Cs resonance frequency with pressure at 20°C.

Cesium was obtained from A.D. Mackay Company. The minimum purity was 99·9 per cent. In Fig. 6 is shown the very great increase in the cesium resonance frequency at 20°C as the pressure is increased. The frequency corresponding to the line center of the ^{133}Cs resonance was 3,720,842 c/s at atmospheric pressure. Again, the broadening makes it difficult to determine the line width with accuracy. However, it appears that the line width increases roughly by a factor of four on increasing the pressure to 8,000 kg/cm².

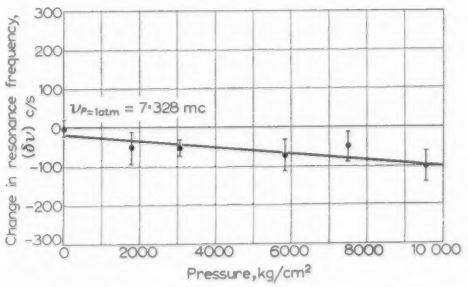

FIG. 7. The change in the ^{63}Cu resonance frequency with pressure at 21°C.

Fine powdered copper from Baker and Adamson was used in the measurements on copper. In Fig. 7 is shown the pressure variation of the resonance frequency at 21°C. The center of the copper line fell at 7·328 Mc at 1 atm. The pressure variation of the resonance frequency is not well determined, because of the broadness (7 kc) of the line and the small compressibility of copper.

U.S.P. powdered aluminum from the Baker Chemical Company was used in the aluminum experiments. Because of the broad (10 kc) line width of the aluminum resonance, the pressure-induced shift in the line center was found to be of the same magnitude as the error involved in determining the line center. We can place an upper limit for the pressure shift at 20°C as being ± 150 c/s up to 10,000 kg/cm^2. Since the resonance frequency at atmospheric pressure was 7·163 Mc, the magnitude of the pressure-induced change in the Knight shift to 10,000 atm is less than 1 per cent.

4. ANALYSIS OF THE DATA

(a) *The Volume-Dependence of the Knight Shift*

The average magnetic resonance frequency (ν) of a nucleus in an external magnetic field H_0 is $\nu = \gamma(H_0 + \Delta H_t)$, where γ is the gyromagnetic ratio of the bare nucleus, and ΔH_t is the average local magnetic field in the direction of H_0 set up by the surrounding electrons. In the case of the alkali metals, in which a clear distinction can be made between the core electrons and the conduction electrons, it is possible to break ΔH_t into three distinct components: $\Delta H_t = \Delta H_1 + \Delta H_2 + \Delta H_3$. ΔH_1 represents the field set up by the diamagnetism of the core electrons. In magnitude, $\Delta H_1/H_0$ ranges from 1×10^{-4} for lithium to 5×10^{-3} for ^{133}Cs. ΔH_2 represents the field set up by the diamagnetism of the conduction electrons. This field is largest at regions far from the nucleus, so that ΔH_2 can be roughly approximated by its spatial average. This yields $\Delta H_2/H_0 \sim 10^{-6}$. ΔH_3 represents the field set up by the paramagnetism of the conduction electrons. The magnitude of this field is enhanced by the lumping of the electron probability density close to the nucleus which occurs when the conduction electron wave function has s character. The Knight shift (K) is proportional to the difference in average local fields between nuclei in a metal and nuclei in a solution of the salt of that metal, both samples being in the same external magnetic field H_0. Symbolically, $K = [(\Delta H_t)_{\text{metal}} - (\Delta H_t)_{\text{metal ion}}]/H_0$. If we presume that the contribution to ΔH_t from the diamagnetism of the core is the same in both metal and ion, then $K = [\Delta H_3 + \Delta H_2]_{\text{metal}}/H_0$. Since the observed values of K range from 10^{-2} to 10^{-4}, we see that ΔH_2 is negligible relative to ΔH_3 and that $K = \Delta H_3/H_0$. A calculation[2,3] of ΔH_3 shows that

$$K = (8\pi/3)\chi_P \Omega P_F. \qquad (1)$$

χ_P is the paramagnetic volume susceptibility, Ω is the atomic volume, and $P_F = \langle|\psi_F(0)|^2\rangle$ is the probability density that an electron whose energy is equal to the Fermi energy can be found at the nucleus. $|\psi|^2$ is assumed normalized over the atomic volume.

When pressure is applied to the metal in a fixed external magnetic field, the local field changes and hence the resonance frequency changes. In the alkali metals, for all pressures used in the present experiments, the volume occupied by the core electrons is considerably less than the atomic volume. It is therefore reasonable that the pressure produces no change in the core contribution to ΔH_t. Furthermore, the smallness of ΔH_2 insures that any change in it will be 10^{-3}–10^{-4} times smaller than the changes in ΔH_3. Therefore, the change in resonance frequency $\delta\nu(P)$ produced by the pressure P can be assumed to result entirely from changes in ΔH_3, i.e. $\delta\nu(P) = \gamma\delta(\Delta H_3)$. Since the Knight shift at atmospheric pressure, $K(0)$, is known, the Knight shift at each pressure is given by

$$K(P) = K(0)[1 + \delta\nu(P)/K(0)\nu_0], \qquad (2)$$

where $\nu_0 = \gamma H_0$.

By using BRIDGMAN's data[19,20] on the P–V isotherms for the alkali metals, it is possible to determine from (2) the volume-dependence of the Knight shift. In Table 1, $K(V)/K(V_0)$ is given as a function of V/V_0 for each of the alkali metals. V_0 is the volume corresponding to $P = 1$ atm and room temperature. V is the volume at pressure P and room temperature.

The volume-dependence of the Knight shift in copper can be determined using the results shown in Fig. 7 in conjunction with BRIDGMAN's data on the P–V isotherms of copper.[12] The result

VOL. 5 1958

Table 1. *The volume-dependence of the Knight shift in the alkali metals*

Li		Na		Rb		Cs	
$K(0) = 0{\cdot}249\times10^{-3}$		$K(0) = 1{\cdot}13\times10^{-3}$		$K(0) = 6{\cdot}53\times10^{-3}$		$K(0) = 14{\cdot}9\times10^{-3}$	
(V/V_0)	$K(V)/K(V_0)$	V/V_0	$K(V)/K(0)$	V/V_0	$K(V)/K(0)$	V/V_0	$K(V)/K(0)$
1·00	1·000	1·00	1·000	1·000	1·000	1·00	1·000
0·99	0·9994	0·98	0·99692	0·97	1·00275	0·97	1·0139
0·98	0·9988	0·96	0·99416	0·94	1·00601	0·94	1·0331
0·97	0·9981	0·94	0·99179	0·91	1·0100	0·90	1·0713
0·96	0·9972	0·92	0·98976	0·88	1·0147	0·87	1·1118
0·95	0·9961	0·90	0·98819	0·85	1·02138	0·84	1·1685
0·94	0·9946	0·88	0·98726	0·82	1·03273	0·81	1·2415
0·93	0·9925	0·87	0·98692	0·79	1·05261	0·79	1·3053
0·92	0·9884			0·77	1·06797	0·76	1·4150

can be expressed simply as $K(V) = 0{\cdot}00232\,(V/V_0)^{(0\cdot7\pm0\cdot3)}$.

(b) *The Volume Dependence of* $\chi_P\Omega$

From equation (1) it is seen that the data of Table 1 represent the volume-dependence of $(\chi_P\Omega)P_F$. Because of the absence of experimental data, we shall use a theoretical prediction for the volume-dependence of χ_P. The free-electron picture, while it explains the temperature-independence of χ_P, is unable to give the magnitude correctly. The collective electron picture of PINES,[9] on the other hand, gives values for χ_P which are in good agreement with direct experimental determinations[10] in lithium and sodium. We shall therefore use PINES' theoretical expression* for the volume-dependence of $\chi_P\Omega$,

$$\chi_P\Omega = 0{\cdot}5325\times10^{-4}/\alpha \quad \text{(Bohr units)}, \tag{3a}$$

$$\alpha = \frac{4{\cdot}911}{(m^{**}/m)r_s^2} - 0{\cdot}814/r_s - 0{\cdot}0432/r_s^{\frac{1}{2}} - \\ -0{\cdot}0032r_s + 0{\cdot}162 \quad \text{(Rydberg units)}. \tag{3b}$$

* In ref. 9, equation (9.14) which describes the slope of the $\chi_P\Omega$ versus r_s curve at $r_s = (r_s)_0$ should be altered to read

$$\alpha = \alpha_0 - [9{\cdot}82/(r_s)_0^2 - 0{\cdot}814/(r_s)_0 - 0{\cdot}0216/(r_s)_0^{\frac{1}{2}} + \\ + 0{\cdot}0032r_s]\gamma.$$

This equation is correct only when $m^{**}/m = 1$ for all values of r_s. It should be noted, in particular for the case of lithium where $\alpha - \alpha_0$ is quite small, that departures of m^{**}/m from unity can affect $\alpha - \alpha_0$ appreciably.

$\chi_P\Omega$ has the dimensions of volume, and in equation (3) the unit of length is taken as the radius of the first Bohr orbit, i.e. $0{\cdot}5292\times10^{-8}$ cm^3. In (3b) α is expressed in units of the Rydberg, i.e., 13·605 eV, and r_s is the radius of the Wigner–Seitz sphere expressed in Bohr units. m^{**}/m is given by

$$\frac{m}{m^{**}} = \frac{m}{m^*}[1 + 2(E_4/E_2)k_0^2], \tag{4}$$

where E_4 and E_2 are defined by the following expansion for $E(k)$:

$$E = E_0 + E_2k^2 + E_4k^4.$$

m is the free electron mass and m^* is the effective mass describing the curvature of the $E(k)$ curve at $k = 0$. k_0 is the value of k for which E is equal to the Fermi energy. In calculating $\chi_P\Omega$ as a function of r_s, we have taken into account the dependence of m^{**}/m on r_s. In Table 2 below are listed values of m^{**}/m versus r_s for the alkali metals, using the results of calculations by BROOKS[8] and BROOKS and HAM.[7]

Using Table 2 and equation (3), it is possible to calculate the volume-dependence of $\chi_P\Omega$ near any value of r_s. In Table 3 are listed the values of r_s at 0°K and 300°K and atmospheric pressure, using the data available from X-ray measurements,[21] density measurements,[22] and thermal-expansion measurements.[23]

For the small changes in r_s which are produced during compression to 10,000 kg/cm^2, it has been found possible to write the dependence of $\chi_P\Omega$ as

Table 2. The dependence of m^{**}/m on the radius of the Wigner–Seitz sphere. r_s is in Bohr units.

Li		Na		Rb		Cs	
r_s	m^{**}/m	r_s	m^{**}/m	r_s	m^{**}/m	r_s	m^{**}/m
3·25	1·38	4·10	0·984	4·0	0·902	4·6	1·70
3·20	1·41	4·00	0·9839	4·4	0·904	5·0	1·16
3·15	1·43	3·90	0·9837	4·8	0·931	5·4	1·02
3·10	1·46	3·80	0·9835	5·2	0·938	5·8	1·00
		3·70	0·9828	5·6	0·941	6·2	0·952

Table 3. The radius of the Wigner–Seitz sphere (r_s) at 0°K and 300°K. r_s is in Bohr units.

T (°K)	Li r_s	Na r_s	Rb r_s	Cs r_s
0	3·22	3·94	5·22	5·58
300	3·24	3·99	5·31	5·79

$\chi_P\Omega = \text{const.}\ V^P$. In Table 4 are listed the results for the alkali metals.

(c) *The Volume-Dependence of P_F*

(i) *Deduction from experiment*

Combining the data in Tables 4 and 1, the volume-dependence of P_F can be deduced by using equation (1). In Figs. 8–11 are shown the deduced volume-dependence of $P_F(V)/P_F(V_0)$ for

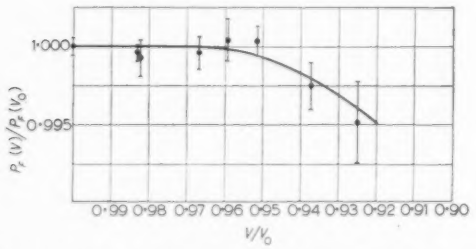

FIG. 8. The deduced volume-dependence of P_F for lithium. V_0 is the volume at room temperature and atmospheric pressure.

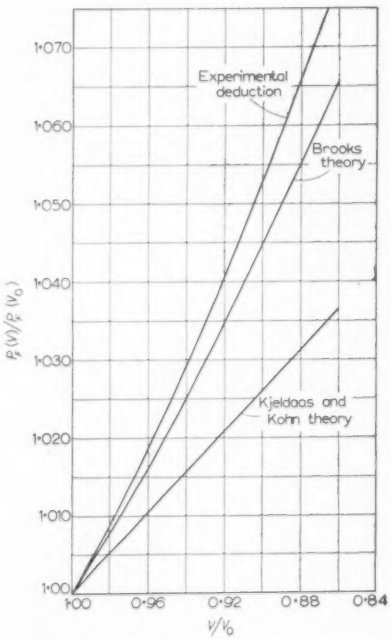

FIG. 9. The deduced volume-dependence of P_F for sodium, and the theoretical predictions.

Table 4. The volume-dependence of $\chi_P\Omega$ (in Bohr units)

Li	Na	Rb	Cs
$2{\cdot}5\times10^{-4}(V/V_0)^{0{\cdot}072}$	$2{\cdot}25\times10^{-4}(V/V_0)^{0{\cdot}600}$	$3{\cdot}36\times10^{-4}(V/V_0)^{0{\cdot}578}$	$4{\cdot}05\times10^{-4}(V/V_0)^{0{\cdot}28}$

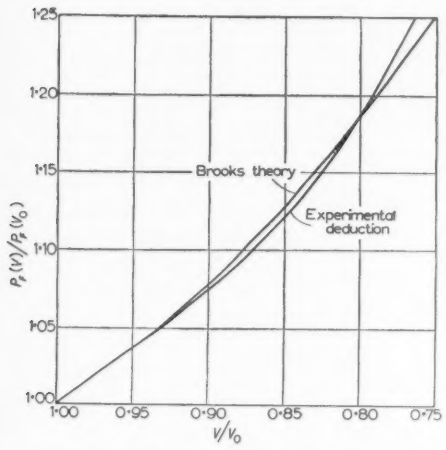

FIG. 10. The deduced volume-dependence of P_F for rubidium, and the theoretical prediction.

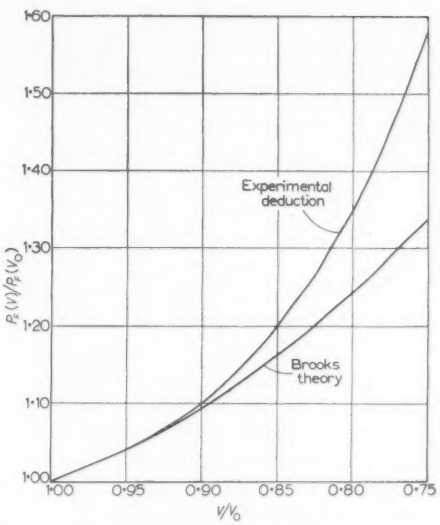

FIG. 11. The deduced volume-dependence of P_F for cesium, and the theoretical prediction.

lithium, sodium, rubidium and cesium. In the case of lithium the deduced volume-dependence is so small that the changes in P_F are of the same size as the accuracy in determination of the Knight shift itself. Therefore, the deduction is given directly at the experimental points along with the corresponding accuracy. The values of $P_F(V_0)$ and $P_F(V_0)/P_A$ are given in Table 5. P_A is the value of $|\psi(0)|^2$ for the free atom and is determined from the observed hyperfine splittings[24] using the equation[25]

$$P_A = \frac{3}{16\pi}\left(\frac{I}{\mu_I}\right)\frac{a(s)}{\mu_B}, \tag{5}$$

where I is the nuclear spin, μ_I is the nuclear magnetic moment, μ_B is the Bohr magneton, and $a(s)$ the hyperfine splitting constant. The entries in the

Table 5. *P_F, P_A, and P_F/P_A at atmospheric pressure and room temperature: comparison of theory and experiment. P_F and P_A are in Bohr units.*

		Experimental	Experimental Deduction	Theory (BROOKS)	Theory (KOHN)
Li	P_F	0·10±0·005	0·119	0·110	0·11
	P_A	0·2312	0·2312	0·242	0·223
	P_F/P_A	0·43±0·02	0·515	0·455	0·49
Na	P_F	0·53±0·05	0·600	0·664	0·555
	P_A	0·7507	0·7507	0·840	0·685
	P_F/P_A	0·705±0·07	0·799	0·790	0·81
Rb	P_F		2·32	1·76	
	P_A	2·337	2·337	2·18	
	P_F/P_A		0·993	0·81	
Cs	P_F		4·39	2·47	
	P_A	3·882	3·882	2·97	
	P_F/P_A		1·131	0·832	

column labelled "experimental" of Table 5 are obtained using the experimentally measured[10] values of χ_P for sodium and lithium, along with the room-temperature values of the atomic volume Ω. The entries in the "experimental deduction" column were obtained using PINES' theoretical values for $\chi_P\Omega$ as listed in Table 4. It will be noted that there is fair agreement between the values of P_F determined in these two different ways.

The analysis of the volume-dependence of the Knight shift in copper requires special consideration. The lattice constant in copper is determined by the repulsion of the cores as they begin to overlap.[26,27] Thus the assumption that the contribution of the core diamagnetism is the same in the ion and in the metal is open to question. If the core contributes to the local field differently in metal and ion, then the expression for the Knight shift must be written as

$$K = \sigma_{\text{metal}} - \sigma_{\text{ion}} + (8\pi/3)\chi_P\Omega P_F, \qquad (6)$$

where

$$\sigma_{\text{ion}} = (\Delta H_1/H_0)_{\text{ion}}, \quad \sigma_{\text{metal}} = (\Delta H_1/H_0)_{\text{metal}}.$$

σ_{ion} has been calculated,[28] using Hartree wave functions for the core electrons. This calculation gives $\sigma_{\text{ion}} = -0{\cdot}238$ per cent. The observed Knight shift for copper is 0·232 per cent. Thus, the diamagnetic core shift is almost the same magnitude as the observed Knight shift. Since the range of chemical shifts in the reference solutions indicates that K varies 3 per cent in going from solution to solution, σ_{metal} must be less than 3 per cent different than σ_{ion} in order that the core diamagnetism makes no observable contribution to the Knight shift. Furthermore, $\sigma_{\text{metal}} - \sigma_{\text{ion}}$ can be expected to be a function of the pressure because of the effect of increasing core overlap. Keeping these difficulties in mind, we can nevertheless calculate the volume-dependence of P_F under the *presumption* that $\sigma_{\text{metal}} = \sigma_{\text{ion}}$ at all pressures. Using PINES' picture for the susceptibility and KAMBE's[26] value for the effective mass, we find that $\chi_P\Omega = 1{\cdot}05\times10^{-4}(V/V_0)^{0{\cdot}667}$ Bohr units. Combining this with the volume-dependence of K given above, we can deduce that

$$P_F = 2{\cdot}6(V/V_0)^{0{\cdot}0\pm0{\cdot}3} \text{ Bohr units.}$$

Thus, under the presumption mentioned above, P_F is almost independent of volume over the range of volume available in a compression to 10,000 atm, viz. $\sim 0{\cdot}7$ per cent.

(ii) *Theoretical calculations of P_F*

Theoretical calculations of P_F have been carried out by KOHN,[29] KJELDAAS and KOHN,[4] and BROOKS.[8] KOHN and KJELDAAS studied lithium and sodium. They solved the Schroedinger wave equation, subject to spherical boundary conditions on the surface of the Wigner–Seitz sphere, with the aid of a variational technique. In their calculations an explicit potential was employed. Their values of $P_F(V_0)$, P_A, and $P_F(V_0)/P_A$ are shown in Table 5. The good agreement between these values and the experimental results should be noted. In the case of sodium, P_F was calculated for two values of r_s, enabling the prediction that $P_F = P_F(V_0)(V/V_0)^{-0{\cdot}26}$. This volume variation of P_F is plotted on Fig. 9 for comparison with the experimental results.

BROOKS has calculated P_F as a function of r_s for all the alkali metals, using the quantum defect method[7] and an extension of the BARDEEN perturbation theory.[7a] His results for P_F, P_A, and P_F/P_A at room temperature and atmospheric pressure are given in Table 5. Strictly speaking, only values of P_F/P_A should be compared with experiment, because there are sizeable relativistic corrections which should be made in both P_F and P_A. However, these corrections should be about the same in both P_F and P_A. It will be observed that BROOKS' value for P_F/P_A is in good agreement with the experimental results for lithium and sodium, and in fair agreement with those for rubidium. They are in disagreement with the deduced results for cesium. His results for $P_F(V)/P_F(V_0)$ are plotted in Figs. 9, 10, and 11 for comparison with the experimentally deduced results. No comparison is made in the case of lithium, because the calculation technique fails at values of r_s only 12 per cent smaller than r_s at $T = 300°\text{K}$, $P = 1$ atm. This affects the magnitude of $(dP_F/dV)_{V_0}$ quite seriously, but apparently does not affect the magnitude of P_F very much. BROOKS' results do indicate, though, that P_F decreases with decreasing volume, in agreement with the experimental deduction. The quantum-defect calculation for sodium and rubidium shows strikingly good agreement with the experimental volume-dependence of

VOL. 5 1958

P_F. Cesium, however, shows a much stronger volume-dependence than is predicted theoretically. In view of the poor agreement between the theoretical and experimental values of $P_F(V_0)/P_A$ in cesium, it is not surprising that the volume-dependence of P_F is not well represented by the theory.

(d) *The Temperature-Dependence of the Knight Shift*

The temperature-dependence of the Knight shift in lithium, sodium, rubidium, and cesium has been measured by McGarvey and Gutowsky.[13] They analyzed their data assuming that the temperature-dependence of the Knight shift results entirely from the thermal expansion; that is, they assumed that the Knight shift has no explicit temperature-dependence. Since we have measured the volume-dependence of the Knight shift, we are in a position to examine the validity of this assumption. This is done by making use of the thermodynamic relation

$$(\partial \ln K/\partial T)_P = (\partial \ln K/\partial \ln V)_T(\partial \ln V/\partial T)_P + \\ +(\partial \ln K/\partial T)_V, \qquad (7)$$

where K is presumed a function of V and T. The left-hand side of equation (7) represents the temperature-dependence of K at constant pressure. The two terms on the right-hand side represent, respectively, the contributions of the thermal expansion and the explicit temperature variation to the observed temperature variation of K. By using data in Table 1, along with thermal-expansion measurements,[21,22,23] we can estimate, using McGarvey and Gutowsky's data, the explicit dependence of K on T. The results for sodium, rubidium and cesium are given in Table 6. No entries are made for lithium because $(\partial \ln K/\partial T)_P$ was found to be zero.

In column 1 are the measured[13] values of the temperature dependence of K at atmospheric pressure. In column 2 is the effect of the volume expansion on K. In column 3 is the explicit temperature-dependence of K. It will be observed that in sodium the thermal expansion and the explicit temperature-dependence of K contribute about equally to $(\partial \ln K/\partial T)_P$; while in rubidium these two contributions are in opposite directions with the explicit temperature-dependence dominating. In the case of cesium $(\partial \ln K/\partial T)_P$ and $(\partial \ln K/\partial \ln V)_T(\partial \ln V/\partial T)_P$ are roughly the same size. Therefore, the choice of the thermal expansion is important in determining $(\partial \ln K/\partial T)V$. We have used $(\partial \ln V/\partial T)_P = 9{\cdot}66 \times 10^{-4}/°\mathrm{K}$. We conclude from Table 6 that the Knight shift is an explicit function of the temperature at constant volume. The magnitude of this effect is such that the Knight shift at room temperature is a few per cent higher than the Knight shift at 0°K, at least for sodium, rubidium, and cesium.

The following physical picture is proposed to explain the observed temperature variation of K at constant volume. As the lattice vibrates, the electronic wave function at each point in the lattice adjusts itself almost instantaneously to the local state of strain. Thus P_F is a time-varying function whose time average value is equal only in the first order to the rigid lattice value. In the second order

Table 6. The contribution to the temperature-dependence of the Knight shift at constant pressure from the thermal expansion and from the explicit temperature-dependence of the Knight shift: comparison with theoretical predictions

	$(\partial \ln K/\partial T)_P \times 10^4$ (°K^{-1})	$\left(\frac{\partial \ln K}{\partial \ln V}\right)_T\left(\frac{\partial \ln V}{\partial T}\right)_P \times 10^4$ (°K^{-1})	$(\partial \ln K/\partial T)_V \times 10^4$ (°K^{-1}) Exp.	$(\partial \ln K/\partial T)_V \times 10^4$ (°K^{-1}) Theory	$\frac{1}{P_F}\cdot\frac{\partial^2 P_F}{\partial (V/V_0)^2}$ Exp. deduction
Na	+1·5	+0·8	+0·7	+0·7	2·6
Rb	+1·7*	−0·4	+2·1	+0·5	1·4
Cs	−1·9	−3·1	+1·2	+0·9	2·5

* In determining $(\partial \ln K/\partial T)_P$ for rubidium, we considered only the temperature range between 265°K and the melting point. No attempt is made to explain the maximum in K observed at 254°K in this metal.

of approximation, the average value of P_F is proportional to the product of the square of the local strains and the second derivative of P_F with respect to the strain. Since the average value of the square of the strains is proportional to the squares of the amplitudes of the normal modes of the lattice vibrations, we can expect the time average of P_F to be a function of the temperature at constant volume. The paramagnetic susceptibility, on the other hand, can be expected to be unaffected by the lattice vibrations. This is because the electron spin relaxation time is 10^{-6}—10^{-9} sec, while the characteristic time of a lattice vibration is 10^{-12} sec. The electron spins therefore cannot follow the lattice vibrations and the susceptibility takes on a value determined by the equilibrium lattice spacing.

Using this picture it is possible to make a semiquantitative prediction for the temperature variation of P_F. Because the dependence of P_F on the shearing strains is not known, we shall consider only the effect of the compressional strains which act to change the volume of the unit cell. Expanding P_F around the volume corresponding to the equilibrium volume V_0 at temperature T, we have for the time average value of P_F

$$\overline{P_F(t)} = P_F(V_0) + \tfrac{1}{2}\frac{\partial^2 P_F}{\partial(V/V_0)^2}\overline{\left(\frac{V(t)-V_0}{V_0}\right)^2} + \cdots \quad (8)$$

The horizontal bar indicates averaging over the time. The term linear in ΔV does not enter because $\overline{V(t)-V_0} = 0$. It can be noted that, even at $T = 0$, $\overline{P_F(t)} \neq P_F(V_0)$ because of the presence of the zero point vibrations. The logarithmic derivative of $\overline{P_F(t)}$ relative to T at constant volume is

$$(\partial \ln \bar{P}_F/\partial T)_V = (\partial \ln K/\partial T)_V = \frac{1}{2P_F(V_0)}\left(\frac{\partial^2 P_F}{\partial(V/V_0)^2}\right)_{V=V_0}\frac{\partial}{\partial T}\overline{\left(\frac{\Delta V}{V_0}\right)^2}. \quad (9)$$

The volume-dependence of P_F can be determined using the experimentally deduced results shown in Figs. 9–11 and Table 5. The values for

$$\left(\frac{1}{P_F}\cdot\frac{\partial^2 P_F}{\partial(V/V_0)^2}\right)_{V_0}$$

at room temperature and atmospheric pressure determined in this way are given in column 5 of Table 6. $\overline{(\Delta V/V_0)^2}$ can be estimated using the Debye picture of lattice vibrations as

$$\overline{(\Delta V/V_0)^2} \approx \frac{1}{\rho c^2}\int_0^{\nu_m} h\nu\left(\frac{1}{e^{h\nu/kT}-1}+\tfrac{1}{2}\right)\frac{4\pi\nu^2}{c^3}d\nu, \quad (10)$$

where ρ is the density and c is the sound velocity. Equation (10) presumes that the wavelength of the lattice vibration is long compared to the interatomic distance. For temperatures well above the Debye temperature, where the wavelength of the lattice vibrations is of the order of the interatomic distances, it can be shown that

$$\overline{(\Delta V/V_0)^2} \approx \beta kT/\Omega, \quad (11)$$

where T is absolute temperature, k is Boltzmann's constant, β is the volume compressibility, and Ω is the atomic volume. Explicit evaluation of $(\partial \ln K/\partial T)_V$, using equations (11) and (9) and the results in column 5 of Table 6, gives the values listed in column 4 of Table 3. Comparison of columns 3 and 4 shows surprisingly good agreement between the theoretical and experimental values of $(\partial \ln K/\partial T)_V$ for sodium and cesium. In view of the semiquantitative nature of the theory and the experimental uncertainties, the agreement between theory and experiment in these metals must be considered fortuitous. In the case of rubidium the results indicate that the theory is capable of predicting roughly the size of the observed effect. Furthermore, the theory is consistent with the observed temperature-independence of the Knight shift in lithium, because in this metal $(\partial^2 P_F/\partial(V/V_0)^2)$ is very nearly zero.

5. CONCLUSION

Using PINES' collective electron picture to determine the volume-dependence of the paramagnetic susceptibility χ_P, we have deduced the volume-dependence of P_F for lithium, sodium, rubidium, cesium and copper from measurements of the pressure-dependence of the Knight shift. Comparison has been made with recent theoretical predictions. At atmospheric pressure it is found that both KOHN and KJELDAAS' variational principle technique and BROOKS' quantum-defect method give results for P_F, P_A, and P_F/P_A for lithium and sodium which are in good agreement with the

VOL. 5 1958

values deduced from experiment. The quantum-defect method results for rubidium are in fair agreement with experiment. However, in the case of cesium this theory gives a result for P_F/P_A which is about 40 per cent too small. Comparison of the theoretical predictions with the deduced volume dependence of P_F shows that the quantum-defect method gives excellent results for sodium and rubidium, but varies too slowly with volume in the case of cesium. Calculations using the variational principle have been made only for sodium, in which case the predicted volume-dependence is considerably smaller than the deduced one.

By comparing the present measurements of the volume-dependence of the Knight shift (K) with the previously observed temperature-dependence of K at atmospheric pressure, it has been found that K is an explicit function of the temperature at constant volume. A theory of this effect is proposed in which the effect of the compressional modes of the lattice vibrations on the time average value of P_F is taken into account. It is found that in the second order P_F is displaced from its equilibrium lattice value by an amount proportional to the mean square of the amplitude of the compressional vibrations. Comparison of this theory with the experimentally results is satisfactory.

Acknowledgements—The authors acknowledge with thanks the help of Professor N. BLOEMBERGEN for his guidance and encouragement, and Professor H. BROOKS for several stimulating discussions and the communication of his results prior to publication. We thank also Mr. GUY BOODRY, who constructed much of the electronic equipment.

REFERENCES

1. KNIGHT W. D. *Phys. Rev.* **76,** 1259 (1949).
2. TOWNES C. H., HERRING C. and KNIGHT W. D. *Phys. Rev.* **77,** 852 (1950).
3. PAKE G. E. *Solid State Physics* Vol. 2, p.1 Academic Press Inc., New York (1956).
4. KJELDAAS T. and KOHN W. *Phys. Rev.* **101,** 66 (1955).
5. KOHN W. and ROSTOKER N. *Phys. Rev.* **94,** 1111 (1954).
6. BROOKS H. *Phys. Rev.* **91,** 1027 (1953).
7. HAM F. *Solid State Physics* Vol. 1, p. 127 Academic Press Inc., New York (1955).

7(a). BARDEEN J. *J. Chem. Phys.* **6,** 367 (1938).
SILVERMAN R. A. *Phys. Rev.* **85,** 227 (1952).

8. BROOKS H. Private Communication.
9. PINES D. *Solid State Physics* Vol. 1, p. 367 Academic Press Inc., New York (1955).
10. SCHUMACHER R. T. and SLICHTER C. P. *Phys. Rev.* **101,** 58 (1955).
11. GUTOWSKY H. S. and MCGARVEY B. R. *J. Chem. Phys.* **20,** 1472 (1952).
12. BRIDGMAN P. W. *The Physics of High Pressures* G. Bell and Sons Ltd., London (1949).
13. MCGARVEY B. R. and GUTOWSKY H. S. *J. Chem. Phys.* **21,** 2114 (1953).
14. KUSHIDA T., BENEDEK G. and BLOEMBERGEN N. *Phys. Rev.* **104,** 1364 (1956).
15. PAUL W. and WARSCHAUER D. *Rev. Sci. Instrum.* **27,** 418 (1956).
16. JACOBSOHN B. A. and WANGSNESS R. K. *Phys. Rev.* **73,** 942 (1948).
17. BLOEMBERGEN N., PURCELL E. and POUND R. *Phys. Rev.* **73,** 679 (1948).
18. DICKINSON W. C. *Phys. Rev.* **81,** 717 (1951).
19. BRIDGMAN P. W. *Proc. Amer. Acad. Arts Sci.* **58,** 166 (1923).
20. BRIDGMAN P. W. *Proc. Amer. Acad. Arts Sci.* **60,** 385 (1925).
21. SIMON F. and VOHSEN E. *Z. phys. Chem.* **133,** 165 (1928).
22. SWENSON C. *Phys. Rev.* **99,** 425 (1955).
23. *International Critical Tables* Vol. II, p. 459 McGraw-Hill New York (1927).
24. KNIGHT W. D. *Solid State Physics* Vol. 2, p. 93 Academic Press Inc., New York (1955).
25. FERMI E. *Z. Phys.* **60,** 320 (1930).
26. KAMBE K. *Phys. Rev.* **99,** 419 (1955).
27. FUCHS K. *Proc. Roy. Soc.* **A151,** 585 (1935).
28. DICKINSON W. C. *Phys. Rev.* **80,** 563 (1950).
29. KOHN W. *Phys. Rev.* **96,** 590 (1954).

J. Phys. Chem. Solids Pergamon Press 1958. Vol. 5. pp. 256–263.

THE DEFORMATION POTENTIAL OF POTASSIUM CHLORIDE

HAZIMU KAWAMURA*

H. H. Wills Physics Laboratory, University of Bristol

(*Received* 2 *July* 1957; *revised* 21 *October* 1957)

Abstract—The calculation of the energy of the lowest state of a conduction electron in potassium chloride is made by means of the cellular method for various lattice parameters. The energy is as high as 8·81 eV for the normal lattice parameter, and is reduced to −3·63 eV by taking into account the exchange and overlap corrections. The deformation potential obtained directly from these values is 5·4 eV per unit dilatation. The trapping state around a dislocation line and the scattering of electrons by acoustical phonons are discussed, making use of this value.

VOL. 5 1958

1. INTRODUCTION

We have obtained evidence that the dislocation lines in alkali halides may trap conduction electrons.[1] The photoconductivity of the coloured alkali halide crystal undergoes such a remarkable decrease upon mechanical working that it can hardly be attributed merely to jogs on dislocation lines. The reduction of photoconductivity occurs in the temperature range from −170 to −100°C, showing that the trap depth is about 0·2–0·3 eV. If the deformation potential is known, we may calculate the state of the electron trapped by the potential around the dislocation line (Section 5).

Since the deformation potential is taken as the change in position of the bottom of the conduction band as a function of volume, we must calculate the energy of the conduction-band edge for various lattice parameters. Although Tibbs[2] has made a calculation for the conduction band of sodium chloride by the cellular method, he employed a Hartree potential without exchange for the field of the ionic core, and further he adopted the value of 4·00 atomic units as the radius of the ionic sphere instead of the true value of 3·15. We have solved the Hartree equations in the ionic spheres, employing the potential arising from the charge distribution coming from the free-ion Hartree–Fock calculation as well as from the charges due to anions and cations outside the spheres (Section 2); moreover, we have taken into account the exchange interaction between conduction electron and core electrons (Section 3) and also the effect of overlap between the conduction electron and the core electrons in the same cell as first-order perturbations (Section 4).

2. SOLUTION OF HARTREE EQUATIONS IN IONIC SPHERES

In accordance with the conventional cellular method, we divide the whole crystal into ionic cells of equal volume, each of which contains a cation or an anion, and solve the Hartree equations in these cells with the appropriate boundary conditions for various lattice parameters. In order to separate the equations in polar co-ordinates, we replace the cubic cells by spheres of equal volume. In most metals the atomic cells are truncated octahedra or dodecahedra, which are very nearly spherical, and this substitution may well be justified; but the replacement of a cube by a sphere, as in the present case, is rather questionable. Something like the method of augmented plane waves[3] may be more suitable. However, if the spherical approximation is allowed, we can separate the wave equation into angular and radial parts. If we write $\Psi(r) = R(r)\,Y(\theta, \phi)$, the radial equation has the form

$$\frac{d^2R}{dr^2} + \frac{2}{r}\frac{dR}{dr} + \left[2E - 2U - \frac{l(l+1)}{r^2}\right]R = 0, \quad (1)$$

* Now at the Department of Physics, Osaka City University, Osaka, Japan.

in atomic units. Since the lowest state of the conduction band is s-like, we can put $l = 0$ and $Y(\theta, \phi) = 1$. If we put $P = rR$, the above equation is further reduced as

$$P_K''(r) - 2[U_K - E]P_K(r) = 0, \quad \text{in } K^+ \text{ sphere} \tag{2a}$$

and

$$P_{Cl}''(r) - 2[U_{Cl} - E]P_{Cl}(r) = 0 \quad \text{in } Cl^- \text{ sphere} \tag{2b}$$

where U_K and U_{Cl} are the potential for extra electrons in each ionic sphere. The boundary condition is not so straightforward, since the ionic cells do not fit exactly into the crystal. Following the conventional method, however, we shall assume the relation $R_K'/R_K = -R_{Cl}'/R_{Cl}$, at the surface of the sphere. This equation is expressed in terms of P as

$$P_K'(r_0)/P_K(r_0) + P_{Cl}'(r_0)/P_{Cl}(r_0) = 2/r_0, \tag{2c}$$

where r_0 is the radius of the ionic sphere.

The potential U can be resolved into: (1) the electrostatic potential due to the ionic core belonging to its own ionic sphere, (2) the potential due to the positive and negative ions outside the ionic sphere, and (3) the effect of the electron cloud coming from the ions belonging to the nearest neighbours. We shall designate these components V, M, and v, respectively. For V, we have adopted the potential due to the free ions of K^+ and Cl^- obtained by the use of HARTREE–FOCK calculations.[4,5] For U, we have taken all the ions to be point charges. The effect of overlap of core electrons on the nearest neighbours is taken into consideration in connection with the third component, v. Therefore, M is represented by the Madelung field. Although this is not constant, we shall take only the spherically symmetric part of the expansion in spherical harmonics, which is closely approximated by $\pm\alpha/a$ at the inside of the ionic sphere, where α is Madelung constant and a the ionic distance. The $+$ sign is for the ionic sphere of potassium and the $-$ sign for chlorine. For v, we have expanded the potential V due to the core electrons of the six nearest neighbours in spherical harmonics about the centre of the ion in question, and taken its spherically symmetric part given by

$$v_K(r) = \frac{6}{2ar}\int_{|a-r|}^{a+r} sV_{Cl}(s)\,ds$$

$$v_{Cl}(r) = \frac{6}{2ar}\int_{|a-r|}^{a+r} sV_K(s)\,ds. \tag{3}$$

Thus the potential in each ionic sphere becomes

$$U_K(r) = V_K(r) + \alpha/a + v_K(r)$$

$$U_{Cl}(r) = V_K(r) - \alpha/a + v_K(r). \tag{4}$$

We have calculated these values for $a = 5{\cdot}7$, $5{\cdot}9$ (normal distance between nearest neighbours), and $6{\cdot}1$. Since, as shown in Fig. 1, these functions are

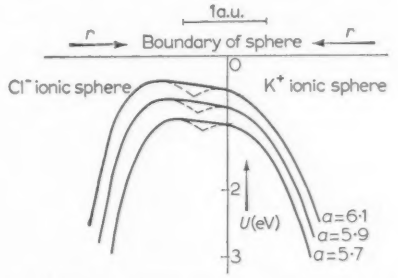

FIG. 1. The potential near the boundaries of each ionic sphere as a function of r for three different lattice parameters.

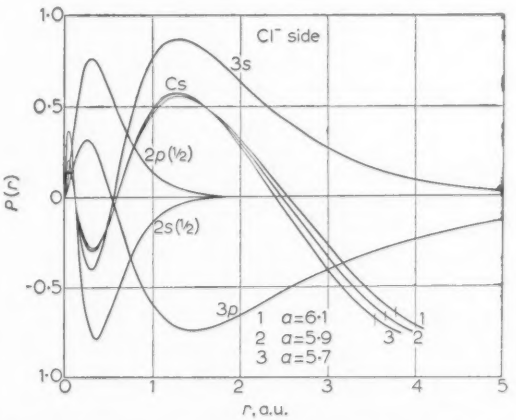

FIG. 2a. The wave functions in K^+ ionic sphere. *Cs* are the wave functions for the bottom of the conduction band for three different lattice parameters calculated by the cellular method. The wave functions for the core electrons for free ion due to HARTREE and HARTREE are also shown.

not strictly continuous near the boundaries of the ionic spheres owing to the rather crude approximation of a cube to a spherical cell, we have joined the two curves by a straight line as indicated by the solid line. This procedure may affect the energy parameter at most by 0·1 eV.

Inserting equations (3) and (4) into (2), we solved the equations numerically for various energy parameters E_0 in K^+ and Cl^- ionic spheres until the boundary condition (equation (2c)) was satisfied.

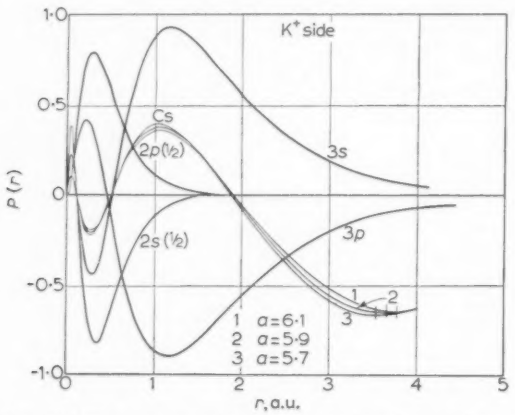

FIG. 2b. The wave function in Cl^- ionic sphere. *Cs* are calculated by the cellular method. The core wave functions for free ion are also due to HARTREE and HARTREE.

The wave functions thus obtained are plotted in Figs. 2a and 2b, together with the wave functions of core electrons. The correct energy parameters for various ionic distances are shown in Table 1.

Table 1

a (atomic unit)	E_0(eV)
5·7	+9·95
5·9	+8·81
6·1	+7·96

3. EXCHANGE CORRECTION

As indicated in Fig. 2, the conduction-electron wave functions have a large overlap with the wave functions of core electrons in the same cell, and hence a considerable exchange effect is to be expected. Since it is difficult to solve the HARTREE–FOCK equation in this case, we have computed the exchange correction as a first-order perturbation of the energy, using the wave function $\Psi(cs|r) = P(cs|r)/r$ obtained in the electrostatic potential of the HARTREE–FOCK core charge distribution. If we let $\Psi(nlm|r) = P(nl|r)\Theta(lm|\theta)\Phi(m|\phi)/r$ be the HARTREE–FOCK core wave functions for free ions, the first-order energy correction due to the exchange interaction between a conduction electron and a core electron is given by

$$E_X = -\iint \Psi(cs|r_1)\Psi(nlm|r_2)\times$$
$$\times\frac{e^2}{r_{12}}\Psi(cs|r_2)\Psi(nlm|r_1)\,d\tau_1\,d\tau_2$$
$$= -\int\int\int\int\int\int P(cs|r_1)P(nl|r_2)\Theta(lm|\theta_2)\times$$
$$\times\Phi(m|\phi_2)\frac{e^2}{r_{12}}P(cs|r_2)P(nl|r_1)\times$$
$$\times\Theta(lm|\theta_1)\Phi(m|\phi_1)\times$$
$$\times\sin\theta_1\sin\theta_2\,dr_1\,dr_2\,d\theta_1\,d\theta_2\,d\phi_1\,d\phi_2. \tag{5}$$

For a closed shell we must sum up over m, which extends from $-l$ to $+l$. Now $1/r_{12}$ is expanded in terms of r_1 and r_2 by making use of Legendre polynomials P as

$$\frac{1}{r_{12}} = \sum_k \frac{{r_1}^k}{{r_2}^{k+1}}P_k(\cos\alpha) \qquad \text{for } r_1 < r_2$$
$$= \sum_k \frac{{r_2}^k}{{r_1}^{k+1}}P_k(\cos\alpha) \qquad \text{for } r_1 > r_2,$$

where α is the angle between $\boldsymbol{r}_1$ and $\boldsymbol{r}_2$. Further, with the use of the properties of spherical harmonics, the integration over θ's and ϕ's may be performed. Finally we get

$$E_X = -2\int_0^\infty dr_1 P(cs|r_1)P(nl|r_1)\times$$
$$\times\frac{1}{{r_1}^{1+l}}\int_0^{r_1} dr_2 P(cs|r_2)P(nl|r_2)r_2\,. \tag{6}$$

Though the above integrations must be carried out from 0 to ∞, we integrated only up to $r = r_0$ for the $1s$, $2s$, and $2p$ shells of K^+ and Cl^- ions, and for the $3s$ and $3p$ shells of the K^+ ion, since these wave functions almost vanish at the outside of the ionic spheres, as indicated in Fig. 2. The results are listed in Table 3 (below) for the three different lattice parameters.

For the $3s$ and $3p$ shells of the Cl^- ion, there is appreciable overlap into the K^+ sphere. Thus it is necessary to compute the exchange interaction between the conduction electron in the K^+ sphere and the part of the $3s$ and $3p$ wave functions which overlap from the six nearest-neighbour Cl^- ions into a given K^+ sphere. We expand these wave functions in spherical harmonics about the potassium nucleus, which is at the distance a from the Cl^- ion. Then the wave function of the Cl^- ion specified by the quantum number n, l, and m is expressed by:

$$\begin{aligned}\Psi_{Cl}(nlm|r) &= k_{lm}\frac{P_{Cl}(nl|r)}{r}P_l^m(\cos\theta)\exp(im\phi)\\ &= k_{lm}\exp(im\phi')\sum_{k=|m|}^{\infty}\alpha_k(nlm|a,r')\times\\ &\quad\times P_k^m(\cos\theta'),\end{aligned}\tag{7}$$

where $r'(r', \theta', \phi')$ is the vector drawn from the potassium nucleus, and $k_{lm}^2 = (2l+1)/4\pi\times$ $\times(l-m)!/(l+m)!$. The expansion coefficients are given by:

$$\begin{aligned}\alpha_k(nlm|a,r') &= 2\pi k_{km}^2\int_0^{\pi}P_{Cl}(nl|r)\times\\ &\quad\times(1/r)P_l^m(\cos\theta)P_k^m(\cos\theta')\sin\theta'\,d\theta',\end{aligned}\tag{8}$$

which is easily obtained by making use of the properties of spherical harmonics. We introduce r as an integration variable instead of θ' by means of the relation

$$r^2 = r'^2+a^2-2ar'\cos\theta',$$

$$\sin\theta'\,d\theta' = (r/ar')\,dr,$$

$$\cos\theta' = (r'^2+a^2-r^2)/2ar',$$

$$\cos\theta = (r^2+a^2-r'^2)/2ar,$$

and

$$r = |a-r'|,\ \text{for}\ \theta = 0,$$

$$r = a+r',\ \text{for}\ \theta = \pi.\tag{9}$$

Further, using the expression for the associated Legendre functions, we can obtain:

$$\alpha_k(nlm|a,r') = \frac{2k+1}{(2a)^l(2ar')^{k+1}}\times$$

$$\times\sum_{s=0}^{l+k}Q_{ks}(nlm|a,r')\int_{|a-r'|}^{a+r'}P_{Cl}(nl|r)r^{2s-l}dr,\tag{10}$$

where $Q_{ks}(nlm|a, r)$ is a homogeneous polynomial in a^2 and r^2 of degree $2(l+k-s)$, which is tabulated in the paper by LÖWDIN.[6] We computed $\alpha_k(300|a, r)$, $\alpha_k(310|a, r)$ and $\alpha_k(311|a, r)$ numerically, using the $3s$ and $3p$ function of the Cl^- ion obtained by HARTREE and HARTREE.

Making use of equations (5) and (7), the exchange energy between the conduction electron and the (nlm) state electrons of the six nearest Cl^- ions in the K^+ ionic sphere is given by:

$$\begin{aligned}E_X'(nlm) &= -6\sum_{k=|m|}^{\infty}C_k(nlm)\\ C_k(nlm) &= 2\frac{1}{2k+1}\times\\ &\quad\times\frac{k_{lm}^2}{k_{km}^2}\int_0^{r_0}dr_1\alpha_k(nlm|a,r_1)\times\\ &\quad\times P_{Cl}(cs|r_1)r_1^{-k}\times\\ &\quad\times\int_0^{r_1}dr_2\alpha_k(nlm|a,r_2)P_{Cl}(cs|r_2)r_2^{k+1}.\end{aligned}\tag{11}$$

Thus for $3s$ and $3p$ states, we have:

$$\begin{aligned}E_X'(3s) &= -6\sum_{k=0}^{\infty}C_k(300)\\ E_X'(3p) &= -6\sum_{k=0}^{\infty}C_k(310)-2\times6\sum_{k=0}^{\infty}C_k(311),\end{aligned}\tag{12}$$

where the factor 2 in the last term comes from

Table 2

	$6C_1(300)$	$6C_1(310)$	$6C_2(310)$	$12C_1(311)$	$12C_2(311)$	$12C_2(311)$
eV	0·013	0·11	0·05	0·005	0·04	0·0002

$m = \pm 1$. We calculated only to the first term of $C_k(300)$, to the second of $C_k(310)$, and to the third of $C_k(311)$. The values are tabulated in the Table 2. The calculation was carried out only for the normal ionic distance ($a = 5{\cdot}9$).

For different lattice parameters, we multiplied by the factor $[P_{Cl}(3l|r_0')/P_{Cl}(3l|r_0)]^2$,* which is taken as the measure of the relative density of electrons outside the ionic sphere. The summary of the calculation of the exchange correction is given in the Table 3. We can see that the total exchange energy is as large as −11·47 eV for the normal lattice parameter.

* r_0' is the ionic radius for the deformed lattice.

Table 3. *Exchange correction* (*in* eV)

	a (atomic unit)	5·7	5·9	6·1
1*s*	K	−0·18	−0·16	−0·14
	Cl	−0·34	−0·31	−0·28
2*s*	K	−0·40	−0·365	−0·33
	Cl	−0·74	−0·70	−0·67
2*p*	K	−0·37	−0·34	−0·30
	Cl	−0·79	−0·75	−0·72
3*s*	K	−1·62	−1·49	−1·34
	Cl E_X	−4·08	−4·03	−4·02
	Cl E_X'	−0·01	−0·01	−0·01
	Cl E_X (total)	−4·09	−4·04	−4·03
3*p*	K	−1·10	−1·02	−0·94
	Cl E_X	−2·08	−2·08	−2·15
	Cl E_X'	−0·26	−0·21	−0·18
	Cl E_X (total)	−2·34	−2·29	−2·33
Total exchange energy		−11·97	−11·47	−11·08

4. OVERLAP CORRECTION

Our wave function is not orthogonal to the core electrons because the latter satisfy different boundary conditions. It is orthogonal to *p*-states owing to the different symmetry. The overlap integrals between *s*-states at the inside of the ionic spheres are shown in Table 4. To 1*s* and 2*s* it is almost orthogonal, but there is appreciable overlap with 3*s*. Hence we must take into account the correction in energy due to this overlap. In the following the orthonormalization is performed only at the inside of each ionic sphere, neglecting the overlap between conduction-band wave function on one ion and the core function overlapping from another ion. Since the fraction of the total charge of the 3*s* electron of Cl outside the ionic sphere is 0·01, the neglected overlap integral may be of the order of 0·1, if the conduction-band wave function is approximated by a plane wave.

Table 4. *Overlap integral*

	a(Å)	5·7	5·9	6·1
1*s*	K		$1{\cdot}03\times10^{-3}$	
	Cl		$2{\cdot}13\times10^{-3}$	
2*s*	K		$1{\cdot}82\times10^{-2}$	
	Cl		$3{\cdot}55\times10^{-2}$	
3*s*	K	0·209	0·199	0·187
	Cl	0·421	0·428	0·431

For simplicity, we shall let ψ_K, ψ_{Cl}, and ψ be the wave functions for 3*s* of K^+, 3*s* of Cl^-, and an extra electron, respectively, and further we shall adopt the following abbreviated symbols:

VOL. 5 1958

$$(\psi|\psi_K) = \int \psi\psi_K \, d\boldsymbol{r}, \quad (\psi|\psi_{Cl}) = \int \psi\psi_{Cl} \, d\boldsymbol{r},$$
$$(\psi|\mathscr{H}|\psi_K) = \int \psi\mathscr{H}\psi_K \, d\boldsymbol{r},$$
$$\alpha = (\psi|\psi_K)/(\psi_K|\psi_K), \quad \beta = (\psi|\psi_{Cl})/(\psi_{Cl}|\psi_{Cl}). \tag{13}$$

We shall assume that ψ_K and ψ_{Cl} vanish outside their own ionic spheres. Hence $(\psi_K|\psi_K)$ and $(\psi_{Cl}|\psi_{Cl})$ are less than unity by 0·003 and 0·01, respectively. This rather crude approximation may be justified, since the overlap correction is very small, as is shown later. The formulation becomes quite simple by virtue of this assumption. The wave function orthonormalized to ψ_K and ψ_{Cl} is given by

$$\phi = (\psi - \alpha\psi_K - \beta\psi_{Cl})/(1-\alpha^2-\beta^2)^{\frac{1}{2}}, \tag{14}$$

and the mean energy for this wave function is given by

$$\begin{aligned}(\phi|\mathscr{H}|\phi) &= (\psi-\alpha\psi_K-\beta\psi_{Cl}|\mathscr{H}|\psi-\alpha\psi_K-\beta\psi_{Cl})/\\ &\qquad (1-\alpha^2-\beta^2)\\ &= E_0+[\alpha^2(\psi_K|\mathscr{H}|\psi_K)-\alpha(\psi|\mathscr{H}|\psi_K)+\\ &\qquad +\beta^2(\psi_{Cl}|\mathscr{H}|\psi_{Cl})-\beta(\psi|\mathscr{H}|\psi_{Cl})]/\\ &\qquad (1-\alpha^2-\beta^2),\end{aligned} \tag{15}$$

where $\mathscr{H}$ is the Hamiltonian for the extra electron and $E_0 = (\psi|\mathscr{H}|\psi)$ is the uncorrected energy for this electron. Now $\mathscr{H}$ may be resolved into the Madelung energy $\pm M = \pm\alpha/a$ and the Hamiltonian for the extra electron attached to the isolated ion in each ionic sphere, if the small correction term due to the electron cloud from the nearest neighbours is neglected. The latter is further resolved into the potential u due to the charge cloud of 3*s* electron and the ion-core Hamiltonian without 3*s*, whose eigenfunction is ψ_K or ψ_{Cl} under proper boundary condition, which we shall designate $\mathscr{H}'$. Thus we have

$$\begin{aligned}\mathscr{H} &= \mathscr{H}_K' + M + u_K(r), \quad \text{in the } K^+ \text{ ionic sphere,}\\ &= \mathscr{H}_{Cl}' - M + u_{Cl}(r), \quad \text{in the } Cl^- \text{ ionic sphere.}\end{aligned} \tag{16}$$

When equation (16) is inserted into (15), we have pairs of terms such as

$$\alpha^2(\psi_K|\mathscr{H}_K'|\psi_K) - \alpha(\psi|\mathscr{H}_K'|\psi_K),$$

which vanish because $\mathscr{H}_K'\psi_K$ is a constant multiple of ψ_K, and only the following terms remain as the correction of energy:

$$\begin{aligned}E_s &= [\alpha^2(\psi_K|u_K|\psi_K)-\alpha(\psi|u_K|\psi_K)+\\ &\quad +\beta^2(\psi_{Cl}|u_{Cl}|\psi_{Cl})-\beta(\psi|u_{Cl}|\psi_{Cl})]/(1-\alpha^2-\beta^2).\end{aligned} \tag{17}$$

These integrations extend into each ionic sphere, and have the value shown in Table 5.

Adding up all these corrections to E_0, we get the final results shown in Table 6. We see that the bottom of the conduction band of the normal lattice is −3·63 eV and the deformation potential is 5·4 eV per unit dilation.

5. DISCUSSION AND APPLICATIONS OF THE RESULT

It is interesting that the exchange correction is as large as −11·47 eV and the total energy becomes negative by virtue of this correction. In this respect our result is far more satisfactory than that

Table 5. Overlap correction (in eV)

	a (atomic units)	5·7	5·9	6·1
K	$(\psi_K\|u_K\|\psi_K)$	+19·1	+19·1	+19·1
	$(\psi\|u_K\|\psi_K)$	+ 5·29	+ 5·12	+ 4·93
	$\alpha^2(\psi_K\|u_K\|\psi_K)-\alpha(\psi\|u_K\|\psi_K)$	− 0·27	− 0·26	− 0·25
Cl	$(\psi_{Cl}\|u_{Cl}\|\psi_{Cl})$	+15·3	+15·3	+15·3
	$(\psi\|u_{Cl}\|\psi_{Cl})$	+ 7·62	+ 7·71	+ 7·81
	$\beta^2(\psi_{Cl}\|u_{Cl}\|\psi_{Cl})-\beta(\psi\|u_{Cl}\|\psi_{Cl})$	− 0·47	− 0·49	− 0·50
E_s		− 0·96	− 0·97	− 0·97

Table 6. Energy and deformation potential (in eV)

a (atomic units)	5·7	5·9	6·1
E_0	+ 9·95	+ 8·81	+ 7·98
E_x	−11·97	−11·47	−11·08
E_s	− 0·96	− 0·97	− 0·97
E (total)	− 2·98	− 3·63	− 4·07
$E_1 = -(1/V)(dE/dV)$		+ 5·4	

of TIBBS,[2] who obtained the value of +3 eV, reducing the uncorrected value by increasing the radius of the ionic sphere (Section 1). Of course, the exact position of the bottom of the conduction band referred to the vacuum potential is changed by the dipole layer on the surface. Therefore, we cannot compare our result directly with the electron affinity estimated by MOTT[7] to be about −0·5 eV for sodium chloride.

The ordinary cellular method is not well suited to a crystal of the sodium chloride type, since the ionic sphere is so different from the true cubic cell. Therefore, the boundary condition (2c) may lead to large errors. A more reasonable procedure may be to separate the whole crystal into ionic spheres of smaller volume surrounding each ion and the residual region between these spheres, where the potential is fairly constant. Thus we should be able to connect naturally the spherically symmetric functions about ions and the plane waves having singularities at the nuclei.

Since the kinetic and potential energies are about 50 eV, the exchange energy amounts to more than 20 per cent of the potential energy. Therefore, it is not very reasonable to take it into account as a first-order perturbation. It is better, of course, to solve the HARTREE–FOCK equation from the beginning, though this may be very difficult.

The deformation potential which we have obtained has no direct relationship to experiment. But it has a physical bearing on electronic processes in ionic crystals, some of which we shall discuss briefly.

(a) *Electron trap along a dislocation line*

About a dislocation line, there is a volume dilatation given by

$$\Delta = \left(\frac{b}{2\pi}\right)\left(\frac{1-2\sigma}{1-\sigma}\right)\frac{\sin\theta}{\rho}, \tag{18}$$

where b and σ are the Burger's vector and Poisson's ratio, respectively, and ρ, θ, z are the cylindrical co-ordinates with the z axis along the dislocation line. We have compression on the side of the extra half plane and dilatation on the other side. If we apply the effective mass approximation, the conduction electron with effective mass m^* has the effective potential:

$$E_1\Delta = -A\sin\theta/\rho,$$

where

$$A = E_1\left(\frac{b}{2\pi}\right)\left(\frac{1-2\sigma}{1-\sigma}\right). \tag{19}$$

LANDAUER[8] had estimated the energy of an electron trapped in this potential to be:

$$E = -0{\cdot}204m^*A^2/\hbar^2, \tag{20}$$

using an error function as the trial function, whose half-breadth and centre position are varied. If we assume 5·4 eV for E_1, the trap depth becomes 0·16 eV. These electrons are trapped only two dimensionally and may be running along the dislocation line as the polarons accompanying the field of polarization. There is also the possibility that the electrons are "self-trapped". In any case the state may be further stabilized by the polarization of the medium due to the trapped electron.

(b) *Mobility of an electron*

According to BARDEEN and SHOCKLEY,[9] the relaxation time due to the collision between an electron and an acoustic phonon is given by

$$\tau = \frac{\pi\hbar^4 c_{ll}}{m^{*2}E_1^2 k_0 T}\cdot\frac{1}{v}. \tag{21}$$

Using our result, the mobility $\mu = (e/m)\tau$ becomes 140 cm²/V sec at room temperature. This is indeed much greater than the mobility due to scattering by optical phonons, which is about 5 cm²/V sec at room temperature for potassium chloride. But at very low temperatures, the acoustic phonon becomes more effective, since the number of optical phonons decreases more rapidly with

temperature than does the number of acoustic phonons. Further, Y. TOYOZAWA has suggested to me that the acoustic phonon is also important for the scattering excitons, because they have no net charge.

Acknowledgements—I should like to express my profound gratitude to Professor M. H. L. PRYCE for his kind guidance throughout this work. I am also much indebted to Professor F. C. FRANK for the deep interest shown in this work. I should also like to take this opportunity to express my sincere gratitude to Science Council of Japan and to the City Council of Osaka for financial support.

OL.
5
958

REFERENCES

1. KAWAMURA H., OKADA J., UEMURA Y. and OKURA H. *International Conference on Semiconductors and Phosphors* (1956).
2. TIBBS S. R. *Trans. Faraday Soc.* **35,** 1471 (1939).
3. SAFFREN M. M. and SLATER J. C. *Phys. Rev.* **92,** 1126 (1953).
4. HARTREE D. R. and HARTREE W. *Proc. Roy. Soc.* **A156,** 45 (1936) (Cl).
5. HARTREE D. R. and HARTREE W. *Proc. Roy. Soc.* **A166,** 450 (1938) (K).
6. LÖWDIN P. O. *Advances in Phys.* **5,** 1 (1956).
7. MOTT N. F. and GURNEY R. W. *Electronic Processes in Ionic Crystals* Oxford University Press (1948).
8. LANDAUER R. *Phys. Rev.* **94,** 1386 (1954).
9. BARDEEN J. and SHOCKLEY W. *Phys. Rev.* **80,** 102 (1950).

J. Phys. Chem. Solids Pergamon Press 1958. Vol. 5. pp. 264–267.

THE LATTICE ENERGY AND HEAT OF FORMATION OF LITHIUM MONOSULPHIDE

D. F. C. MORRIS

Department of Chemistry, Brunel College of Technology, London W.3.

(*Received* 18 *September* 1957)

Abstract—A term-by-term theoretical calculation of the lattice energy of lithium monosulphide is reported. The lattice energy is computed to be $U_0 = 588{\cdot}7$ kcal/mole (0°K). This value, in conjunction with known thermodynamic data, has been used to estimate the heat of formation of the compound, $\Delta Hf = -117{\cdot}7$ kcal/mole (298°K).

VOL.
5
195

1. INTRODUCTION

CALCULATIONS have recently been made by MORRIS[1] of the lattice energies of the alkali monosulphides Na_2S, K_2S, and Rb_2S, and the results have been used to derive the affinity of sulphur for two electrons. In the present paper the theoretical calculation of the lattice energy of lithium monosulphide is reported. Since no experimental figure for the heat of formation of this compound appears to be available in the literature, a value has been estimated from the lattice energy and other thermodynamic data.

The values computed are for the lattice energy, $U_0 = 588{\cdot}7$ kcal/mole (0°K), for the heat of formation, $\Delta Hf = -117{\cdot}7$ kcal/mole (298°K).

2. THE LATTICE ENERGY

The calculation of the lattice energy is based on the theory of BORN and MAYER,[2] and the assumption is made that the chemical bonding in lithium monosulphide is of the straightforward ionic type. The general procedure employed is similar to that used by MORRIS for alkali monoxides[3] and other alkali monosulphides.[1]

The lattice energy per mole at 0°K of an ionic crystal may be expressed in the following form:[2,4]

$$U_0 = U_E - U_R + U_W - U_Z, \tag{1}$$

where U_E represents the Coulomb or electrostatic energy of attraction between the ions, U_R the repulsion energy, U_W the van der Waals energy, and U_Z the zero-point energy. By evaluating the terms U_E, U_R, U_W, and U_Z, the lattice energy of the crystal may be determined.

In the case of lithium monosulphide, the terms may be assumed to be represented by the following equations:

$$U_E = \frac{e^2 NA}{r_0} \tag{2}$$

$$U_R = bN[nc_{+-}\exp\{(r_+ + r_- - r_0)/\rho\} + n'c_{++}\exp\{(2r_+ - k_1 r_0)/\rho\} + \tfrac{1}{2}n''c_{--}\exp\{(2r_- - k_2 r_0)/\rho\}] \tag{3}$$

$$U_W = N\left\{\frac{C}{r_0^6} + \frac{D}{r_0^8}\right\} \tag{4}$$

$$U_Z = \frac{27}{8}Nh\nu_{\max.} \tag{5}$$

The symbols in these equations have the following significance:

N = Avogadro's number = $6{\cdot}02283 \times 10^{23}$.
e = electron charge = $4{\cdot}8024 \times 10^{-10}$ e.s.u.
A = Madelung constant, referred to r_0, for the antifluorite (and fluorite) lattice.
r_0 = shortest equilibrium Li–S distance. For Li_2S with the antifluorite lattice, $r_0 = \sqrt{3}a_0/4$, where a_0 is the lattice constant.
b = a repulsion constant obtainable from the condition $(dU_0/dr)_{r=r_0} = 0$.

n = the number of nearest unlike neighbours of a sulphide ion.
n', n'' = the number of nearest like neighbours of a lithium ion and a sulphide ion, respectively.
r_+ = "basic radius" for a lithium ion.
r_- = "basic radius" for a sulphide ion.
$c_{+-}c_{++}, c_{--}$ = factors introduced by PAULING[5] for the dependence of the repulsion of two ions on their charges and the number of electrons in their outermost shells.
ρ = a constant obtainable from compressibility data.[2]
k_1 = ratio of the shortest Li–Li distance to r_0.
k_2 = ratio of the shortest S–S distance to r_0.
C, D = van der Waals constants, calculated as described below.
h = Planck's constant = $6{\cdot}6242\times10^{-27}$ erg sec.
ν_{max} = characteristic Debye frequency for the solid oxide.

The experimental lattice constant employed in the present calculations is that listed by WYCKOFF.[6] The constant ρ has been taken as having the value $\frac{1}{3}\times10^{-8}$ cm due to HUGGINS,[4] and the basic radii of Li^+ and S^{2-} are the values derived by HUGGINS[4] and by HUGGINS and SAKAMOTO.[7]

The van der Waals energy term

The term U_W contributes relatively little to the lattice energy. The constants C and D refer to dipole–dipole and quadrupole–dipole attraction, respectively. They may be evaluated using the following equations

$$C = S_6'd_{+-}+\tfrac{1}{2}S_6''d_{++}+\tfrac{1}{2}S_6'''d_{--} \qquad (6)$$

$$D = S_8'q_{+-}+\tfrac{1}{2}S_8''q_{++}+\tfrac{1}{2}S_8'''q_{--} \qquad (7)$$

$$d_{1,2} = \tfrac{3}{2}\alpha_1\alpha_2\frac{\epsilon_1\epsilon_2}{\epsilon_1+\epsilon_2};\ q_{1,2} = \frac{9d_{1,2}}{4e^2}\left(\frac{\alpha_1\epsilon_1}{p_1}+\frac{\alpha_2\epsilon_2}{p_2}\right) \qquad (8)$$

where α refers to the polarizability of an ion, ϵ refers to an energy characteristic of the oscillators in the ion, and p refers to the effective number of outermost electrons.

In the present calculations, the values of the S constants for the antifluorite lattice are taken from MORRIS.[3] The value of PAULING[8] for the polarizability of the lithium ion α_+ has been employed and, following MAYER,[9] ϵ_+ has been given the value $0{\cdot}75\ I_2$, where I_2 is the ionization potential of Li^+. The value α_- for the polarizability of the sulphide ion has been chosen from an examination of the data of FAJANS and JOOS[10] and TESSMAN, *et al.*[11] The value of ϵ_- for the sulphide ion has been obtained from the approximation equation

$$\epsilon = (h^2e^2p/4\pi^2m\alpha)^{\frac{1}{2}} \qquad (9)$$

due to HERZFELD and WOLF.[12] Although there are two electrons in the outermost shell of the lithium ion and eight electrons in the outermost shell of the sulphide ion, MAYER[9] has calculated 3·2 as the "effective number" for the chloride ion in NaCl and KCl, and 4·0 for the iodide ion in KI. HERZFELD and WOLF[13] have computed p values of 4·6 for argon and 5·6 for xenon. In the present work, a value of 1 has been taken for the lithium ion and 3·2 for the sulphide ion.

The choice of values of some of these quantities employed in calculating the van der Waals energy is subject to uncertainty. However, owing to the use of an empirical repulsive potential, determined from the attractive potential and the constants of the crystal, the magnitude of error introduced into the computation of lattice energy by an error in the values of C and D is less than that introduced into the van der Waals energy.

Results

The results of the term-by-term calculations are summarized in Table 1, and the data employed in the computation of the different terms are listed in Table 2. The value quoted for the lattice energy, 588·7 kcal/mole (0°K), is probably reliable to within *ca.* ±3 kcal.

Table 1. *Lattice energy* U_0, *of lithium monosulphide calculated term by term. Values in kcal/mole at* 0°*K.*

U_E	$-U_R$	U_W	$-U_Z$	U_0
676·9	−94·4	8·8	−2·6	588·7

3. THE HEAT OF FORMATION

The heat of formation ΔHf of lithium monosulphide may be obtained from the lattice energy and other thermodynamic data by use of the BORN HABER cycle. For Li_2S the cycle is shown below:

Table 2. Data employed for calculation of the terms

Crystal type	antifluorite	$10^{24}\alpha_+$ (cm^3)	0·029
r_0 (Å)	2·471	$10^{24}\alpha_-$ (cm^3)	4·8
A	5·039	$10^{12}\varepsilon_+$ (erg ion^{-1})	90·8
$10^{12}b$ (erg mol^{-1})	1·13	$10^{12}\varepsilon_-$ (erg ion^{-1})	13·7
n	8	S'_6	8·709
n'	6	S''_6	1·524
n''	12	S'''_6	0·762
k_1	1·154	S'_8	8·208
k_2	1·633	S''_8	0·506
r_+ (Å)	0·57	S'''_8	0·253
r_- (Å)	1·69	$10^{60}d_{+-}$ (erg cm^6)	2·5
c_{+-}	1·25	$10^{60}d_{++}$ (erg cm^6)	0·057
c_{++}	2	$10^{60}d_{--}$ (erg cm^6)	237
c_{--}	0·5	$10^{76}q_{+-}$ (erg cm^8)	5·6
$10^8\rho$ (cm)	0·3333	$10^{76}q_{++}$ (erg cm^8)	0·29
$10^{60}C$ (erg cm^6)	112	$10^{76}q_{--}$ (erg cm^8)	950
$10^{76}D$ (erg cm^8)	167	$10^{12}\nu_{max}$ (s^{-1}) estd.	8

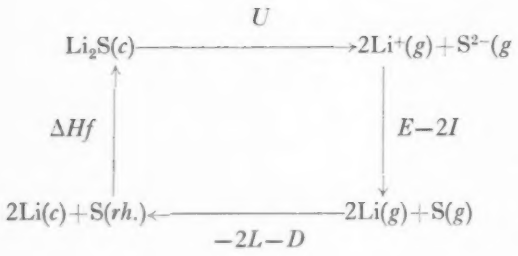

The symbols are defined by the following thermochemical equations:

$$\mathrm{Li_2S}(c) = 2\mathrm{Li^+}(g) + \mathrm{S^{2-}}(g)$$
$$\Delta H_{298} = U, \text{ lattice energy at } 298°\mathrm{K}.$$

$$\mathrm{Li_2S}(c) = 2\mathrm{Li}(c) + \mathrm{S}(rh.)$$
$$\Delta H_{298} = -\Delta Hf, \text{ heat of formation.}$$

$$\mathrm{Li}(c) = \mathrm{Li}(g)$$
$$\Delta H_{298} = L, \text{ heat of sublimation.}$$

$$\mathrm{S}(rh.) = \mathrm{S}(g)$$
$$\Delta H_{298} = D, \text{ heat of atomization.}$$

$$\mathrm{Li}(g) = \mathrm{Li^+}(g) + e$$
$$\Delta H_0 = I, \text{ ionization potential.}$$

$$\mathrm{S^{2-}}(g) = \mathrm{S}(g) + 2e$$
$$\Delta H_0 = E, \text{ double electron affinity.}$$

The changes in enthalpy must add up to zero, and hence

$$\Delta Hf = D + 2L + 2I - U - E. \qquad (10)$$

The heat of formation ΔHf obtained from this equation may be regarded as refering to 298°K. If the assumption is made that the heat capacity of $\mathrm{Li^+}(g)$ is the same as that of $\mathrm{Li}(g)$, then the change of ionization potential with temperature will depend only upon the heat capacity of the electron. If the corresponding assumption is made concerning $\mathrm{S^{2-}}(g)$ and $\mathrm{S}(g)$, then the change of electron affinity with temperature will similarly depend upon the heat capacity of the electrons. Since E and $2I$ enter into equation (10) with opposite sign, an error introduced by neglecting the thermal energy of the electrons is cancelled. The value for U to be employed in equation (10) should refer to 298°K; however, owing to the lack of requisite heat-capacity data, the small enthalpy change for the lattice energy between 0 and 298°K cannot be computed. Nevertheless, a rough estimate of this has been made in deriving U for 298°K.

The value for the heat of formation ΔHf of lithium monosulphide and the necessary thermodynamic data for its calculation from equation (10) are listed in Table 3. The result, $\Delta Hf = -117{\cdot}7$ kcal/mole (298°K), is probably reliable to within *ca.* ± 5 kcal.

Table 3. Heat of formation, ΔHf (in kcal/mole), of lithium monosulphide from the BORN–HABER *cycle*

D	$2L$	$2I$	$-U$	$-E$	ΔHf
53·25[a]	74·14[a]	248·6[b]	−588·2[c]	94·5[d]	−117·7

Data from (*a*) ROSSINI *et al.*,[14] (*b*) FINKELNBURG and HUMBACH,[15] (*c*) present paper, and (*d*) MORRIS.[1]

REFERENCES

1. MORRIS D. F. C. *Acta Cryst.* (In the press).
2. BORN M. and MAYER J. E. *Z. Phys.* **75,** 1 (1932).
3. MORRIS D. F. C. *Proc. Roy. Soc.* **242,** 116 (1957).
4. HUGGINS M. L. *J. Chem. Phys.* **5,** 143 (1937).
5. PAULING L. *Z. Krist.* **67,** 377 (1928).
6. WYCKOFF R. W. G. *Crystal Structures* Interscience Publishers Inc., New York (1951).
7. HUGGINS M. L. and SAKAMOTO Y. *J. Phys. Soc. Japan* **12,** 241 (1957).
8. PAULING L. *Proc. Roy. Soc.* **A114,** 181 (1927).
9. MAYER J. E. *J. Chem. Phys.* **1,** 270 (1933).
10. FAJANS K. and JOOS G. *Z. Phys.* **23,** 1 (1924).
11. TESSMAN J. R., KAHN A. H., and SHOCKLEY W. *Phys. Rev.* **92,** 890 (1953).
12. HERZFELD K. F. and WOLF K. L. *Ann. Phys. (Leipzig)* **78,** 195 (1925).
13. HERZFELD K. F. and WOLF K. L. *Ann. Phys. (Leipzig)* **76,** 71 (1925).
14. ROSSINI F. D., WAGMAN D. D., EVANS W. H., LEVINE S. and JAFFE I. *Circ. Nat. Bur. Stand.* No. 500 (1952).
15. FINKELNBURG W. and HUMBACH W. *Naturwissenschaften,* **42,** 35 (1955).

J. Phys. Chem. Solids Pergamon Press 1958. Vol. 5. pp. 268–287.

PARAMAGNETIC RESONANCE ABSORPTION OF A V CENTER IN LiF

TRUMAN O. WOODRUFF and WERNER KÄNZIG

General Electric Research Laboratory, Schenectady, New York

(*Received* 26 *September* 1957)

Abstract—By X-irradiation of LiF at liquid-nitrogen temperature, an electron-deficiency center is created that can be described as a F_2^- molecule-ion, as was shown in previous work by CASTNER and KÄNZIG. The present paper contains a more rigorous and complete study of the paramagnetic resonance absorption spectrum of this center. The spin energy matrix based on the spin Hamiltonian proposed in the previous paper has been diagonalized, and it is shown that the "allowed" and "forbidden" transitions between the resulting energy levels are in good agreement with the observed paramagnetic resonance lines, for any orientation of the crystal in the d.c. magnetic field.

VOL. 5 1958

1. INTRODUCTION

THE exposure of an alkali halide crystal to X-rays may produce interesting changes in almost every one of its optical, electrical, magnetic, and mechanical properties. The extent to which a particular property is changed depends on the imperfections initially present in the specimen and the conditions of the exposure to X-rays, such as the duration of the exposure, the wavelengths contained in the incident X-ray beam, and the temperature of the crystal during and after irradiation. These property changes are believed to be associated with the formation of localized imperfections in the crystal. The imperfections that absorb light have been studied in detail by a great number of workers; they are called "color centers". Structures for a number of color centers have been proposed and related with varying degrees of success to the property changes.* In this paper we describe an investigation of the paramagnetic resonance absorption observed under particular conditions in single crystals of LiF which have been exposed to X-rays at liquid-nitrogen temperature and kept at this temperature. We have found about a dozen paramagnetic centers in these crystals after such irradiation, but by a suitable choice of the experimental conditions (microwave power level, temperature, tuning, modulation) we can generally isolate and study the resonance spectrum of a single center. In this particular case the paramagnetic resonance absorption for very low power levels was observed at liquid-nitrogen temperature. CASTNER and KÄNZIG,[2] in a paper hereafter referred to as (I), have given evidence that this paramagnetic resonance absorption is due to a diatomic molecular ion F_2^- in the LiF crystal, which can be thought of as formed from two neighboring fluoride ions by removing one electron in

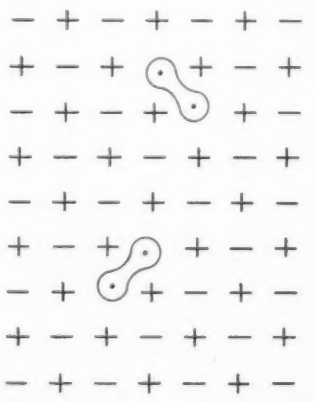

FIG. 1. Model for the V center whose paramagnetic resonance absorption is discussed here.
F_2 molecule + ions in LiF lattice.

* For a summary of this work, with references, see SEITZ.[1]

such a way that the resulting electron deficiency is shared equally by the two ions, as indicated schematically in Fig. 1 and in Fig. 5 of (I). Their results indicate that such a configuration is not associated with any other imperfection; if this is so, it may be regarded as a self-trapped hole. We refer to it as a V center.

This imperfection is so fundamental that any structure which is proposed for it should be thoroughly tested. Therefore, it seemed to us important to study certain aspects of the analysis of the paramagnetic resonance spectrum in more detail than did CASTNER and KÄNZIG.[2] We were especially eager to obtain a better understanding of the way in which the paramagnetic resonance absorption spectrum of this center depends on the angle θ between its axis and the d.c. magnetic field, since the approximate analysis of (I) did not yield a satisfactory description of this dependence for θ approaching 90°. A comparison of the V center spectra of four different kinds of alkali-halide crystals (LiF, KCl, NaCl, and KBr) reproduced in (I) will make clear why we chose to concentrate on the LiF spectrum. The LiF V center spectrum is simpler than the others because there is only one naturally occurring fluorine isotope, ^{19}F, and it has spin $\frac{1}{2}$. Hence the individual lines, particularly in the 90° pattern, are much better resolved.

The principal object of the work described here was to make an accurate and complete comparison of the experimental observations of the spectra for various orientations of the crystal in the d.c. magnetic field, summarized in Section 2, with the implications of the spin Hamiltonian proposed in (I). As indicated in Section 3, it was possible to do this only by determining the exact eigenvalues of this spin Hamiltonian. We found that the line positions obtained from these exact eigenvalues for a particular choice of the constants in the spin Hamiltonian agreed in all cases with the measured positions to within a few gauss. We consider this agreement remarkably good, in view of the fact that the spectra spread over a range of nearly 1800 G. Initially, we were concerned only with describing and interpreting our observations of the "allowed" paramagnetic resonance absorption lines, by which we mean the absorption lines excited by the component of the oscillating magnetic field normal to the d.c. magnetic field. When that work was almost finished, improvements in the sensitivity of the apparatus enabled us to observe the "forbidden" lines—the lines excited by the component of the oscillating magnetic field parallel to the d.c. magnetic field. These results are included in Section 4, which contains a description and interpretation of the "forbidden" lines in the LiF V center spectrum together with some more general considerations on line intensities and selection rules in paramagnetic resonance.

2. OBSERVATIONS

We first describe a typical experiment and then present the data obtained from a series of such experiments. Single crystals of LiF supplied by the Harshaw Chemical Company were cut to fit with a desired orientation into the resonant cavity of a high-sensitivity paramagnetic resonance spectrometer. The apparatus was arranged so that the resonant cavity could be maintained at the temperature of an appropriate coolant (liquid nitrogen, liquid hydrogen, or liquid helium) and either exposed to the radiation from an X-ray tube or placed between the poles of a Varian 12-in. magnet. The orientation of the crystal in the magnetic field could be very precisely adjusted by rotating the magnet and tilting the cryostat. After the crystal had been cemented into the cavity, it was cooled and irradiated. The irradiation took place at liquid-nitrogen temperature and was such as to produce roughly 10^{17} V centers/cm^3. The intensity and distribution of wavelengths in the X-ray beam used for the irradiation and the length of the exposure can be varied within wide limits, the only effect on the V center resonance being to change its intensity. Typically, the crystal was exposed for 6 hr at a distance of 2 in. from the focus of an X-ray diffraction tube with a tungsten target operated at 50 kV and 20 mA, with the equivalent of about 2 mm of aluminum interposed between tube and crystal. While we believe that ultraviolet radiation can produce V centers with high efficiency provided that electron traps are present, it is convenient to use penetrating X-ray quanta, so that the centers are produced uniformly throughout the volume of the crystal, rather than in a surface layer.

Upon completion of the irradiation, the crystal was precisely oriented with respect to the d.c. magnetic field by a procedure depending upon observation of the effects of small rotations of the

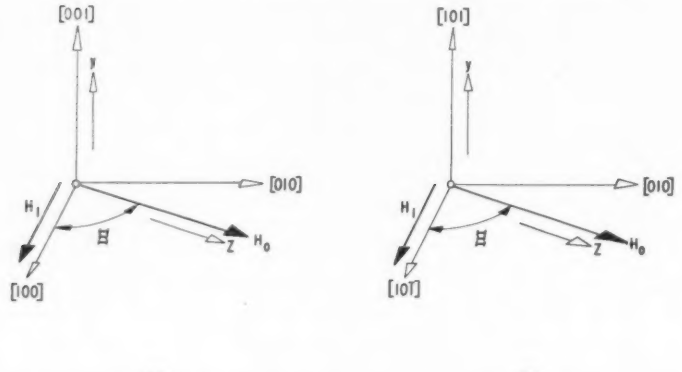

FIG. 2. The relative orientations of the LiF crystal, $\boldsymbol{H}_0$ and $\boldsymbol{H}_1$ in : (A) the first sequence of experiments (in that sequence Ξ was varied from 90° to 45°); (B) the second sequence of experiments (in that sequence Ξ was varied from 90° to 35·26°).

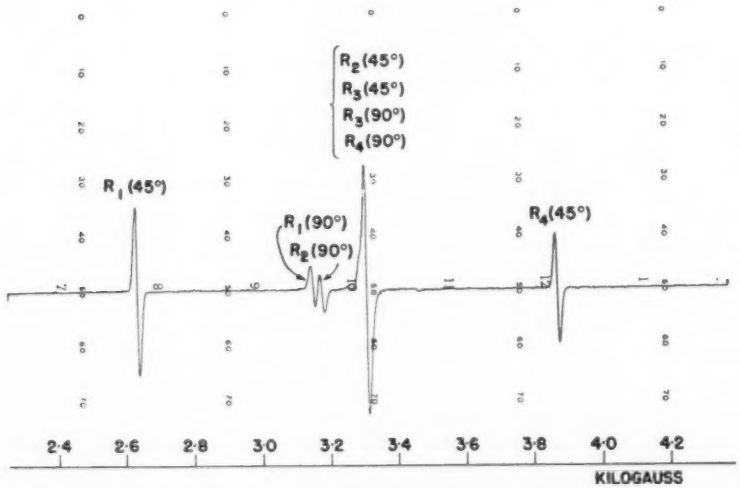

FIG. 3. "Allowed" paramagnetic resonance absorption of V centers in LiF observed at 9·319 kMc with the d.c. magnetic field $\boldsymbol{H}_0$ parallel to the [010] direction in the crystal. As usual, the derivative of absorption is plotted. The significance of the labels attached to the various lines is explained in Section 2.

magnet or tilts of the cryostat on the observed spectrum. By this procedure a particular crystal axis can be lined up with the magnetic field to within a few hundredths of a degree. After orientation of the crystal, the paramagnetic resonance absorption spectrum was recorded at liquid-nitrogen temperature, using a frequency of about 9·3 kMc.

Because our paramagnetic resonance equipment was arranged so that the magnet which produced the d.c. field could be rotated about the cryostat containing the microwave cavity, it was possible to make observations for different values of the angle Ξ between the microwave magnetic field $\boldsymbol{H}_1$ (with respect to which the crystal was fixed) and the d.c. magnetic field $\boldsymbol{H}_0$. In all the experiments described in this section, there was a component of $\boldsymbol{H}_1$ normal to $\boldsymbol{H}_0$, and only this component was effective in producing the observed absorption. In

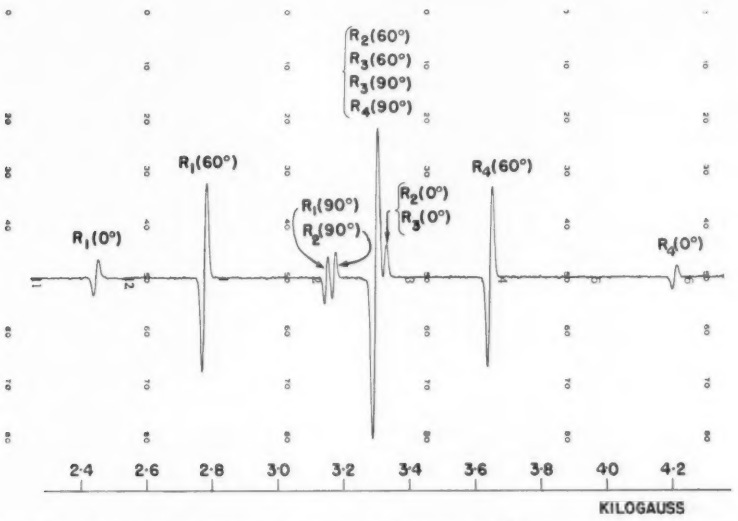

FIG. 4. "Allowed" paramagnetic resonance absorption of V centers in LiF observed at 9·319 kMc with the d.c. magnetic field $\boldsymbol{H}_0$ parallel to the [110] direction in the crystal.

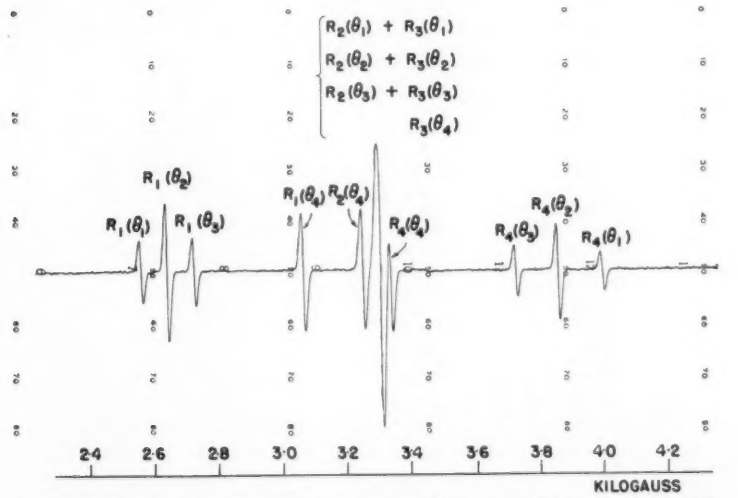

FIG. 5. "Allowed" paramagnetic resonance absorption of V centers in LiF observed at 9·319 kMc with the crystal and the fields $\boldsymbol{H}_1$ and $\boldsymbol{H}_0$ oriented as in Fig. 8 with $\theta_1 = 35°$ corresponding to $\Xi = 80°$ in Fig. 2(A).

Section 4 we shall mention observations made at higher gain with $\boldsymbol{H}_1$ parallel to $\boldsymbol{H}_0$.

Spectra were recorded for two different orientations of the crystal in the cavity. In one sequence of experiments the crystal was mounted so that the microwave magnetic field $\boldsymbol{H}_1$ was directed along the [100] axis of the crystal; the d.c. magnetic field $\boldsymbol{H}_0$ was directed normal to the [001] axis and was rotated about this axis in steps of a few degrees from the [010] axis to the [110] axis. The important geometrical relationships for this sequence are indicated in Fig. 2(A). Figs. 3 and 4 show the

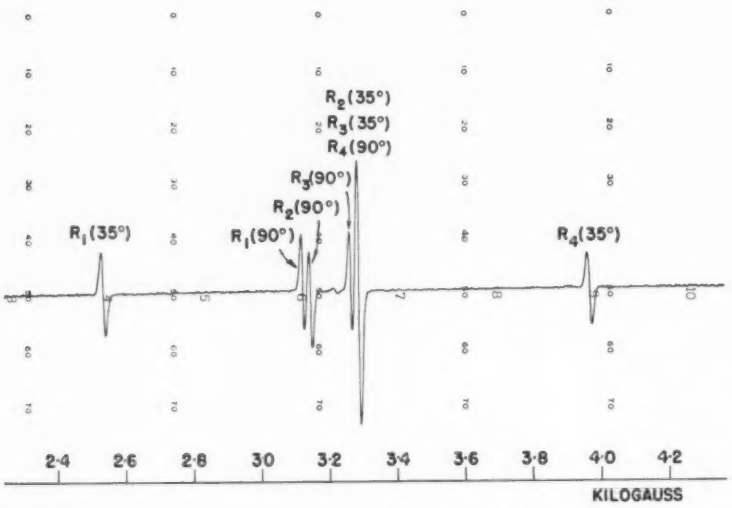

FIG. 6. "Allowed" paramagnetic resonance absorption of V centers in LiF observed at 9·246 kMc with the d.c. magnetic field H_0 parallel to the [111] direction in the crystal.

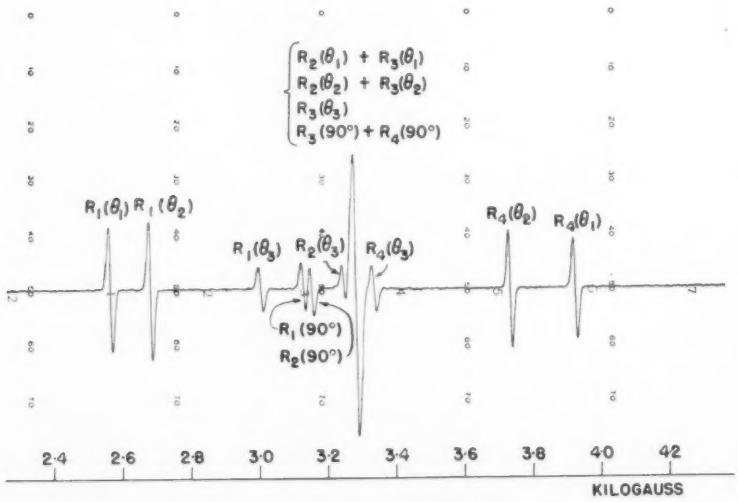

FIG. 7. "Allowed" paramagnetic resonance absorption of V centers in LiF observed at 9·246 kMc with the crystal and the fields H_1 and H_0 oriented as in Fig. 9, corresponding to $\Xi = 80°$ in Fig. 2(B).

(derivative) absorption spectra with H_0 along the [010] and [110] axes, respectively, and Fig. 5 shows the spectrum for H_0 in an intermediate orientation making an angle of 10° with the [010] axis ($\Xi = 80°$). In a second sequence of experiments, the crystal was mounted so that H_1 was along its [10$\bar{1}$] axis; H_0 was normal to the [101] axis and was rotated about this axis in steps of a few degrees from the [010] axis to the [11$\bar{1}$] axis. For this sequence the geometry is shown in Fig.

2(B). Fig. 6 shows the spectrum when $\boldsymbol{H}_0$ is along the $[11\bar{1}]$ axis and Fig. 7 when the angle between $\boldsymbol{H}_0$ and the [010] axis is 10° ($\Xi = 80°$).

In (I) it was shown that the V centers giving these spectra are F_2^- molecule-ions with their axes randomly and equally distributed over the six face-diagonal axes [110], [101], [011], $[1\bar{1}0]$, $[10\bar{1}]$, $[01\bar{1}]$. Therefore, for a general direction of the applied d.c. magnetic field $\boldsymbol{H}_0$, the molecule-ions fall into six classes or sets, characterized by the angle θ between the molecular axis and $\boldsymbol{H}_0$. The hyperfine interaction for a given set splits the electronic resonance into four lines, R_1, R_2, R_3, R_4, because each of the two ^{19}F nuclei has two spin states. The two center lines, R_2 and R_3, are not resolved in most cases.

of (I)). The form of the spectrum depends on the direction cosines (l', m', n') of the d.c. magnetic field $\boldsymbol{H}_0$ in the $x'y'z'$ system. (The unprimed letters xyz are reserved for use with a coördinate system having its z axis in the direction of the d.c. field $\boldsymbol{H}_0$.) To a very good approximation, however, the V center in LiF has cylindrical symmetry about z', as it was found that its spectrum depends almost entirely on n'. Thus, throughout this paper, we regard the V center in LiF as cylindrically symmetrical and assume that the location of lines in its spectrum is a function only of the angle θ between the axis of the center and the d.c. magnetic field $\boldsymbol{H}_0$.

It is clear that for any orientation of the d.c. magnetic field several different spectra (in the general case six) are simultaneously observed, each

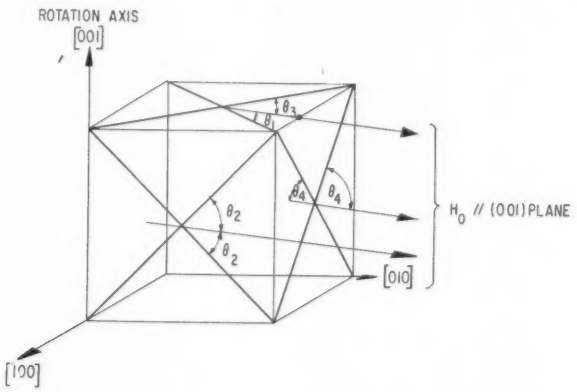

FIG. 8. Orientation of the d.c. magnetic field $\boldsymbol{H}_0$ with respect to the six face-diagonal directions of the LiF crystal for which the spectrum of Fig. 5 was obtained.

Different sets have different hyperfine splittings for the following reason. The structure of the V center and its crystalline environment make it have orthorhombic symmetry; hence the magnitude of the hyperfine splitting depends on the orientation of the d.c. field with respect to the axes of the V center. Thus for the accurate analysis of the spectrum of a single V center it is appropriate to set up an $x'y'z'$ coördinate system with the z' axis along the line joining the two nuclei in the center, which, for example, we take to be the $[\bar{1}\bar{1}0]$ direction in the crystal, with the y' axis in the [001] direction, and the x' axis in the $[1\bar{1}0]$ direction, the three axes forming a right-handed orthogonal set (see Fig. 5

spectrum associated with a different set. For specialized directions of the d.c. magnetic field, the number of sets is reduced. As a simple example, consider the situation with $\boldsymbol{H}_0$ lying along the [010] crystal axis, as is the case for the spectrum of Fig. 3. Using the ideas which we have just described, this spectrum can be decomposed into two sets of four lines each. With the help of a figure like Fig. 8, except that $\theta_1 = \theta_2 = \theta_3 = 45°$, $\theta_4 = 90°$, we can easily see that the V centers associated with four of the six face-diagonal directions will make an angle of 45° with $\boldsymbol{H}_0$, and the V centers associated with the remaining two face-diagonal directions will make an angle of 90° with

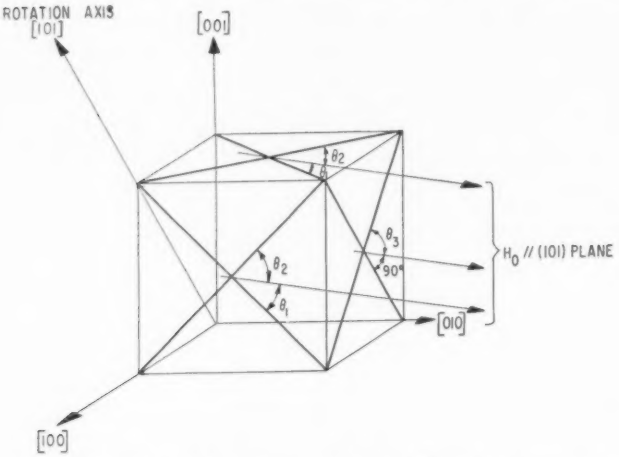

FIG. 9. Orientation of the d.c. magnetic field H_0 with respect to the six face-diagonal directions of the LiF crystal with which the spectrum of Fig. 7 was obtained.

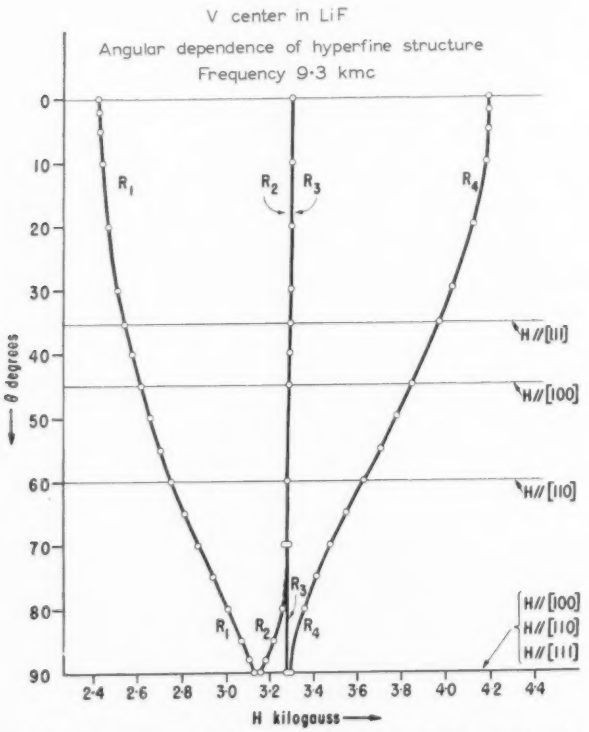

FIG. 10. The magnetic fields for which the four "allowed" lines in the spectrum of a single set of V centers are observed with a microwave frequency of about 9·3 kMc plotted as a function of the angle θ between the axis of the centers and the d.c. magnetic field H_0.

$\boldsymbol{H}_0$. Thus we expect one four-line pattern associated with $\theta = 45°$ of intensity 4 (in arbitrary units) and one four-line pattern associated with $\theta = 90°$ of intensity 2 (in the same arbitrary units). The lines in Fig. 3 have been labelled $R_1(\theta)$, $R_2(\theta)$, $R_3(\theta)$, $R_4(\theta)$ with $\theta = 45°$ or $90°$ in accordance with this analysis. The spectrum given in Fig. 5 corresponds to a more general orientation of $\boldsymbol{H}_0$ and hence is more complicated. It is to be interpreted with the aid of Fig. 8, which defines the angles θ_j. Similarly the angles used as labels in Fig. 7 are defined by Fig. 9. Consideration of these illustrative cases will convince the reader that all of the other spectra we obtained, including those of Figs. 4 and 6, can be decomposed into four-line patterns in such a way that the designations of all lines in all patterns are internally consistent. In Fig. 10 we have summarized the results obtained from the decomposition in this fashion of each of the spectra we observed (only a few of which are illustrated). In this figure we have a complete description of the observations on the dependence of the paramagnetic resonance absorption on the angle θ between the axis of the V center and the d.c. magnetic field $\boldsymbol{H}_0$. Because of the width of the individual lines (about 12 G on the average) and the overlapping of lines coming from different sets of V centers, there is some uncertainty ($\sim$ 2–3 G) as to the exact positions of the lines labelled R_2 and R_3. For certain angles these positions had to be established by the approximate graphical decomposition of two or three unresolved lines.

3. THE SPIN HAMILTONIAN

The spin Hamiltonian for an atomic system is an operator which transforms the eigenfunctions of the electronic and nuclear spin operators of the system.[3–5] Its eigenvalues E_j are the energies associated with a given orbital level of the atomic system in a magnetic field. For the case in which we are interested, these energy levels are the Zeeman levels of the ground state of a diatomic molecule-ion embedded in a crystal of LiF. This is a group of $2(2I_1+1)(2I_2+1)$ levels, where I_1 and I_2 are the spins of nuclei 1 and 2 in the molecule. All other energy levels of the system (orbitally excited levels) lie higher than the lowest group by an amount of energy large compared to the total energy spread of this lowest group of levels; they are neglected except insofar as their presence may modify coefficients in the spin Hamiltonian. Paramagnetic resonance absorption lines are observed when transitions between two of the Zeeman levels, i and j, separated by an energy $\Delta E_{ij} = E_i - E_j$, are stimulated by a magnetic field $\boldsymbol{H}_1$ alternating at a frequency ν such that

$$h\nu = \Delta E_{ij}. \tag{1}$$

For particular relative orientations of the d.c. field $\mathbf{H}_0$, the alternating field $\boldsymbol{H}_1$, and the molecular axis, transitions can be stimulated between only a fraction of all the pairs of levels E_j, regardless of the magnitudes of ν, $\boldsymbol{H}_0$, and $\boldsymbol{H}_1$. We defer discussion of the selection rules and transition probabilities to the next section. It is sufficient here to note that when transitions between levels i and j can be stimulated, we can find particular values of $\boldsymbol{H}_0$ and of ν, for which we observe an absorption line, and we can obtain $(\Delta E_{ij})_{\text{obs}} = (E_i - E_j)_{\text{obs}}$ from equation (1), using the experimentally determined ν. We can then compare this measurement of $(E_i - E_j)$ with the predictions of any spin Hamiltonian. We consider a particular spin Hamiltonian as satisfactory if for the experimentally measured value of $\boldsymbol{H}_0$ associated with the absorption, which we may call $(\boldsymbol{H}_0)_{ij}$, it has eigenvalues E_i and E_j which can be associated in a consistent way with the experimentally observed absorption line and for which the difference $(\Delta E_{ij})_{\text{calc}}$ satisfies the relation

$$\frac{|(\Delta E_{ij})_{\text{calc}} - (\Delta E_{ij})_{\text{obs}}|}{|\Delta E_{ij}|_{\text{obs}}} \ll 1. \tag{2}$$

We now investigate the adequacy of a spin Hamiltonian of the type proposed in (I) for the LiF V center, using this criterion.

In (I) it was seen that the diatomic molecule-ion model leads to a spin Hamiltonian of the form

$$\begin{aligned}\mathcal{H} = {} & \beta_0(g_{z'z'}H_{z'}S_{z'} + g_{x'x'}H_{x'}S_{x'} + g_{y'y'}H_{y'}S_{y'}) + \\ & + A_{z'z'}I_{z'}S_{z'} + A_{x'x'}I_{x'}S_{x'} + A_{y'y'}I_{y'}S_{y'} + \\ & + g_N\beta_N \boldsymbol{H}\cdot\boldsymbol{I},\end{aligned} \tag{3}$$

with

$$\boldsymbol{I} = \boldsymbol{I}_1 + \boldsymbol{I}_2,$$

where $\boldsymbol{I}_1$ and $\boldsymbol{I}_2$ are the nuclear spin operators of the two nuclei in the molecule. $H_{z'}$ is the z' component of $\boldsymbol{H}_0$ (the subscript zero is omitted in the rest of this section), and $H_{x'}$, $H_{y'}$ are defined similarly.

The quantities g_{jj} and A_{jj} ($j = x', y', z'$) are the principal components respectively of the spectroscopic-splitting tensor and the hyperfine-interaction tensor. β_0 and β_N stand for the Bohr magneton and the nuclear magneton, respectively, and g_0 and g_N are the (dimensionless) spectroscopic splitting factors for the free electron and the free ^{19}F nucleus respectively. We used the following numerical values of these constants:

$$\beta_0 = 0{\cdot}927120\times 10^{-20}\ \text{erg}\,G^{-1}$$
$$\beta_N = \beta_0/1836{\cdot}14$$
$$g_0 = 2{\cdot}00229$$
$$g_N = 2{\cdot}628$$

In the cylindrical approximation, equation (3) reduces to

$$\mathcal{H} = g_{\parallel}\beta_0 H_{z'}S_{z'}+g_{\perp}\beta_0(H_{x'}S_{x'}+H_{y'}S_{y'})+ +g_0\beta_0(a\boldsymbol{I}\cdot\boldsymbol{S}+bI_{z'}S_{z'})+g_N\beta_N\boldsymbol{H}\cdot\boldsymbol{I} \tag{4}$$

where

$$g_{\parallel} = g_{z'z'}$$
$$g_{\perp} = g_{x'x'} = g_{y'y'}$$
$$g_0\beta_0 a = A_{x'x'} = A_{y'y'}$$
$$g_0\beta_0(a+b) = A_{z'z'}.$$

As shown in (I), this spin Hamiltonian takes the form

$$\begin{aligned}\mathcal{H}/g_0\beta_0 = {}&(g/g_0)HS_z+[(a\sin\phi+b\sin^2\theta\sin\phi+\\ &+b\sin\theta\cos\theta\cos\phi)I_{z''}+(a\cos\phi+\\ &+b\sin^2\theta\cos\phi-b\sin\theta\cos\theta\sin\phi)I_{x''}]S_x+\\ &+aI_{y''}S_y+[(a\cos\phi+b\cos^2\theta\cos\phi+\\ &+b\sin\theta\cos\theta\sin\phi)I_{z''}+(-a\sin\phi-\\ &-b\cos^2\theta\sin\phi+b\sin\theta\cos\theta\cos\phi)I_{x''}]S_z+\\ &+(g_N\beta_N/g_0\beta_0)(HI_{z''}\cos\phi-HI_{x''}\sin\phi)\end{aligned} \tag{5}$$

when the electron spin operator $\boldsymbol{S}$ is referred to the xyz axis system (θ is the angle between the z and z' axes) and the nuclear spin operators $\boldsymbol{I}_1$, $\boldsymbol{I}_2$, and $\boldsymbol{I}$ are referred to the $x''y''z''$ axis system defined in (I) (ϕ is the angle between the z and z'' axes).

$$g = (g_{\parallel}{}^2\cos^2\theta+g_{\perp}{}^2\sin^2\theta)^{\frac{1}{2}}. \tag{6}$$

With the methods for finding the eigenvalues of $\mathcal{H}$ used in this paper, it is not necessary to introduce the $x''y''z''$ system and ϕ. However, we have introduced them and used expression (5) for the spin Hamiltonian in order to facilitate comparison of this paper with (I). In actual calculations we always took $\phi = 0$.

For the basis set of state vectors transformed by $\mathcal{H}$ we can choose the following complete set of eight:

$$|S, m_S\rangle|I_1, m_{I_1}\rangle|I_2, m_{I_2}\rangle \tag{7}$$

with

$$S = \tfrac{1}{2}$$
$$I_1 = I_2 = \tfrac{1}{2}$$
$$m_S = \pm\tfrac{1}{2}$$
$$m_{I_1} = \pm\tfrac{1}{2}$$
$$m_{I_2} = \pm\tfrac{1}{2}.$$

The values for the electron spin quantum number $\boldsymbol{S}$ and the nuclear spin quantum numbers $\boldsymbol{I}_1$, $\boldsymbol{I}_2$ follow from the fact that we are dealing with a molecular state of resultant electronic spin $\frac{1}{2}$ and two fluorine nuclei each with spin $\frac{1}{2}$.

By taking singlet and triplet combinations of the nuclear spin functions, we may relabel the states (7) in accordance with the scheme $|S, m_S\rangle|I, m_I\rangle$ as follows:

$$\left.\begin{aligned}|1'\rangle &= |\tfrac{1}{2},\tfrac{1}{2}\rangle|1,1\rangle\\ |2'\rangle &= |\tfrac{1}{2},\tfrac{1}{2}\rangle|1,0\rangle\\ |3'\rangle &= |\tfrac{1}{2},\tfrac{1}{2}\rangle|1,-1\rangle\\ |4'\rangle &= |\tfrac{1}{2},-\tfrac{1}{2}\rangle|1,-1\rangle\\ |5'\rangle &= |\tfrac{1}{2},-\tfrac{1}{2}\rangle|1,0\rangle\\ |6'\rangle &= |\tfrac{1}{2},-\tfrac{1}{2}\rangle|1,1\rangle\\ |7'\rangle &= |\tfrac{1}{2},\tfrac{1}{2}\rangle|0,0\rangle\\ |8'\rangle &= |\tfrac{1}{2},-\tfrac{1}{2}\rangle|0,0\rangle\end{aligned}\right\} \tag{8}$$

To obtain the eigenvalues and eigenfunctions of $\mathcal{H}$, it is necessary to diagonalize the 8×8 matrix $[\langle i'|\mathcal{H}|j'\rangle]$. It is easy to obtain this matrix in explicit form, as given in Table 1, by using the well-known expressions for angular momentum matrices.[6]

VOL. 5 1958

Table 1. V *center in* LiF*: spin energy matrix* $[\langle i'|\mathcal{H}/g_0\beta_0|j'\rangle]$

	$\|1'\rangle$	$\|3'\rangle$	$\|5'\rangle$	$\|4'\rangle$	$\|6'\rangle$	$\|2'\rangle$	$\|7'\rangle$	$\|8'\rangle$
$\langle 1'\|$	$\frac{1}{2}(F+C)+G_0$	0	$8^{-\frac{1}{2}}(A-B)$	0	$\frac{1}{2}D_1$	$2^{-\frac{1}{2}}(\frac{1}{2}D_0-G_1)$	0	0
$\langle 3'\|$	0	$\frac{1}{2}(F-C)-G_0$	$8^{-\frac{1}{2}}(A+B)$	$-\frac{1}{2}D_1$	0	$2^{-\frac{1}{2}}(\frac{1}{2}D_0-G_1)$	0	0
$\langle 5'\|$	$8^{-\frac{1}{2}}(A-B)$	$8^{-\frac{1}{2}}(A+B)$	$-\frac{1}{2}F$	$-2^{-\frac{1}{2}}(\frac{1}{2}D_0+G_1)$	$-2^{-\frac{1}{2}}(\frac{1}{2}D_0+G_1)$	0	0	0
$\langle 4'\|$	0	$-\frac{1}{2}D_1$	$-2^{-\frac{1}{2}}(\frac{1}{2}D_0+G_1)$	$-\frac{1}{2}(F-C)-G_0$	0	$8^{-\frac{1}{2}}(A-B)$	0	0
$\langle 6'\|$	$\frac{1}{2}D_1$	0	$-2^{-\frac{1}{2}}(\frac{1}{2}D_0+G_1)$	0	$-\frac{1}{2}(F+C)+G_0$	$8^{-\frac{1}{2}}(A+B)$	0	0
$\langle 2'\|$	$2^{-\frac{1}{2}}(\frac{1}{2}D_0-G_1)$	$2^{-\frac{1}{2}}(\frac{1}{2}D_0-G_1)$	0	$8^{-\frac{1}{2}}(A-B)$	$8^{-\frac{1}{2}}(A+B)$	$\frac{1}{2}F$	0	0
$\langle 7'\|$	0	0	0	0	0	0	$\frac{1}{2}F$	0
$\langle 8'\|$	0	0	0	0	0	0	0	$-\frac{1}{2}F$

$|1'\rangle = |\frac{1}{2}, \frac{1}{2}\rangle|1, 1\rangle$
$|2'\rangle = |\frac{1}{2}, \frac{1}{2}\rangle|1, 0\rangle$
$|3'\rangle = |\frac{1}{2}, \frac{1}{2}\rangle|1, -1\rangle$
$|4'\rangle = |\frac{1}{2}, -\frac{1}{2}\rangle|1, -1\rangle$
$|5'\rangle = |\frac{1}{2}, -\frac{1}{2}\rangle|1, 0\rangle$
$|6'\rangle = |\frac{1}{2}, -\frac{1}{2}\rangle|1, 1\rangle$
$|7'\rangle = |\frac{1}{2}, \frac{1}{2}\rangle|0, 0\rangle$
$|8'\rangle = |\frac{1}{2}, -\frac{1}{2}\rangle|0, 0\rangle$

$A = (a+b\sin^2\theta)\cos\phi - b\sin\theta\cos\theta\sin\phi$
$B = a$
$C = b\sin\theta\cos\theta\sin\phi + (a+b\cos^2\theta)\cos\phi$
$D_0 = b\sin\theta\cos\theta\cos\phi - (a+b\cos^2\theta)\sin\phi$
$D_1 = (a+b\sin^2\theta)\sin\phi + b\sin\theta\cos\theta\cos\phi$
$F = (g/g_0)H$
$G_0 = (g_N\beta_N/g_0\beta_0)H\cos\phi$
$G_1 = (g_N\beta_N/g_0\beta_0)H\sin\phi$

In evaluating this matrix we have omitted the term in $\boldsymbol{H} \cdot \boldsymbol{I}$ which is small compared to the other terms in $\mathscr{H}$ and does not affect $E_i - E_j$ for the allowed transitions. It is easy to find the modifications in the matrix of Table 1 which are introduced by including this term. As already noted, ϕ can be chosen arbitrarily; in all of the calculations described here, we put $\phi = 0$.

Table 1 shows that our choice of basis functions has led to factorization of the secular determinant of the matrix into a 6×6 block and a 2×2 block.

The energy levels obtained from the diagonalization of $[\langle i'|\mathscr{H}|j'\rangle]$ for four different values of H_0 and some value of θ not too close to 90° are shown schematically in Fig. 11. The values $\boldsymbol{H}_0$ are chosen so that in each case there are two levels (connected by an arrow in each of the four diagrams) almost symmetrical with respect to the zero of energy, and separated by the same energy. The application of a properly directed microwave field of constant frequency ν such that $h\nu$ is just equal to this energy separation will stimulate transitions between the

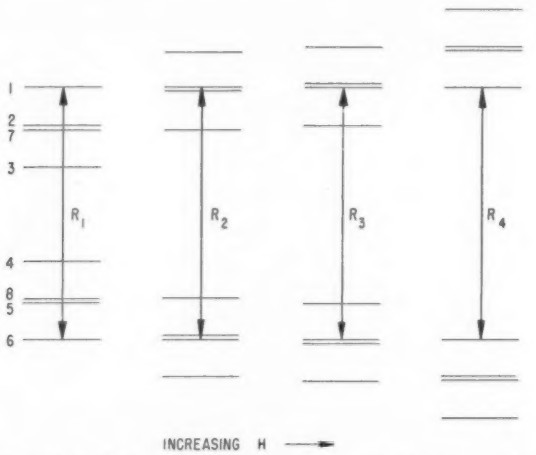

FIG. 11. LiF V center: schematic energy-level diagrams for the four different values of $\boldsymbol{H}$ at which "allowed" paramagnetic resonance absorption occurs. The length of the double-headed arrow is proportional to the energy of the microwave quantum.

The 6×6 block is also factored into smaller blocks for $\theta = 0$, $\phi = 0$ and $\theta = \pi/2$, $\phi = 0$. For a particular set of values of the constants $g_\parallel$, $g_\perp$, a, b and for a particular d.c. magnetic field ($\boldsymbol{H}$ and θ) two of the eigenvalues and associated eigenvectors of $\mathscr{H}$ are now obvious by inspection; the other six can be determined by numerical procedures. In our work the numerical diagonalization was carried out for as many cases as required by an automatic digital computer (I.B.M. 650)*

two levels, and under these circumstances absorption of the microwave energy will occur for each of the four values of $\boldsymbol{H}_0$. In Section 4 we show that these transitions are excited when the oscillating field $\boldsymbol{H}_1$ has a component normal to $\boldsymbol{H}_0$. We shall also see that the probability of exciting other transitions than the four indicated in Fig. 11 is very small when $\boldsymbol{H}_1 \perp \boldsymbol{H}_0$, even if $\boldsymbol{H}_0$ is adjusted so that the resonance condition

$$h\nu = \Delta E$$

is satisfied. Thus for the usual arrangement of fields in a paramagnetic resonance absorption experiment ($\boldsymbol{H}_1 \perp \boldsymbol{H}_0$), we expect to obtain absorption lines from any one set of F_2^- molecule-ions

* Prior to our work a program for this matrix diagonalization had been prepared by Dr. W. W. PIPER of this laboratory. We are indebted to him and to Mrs. MARY T. GRAY for enabling us to use this program and for other generous assistance in connection with the numerical diagonalizations.

VOL. 5 1958

at four different values of H_0 (a four-line spectrum), consistent with the data of Fig. 10.

To test whether or not the spin Hamiltonian (3) leads to the observed angular variation in the paramagnetic resonance spectrum (Fig. 10), we chose values for the four constants $g_\parallel$, $g_\perp$, a, and b to fit four of the experimental data and then from the numerical diagonalization of $[\langle i'|\mathcal{H}|j'\rangle]$ computed the positions of each of the four resonance lines in the spectrum of a single set of centers for 5 different values of the angle θ.

The four experimental data were:

(1) the position of line R_3 for $\theta = 0°$, used to determine $g_\parallel$;

(2) the position of line R_3 for $\theta = 90°$, used to determine $g_\perp$;

(3) the separation of lines R_1 and R_4 in the spectrum for $\theta = 0°$, used to determine $(a+b)$; and

(4) the position of line R_1 in the $\theta = 90°$ spectrum from which we obtain $|a|$.

We were unable to determine the sign of a from these observations. Here R stands for a line (resonance) and the subscripts 1, 2, 3, 4 refer to the order in which the four lines of the spectrum from a single class of centers are observed as the magnetic field is increased (see Figs. 10 and 11). The constants were determined in the order indicated above because the determination of the latter constants in this sequence requires a knowledge of some of the earlier ones. A further complication is that to determine b one must have an estimate of $|a|$. Fortunately a very crude estimate suffices, since the separation of lines R_1 and R_4 in the $\theta = 0°$ spectrum depends primarily on b and is very insensitive to $|a|$. Conversely, in the $\theta = 90°$ spectrum the line separations depend mainly on $|a|$ and are insensitive to b.

In adjusting the constant $|a|$ to fit the experimental data, we made use of a well-known perturbation theorem. Consider a Hermitian matrix $[H_{ij}]$ and a normalized eigenvector (x_j) such that

$$\sum_j H_{ij}x_j = Ex_i$$

(the eigenvalue E is necessarily real). We assume that there is no second eigenvector (y_j) linearly independent of (x_j) associated with E (no degeneracy). Then if we add to $[H_{ij}]$ the Hermitian matrix $\epsilon[h_{ij}]$, where $\epsilon \ll 1$, and find a normalized eigenvector (x_j') and eigenvalue E' such that

$$\sum_j (H_{ij}+\epsilon h_{ij})x_j' = E'x_i',$$

and such that $\lim_{\epsilon \to 0} E' = E$, then

$$E' = E+\epsilon \sum_{i,j} h_{ij}x_i^* x_j + 0(\epsilon^2).$$

Table 2. V center in LiF*: comparison of experimental and calculated line positions (in* G)

Frequency = 9·3 kMc

θ		0°	35¼°	45°	60°	90°
R_1	exp.	2422·0	2540·3	2608·5	2753·5	3129·3
	calc.	2417·1	2533·0	2602·1	2747·0	3129·3*
R_2	exp.	3304·0	3297·2	3287·1	3279·0	3155
	calc.	3303·0	3294·0	3285·5	3276·5	3153·4
R_3	exp.	3304·0	3297·2	3287·1	3279·0	3273·6
	calc.	3304·0*	3295·2	3286·9	3279·1	3273·6*
R_4	exp.	4194·8	3974·3	3847·3	3629·9	3297
	calc.	4189·9	3977·5	3852·4	3633·2	3297·4

* Fitted.

In other words, the first-order change in E when we add h_{ij} to H_{ij} is simply

$$\sum_{i,j} h_{ij} x_i^* x_j.$$

Thus, once we had an eigenvector (x_j) and eigenvalue E of the matrix of Table 1, we could easily find how E changed with any small change in the matrix elements, such as is produced by a small change in $|a|$, b, H, or θ.

Using

$$\left.\begin{aligned} g_{\parallel} &= 2{\cdot}0031 \\ g_{\perp} &= 2{\cdot}0230 \\ (a+b) &= 887 \\ |a| &= 59 \end{aligned}\right\} \quad (9)$$

the fields for which lines are predicted have been determined and are given in Table 2, which also contains the corresponding experimental results. The table demonstrates that the simple spin Hamiltonian (3) leads to an almost exact description of the angular dependence of the spectrum. For later use we also exhibit in Table 3 the energy eigenvalues for $\theta = 90°$, $\boldsymbol{H} = 3129{\cdot}27$ G.

Table 3. Spin energy levels for $\theta = 90°$, $\boldsymbol{H} = 3129{\cdot}27$ G.

(Energies are given in G)

i	W_i
1	1650·90
2	1642·00
3	1572·03
4	−1566·34
5	−1642·14
6	−1656·45
7	1580·79
8	−1580·79

The approximate method of obtaining the eigenvalues of (3) which was used in (I) corresponds to neglecting all matrix elements except those between the first state and all other states, i.e. to the diagonalization of a matrix with only one row and column of non-vanishing off-diagonal elements.[7] If the neglected elements are indeed small compared with those retained, the approximation can be justified, but in the case of the matrix of Table 1 with $\theta = 90°$, these elements are too large to be neglected.

4. LINE INTENSITY

In the preceding section we discussed the determination of the energies of the lowest-lying stationary states of a molecular system in a magnetic field. The specific molecular system which we were considering was a single V center (F_2^- molecule-ion) in a LiF crystal, though some of our discussion applies equally well to other systems. In this section we analyze experiments involving the stimulation of transitions between pairs of these low-lying levels. Again, much of the analysis is not really limited to the V center in LiF, though the specific calculations which follow are for that system. We first discuss the probability for the excitation of a transition between two levels of a single V center by a magnetic field $2\boldsymbol{H}_1 \cos \omega t$, where ω is a microwave frequency, for an arbitrary angle Ξ between $\boldsymbol{H}_1$ and $\boldsymbol{H}_0$. We then discuss the excitation of transitions by the field $2\boldsymbol{H}_1 \cos \omega t$ for $\Xi = 90°$ and $0°$. Finally, we recall how these probabilities enter into the determination of the intensities of the absorption lines in paramagnetic resonance absorption experiments in which transitions up and down between corresponding levels of a large number of identical paramagnetic centers are simultaneously stimulated.

From equation (3) we see that placing our system in the field $2\boldsymbol{H}_1 \cos \omega t$ can be described by the addition to the spin Hamiltonian of a time-varying part

$$\mathscr{H}' = 2\beta_0 \cos \omega t [g_{\parallel} H_{1z} + g_{\perp}(H_{1x} + H_{1y})]$$

The effect of $\mathscr{H}'$ on the system can be analyzed by the standard methods of time-dependent perturbation theory.[8] For our system this analysis is very similar to that described by PAKE.[9] It leads to a probability $w_{ik}dt$ that the field $2\boldsymbol{H}_1 \cos \omega t$ will excite a transition from state i to state k in time dt, with

$$w_{ik} = (\beta_0/h)^2 |\langle i|g_{\parallel} H_{1z} S_z + g_{\perp}(H_{1x} S_x + H_{1y} S_y)|k\rangle|^2 f_{ik}(\nu). \quad (10)$$

In this expression $f_{ik}(\nu)$ with $\nu = \omega/2\pi$ is a function which is introduced to take account of the fact that an absorption line always has a finite

width and hence a shape; $f_{ik}(\nu)$ describes this shape. It is peaked around a frequency

$$\nu_{ik} = h^{-1}(E_i - E_k) \tag{11}$$

(we assume $E_i > E_k$), and for values of ν greater and less than this frequency it falls off and approaches zero.

$$\int_0^\infty f_{ik}(\nu)\, d\nu = 1.$$

In cases such as ours where the lines are not homogeneous, $f_{ik}(\nu)$ describes the shape of a homogeneous component of the absorption line.[10] For the component of an absorption line associated with transitions from level i to level k of the individual V centers, $f_{ik}(\nu)d\nu$ can be regarded as the probability that the ν_{ik} of a particular center lies between ν and $\nu+d\nu$.

It is easy to determine from (10) the probability for the excitation of transitions between any two of the eight spin states of the LiF V center by a field $2\boldsymbol{H}_1 \cos \omega t$. In the usual paramagnetic resonance absorption experiments, including those described in Section 2, the effective oscillating magnetic field is normal to the d.c. field. In this case, we can set up our xyz coördinate system so that the x axis is in the direction of $\boldsymbol{H}_1$. Then

$$w_{ik} = (g_\perp \beta_0 H_{1x}/h)^2 |\langle i|S_x|k\rangle|^2 f_{ik}(\nu) \tag{12}$$

If $x_{ij'}$ represents the diagonalizing transformation for the matrix of Table 1, then (12) may be written

$$\begin{aligned} w_{ik} &= (g_\perp \beta_0 H_{1x}/h)^2 \Big| \sum_{j',l'} x_{ij'} x_{kl'} \langle j'|S_x|l'\rangle \Big|^2 f_{ik}(\nu) \\ &= (g_\perp \beta_0 H_{1x}/h)^2 f_{ik}(\nu) |x_{i1'}x_{k6'} + x_{i2'}x_{k5'} + \\ &\quad + x_{i3'}x_{k4'} + x_{i4'}x_{k3'} + x_{i5'}x_{k2'} + x_{i6'}x_{k1'} + \\ &\quad + x_{i7'}x_{k8'} + x_{i8'}x_{k7'}|^2. \end{aligned} \tag{13}$$

In what follows we shall be concerned only with the relative probabilities of transitions between different pairs (i, k) of levels for equal values of $g_\perp$, H_{1x} and $f_{ik}(\nu)$, or at least for values of these quantities which differ by an amount too small to affect our approximate measurements of intensity. For this reason it is convenient to define and use a relative transition probability $\tilde{w}_{ik}$,

$$\begin{aligned} \tilde{w}_{ik} &= |x_{i1'}x_{k6'} + x_{i2'}x_{k5'} + x_{i3'}x_{k4'} + x_{i4'}x_{k3'} + \\ &\quad + x_{i5'}x_{k2'} + x_{i6'}x_{k1'} + x_{i7'}x_{k8'} + x_{i8'}x_{k7'}|^2. \end{aligned} \tag{14}$$

In general $x_{ij'} \neq 0$ for any i or j', and there is a finite probability for observing transitions between any two spin-energy levels. Thus for a system of eight spin states the maximum possible number of absorption lines in the general case is $(8\times7)/2$. For our special case, the V center in LiF, with the effective component of $\boldsymbol{H}_1$ normal to $\boldsymbol{H}_0$, only four lines are observed, as illustrated in Fig. 11, because many of the $x_{ij'}$ vanish or are small, and because partial cancellation of terms in the sum of (14) occurs in certain cases, as will appear presently. For example, from the form of the spin energy matrix (Table 1) we see that the basis states $|7'\rangle$ and $|8'\rangle$ cannot enter into any eigenstate $|i\rangle$ which includes a state $|j'\rangle$ for which $1 \leqq j \leqq 6$. That is, $x_{ij'} = 0$ if $i = 7$ or 8 and $1 \leqq j \leqq 6$. Also it is obvious that $|7\rangle = |7'\rangle$ and $|8\rangle = |8'\rangle$, so that the only transitions in which levels 7 and 8 appear is the transition between 7 and 8 giving rise to line R_3. Here we have to do with an absolute selection rule based on symmetry. Triplet and singlet nuclear spin states behave differently under interchange of the two nuclear spins, and this leads to an absolute prohibition of transitions between such states. It is obvious, too, that many of the $x_{ij'}$ vanish for special values of θ, such as $\theta = 0°$ and $\theta = 90°$. For illustrative purposes the $x_{ij'}$ for

Table 4. $x_{ij'} = \langle j'|i\rangle$ for $\theta = 45°$, $\boldsymbol{H} = 2608{\cdot}46$ G

i \ j'	1′	2′	3′	4′	5′	6′
1	0·865794	0·473887	0·129821	0·013081	0·046268	0·081655
2	−0·479590	0·747118	0·459945	0·005612	0·005116	0·014161
3	−0·119753	0·456779	−0·868252	0·122210	−0·086069	0·028424
4	0·020201	−0·072621	0·129835	0·879089	−0·439111	0·108834
5	0·005482	−0·010561	0·022264	−0·443367	−0·762348	0·470760
6	−0·074937	−0·056689	−0·019568	0·124462	0·465223	0·871128

Table 5. $x_{ij'} = \langle j'|i\rangle$ for $\theta = 90°$, $\boldsymbol{H} = 3129{\cdot}27$ G

i \ j'	1′	2′	3′	4′	5′	6′
1	0·899384	0	0·418965	0	0·124806	0
2	0	0·990647	0	0·090797	0	0·101858
3	−0·427974	0	0·902058	0	0·055946	0
4	0	−0·047834	0	0·930186	0	−0·363958
5	−0·089142	0	−0·103731	0	0·990603	0
6	0	−0·127794	0	0·355681	0	0·925829

particular values of θ and $\boldsymbol{H}$ are given in Tables 4 and 5.

With the aid of these tables and equation (14) we can compute, for example, that for

$$\theta = 45° \text{ with } \boldsymbol{H} = 2608{\cdot}46 \text{ G},$$

$$\tilde{w}_{16} = 0{\cdot}964010$$

and that for $\theta = 90°$ with $\boldsymbol{H} = 3129{\cdot}27$ G.

$$\tilde{w}_{16} = 0{\cdot}932663.$$

We note that the two probabilities are nearly equal. In the same way, using different tables of the elements $x_{ij'}$, we can compute the relative probabilities $\tilde{w}_{ik}$ of the four transitions associated with R_1, R_2, R_3, and R_4 for $\theta = 0°$, 45°, 60°, and 90°. These probabilities are all approximately 0·96; their exact values are not of interest. It should be noted that the matrix $x_{ij'}$ is a function of $\boldsymbol{H}$ as well as θ; since the paramagnetic resonance absorption lines in the spectrum of a single V center are observed for different values of $\boldsymbol{H}$, in accurate work a different set of $x_{ij'}$ values must be used for the computation from equation (14) of the relative intensity of each line in the spectrum. However, since $x_{ij'}$ is a slowly varying function of $\boldsymbol{H}$, a single matrix $x_{ij'}$ may be used to obtain a rough estimate of the intensities of all the lines in the spectrum. Thus we can also use Table 4 to estimate $\tilde{w}_{15}$ for $\theta = 45°$:

$$\begin{aligned}\tilde{w}_{15} = (&+0{\cdot}407581 - 0{\cdot}361267 - 0{\cdot}057558 + \\ &+0{\cdot}000291 - 0{\cdot}000489 + 0{\cdot}000448) \\ &= 0{\cdot}000121.\end{aligned}$$

Here the small probability does not result from the vanishing of any of the $x_{ij'}$ but from the arrangement of signs in the matrix $x_{ij'}$ which leads to an almost complete cancellation of the terms in equation (14). Similar cancellations insure small values for the probabilities of all the transitions between levels 1, 2, 3, and 4, 5, 6, except w_{16}, w_{25}, and w_{34}, associated respectively with R_1, R_2, and R_4.

Now let us investigate the implications of equation (10) as to the probabilities for the excitation of transitions by $2\boldsymbol{H}_1 \cos \omega t$ when $\boldsymbol{H}_1$ is parallel to $\boldsymbol{H}_0(\Xi = 0°)$. Then $H_{1x} = H_{1y} = 0$ in (10), which becomes

$$w_{ik} = (g_{\parallel}\beta_0 H_{1z}/h)^2 \, |\langle i|S_z|k\rangle|^2 f_{ik}(\nu). \qquad (15)$$

Introducing the transformation matrix and the relative transition probability $\tilde{w}_{ik}$ as before, we have

$$\begin{aligned}\tilde{w}_{ik} = |&x_{i1'}x_{k1'} + x_{i2'}x_{k2'} + x_{i3'}x_{k3'} - x_{i4'}x_{k4'} - \\ &- x_{i5'}x_{k5'} - x_{i6'}x_{k6'} + x_{i7'}x_{k7'} - x_{i8'}x_{k8'}|^2. \qquad (16)\end{aligned}$$

For $\theta = 90°$ we find that all the transition probabilities vanish except

$$\tilde{w}_{26}\,(\boldsymbol{H} = 3129{\cdot}27 \text{ G}) = 0{\cdot}064109$$

$$\tilde{w}_{15}\,(\boldsymbol{H} = 3129{\cdot}27 \text{ G}) = 0{\cdot}061140$$

$$\tilde{w}_{35}\,(\boldsymbol{H} = 3297{\cdot}00 \text{ G}) = 0{\cdot}011862$$

$$\tilde{w}_{24}\,(\boldsymbol{H} = 3297{\cdot}00 \text{ G}) = 0{\cdot}008626.$$

Thus we expect to find "forbidden" lines associated with these four transitions: $2 \leftrightarrow 6$, $1 \leftrightarrow 5$, $3 \leftrightarrow 5$, $2 \leftrightarrow 4$; hereafter we refer to them as ρ_1, ρ_2, ρ_3, ρ_4, respectively. From Table 3 we can estimate the magnetic fields at which these transitions could be excited with $\nu = 9{\cdot}262$ kMc.

$$\boldsymbol{H}(\rho_1) = 3138 \text{ G}$$

$$\boldsymbol{H}(\rho_2) = 3143 \text{ G}$$

$$\boldsymbol{H}(\rho_3) = 3222 \text{ G}$$

$$\boldsymbol{H}(\rho_4) = 3228 \text{ G}.$$

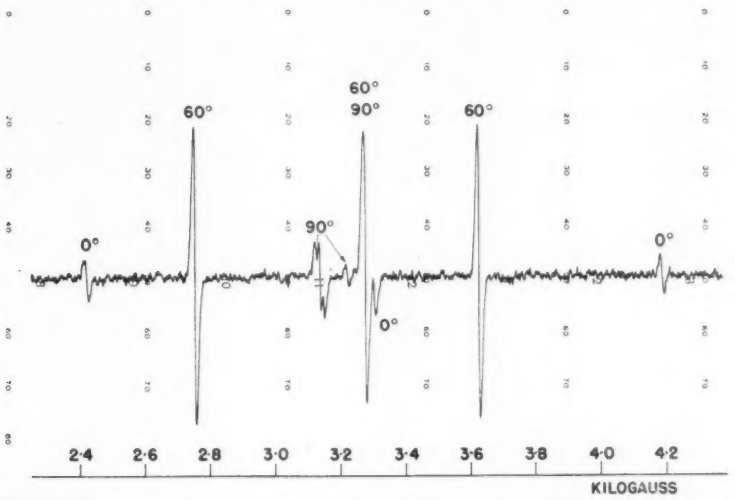

FIG. 12. Paramagnetic resonance absorption of V centers in LiF observed at 9·246 kMc with the d.c. magnetic field $\boldsymbol{H}_0$ parallel to a [110] direction in the crystal and the (spatial) average oscillating field $\overline{\boldsymbol{H}}_1$ parallel to $\boldsymbol{H}_0$.

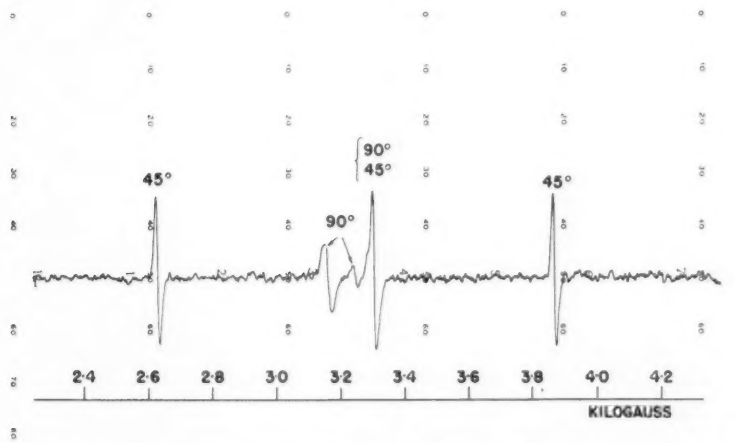

FIG. 13. Paramagnetic resonance absorption of V centers in LiF observed at 9·319 kMc with the d.c. magnetic field $\boldsymbol{H}_0$ parallel to a [100] direction in the crystal and the (spatial) average oscillating field $\overline{\boldsymbol{H}}_1$ parallel to $\boldsymbol{H}_0$.

We can make the specification of the positions of these lines relatively independent of the frequency ν by giving their displacements form $R_1(90°)$:

$$\Delta(\rho_1) = \boldsymbol{H}[\rho_1] - \boldsymbol{H}[R_1(90°)] = 9 \text{ G}$$
$$\Delta(\rho_2) = \boldsymbol{H}[\rho_2] - \boldsymbol{H}[R_1(90°)] = 14 \text{ G}$$
$$\Delta(\rho_3) = \boldsymbol{H}[\rho_3] - \boldsymbol{H}[R_1(90°)] = 93 \text{ G}$$
$$\Delta(\rho_4) = \boldsymbol{H}[\rho_4] - \boldsymbol{H}[R_1(90°)] = 99 \text{ G}.$$

For $\theta = 60°$ we find finite probabilities for all possible transitions from levels 1, 2, 3, to levels 4, 5, 6, but only $\tilde{w}_{16}$ and $\tilde{w}_{34}$ are large enough to be detected with our present apparatus.

$$\tilde{w}_{16}(\boldsymbol{H} = 2608{\cdot}46 \text{ G}) = 0{\cdot}035558$$

$$\tilde{w}_{34}(\boldsymbol{H} = 3847{\cdot}30 \text{ G}) = 0{\cdot}035444.$$

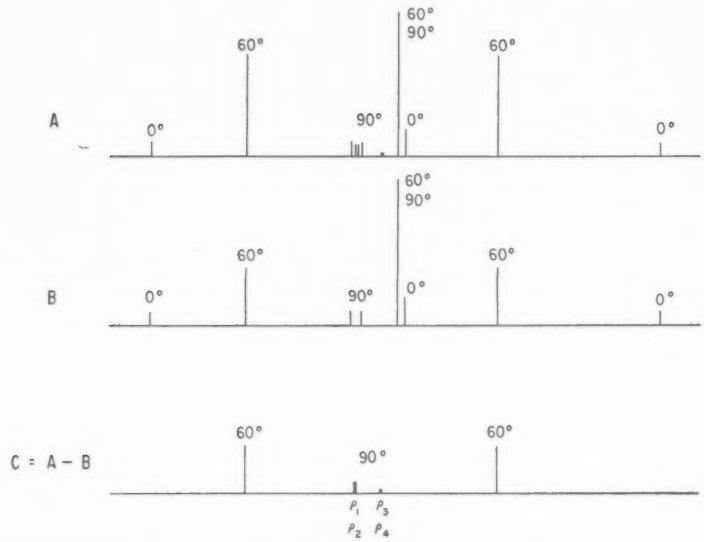

FIG. 14. Line drawings showing schematically how the spectrum of Fig. 12 (represented here by A) can be approximately decomposed into the "allowed" part (B) and the "forbidden" part (C). The lengths of the vertical lines are roughly proportional to the integrated intensities of the lines they represent.

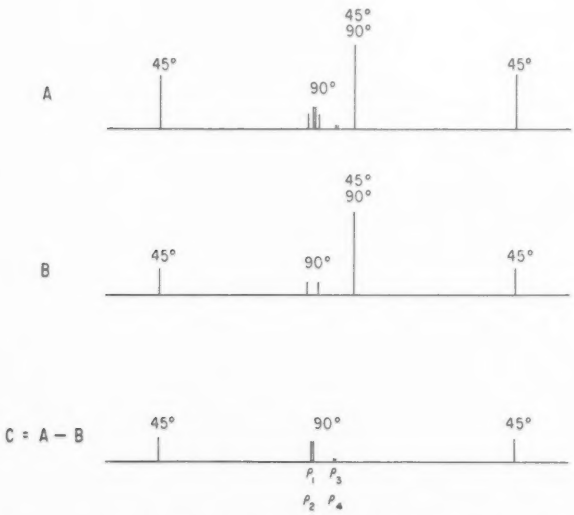

FIG. 15. Line drawings showing schematically how the spectrum of Fig. 13 (represented here by A) can be approximately decomposed into the "allowed" part (B) and the "forbidden" part (C). The lengths of the vertical lines are roughly proportional to the integrated intensities of the lines they represent.

For $\theta = 45°$, the situation is as for $\theta = 60°$; the only significant probabilities are

$$\tilde{w}_{16}\,(H = 2753{\cdot}47\text{ G}) = 0{\cdot}053111$$
$$\tilde{w}_{34}\,(H = 3629{\cdot}93\text{ G}) = 0{\cdot}052095.$$

For $\theta = 0°$ the probabilities of all possible transitions from any one of levels 1, 2, 3, 7 to any one of levels 4, 5, 6, 8 vanish.

We shall see presently that in some circumstances the intensity of a line is proportional to $\tilde{w}_{ik}$. Then, the above values of $\tilde{w}_{ik}$ for various angles imply that with $\Xi = 0°$ and $\boldsymbol{H}_0$ along a [110] axis in the crystal the "forbidden" paramagnetic resonance absorption spectrum should have the structure indicated in Fig. 14(C). With $\boldsymbol{H}_0$ along a [100] crystal axis, the "forbidden" paramagnetic resonance absorption spectrum should look as indicated in Fig. 15(C). According to our analysis, new lines (lines not included in the "allowed spectrum") can be excited by $\boldsymbol{H}_1 \,||\, \boldsymbol{H}_0$ for $\theta = 90°$. We have called these new lines ρ_1, ρ_2, ρ_3, ρ_4 in Figs. 14(C) and 15(C).

In order to check these predictions, we set up the apparatus so that $\boldsymbol{H}_0$ was parallel to $\boldsymbol{H}_1$ ($\Xi = 0°$) and obtained the spectra of Figs. 12 and 13 for two different orientations of the crystal in the microwave cavity. The spectrum of Fig. 12 was obtained with $\boldsymbol{H}_1$ and $\boldsymbol{H}_0$ parallel to a [110] axis; that of Fig. 13 with $\boldsymbol{H}_1$ and $\boldsymbol{H}_0$ parallel to a [100] axis. At this point we must qualify the statement that $\boldsymbol{H}_0$ was parallel to $\boldsymbol{H}_1$. While the $\boldsymbol{H}_0$ field in our apparatus is practically homogeneous throughout the crystal, the oscillating field $\boldsymbol{H}_1$ is only in first approximation unidirectional over that part of the resonant cavity occupied by the crystal. The crystal has a thickness of about 3 mm and the same cross-section as the cavity, which is excited in the TE_{101} mode. There are always regions in the crystal with a small component of $\boldsymbol{H}_1$ normal to $\overline{\boldsymbol{H}}_1$ (this symbol we use to denote the average of $\boldsymbol{H}_1$ over the whole volume of the crystal). For the considerations of Section 3 it was entirely proper to neglect the existence of this small $\boldsymbol{H}_1$ field normal to $\overline{\boldsymbol{H}}_1$, because it produced no new observable effects; the transitions which it is capable of stimulating are either the same as are normally excited or else they are much less strongly excited than those excited by the large component of $\boldsymbol{H}_1$. But in looking at the "forbidden" spectrum the situation is very different. Since the probability of excitation of the lines of this spectrum for a given magnitude of $\boldsymbol{H}_1$ parallel to $\boldsymbol{H}_0$ is of the order of one-tenth that for the excitation of the allowed lines for the same magnitude of $\boldsymbol{H}_1$ normal to $\boldsymbol{H}_0$, if in even a small part of the crystal $\boldsymbol{H}_1$ is normal to $\overline{\boldsymbol{H}}_1$ the allowed line will be excited with an intensity comparable to that of the forbidden line. Neglecting interference effects which will be discussed below, it is possible to determine fairly accurately for the paramagnetic resonance spectra of Figs. 12 and 13 how much of each spectrum is really "forbidden" and how much is excited by the residual $\boldsymbol{H}_1$ field normal to $\boldsymbol{H}_0$. For the case of Fig. 12 (represented schematically by Fig. 14(A)) the two extreme lines belong to the 0° pattern. Since we know that these transitions cannot be excited at all by the component of $\boldsymbol{H}_1$ parallel to $\boldsymbol{H}_0$, they must be the allowed transitions excited by the residual component of $\boldsymbol{H}_1$ perpendicular to $\boldsymbol{H}_0$. This enables us to estimate how much of the total spectrum is excited in an allowed fashion by this residual component of $\boldsymbol{H}_1$. This allowed part is represented schematically in Fig. 14(B) and has to be subtracted from the total spectrum (Fig. 14(A)) in order to arrive at the pure forbidden spectrum (Fig. 14(C)).

The spectrum of Fig. 13 can be analyzed in the same way (Fig. 15), using the fact that the large central line must be wholly due to "allowed" stimulation of transitions, since the probability for the stimulation of "forbidden" transitions in this region is so small that it can be neglected.

The most obvious new feature of the spectra of Figs. 12 and 13 is the small line structure at about 3250 G belonging to the 90° set. While it is not possible to decompose this structure unambiguously into two separate lines, the data are consistent with such a decomposition into two lines 4–8 G apart with the center of the doublet at a field 99 G higher than that of $R_1(90°)$. We associate these lines with the ρ_3 and ρ_4 which according to our approximate calculations should appear 93 and 99 G higher than $R_1(90°)$. It is also clear that in Figs. 12 and 13 new lines are present in the region between R_1 and R_2 of the 90° "allowed" spectrum. When the "allowed" spectrum is subtracted out, in the manner we have described, the residual structure can be consistently interpreted as composed of two lines, 4–10 G apart with the center of the doublet at a field about 12 G higher than that of R_1. These

two lines we identify with ρ_1 (expected 9 G above R_1) and ρ_2 (expected 14 G above R_1).

As a further test of the correctness of our interpretation of the spectra of Figs. 12 and 13 and the accuracy of the spin wave functions for $\theta = 90°$ obtained by diagonalizing the matrix of Table 1, we compared the theoretical and experimental values of the ratio

$$\lambda = \frac{Z[R_1(90°)]+Z[R_2(90°)]}{Z[\rho_1]+Z[\rho_2]}, \tag{17}$$

where $Z[R]$ means the intensity of line R. The theoretical value, computed by using Table 5 and equations (14) and (16) is $\lambda = 14{\cdot}8482$. The experimental value is $\lambda = 15 \pm 3$. The graphical integration of the absorption lines and the corrections for saturation are the main error sources.

The decomposition of the 45° and 60° lines observed with $\overline{\boldsymbol{H}_1} \| \boldsymbol{H}_0$ which we discussed above in connection with Figs. 12–15 is only qualitative because it ignores the very important interference between "allowed" and "forbidden" excitation of a single line. From equation (10) we see that the probability of excitation of a line when $\boldsymbol{H}_1$ has both x and z compohents is proportional to

$$\begin{aligned} |\langle i|g_{\parallel}H_{1z}S_z+g_{\perp}H_{1x}S_x|k\rangle|^2 &= \langle i|g_{\parallel}H_{1z}S_z|k\rangle^2+ \\ &+\langle i|g_{\perp}H_{1x}S_x|k\rangle^2+2\langle i|g_{\parallel}H_{1z}S_z|k\rangle\times \\ &\times\langle i|g_{\perp}H_{1x}S_x|k\rangle \end{aligned} \tag{18}$$

where we have used the fact that with our choice of coördinates the matrix elements are always real. The last term of (18) we refer to as the interference term; thus far we have neglected it in discussing the excitation of the forbidden lines. This neglect was quite unjustified, in that the interference term is probably comparable in magnitude to the "allowed" term (the second in equation (18)), for the $\theta = 45°$ and $\theta = 60°$ lines appearing in Figs. 12 and 13. In our experiment the direction of $\boldsymbol{H}_1$ at any instant varies throughout the LiF crystal in a complicated and quantitatively unknown way, so that we are simply unable to resolve the intensities of the low and high field lines for $\theta = 45°$ and $\theta = 60°$ into "forbidden," "allowed," and interference parts. Each line includes contributions from many centers and for some of these centers the ratio $H_{1z} : H_{1x}$ is different than for others. Because of these interference contributions varying from center to center, it is not possible with our data to analyze and understand with any precision the relations between the intensities of the 45° and 60° lines of Figs. 12 and 13 and those obtained with $\boldsymbol{H}_1 \perp \boldsymbol{H}_0$. Thus a detailed test of our theoretical predictions of the line intensities to be expected from the excitation of V centers with $\theta = 45°$ and $\theta = 60°$ and with $\boldsymbol{H}_1$ parallel to $\boldsymbol{H}_0$ at every center, requires data from a different experimental arrangement, one such that the variation in the direction of $\boldsymbol{H}_1$ over the volume of the crystal is either very small or else accurately known.

This difficulty does not arise in connection with the 90° pattern. The four main lines of the 90° "forbidden" spectrum are all different from the four main lines of the 90° "allowed" spectrum, so that they are excited without interference effects and their intensities can be compared simply. We have already made this comparison using the ratio defined in equation (17), and it confirms that our spin Hamiltonian analysis of the V center in LiF is essentially correct.

In order to relate the observed line intensities to the probabilities given by (10), it is necessary to show that the r.f. intensity is sufficiently small so that no saturation effects are present.[11] This was done by varying $\boldsymbol{H}_1$ and showing that the power absorbed in stimulating transitions between levels i and j, P_{ij}^{abs}, was proportional to $\boldsymbol{H}_1^2$.

There is another class of effects which in our work may have impaired the exact proportionality of P_{ij}^{abs} to w_{ij}: the "fast-passage" effects. These effects, discussed by BLOCH[12] and by HONIG and COMBRISSON[13] are modifications of the shapes of resonance lines which result when the period of modulation of the d.c. field $\boldsymbol{H}_0$ is comparable to or shorter than the relaxation times of the resonating spin system. For the observations discussed in this paper the modulation period was $\frac{1}{8}$ sec. We believe that some of the important relaxation times for the V center in LiF at liquid-nitrogen temperature are comparable with or perhaps much longer than this period. There are slight differences between the intensities of lines 1 and 4 for some values of θ which we attribute to effects of this kind. We are at present studying these fine-scale intensity variations in connection with an investigation of the paramagnetic relaxation of the LiF V center.

VOL. 5 1958

5. DISCUSSION OF RESULTS

We have presented evidence that the spin Hamiltonian (3) proposed by CASTNER and KÄNZIG[2] to account for the paramagnetic resonance absorption at liquid-nitrogen temperature of LiF irradiated with X-rays at the same temperature does indeed account completely and with considerable accuracy for the spectrum which is observed for any orientation of the constant magnetic field with respect to the axes of the LiF crystal when the constants $g_\parallel$, $g_\perp$, $|a|$, b, which enter into (3) have the values (9). The spin Hamiltonian (3) is consistent with and in fact was suggested by the assumption that this absorption arises from the paramagnetic resonance of localized crystal imperfections each of which is most simply described as an F_2^- molecule-ion with its axis along one of the [110] directions in the crystal. The agreement between the predictions based on this molecule-ion model and the very complex behavior of the spectrum as a function of magnetic field direction in the crystal is sufficiently complete to give strong confirmation of the essential correctness of the molecule-ion model. However, as can be seen from Table 2, the line positions predicted by the spin Hamiltonian (3) do not agree exactly with the observed line positions. This is partly due to the approximation of axial symmetry. The agreement can be improved if the actual orthorhombic symmetry of the molecule-ion is taken into account. It appears, however, that perfect agreement could only be achieved by making also other slight modifications in the form of the spin Hamiltonian.

One of the interesting theoretical problems suggested by the work described in this paper is the computation from the fundamental principles of quantum mechanics of the constants $g_\parallel$, $g_\perp$, a, and b appearing in (3). First attempts at a solution of this problem have been made.[2,14,15] It is easy to see that these treatments are in many respects incomplete and inaccurate, but with the presently available calculational methods of the quantum theory of molecules and crystals, it is difficult to improve them.

In summary, the information obtained by paramagnetic resonance methods has made possible the deduction of the most important features of the electronic structure of one kind of V center, but it is not sufficient to elucidate all of the finer details of this structure. In addition to the data given here and in (I), extensive quantum-mechanical analysis and possibly further experiments are required to reach that goal.

REFERENCES

1. SEITZ F. *Rev. Mod. Phys.* **26,** 7 (1954).
2. CASTNER T. G. and KÄNZIG W. *J. Phys. Chem. Solids* **3,** 178 (1957).
3. PRYCE M. H. L. *Proc. Phys. Soc.* **A63,** 25 (1950).
4. BLEANEY B. and STEVENS K. W. H. *Rep. Progr. Phys.* **16,** 108 (1953).
5. BOWERS K. D. and OWEN J. *Rep. Progr. Phys.* **18,** 304 (1955).
6. CONDON E. U. and SHORTLEY G. H. *The Theory of Atomic Spectra* Cambridge University Press, Cambridge (1951).
7. LENNARD-JONES J. E. *Proc. Roy. Soc.* **A129,** 598 (1930) See §4.
8. SCHIFF L. I. *Quantum Mechanics* §29 McGraw-Hill Book Co., New York (1949).
9. PAKE G. E. *Solid State Phys.* **2,** 1 (1956). See §4.
10. PORTIS A. M. *Phys. Rev.* **91,** 1071 (1953).
11. BLOEMBERGEN N., PURCELL E. M. and POUND R. V. *Phys. Rev.* **73,** 679 (1948).
12. BLOCH F. *Phys. Rev.* **70,** 460 (1946).
13. HONIG A. and COMBRISSON J. *Phys. Rev.* **102,** 917 (1956).
14. INUI T., HARASAWA S., and OBATA Y. *J. Phys. Soc., Japan* **11,** 612 (1956).
15. COHEN M. H. *Phys. Rev.* **101,** 1432 (1956).

J. Phys. Chem. Solids Pergamon Press 1958. Vol. 5. pp. 288–292.

TOPOLOGICAL METHODS OF LOCATING CRITICAL POINTS

JAMES C. PHILLIPS

Bell Telephone Laboratories, Inc.,
Murray Hill, New Jersey

and

HERBERT B. ROSENSTOCK

U.S. Naval Research Laboratory,
Washington, D.C.

(*Received* 23 *September*, 1957)

VOL.
5
1958

Abstract—Relations between the critical points of a function on and interior to a closed surface are presented. The derivation uses the rigorous formalism developed by MORSE, and extends results previously presented here by one of the authors. A discussion of the limitations of the previous treatment is given. The previous treatment is then refined and the results compared with those of the MORSE theory.

INTRODUCTION

IN many problems in physics one is concerned with a function F which is defined only implicitly on some domain $\mathscr{D}$. Obtaining a complete solution for F throughout $\mathscr{D}$ often proves to be quite laborious. In some cases, however, some of the important qualitative features of F can be obtained from a knowledge of its critical points (c.p.) in $\mathscr{D}$. (By a c.p. we mean a point where $\nabla F = 0$.) For instance, VAN HOVE[1] and each of us[2, 3] have discussed the importance of c.p. for the qualitative behavior of frequency surfaces of lattice vibrations or energy surfaces of electronic energy bands. In particular, it has been shown[3] that the smallest set of c.p. consistent with the requirements of both symmetry and connectivity (more formally, group theory and topology) often exhausted all the c.p. present.

This treatment, however, was applicable only to domains such as Brillouin zones which are topologically equivalent to toroids because, on account of the periodicity of F, opposite faces may be identified. Figuratively speaking, one has taken advantage of the fact that $\mathscr{D}$ is closed but has no bounding surface. Recently one of us[2, 4] has extended the methods to more general domains $\mathscr{D}$ bounded by surfaces $\mathscr{S}$. The results then relate the c.p. of $\mathscr{D}$ to those of $\mathscr{S}$. Since the c.p. of F on $\mathscr{S}$ are usually much easier to locate, the relations may provide material simplifications of the problem of finding the c.p. of F in $\mathscr{D}$.

Further investigation, however, has shown that the relations so derived are not always correct. However, it has proved possible to derive relations of the desired form rigorously from MORSE's theory of c.p.[5] We shall present these results and their derivation in the body of the paper.

In addition, we have extended the previous intuitive considerations, and obtained more detailed results which are consistent with the MORSE relations. Since these results have not been obtained rigorously, we present them in the Appendix. The Appendix also contains a comparison of the intuitive results with those obtained from the MORSE theory.

DERIVATION FROM THE MORSE RELATIONS

Since an elementary discussion of MORSE's methods has already been given,[3] we shall only outline the results. We consider a domain $\mathscr{D}$ homeomorphic to a solid l-dimensional sphere. (We shall derive explicit results only for $l = 2$

and 3, but the method can readily be extended to higher values of l.) The surface of $\mathscr{D}$ is denoted by $\mathscr{S}$. We assume that F is analytic and that all its c.p. are non-degenerate in the mathematical sense.* We first establish a notation for c.p. within and on the boundaries of two- and three-dimensional domains. The c.p. of two-dimensional regions are denoted by p_0 (minimum), p_1 (saddle point), and p_2 (maximum). One-dimensional maxima and minima of F restricted to the bounding curve C are denoted by c_1 and c_0, respectively. These points on the boundary may be further divided into those for which the function increases along the normal to the boundary going into D and those for which it decreases. These differences are denoted by $+$ and $-$ superscripts, respectively. In a similar way we denote c.p. of index j belonging to three-dimensional regions by P_j, and let $p_j^{\pm}$ denote c.p. of index j of F restricted to the two-dimensional bounding surfaces $\mathscr{S}$. Again the superscripts refer to the sign of the inward normal derivative.

To simplify the discussion, we present the case $l = 2$ in detail.† Then we have a two-dimensional domain D bounded by a curve C (Fig. 1). We

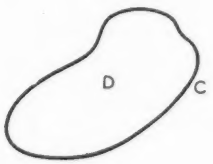

FIG. 1. A two-dimensional domain D with bounding curve C.

shall now show that the following relations hold between the c.p. of D and those of F restricted to C:

$$2n_0+b_0^+ \geqslant 1, \tag{1}$$

$$(2n_0+b_0^+)-(2n_1+b_1^++b_0^-) \leqslant 1, \tag{2}$$

$$(2n_0+b_0^+)-(2n_1+b_1^++b_0^-)+(2n_2+b_1^-) = 2, \tag{3}$$

$$n_0-n_1+n_2+b_1^+-b_0^+ = 1. \tag{4}$$

Here n_j denotes the total number of p_j points in D and $b_j^{\pm}$ denotes the total number of $c_j^{\pm}$ points on C.

These relations can be proved in the following way, which was suggested to the authors by Professor E. H. SPANIER. We imagine D homeomorphically mapped first onto the upper half surface of a three-dimensional sphere, whose surface we denote by Σ, so that C coincides with the sphere's equator, and then onto the lower half surface, C again coinciding with the equator and with itself, as obtained from the first mapping. By this process every c.p. of D appears twice on Σ, and every one-dimensional c.p. of F restricted to C becomes a c.p. of the two-dimensional surface Σ. For instance, as is indicated in Fig. 2, a c_1^+

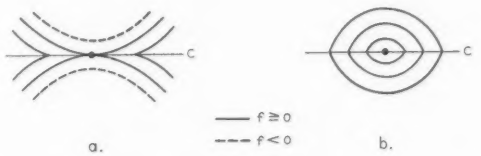

FIG. 2. (a) A c_1^+ point on Σ. (b) A c_1^- point on Σ.

point becomes a p_1 point on Σ, while a c_1^- point becomes a p_2 point. The correspondence between the points of C and their images on Σ is listed in Table 1. Now, the connectivity numbers‡ of Σ are $R_0 = R_2 = 1$ and $R_1 = 0$. If one now writes out the MORSE relations for Σ, one obtains the relations (1)—(3). On the other hand, the MORSE relations applied to C yield

$$(b_1^-+b_1^+)-(b_0^++b_0^-) = 0, \tag{5}$$

and if equation (5) is substituted into (3) one obtains (4).

The same method yields similar relations for l-dimensional domains. We content ourselves here with listing the results for $\mathscr{D}$ when $l = 3$, which is the case of greatest practical interest. The correspondence between the points of $\mathscr{S}$ and their images on Σ can be obtained from the behavior

* A c.p. is non-degenerate if the Hessian of F does not vanish at the c.p. (Cf. ref. (5)).

† The proof for $l > 2$ will be published elsewhere.

‡ The connectivity numbers of a domain and type numbers of c.p. are defined in the Appendix of ref. (3), which also gives the general form of the MORSE relations. The intuitive meaning of connectivity numbers, sometimes called Betti numbers is discussed in ref. (2).

Table 1. *Correspondence between c.p. of* C *and their images on* Σ.

C	Σ
c_1^-	p_2
c_1^+	p_1
c_0^-	p_1
c_0^+	p_0

of F along its principal axes in and normal to $\mathscr{S}$; the results are listed in Table 2. Now we obtain:

$$2N_0+n_0^+ \geqslant 1, \tag{6}$$

$$2N_0+n_0^+-(2N_1+n_1^+ +n_0^-) \leqslant 1, \tag{7}$$

$$2N_0+n_0^+-(2N_1+n_1^+ +n_0^-)+ +(2N_2+n_2^+ +n_1^-) \geqslant 1, \tag{8}$$

$$2N_0+n_0^+-(2N_1+n_1^+ +n_0^-)+ +(2N_2+n_2^+ +n_1^-)-(2N_3+n_2^-) = 0, \tag{9}$$

$$N_0-N_1+N_2-N_3+n_0^+-n_1^+ +n_2^+ = 1. \tag{10}$$

Table 2. *Correspondence between c.p. of* $\mathscr{S}$ *and their images on* Σ.

$\mathscr{S}$	Σ
p_2^-	P_3
p_2^+	P_2
p_1^-	P_2
p_1^+	P_1
p_0^-	P_1
p_0^+	P_0

Here N_j denotes the total number of P_j points in $\mathscr{D}$, while $n_j^\pm$ denotes the total number of $p_j^\pm$ points on $\mathscr{S}$.

Some of these results have already been obtained by MORSE[6] in the special case that F always decreases from $\mathscr{S}$ toward the interior of $\mathscr{D}$. Our equations (1)–(10) can be obtained from his when we take $b_j^+ = n_j^+ = 0$.

We have assumed so far that F was an analytic function. This is not essential to the general argument; F need only satisfy the condition that it is differentiable and has a finite number of c.p. having finite type numbers. In this event, the above relations will still hold, providing that each non-analytic c.p. is assigned a suitable topological weight.

APPENDIX

In this Appendix we are concerned with relations between c.p. that can be arrived at by the intuitively simple, but mathematically less rigorous, methods used in references (2) and (4). Three things are done. First, we find it possible to extend earlier relations because we had not previously distinguished between maxima P_3 and minima P_0, nor between saddle points P_1 and saddle points P_2. Second, we show that in the derivation of these relations a certain class of functions was ignored, and that the results are therefore not completely general as they stand; we show how these results must be modified to be generally correct, or how the old ones can be reinterpreted to serve the same purpose. Third, we give an example of the usefulness of the relations derived in this paper.

(1) We first recall that in ref. (4) we distinguished two kinds of two-dimensional saddle points, there called S_1^1 and S_2^2 respectively, on the basis of whether the 1-gons they form on $\mathscr{S}$, or the 2-gon, are (is) connected by a contour surface inside $\mathscr{D}$. This distinction is discussed in greater detail in the appendix to ref. (4); we have had no occasion to use it so far in the present paper.* Consistent with present notation, we refer to these saddle points as ${}_1p_1^\pm$ and ${}_2p_1^\pm$, respectively.

We now wish to include in the results of ref. (4) the effects of distinguishing between P_0 and P_3 points, and between P_1 and P_2 points. The derivation may be repeated step by step with little additional difficulty, but some increase in complexity; instead of the four equations there labelled (2) containing two auxiliary quantities, one obtains eight such equations with four auxiliary quantities. After eliminating these, one obtains, corresponding to equation (3) of ref. (4);

$$N_3-N_2 = n_2^+-{}_2n_1^+ = 1+{}_1n_1^--n_2^-, \tag{11}$$

$$N_0-N_1 = n_0^--{}_2n_1^- = 1+{}_1n_1^+-n_0^+. \tag{12}$$

* The fact that the sign of the inward normal was not considered in ref. (4) causes no additional difficulty here: if any one of a set of "joined" saddle points is n_1^+ (or n_1^-, respectively), then all saddle points of that set are n_1^+ (or n_1^-, respectively).

Equation (3) of ref. (4) may be obtained by adding equations (11) and (12).

(2) The critical surface through a saddle point has the shape of two cones meeting at the saddle point (Fig. 3a) and if these two cones either extend beyond the boundary or are closed up separately (Fig. 3b) the critical surface divides space up into three distinct regions. In that case equations (11) and (12), as well as equation (3) of ref. (4), apply directly. We may call such surfaces "incomplete saddle surfaces". In addition, however, it is possible that a saddle-point surface may be so connected that it divides space up into only two distinct regions.

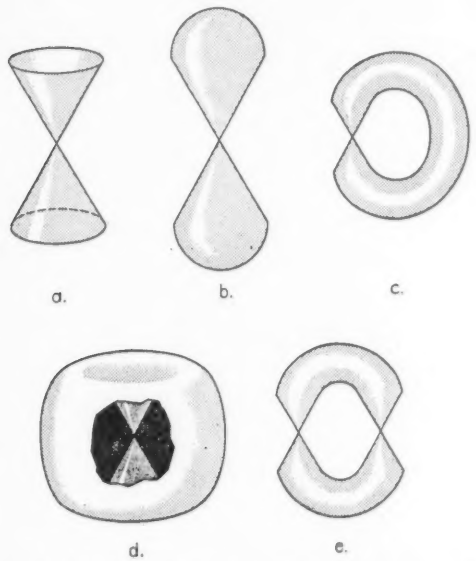

FIG. 3. Critical surfaces of three-dimensional saddle points.

Such "complete saddle surfaces" may be constructed in two ways: first, by bending the two cones of Fig. 3a to the same side until the cut surfaces meet there (illustrated in Fig. 3c), second, by turning each of the surfaces "inside out" until they meet at the equator (as shown in Fig. 3d); here part of the surface has been cut away to present the situation more clearly. Surfaces near a complete critical surface of the first kind (*ccs*1) are topological toroids, surfaces near a critical surface of the second kind (*ccs*2) are topological spheres. *Ccs*1 may also be constructed by joining together more than one saddle point (Fig. 3e illustrates the case of two saddle points). Note that a *ccs*1 consisting of n saddle points contains n maxima or minima inside it; and that any *ccs*2 contains a *ccs*1 inside it. It must now be observed that *ccs* were not taken into account explicitly in the derivation of equation (3) of ref. (4), nor of equations (11) and (12) of the present paper. This will be realized by referring to Fig. 3d of ref. (4). It is possible not only to introduce a new incomplete saddle point in the same manner as before, but also to introduce one that will complete the saddle-point surface already inside the boundary, thereby forming a *ccs*1 as in Fig. 3e of the present paper. To take account of the *ccs*, we recall that the surface outside a *ccs*2 is a sphere and that its effect on a boundary will therefore be that of a maximum or minimum, and that the region inside it must contain one *ccs*1 (which, in turn, consists of n saddle points and n minima or maxima). We therefore stipulate that in equations (11) and (12) N_1 and N_2 are to be interpreted as the number of incomplete P_1 and P_2 points, respectively; that N_0 is the number of P_0 plus the number of structures consisting of one complete P_2 of the second kind and a *ccs*1 containing n P_1 and n P_0; and that N_3 is the number of P_3 plus the number of structures consisting of one complete P_1 of the second kind and one *ccs*1 containing n P_2 and n P_3.

More explicitly, we may write equations (11) and (12) as follows:

$$N_3+Q_3-N_2^{i} = n_2^{+}-{}_2n_1^{+} = 1+{}_1n_1^{-}-n_2^{-}, \tag{13}$$

$$N_0+Q_0-N_1^{i} = n_0^{-}-{}_2n_1^{-} = 1+{}_1n_1^{+}-n_0^{+}. \tag{14}$$

where superscripts i indicate the number of incomplete saddle points of the appropriate kind, and where Q_3 and Q_0 are the numbers of structures whose topological effect is equivalent to maxima and minima, respectively; i.e. the number of *ccs*1 with a saddle point forming a *ccs*2 at the center.

Equations (13) and (14) describe the situation more completely than (11) and (12) did, but have the disadvantage that these values of the quantities Q_0 and Q_3 are not apparent from a knowledge of F on $\mathcal{S}$ alone. An equation which does not have this disadvantage, but is necessarily weaker, and, in fact, equivalent to (10) can be obtained by subtracting (13) from (14):

$$N_0-N_1+N_2-N_3 = 1+n_1^{+}-n_0^{+}-n_2^{+} = -1-n_1^{-}+n_0^{-}+n_2^{-}. \tag{15}$$

Here we have put $n_1^{+} = {}_1n_1^{+}+{}_2n_1^{\pm}$, and used $Q_0+N_2^{i} = N_2$, $Q_3+N_1^{i} = N_1$ together with the fact that each *ccs*1 contains an equal number of P_0 and P_1, and an equal number of P_2 and P_3 points.

(3) We conclude with a simple example of the use of the relations derived. Consider $F = \mu_1(c_1, c_2, c_3)$, the function which occurs in the study of the body-centered cubic lattice in ref. (2). Its behavior on the surface of the cube $-1 \leqslant (c_1, c_2, c_3) \leqslant 1$ is given in the top left drawing of Fig. 8 of ref. (2). The nature of the two-dimensional c.p. on that surface can be established by expanding the secular determinant about them and, in case of the saddle points, by subsequent use of the rules derived in the appendix of ref. (4). We find:

$$n_0^+ = 4, \qquad n_0^- = 0$$

$$_1n_1^+ = 3, \qquad _1n_1^- = 0$$

$$_2n_1^+ = 3, \qquad _2n_1^- = 0$$

$$n_2^+ = 0, \qquad n_2^- = 4.$$

The equations we have derived then yield the following: From (13)

$$N_3+Q_3-N_2^i = -3 \tag{16}$$

from (14)

$$N_0+Q_0-N_1^i = 0 \tag{17}$$

from (9), (10), and (15)

$$N_0-N_1+N_2-N_3 = 3 \tag{18}$$

from (6)

$$N_0 \geqslant -1 \tag{19}$$

from (7)

$$N_1 \geqslant N_0-2 \tag{20}$$

from (8)

$$N_2 \geqslant N_1-N_0+2. \tag{21}$$

Since the number of any kind of c.p. is necessarily an integer, fractional numbers β in expressions $N_i \geqslant \beta$ have been replaced by the smallest integer larger than β. The relations most useful for constructing solutions $\mu_1(c_1, c_2, c_3)$ inside the cube are (16)–(18). Of the inequalities, (19) is useless (because the number of N_0 points is non-negative by definition), but (20) and (21) eliminate a large number of otherwise possible solutions. The simplest solution consistent with both equations (16)–(21) and with symmetry requirements (not discussed here) is $(N_0, N_1, N_2, N_3) = (0, 0, 4, 1)$ as exhibited in ref. (2) (footnote 25 and bottom left drawing of Fig. 8).

REFERENCES

1. Van Hove L. *Phys. Rev.* **89**, 1189 (1953).
2. Rosenstock H. B. *Phys. Rev.* **97**, 290 (1955).
3. Phillips J. C. *Phys. Rev.* **104**, 1263 (1956).
4. Rosenstock H. B. *J. Phys. Chem. Solids* **2**, 44 (1957).
5. Morse M. *Functional Topology and Abstract Variational Theory* (Memorial Sciences Mathematiques, Fascicule 92) Gauthier-Villars, Paris (1938).
6. Morse M. *Trans. Amer. Math. Soc.* **27**, 345 (1925).

VOL.
5
1958

J. Phys. Chem. Solids Pergamon Press 1958. Vol. 5. pp. 293–298.

NEW MAGNETIC COMPOUNDS OF THE ILMENITE-TYPE STRUCTURE

T. J. SWOBODA, R. C. TOOLE and J. D. VAUGHAN

Central Research Department,* Experimental Station,

E. I. du Pont de Nemours and Company, Wilmington, Delaware

(*Received* 17 *October* 1957)

Abstract—Two new ferromagnetic oxides, $CoMnO_3$ and $NiMnO_3$, have been synthesized by reacting the appropriate binary oxides under hydrothermal conditions. These compounds have rhombohedral, ilmenite-type crystal structures, i.e. they are isomorphous with $FeTiO_3$ and are believed to be the first oxides with this structure reported to be ferromagnetic. The specific moment of each oxide is of the order of 14 cgs units/g at room temperature. Intrinsic coercive forces as high as 9000 Oe for $CoMnO_3$ and 1240 Oe for $NiMnO_3$ have been observed for samples of these oxides that have been severely cold worked. The magnetic properties of $CoMnO_3$ and $NiMnO_3$ indicate that they possess high magnetocrystalline anisotropies and that their direction of easy magnetization does not lie along the principal crystallographic symmetry axis but lies probably in the basal plane.

1. INTRODUCTION

In recent years ferromagnetic oxides have become of increasing interest both for theoretical and practical reasons. The number of oxide crystal structures in which ferromagnetism is known to occur is, however, very limited. The recognized structures for which examples of magnetic oxides are known include the isometric spinel structure of the ferrites such as Fe_3O_4 and its numerous isomorphs, the hexagonal magnetoplumbite and related structures of $BaFe_{12}O_{19}$ and similar oxides,[1] and the perovskite structure of complex oxides such as $La_{1-x}Sr_xMnO_3$.[2] Most recently, the isometric garnet structure, as illustrated by compounds such as $Y_3Fe_5O_{12}$,[3] has been added to the list of known structure types for which ferromagnetism has been observed.

Two new ferromagnetic oxides of cobalt and manganese and of nickel and manganese, respectively,[4] have now been prepared. Of particular interest is the fact that these oxides possess a rhombohedral ilmenite-type crystal structure. Their stoichiometries correspond to the formulae $CoMnO_3$ and $NiMnO_3$, which are typical of the ilmenite-type oxides, and both are magnetic well above room temperature. Before discovery of these compounds, the only ilmenite-type oxides reported to be ferromagnetic were solid solutions of hematite, Fe_2O_3, and ilmenite, $FeTiO_3$, in a narrow range of compositions near $Fe_2O_3 \cdot 2Fe_2TiO_3$.[5] That a critical relationship exists between crystal structure and magnetic properties of solids is well recognized, but the exact manner in which structure is related to ferromagnetism in the oxides has been difficult to establish because so few crystal types have been found in which this phenomenon occurs. The discovery of magnetic cobalt manganese oxide and nickel manganese oxide which are simple stoichiometric compounds of novel crystal type for the occurrence of ferromagnetism should thus assist in the further development of theories of ferromagnetism.

The magnetic cobalt manganese and nickel manganese oxides have the same rhombohedral-type structure as do many of the sesquioxides of the transition metals and the related ilmenite-type ternary oxides of these metals. The oxides Cr_2O_3,[6] α-Fe_2O_3,[7] and V_2O_3[8] have been reported to be antiferromagnetic. However, neutron-diffraction studies have shown that Cr_2O_3[9] and Fe_2O_3[10] have different magnetic lattices. The dissimilarities in lattice have been attributed to the

* Contribution No. 450.

difference in extent to which the 3*d*-orbitals of Cr^{+3} and Fe^{+3} cations are occupied.[11] Stoichiometric $FeTiO_3$ is paramagnetic at room temperature,[12] but has recently been shown to become antiferromagnetic at very low temperatures.[13] In contrast, cobalt manganese and nickel manganese oxides are ferromagnetic from 0 to 391 and 437°K, respectively. The semi-empirical argument concerning extent to which 3*d*-orbitals are filled cannot be simply applied to these ternary compounds, since this concept would suggest that all three have similar magnetic properties. Study of the magnetic cobalt manganese and nickel manganese oxides should help to elucidate further the magnetic behavior of this rhombohedral group of transition oxides.

2. SYNTHESES

The ferromagnetic ilmenite-type oxides were synthesized from the simple oxides of cobalt, nickel, and manganese by hydrothermal methods. The reactions described below are preferred syntheses typical of the most successful preparations of each of the oxides.

To prepare the cobalt manganese oxide, a mixture of one mole part of Co_3O_4 and three mole parts of MnO_2 was intimately ground together. This mixture and an amount of 5 per cent aqueous sulfuric acid solution corresponding to 0·3 g of solution/g of oxide mixture were sealed in a thin-walled collapsible platinum tube ($\frac{3}{8}$ in. diam., 6 in. long and 0·007 in. wall). The tube and its contents were heated and pressured to 625°C and 3000 atm in a static, fluid-pressured bomb for 3 hr. The tube contents, which consisted of a gray coarsely crystalline solid and a pink solution, were then washed into a large volume of water. The magnetic portion of the crystalline solid, consisting primarily of cobalt manganese oxide, was extracted from this slurry with strong permanent magnets. The amount of material recovered in this manner corresponded to 85 per cent of the theoretical yield of magnetic ilmenite-type oxide. Unreacted oxides of cobalt and manganese and minor amounts of unidentified materials made up the remaining nonmagnetic portion of the product. The over-all reaction that occurred can be represented by

$$Co_3O_4+3MnO_2 \rightarrow 3CoMnO_3+\tfrac{1}{2}O_2.$$

The magnetic oxide of nickel and manganese was prepared in a similar manner from one mole part of NiO (black oxide, free of metallic nickel) and two mole parts of MnO_2 in a 5 per cent aqueous sodium hydroxide solution (0·3 g/g of oxide). This charge was sealed in a platinum tube and held at 700°C and 3000 atm for 3 hr. At the end of the reaction, the solids were isolated by filtration and then extracted with a large volume of concentrated hydrochloric acid at room temperature to remove the excess MnO_2. An undissolved magnetic residue of nickel manganese oxide was recovered which corresponded to 70 per cent of the theoretical yield of magnetic ilmenite-type oxide based on the amount of NiO charged. This synthesis reaction can be represented by,

$$NiO+MnO_2 \rightarrow NiMnO_3.$$

Most critical of the variables involved in the hydrothermal syntheses of the magnetic ilmenite-type oxides are the temperature and pressure. High pressures are obviously necessary to maintain a high-density aqueous reaction medium at the temperatures employed. Equally important is the maintenance within the closed reaction systems of high partial pressures of oxygen which render the ilmenite-type phases stable at the reaction temperatures. In the case of cobalt manganese oxide, excess oxygen arises naturally from the stoichiometry of the reaction equation whereas the use of excess MnO_2 makes oxygen available in the synthesis of nickel manganese oxide. However, a decrease in yield of the magnetic phase appears to be the only significant effect of using the stoichiometric amount of MnO_2.

Significant yields of the ilmenite-type oxides were obtained from hydrothermal syntheses at pressures as low as 1000 atm. Best results were obtained at temperatures of 600°C and above while little or no reaction occurred at temperatures below 500°C. An acidic aqueous reaction medium gave the best yields of cobalt manganese oxide, but *p*H of the reaction medium appeared to be of minor importance in syntheses of nickel manganese oxide. The amount of aqueous solution used was not critical. In general, the reaction tubes were first pressured and then heated to the reaction temperature over a period of approximately 1 hr. The rate of cooling after reaction had occurred appeared unimportant.

3. STRUCTURE AND STOICHIOMETRY

X-ray powder patterns obtained for products of the hydrothermal syntheses consistently showed the ilmenite-type phase to be the major component. Diffraction patterns typical of those observed for these products were obtained for the cobalt manganese and nickel manganese products described in the previous section. The patterns were obtained

VOL. 5 1958

Table 1. *X-ray powder patterns of magnetic ilmenite-type cobalt manganese oxide and nickel manganese oxide products*

hkl	$CoMnO_3$		$NiMnO_3$	
	Interplanar spacings (Å)	Relative intensities	Interplanar spacings (Å)	Relative intensities
102	3·63	4	3·61	5
	MnO_2—3·11	1	MnO_2—3·11	< 1
	?—2·92	< 1	?—2·92	< 1
104	2·67	10	2·66	10
110	2·467	7	2·455	6
	Co_3O_4—2·44	< 1		
	MnO_2—2·41	< 1	NiO, MnO_2—2·41	1
105	2·307	< 1	2·290	< 1
006	2·286	2	2·264	1
113	2·169	2	2·156	2
			NiO—2·09	1
	?—2·03	< 1	?—2·03	< 1
204	1·814	2	1·801	2
116	1·675	6	1·664	5
	MnO_2—1·62	< 1	MnO_2—1·62	< 1
108	1·590	1	1·577	< 1
	Co_3O_4, MnO_2—1·56	< 1	MnO_2—1·56	< 1
009	1·523	< 1		
			NiO—1·48	< 1
214	1·460	2	1·451	2
	Co_3O_4—1·434	< 1		
300	1·424	2	1·416	2
214	1·391	< 1		
10·10	1·305	3	1·293	2
119	1·296	1	1·285	< 1
			NiO—1·26	< 1
220	1·233	1	1·226	1
	?—1·215	< 1		
306	1·209	< 1		
10·11	1·196	1		

on a General Electric XRD-3 spectrometer, using Cr K_α radiation and are given in Table 1. The observed reflections are indexed to correspond to the rhombohedral ilmenite-type structure. Excellent agreement was found between the observed interplanar spacings and those calculated using cell constants of $a_0 = 4{\cdot}933$ and $c_0 = 13{\cdot}71$ Å for cobalt manganese oxides and $a_0 = 4{\cdot}905$ and $c_0 = 13{\cdot}59$ Å for nickel manganese oxide. Good qualitative agreement was also observed between the experimentally recorded reflection intensities and those reported in the literature[14] for ilmenite and its isomorphs. The minor differences in the observed intensities for cobalt manganese oxide and nickel manganese oxide are not considered significant, since equally large variations were observed from sample to sample of either oxide. A number of very weak reflections were observed in addition to the reflections of the ilmenite-type phases. These are also given in Table 1 and are seen to correspond in most instances to the strongest reflections expected for the reactants Co_3O_4, NiO, or MnO_2. The rhombohedral ilmenite-type structures of the magnetic cobalt manganese and nickel manganese oxides have been confirmed in X-ray precession camera studies of single crystals.[15]

Chemical analyses for cobalt or nickel and manganese were carried out for the two magnetic fractions discussed above. The results are given in

Table 2. The observed weight percentages of the metals in each oxide agree quite well with the calculated values assuming the ideal formulae $CoMnO_3$ and $NiMnO_3$ for the two products. The presence of small amounts of unchanged reactants

Table 2. Chemical analyses of cobalt manganese and nickel manganese oxides

Cobalt manganese oxide		
	Calc'd. for $CoMnO_3$	Found
Co, wt.-per cent	36·45	37·40
Mn, wt.-per cent	34·00	32·31
Nickel manganese oxide		
	Calc'd. for $NiMnO_3$	Found
Ni, wt.-per cent	36·35	36·51
Mn, wt.-per cent	33·95	33·23

as indicated by the X-ray analyses is probably responsible for the discrepancies between observed and calculated analyses. The theoretical densities of $CoMnO_3$ and $NiMnO_3$, calculated from the X-ray cell dimensions and stoichiometry of the phases, are 5·55 and 5·65, respectively. The density of a powder sample of cobalt manganese oxide was found experimentally to be 5·57.

While no X-ray evidence was obtained which suggested the presence of metallic cobalt or nickel in these products, the conclusion that the free metals were absent was also checked in another manner. A simple tripping balance was constructed which enabled a qualitative estimation of the magnetization of small samples of these products as a function of temperature. This balance was arranged so that the force on a sample due to the non-homogeneous field near the poles of a large permanent magnet (3000 G) could be measured at a series of temperatures. Typical curves obtained in this manner are plotted in Fig. 1. Cobalt manganese oxide was found to become completely non-magnetic just above 118°C, while nickel manganese

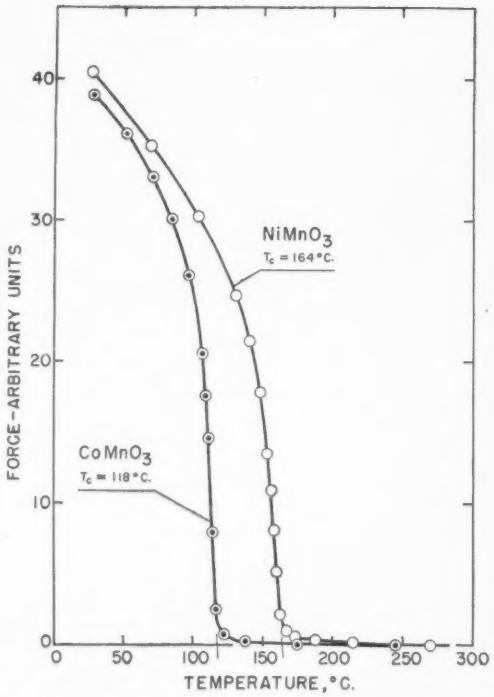

FIG. 1. Curie-temperature curves of magnetic cobalt manganese and nickel manganese oxides.

oxide became completely non-magnetic just above 164°C. Since cobalt and nickel have Curie temperatures of 1130 and 358°C, respectively, it is clear that the free metal is not present in either product. Curves similar to those of Fig. 1 were obtained for previously known magnetic materials such as Fe_3O_4, nickel and iron. By extrapolating the straight portion of the curves to zero force, as was done in Fig. 1, the Curie temperatures of these materials as reported in the literature[16] were accurately reproduced. Therefore, Fig. 1 indicates the Curie temperature of cobalt manganese oxide and nickel manganese oxide to be approximately 118 and 164°C, respectively.

4. MAGNETIC PROPERTIES

The cobalt manganese and nickel manganese oxides were synthesized as finely divided powders. Electron micrographs showed these crystalline powders to be composed of particles with diameters in the range of 0·5–5μ. Magnetic measurements were obtained by preparing cylindrical

VOL. 5 1958

compacts of these powders having densities roughly 0·6 of the theoretical density and length to diameter ratios of 16 : 1. Measurements of magnetic moments and coercive forces were made using instruments similar to those described by DAVIS and HARTENHEIM[17] and BARDELL.[18] This equipment employed a long air-core solenoid to magnetize and demagnetize samples and a small concentrically mounted detection coil in series with a sensitive deflection galvanometer to detect the magnetization of the samples as they were flipped out of the detection coil along the common axis of the two coils. The 2–3000-G fields of the solenoid proved inadequate for saturating some of the samples encountered. In such cases a 12-in Varian magnet capable of fields of 14,000 G was used in place of the air-core solenoid.

In magnetizing fields of 2–3000 G, specific moments as high as 14 cgs units/g were obtained for the best samples of both cobalt manganese and nickel manganese oxides. Qualitative observations in fields up to 14,000 G suggested that the 2–3000-G fields had not completely saturated the samples. Variations in the specific moments from sample to sample suggested that even the best samples may have been contaminated with some non-magnetic impurities. It is therefore felt that the saturation specific moments at room temperature are somewhat higher than 14 cgs units/g. The measured moments correspond to approximately 0·4 Bohr magnetons per molecule for each of the oxides. Remanent moments observed in zero field were 0·65–0·70 of the moments observed in magnetizing fields of 2–3000 G. These remanent moments are distinctly higher than the value of 0·5 which would be expected for randomly oriented uniaxial crystals having their magnetization vector along the symmetry axis. There was no reason to suspect crystallite orientation in the cylindrical test specimens which might have given rise to high remanent moments. Obviously, the low density of the compacts tended to shear the demagnetization curves, so that remanent moments for specimens of theoretical density should be even higher than the values observed. The results of these measurements indicated that the direction of easy magnetization is not along the principal symmetry axis of the rhombohedral crystals, and this possibility has been confirmed in subsequent ferromagnetic resonance studies.[19]

Intrinsic coercive forces (iHc at $(B\text{-}H) = 0$) observed for the two oxides were quite high. For example, values ranging from 200 to 400 Oe were observed after magnetization in 2–3000-G fields. However, it was found that severe cold working of the powders raised the coercive forces to much higher values, particularly in the case of cobalt manganese oxide. Coercive forces as high as 9000 Oe were observed for cold-worked samples of cobalt manganese oxide and as high as 1240 Oe for nickel manganese oxide samples that had been magnetized in fields of 14,000 G. The highest values of coercive force were obtained after passing the oxide powders through the polished rolls of a rubber mill where they were subjected to a combination of severe compression and shear. However, very large increases in coercive force were also obtained by merely ball milling the oxides. Electron micrographs of a sample of cobalt manganese oxide before and after rubber milling were obtained. While a small amount of fragmentation was apparent, in general, there was no significant difference in the size or shape of the particles. X-ray diffraction patterns of the oxide before and after milling were more informative. Retention of the characteristic reflections of large interplanar spacings assigned to the rhombohedral oxide indicated that no major structural or chemical alteration of the magnetic phase had taken place. However, reflections of small interplanar spacings in the back-reflection region had been almost completely obliterated, and reflections of large interplanar spacings had been considerably broadened. Qualitatively, the observed patterns indicated that regions of continuous crystallographic order had been reduced in size to the range of only hundreds of ångströms by milling. Cold working may therefore have reduced the effective crystallite size to the critical diameter necessary for single-domain behavior. The large magnitude of the coercive forces observed for these crystallites indicates a high magnetocrystalline anisotropy for these oxides. This conclusion was confirmed subsequently by ferromagnetic-resonance experiments.[19]

REFERENCES

1. WENT J. J., RATHENAU G. W., GORTER E. W. and VAN OOSTERHAUT G. W. *Philips Tech. Rev.* **13,** 194 (1952).

2. VAN SANTEN J. H. and JONKER G. H. *Physica* **16,** 337, 599 (1950).
3. BERTAUT F. and FORRAT T. *C.R. Acad. Sci.* (*Paris*) **242,** 382 (1956).
4. TOOLE R. C. *U.S. Patent* 2,770,523 (November 13, 1956).
5. POUILLARD E. and MICHEL A. *C.R. Acad. Sci.* (*Paris*) **228,** 1232 (1949).
6. FOEX J. and GRAFF M. *C.R. Acad. Sci.* (*Paris*) **209,** 160 (1939).
7. NÉEL L. *Ann. Phys.* (*Paris*) **4,** 249 (1949).
8. HASCHEK E. and KLEMM W. *Z. anorg. allgem. Chem.* **242,** 63 (1939).
9. BROCKHAUSE B. N. *J. Chem. Phys.* **21,** 961 (1953).
10. SHULL C. G., STRAUSER W. A. and WOLLAN E. O. *Phys. Rev.* **83,** 333 (1951).
11. LI Y. Y. *Phys. Rev.* **102,** 1015 (1956).
12. CHEVALLIER R. *Bull. Soc. Chim. France* **20,** 973 (1953).
13. BIZETTE H. and TSAI B. *C.R. Acad. Sci.* (*Paris*) **242,** 2124 (1956).
14. BARTH T. F. W. and POSNJAK E. *Z. Krist.* **88,** 265 (1934).
15. CLOUD W. H. To be published.
16. BOZORTH R. M. *Ferromagnetism* p. 723 Van Nostrand New York (1951).
17. DAVIS C. W. and HARTENHEIM M. *Rev. Sci. Instrum.* **7,** 147 (1936).
18. BARDELL T. R. *Magnetic Materials in the Electronic Industry* pp. 226–8 Philosophical Library, New York (1955).
19. JARRETT H. S. and WARING R. K. To be published.

VOL.
5
195

J. Phys. Chem. Solids Pergamon Press 1958. Vol. 5. pp. 299–301.

FERROMAGNETIC MOMENT OF $CoMnO_3$

R. M. BOZORTH and DOROTHY E. WALSH

Bell Telephone Laboratories, Inc., Murray Hill, N.J.

(*Received* 14 *October* 1957)

Abstract—$CoMnO_3$ and $NiMnO_3$ have the rhombohedral structure of ilmenite and are ferromagnetic, as reported by SWOBODA, TOOLE, and VAUGHAN. The magnetic moment of $CoMnO_3$, extrapolated to 0°K and infinite field strength, is 0·72 Bohr magneton per molecule. This is interpreted as antiferromagnetic coupling between layers of cobalt and manganese ions, the difference in moment being attributed to the orbital moment of the cobalt ion.

1. INTRODUCTION

SWOBODA *et al.*[1] have prepared $CoMnO_3$ and $NiMnO_3$, and shown that these compounds are ferromagnetic with Curie points of 118 and 164°C, respectively, and that they have the rhombohedral crystal structure of ilmenite, $FeTiO_3$. We have measured the magnetic moment of the materials prepared by them, from 2°K to room temperature in fields of 3900, 7700, and 10,800 Oe.

2. MEASUREMENTS

Measurements were made in apparatus simila to that previously described.[2] The sample wa fixed at the lower end of a 57-in. pendulum, in the field of a Varian magnet fitted with poles of the Sucksmith type, giving a gradient of about 220 Oe/cm at the maximum field of 10,800 Oe. Deflection of the pendulum was detected with strain gauges at the top of the pendulum, and was balanced by a measured current in a calibrated coil surrounding the specimen. Temperature was determined with the aid of a carbon resistor held in contact with the specimen and calibrated at the helium, hydrogen, nitrogen, C_2H_5OH, CO_2, and H_2O points and at room temperature.

The observed moments for the three field strengths are plotted against the Kelvin temperature, T, in Fig. 1. At temperatures below 300°K the broken line represents the saturation moment per mole, σ_s, obtained by plotting the observed moments against $1/H$ and extrapolating to $1/H=0$. The amount of this extrapolation is about 6 per cent.

The moment per mole, extrapolated to $H = \infty$, $T = 0$ is $\sigma_0 = 4000$ cgs units, corresponding to $n_B = 0{\cdot}72$ Bohr magneton per molecule.

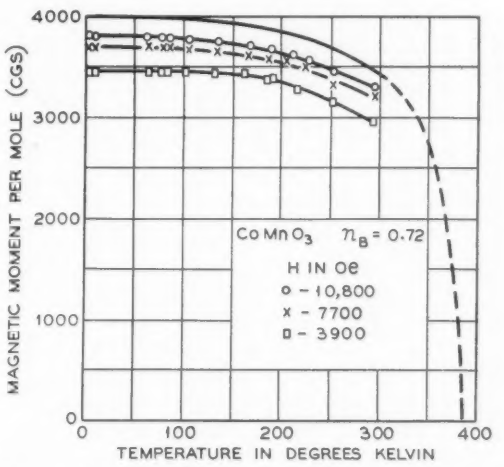

FIG. 1. Magnetic moment per mole of $CoMnO_3$ at various field strengths, and moment extrapolated to $H = \infty$.

Moments have not been determined above room temperature; the broken line in the figure is drawn toward zero at the Curie point, $\theta = 114$°C, as determined by SWOBODA *et al.*[1] This line lies somewhat above that corresponding to $\sigma_s/\sigma_0 = \tanh(T/\theta)$.

Measurement of the magnetic moment of non-stoichiometric $NiMnO_3$ gave a Bohr magneton number of 0·61.

3. DISCUSSION

It has been established[1] by X-ray diffraction that $CoMnO_3$ has the crystal structure of ilmenite, $FeTiO_3$. In the latter compound the iron and titanium ions, presumably Fe^{2+} and Ti^{4+}, lie in alternate layers perpendicular to the rhombohedral axis, with plane layers of oxygen ions interleaved with the layers of metal ions. The metal ions in each layer do not lie exactly in the same (111) plane but are "staggered", neighboring ions being slightly displaced on opposite sides of the median plane. It is known that ilmenite is antiferromagnetic,[3] with a Néel point of 55–70°K.

Structures similar to that of ilmenite are found in Fe_2O_3 and Cr_2O_3, which are also antiferromagnetic with Néel points of 950 and 307°K. In the latter oxides neutron diffraction shows that the magnetic structures are different; in Fe_2O_3 the layers of ions are each ferromagnetic and neighboring layers are antiferromagnetically coupled,[4] while in Cr_2O_3 each layer is internally antiferromagnetic.[5] These three structures may be described as (*a*) $(Fe^{2+})(Ti^{4+})(Fe^{2+})(Ti^{4+})$, (*b*) $(+Fe^{3+})(-Fe^{3+})(+Fe^{3+})(-Fe^{3+})$, and (*c*) $(\pm Cr^{3+})(\pm Cr^{3+})(\pm Cr^{3+})(\pm Cr^{3+})$. Although the magnetic structure of (*a*) has not been determined, both $(a_1)(\pm Fe^{2+})(Ti^{4+})(\pm Fe^{2+})(Ti^{4+})$ and (a_2) $(+Fe^{2+})(Ti^{4+})(-Fe^{2+})(Ti^{4+})$ have been proposed.[6,7]

In $CoMnO_3$ the obvious possibility for the magnetic structure is $(+Co^{2+})(-Mn^{4+})(+Co^{2+})$ $(-Mn^{4+})$, or a similar structure with different combinations of valences. $(\pm Co)(\pm Mn)(\pm Co)$ $(\pm Mn)$ would have zero net moment. The net moment of $(+Co^{2+})(-Mn^{4+})(+Co^{2+})(-Mn^{4+})$ is zero if the moments of cobalt and manganese ions are equal. They are equal if their orbital moments are completely quenched and they have spin-only values. In that case the moments of Co^{3+} and Mn^{3+} are each 4 Bohr units, those of Co^{2+} and Mn^{4+} each 3. Calculation shows that any combinations of valencies of Co^{m+}, Co^{n+}, Mn^{p+}, and Mn^{q+} will have zero net moment as long as: (1) the overall balance of valences is preserved, (2) the ions in any one layer are of the same metal, and (3) the moments are spin-only, or have free-ion values, or when plotted against number of electrons per ion, lie on a curve symmetrical about the line for Mn^{2+} (or Co^{4+}), when the 3*d* shell is half filled.

In order to account for the observed ferrimagnetism, we discard (3) and suppose that the orbital moments of the ions make contributions which are different for cobalt and manganese ions. This is in accord with the data on paramagnetic salts of the iron group, as collected by STONER.[8] The average effective moments of ions containing 3, 4 6, and 7 electrons in the *d*-shell, corresponding to Mn^{4+}, Mn^{3+}, Co^{3+}, and Co^{2+}, are respectively 3·9, 4·9, 5·3, and 4·8 Bohr units. The difference between the moments of Mn^{3+} and Co^{3+} is then 0·4, and between Mn^{4+} and Co^{2+} it is 0·9. The observed moment of 0·7 is intermediate between these differences, and suggests that each of the ions Mn^{4+}, Co^{2+}, Mn^{3+}, and Co^{3+}, are present.

The orbital contribution to the moments between the cobalt and the manganese ions is also prominent in the ferrites $MnFe_2O_4$ and $CoFe_2O_4$. If the ions in these compounds had spin-only values the molecular moments of the compounds, assumed to be inverse spinels, would be respectively 5 and 3, whereas the observed values[9] are 4·4–5·0 and 3·7–3·9.

Further tests of the proposed structure and atomic moments of $CoMnO_3$ could be made with neutron-diffraction experiments, and with magnetic resonance, using the theory of WANGSNESS.[10]

One can conclude from the measurement of 0·61 Bohr magneton for the non-stoichiometric $NiMnO_3$ that it is not inconsistent with the model given here. Antiparallel nickel and manganese ions, of whatever valence, would give 1·0 for spin-only moments, and a somewhat smaller value if the nickel ion has a larger orbital contribution than the manganese ion, as in fact previous measurements indicate.

Ferrimagnetism of the kind here described may be termed "orbital ferrimagnetism".

Acknowledgements—We are glad to acknowledge the benefit of discussions with P. W. ANDERSON, and the assistance of A. J. WILLIAMS with the measurements. We appreciate having received the materials investigated, and information regarding them, from M. S. SADLER, T. J. SWOBODA, R. C. TOOLE, and J. D. VAUGHAN of the Central Research Department of the du Pont Company before publication.

REFERENCES

1. SWOBODA T. J., TOOLE R. C., and VAUGHAN J. D. See preceding article.

VOL. 5 1958

2. Bozorth R. M., Williams H. J., and Walsh Dorothy E. *Phys. Rev.* **103,** 572 (1956).
3. Bizette H. and Tsai B. *C.R. Acad. Sci.* (*Paris*) **242,** 2124 (1956).
Shomate C. H. *J. Amer. Chem. Soc.* **68,** 964 (1946).
4. Shull C. G., Strauser W. A., and Wollan E. O. *Phys. Rev.* **83,** 333 (1951); see also ref. 7, pp. 5–227.
5. Brockhouse B. N. *J. Chem. Phys.* **21,** 961 (1953).
6. Li Y. Y. *Phys. Rev.* **102,** 1015 (1956); see also ref. 3.
7. Néel L. *Advances in Phys.* **4,** 191 (1955).
8. Stoner E. C. *Magnetism* p. 59 Methuen and Co., Ltd., London (1948).
9. *American Institute of Physics Handbook* p. 5–211 American Institute of Physics, New York (1957).
10. Wangsness R. K. *Phys. Rev.* **93,** 68 (1954).

OL.
5
958

J. Phys. Chem. Solids Pergamon Press 1958. Vol. 5. pp. 302–315.

SOME TRANSIENT ELECTRICAL EFFECTS OF PLASTIC DEFORMATION IN NaCl CRYSTALS*

D. B. FISCHBACH† and A. S. NOWICK‡

Yale University, New Haven, Connecticut

(*Received* 22 *October* 1957)

Abstract—Transient electrical effects of plastic deformation in NaCl crystals have been investigated. Two such effects have been observed: (1) a temporary increase in the ionic conductivity and (2) a deformation-induced charge flow with no applied electric field. The first effect, which is observable for about an hour at room temperature, is attributed to excess vacancies freed by moving dislocations. It is suggested that an important source of these vacancies may be the breaking-up by the deformation of associated complexes between cation vacancies and multivalent cation impurities. The second effect is observed only after inhomogeneous plastic deformation, and it ceases abruptly when the stress increment producing it is removed. Possible sources for this deformation-induced charge flow are discussed, and an explanation is offered in terms of electrically charged dislocations.

VOL. 5 1958

1. INTRODUCTION

SEVERAL observations of transient effects of plastic deformation upon the ionic conductivity of alkali halide crystals are reported in the early literature. GYULAI and HARTLY[1] found that plastic deformation produced a large transient increase in the conductivity of natural rock-salt crystals at 40°C. This increase, which was sometimes more than a factor of 100 for large stress increments (100–200 kg/cm²), decayed rapidly and disappeared completely (within the accuracy of the measurements) in about 15 min. The stress required to produce the first substantial conductivity increase agreed roughly with the yield stress. If the load increment which produced the conductivity increase was left on until the current returned to its original value, removal and reapplication of the same load had no further effect; a new transient increase was observed only if the previous total load was exceeded. If, however, the load was removed within a few seconds after application, reloading was accompanied by a second, smaller current increase. BOROS and GYULAI[2] later used the transient-conductivity increase observed with moderate deformation (about 50 kg/cm²) to investigate the rate of recovery of work-hardened rock salt with annealing. In view of the space-charge polarization§ in these crystals, it is not clear from the GYULAI–HARTLY experiments whether or not part of the current increase may have been due to a change in the state of polarization.

STEPANOW[3] repeated the experiments of GYULAI and HARTLY and confirmed the existence of a temporary increase in the conductivity after plastic deformation. Furthermore, experiments were performed which demonstrated that the GYULAI–HARTLY effect could not be ascribed to a

* This research was supported by the U.S. Air Force through the Office of Scientific Research of the Air Research and Development Command under contract No. AF 18(600)–850. Reproduction in whole or in part is permitted for any purpose of the United States Government.

† Now at the Jet Propulsion Laboratory, California Institute of Technology, Pasadena, California.

‡ Now at the IBM Watson Laboratory, Columbia University, New York City.

§ Below about 300°C, the apparent conductivity (defined as the ratio of the current density to the externally applied field) is time-dependent. The current decreases with time after application of the field from a finite initial value to a steady-state value. Thus, two conductivities may be defined: the initial conductivity, σ_0, which exists at the instant the field is applied, and the steady-state conductivity, σ_∞, which remains after the transient process is completed. This effect is the well-known space-charge polarization phenomenon characteristic of most dielectric materials. (See, for example, JOFFE A. *The Physics of Crystals* McGraw-Hill, New York (1928) especially Chaps. 7–9.)

change in the state of space-charge polarization in the crystal produced by the deformation. Finally, measurements by STEPANOW over the temperature range 30–170°C showed that, although the relative increase in the conductivity produced by deformation was much smaller at 170 than at 30°C, the amount of excess charge flow produced by a given stress was larger at the higher temperature. This was attributed to the larger amount of plastic deformation produced by a given load at the higher temperature.

In addition to the enhancement of the conductivity by plastic flow, STEPANOW found that, under certain conditions, when a crystal was deformed a charge flow was produced in the external circuit, even in the absence of an applied electric field. Although he could not explain this effect, STEPANOW was able to make it negligibly small (by proper choice of experimental conditions) during his measurements on the effect of deformation on the conductivity. Since this "deformation-induced charge flow" will be studied in the present paper, further information concerning STEPANOW's experiments will be given in Section 3.

In the experiments of GYULAI and HARTLY and in those of STEPANOW, the crystals were deformed in compression, with the load applied to the electrode surfaces of the crystal. Thus, there remained the possibility that changes in the nature of the contact between the electrodes and the crystal surface were involved in the observed deformation effects. To check on this possibility, KASSEL[4] deformed in tension crystals with electrodes applied either parallel or perpendicular to the tension axis. He confirmed the existence of a transient change in conductivity for applied stresses greater than a minimum "electrical" yield stress, in the temperature range 40–100°C. However, he reported that the change observed could be either an increase or a decrease, depending on the particular crystal specimen. The transient effects observed by KASSEL decayed very rapidly, disappearing within 1 min. He also observed transient changes in the opposite direction on unloading. Thus, the effect observed by KASSEL appears to be different from the enhancement of conductivity found by GYULAI and HARTLY and by STEPANOW. It should be noted that the loads used by KASSEL were relatively small, since rock salt breaks in tension under a stress of the order of 30 kg/cm^2.

Recent advances in the theory of imperfections in solids have suggested interpretations for some of these early observations. It is now generally accepted that the ionic conductivity of alkali halide crystals is due to the migration of positive-ion vacancies under the influence of the applied electric field.[5] Accordingly, SEITZ[6] has interpreted the results of GYULAI and HARTLY and those of STEPANOW as an enhancement of the ionic conductivity resulting from the production of free lattice vacancies by moving dislocations. It is then possible to infer that about 10^{18} Schottky defects per cm^3 were generated by the deformation of about 10 per cent which produced the 100-fold conductivity increase reported by GYULAI and HARTLY.

The interpretation of SEITZ has not been regarded as the only possible explanation for the enhanced conductivity after deformation. TYLER[7] has suggested that the GYULAI–HARTLY effect may be due at least in part to an electronic contribution resulting from the freeing of electrons into the conduction band by the motion of dislocations. He cited as evidence the experiments of GYULAI and BOROS,[8] in which fast decaying currents were observed upon deformation (under stresses of about 10 kg/cm^2) both for normal crystals and for crystals colored with *F*-centers. The size of the conductivity increase was about twice as large in the colored crystals as in the normal (uncolored) crystals; in both types of crystal, however, the decay time was about the same, viz. of the order of a few seconds. Such decay times are not inconsistent with the anticipated lifetime of conduction electrons, so that the effects of GYULAI and BOROS may well be due to electronic conductivity. It should be recalled, however, that in the original observations of GYULAI and HARTLY (with crystals under much larger loads) the duration of the transient effect was considerably longer (of the order of several minutes).

JOHNSTON[9] has recently investigated the conductivity increase produced in AgBr by plastic deformation at and below room temperature. Hundreds of hours were required at room temperature for the enhanced conductivity to decay to its normal value. On the basis of the long recovery time and other characteristics of the observed conductivity increase, he concluded that the mechanism proposed by SEITZ is not responsible for the

behavior of AgBr. JOHNSTON proposed instead that the transient effect in AgBr may be attributed to the formation of regions of disorder by the deformation process. These regions of disorder form low-resistance paths through the crystal and hence increase the conductivity. A similar interpretation was recently given for a high-temperature transient phenomenon in KCl crystals.[10]

Further evidence in conflict with SEITZ's interpretation is reported by CAFFYN and GOODFELLOW.[11] These authors have confirmed the existence of the GYULAI–HARTLY effect in some alkali halide crystals but not in others, depending upon the source of the crystal. This result implies a dependence of the effect on crystal purity, which is not readily accounted for in terms of SEITZ's suggestion.

In view of the uncertainties in the interpretation of the various experiments dealing with the effects of deformation on the electrical properties of the alkali halides, it appeared desirable to repeat and expand these experiments. The present work was undertaken with this purpose in mind. We shall be concerned in what follows only with the transient effects of plastic deformation. Permanent effects of deformation on the conductivity have been discussed elsewhere.[12]

2. EXPERIMENTAL APPARATUS AND PROCEDURE

All charge and current measurements were made with a vacuum-tube electrometer amplifier based on the two-tube bridge-type circuit of DU BRIDGE.[13] Victoreen type-5800 electrometer tetrodes were employed, with a sensitive galvanometer as the indicating instrument. The current sensitivity of the instrument was 5×10^{-16} A/mm with a $10^{11}\Omega$ grid resistor, and the zero drift was about 1–2 cm/hr. The response time of the measuring circuit, which was about 10 sec, was determined largely by the period of the galvanometer. In order to obtain some information on the very early portions of the transient effects, a rough calibration of the ballistic response of the system was also made. Two methods were used: charge and discharge of the parallel-plate air capacitor formed by the electrodes, and application of known compressive loads to an X-cut quartz crystal plate between the electrodes. Both methods gave a ballistic sensitivity of about $2{\cdot}5\times10^{-15}$ C/mm.

To permit measurements of the conductivity and charge flow during plastic deformation, the electrodes, which were of steel, formed the platens of a subpress assembly. The lower electrode rested on a fused-quartz disc insulator. Compressive stress could be applied to the crystal by placing weights on a pan attached rigidly to the upper electrode through a cylinder sliding in a long guide bearing. A sponge-rubber pad on the weight pan helped to prevent impact shocks when weights were placed on the pan. The crystal was heated by a short cylindrical electric furnace which surrounded the crystal and electrodes. The temperature, which was measured with a Chromel/Alumel thermocouple located adjacent to the crystal, was regulated to $\pm0{\cdot}25$°C. The furnace was provided with two narrow window slits to permit observation of the crystal by transmitted light through a low-power microscope. Rock salt becomes birefringent on plastic deformation, so that the use of a polarizer and analyzer in the optical system provided a simple means of observing qualitatively the degree of plastic deformation undergone by the crystal as the load was increased. The entire apparatus, including the electrometer tubes and the grid resistor, R_g, was enclosed in a brass can which was first evacuated and then filled with dry air or helium before the measurements were made. Fig. 1

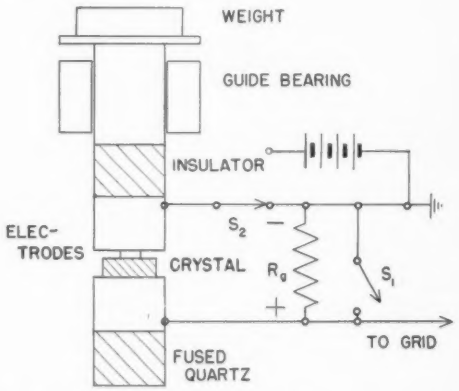

FIG. 1. Schematic diagram of the apparatus. Switch S_2 is shown in position for measuring the deformation-induced charge flow without an applied electric field. For conductivity measurements S_2 is placed in the upper position.

shows a schematic diagram of the apparatus, for the particular case in which the deformation was made inhomogeneous through the use of a small metal disc placed directly above the crystal.

The specimens were in the form of thin plates 1–2 mm thick and 5–10 mm on a side cleaved from single-crystal blocks of NaCl obtained from the Harshaw Chemical Co. The plates were annealed at 650°C for several hours in either air or helium, and furnace-cooled. After annealing, electrodes of colloidal graphite were painted on opposite faces of some of the crystals; others were studied without such electrodes.

For conductivity measurements, a potential difference of 1·5–100 V was applied across the crystal in series with the grid resistor (S_2 up in Fig. 1). This field was reversed on successive measurements to avoid cumulative effects of electrolysis of the crystal. In most of the measurements

the current was allowed to decay to a constant (steady-state) value; a compressive stress was then applied to the crystal, and the current through R_g measured as a function of time after loading. For measurements of the effect of deformation with no applied field, the two electrodes were connected together through the grid resistor (S_2 horizontal in Fig. 1). In both cases, the grid was grounded (using S_1) at intervals of about 2 min and the position of the zero noted, so that the data could be corrected for zero drift of the amplifier. The electrometer calibration was checked with a potentiometer, inserted in series with the grid bias, prior to each set of measurements.

3. RESULTS

(a) *Observations with No Applied Field*

In the course of some experiments preliminary to the investigation of the transient effects of plastic deformation on the conductivity, it was found that charge flow was produced in the external circuit by plastically deforming a crystal, even when no electric field was applied. The current resulting from the deformation decayed with time in an approximately hyperbolic fashion when the load was left on, such that it decreased by approximately a factor of ten in a time between 10 and 100 sec. As the crystal was loaded up in 1-kg increments, the effect repeated with each new addition to the load. Since the initial decay rate of the current was too rapid to be followed by the galvanometer, the ballistic deflection of the galvanometer was used as a measure of the total charge that flowed in the first few seconds after the deformation. The residual current flowing at times greater than 10 sec was then measured as a function of time. The total charge flow produced by a stress increment of 1 kg/cm^2 was of the order of 10^{-12} C.

A preliminary account of these results has been published previously;[14] more recently, CAFFYN and GOODFELLOW[11] described their independent observations of this effect. As mentioned in the Introduction, the deformation-induced charge flow was apparently first observed by STEPANOW,[3] also in connection with an investigation of the effect of deformation on the conductivity. STEPANOW found that the effect appeared independently of the kind of electrodes used (tin foil, painted graphite, or sputtered platinum) and of the orientation of the electrodes with respect to the applied stress, and he concluded that the charge flow could not be ascribed to frictional (contact) emf at the electrodes. He reported that with repeated application of the same load the effect disappeared and that a new charge flow was produced only if the previous total load was exceeded. STEPANOW was unable to predict the direction of the charge flow produced by the deformation, and reported that it varied from crystal to crystal. However, he did observe that the amount of charge released was larger for rod-shaped specimens than for thin plates, and therefore used the latter in his investigation of the effects of deformation on the conductivity.

Since it appeared possible that the phenomenon of deformation-induced charge flow in the absence of an applied field was linked in a fundamental way with the properties of the imperfections found in ionic crystals, a more thorough investigation of the effect was undertaken. Because of the cubic symmetry of the NaCl crystal, the direction of the observed charge flow produced can only be determined by some anisotropy imposed on the crystal by the experimental arrangement. In view of the fact that the charge flow is produced by plastic deformation, it seems reasonable to suppose that the direction of the current is determined by the inhomogeneity of the deformation. This hypothesis was confirmed experimentally when a crystal was purposely deformed in a strongly inhomogeneous fashion by applying the load to a smaller area on one side of the crystal than on the other, in the manner illustrated in Fig. 1. It was found that the current flow in R_g was then in such a direction that negative charge flowed from the crystal face to which the higher compressive stress had been applied. Both the ballistic effect (initial flow) and the residual charge flow were in the same direction, and the total charge was divided approximately equally between them.

Sometimes, it was found that the initial one or two load increments produced currents in the opposite direction to that expected from the sense of the applied stress gradient. In some of these cases, this behavior was clearly observed to be associated with the occurrence of localized plastic deformation on the side of the crystal opposite to that on which the stress concentration was applied. The regions where deformation occurred could easily be identified by viewing the crystal in polarized light. Such deformation on the "wrong" side of the crystal was presumably due to localized stress concentrations caused by irregularities at the

crystal surface (e.g. brush marks, cleavage steps, or other small discontinuities on the crystal surface itself). In each crystal for which an initial "wrong" sign was observed, the current flow reversed direction at higher loads when the intended stress geometry became effective. Thus, these observations give further confirmation to the hypothesis that the current flow is produced by inhomogeneous plastic deformation.

A number of different geometries were used to apply the stress to the crystal inhomogeneously. One crystal was deformed by bending about a [100] axis; in others, compressive stress was applied through a small metal block, ball, rod, or washer, placed on one face of the crystal. The results obtained for previously undeformed crystals in all these cases were similar, and the direction of the charge flow observed (after the first few load increments) was always determined by the sense of the applied stress gradient as stated above. About ten crystals were investigated in all.

Crystals which had been previously deformed inhomogeneously generally showed anomalous or irregular behavior in succeeding experiments with a stress geometry different from that originally employed. For example, one crystal gave completely regular results when originally deformed with a small rectangular plate on one side. However, in a second set of measurements on this crystal with a steel rod placed along a [110] direction on the surface, the current direction was consistently opposite to that expected. In a third series of observations on this crystal, in which the stress was applied through a steel ball, the ballistic charge flow was in the expected direction, but the residual current was small and reversed in sign. The irregular results obtained in successive measurements on the same crystal with different geometries of deformation are probably connected with the different patterns of work-hardening produced in the crystal.

Several experiments were performed to ensure that the current flow did not originate in some trivial change in the experimental arrangement, but rather that it stemmed from changes produced in the crystal by the inhomogeneous deformation. Thus, it was found that the effect was unchanged if the load was applied to the crystal with the grid of the electrometer amplifier grounded (crystal shorted); the residual current observed on ungrounding the grid in this case was the same as that obtained (at the same time after deformation) when the crystal was deformed with R_g in the circuit. Therefore, the RC time constant of the circuit is not a significant factor in this phenomenon. The effect was essentially the same in crystals without painted-on electrodes as in crystals with graphite electrodes on both faces. Moreover, the deformation-induced charge flow was also observed when a crystal in the form of a notched bar, with electrodes painted on the sides, was compressed in a direction parallel to the electrodes. These results indicate that the observed phenomenon cannot be ascribed to contact potential differences produced by the deformation.

The decay with time of the current produced in the external circuit by inhomogeneous deformation was found to be linear on a plot of log D versus log t, where D is the galvanometer deflection and t is the time elapsed after application of the stress increment. This result implies a time-dependence for the current flow during the observed time interval, of the form

$$D = At^{-n} \qquad (1)$$

where A and n are constants. Typical data, obtained on one crystal, are shown in Fig. 2. The values of n (the negative slope of the linear log/log plot) observed for several crystals ranged from 1·5 to 0·70. In general, when the crystal was loaded in a succession of equal increments for the first time, the magnitude of the effect, and also the n-value observed, decreased with increasing total load, as illustrated by curves A, B, and C of Fig. 2. If the current flow is allowed to decay to zero and the load increment that produced it is then removed, the magnitude of the effect obtained upon reapplication of the same load increment is considerably smaller than the original effect. This fact, which is illustrated by a comparison of curves B and E in Fig. 2, is clearly due to work-hardening.

The charge flow decayed to zero in a continuous fashion if the stress increment producing it was left on. However, if the stress increment was removed before the current had completely decayed, the current generally dropped abruptly to a value near zero in approximately the time constant of the instrument ($\sim$ 10 sec). This is shown in the first curve of Fig. 3. In one experiment, only half of the applied load increment was removed, with the

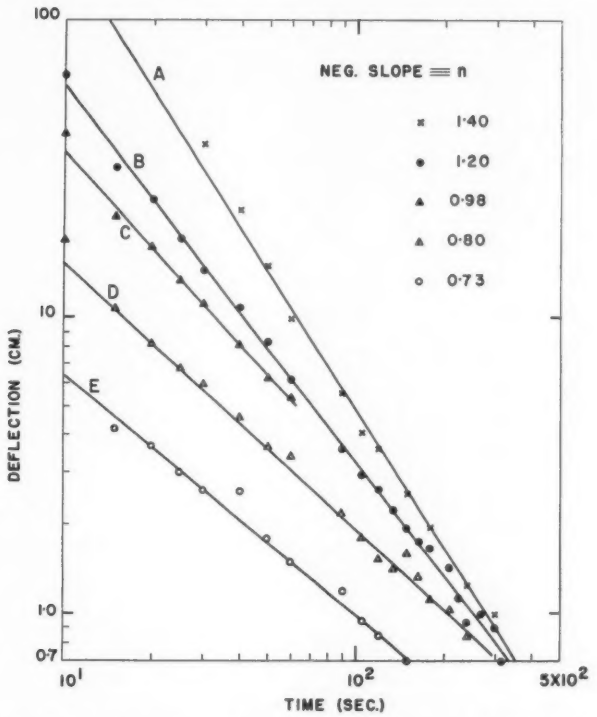

FIG. 2. Variation of the deformation-induced current at 30°C with time. In all cases a 1-kg load increment was applied at zero time. Curves A, B, and C represent initial attainments of total loads of 2, 5, and 6 kg, respectively. The 1-kg increment was removed in the case of curve B after the current had decayed to zero; reapplication of this increment gave curve E. In the case of C, the 1-kg increment was removed after 1 min; reloading gave curve D. To convert deflection to current multiply by $5{\cdot}3 \times 10^{-15}$ amp/cm.

result that only part of the current disappeared, as shown in Fig. 4. In some cases removal of a load increment produced a small ballistic charge flow in the direction opposite to that which took place on applying the load. This affect generally occurred only after the load increment had been removed and reapplied several times in succession, or when the load was removed after the current had decayed to zero. In all cases this effect was very small (only about 10^{-3} of the ballistic charge on first loading).

Reapplication of a load increment, removed before the current had decayed to zero, produced a new charge flow in the same direction as the initial one but smaller in magnitude. This is shown by a comparison of curves C (initial) and *D* (reload) in Fig. 2. The current flow produced by reloading in this case is distinctly larger than for the case where the initial load increment was left on until the current decayed to zero (compare curves *B* and *E*). If care was taken to avoid impact shocks, periodic removal and reapplication of a given load increment produced a smaller charge flow on each successive cycle, as illustrated in Fig. 3. It is worth emphasizing that in experiments such as those of Figs. 3 and 4, only the relatively small load *increment* is removed and reapplied; the major part of the total load remains applied to the crystal.

No strong temperature-dependence was observed for the deformation-induced charge flow. In fact measurements at 30 and 90°C on the same crystal indicated essentially no difference in the magnitude of the effect or in the decay rate of the

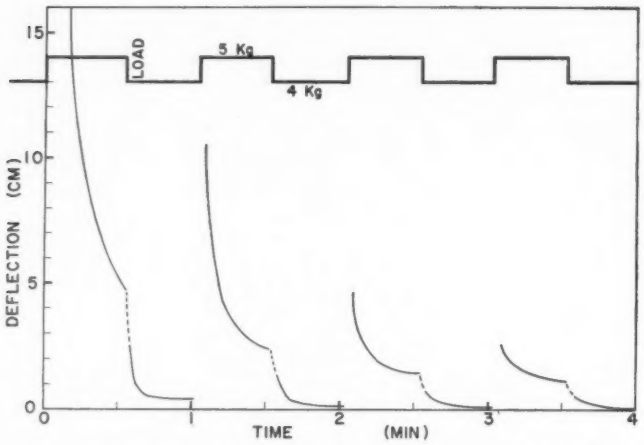

FIG. 3. Effect on the deformation-induced charge flow (at 25°C) of removing and reapplying a load increment. The loading schedule is indicated by the heavy line at the top of the diagram. The ballistic charges resulting from the four successive applications of the 1-kg increment were approximately 7, 2·7, 1·2, and $0{\cdot}66 \times 10^{-13}$ C respectively. Area of crystal and of stress concentrating plate about 0·9 and 0·2 cm², respectively, in Figs. 3–6.

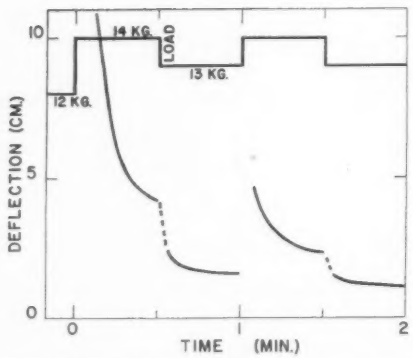

FIG. 4. Effect on the deformation-induced charge flow (at 23°C) of removing only half of the originally applied load increment. Heavy line at top shows loading schedule.

current at these two temperatures. This is in agreement with the results of CAFFYN and GOODFELLOW,[11] who reported that the effect was essentially temperature-independent up to 180°C. There were, however some differences between the effects of deformation at 30 and 90°C. A "jerky" type of charge flow often occurred in the crystal at 90°C, i.e. instead of decaying smoothly with time, the current/time curve obtained at 90°C was interrupted at random intervals by sudden brief rises in the current. These rises were in the same direction as the initial increase on application of the load increment. In addition it was found that deformation by a given load at 90°C hardened the crystal to considerably higher loads for subsequent deformation at room temperature.

(b) *The Transient Effect of Deformation on the Conductivity*

Deformation experiments were also carried out with an electric field applied to the crystal. Sufficient time was allowed, after application of the field, for the conduction current in the crystal to decay to its steady-state value (corresponding to the steady-state conductivity, σ_∞) before the crystal was deformed.

The presence of an applied field does not appear to influence the deformation-induced charge-flow effect resulting from inhomogeneous deformation. Thus, even with an opposing field as large as 10^3 V/cm, the direction of the initial charge flow produced by inhomogeneous deformation is determined by the sense of the stress gradient rather than by the direction of the applied electric field. This statement is illustrated in Fig. 5. Here, the

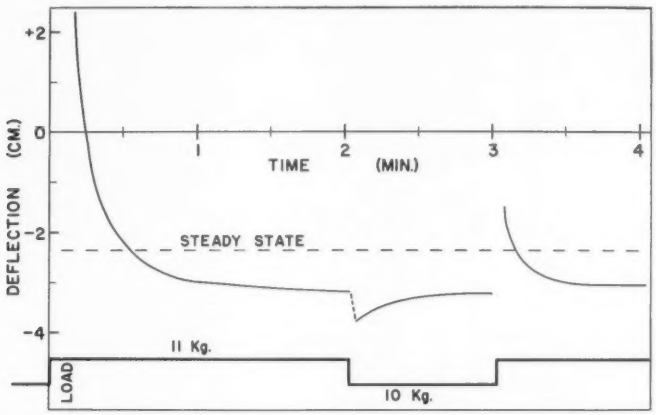

FIG. 5. The effect of inhomogeneous plastic deformation (at 22°C) with an applied electric field directed so as to oppose the deformation-induced charge flow. The electric field alone gives rise to a steady-state conduction current indicated by the dashed line, which corresponds to a conductivity $\sigma_\infty = 2{\cdot}06 \times 10^{-17}(\Omega\text{-cm})^{-1}$. Heavy line at the bottom shows the loading schedule.

stress gradient was in such a direction as to produce a positive deflection on deformation, while the applied field gave rise to a negative deflection. Instead of decreasing with time to its original value prior to deformation (the "steady-state" value in Fig. 5), the current is observed to decay toward a value which corresponds to an increased conduction current. When the load increment producing the deformation is removed, the charge flow due to the inhomogeneous character of the deformation essentially disappears, as demonstrated earlier (see Fig. 3); however, the enhancement of the conduction current produced by the deformation remains, as shown in Fig. 5. An analogous behavior is observed in the case where the stress gradient and the applied field are such as to produce currents in the same direction, as shown in Fig. 6. There are thus two effects superimposed in Figs. 5 and 6: (*a*) the transient charge flow produced by the inhomogeneous deformation, which goes to zero as soon as the load increment that produced the deformation is removed; and (*b*) an increased conduction current, corresponding to a temporary enhancement of the conductivity. The direction of component (*a*) is determined only by the sense of the applied stress gradient, while that of component (*b*) is, of course, determined by the direction of the applied field. This second component is presumed to be the GYULAI–HARTLY effect.

After times which are long compared to the

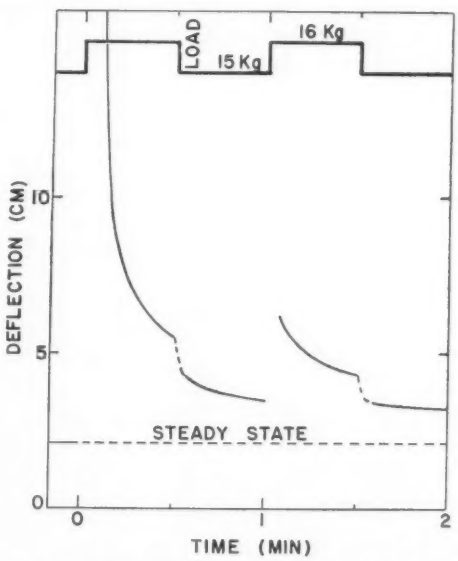

FIG. 6. The effect of inhomogeneous plastic deformation (at 23°C) with an applied electric field directed so as to enhance the deformation-induced charge flow. Loading schedule at top. $\sigma_\infty = 2{\cdot}05 \times 10^{-17}(\Omega\text{-cm})^{-1}$.

scale of Figs. 5 and 6, the conductivity decays back to the steady-state value which existed prior to the deformation. (The cold work produced in these experiments was not sufficient to cause any noticeable change in the steady-state value of the conductivity of the type that occurs for more heavily deformed specimens.[12]) In these experiments, only the tail of the GYULAI–HARTLY effect was observed, since the increase in conductivity immediately after application of the load was generally masked by the deformation-induced charge flow. Fig. 7 shows that the time-dependence of the conductivity increase appears to be of the form of equation (1) with n approximately equal to unity (i.e. roughly hyperbolic). Although the deformation in this experiment was not intentionally inhomogeneous, the existence of the deformation-induced charge flow is indicated by the sudden drop in current when the load increment was removed.* Even with the relatively small deformations employed in these measurements, the observed conductivity at 30 sec after deformation was higher than that prior to deformation by about a factor of two. As much as an hour was required for the conductivity to return to its original value at room temperature.

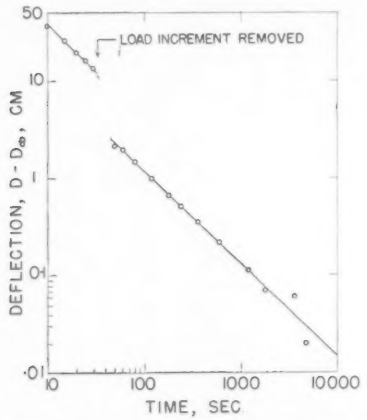

FIG. 7. Time-dependence of the conductivity increase following plastic deformation at 30·5°C. A load increment of 7 kg was applied at $t = 0$ (bringing total load to 9 kg) and removed after 30 sec. D_∞ is the steady-state deflection (= 1·90 cm) corresponding to $\sigma_\infty = 4{\cdot}67 \times \times 10^{-17}(\Omega\text{-cm})^{-1}$. Crystal area approximately 0·6 cm².

The present experiments show that a transient increase in the conductivity is produced when a crystal is deformed after it has reached the steady-state value, σ_∞. The question therefore arises as to whether this increase may be ascribed to a change in the state of the space-charge polarization in the crystal produced by the deformation, rather than to a change in σ_∞. As stated in the Introduction, STEPANOW[3] concluded from his experiments that the transient effect of deformation was not associated with the polarization phenomenon. To confirm this conclusion, the writers repeated experiments similar to those performed by STEPANOW. An unpolarized crystal was first deformed and the load removed immediately, after which an electric field was applied. The transient charging current observed in this experiment was considerably larger than that observed in an undeformed crystal; therefore, even in an unpolarized crystal, deformation apparently produces a conductivity increase. When the discharge current was then observed on shorting the polarized crystal, it was found to be essentially unchanged from the case of the undeformed crystal. The discharge current was in fact, unchanged both for the case of deformation before application of the field, and for deformation just prior to shorting the polarized crystal. These results show that deformation, at the stress levels used in the present experiments, does not disturb the space charge polarization process in the crystal, but rather produces a true enhancement of the steady-state conductivity.

4. DISCUSSION

(a) *The* GYULAI–HARTLY *Effect*

The results described in Section 3(b) confirm the existence of a transient increase in the conductivity produced by plastic deformation (the GYULAI–HARTLY effect). SEITZ[6] has ascribed this enhancement of the conductivity by deformation to the generation of excess free vacancies by the motion of dislocations during the deformation. It was observed here that a conductivity increase of the order of a factor of two remained at 30 sec after deformation by a stress of the order of 10^7 dynes/cm² at room temperature (e.g. see Fig. 7). In Appendix I it is shown that the room-temperature concentration of free positive-ion vacancies in

* The birefringence pattern in the strained crystal confirmed the fact that the deformation actually occurred inhomogeneously.

VOL. 5 1958

the undeformed crystals used in this work appears to be of the order of $10^{15}/cm^3$. Thus, to increase the conductivity by a factor of two, about $10^{15}/cm^3$ free positive-ion vacancies must be produced by the deformation. If it is assumed that a dislocation density of about $10^9/cm^2$ contributes to the deformation, we conclude that of the order of one positive-ion vacancy must be produced for about 30 ionic lengths of dislocation line active in the deformation process. Actually, the *instantaneous* conductivity increase (immediately after deformation) was probably in excess of a factor of ten, which corresponds to roughly one vacancy for each ionic length of dislocation line. Such an estimate seems unreasonably high, even if it is reduced somewhat by assuming a larger effective dislocation density. Another diffculty for SEITZ's interpretation appears when one considers the experiments of CAFFYN and GOODFELLOW.[11] These authors reported that the magnitude of the GYULAI–HARTLY effect varies widely with the source of the crystal and that no enhancement of the conductivity at all is produced by deformation of some (presumably very pure) crystals. This result is difficult to understand in terms of the geometrical mechanisms of vacancy generation which SEITZ has proposed as the source of the enhanced conductivity.

It is well known that in crystals of average purity the positive-ion vacancy concentration (which controls the conductivity) is determined, at temperatures below about 500°C, principally by the concentration of divalent positive-ion impurities in the crystal; each such impurity ion brings with it a cation vacancy to preserve electrical neutrality of the crystal. Furthermore, a considerable fraction of these vacancies may be bound to the impurity ions to form associated complexes at room temperature, and are therefore not free to participate in the conduction process.[5] In fact, although the number of positive-ion vacancies introduced by the probable impurity content is at least of the order of $10^{17}/cm^3$ in the crystals used in this investigation, association is so nearly complete that the concentration of free cation vacancies which contribute to the conductivity is probably only of the order of $10^{15}/cm^3$ (see Appendix I). This estimate, together with the observations of CAFFYN and GOODFELLOW, suggests that the conductivity increase produced by deformation may be due in large part to vacancies freed by the breaking-up of associated complexes by moving dislocations. The period of about an hour required for the complete decay of the excess conductivity at room temperature is a reasonable time for the recombination of vacancies with impurity ions to form complexes, in view of the estimated jump time ($\sim$ 1 sec) for cation vacancies in NaCl at room temperature.[5] Further experimental investigation of the relationship between the magnitude of the GYULAI–HARTLY effect and the impurity content is required to evaluate this interesting possibility.

As mentioned in the Introduction, TYLER[7] has suggested that at least a part of the GYULAI–HARTLY effect may be due to the release of electrons into the conduction band by deformation. The long time for the decay of the effect could then reasonably be explained only on the assumption that there is a continuous production of free electrons through the action of a time-dependent deformation process (creep). This suggestion is refuted by the present experiments, which show that a substantial portion of the enhanced conductivity remains when the load increment producing the deformation is removed, so that appreciable creep surely could not be taking place. It appears hard to believe, therefore, that the long-time effect could be electronic in origin.

(b) *The Deformation-Induced Charge Flow*

The experiments described in Section 3 show that the charge flow observed, when NaCl crystals are deformed in the absence of an applied electric field, has the following characteristics:

(*a*) It is associated with inhomogeneous plastic deformation, the direction of the transient current being determined by the sense of the applied stress gradient (see Fig. 1).

(*b*) The transient current decays with time in an approximately hyperbolic manner, and is observable for a time of the order of minutes when the stress increment which produced it is left on (Fig. 2).

(*c*) The current drops almost to zero abruptly when the stress increment which produced it is removed (Fig. 3). In this case, a greater current is observed on reloading than for the case in which the original current had been allowed to decay to zero with the deforming load on.

(*d*) The magnitude of the current that flows at a given time after deformation by a given stress increment decreases slowly with increasing total stress (Fig. 2).

(*e*) The current is insensitive to temperature, at least in the range between room temperature and 100°C.

(*f*) The deformation-induced current is observed even with an opposing applied electric field of 10^3 V/cm (Fig. 5).

These characteristics are sufficient to eliminate from consideration several readily conceived explanations for the effect and to suggest a model which appears capable of explaining the observations. For example, the effect might be regarded as due to a potential difference between the two sides of the crystal which originates either in a contact potential difference or in thermal effects due to the deformation. The experiment with the electrodes parallel to the axis of applied stress tends to eliminate such possibilities. More convincing, however, is characteristic (*f*) which shows that the deformation-induced charge flow is a *current* flow and not a voltage effect, since it seems inconceivable that potential differences of the order of 100 V or higher can be developed between the two faces of the crystal by deformation.* Finally, characteristic (*c*) is also difficult to account for in terms of thermal or contact potential differences. Therefore, it appears that the charge flow produced by inhomogeneous deformation must be attributed to some mechanism occurring within the volume of the crystal.

In order to produce the observed current flow in the external circuit, charge must be separated within the crystal by the deformation. The external charge flow may be conveniently divided up into an initial (almost instantaneous) effect, which accompanies the initial plastic deformation and is responsible for the ballistic throw, and a longer time effect which provides the decreasing current over a period of minutes. The possibility that the time effect could be due to a recombination of charges separated in the crystal by the initial deformation is ruled out by the fact that both the ballistic and the residual currents are in the same direction. It must therefore be concluded that the time effect must involve a continuing charge separation in the crystal in the manner of the initial effect. From the fact that removal of the load increment stops the time effect without producing a substantial reverse current, it must be concluded that the charges separated while the full load was on recombine only very slowly, if at all. Thus, unlike the space-charge polarization under an applied electric field, the charge displacements in the present case are relatively permanent.

One type of mechanism for the time effect is one in which free charges generated by the initial deformation, may be caused to separate under the influence of the *elastic* stress gradient in the crystal. A specific mechanism of this type is the diffusion in the stress gradient of free vacancies produced by the initial deformation. This type of mechanism does not seem to be capable of explaining the observed disappearance of the deformation-induced current on removing the increment of stress responsible for the deformation. For example, in Fig. 3 it is seen that a decrease in load of 20 per cent causes an immediate drop of at least 90 per cent in the observed current; a similar large decrease in current is observed even when the change in stress is less than 10 per cent (at higher total loads). (See, for example, Fig. 4.) Thus, the effect of removal of the stress increment on the current is far out of proportion to the change in elastic stress produced. Therefore, it appears that if free charges are generated only on the initial (instantaneous) deformation, the inhomogeneous elastic stress field cannot account for their separation with increasing time. Accordingly it must be assumed that a continuing separation or generation of free charge in the crystal must take place through a creep process which follows the initial deformation.

Let us consider as possible charge carriers either vacancies or electrons and holes. In neither case does it seem possible that continuous creep could provide a means for separation of the charge carriers if they are generated only upon the initial instantaneous plastic deformation. It is therefore necessary to assume that these charge carriers are continuously generated during creep following the deformation and separated through the action of

* The fact that the effect is a current flow rather than a voltage effect was clearly established by additional experiments of P. SUTTER (Yale University) who showed that a decrease in R_g (Fig. 1) by a factor of ten reduced the electrometer output by the same factor.

VOL. 5 1958

the elastic stress gradient. In view of the low creep rate of NaCl at room temperature, however, there may not be sufficient dislocation kinetic energy to generate free charges in the creep process. Another serious drawback to the assumption that vacancies or free electrons are generated in creep and moved by the inhomogeneous elastic stress field is that the predicted direction of current flow is then opposite to that actually observed. For the case of vacancies as charge carriers, the calculations of MOTT and LITTLETON[15] show that the lattice of NaCl is expanded in the vicinity of a vacancy. Vacancies would therefore be expected to diffuse away from the region of high compressive stress. Since only the positive-ion vacancy is mobile, and it has an effective negative charge, this model predicts a flow of negative charge in the external circuit toward the side of the crystal on which the compressive stress is a maximum. The observed current flow is opposite to this prediction. An electron in the conduction band of NaCl may be thought of as a sodium atom which exists temporarily when the electron is held by a given sodium ion. Since the sodium atom is considerably larger than the sodium ion, electrons would also be expected to flow away from the highly compressed region of the crystal, contrary to the observed current direction.

The most satisfactory type of model for the deformation-induced charge flow is one which provides for the generation of free charges only by the initial instantaneous deformation and the subsequent separation of these charges with time under the influence of the increment in stress, in such a way that positive charge flows away from the region of high compressive stress and into the crystal. The only suitable charge carrier to fit this description appears to be the electrically charged dislocation. SEITZ[16] has pointed out that jogs on edge dislocations lines in NaCl may have an effective charge of $\pm e/2$, the sign depending on whether the jog occurs at a positive or negative ion. (Both charged and uncharged jogs may exist, as discussed in Appendix II.) In the normal state of the crystal, a dislocation line is expected to have as many negative as positive jogs and therefore to be electrically neutral. However, when a dislocation line is in motion, vacancies may be "evaporated" at a jog, thereby changing the sign of the charge at the jog. Thus, when a negatively charged jog generates a positive-ion vacancy, it becomes a positively charged jog.* A dislocation in motion may be expected to have equal numbers of negative and positive jogs only if cation and anion vacancies are formed with equal ease. The calculations of MOTT and LITTLETON[15] indicate, however, that the energy required to form a negative-ion vacancy is somewhat larger than that required to form a positive-ion vacancy. Therefore, a moving edge dislocation line may be expected to acquire a net positive charge due to the preferential loss of positive-ion vacancies from jogs. Since these positively charged dislocations move into the crystal from the regions of stress concentration leaving behind a net excess of (negatively charged) cation vacancies, this model correctly predicts the sign of the observed charge flow. It will be shown below that it also explains qualitatively the other characteristics of the phenomenon.

When a load is applied to the crystal, large numbers of dislocations carrying a net charge, are generated and set in motion in the region of high compressive stress. Initially these dislocations have a high kinetic energy, but as they move into regions of lower stress they may be expected to slow down and finally to become stuck at obstacles. Further motion of the dislocations, which leads to further charge separation, will then be a time-dependent (creep-type) motion. The immediate cessation of the current flow on removing the stress increment which produced the deformation is explained by the fact that the creep motion of dislocations is very strongly stress-dependent (i.e. it is a highly nonlinear phenomenon). When the load increment is reapplied, the creep deformation resumes and a current is again produced in the external circuit. If the load is left on, the charge flow continues until the charged dislocations have either moved completely across the crystal or become permanently stuck at obstacles. Removal and reapplication of the load increment at this stage would be expected to produce little further effect, in agreement with the observations. The occasionally observed small negative deflection which occurred on removing the load may be attributed to the sliding back of dislocations which have piled up at obstacles.

* Charged jogs may also be formed through dislocation intersections, as shown in Appendix II. On the other hand, in the case of an intersection mechanism, the number of positive and negative jogs should be the same.

The observed total charge flow produced by a 1 kg/cm^2 stress increment in a slightly cold-worked crystal is of the order of 10^{-12} C, or about 10^7 electronic charges. If it is assumed that the crystal has a dislocation density of 10^8/cm^2, the specimen crystal (with volume $1\times1\times0{\cdot}1$ cm^3) contains about 10^7 cm of dislocation line, or about 10^{15} ionic lengths of dislocation line. Thus, on the average, only one site in each 10^8 along the dislocation line carries a net positive charge. Actually, only those dislocations located in the small volume of the crystal where the stress is concentrated will participate, but here we expect the density of dislocation lines to be higher owing to the operation of dislocation sources in the high stress field. Thus, if only 10^{-3} of the total crystal volume is involved and the dislocation density in this region is of the order of 10^{10}/cm^2, we still find that about one dislocation site in 10^7 carries a net charge, an estimate which is not unreasonable.

It seems likely that deformation-induced charge-flow phenomenon contributed in some degree to many of the early observations on the effect of plastic deformation on the conductivity of alkali halide crystals, though no one except STEPANOW appears to have suspected it. The effect should be particularly prominent in experiments at low and medium applied stresses, where the actual conductivity enhancement is relatively small and the chance of stress inhomogeneities large. For example, KASSEL's observations that either an increase or a decrease in conductivity, with a very short decay time, could be produced by deforming rock salt in tension are easily understood in this way. It is also possible that a significant part of the observations of GYULAI and HARTLY were a result of the deformation-induced charge flow. This possibility is indicated, first, by the reported enhancement of the current increase by means of intentionally inhomogeneous deformation,[1] and second, by the fact that for most of the crystals deformed by GYULAI and HARTLY, the conductivity increase was observed only in the early stages of the deformation and no longer appeared for high loads. This is the behavior which would be expected for unintentionally inhomogeneous deformation. It is necessary to assume, however, that due to some peculiarity in their apparatus, the stress gradient was always in such a direction that the sign of the deformation-induced current was the same as that of the conduction current.

Although the concept of the generation of free vacancies by dislocation motion may prove inadequate to account for the GYULAI–HARTLY effect (as discussed in Section 4a), its application to the deformation-induced charge flow apparently provides the only reasonable mechanism. There are two reasons why the concept of dislocation-produced vacancies works well in describing one phenomenon and not the other. First, the excess number of vacancies which are required to account for the deformation-induced charge flow is considerably less than that required for the GYULAI–HARTLY effect. For example, even if the *excess* of positive-ion over negative-ion vacancies is only 1 per cent, the total number of vacancies which must be generated to account for the deformation-induced charge flow is only 10^{-5} of that required to account for the GYULAI–HARTLY effect. Second, even if the vacancies generated in the deformation-induced charge flow are left in the form of large (immobile) clusters, the effect would be observed, since it is the *dislocations* which are the mobile charge carriers. In the case of the GYULAI–HARTLY effect, on the other hand, only mobile aggregates (presumably, only single or paired vacancies) can produce the effect.

Acknowledgements—One of the authors (D.B.F.) held a Du Pont Graduate Fellowship in Physics during part of this work.

This paper represents part of a dissertation submitted by D. B. FISCHBACH for the degree of Doctor of Philosophy at Yale University.

APPENDIX I

The concentration of charge carriers, n, may be calculated from the measured conductivity value, σ, using the expression $\sigma = ne\mu$ if the mobility, μ, is known (e is the electronic charge). In principle, μ for NaCl may be determined by measuring σ of crystals containing known concentrations of divalent positive-impurity ions. Each such impurity ion brings with it into the crystal a positive-ion vacancy to maintain electrical neutrality of the crystal. Since the impurity concentration is normally large compared with the concentration of vacancies in thermal equilibrium in a pure crystal (for temperatures below about 600°C), the quantity n should be equal to the measured impurity concentration. Actually, even in this low temperature region, n is a function of temperature due to the formation of associated complexes consisting of positive-ion vacancies and multivalent positive-

impurity ions. However, the amount of association decreases with increasing temperature; therefore, in the range just below the knee of the plot of $\ln\sigma$ versus $1/T$, the assumption that n equals the divalent impurity content may be expected to be most reliable. BEAN[17] has found that the mobility of positive-ion vacancies in the region $550° < T < 680°C$ in NaCl crystals doped with cadmium is given by

$$\mu = 6{\cdot}5 \times 10^5/T \exp(-\epsilon/kT),$$

where $\epsilon = 0{\cdot}78 \pm 0{\cdot}02$ eV. Using this expression for μ and data on the initial conductivity (before space-charge polarization develops) near room temperature of a sample of Harshaw NaCl, the number of free positive-ion vacancies is found to be of the order of $10^{15}/cm^3$. On the other hand, spectrographic analyses of several samples of Harshaw NaCl, published by DUERIG and MARKHAM,[18] indicate that there probably is of the order of 10^{17} to $10^{18}/cm^3$ of positive-ion vacancies due to the divalent and trivalent positive-ion impurity content of the crystal. The discrepancy between these two estimates indicates a high degree of association at room temperature.

APPENDIX II

It is necessary to distinguish between two types of jogs in edge dislocation lines in NaCl:

(*a*) What may be called a "full jog", in which the dislocation line jogs a full lattice spacing, i.e. two rows of ions, along the bottom of the extra half plane. The jog height perpendicular to the slip plane is then $a\sqrt{2}/2$, where a is the lattice parameter.

(*b*) A "half jog", in which the dislocation jogs only one row of ions. In this case the jog height is $a\sqrt{2}/4$.

Case (*b*) is the type of jog discussed by SEITZ and will have an effective charge of $\pm e/2$. In case (*a*) the jog will have a dipole field, but no net charge. Both types of jog may be produced by diffusion. Either type of jog may also be produced by the intersection of two dislocation lines, the resulting jog type depending upon the details of the intersection.* In NaCl, the slip plane is (110) and the slip direction $[1\bar{1}0]$; thus slip planes intersect both normally and obliquely. According to READ,[20] when two dislocations intersect, the jog acquired by each is equal to the component perpendicular to its own slip plane of the Burgers vector of the other dislocation. Then it follows that type-(*a*) jogs will result from an intersection of an edge dislocation with a screw dislocation on a perpendicular slip plane. For example, consider an edge dislocation in the (110) plane with Burgers vector $\boldsymbol{b} = a/2[1\bar{1}0]$ cutting a screw dislocation in the $(1\bar{1}0)$ plane with $\boldsymbol{b} = a/2[110]$. Type-(*b*) jogs, which are of interest here, are produced by an intersection of an edge dislocation with a dislocation (either edge or screw) on a slip plane which intersects that of the first dislocation obliquely. An example of this is an edge dislocation on the (110) plane with $\boldsymbol{b} = a/2[1\bar{1}0]$ intersecting either a screw or an edge dislocation on the (011) plane with $\boldsymbol{b} = a/2[0\bar{1}1]$.

* SEEGER has stated[19] that only jogs of type (*a*) may be formed by the intersection of dislocations, but the discussion which follows shows that his statement is incorrect.

REFERENCES

1. GYULAI Z. and HARTLY D. *Z. Phys.* **51,** 378 (1928).
2. BOROS J. and GYULAI Z. *Z. Phys.* **96,** 355 (1935).
3. STEPANOW A. W. *Phys. Z. Sowjet.* **4,** 609 (1933); *Z. Phys.* **81,** 560 (1933).
4. KASSEL M. *Z. Phys.* **90,** 287 (1934).
5. See, for example, SEITZ F. *Rev. Mod. Phys.* **27,** 7 (1954) especially pp. 11–26.
6. SEITZ F. *Phys. Rev.* **80,** 239 (1950); *Advances in Phys.* **1,** 43 (1952).
7. TYLER W. W. *Phys. Rev.* **86,** 801 (1952).
8. GYULAI Z. and BOROS J. *Math. naturw. Anz. Ungar Akad. Wiss.* **59,** 115 (1940).
9. JOHNSTON W. G. *Phys. Rev.* **98,** 1777 (1955).
10. BURMEISTER J. *Z. Phys.* **148,** 402 (1957).
11. CAFFYN J. E. and GOODFELLOW T. L. *Nature (London)* **176,** 878 (1955).
12. FISCHBACH D. B. and NOWICK A. S. *J. Phys. Chem. Solids* **2,** 226 (1957).
13. DUBRIDGE L. A. *Phys. Rev.* **37,** 392 (1931).
14. FISCHBACH D. B. and NOWICK A. S. *Phys. Rev.* **99,** 1333 (1955).
15. MOTT N. F. and LITTLETON M. J. *Trans. Faraday Soc.* **34,** 485 (1938).
16. SEITZ F. *Rev. Mod. Phys.* **23,** 328 (1951).
17. BEAN C. P. *Thesis, University of Illinois* (1952); see ref. 5, p. 12–14.
18. DUERIG W. H. and MARKHAM J. J. *Phys. Rev.* **88,** 1043 (1952).
19. SEEGER A. *Report on the Conference on Defects in Crystalline Solids* p. 391. The Physical Society, London (1955).
20. READ W. T. *Dislocations in Crystals* p. 85. McGraw Hill, New York (1953).

J. Phys. Chem. Solids Pergamon Press 1958. Vol. 5. pp. 316–327.

STUDIES ON THE LOWER OXIDES OF TITANIUM*

A. DAVID PEARSON†

Laboratory for Insulation Research,
Massachusetts Institute of Technology, Cambridge, Massachusetts

(*Received* 11 *October* 1957)

Abstract—Pure TiO is face-centered cubic above ~ 950°C. The structure of samples annealed below this temperature is complex, consisting of two or possibly three phases not in equilibrium. Impurities and excess of oxygen stabilize the face-centered cubic form at room temperature. The electrical resistivity of TiO (prepared by melting) is $2{\cdot}81 \times 10^{-4}$ Ω cm at room temperature, and increases with temperature between —162 and 362°C. The thermoelectric e.m.f. of TiO is of the same order of magnitude as that of metals. The measured density is less than the X-ray density, indicating that 14·6 per cent of the lattice positions are unoccupied. The properties of our products suggest that the TiO-phase oxides may be considered solid solutions of oxygen in titanium.

X-ray investigations indicate that Ti_3O_4 probably does not exist.

The trigonal unit cell of Ti_2O_3 between room temperature and 350°C is confirmed. The lattice parameters change rapidly between 160 and 200°C, corresponding to the rapid increase in magnetic susceptibility. Ti_2O_3 is antiferromagnetic; $\chi_m = 1{\cdot}09 \times 10^{-6}$ cgs units at 20°C. The thermal activation energy of electrical conduction of Ti_2O_3 in the room-temperature region is about half of the observed optical activation energy. The material is a *p*-type semiconductor at room temperature.

1. INTRODUCTION

STUDIES on the transition stages from insulators to metals are one of the long-range projects of the Laboratory for Insulation Research. They are being pursued on the VIb group of the Periodic System and on oxides which can be reduced from insulators to metals. Work on titanium dioxide and reduced rutile was started[1] during the war and continued in the investigation of CRONEMEYER.[2] The purpose of the present study is to narrow further the gap between TiO_2 and titanium metal.

Two intermediate oxides, Ti_2O_3 and TiO, have been previously identified with certainty. Ti_2O_3 contains titanium and oxygen ions in their +3 and —2 oxidation states, respectively. The crystal structure is of the α-Al_2O_3 type with a trigonal (also known as rhombohedral) unit cell.[3–5] Measurements of the physical properties indicate a transition near 200°C.[6,7] TiO has hitherto been assumed to be the divalent oxide of titanium. It is reported as having a face-centered cubic, NaCl-type crystal structure, existing over a composition range from $TiO_{0.6}$ to $TiO_{1.25}$, and an experimentally determined density appreciably less than the X-ray density.[3] Heat-content data indicate a transition in TiO at about 990°C.[6]

2. PREPARATION OF TITANIUM OXIDES

(a) *Preparation of titanium monoxide*

The oxides of the TiO phase may be prepared by reduction of titanium dioxide (rutile) with titanium metal:[6,8] $Ti + TiO_2 \rightarrow 2TiO$. The advantage of this method over reduction by carbon, magnesium,[9,10] or calcium,[10] is that it does not introduce foreign substances. The reaction may be carried out either in the solid state, leading to a sintered product, or by melting.

Solid-state reaction. For the preparation of oxides by the reaction of intimately mixed components, pure titanium metal in the form of fine powder was required, but this is not commercially available.

* Sponsored by the U.S. Office of Naval Research, the Army Signal Corps, the Air Force, the Ordnance Materials Research Office and the Atomic Energy Commission; based on a thesis submitted in partial fulfillment of the requirements for the degree of Doctor of Philosophy in Inorganic Chemistry at the Massachusetts Institute of Technology.

† Present Address: Bell Telephone Laboratories, Inc., Murray Hill, N.J.

VOL. 5 1958

For this study small pieces of titanium, chiseled from a bar of the metal,* were heated in an alundum boat placed in a Vycor combustion tube. A stream of pure hydrogen was passed through the tube while the temperature was raised and held at 950°C for 1 hr. After cooling in hydrogen, the material was crushed to small lumps in a diamond-steel mortar, again placed in the combustion tube, and the hydrogen treatment repeated. The hydride, crushed to a fine powder, was completely decomposed at 950°C *in vacuo* in an alundum boat. After being cooled *in vacuo*, the slightly sintered metal was finely powdered and sieved through bolting cloth.

Analysis[11] showed that no contamination by aluminum from the alundum boat had occurred and that the iron content (from the chisel) had increased by only 0·01 per cent.

A stoichiometric mixture of pure, dry titanium dioxide and powdered titanium was pressed at 65,000 lb/in^2 into a disk. This was heated in an alundum boat to 1350°C for 1 hr under a pressure of 10^{-4} mm Hg or less in the ceramic combustion tube of a Globar furnace. After being cooled *in vacuo*, the product was ground, then pressed at 65,000 lb/in^2 into cylinders ($\frac{1}{4}$ in dia$\times\sim\frac{1}{2}$ in long) and refired under the same conditions. A hard, brass-colored solid resulted.

Preparation by melting.† Compressed pellets of pure titanium dioxide were placed, together with a stoichiometric amount of massive pure titanium,‡ in the water-cooled copper crucible of an arc furnace, containing an atmosphere of argon. The titanium melted and reacted quickly with the dioxide, forming the monoxide, which was then remelted several times to ensure homogeneity.

Previous workers[12,13] have shown that the compositions of the products obtained by both methods correspond closely to theory. To confirm this, several analyses were made by oxidizing a weighed amount of the material to titanium dioxide in pure oxygen at 900°C for 45 min (Table 1).

Table 1. *Analysis of titanium–oxygen compounds*

Formula	Percentage Found*
$TiO_{0\cdot95}$	99·9
TiO	98·9
TiO	99·4
Ti_2O_3	99·3

* Accounted for by the observed oxygen uptake.

(b) *Attempted preparation of* Ti_3O_4

BILLY[9] claims to have prepared Ti_3O_4 by reduction of TiO_2 with titanium at 1100–1200°C, and WYSS[10] with magnesium at 750–875°C. Their evidence seems to be restricted to chemical analysis of their products. To check this, an X-ray examination was made of materials with compositions corresponding to Ti_3O_4.

An intimate mixture of the stoichiometric proportions of titanium powder and titanium dioxide was prepared, pressed into a pellet, fired at 1350°C *in vacuo* for 1 hr, ground, repressed, fired again, and furnace-cooled. A powder pattern of the product showed only the diffraction lines of TiO and Ti_2O_3. Two portions of the pellet were then annealed for 1 hr at 1200°C and 4 hr at 750°C, respectively, followed by quenching in cold water. In both cases only TiO and Ti_2O_3 lines were observed.

If a solid homogeneous phase existed in the region of Ti_3O_4, it would have to be bounded on both sides by two-phase regions, one of TiO and Ti_3O_4 and the other of Ti_3O_4 and Ti_2O_3. In this case it would be impossible to obtain an annealed specimen with TiO and Ti_2O_3 present at the same time. Even if Ti_3O_4 existed at high temperatures and disproportionated into TiO and Ti_2O_3 on cooling, the disproportionation products would probably not be homogeneous. The observations that only diffraction lines of TiO and Ti_2O_3 occur, and the sharpness of these lines, seems to exclude the existence of Ti_3O_4.

(c) *Preparation of* Ti_2O_3

Titanium sesquioxide has been prepared by BILLY,[9] SHOMATE,[8] NAYLOR,[6] and LUNDE.[4] All methods involved reduction of titanium dioxide by a reducing agent other than metallic titanium.

* Foote Mineral Co., Philadelphia, Pa., "iodide" titanium, 99·97 per cent pure; in preliminary experiments, a material of the same composition, kindly given by Dr. R. J. WEISS, Watertown Arsenal, was used.

† Thanks are due to Dr. E. P. ABRAHAMSON, Massachusetts Institute of Technology, for making the TiO melts.

‡ Foote Mineral Co., Philadelphia, Pa., "iodide" titanium, 99·97 per cent pure.

In the present work, the sesquioxide has been successfully prepared by reduction of titanium dioxide with the stoichiometric amount of titanium metal, $Ti + 3\ TiO_2 \rightarrow 2\ Ti_2O_3$, in the solid state.

The sintered product is a deep-violet, friable solid which crushes to a fine, deep-violet powder. Analysis by oxidation (Table 1) indicates that the composition is very close to that of Ti_2O_3.

The sesquioxide may also be prepared by melting, but cohesion between the crystals after cooling is not great enough to allow cutting of samples.

3. MEASUREMENTS ON TiO-PHASE MATERIALS

(a) *Structural Features*

(1) *Phase transitions*

TiO is reported to have a face-centered cubic structure.[3,14,15] X-ray powder photographs of samples prepared from pure metal and dioxide did not show this structure more than superficially. The diffraction lines had split into doublets and triplets, and numerous additional faint lines were observed. A series of oxides, $TiO_{0.8}$, TiO, $TiO_{1.05}$, showed these deviations, while $TiO_{1.1}$, $TiO_{1.15}$, and $TiO_{1.2}$ had rock-salt structures. In order to examine the structure of stoichiometric TiO at high temperatures, a pressed pellet contained in an alundum thimble was placed in a quartz ampule, outgassed, and cooled to room temperature. The calculated amount of pure helium to produce 1 atm pressure at the selected annealing temperature was admitted and the ampule sealed. The helium prevents the collapse of the ampule at high temperatures and allows rapid quenching by conducting heat from the sample. After being held at 1350°C for 1 hr, the ampule was cooled in air for 10 sec and then quenched in cold water. A powder photograph of the product showed only the rock-salt pattern.

From heat-content measurements, NAYLOR[6] reported a transition in TiO at ~ 990°C. A series of samples was therefore annealed and quenched from 1100, 1000, 950, 900, and 850°C. These showed sharp rock-salt structure powder patterns for the first three and deviations from this pattern for the last two, indicating a phase transition between 900 and 950°C. WANG and GRANT[16] have since reported this transition; SCHOFIELD and BACON[16] also mention it in their study of the titanium–titanium dioxide phase diagram.

By annealing for 68 hr at 710°C and an additional 68 hr at 780°C, TiO samples were obtained whose powder patterns proved sufficiently strong and sharp to permit accurate calculation of the *d* spacings. We found that addition of ~ 2·5 per cent aluminum to a sample of $TiO_{0.8}$ (which had undergone the phase transition when pure) stabilized the rock-salt structure so that no transition occurred.

(ii) *Structure of* TiO *below* 900°C.

X-ray study. Prolonged efforts to index the diffraction pattern of TiO (quenched from 780°C) by use of Hull–Davey charts and by ITO's[17] method were unsuccessful. It seemed likely that the material was either multiphased or else a single phase of low symmetry.

To ascertain if the material represented a two-phase equilibrium system, a powder pattern of $TiO_{0.95}$ (annealed at 710 and 780°C for 68 hr each) was compared with that of an identically annealed sample of TiO. The intensities of the diffractions, and the fact that there was a change in the *d* spacings, showed that the materials did not represent a two-phase equilibrium system. However, the possibility of a non-equilibrium system of two phases still remained.

Metallographic study. Two samples, cut with a diamond wheel from a melted button of TiO, were annealed, one at 825°C for 250 hr and air-cooled, the other at 1350°C for 1 hr and quenched. A powder photograph of the first sample showed that the transition had taken place. Both samples were metallographically polished, and etched with a solution containing 1 per cent HF, 1 per cent HNO_3, and 2 per cent HCl. The high-temperature material showed a single-phase system of grains (Fig. 1a); the low-temperature material consisted of two types of grains, one apparently the same as the face-centered cubic phase, and the other distinctly darker in color. Within the darker grains a dendritic precipitate was observed which crossed grain boundaries in places, indicating that a recrystallization process had taken place, and adding further evidence for the existence of the phase transition (Fig. 1b). A third sample, annealed at 825°C for 3 hr showed the same grain structure (Fig. 1c) as the 250-hr sample, indicating that longer annealing did not cause further transformation.

VOL. 5 1958

(a) 1350°C for 1 hr. × 100

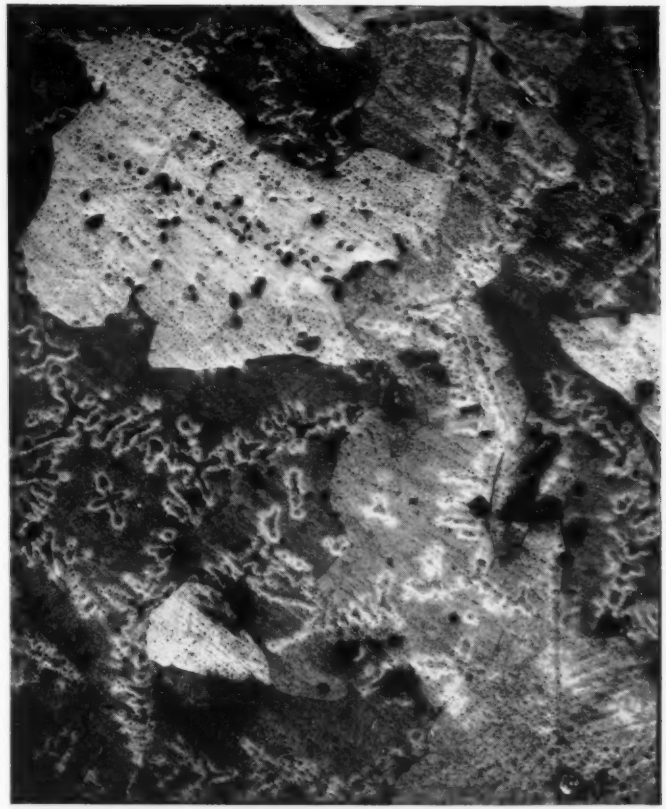

(b) 825°C for 250 hr. × 100

FIG. 1. Titanium monoxide annealing temperatures.

[Facing page 318

VOL.
5
1958

(c) 825°C for 3 hr. × 100.

(iii) *Lattice parameter of* TiO *single crystal*

A fragment ($\sim 0{\cdot}1\times0{\cdot}03\times0{\cdot}03$ mm) from a button of TiO was mounted on a universal goniometer head, and precession-orientation X-ray photographs were taken until a four-fold axis was found. Zero-level precession photographs indicated that the piece was a single crystal of the high-temperature form, face-centered cubic, with $a = 4{\cdot}17 \pm 0{\cdot}005$ Å.

(b) *Electrical Conductivity of* TiO

(i) *Conductivity of* TiO*-phase oxides*

Equipment. The resistivity of TiO was measured on a four-terminal a.c. bridge (Fig. 2). To minimize inductive effects and noise, an 18-cycle/sec oscillator was used, together with a detector of narrow band width. The detector rejected 60 cycles at the ratio of 10,000 to 1; the minimum detectable 18-cycle signal was 2×10^{-8} V. When the resistance across the sample is small in comparison to R_1, and $R_1 \ll R_2$, the resistance R across the probes is given by $R = R_1 \times R_{\text{decade}}/R_2$. The sensitivity of the bridge was 10^{-6} Ω.

The sample-holder (Fig. 3) was enclosed in a Pyrex envelope, closed with a brass end-plate and rubber gasket. Insulated Kovar seals carried the thermocouple and sample-holder connections through the plate, into which was sealed a brass tube connected to the vacuum system. Evacuation of the Pyrex tube permitted resistivity measurements up to 400°C (electric furnace) without surface oxidation. Measurements down to liquid-nitrogen temperature were also made.

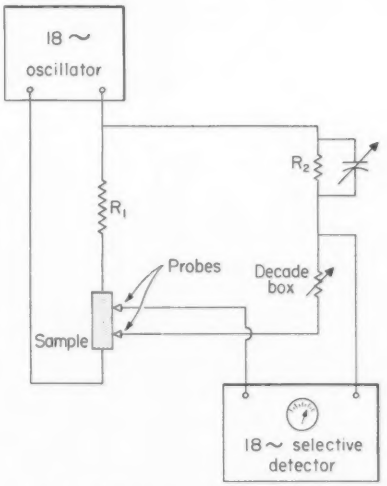

Fig. 2. Four-terminal a.c. bridge.

Resistivity of TiO *versus temperature*. A sample of TiO in the face-centered cubic form was cut from a button made by melting. After it had been mounted in the sample-holder, the resistance across the probes was measured as a function of temperature from −162 to 362°C, with vacuum maintained at 10^{-4} mm Hg for all measurements

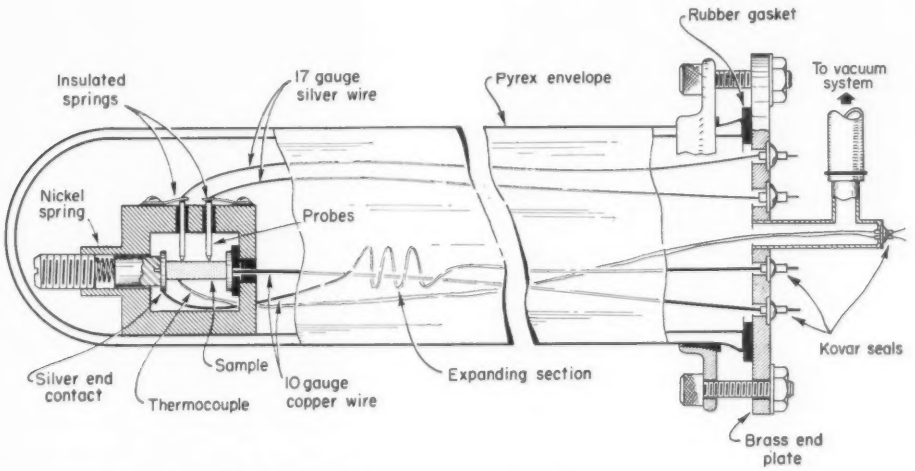

FIG. 3. Sample-holder for resistance measurements.

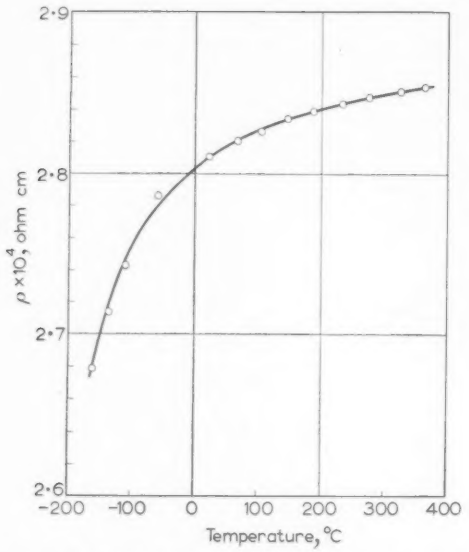

FIG. 4. Resistivity versus temperature characteristic for TiO.

above room temperature (Fig. 4). Although the furnace temperature was raised rapidly between readings, 20 min were allowed at each temperature to ensure thermal equilibrium between sample and sample-holder before measuring the resistance.

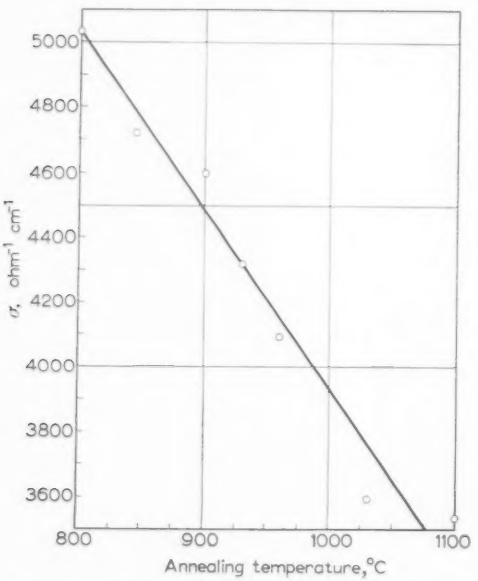

FIG. 5. Effect of annealing on conductivity of TiO.

Effects of annealing on conductivity of TiO. In order to establish the effect of the phase transformation, a series of samples (produced by melting) was sealed in quartz ampules, as previously described and quenched from various temperatures. The resistivities were measured at room temperature and the conductivities were calculated. The results (Fig. 5) show that the phases present below 950°C have conductivities higher than that of face-centered cubic TiO.

Effect of composition on conductivity in the range $Ti \rightarrow TiO_{1.2}$. Four solid solutions of oxygen in titanium metal were prepared by the sintering method from the metal and TiO_2.

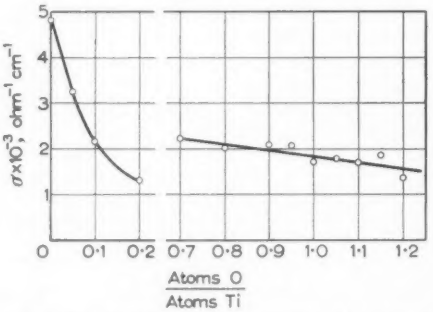

FIG. 6. Conductivity versus composition for sintered titanium oxides.

Nine mixtures of titanium powder with titanium dioxide (ranging from $TiO_{0.7}$ to $TiO_{1.2}$) were also prepared and fired as previously described. The sintered products were annealed at 1200°C for 1 hr and quenched in cold water. The colors of the products ranged from silver with a slight yellow tinge ($TiO_{0.7}$) to bright golden yellow ($TiO_{1.2}$). Conductivities were calculated from the resistances measured at room temperature (Fig. 6).

(c) *Thermoelectric E.M.F. of* TiO

To obtain additional information on electrical conduction in TiO, the thermovoltage was measured by clamping the sample between two copper blocks, one of which was maintained at room temperature while the other was heated electrically. The thermoelectric e.m.f. (Fig. 7), measured with a potentiometer, varies almost linearly with temperature difference, as determined with thermocouples.

The sign of the thermoelectric e.m.f. was the same for oxygen-rich and oxygen-deficient oxides, increasing in magnitude for $TiO_{1\cdot2}$ and decreasing for $TiO_{0\cdot8}$.

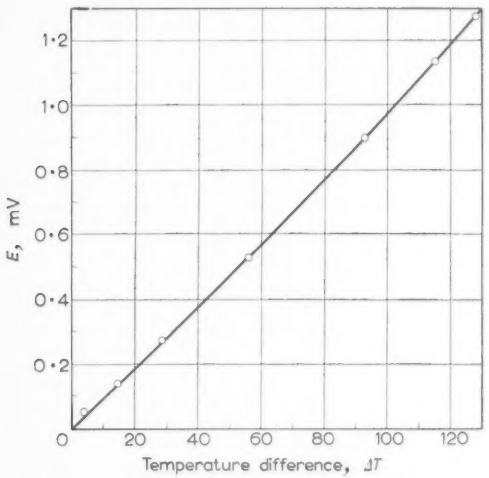

FIG. 7. Thermoelectric e.m.f. of polycrystalline TiO.

(d) *Density of* TiO

The density of the TiO formed by the melting procedure was determined by hydrostatic weighing in ethylene dibromide, using a large single crystal of pure quartz as a standard. The directly determined value is 4·958 g/cm³, while the density calculated from the lattice constant is 5·807 g/cm³, indicating that 14·6 per cent of the lattice positions are unoccupied.

The density of sintered TiO, determined from the sample dimensions and weight, was found to be $\sim$ 4 g/cm³, which probably accounts for the differences in conductivity between sintered and melted materials.

(e) *Discussion of the Results Obtained for* TiO

(i) *Structure of* TiO

The X-ray study on quenched material indicates that pure TiO-phase samples of compositions $< TiO_{1\cdot1}$ undergo a phase transition at about 950°C. Above this temperature, powder and single-crystal data confirm the structure of the phase as face-centered cubic, and for stoichiometric TiO, $a = 4\cdot1807 \pm 0\cdot0003$ Å. The value obtained by EHRLICH[3] was 4·173 Å. Impure samples and samples with an oxygen content corresponding to or greater than $TiO_{1\cdot1}$ do not undergo the transition, but remain face-centered cubic on furnace-cooling from high temperatures.

Microscopic study of metallographically polished and etched samples confirmed that the system below 950°C is a multiphase one. Although two types of grains and a dendritic precipitate have been observed, it is not possible to say whether the system, which does not appear to be in equilibrium, consists of two or three phases. Under these circumstances it is not feasible to index the power patterns, and the new phases precipitated in such fine grains that the selection of a single crystal from fragments proved impossible.

(ii) *General features of face-centered cubic* TiO

In the past TiO has been considered an ionic metal oxide containing Ti^{2+} ions, but in the light of the present results this view must be re-examined. The only other compounds known with any certainty to contain divalent titanium are the dihalides, but these are not easily prepared in a pure state and are somewhat unstable. On the other hand, TiO is easily prepared and may be kept in air at room temperature indefinitely without decomposition or oxidation.

The high conductivity of TiO, coupled with the decrease of conductivity with increasing temperature, indicates near-metallic conduction. Metal oxides which exhibit electronic conductivity are normally semiconductors of appreciably lower conductivity. Another notable exception of very high conductivity is PbO_2, which, with excess lead, behaves nearly like a metal.[18] The thermoelectric e.m.f. of TiO is of the same order of magnitude as that of metals, and the sign of the e.m.f. is the same for oxygen-rich and titanium-rich samples.

If TiO were an ionic crystal containing Ti^{2+}, it might be expected to conduct by means of an electron-transfer process between titanium ions of different valences, which would be present at all times except when the composition is exactly stoichiometric. This type of conduction is seen in magnetite (Fe_3O_4), where electrons may be transferred between the Fe^{2+} and Fe^{3+} ions. In this case stoichiometric TiO would have minimum conductivity, the value of which would increase for moderate departures from stoichiometry toward both the titanium-rich and oxygen-rich regions.

Table 2. Comparison of some physical properties of TiC, TiN, *and* TiO

	TiC	TiN	TiO
Structure	f.c.c.[20]	f.c.c.[20]	f.c.c.* (above 950°C)
a (Å)	4·326[21]	4·234[20]	4·181*
Melting point (°K)	3430[22,23]	3470[22,24]	2020[12,15]
Resistivity (Ω cm)	$1·8–2·5 \times 10^{-4}$[22,23]	$1·3 \times 10^{-4}$[22,24]	$2·8 \times 10^{-4}$*
Temperature coefficient of resistance	Positive[22,23]	Positive[25]	Positive*
Density observed (g/cm³)	4·92[20]	5·22[21]	4·958*
Density calculated (g/cm³)	4·915[21]	5·424†	5·807*

* From author's results. † Calculated by the author.

Experimental results (Fig. 6) show that this is not the case for TiO, and that conductivity decreases steadily from $TiO_{0·7}$ to $TiO_{1·2}$. The conductivities of the samples of titanium metal with oxygen in solid solution are of the same order of magnitude as those of the TiO-phase materials, even though the oxygen content of the latter is at least five times larger. This is not in conflict with the idea of a metallic structure and hence a similar conduction process in both cases, since the oxygen dissolved in the metal is probably randomly distributed throughout the interstices, but ordered in TiO. As is well known, an ordered arrangement of scattering sites (in this case, oxygen) disturbs the conductivity of a material less than the same number of sites randomly distributed.

In Table 2 some physical properties of TiO, TiN, and TiC are compared. TiC and TiN are considered metallic interstitial compounds, and it is significant to note the similarities of the three substances. Finally, the metallic radius of titanium (1·475 Å) and the atomic radius of oxygen (0·66 Å) would give a lattice parameter of 4·27 Å for the face-centered cubic structure, compared with the measured value of 4·18 Å.

Thus the evidence of the present paper suggests that TiO is close in properties to metals and therefore should probably be classified with the interstitial metal-like materials.

4. MEASUREMENTS ON TITANIUM SESQUIOXIDE

(a) *Crystal Structure*

(i) *Unit cell of* Ti_2O_3

Titanium sesquioxide is reported to have a corundum-type lattice, with two molecules to the trigonal unit cell.[3–5]

To obtain powder photographs with clearly visible and more numerous diffraction lines than had previously been observed, a new developing technique was employed. This process was designed to avoid the effect of the fluorescence of titanium and its compounds under X-ray irradiation from the commonly employed target materials. Normally developed photographs were so badly blackened by the fluorescence that only the strongest diffraction lines could be discerned. Examination of the developed photographs before fixing showed that only the emulsion on the side of the film facing the specimen was blackened, and that the background on the opposite side was low. After scraping off the blackened emulsion and fixing, the diffraction lines were clearly visible. Thus the first layer of emulsion acted as absorber of the fluorescent radiation, while the diffracted X-rays passed through both layers. This technique was later improved by covering the inside surface of the film with masking tape before developing, and removing the tape before fixing.[19] Low-background powder patterns were obtained that showed about twice the number of lines reported by HALLA.[5]

To check the unit cell proposed by HALLA, our pattern was indexed, in the hexagonal system for ease of computation, and the lattice parameters refined by the method of least squares.

The unit cell is trigonal, as previously reported, with parameters $a = 5·428$ Å and $\alpha = 56°39'$. The agreement between calculated and observed d values is good.

(ii) *Effect of temperature on the* Ti_2O_3 *lattice*

A transition has been reported in titanium sesquioxide near 200°C[6,7] on the basis of sharp changes in its heat content, electrical conductivity, and coefficient of thermal expansion, but no structural data to account for this transition have been published.

To obtain X-ray diffraction photographs at elevated temperatures, a powder sample was sealed in a thin-walled Pyrex capillary and heated by a stream of hot air during the exposures. A powder pattern taken at 280°C was indexed completely to check the unit cell. This was still trigonal, and the visually estimated intensity relationships of the lines did not indicate any departure from the room-temperature crystal structure. Powder photographs were then taken at 150, 200, and 350°C, and the d spacings of the 419 and 154 lines calculated for each temperature.

The expression:

$$d = 1\Big/\left[\frac{4}{3a^2}(h^2+k^2+hk)+\frac{l^2}{c^2}\right]^{\frac{1}{2}}$$ for the

hexagonal unit cell was solved simultaneously at each temperature for the hexagonal parameters a and c. The a parameter decreases with increasing temperature, while c increases (Fig. 8 a,b). The angle α of the trigonal cell, calculated as: $\cos\alpha = (-3a_{hex}^2+2c_{hex}^2)/(6a_{hex}^2+2c_{hex}^2)$, decreases as the temperature is raised (Fig. 8c). Thus there is no change in crystal structure to account for the transition near 200°C in Ti_2O_3, but the lattice parameters of the unit cell change rapidly between ~ 160 and 200°C.

(b) *Conductivity of Sintered* Ti_2O_3 *as a Function of Temperature*

The resistance of sintered Ti_2O_3 was measured from liquid-nitrogen temperature to 400°C, using the a.c. bridge and sample-holder previously described. Surface oxidation of the samples proved negligible when the air pressure in the Pyrex envelope was less than 10^{-4} mm Hg. The conductivities are plotted in Fig. 9, which also shows

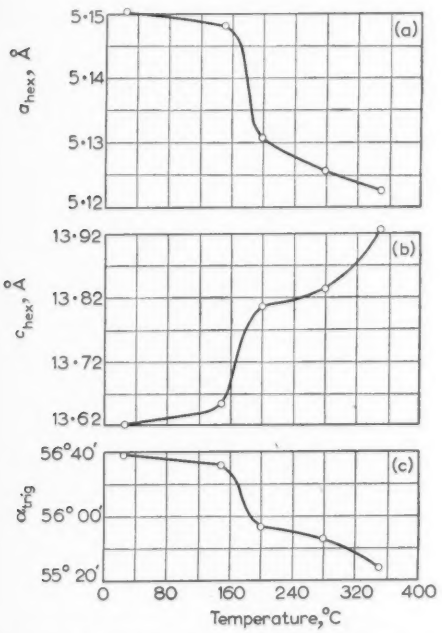

FIG. 8. Lattice parameters of Ti_2O_3 versus temperature: (a) a_{hex}; (b) c_{hex}; (c) α_{trig}.

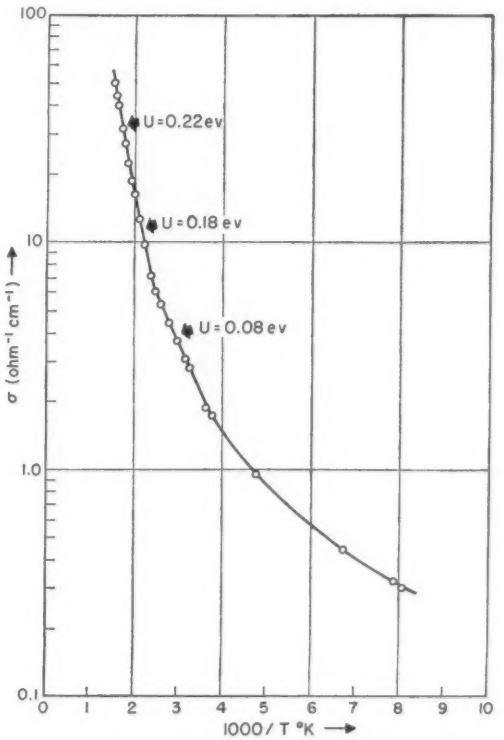

FIG. 9. Conductivity/temperature characteristic for Ti_2O_3.

thermal activation energies. Rough measurements on Ti_2O_3 prepared by melting indicate that its conductivity is much higher than that of the sintered material, but samples for accurate measurements could not be cut.

(c) *Paramagnetic Susceptibility of* Ti_2O_3

EHRLICH[3] reported that all phases of the titanium–titanium dioxide system except pure TiO_2 are paramagnetic. In the hope that the variation in magnetic properties near 200°C might throw further light on the transition in Ti_2O_3, paramagnetic susceptibility measurements were made from —185 to 350°C in a Gouy balance. The equipment was calibrated using ferrous ammonium sulphate ($\chi_{20°} = 32{\cdot}3 \times 10^{-6}$ cgs units) as a standard. The ratio of forces on the Ti_2O_3 and standard under identical field conditions equals the ratio of susceptibilities. Temperatures up to 350°C, maintained by a vertical tube furnace, were measured by thermocouples located above and below the specimen. Up to 100°C, temperature differences between these two points were less than 1° and at 350°C increased to about 10°.

The sample tube was evacuated and sealed to prevent oxidation of the Ti_2O_3 at high temperatures. The force difference between O($H \simeq 8 \times 10^3$ A/m) and full magnet excitation ($H = 5{\cdot}4 \times 10^5$ A/m) was determined from —185 to 350°C. At least 15 min were allowed before each measurement to ensure temperature equilibrium. Several temperature cycles were traversed; the consistency of the results with waiting periods of 15 and 30 min indicates that temperature lag was negligible. The results are shown in Fig. 10.

(d) *Thermoelectric E.M.F. of* Ti_2O_3

The thermoelectric e.m.f. of Ti_2O_3 was measured as described in Section 3(c). The thermoelectric effect for Ti_2O_3 is much larger than for TiO, and, as expected for a semiconductor, shows considerable nonlinearity throughout. The e.m.f./ΔT curve levels off between 100 and 250°C, and decreases beyond this region (Fig. 11). The e.m.f.

VOL. 5 1958

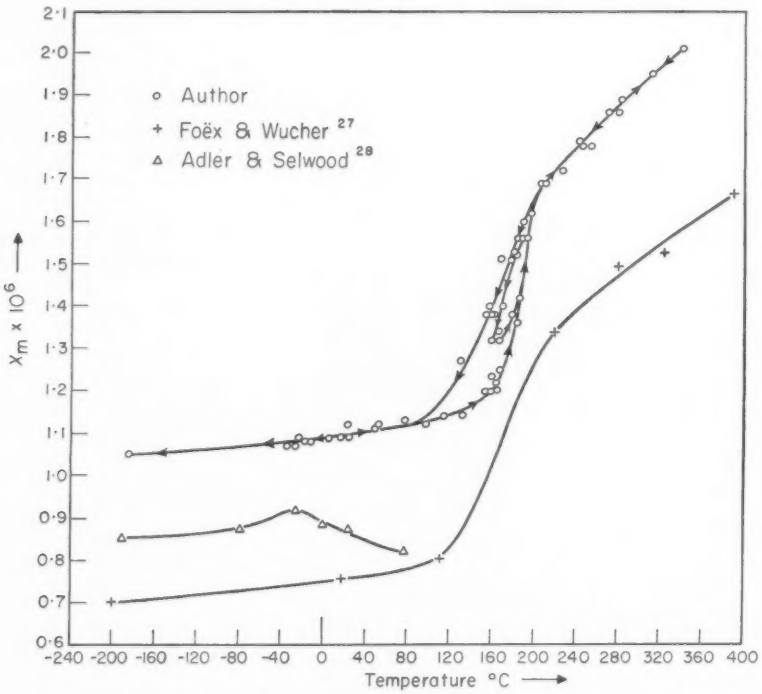

FIG. 10. Magnetic susceptibility of Ti_2O_3 versus temperature.

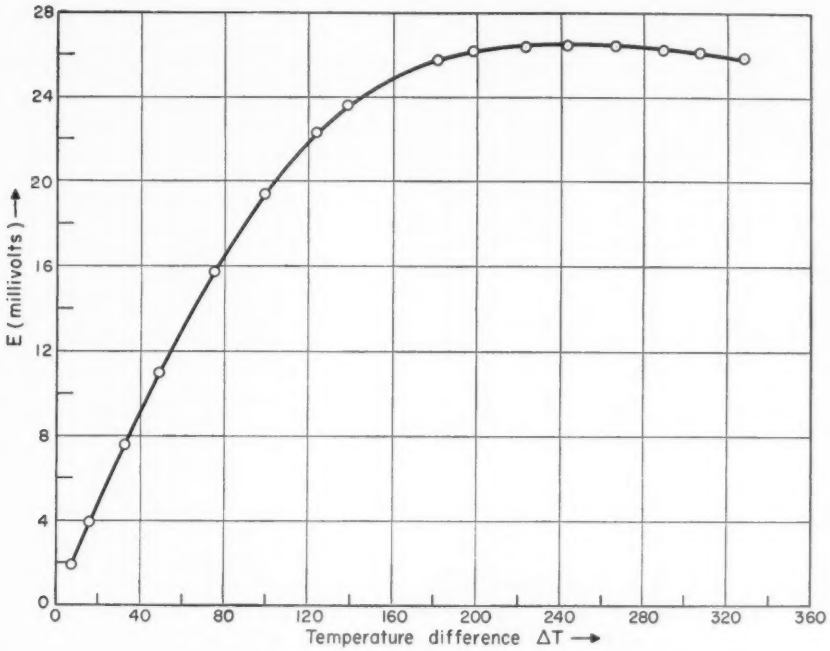

FIG. 11. Thermoelectric e.m.f. of polycrystalline Ti_2O_3.

produced is such that the hot junction becomes negative.

(e) *Spectroscopic Study*

To determine the position of electronic transitions in Ti_2O_3, the absorption spectrum of the material was examined in the visible and infrared regions. For this purpose a mixture of 4 mg of finely powdered Ti_2O_3 and $\sim$ 0·8 g finely powdered potassium bromide was pressed into a disk according to the methods of STIMSON and SCHIEDT.[26] Spectra were recorded in the infrared region on a Beckman IR3 spectrophotometer. In the visible region a Cary 12 M spectrophotometer was used. Fig. 12 shows the absorbance of Ti_2O_3 as a function of frequency. The narrow band at 520 cm^{-1} lies in the region of infrared lattice vibration bands for numerous metallic oxides. The broad, intense band, centered at about 6000 cm^{-1}, probably corresponds to electronic excitations. The optical activation energy calculated from the position of the absorption edge (1200 cm^{-1}) is 0·15 eV.

(f) *Discussion of the Results Obtained for* Ti_2O_3

(1) *Charge carriers*

The rapid increase in the conductivity of Ti_2O_3 with increasing temperature and the room-temperature conductivity of $\sim$ 3 Ω^{-1} cm^{-1} testify that the material is a semiconductor. The logarithmic conductivity plot (Fig. 9) shows the dominance of impurity and imperfection effects from 124 to 266°K. From 266°K to the highest temperature reached (669°K), the plot consists of straight lines, with breaks at about 425 and 500°K. The activation energies U calculated from a Boltzman term $\sigma = \sigma_0 e^{-U/kT}$ are indicated in Fig. 9. The observed thermal activation energy (0·08 eV) for the room-temperature region is therefore about half the optical activation energy (0·15 eV) calculated from the position of the absorption edge.

The thermoelectric effect shows that the semiconductor is dominantly a hole conductor (i.e. p-type) in the region investigated, but that n-type conduction comes in at an increasing rate at higher temperatures. Therefore, a maximum is traversed in the e.m.f./ΔT curve (Fig. 11).

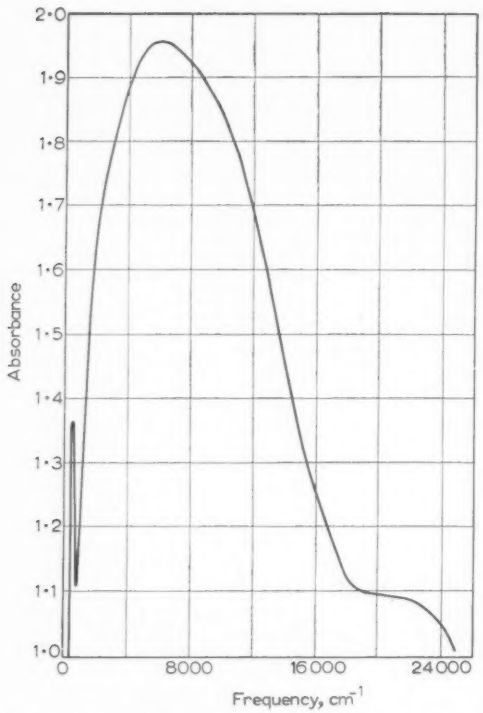

FIG. 12. Absorption spectrum of Ti_2O_3 (1·3 mg/cm² in pressed KBr disk).

(ii) *Structure of* Ti_2O_3

The trigonal unit cell proposed by HALLA[5] is confirmed. X-ray data up to 350°C do not indicate a change in crystal structure, but the lattice parameters change rapidly in the region from about 160 to 200°C.

(iii) *Magnetic properties of* Ti_2O_3

The increase of the magnetic susceptibility χ_m with temperature indicates that the magnetic structure of Ti_2O_3 is ordered, since χ_m decreases with increasing temperature for randomly oriented paramagnetic materials (Curie law). The material is probably completely antiferromagnetic; if any spontaneous moment exists it must be less than 10^{-2} e.m.u.

The susceptibility rises slowly with temperature to ~ 160°C, then increases by ~ 40 per cent to 205°C. From this temperature to 350°C, χ_m continues to increase slowly, but still at a faster rate than is observed at low temperatures. The general form of the curve is therefore similar to that obtained by FOËX and WUCHER.[27] The peak reported by ADLER and SELWOOD[28] was not observed; possibly these authors were dealing with a ferromagnetic impurity.

Detailed study of the transition region indicates that it is a region of rapid change in χ_m rather than a discontinuity. A temperature hysteresis was observed through repeated temperature cycles, and on maintaining the temperature at 160–165°C for periods up to 2 hr, repeated measurements gave values of χ_m differing by 14 per cent, the lower value being obtained during increasing temperature runs and the higher when the temperature was being decreased.

The rapid increase in susceptibility is similar to that observed in Fe_2O_3 at −20°C, where a change in the direction of the magnetic axis takes place.[29] Positive proof of this interpretation in the case of Ti_2O_3 has to await neutron diffraction studies, but it appears to be supported by the fact that the temperature region over which the rapid increase in χ_m occurs corresponds to that in which the lattice parameters of Ti_2O_3 change rapidly.

Acknowledgements—The author is grateful to Professor ARTHUR R. VON HIPPEL for suggesting the problem and for his continuous interest and guidance, and to Professor WALTER C. SCHUMB for his encouragement and advice during the course of this work.

Thanks are also due to Professors DAVID P. SHOEMAKER, NICHOLAS J. GRANT, and CARL W. WAGNER for stimulating discussions and advice.

REFERENCES

1. VON HIPPEL A. *et al. High-Dielectric-Constant Ceramics I and II, N.D.R.C. Rep.* No. 300 (Aug. 1944); No. 540 (Oct. 1945).
   VON HIPPEL A., BRECKENRIDGE R. G., CHESLEY F. G. and TISZA L. *Industr. Engng. Chem.* **38,** 1097 (1946).
   VON HIPPEL A. *Rev. Mod. Phys.* **22,** 221 (1950).
2. CRONEMEYER D. C. *Phys. Rev.* **87,** 876 (1952).
3. EHRLICH P. *Z. Elektrochem.* **45,** 362 (1939).
4. LUNDE G. *Z. anorg. allgem. Chem.* **164,** 341 (1927).
5. HALLA F. *Z. anorg. allgem. Chem.* **184,** 421 (1929).
6. NAYLOR B. F. *J. Amer. Chem. Soc.* **68,** 1077 (1946).
7. FOËX M. and LORIERS J. *C.R. Acad. Sci. (Paris)* **226,** 901 (1948).
8. SHOMATE C. H. *J. Amer. Chem. Soc.* **68,** 310 (1946).
9. BILLY M. *Ann. chim.* **16,** 5 (1921).
10. WYSS R. *Ann. chim.* **3,** 215 (1948).
11. FEIGL F. and STERN R. *Z. anal. Chem.* **60,** 1 (1921).
    THOMPSON J. M. *Analyt. Chem.* **25,** 1231 (1953).

VOL. 5 1958

12. BUMPS E. S., KESSLER H. D. and HANSEN M. *Trans. Amer. Soc. Metals* **45,** 1008 (1953).
13. GRANT N. J. Private communication.
14. BRÄKKEN H. *Z. Krist.* **67,** 547 (1928).
CARSTENS C. W. *K. Norske Vidensk Selsk. Forhandl.* I, 1926–28, Medd. No. 20, 56 (1929).
15. DAWIHL W. and SCHRÖTER K. *Z. anorg. allgem. Chem.* **233,** 178 (1937).
16. WANG C. C. and GRANT N. J. *J. Metals* **8,** 184 (1956).
SCHOFIELD T. H. and BACON A. E. *J. Inst. Metals* **84,** 47 (1955).
17. ITO T. *X-Ray Studies on Polymorphism* Appendix VII Maruzen Co., Tokyo (1950).
18. THOMAS U. B. *Trans. Electrochem. Soc.* **94,** 42 (1948).
19. PARRISH W. *Norelco Reporter* **2,** No. 4, 67 (1955).
20. EHRLICH P. *Z. anorg. allgem. Chem.* **259,** 1 (1949).
21. SKINNER G., JOHNSTON H. L. and BECKETT C. *Titanium and its Compounds* JOHNSTON Enterprises, Columbus, O. (1954).
22. FRIEDRICH E. *Z. Phys.* **31,** 813 (1925).
23. FRIEDRICH E. and SITTIG L. *Z. anorg. allgem. Chem.* **144,** 169 (1925).
24. FRIEDRICH E. and SITTIG L. *Z. anorg. allgem. Chem.* **143,** 293 (1925).
25. MOERS K. *Z. anorg. allgem. Chem.* **198,** 262 (1931).
26. STIMSON M. M. and O'DONNELL M. J. *J. Amer. Chem. Soc.* **74,** 1805 (1952); SCHIEDT U. and REINWEIN H. *Z. Naturforsch.* **7b,** 270 (1952); *Appl. Spectrosc* **7,** 75 (1953).
27. FOX M. and WUCHER J. *C.R. Acad. Sci. (Paris)* **241,** 184 (1955).
28. ADLER S. F. and SELWOOD P. W. *J. Amer. Chem. Soc.* **76,** 346 (1954).
29. SHULL C. G., STRAUSER W. A. and WOLLAN E. O. *Phys. Rev.* **83,** 333 (1951).

J. Phys. Chem. Solids Pergamon Press 1958. Vol. 5. pp. 328–336.

THE EFFECT OF PRESSURE ON COLOR CENTERS IN ALKALI HALIDE CRYSTALS*

W. G. MAISCH and H. G. DRICKAMER

Department of Chemistry and Chemical Engineering, University of Illinois, Urbana, Illinois

(*Received* 28 *October* 1957)

Abstract—The absorption spectra of both X-irradiated and additively colored alkali halides have been studied under pressure up to 50,000 atm. These experiments were conducted at room temperature and, with a few exceptions, only those bands occurring in or near the visible region of the spectrum were studied. Frequency shifts and bleaching effects, the latter induced both by radiation and by plastic deformation, were observed. An apparently new band, intimately related to the *F* center and appearing at the expense of the *F* band, has been studied.

Several related experiments were run at 1 atm. It has been shown that atmospheric oxidation is one of the mechanisms responsible for the bleaching of plastically deformed crystals.

VOL. 5 1958

1. INTRODUCTION

In recent years there have been several investigations[1] of the effect of pressure and plastic deformation on the spectra of colored alkali halides. Jacobs[1] studied the shift of frequency of the *F* band with pressure to 8000 atm, using a silicone liquid as the pressure-transmitting fluid. He found that a plot of log ν_m versus log a gave a straight line for all seven salts studied. (ν_m = frequency of maximum absorption, a = lattice parameter.) These results were independent of the method of coloration of the crystal. In a treatment relating the pressure and temperature coefficients of the dependence of ν_m on a, Jacobs concluded that the former depends only on local interionic distance, at the *F* center while the latter also is influenced by interaction of the *F* center electron with the optical vibration of the lattice.

Kiyama *et al.*[2] have studied the after-effects of hydrostatic pressure and of plastic deformation on the frequency, band width, and bleaching characteristics of the *F* band, and the frequency of the colloid band, using electrolytically colored crystals.

They found that after releasing hydrostatic pressure there was a blue shift and a broadening of the *F* band which diminished with time. ν_m for the colloid band shifted to the blue. The production of *R* and *M* bands by bleaching with light in the *F* center region is enhanced after compression. In KI the band at 5200 Å increases with exposure to light. (The 5200 Å band appeared before compression in paper 5, after compression in paper 3.)

After plastic deformation at 5000 kg/cm², the *F* band in NaCl was stable, but in KCl, KBr, and KI it diminished with time in the dark. Electrolytically colored NaCl annealed at 400°C and plastically deformed material showed some formation of the *F* and *M* bands at the expense of the colloid band. After plastic deformation, NaCl crystals colored more rapidly when exposed to ^{60}Co. They also bleached more rapidly when exposed to *F* light.

2. EXPERIMENTAL PROCEDURE

This paper presents the results of optical studies to 50,000 atm on the spectra of both X-irradiated and additively colored crystals. Spectral shifts were measured on both types, while the bleaching experiments were performed on the additively colored crystals. The crystals studied include NaCl, KCl, KBr, KI, CsCl, and CsBr. A few measurements were made on the *M* band of LiF. All of these except CsCl were single-crystal materials obtained from the Harshaw Chemical Co. The CsCl was Mackay and Co. C.P. powder pressed into a pellet.

* This work was supported in part by the Atomic Energy Commission.

The pressure apparatus has been described elsewhere.[3] The pressure-transmitting "fluid" was NaCl. From the appearance of the samples at the end of the run, it is clear that no gross plastic deformation has taken place. The agreement with JACOBS' data in the low-pressure range and evidence from other studies indicate that the static pressure was substantially hydrostatic. The fading of X-irradiated crystals at atmospheric pressure after pressure release and other evidence presented later indicate that there was significant plastic deformation while applying and changing the pressure.

The irradiated crystals were cleaved to $2\frac{1}{2}\times 5\times\frac{1}{2}$ mm and exposed at a distance of 1 in. for times varying from 10 min to several hours to an X-ray tube with tungsten target and beryllium windows operated at 40 kV and 25 mA. Except for the CsCl pellets which bleached rapidly, all crystals were held in the dark for 24 hr before being used.

NaCl, KCl, KBr, KI, and CsBr were additively colored by exposure to potassium vapor at 550°C for 15–18 hr. NaCl was also colored with sodium vapor. The additively colored KCl and KBr showed absorption in the *F* center region only, but NaCl, KI, and CsBr showed varying amounts of colloid band. No attempt was made to remove this by quenching, since, as explained later, the same effect was obtained by the application of pressure. The crystals were not generally uniformly colored, but small uniform pieces were cut from the center of the exposed crystal.

The concentration of *F* centers, as indicated by intensity of absorption, varied little among the various crystals, but, in general, it was a little higher in the X-irradiated crystals. By the use of DEXTER'S[4] form of the Smakula equation, the concentration of *F* centers in additively colored KCl was found to be $1\text{–}2\times 10^{16}/\text{cm}^3$.

A Beckmann DUR, equipped with a wavelength drive and supplementary lens system to be described elsewhere, was used as a monochromator. Both hydrogen and tungsten lamps were used. The single-beam optics and a non-linear amplifier used in much of the work made intensity determinations difficult. A linear amplification system adopted late in the work permitted the concentration determination given above. Many of the atmospheric runs were made on a Cary Model 13 Spectrometer.

The points shown are for increasing pressure. It was found that when the apparatus was allowed to sit at each decreasing pressure for a short time, the results approached those obtained with increasing pressure. All spectra were run in duplicate at each pressure. Bleaching under pressure utilized monochromated light from the tungsten lamp.

The plastically deformed crystals mentioned below were made in a pellet press. Those bleached in the absence of air were sealed in evacuated Pyrex tubing. The pellets were large enough so that the 10 min exposure to air during transfer and sealing gave negligible oxidation bleaching.

3. RESULTS

The results are plotted as energy versus pressure and, for several crystals,

$$\log\frac{\nu_{m_p}}{\nu_{m_0}} \text{ versus } \log\frac{\rho_p}{\rho_0},$$

ρ being the density. The density data of BRIDGMAN[5] were used. In every case a shift of ν_m to higher energies with increasing pressure was noted. Where available JACOBS' data fit ours quite well. For several of the crystals a new band, called here the K' band appeared on the high-energy side of the *F* band at higher pressures, and, in general, increased in intensity with pressure at the expense of the *F* band. The results of bleaching experiments are also noted.

(a) NaCl

The results for the frequency shift appear in Figs. 1 and 8. No difference in behavior between X-irradiated and additively colored crystals was noticed. At lower pressure the plot of $\ln\nu_{m_p}/\nu_{m_0}$ versus $\ln\rho_p/\rho_0$ can be fitted by a straight line, but at higher pressures the frequency shifts fall below the line.

The band width at the highest pressure was 10–15 per cent wider than at 1 atm. The width after releasing pressure was substantially the same as before the run. As mentioned earlier, the colloid band could be destroyed and the *F* band introduced by the application of pressure. The maximum intensity of the *F* band was obtained by raising and lowering the pressure several times between 1000 and 50,000 atm.

Additively colored crystals were bleached at 16,700 atm with *F* light, using a tungsten lamp and

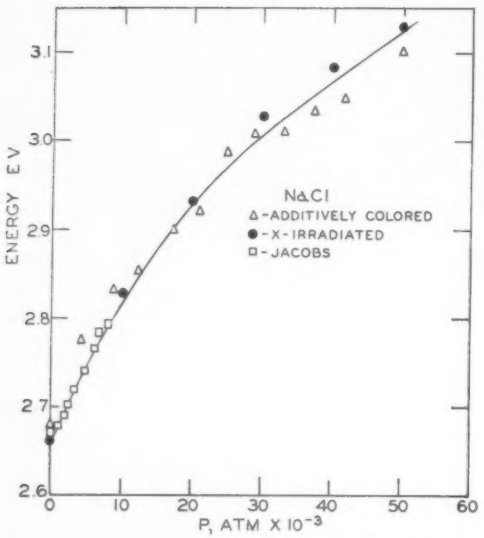

FIG. 1. Pressure versus energy (ν_m): F band—NaCl.

a Beckmann monochromator with a spectral slit width 65 Å. The F band diminished noticably in 30 min and a new band at 5200 Å appeared. After several hours the F band had substantially disappeared, and two additional bands at 5680 and 7005 Å were present. The 5200 Å band and the 7005 Å band were of about equal intensity (less than that of the original F band), while the 5680 Å band was quite weak. Intense irradiation in the region of the strong bands did not bleach them, nor did it enhance the F band. However, a change of pressure destroyed all three bands and restored, the F band. This was apparently a result of plastic deformation rather than pressure *per se*, as it occurred upon changing pressure at high or low pressures.

Additively colored crystals pressed in a pellet press to 20,000 atm appeared yellow, but turned blue in 5 min when exposed to light with broad bands at 5520 and 6365 Å. If the yellow pellets were kept in the dark, they retained their color indefinitely (over a period of several months). Unlike the pellets made from other alkali halides, the bleaching of NaCl pellets was not affected by the atmosphere. The values mentioned above can be compared with those found for unquenched crystals and crystals quenched at various temperatures (see Table 1).

(b) *Stassfort blue*

A series of experiments were performed on a naturally colored halite, "Stassfort blue." Plastic deformation turned these crystals yellow, but the F band was much less intense (less than 1 per cent) than for the artificially colored NaCl. However, when irradiated with ultraviolet light from an AH4 lamp, the resulting band structure in Stassfort blue is quite different from that observed in additively colored crystals similarly irradiated (see Table 1).

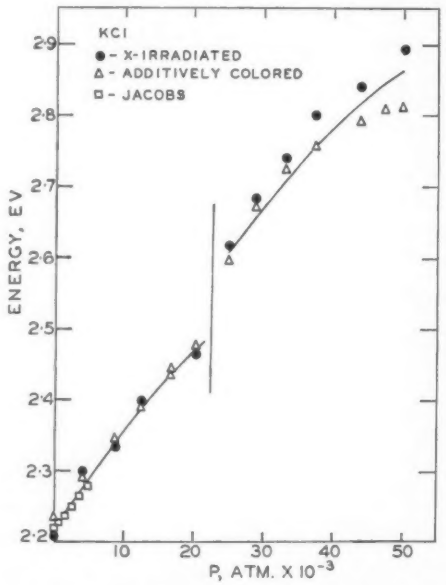

FIG. 2. Pressure versus energy (ν_m): F band—KCl.

(c) KCl

The shifts with pressure and density are shown in Figs 2 and 8. As with NaCl, the F band could be bleached with pressure and restored by further application of pressure. With the detection system used, it was not possible to observe the long-wavelength bands probably produced by bleaching.

Some interesting effects are observed at the phase transition at 19,500 atm when KCl goes from the face-centered cubic (NaCl) structure to the simple cubic (CsCl). Internal shearing during the transition greatly reduced transparency, but this was restored above the transition.

Table 1. *Frequency* (Å) *for maximum intensity of bands for* NaCl *and Stassfort blue crystals*

Condition of crystal	Bands	Intensity*
NaCl		
Unquenched, additively colored	4680–4750	m
	5700	m
	6155	m
Quenched from 400°C	4670	vw
	5570	s
Quenched from 700°C	4560	s
Pellet pressed to 20,000 atm, exposed to light and air	6365	m
	5521	m
U.V.-irradiated NaCl		
short exposure	4550–4650	vs
	5560	w
	5630	w
	7230	s
	8460	s
long exposure	5640–5730	w
	6190	vs
pellet from above pressed to 20,000 atm	5570	m
	6310	m
Bands produced in NaCl bleached with *F* light at 16,700 atm	5200 (R_1)	m
	5681 (R_2)	w
	7005 (M)	m
Stassfort blue		
Natural crystal	4387	w
	5289	w
	6555	s
	7902	w
U.v-irradiated	4375	w
	5254	w
	6050	w
	6835	m
Pellet from untreated crystal	5793	m

* Key to intensities: w = weak, vw = very weak, m = medium, s = strong, vs = very strong.

There was a large discontinuous increase in ν_m at the transition, as well as a change in the slope of the energy versus pressure curve.

Bleaching experiments were conducted both below and above the transition, at 10,000, 16,000, 30,000 and 50,000 atm. In all cases the *F* band could be bleached from 50 to 70 per cent and restored by passing through the transition. Repetition of this process gradually decreased the intensity of the *F* band, particularly in X-irradiated crystals. Another weak band appears at 4325 Å at both 16,000 and 30,000 atm.

KCl pellets were pressed at 16,000 and 30,000 atm. and exposed to the atmosphere. Those kept in the dark faded irregularly, especially at the surface and near cracks. The ones pressed at 30,000 atm faded more rapidly. After 5 hr the pellets were essentially colorless. There was no change in the frequency of ν_m during this process. Exposure to light increased the rate of fading and shifted ν_m from 5500 to 5725 Å. Pellets placed in a vacuum in the dark did not fade. Pellets in a vacuum exposed to light changed color but did not fade. Repressing restored the original color of the pellets. Heating to

Table 2. Frequency (Å) *for maximum intensity of bands for* KCl *crystals*

	Band	Intensity*
Additively colored crystal	4630	vw
	5550 (F)	s
	6750 (R_1)	w
	7360 (R_2)	m
	8250 (M)	m
Pellet pressed to 16,000 atm bleached in vacuum	5270	w
	7990	m
Pellet pressed to 16,000 atm, not exposed to light	5450–5530	s

* Key to intensities as for Table 1.

550°C for 5 min also restored the original color. Several hours' heating at 100°C had no effect. Crystals heated to 550°C became stable to exposure to light and air, whereas repressed pellets, of course, bleached as before.

The value of ν_m found in the above experiments as well as for untreated additively colored crystals are found in Table 2.

(d) KBr

The results for KBr are shown in Fig. 3. The most remarkable feature is the appearance of a new band under pressure on the high-frequency side of the F band. At 8300 atm this (K') band is about 0·1 times as intense as the F band. It increases in intensity with pressure, while the F band diminishes. At 12,500 atm the F band has 0·1 times the intensity of the K' band, and at 16,700 atm the F band has disappeared. The intensity of the K' band at 16,700 atm is approximately that of the F band at 4000 atm and the band widths are about equal. The transition between the F and K' bands is reversible, the F band reappearing at 12,500 atm with descending pressure.

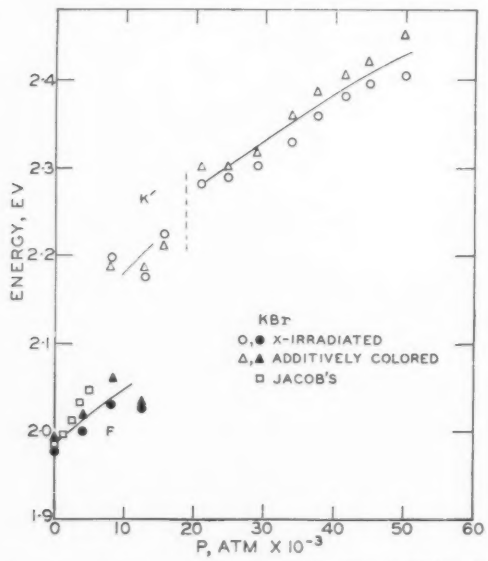

FIG. 3. Pressure versus energy (ν_m): F and K' bands—KBr.

In general, the shift with pressure is to higher energies. In the region 8000–16,000 atm, the bands overlap partially and lie on a steep part of the background curve so that accurate determination of ν_m is difficult. Below the phase transition (18,400 atm) the K' band shift appears to form a continuation of the F band shift and for thick crystals where they are unresolved a smooth continuous curve is obtained.

At 8300 and 12,500 atm where both bands exist both are bleached equally (75 per cent) when irradiated with narrowly monochromated light in either band. The K' band also bleached about the transition at 30,000 atm. With the present detection system no low-frequency bands were found. Irradiation of the bleached crystal did not bring back the F or K' band.

Either band could be restored by changing the pressure in the appropriate region. X-irradiated crystals bleached significantly on passing through the transition. Even for additively colored crystals the K' band diminished on going through the transition with increasing pressure, but this was

VOL. 5 1958

largely restored on lowering the pressure below 17,000 atm.

The phenomena in plastically deformed KBr pellets resembled those in KCl except that bleaching was, in all stages, more rapid.

(e) KI

The results for KI are shown in Fig. 4. Below the phase transition, with increasing pressure the

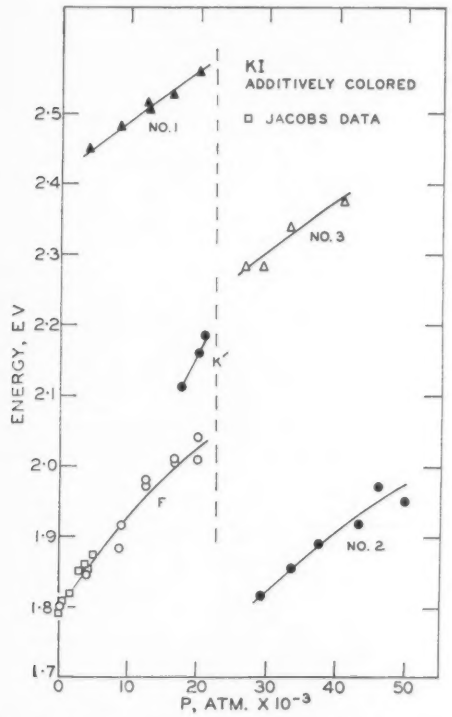

FIG. 4. Pressure versus energy (v_m): F, K', and other bands—KI.

behavior of KI is much like KBr. Above the phase transition there appears a very weak band (No. 3) at relatively higher energies and a strong band (No. 2) (but less intense than the K' band) at frequencies well below that of the K' band. Band No. 2 diminished in intensity with pressure changes, but never disappeared. No. 3 was unaffected by pressure changes. When the pressure was reduced below the transition bands No. 2 and No. 3 disappeared, and the F and K' bands returned, but another band (No. 1) appeared at higher frequencies than K' or No. 3. It was stable in intensity to pressure changes. Band width could not be obtained on No. 2 or No. 3. Band No. 1 had a width about two-thirds of that of the F band in KCl or KBr.

Optical bleaching of the F and K' band was the same as in KBr. Band No. 3 did not bleach, but irradiation in band No. 2 tended to increase No. 3 slightly. Band No. 1 bleached very rapidly, but since it was much weaker than the F and K' bands, it was difficult to determine whether bleaching it increased F and K'.

Results obtained for the bleaching of pellets were similar to those obtained with KBr and KCl, with the rate of bleaching intermediate between these two.

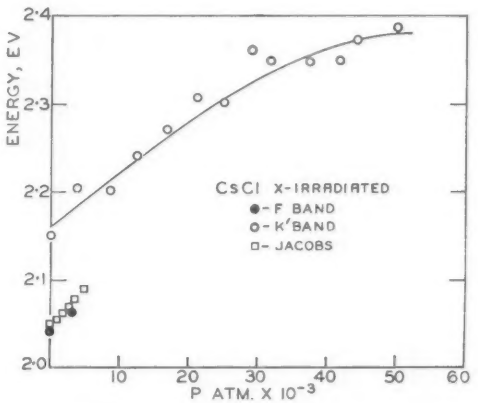

FIG. 5. Pressure versus energy (v_m): F and K' bands—CsCl.

(f) CsCl

A few runs were made on X-irradiated CsCl made by compressing powder. Since it bleached easily and was optically poor, only the shifts with pressure were noted (see Fig. 5). At 1 atm both the F and K' band are present. At higher pressures only the K' band was detected.

(g) CsBr

The results are shown in Figs. 6 and 8. Both the F and K' band were present at atmospheric pressure. With increasing pressure the K' band increases at the expense of the F band, but at 50,000 atm the F band still represents about 10 per cent of the total absorption. Over the pressure range the F

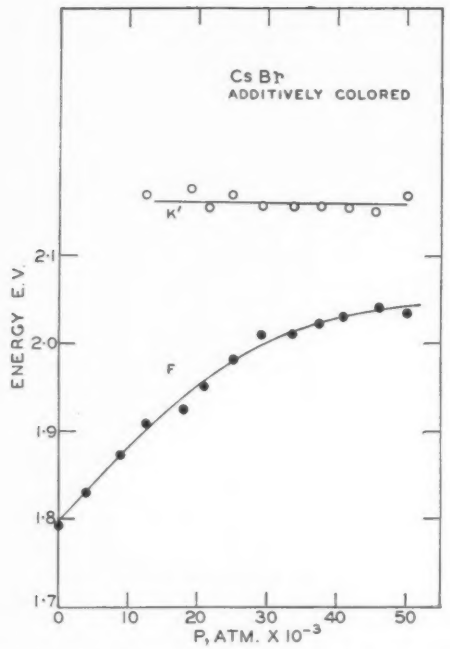

FIG. 6. Pressure versus energy (ν_m): F and K' bands—CsBr.

band gradually shifts to higher energy, while the K' band ν_m is independent of pressure. CsBr, like NaCl, has a large colloid band which is removable with pressure.

Plastically formed pellets bleach slowly in the atmosphere. In the dark they appear to retain their color.

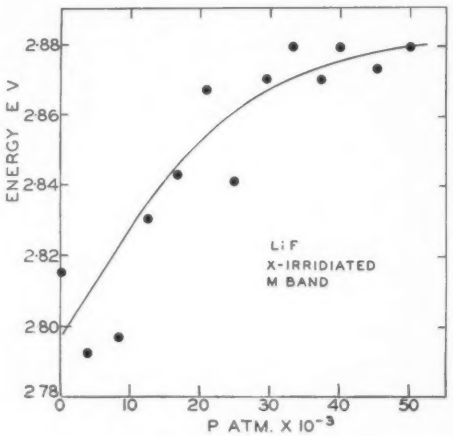

FIG. 7. Pressure versus energy (ν_m): M band—LiF.

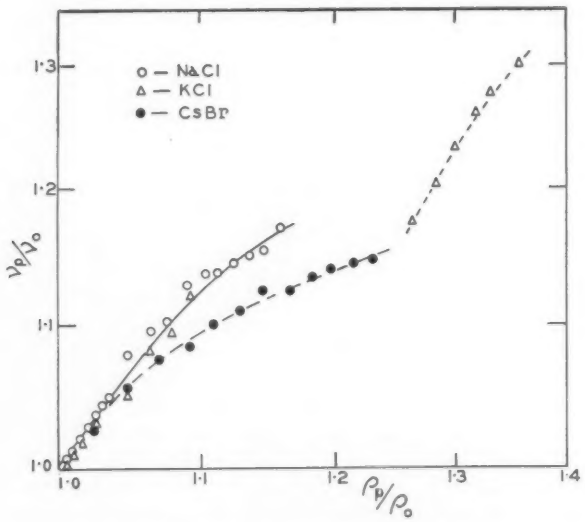

FIG. 8. Relative density versus relative energy (ν_m). NaCl, KCl, CsBr.

VOL. 5 1958

(h) LiF

Because it was difficult, with our apparatus, to make observations in the region of the F band of LiF (2500 Å), our studies with this crystal were limited to the shift of the M band. Fig. 7 shows the shift of ν_m with pressure. The shift is small compared with the shift of $\nu_m(F)$ for most crystals, but, based on limited observation, the shift of $\nu_m(M)$ is small in most crystals. The band width was substantially independent of pressure. Although these were X-irradiated crystals, the intensity was not affected by pressure. For most crystals the M band is quite unstable to changes in pressure.

4. DISCUSSION

(a) *Frequency shifts*

In general a shift to higher energies occurred for all bands with pressure (except the K' band in CsBr) as long as no phase transition occurred. Below 10,000 atm a straight line was obtained on a logarithmic plot of $\nu_m(F)a$ (lattice parameter), in agreement with the particle in the box, with JACOBS treatment, and with the empirical relationship of MOLLWO[6] and IVEY.[7] A more sophisticated treatment is needed to explain the high-pressure data. Such treatments presently available are difficult to apply directly because they contain parameters which depend on interionic distance. It is doubtful, in any case, if these would apply over relatively large changes in lattice parameter. It would be impossible to try to predict the shifts in the other bands until they are positively identified. The shifts across the phase transition are complicated by the fact that it is difficult to relate in a definite way the bands appearing above the transition to those occurring below.

(b) *K' Band*

One of the most interesting results of the work is the appearance of a new band on the high-frequency side of the F band at higher pressures. It occurs in KBr, KI, CsCl, and CsBr, in both X-irradiated and additively colored crystals. The appearance of the K' band is accompanied by a decrease of the F band. The phenomena are completely reversible with pressure. Bleaching with light in one band bleaches the other band. Clearly the same electron is responsible for both the K' and F bands. Possibly the absence of the K' band in NaCl is associated with the fact that it is not near a phase transition. The potassium halides all have a transition near 19,000 atm at room temperature, while the cesium halides transform at 450°C at 1 atm. It is not clear whether the band in KCl above the transition is the K' band.

We can think of five possible explanations, although these are not equally probable.

(1) The K' band involves a transition to a higher-energy level of the F center.

Since the excited state of the F center at 1 atm lies relatively near the conduction band,[8] the higher level would be in the conduction band unless the pressure effected a radical change in the energy levels. In any case, the K' center should bleach much faster than the F center, but it does not do so. Also, the change in relative intensities of the two bands would require the relative transition probabilities to change from 0–1 and from 1–0 which seems unlikely.

(2) The energy-level scheme might undergo a discrete change at high pressure, replacing the first excited band of the F center with a new level. It seems more likely that such a change would be continuous rather than discrete.

(3) A change of configuration, possibly related to the phase transition in the bulk of the crystal, could take place near the F center. Each center could change back and forth between configurations. The results including bleaching could be explained on this basis. However, the energetic requirements for such local rearrangements might be large.

(4) A center located in another part of the lattice might interact with the F center. The equilibrium times of the electron in the two centers would depend on the pressure. Thermal energy could be responsible for the transfer of the electron. LAMBE and COMPTON[9] in a study of luminescence involving F and M centers have shown that strong interaction exists between these centers. Since the F–K' equilibrium occurs in X-irradiated crystals as well as in additively colored ones, the centers would have to be close enough so that electrons would not be captured by holes.

(5) A new center may form at the same site as the F center due to interaction with a lattice imperfection, possibly to the F center by motion of dislocations created by plastic deformation during pressure changes. SEITZ[10] demonstrated that cold

working can cause bleaching of X-irradiated crystals, and our work shows that the colloid band can be dispersed by the same process. Whether the imperfection is more probably an impurity ion or a dislocation cannot be stated at present.

At this point the relation between the K band previously discussed in the literature and the K' band should be mentioned. The K band has been found on the high-frequency side of the F band in KCl and KBr. Bleaching the F band increases the K band intensity. In our work, the band which appears at 4325 Å in KCl as a result of bleaching in the F band at 16,000 atm is undoubtedly the K band. In KBr the K band appears at 5300 Å at 1 atm, while the K' band appears at 5700 Å at 8300 atm. One concludes that the K and K' bands are not identical.

Of the explanations offered, No. 5 is the most probable, although the nature of the imperfection is indefinite. No. 3 and No. 4 cannot be eliminated, although No. 3 has serious energetic objections.

(c) *Bleaching*

The optical bleaching of the crystals under pressure produces the same bands as at 1 atm, at least in NaCl. At 16,700 atm, irradiation of NaCl with F light produces bands at 5200, 5680, and 7005 Å. These undoubtedly correspond to the R_1, R_2, and M bands which appear at 5450, 5960, and 7150 Å at 1 atm. The bleaching, at 1 atm, of plastically deformed crystals is not so easy to interpret. In NaCl the band appearing at 5520 Å is probably the R_1 band, the band at 6365 Å, and the band at 5726 Å in KCl, do not fit with known bands.

(d) *Plastic deformation*

The destruction of the R_1, R_2, and M bands and dispersion of the colloid band under pressure, as well as the production of band No. 1 in KI are probably the effects of plastic deformation. The dispersion of the colloid band is particularly interesting, because it involves the movement of large amounts of material.

Crystals deformed and kept at 1 atm behave differently than those deformed and held under pressure. High pressure, like high temperature, apparently anneals the crystal. Exposure to air causes deformed crystals to bleach permanently, so that deformation accelerates diffusion. The absence of this effect in NaCl can be correlated with the slow rate of additive coloring in this salt, which is due to slow diffusion rates.

(e) KI

Band Nos. 1, 2, and 3 in KI must still be identified. Band No. 2, which is fairly intense and stable to pressure, is probably the K' center in the CsCl lattice. Bands No. 1 and No. 3 are probably the same band above and below the transition. The frequency shift at the transition is consistent with the shift from the K' band below to band No. 2 above.

A band at 5200 Å has been reported by KIYAMA and OKAMOTO[2] and by KIYAMA and SCHIMUYU.[2] The former report this to result from plastic deformation at 5000 kg/cm², while the latter report that it increases in intensity with exposure of the crystal to F light. Although band No. 1 occurs in this region (5050 Å at 4000 atm), the behavior of these two bands is not consistent, and they are probably not the same band.

Acknowledgements—The authors wish to acknowledge many helpful suggestions and discussions with F. SEITZ and R. J. MAURER.

REFERENCES

1. JACOBS D. S. *Phys. Rev.* **93,** 993 (1954).
   BURSTEIN E., OBERLY J. J. and DAVISSON J. W. *ibid.* **85,** 729 (1952).
   BURSTEIN E., SMITH P. L. and DAVISSON J. W. *ibid.* **86,** 615 (1952).
2. KIYAMA R. and OKAMOTO F. *Rev. Phys. Chem. Japan* **25,** 1, 6, 49 (1955).
   KIYAMA R. and SHIMUYU K. *ibid.* **25,** 101 (1955).
   KIYAMA R., MINOMURA S. and OURA S. *ibid.* **24,** 61 (1955).
   MINOMURA S. *ibid.* **24,** 28 (1955).
3. FITCH R. A., SLYKHOUSE T. E. and DRICKAMER H. G. *J. Opt. Soc. Amer.* (1957).
4. DEXTER D. L. *Phys. Rev.* **101,** 48 (1956).
5. BRIDGMAN P. W. *Proc. Amer. Acad. Arts Sci.* **76,** 1 (1945).
6. MOLLWO E. *Z. Phys.* **59,** 603 (1929/30).
7. IVEY H. F. *Phys. Rev.* **72,** 341 (1947).
8. DORENDORF F. and PICK K. *Z. Phys.* **128,** 106 (1950).
9. LAMBE J. and COMPTON W. D. *Phys. Rev.* **106,** 684 (1957).
10. SEITZ F. *Phys. Rev.* **80,** 239 (1950)

VOL. 5 1958

J. Phys. Chem. Solids Pergamon Press 1958. Vol. 5. pp. 337–355.

DÉTERMINATION DES LOIS DE FORCE DANS LES CRISTAUX DU TYPE DU DIAMANT

D. SAINT-JAMES

Centre d'Études Nucléaires Saclay, France

Received 3 *June* 1957; *revised* 12 *November* 1957)

Abstract—Laval's theory makes a distinction between dynamic and static elasticity. It introduces, instead of the 21 coefficients of Voigt, 45 for the description of the solid behaviour. Particularly, in holoedric cubic systems when each atom is not a symmetry centre, *four* different coefficients are necessary. It follows that compressibility cannot be expressed with the dynamic elastic coefficients as measured by sound velocity. In fact a new relation is available which, in the case of diamond structure, allows the calculation of five force constants between the two nearest neighbours, with the help of the Raman frequency and the dynamic elastic constants. These force constants are general; no assumption is made concerning their form (e.g. central forces). More general forces than two-body forces are involved in the values obtained. The results are very different from those of SMITH. The results of the experimental measurements for diamond are compared, and an attempt is made to apply the same calculation to silicon and germanium where the Raman frequency is unknown, and to discuss the infra-red absorption spectra of these elements.

Résumé—La théorie de LAVAL distingue entre élasticité dynamique et élasticité statique. Elle introduit, au lieu des 21 coefficients de Voigt, 45 coefficients pour décrire les propriétés d'un solide. En particulier dans les corps cubiques holoédriques, où chaque atome n'est pas centre de symétrie, quatre coefficients différents sont nécessaires. Il s'ensuit que la compressibilité ne peut être exprimée avec les coefficients dynamiques déduits de la mesure de la vitesse du son. On obtient donc une relation supplémentaire qui, dans le cas de la structure du type du diamant, permet le calcul de cinq constantes de force entre les deux premiers voisins, à l'aide de la fréquence Raman et des coefficients d'élasticité dynamique. Ces constantes de forces sont générales et ne supposent pas de formes particulières de ces forces (centrales. . .). Des forces plus générales que les forces à deux corps sont comprises dans les valeurs obtenues. Les résultats sont très différents de ceux de H. J. SMITH. L'auteur compare entre elles les diverses mesures expérimentales pour le diamant, et tente d'appliquer le même calcul au silicium et au germanium où la fréquence Raman est inconnue, et de discuter les spectres d'absorption infra-rouge de ces éléments.

1. INTRODUCTION

LA détermination des lois de force entre atomes à l'intérieur d'un cristal est un problème fondamental de la Physique du solide et a été l'objet de nombreuses études tant expérimentales que théoriques.

Pour ces dernières on a beaucoup utilisé le calcul des forces à partir des coefficients d'élasticité. Les résultats sont cependant entachés d'erreur si on utilise directement, sans précautions, la théorie de Born.

LAVAL[1] a montré, en effet, qu'il faut distinguer deux sortes de coefficients d'élasticité appelés par lui *dynamiques* et *statiques*, qui sont, dans la théorie classique, confondus.

L'originalité, et, par conséquent, le perfectionnement apportés par LAVAL et par LE CORRE[2] est de reprendre à la base la théorie de Voigt de l'élasticité statique. Laval montre que les déformations ne sont pas obligatoirement *irrotationnelles* (ou pures) et Le Corre que l'équilibre d'un petit cube est possible même si la tension T_γ^α appliquée sur les plans réticulaires n'est pas symétrique en α et γ.

En considérant des déformations *rotationnelles* (à l'échelle macro et microscopique), on introduira des couples (« massiques ») (interactions à longue distance) non nuls, en général, pour des forces électromagnétiques produisant ces déformations, et responsables de la dissymétrie de T_α^γ. Ces couples sont en général négligés car ils sont nuls:

(1) En mécanique classique des milieux élastiques continus

(2) Dans la théorie de Voigt

(3) Si les forces sont centrales ou si chaque atome est centre de symétrie.

On pourra les considérer comme petits en général, sauf dans des cas particuliers comme ceux envisagés par LE CORRE.

En élasticité dynamique même, ces petits « couples massiques » peuvent exciter des oscillations rotationnelles qui se perpétuent grâce aux forces d'inertie (fortes dès que les oscillations entraînent le déplacement des noyaux atomiques) et qui peuvent être importantes (cf. LAVAL).

Dans les cas le plus général il faut introduire 45 coefficients d'élasticité au lieu des 21 coefficients classiques. De ces 45 coefficients on déduit les coefficients d'élasticité dynamique et les coefficients d'élasticité statique. Si la déformation statique peut être considérée comme irrotationnelle (et c'est le cas des cristaux cubiques holoédriques cf. *infra*. II B et C), ces derniers prennent la symétrie des coefficients de Voigt et se confondent avec eux; mais ils restent différents des coefficients dynamiques à moins que les forces ne soient centrales, ou que chaque atome ne soit centre de symétrie. Si ces deux éventualités se produisent ensembles, le cristal obéit aux relations de Cauchy.

Dans ce qui suit, nous appliquerons la théorie de Laval aux corps ayant la structure du diamant. Ils bénéficient de la symétrie cubique holoédrique sans que chaque atome soit centre de symétrie. En nous bornant aux forces entre deux premiers voisins, nous donnerons l'expression des coefficients d'élasticité (statiques et dynamiques), de la compressibilité, de la fréquence Raman et nous en déduirons cinq constantes de forces.

Nous verrons qu'on ne peut pas considérer que les coefficients de la matrice dynamique $C\binom{m-p}{j\ k}_{\alpha\beta}$ sont symétriques en α et β. Ceci conduira à introduire une constante de force supplémentaire, mais qui n'intervient pas explicitement dans les coefficients d'élasticité.

La limitation à deux voisins n'exclut pas les forces autres que deux par deux, comme on peut s'en rendre compte lors du calcul des coefficients.

Nous donnons dans une première partie l'essentiel de la théorie de LAVAL.

2. THEORIE DE L'ELASTICITE

(a) *Elasticité dynamique*

Pour un cristal à la température T, on pourra écrire l'énergie potentielle sous la forme:

$$W=\frac{1}{2!}W_2+\frac{1}{3!}W_3+\ \dots\ . \qquad (2.1)$$

On a supposé le champ de force conservatif. Chacun des termes W_2, W_3 etc. représentent des termes de l'énergie potentielle dus à des actions deux par deux, trois par trois etc. Les termes d'ordre supérieur à deux doivent être introduits à cause de l'interpénétration des atomes qui ne sauraient conserver la symétrie sphérique. Chacun de ces termes n'est fonction que des coordonnées des atomes, et on pourra les développer en puissances entières des déplacements relatifs à partir des positions moyennes:

$$\boldsymbol{u}\binom{m-p}{j\ k}=\boldsymbol{u}\binom{m}{j}-\boldsymbol{u}\binom{p}{k},$$

(l'atome $\binom{m}{j}$ de la maille $\boldsymbol{m}=m_1\boldsymbol{l}_1+m_2\boldsymbol{l}_2+m_3\boldsymbol{l}_3$ (m_1, m_2, m_3 entiers; $\boldsymbol{l}_1, \boldsymbol{l}_2, \boldsymbol{l}_3$: translations principales du réseau) est repéré à l'intérieur de cette maille par le vecteur $\boldsymbol{j}$). On écrira:

Entre deux atomes

$$W\binom{m-p}{j\ k}=W_0\binom{m-p}{j\ k}-\sum_{\alpha}B_2\binom{m-p}{j\ k}_{\alpha}\boldsymbol{u}\binom{m-p}{j\ k}^{\alpha}-\frac{1}{2}\sum_{\alpha\beta}C_2\binom{m-p}{j\ k}_{\alpha\beta}\boldsymbol{u}\binom{m-p}{j\ k}^{\alpha}\boldsymbol{u}\binom{m-p}{j\ k}^{\beta}+\ \dots$$

où:

$$B_2\binom{m-p}{j\ k}_{\alpha}=-\frac{\partial W\binom{m-p}{j\ k}}{\partial x\binom{m-p}{j\ k}^{\alpha}};\quad C_2\binom{m-p}{j\ k}_{\alpha\beta}=-\frac{\partial^2 W\binom{m-p}{j\ k}}{\partial x\binom{m-p}{j\ k}^{\alpha}dx\binom{m-p}{j\ k}^{\beta}};\quad x\binom{m-p}{j\ k}^{\alpha}=(\boldsymbol{m}+\boldsymbol{j}-\boldsymbol{p}-\boldsymbol{k})^{\alpha}$$

et entre trois atomes:

$$W\begin{pmatrix} m-p-q \\ j\ k\ l \end{pmatrix} = W_0\begin{pmatrix} m-p-q \\ j\ k\ l \end{pmatrix} - \sum_{\alpha}\left\{B_3\begin{pmatrix} m-p \\ j\ k \end{pmatrix}_\alpha u\begin{pmatrix} m-p \\ j\ k \end{pmatrix}^\alpha + B_3\begin{pmatrix} p-q \\ k\ l \end{pmatrix}_\alpha u\begin{pmatrix} p-q \\ k\ l \end{pmatrix}^\alpha + B_3\begin{pmatrix} q-m \\ l\ j \end{pmatrix}_\alpha u\begin{pmatrix} q-m \\ l\ j \end{pmatrix}^\alpha\right\} -$$

$$-\frac{1}{2}\sum_{\alpha\beta}\left\{C_3\begin{pmatrix} m-p \\ j\ k \end{pmatrix}_\alpha\begin{pmatrix} m-p \\ j\ k \end{pmatrix}_\beta u\begin{pmatrix} m-p \\ j\ k \end{pmatrix}^\alpha u\begin{pmatrix} m-p \\ j\ k \end{pmatrix}^\beta +\right.$$

$$+C_3\begin{pmatrix} m-p \\ j\ k \end{pmatrix}_\alpha\begin{pmatrix} p-q \\ k\ l \end{pmatrix}_\beta u\begin{pmatrix} m-p \\ j\ k \end{pmatrix}^\alpha u\begin{pmatrix} p-q \\ k\ l \end{pmatrix}^\beta + C_3\begin{pmatrix} m-p \\ j\ k \end{pmatrix}_\alpha\begin{pmatrix} q-m \\ l\ j \end{pmatrix}_\beta u\begin{pmatrix} m-p \\ j\ k \end{pmatrix}^\alpha u\begin{pmatrix} q-m \\ l\ j \end{pmatrix}^\beta +$$

$$+C_3\begin{pmatrix} p-q \\ k\ l \end{pmatrix}_\alpha\begin{pmatrix} m-p \\ j\ k \end{pmatrix}_\beta u\begin{pmatrix} p-q \\ k\ l \end{pmatrix}^\alpha u\begin{pmatrix} m-p \\ j\ k \end{pmatrix}^\beta +$$

$$+C_3\begin{pmatrix} p-q \\ k\ l \end{pmatrix}_\alpha\begin{pmatrix} p-q \\ k\ l \end{pmatrix}_\beta u\begin{pmatrix} p-q \\ k\ l \end{pmatrix}^\alpha u\begin{pmatrix} p-q \\ k\ l \end{pmatrix}^\beta + C_3\begin{pmatrix} p-q \\ k\ l \end{pmatrix}_\alpha\begin{pmatrix} q-m \\ l\ j \end{pmatrix}_\beta u\begin{pmatrix} p-q \\ k\ l \end{pmatrix}^\alpha u\begin{pmatrix} q-m \\ l\ j \end{pmatrix}^\beta +$$

$$+C_3\begin{pmatrix} q-m \\ l\ j \end{pmatrix}_\alpha\begin{pmatrix} m-p \\ j\ k \end{pmatrix}_\beta u\begin{pmatrix} q-m \\ l\ j \end{pmatrix}^\alpha u\begin{pmatrix} m-p \\ j\ k \end{pmatrix}^\beta +$$

$$\left.+C_3\begin{pmatrix} q-m \\ l\ j \end{pmatrix}_\alpha\begin{pmatrix} p-q \\ k\ l \end{pmatrix}_\beta u\begin{pmatrix} q-m \\ l\ j \end{pmatrix}^\alpha u\begin{pmatrix} p-q \\ k\ l \end{pmatrix}^\beta + C_3\begin{pmatrix} q-m \\ l\ j \end{pmatrix}_\alpha\begin{pmatrix} q-m \\ l\ j \end{pmatrix}_\beta u\begin{pmatrix} q-m \\ l\ j \end{pmatrix}^\alpha u\begin{pmatrix} q-m \\ l\ j \end{pmatrix}^\beta\right\} + \ldots ;$$

où:

$$B_3 = -\frac{\partial W\begin{pmatrix} m-p-q \\ j\ k\ l \end{pmatrix}}{\partial x\begin{pmatrix} m-p \\ j\ k \end{pmatrix}^\alpha} \text{ et } C_3 = -\frac{\partial^2 W\begin{pmatrix} m-p-q \\ j\ k\ l \end{pmatrix}}{\partial x\begin{pmatrix} m-p \\ j\ k \end{pmatrix}^\alpha \partial x\begin{pmatrix} p-q \\ k\ l \end{pmatrix}^\beta}. \tag{2.3}$$

α, β, γ représentent les trois directions, de coordonnées. $u\binom{m}{j}^\alpha$ représente la projection du vecteur $\boldsymbol{u}\binom{m}{j}$ sur la direction α etc. La position des indices est fonction de la variance : covariants en bas, contrevariants en haut.

Les atomes dans leur position moyenne sont en équilibre, la résultante des termes du premier ordre est nulle et on écrira :

$$W = A + \frac{1}{2}\sum_{\binom{m-p}{j\ k}}\sum_{\alpha\beta} C\begin{pmatrix} m-p \\ j\ k \end{pmatrix}_{\alpha\beta} u\begin{pmatrix} m \\ j \end{pmatrix}^\alpha u\begin{pmatrix} p \\ k \end{pmatrix}^\beta + \ldots; \tag{2.4}$$

avec

$$A = \frac{1}{2}\sum_{\binom{m-p}{j\ k}} W_0\begin{pmatrix} m-p \\ j\ k \end{pmatrix} + \frac{1}{3!}\sum_{\binom{m-p-q}{j\ k\ l}} W_0\begin{pmatrix} m-p-q \\ j\ k\ l \end{pmatrix} + \ldots; \tag{2.5}$$

$$C\begin{pmatrix} m-p \\ j\ \ k \end{pmatrix}_{\alpha\beta} = C_2\begin{pmatrix} m-p \\ j\ \ k \end{pmatrix}_{\alpha\beta} + \sum_{\substack{q \\ \left(\begin{smallmatrix} p \neq q \neq m \\ k \neq l \neq j \end{smallmatrix}\right)}} C_3\begin{pmatrix} m-p \\ j\ \ k \end{pmatrix}_{\alpha}\begin{pmatrix} m-p \\ j\ \ k \end{pmatrix}_{\beta} + C_3\begin{pmatrix} q-m \\ l\ \ j \end{pmatrix}_{\alpha}\begin{pmatrix} p-q \\ k\ \ l \end{pmatrix}_{\beta} -$$

$$-C_3\begin{pmatrix} m-p \\ j\ \ k \end{pmatrix}_{\alpha}\begin{pmatrix} p-q \\ k\ \ l \end{pmatrix}_{\beta} - C_3\begin{pmatrix} p-m \\ l\ \ j \end{pmatrix}_{\alpha}\begin{pmatrix} m-p \\ j\ \ k \end{pmatrix}_{\beta} + \ldots; \qquad (2.5\text{ bis})$$

Dans la somme donnant W, et pour éviter toute restriction, on a posé :

$$C\begin{pmatrix} m-m \\ j\ \ j \end{pmatrix}_{\alpha\beta} = -\sum_{\substack{p \\ \left(\begin{smallmatrix} p \neq m \\ k \neq j \end{smallmatrix}\right)}} C\begin{pmatrix} m-p \\ j\ \ k \end{pmatrix}_{\alpha\beta}. \qquad (2.6)$$

D'où la relation générale:

$$\sum_{\substack{p \\ k}} C\begin{pmatrix} m-p \\ j\ \ k \end{pmatrix}_{\alpha\beta} = 0. \qquad (2.7)$$

L'énergie prend donc la forme classique (2.4) mais il a été nécessaire d'introduire des forces autres que deux par deux dans la définition des coefficients $C\binom{m-p}{j\ \ k}_{\alpha\beta}$. Ces coefficients obéissent à la relation fondamentale :

$$C\begin{pmatrix} m-p \\ j\ \ k \end{pmatrix}_{\alpha\beta} = C\begin{pmatrix} p-m \\ k\ \ j \end{pmatrix}_{\beta\alpha} \qquad (2.8)$$

car on peut intervertir les dérivations mais ils n'ont pas de raison d'être symétriques en α et β comme on le suppose généralement car :

$$\frac{\partial^2 W}{\partial x\binom{m}{j}^{\beta}\partial x\binom{p}{k}^{\alpha}} \neq \frac{\partial^2 W}{\partial x\binom{m}{j}^{\alpha}\partial x\binom{p}{k}^{\beta}}.$$

Si on tente d'écrire l'équilibre de deux parties A et B d'un cristal, les équations obtenues se réduisent à une identité si les coefficients C sont symétriques en α et β. La condition est suffisante mais elle n'est pas nécessaire et nous ne supposerons pas les coefficients symétriques.

(1) *Matrice* Γ *et matrice atomique.* Nous définissons maintenant la matrice Γ par les relations:

$$\Gamma(jk)_{\alpha\beta} = \sum_{b} C\begin{pmatrix} b \\ jk \end{pmatrix}_{\alpha\beta} e^{i\sigma q(b+j-k)} \qquad (2.9)$$

avec

$$\boldsymbol{b} = \boldsymbol{m} - \boldsymbol{p},\ |\boldsymbol{q}|^2 = 1.$$

$\sigma\boldsymbol{q}$ est le vecteur d'onde associé aux ondes élastiques, Γ traduit cette décomposition classique en ondes.

Considérons la composante des oscillations

$$a\begin{pmatrix} m \\ j \end{pmatrix}_{\alpha} = \xi(j)_{\alpha} e^{i\omega t} e^{-i\sigma q(m+j)}. \qquad (2.10)$$

L'équation de d'alembert* (μ_j est la masse de l'atome j)

$$-\mu_j \ddot{a}\begin{pmatrix} m \\ j \end{pmatrix}_{\alpha} + \sum_{pk} C\begin{pmatrix} m-p \\ j\ \ k \end{pmatrix}_{\alpha\beta} a\begin{pmatrix} p \\ k \end{pmatrix}^{\beta} = 0, \qquad (2.11)$$

équivaut au système de 3 équations :

$$\mu_j \omega^2 \xi(j)_{\alpha} + \sum_{k\beta} \Gamma(jk)_{\alpha\beta}\xi(k)^{\beta} = 0$$

qui n'a de solution différente de zéro que si :

$$|\Gamma + \mu\omega^2 I| = 0\ (I_{\alpha\beta} = \delta_{\alpha\beta}). \qquad (2.12)$$

S'il y a g atomes dans la maille, cette équation séculaire sera de degré $3g$. Elle détermine les oscillations du milieu cristallin en fonction de σ. Trois racines tendent vers zéro avec σ, ce sont les branches acoustiques, les $3g-3$ racines restantes forment les branches optiques.

Nous allons ne prendre compte que des oscillations de basse fréquence et nous pourrons écrire :

$$\omega^2 = v^2_{\text{son}}\sigma^2 = \eta\sigma^2.$$

Γ est développable en série des puissances de σ selon l'équation (2.9 bis).

* Le tenseur métrique n'a pas été indiqué explicitement; il doit être rétabli pour passer de a_{α} à a^{α} etc.

VOL. 5 1958

$$(2.9\text{ bis})\quad \begin{cases} \Gamma(jk)_{\alpha\beta} = \Gamma^0(jk)_{\alpha\beta}+\Gamma^1(jk)_{\alpha\beta}\sigma+\Gamma^2(jk)_{\alpha\beta}\sigma^2+\ \ldots \\ \Gamma^0(jk)_{\alpha\beta} = \sum_b C\binom{b}{jk}_{\alpha\beta} \\ \Gamma^1(jk)_{\alpha\beta} = i\sum_b C\binom{b}{jk}_{\alpha\beta}\boldsymbol{q}(\boldsymbol{b}+\boldsymbol{j}-\boldsymbol{k}) \\ \Gamma^2(jk)_{\alpha\beta} = -\tfrac{1}{2}\sum_b C\binom{b}{jk}_{\alpha\beta}[\boldsymbol{q}(\boldsymbol{b}+\boldsymbol{j}-\boldsymbol{k})]^2. \end{cases}$$

Développant également

$$\xi(j)^\alpha = u(j)^\alpha+v(j)^\alpha\sigma+w(j)^\alpha\sigma^2+\ \ldots$$

et en reportant dans (2.11) il vient

$$\sum_{k\beta}\Gamma^0(jk)_{\alpha\beta}u(k)^\beta+\sum_{k\beta}[\Gamma^0(jk)_{\alpha\beta}v(k)^\beta+ +\Gamma^1(jk)_{\alpha\beta}u(k)^\beta]\sigma+\Big\{\eta\mu_j u(j)\alpha+ +\sum_{k\ \beta}[\Gamma^0(jk)_{\alpha\beta}W(k)^\beta+\Gamma^1(jk)_{\alpha\beta}v(k)^\beta+ +\Gamma^2(jk)_{\alpha\beta}u(k)^\beta]\Big\}\sigma^2+\ \ldots=0. \tag{2.13}$$

Comme σ peut prendre n'importe quelle valeur, il en résulte trois égalités

(1) $$\sum_{k\beta}[\Gamma^0(jk)_{\alpha\beta}u(k)^\beta]=0;$$

$3g$ équations montrant que :

$$u(j)^\beta = u(k)^\beta = \ldots = u^\beta.$$

(2) $$\sum_{k\beta}[\Gamma^0(jk)_{\alpha\beta}v(k)^\beta+\Gamma^1(jk)_{\alpha\beta}u^\beta]=0;$$

c'est-à-dire en remarquant que β est un indice muet et en posant :

$$v(k)^\epsilon = \sum_\beta y(k)_\beta{}^\epsilon u^\beta,$$

$$\sum_{k\epsilon\beta}\Gamma^0(jk)_{\alpha\epsilon}y(k)_\beta{}^\epsilon u^\beta+\sum_{k\beta}\Gamma^1(jk)_{\alpha\beta}u^\beta=0. \tag{2.14}$$

(3) $$\sum_{k\beta}\Gamma^0(jk)_{\alpha\beta}w(k)^\beta = -\mu_j\eta u(j)_\alpha- -\sum_{k\beta}[\Gamma^1(jk)_{\alpha\beta}v(k)^\beta+\Gamma^2(jk)_{\alpha\beta}u^\beta],$$

Système de 3 équations à 3 inconnues $w(k)\beta$ qui compte tenu de la relation :

$$\sum_j\Gamma^0(jk)_{\alpha\beta}=\sum_k\Gamma^0(jk)_{\alpha\beta}=0, \tag{2.14b}$$

n'a de solution différente de zéro que si :

$$\sum_j[\mu_j\eta u_\alpha+\sum_{k\epsilon}\Gamma^1(jk)_{\alpha\epsilon}v(k)^\epsilon+\sum_{k\beta}\Gamma^2(jk)_{\alpha\beta}u^\beta]=0,$$

En posant $m=\sum_j\mu j$ (masse du motif cristallin) on aura :

$$m\eta u_\alpha+\sum_\beta[\sum_{jk}\sum_\epsilon\Gamma^1(jk)_{\alpha\epsilon}y(k)_\beta{}^\epsilon+ +\sum_{jk}\Gamma^2(jk)_{\alpha\beta}]u^\beta=0. \tag{2.15}$$

Pour retrouver l'équation familière de la théorie classique on définira la matrice atomique $(A\alpha\beta)/m$ symétrique en α et β telle que :

$$A_{\alpha\beta}=\sum_\epsilon\sum_{jk}\Gamma^1(jk)_{\alpha\epsilon}y(k)_\beta{}^\epsilon+\sum_{jk}\Gamma^2(jk)_{\alpha\beta} \tag{2.16}$$

et (2.15) aura la forme matricielle :

$$\eta u+\frac{A}{m}u=0;$$

qui n' a de solution différente de zéro que si :

$$\left|\frac{A}{m}+\eta I\right|=0. \tag{2.17}$$

C'est l'équation séculaire de la théorie classique; mais nous avons été obligés ici de faire appel à la matrice atomique.

Nous allons essayer de relier celle-ci au plus petit nombre de coefficients d'élasticité indépendants. Définissons les coefficients d'élasticité par la relation :

$$\frac{A_{\alpha\beta}}{m}=-\frac{v}{m}\sum_{\gamma\delta}N_\alpha{}^{\gamma}|_\beta{}^\delta q_\gamma q_\delta, \tag{2.18}$$

où v est le volume du motif cristallin.

Tout naturellement nous poserons

$$N_\alpha{}^\gamma|_\beta{}^\delta = M_\alpha{}^\gamma|_\beta{}^\delta + M'_\alpha{}^\gamma|_\beta{}^\delta$$

où

$$-v\sum_{\gamma\delta} M_\alpha{}^\gamma|_\beta{}^\delta q_\gamma q_\delta = \sum_{jk}\Gamma^2(jk)_{\alpha\beta}. \qquad (2.19)$$

$$-v\sum_{\gamma\delta} M'_\alpha{}^\gamma|_\beta{}^\delta q_\gamma q_\delta = \sum_{\epsilon jk}\Gamma^1(jk)_{\alpha\epsilon}y(k)_\beta{}^\epsilon. \qquad (2.19\text{ bis})$$

On voit que :

$$M_\alpha{}^\gamma|_\beta{}^\delta = \frac{1}{2v}\sum_{bjk} C\binom{b}{jk}_{\alpha\beta}(b^\gamma + j^\gamma - k^\gamma)(b^\delta + j^\delta - k^\delta). \qquad (2.20)$$

$M_a^{\gamma}{}_{|\beta}^{\delta}$ est une densité tensorielle symétrique en α et β et γ et δ.

Pour reconnaître les caractères de symétrie des $M'_a{}^{\gamma}{}_{|\beta}^{\delta}$ nous devons donner une expression de ceux-ci que l'on obtient par l'intermédiaire du calcul des racines $y(k)_\beta^\epsilon$:

$$\sum_{k\epsilon}\Gamma^0(jk)_{\alpha\epsilon}y(k)_\beta{}^\epsilon = -\sum_k \Gamma^1(jk)_{\alpha\beta}. \qquad (2.20\text{ bis})$$

Cette relation liée à (2.14b) montre que Γ^0 n'est que de rang $3g-3$ et que trois racines $y(k)_\beta^\epsilon$ peuvent être choisies arbitrairement. Seules les différences sont déterminées, et on les définira par rapport à une racine $y(n)_\beta^\epsilon$ où n est constant. L'équation ci-dessus devient

$$\sum_{k\epsilon}\Gamma^0(jk)_{\alpha\epsilon}\Delta(k-n)_\beta{}^\epsilon = -\sum_k \Gamma^1(jk)_{\alpha\beta},$$

$$\Delta(k-n)_\beta{}^\epsilon = y(k)_\beta{}^\epsilon - y(n)_\beta{}^\epsilon;$$

Les $\Gamma^0(jk)_{\alpha\epsilon}$ forment en fait une matrice $\Gamma^0(n)$ qui n'est que de rang $(3g-1)(3g-1)$, obtenue en supprimant dans Γ^0 les trois lignes et les trois colonnes $n\varepsilon(\varepsilon = 1, 2, 3)$. Cette matrice admet une matrice réciproque $\underset{n}{G}$ et on écrira :

$$\Delta(k-n)_\beta{}^\epsilon = -iv\sum_\delta\Big(\sum_{j\zeta}\underset{n}{G}(kj)^{\epsilon\zeta}L(j)^\delta_{\zeta\beta}\Big)q_\delta. \qquad (2.20\text{ ter})$$

La valeur $j = n$ est exclue de la somme.

On a défini ainsi les coefficients d'élasticité secondaires L tels que :

$$L(j)_{\alpha\beta}{}^\gamma = \frac{1}{v}\sum_{bk} C\binom{b}{jk}_{\alpha\beta}(b^\gamma + j^\gamma - k^\gamma). \qquad (2.21)$$

Mais $\sum_{jk}\Gamma^1(jk)_{\alpha\epsilon} = 0$ il s'ensuit que :

$$\sum_{jk\epsilon}\Gamma^1(jk)_{\alpha\epsilon}y(k)_\beta{}^\epsilon = \sum_{jk\epsilon}\Gamma^1(jk)_{\alpha\epsilon}\Delta(k-n)_\beta{}^\epsilon,$$

c'est-à-dire :

$$\sum_{jk\epsilon}\Gamma^1(jk)_{\alpha\epsilon}y(k)_\beta{}^\epsilon = -v\sum_{\gamma\delta}\Big[v\sum_{jk,\epsilon\zeta}L(k)^\gamma_{a\epsilon}\underset{n}{G}(kj)^{\epsilon\zeta}L(j)^\delta_{\zeta\beta}\Big]q_\gamma q_\delta;$$

D'où la valeur de $M'^{\gamma}_{a}{}_{|\beta}^{\delta}$

$$M'_\alpha{}^\gamma|_\beta{}^\delta = v\sum_{jk,\epsilon\zeta}L(k)^\gamma_{a\epsilon}\underset{n}{G}(kj)^{\epsilon\zeta}L(j)^\delta_{\zeta\beta}. \qquad (2.22)$$

L'indice n est exclu de la sommation sur j et k. $\underset{n}{G}(kj)^{\epsilon\zeta}$, inverse de $\Gamma^0(n)$ obéit aux relations :

$$\begin{cases}\sum_{j\zeta}\underset{n}{G}(kj)^{\epsilon\zeta}\underset{n}{\Gamma^0}(jk')_{\zeta\beta} = \delta_{kk'}\delta_{\epsilon\beta},\\ \sum_{k\epsilon}\underset{n}{\Gamma^0}(jk)_{\alpha\epsilon}\underset{n}{G}(kj')^{\epsilon\zeta} = \delta_{jj'}\delta_{\alpha\zeta}.\end{cases} \qquad (2.22\text{ bis})$$

Dans cette notation $\underset{n}{\Gamma}{}^0(jk)_{\zeta\beta}$ représente les éléments des matrices Γ^0 où l'on a supprimé les lignes et les colonnes correspondant à n. Dans la somme la valeur j ou $k = n$ est évidemment exclue.

$L(j)^\gamma_{a\epsilon}$ est une densité tensorielle symétrique en α et ε. En effet :

$$L(j)^\gamma_{a\epsilon} = \sum_{b,l} C\binom{b}{jl}_{\alpha\epsilon}(b^\gamma + j^\gamma - l^\gamma)$$

$$L(j)^\gamma_{\epsilon a} = \sum_{b,l} C\binom{l}{jl}_{\epsilon\alpha}(b^\gamma + j^\gamma - l^\gamma).$$

Cette dernière expression s'écrit d'après (2.8)

$$L(j)^\gamma_{\epsilon\alpha} = \sum_{b,l} C\binom{-b}{lj}_{\alpha\epsilon}(b^\gamma + j^\gamma - l^\gamma)$$

$$= -\sum_{b,l} C\binom{b}{lj}_{\alpha\epsilon}(b^\gamma + l^\gamma - j^\gamma).$$

$L(j)^\gamma_{a\epsilon}$ peut être considéré comme proportionnel à l'ensemble des forces statiques exercées par tous les atomes du cristal sur l'atome $\binom{m}{j}$. $-L(j)^\gamma_{\epsilon a}$ comme proportionnel (avec la même constante) à l'ensemble des forces statiques exercées par l'atome $\binom{m}{j}$ sur tous les atomes. Le cristal devant être en équilibre, ces forces sont égales et opposées, il s'ensuit la symétrie de L.

On voit donc que $M'^{\gamma}_{a}{}_{|\beta}^{\delta}$ est une densité tensorielle symétrique en $\alpha\gamma$ et $\beta\delta$ mais non symétrique indépendamment pour chaque indice. Il en est de même pour les coefficients :

$$N_\alpha{}^\gamma|_\beta{}^\delta = N_\beta{}^\delta|_\alpha{}^\gamma.$$

VOL. 5 1958

$\alpha\gamma$ et $\beta\delta$ peuvent prendre neuf valeurs distinctes. Il en résulte qu'il y a en principe 81 coefficients d'élasticité, qui se réduisent à 45 du fait de la symétrie $\alpha\gamma$, $\beta\delta$. On pourra donc écrire les $N_\alpha^\gamma|_\beta^\delta$ sous la forme d'un tenseur à neuf lignes et neuf colonnes (repérées par les couples $\alpha\beta$ et $\gamma\delta$), symétrique par rapport à sa diagonale.

Les coefficients N sont les coefficients d'élasticité fondamentaux et ils permettent de déduire la matrice atomique par la relation (2.18).

Mais la matrice $A_{\alpha\beta}$ est symétrique,* il s'ensuit que n'interviennent en fait que les coefficients N' tels que :

$$N'^{\gamma\delta}_{\overline{\alpha|\beta}} = \tfrac{1}{2}(N_\alpha{}^\gamma|_\beta{}^\delta + N_\alpha{}^\delta|_\beta{}^\gamma). \qquad (2.23)$$

Ces coefficients sont au nombre de 36, et ils peuvent s'écrire sous forme d'une matrice à 6 lignes et 6 colonnes.

Dans tout ce qui concerne l'élasticité dynamique les coefficients N n'apparaissent pas individuellement mais seulement la forme N' est utilisée. On ne peut donc déduire les coefficients N' des mesures dynamiques comme la vitesse du son par exemple. Nous verrons ci-dessous que les coefficients N interviennent séparément en élasticité statique ce qui justifie leur introduction.

(b) *Elasticité statique. Déformations linéaires du milieu cristallin. Coefficients d'élasticité statiques*

Les déformations dues aux ondes élastiques que nous avons envisagées jusqu'ici ne déforment pas le réseau et nous ont amené à définir les coefficients N'. Une déformation statique au contraire modifie les positions moyennes des atomes et par conséquent le réseau et les coefficients $C\binom{m-p}{j\ k}_{\alpha\beta}$.

Les énergies d'agitation thermique avant et après déformation sont différentes. Cependant si l'on se borne à des déformations légères obéissant à la loi de Hooke, cette différence devient négligeable devant l'énergie nécessaire à faire passer les atomes de leur ancienne à leur nouvelle position d'équilibre, et l'énergie de déformation se réduit à cette dernière.

Si de plus on impose à cette déformation d'être linéaire au sens de LAVAL, c'est-à-dire de conserver la triple périodicité du réseau, on pourra considérer les coefficients $C_{\alpha\beta}$ comme constants, indépendants des déplacements relatifs, et confondus avec les coefficients des forces de rappel des oscillations.

La densité d'énergie de déformation par unité de volume sera :

$$\epsilon = \frac{w}{v} = \frac{1}{4v}\sum_{mp}\sum_{jk}\sum_{\alpha\beta} C\binom{m-p}{j\ k}_{\alpha\beta} \times$$

$$\times u\binom{m-p}{j\ k}^\alpha u\binom{m-p}{j\ k}^\beta + \ldots; \qquad (2.25)$$

Les termes du premier ordre sont nuls car le cristal abandonné à lui-même doit être stable. La déformation linéaire a pour tenseur constant $t_\gamma{}^\alpha = \partial u^\alpha/\partial x^\gamma$.

Ce tenseur communique aux atomes des déplacements uniformes de *leurs positions moyennes*, que nous désignerons par $u\binom{m}{j}$ tels que:

$$u\binom{m}{j}^\alpha = d(j)^\alpha + t_\gamma{}^\alpha(m^\gamma + j^\gamma) \qquad (2.26)$$

où $d(j)^\alpha$ correspond au déplacement du réseau d'atomes. A l'aide des relations (2.12 bis) et (2.19), (2.21) et (2.26) l'énergie (2.25) prendra la forme :

$$\epsilon = \frac{1}{2v}\sum_{jk\alpha\beta}\Gamma^0(jk)_{\alpha\beta}\, d(j)^\alpha d(k)^\beta +$$

$$+ \sum_{j\alpha\beta\delta} L(j)^\delta_{\alpha\beta} d\,(j)^\alpha t_\delta{}^\beta + \tfrac{1}{2}\sum_{\alpha\beta\gamma\delta} M_\alpha{}^\gamma|_\beta{}^\delta t_\gamma{}^\alpha t_\delta{}^\beta. \qquad (2.27)$$

Les forces de rappel subies par un atome supposé au repos ont une résultante nulle, c'est-à-dire :

$$-\sum_{pk\beta} C\binom{m-p}{j\ k}_{\alpha\beta} u\binom{m-p}{j\ k}^\beta = 0,$$

ou

$$\sum_{k\beta}\Gamma^0(jk)_{\alpha\beta}\, d(k)^\beta = v\sum_{\beta\delta} L(j)^\delta_{\alpha\beta} t_\delta{}^\beta.$$

Soit d'après (2.20 bis)

$$d(k)^\epsilon = -\sum_\beta y(k)_\beta{}^\epsilon \frac{t_\delta{}^\beta}{q_\delta},$$

* q_γ et q_δ peuvent être permutés.

ou encore d'après (2.20 ter) :

$$d(k-n)^{\epsilon} = v \sum_{\delta\beta} \Big(\sum_{j\zeta} \underset{n}{G}(kj)^{\epsilon\zeta}{}_{\alpha}\, (j)^{\delta}_{\zeta\beta} \Big) t_{\delta}{}^{\beta}.$$

Ainsi les déplacements relatifs subis par les réseaux d'atomes correspondent à la propagation non uniforme des oscillations du motif cristallin. Il en résulte que l'expression (2.27) devient :

$$\epsilon = \tfrac{1}{2} \sum_{j\alpha\beta\delta} L(j)^{\delta}_{\alpha\beta}\, d(j)^{\alpha} t_{\delta}{}^{\beta} + \tfrac{1}{2} \sum_{\alpha\beta\gamma\delta} M_{\alpha}{}^{\gamma}|_{\beta}{}^{\delta} t_{\gamma}{}^{\alpha} t_{\delta}{}^{\beta}$$

$$= \tfrac{1}{2} \sum_{\alpha\beta\gamma\delta} N_{\alpha}{}^{\gamma}|_{\beta}{}^{\delta} t_{\gamma}{}^{\alpha} t_{\delta}{}^{\beta}. \qquad (2.28)$$

On voit que si $t_{\gamma}{}^{\alpha}$ n'est pas un tenseur symétrique en α et γ les coefficients N apparaissent indépendamment.

Pour ne pas alourdir l'exposé, nous nous bornerons comme en élasticité classique au cas des déformations pures, c'est-à-dire telles que $t_{\gamma}{}^{\alpha} = t_{\alpha}{}^{\gamma} = t(\alpha\gamma)$. On aura alors :

$$\epsilon = \tfrac{1}{2} \sum_{\alpha\beta,\gamma\delta} \tfrac{1}{4} (N_{\alpha}{}^{\gamma}|_{\beta}{}^{\delta} + N_{\gamma}{}^{\alpha}|_{\beta}{}^{\delta} +$$

$$+ N_{\gamma}{}^{\alpha}|_{\delta}{}^{\beta} + N_{\alpha}{}^{\gamma}|_{\delta}{}^{\beta}) t(\alpha\gamma) t(\beta\delta),$$

$$= \tfrac{1}{2} \sum_{\alpha\beta,\gamma\delta} \Lambda(\alpha\beta, \gamma\delta) t(\alpha\gamma) t(\beta\delta).$$

On a retrouvé ainsi les 21 coefficients de Cauchy-Voigt. Mais ces coefficients Λ se rapportent uniquement aux déformations pures et ils sont à manier avec précaution dans les cas généraux.*

(2) *Cas particulier des forces centrales et des corps où chaque atome est centre de symétrie.* Si chaque atome est centre de symétrie on voit aisément que tous les coefficients $L(j)^{\gamma}_{\alpha\beta}$ seront nuls ainsi que la matrice Γ^1, la matrice Γ étant réelle. Le coefficient N se réduit au coefficient M et prend la symétrie des coefficients de Voigt.

Si les forces sont centrales, LAVAL a montré que $L(j)^{\gamma}_{\alpha\beta}$ devient symétrique en α, β et γ, donc que M' et N sont symétriques en $\alpha\gamma$ et $\beta\delta$ comme les coefficients de Voigt. Si de plus chaque atome est centre de symétrie, les cristal obéira aux relations de Cauchy.

(c) *Application aux corps cubiques holoédriques*

Pour un corps cubique holoédrique, où la symétrie cristalline est élevée, on montre que les déformations sont *toujours* pures.(1) Autrement dit nous pourrons définir des coefficients tels que Λ, c'est-à-dire les coefficients de Voigt. Il est intéressant de comparer ici les résultats obtenus pour les coefficients Λ et les coefficients N'.

Les coefficients N tombent au nombre de quartre.

(1) $N_1{}^1|_1{}^1 = N_2{}^2|_2{}^2 = N_3{}^3|_3{}^3$

(2) $N_3{}^2|_3{}^2 = N_1{}^3|_1{}^3 = N_2{}^1|_2{}^1 = N_2{}^3|_2{}^3 = N_3{}^1|_3{}^1 = N_1{}^2|_1{}^2$

(3) $N_2{}^2|_3{}^3 = N_3{}^3|_1{}^1 = N_1{}^1|_2{}^2 = N_3{}^3|_2{}^2 = N_1{}^1|_3{}^3 = N_2{}^2|_1{}^1$

(4) $N_2{}^3|_3{}^2 = N_3{}^1|_1{}^3 = N_1{}^2|_2{}^1 = N_3{}^2|_2{}^3 = N_1{}^3|_3{}^1 = N_2{}^1|_1{}^2$

Tous les autres coefficients sont nuls.

Les coefficients Λ n'ont que trois valeurs et se confondent avec ceux de Voigt :

$$\Lambda(11,11) = N_1{}^1|_1{}^1 = C_{11}$$

$$\Lambda(22,33) = N_2{}^2|_3{}^3 = C_{23} = C_{12} = \ldots \qquad (2.30)$$

$$\Lambda(23,32) = \frac{N_3{}^2|_2{}^3 + N_2{}^3|_2{}^3}{2} = C_{44}$$

Dans la matrice atomique les coefficients N' se réduisent également à trois:

$$N'{}_1{}^1|_1{}^1 = N_1{}^1|_1{}^1$$

$$N'{}_2{}^2|_3{}^3 = \frac{N_2{}^2|_3{}^3 + N_3{}^2|_2{}^3}{2} \qquad (2.30b)$$

$$N'{}_2{}^3|_2{}^3 = N_2{}^3|_2{}^3.$$

Nous allons comparer la matrice classique des oscillations à la matrice atomique, elle s'écrit :

* On trouvera une discussion complète des cas où les déformations ne peuvent être considérées comme pures dans LAVAL(1) et LE CORRE.(2)

$$\begin{vmatrix} C_{11} & C_{44} & C_{44} & 0 & 0 & 0 \\ C_{44} & C_{11} & C_{44} & 0 & 0 & 0 \\ C_{44} & C_{44} & C_{11} & 0 & 0 & 0 \\ 0 & 0 & 0 & \frac{C_{44}+C_{12}}{2} & 0 & 0 \\ 0 & 0 & 0 & 0 & \frac{C_{44}+C_{12}}{2} & 0 \\ 0 & 0 & 0 & 0 & 0 & \frac{C_{44}+C_{12}}{2} \end{vmatrix} \quad \bar{a} \text{ compares } \bar{a} \quad \begin{vmatrix} N'_1{}^1|_1{}^1 & N'_2{}^3|_2{}^3 & N'_2{}^3|_2{}^3 & 0 & 0 & 0 \\ N'_2{}^3|_2{}^3 & N'_1{}^1|_1{}^1 & N'_2{}^3|_2{}^3 & 0 & 0 & 0 \\ N'_2{}^3|_2{}^3 & N'_2{}^3|_2{}^3 & N'_1{}^1|_1{}^1 & 0 & 0 & 0 \\ 0 & 0 & 0 & N'_2{}^2|_3{}^3 & 0 & 0 \\ 0 & 0 & 0 & 0 & N'_2{}^2|_3{}^3 & 0 \\ 0 & 0 & 0 & 0 & 0 & N'_2{}^2|_3{}^3 \end{vmatrix}$$

Les coefficients de cette matrice sont les coefficients dynamiques et pour les distinguer des coefficients de Voigt nous les désignons par la lettre $\mathcal{C}$

$$\mathcal{C}_{11} = N'_1{}^1|_1{}^1 = N_1{}^1|_1{}^1$$

$$\mathcal{C}_{44} = N'_2{}^3|_3{}^2 = \frac{N_2{}^2|_3{}^3 + N_3{}^2|_2{}^3}{2} \qquad (2.30\text{ ter})$$

$$\mathcal{C}_{12} = 2N'_2{}^2|_3{}^3 - N'_2{}^3|_2{}^3 = N_2{}^2|_3{}^3 + \\ + N_3{}^2|_2{}^3 - N_2{}^3|_2{}^3$$

Les coefficients $\mathcal{C}$, à part $\mathcal{C}_{11}$, sont différents des coefficients C. On ne peut les déduire les uns des autres.

Une autre manière d'exprimer ce fait est de dire que les coefficients N' ont gardé un caractère de densité tensorielle qui a disparu des coefficients Λ. Si les forces sont centrales *ou* si chaque atome est centre de symétrie, $N_\alpha^\gamma|_\beta^\delta$ devient symétrique en $\alpha\beta$ et $\gamma\delta$ et :

$$N_2{}^3|_2{}^3 = N_3{}^2|_2{}^3$$

c'est-à-dire: $C_{11} = \mathcal{C}_{11}$, $C_{12} = \mathcal{C}_{12}$, $C_{44} = \mathcal{C}_{44}$, les coefficients indépendants sont au nombre de trois. Si les forces sont centrales *et* si chaque atome est centre de symétrie, les relations de Cauchy sont alors vérifiées

$$C_{11} = \mathcal{C}_{11} = 2C_{12} = 2\mathcal{C}_{12} = 2C_{44} = 2\mathcal{C}_{44}.$$

(3) *Coefficient de compressibilité.* Dans le cas général où les forces ne sont pas centrales et où chaque atome n'est pas centre de symétrie, les mesures de vitesse du son conduiront à la détermination des coefficients $\mathcal{C}_{11}$, $\mathcal{C}_{12}$, $\mathcal{C}_{44}$, et non à celle de C_{11}, C_{12}, C_{44}. Par contre ceux-ci seront combinés dans la compressibilité K et on démontre, aisément* que dans le cas d'une compression pure :

$$\frac{1}{K} = \frac{1}{9}\{\Lambda(11,11)+\Lambda(22,22)+\Lambda(33,33)+ \\ +2[\Lambda(11,22)+\Lambda(22,33)+\Lambda(33,11)]\}$$

c'est-à-dire pour un cristal cubique, et d'après (2.30)

$$\frac{1}{K} = \frac{1}{3}(C_{11})+2C_{12}). \qquad (2.31)$$

On ne pourra donc utiliser dans (2.31) les valeurs des $\mathcal{C}$ déduites des mesures de vitesse du son que si chaque atome est centre de symétrie, ou si les forces peuvent être considérées comme centrales.

3. LES CORPS DU TYPE DU DIAMANT

Dans ce qui suit nous allons appliquer la théorie de J. LAVAL à un corps cubique holoédrique où chaque atome n'est pas centre de symétrie. Il est naturel de choisir pour cette étude les corps du type du diamant. Uneétude analogue a été faite par SMITH[3] et pour permettre la comparaison nous suivons le même processus que cet auteur. Nous déterminerons donc les coefficients $C_{\alpha\beta}$, puis lamatrice Γ et la matrice atomique, c'est-à-dire les coefficients N', ensuite nous déterminerons les coefficients N et calculerons la compressibilité.

Nous introduirons, pour faire ces calculs, les actions entre premiers et deuxièmes voisins sans faire aucune hypothèse sur les forces qui agissent entre eux. Un certain nombre de paramètres compatibles avec les symétries du diamant seront

* SEITZ F. *Modern Theory of Solids* pp. 373–4. McGraw-Hill, New York (1940).

Tableau 1. *Premiers voisins*

Voisins de l'atome	x_1	x_2	x_3	k_1	k_2	k_3	b_1	b_2	b_3	k	j	b
	$\frac{a}{2}$	$\frac{a}{2}$	$\frac{a}{2}$	$\frac{a}{2}$	$\frac{a}{2}$	$\frac{a}{2}$	0	0	0	2	1	$\bar{1}$
1	$-\frac{a}{2}$	$-\frac{a}{2}$	$\frac{a}{2}$	$\frac{a}{2}$	$\frac{a}{2}$	$\frac{a}{2}$	a	a	0	2	1	$\bar{2}$
0 0 0	$-\frac{a}{2}$	$\frac{a}{2}$	$-\frac{a}{2}$	$\frac{a}{2}$	$\frac{a}{2}$	$\frac{a}{2}$	a	0	a	2	1	$\bar{3}$
	$\frac{a}{2}$	$-\frac{a}{2}$	$-\frac{a}{2}$	$\frac{a}{2}$	$\frac{a}{2}$	$\frac{a}{2}$	0	a	a	2	1	$\bar{4}$
Voisins de l'atome	0	0	0	0	0	0	0	0	0	1	2	1
$\bar{1}$	a	a	0	0	0	0	$-a$	$-a$	0	1	2	2
$\frac{a}{2}$ $\frac{a}{2}$ $\frac{a}{2}$	a	0	a	0	0	0	$-a$	0	$-a$	1	2	3
	0	a	a	0	0	0	0	$-a$	$-a$	1	2	4

utilisés. Nous tenterons de les calculer numériquement grâce aux valeurs expérimentales de la vitesse du son, de la compressibilité et de l'effet Raman.

(a) *La matrice dynamique des corps de type diamant*

Dans ce qui suit nous allons prendre des notations aussi voisines que possible de celle de SMITH.

Les corps du type diamant peuvent être considérés comme formés de deux sous-réseaux cubiques à faces centrées s'interpénétrant. La maille élémentaire (rhomboèdre) possède deux atomes un sur chacun des deux sous-réseaux, ses trois translations sont :

$$\boldsymbol{a}_1 = a(\boldsymbol{i}_2+\boldsymbol{i}_3)$$

$$\boldsymbol{a}_2 = a(\boldsymbol{i}_3+\boldsymbol{i}_1)$$

$$\boldsymbol{a}_3 = a(\boldsymbol{i}_1+\boldsymbol{i}_3).$$

($\boldsymbol{i}_1$, $\boldsymbol{i}_2$, $\boldsymbol{i}_3$ sont les trois vecteurs unitaires des axes cartésiens rectangulaires).

Un certain nombre de conventions, semblables à celles de SMITH seront utilisées. Les vecteurs b sont repérés par des chiffres—2, 3, 4 etc. pour les atomes voisins de l'atome (0, 0, 0), $\bar{2}$, $\bar{3}$, $\bar{4}$, etc. pour les atomes voisins de l'atome. $\left(\frac{a}{2}, \frac{a}{2}, \frac{a}{2}\right)$

Les vecteurs j ou k ne peuvent avoir que deux valeurs suivant le sous-réseau de l'atome :

l'une repérée par

$$: 1 : \quad 0 \quad 0 \quad 0$$

l'autre par

$$: 2 : \frac{a}{2}\boldsymbol{i}_1+\frac{a}{2}\boldsymbol{i}_2+\frac{a}{2}\boldsymbol{i}_3.$$

La liste des premiers voisins est dressée sur le Tableau 1, celle des seconds voisins sur le Tableau 2.

On voit que pour les premiers voisins les coefficients $C\binom{b}{jk}$ n'auront que les possibilités $j = 1$; $k = 2$ ou $j = 2$; $k = 1$ suivant le signe de b. A l'aide des six transformations fondamentales du diamant et compte tenu de la relation (2.8) on montre que :

$$c^1 = c^{\bar{1}} = -\begin{vmatrix} \alpha & \beta & \beta \\ \beta & \alpha & \beta \\ \beta & \beta & \alpha \end{vmatrix} \qquad c^2 = c^{\bar{2}} = -\begin{vmatrix} \alpha & \beta & -\beta \\ \beta & \alpha & -\beta \\ -\beta & -\beta & \alpha \end{vmatrix}$$

$$c^3 = c^{\bar{3}} = -\begin{vmatrix} \alpha & -\beta & \beta \\ -\beta & \alpha & -\beta \\ \beta & -\beta & \alpha \end{vmatrix} \qquad c^4 = c^{\bar{4}} = -\begin{vmatrix} \alpha & -\beta & \beta \\ -\beta & \alpha & \beta \\ \beta & \beta & \alpha \end{vmatrix} \qquad (3.1)$$

Tableau 2. Deuxièmes voisins

Deuxièmes voisins de l'atome 1

x_1	x_2	x_3	k_1	k_2	k_3	b_1	b_2	b_3	k	j	b
0	a	a	0	0	0	0	$-a$	$-a$	1	1	$\bar{5}$
0	a	$-a$	0	0	0	0	$-a$	a	1	1	$\bar{6}$
a	0	a	0	0	0	$-a$	0	$-a$	1	1	$\bar{7}$
a	0	a	0	0	0	a	0	$-a$	1	1	$\bar{8}$
a	a	0	0	0	0	$-a$	$-a$	0	1	1	$\bar{9}$
a	$-a$	0	0	0	0	$-a$	a	0	1	1	$\bar{10}$
0	$-a$	$-a$	0	0	0	0	a	a	1	1	$\bar{11}$
0	$-a$	a	0	0	0	0	a	$-a$	1	1	$\bar{12}$
$-a$	0	$-a$	0	0	0	a	0	a	1	1	$\bar{13}$
a	0	$-a$	0	0	0	$-a$	0	a	1	1	$\bar{14}$
$-a$	$-a$	0	0	0	0	a	a	0	1	1	$\bar{15}$
$-a$	a	0	0	0	0	a	$-a$	0	1	1	$\bar{16}$

Deuxièmes voisins de l'atome $\bar{1}$

x_1	x_2	x_3	k_1	k_2	k_3	b_1	b_2	b_3	k	j	b
a	$-a$	$-a$	a	a	a	0	a	a	2	2	5
$\bar{2}$	$\bar{2}$	$\bar{2}$	$\bar{2}$	$\bar{2}$	$\bar{2}$						
a	$-a$	$3a$	a	a	a	0	a	$-a$	2	2	6
$\bar{2}$	$\bar{2}$	$\bar{2}$	$\bar{2}$	$\bar{2}$	$\bar{2}$						
$-a$	a	$-a$	a	a	a	a	0	a	2	2	7
$\bar{2}$	$\bar{2}$	$\bar{2}$	$\bar{2}$	$\bar{2}$	$\bar{2}$						
$3a$	a	$-a$	a	a	a	$-a$	0	a	2	2	8
$\bar{2}$	$\bar{2}$	$\bar{2}$	$\bar{2}$	$\bar{2}$	$\bar{2}$						
$-a$	$-a$	a	a	a	a	a	a	0	2	2	9
$\bar{2}$	$\bar{2}$	$\bar{2}$	$\bar{2}$	$\bar{2}$	$\bar{2}$						
$-a$	$3a$	a	a	a	a	a	$-a$	0	2	2	10
$\bar{2}$	$\bar{2}$	$\bar{2}$	$\bar{2}$	$\bar{2}$	$\bar{2}$						
a	$3a$	$3a$	a	a	a	0	$-a$	$-a$	2	2	11
$\bar{2}$	$\bar{2}$	$\bar{2}$	$\bar{2}$	$\bar{2}$	$\bar{2}$						
a	$3a$	$-a$	a	a	a	0	$-a$	a	2	2	12
$\bar{2}$	$\bar{2}$	$\bar{2}$	$\bar{2}$	$\bar{2}$	$\bar{2}$						
$3a$	a	$3a$	a	a	a	$-a$	0	$-a$	2	2	13
$\bar{2}$	$\bar{2}$	$\bar{2}$	$\bar{2}$	$\bar{2}$	$\bar{2}$						
$-a$	a	$3a$	a	a	a	a	0	$-a$	2	2	14
$\bar{2}$	$\bar{2}$	$\bar{2}$	$\bar{2}$	$\bar{2}$	$\bar{2}$						
$3a$	$3a$	a	a	a	a	$-a$	$-a$	0	2	2	15
$\bar{2}$	$\bar{2}$	$\bar{2}$	$\bar{2}$	$\bar{2}$	$\bar{2}$						
$3a$	$-a$	a	a	a	a	$-a$	a	0	2	2	16
$\bar{2}$	$\bar{2}$	$\bar{2}$	$\bar{2}$	$\bar{2}$	$\bar{2}$						

Toutes ces matrices sont compatibles avec les symétries du diamant.

Pour les deuxièmes voisins $j = k = 1$ ou 2. La relation (2.8) montre que :

$$c^{\rho} = \tilde{c}^{\rho+6} \text{ et } c^{\bar{\rho}} = \tilde{c}^{(\bar{\rho}-6)}$$

A l'aide des transformations fondamentales, et compte tenu du fait que les coefficients *ne sont pas symétriques en* α et β, on voit que la forme générale de la matrice c^{ρ} est :

$$\begin{vmatrix} \mu & \nu & \tau \\ \nu & \mu & \tau \\ -\tau & -\tau & \lambda \end{vmatrix}$$

Par conséquent :

$$c^5=c^{\bar 5}=\tilde c^{11}=\tilde c^{\bar 1\bar 1}=-\begin{vmatrix}\lambda&-\tau&-\tau\\ \tau&\mu&\nu\\ \tau&\nu&\mu\end{vmatrix},\qquad c^6=c^{\bar 6}=\tilde c^{12}=\tilde c^{\bar 1\bar 2}=-\begin{vmatrix}\lambda&\tau&-\tau\\ -\tau&\mu&\nu\\ \tau&\nu&\mu\end{vmatrix}$$

$$c^7=c^{\bar 7}=\tilde c^{13}=\tilde c^{\bar 1 3}=-\begin{vmatrix}\mu&\tau&\nu\\ -\tau&\lambda&-\tau\\ \nu&\tau&\mu\end{vmatrix},\qquad c^8=c^{\bar 8}=\tilde c^{14}=\tilde c^{\bar 1\bar 4}=-\begin{vmatrix}\mu&\tau&-\nu\\ -\tau&\lambda&\tau\\ -\nu&-\tau&\mu\end{vmatrix}\qquad (3.1b)$$

$$c^9=c^{\bar 9}=\tilde c^{15}=\tilde c^{\bar 1 5}=-\begin{vmatrix}\mu&\nu&\tau\\ \nu&\mu&\tau\\ -\tau&-\tau&\lambda\end{vmatrix},\qquad c^{10}=c^{\bar 1 0}=\tilde c^{16}=\tilde c^{\bar 1 6}=-\begin{vmatrix}\mu&-\nu&-\tau\\ -\nu&\mu&\tau\\ -\tau&\tau&\lambda\end{vmatrix}$$

Ces matrices sont toutes compatibles avec les symétries du diamant. Le fait de ne pas avoir introduit la symétrie en α, β des coefficients c, nous conduit à ajouter un coefficient τ supplémentaire.

Les coefficients c^0 définis par l'équation (2.6) prennent la forme :

$$C^{(0}_{11)}=C^{(0}_{22)}=4\alpha\begin{vmatrix}1&0&0\\0&1&0\\0&0&1\end{vmatrix}+4(\lambda+2\mu)\begin{vmatrix}1&0&0\\0&1&0\\0&0&1\end{vmatrix}.$$

Les valeurs de la matrice Γ se déduisent immédiatement :

$$\Gamma^0(11)=4\alpha\begin{vmatrix}1&0&0\\0&1&0\\0&0&1\end{vmatrix}=\Gamma^0(22).$$

$$\Gamma^0(12)=-4\alpha\begin{vmatrix}1&0&0\\0&1&0\\0&0&1\end{vmatrix}=\Gamma^0(21).$$

$$\Gamma^1(jj)_{\alpha\beta}=0.$$

En reportant dans l'équation (2.14) on tire immédiatement en faisant $j=1$ par example

$$y^2-y^1=-\frac{ia\beta}{2a}\begin{vmatrix}0&q_3&q_2\\q_3&0&q_1\\q_2&q_1&0\end{vmatrix},\qquad (3.4)$$

équation qui correspond au fait que seules les différences sont déterminées. En reportant dans (2.15) et en remarquant que $m=2\mu_A$ on tire la matrice atomique.

Nous avons ainsi determiné les coefficients N' :

$$N'_1{}^1|_1{}^1=N'_2{}^2|_2{}^2=N'_3{}^3|_3{}^3=\frac{\alpha+8\mu}{2a}$$

$$N'_1{}^2|_1{}^2=N'_1{}^3|_1{}^3=N'_3{}^1|_3{}^1=N'_3{}^2|_3{}^2=N'_2{}^1|_2{}^1$$
$$=N'_2{}^3|_2{}^3=\frac{1}{2a}\left[\alpha-\frac{\beta^2}{\alpha}+\tau(\lambda+\mu)\right]$$

$$\Gamma^1(12)=-\Gamma^1(21)=2ia\beta\begin{vmatrix}0&q_3&q_2\\q_3&0&q_1\\q_2&q_1&0\end{vmatrix},$$

$$\Gamma^2(12)=-\frac{a^2}{2}\begin{vmatrix}\alpha(q_1{}^2+q_2{}^2+q_3{}^2)&2\beta q_1q_2&2\beta q_3q_1\\2\beta q_2q_1&\alpha(q_1{}^2+q_2{}^2+q_3{}^2)&2\beta q_2q_3\\2\beta q_1q_3&2\beta q_3q_2&\alpha(q_1{}^2+q_2{}^2+q_3{}^2)\end{vmatrix}=\Gamma^2(21),$$

$$\Gamma^2(22)=\Gamma^2(11)=-2a^2\begin{vmatrix}2\mu q_1{}^2+(\lambda+\mu)(q_2{}^2+q_3{}^2)&2\nu q_1q_2&2\nu q_3q_1\\2\nu q_2q_1&2\mu q_2{}^2+(\lambda+\mu)(q_3{}^2+q_2{}^2)&2\nu q_2q_3\\2\nu q_3q_1&2\nu q_2q_3&2\mu q_3{}^2+(\lambda+\mu)(q_1{}^2+q_2{}^2)\end{vmatrix}.$$

VOL. 5 1958

$$N'^{2}{}_{2}|^{3}{}_{3} = N'^{3}{}_{3}|^{1}{}_{1} = N'^{1}{}_{1}|^{2}{}_{2} = \frac{1}{2a}\left[\frac{\beta}{2}\left(2-\frac{\beta}{\alpha}\right)+4\nu\right].$$

Les constantes mesurées par la vitesse du son sont donc :

$$\mathcal{C}_{11} = \mathcal{C}_{22} = \mathcal{C}_{33} = \frac{\alpha+8\mu}{2a}$$

$$\mathcal{C}_{44} = \mathcal{C}_{55} = \mathcal{C}_{66} = \frac{1}{2a}\left[\alpha - \frac{\beta^2}{\alpha} + 4(\lambda+\mu)\right] \tag{3.6}$$

$$\mathcal{C}_{12} = \mathcal{C}_{31} = \mathcal{C}_{23} = \frac{1}{2a}[2\beta-\alpha-4\lambda-4\mu+8\nu].$$

Toutes ces valeurs ne dépendent pas, comme il fallait s'y attendre, du paramètre τ.

(b) *Calcul des coefficients N. Valeur de la compressibilité*

Ce calcul ne représente aucune difficulté. Le calcul des coefficients M a été fait indirectement lors du calcul de Γ^2. Avec la relation (2.20) on voit immédiatement que :

$$M^{\delta\delta}_{\delta\delta} = \frac{8\mu}{2a}+\frac{\alpha}{2a}, \quad M^{\gamma\zeta}_{\delta\epsilon} = 0 \quad \text{pour} \begin{cases} \delta \neq \epsilon \\ \gamma \neq \epsilon \\ \zeta \neq \epsilon, \\ \gamma \neq \delta \\ 8 \neq \epsilon \end{cases}$$

$$M_{\delta}{}^{\delta}|_{\epsilon}{}^{\epsilon} = M_{\delta}{}^{\epsilon}|_{\epsilon}{}^{\delta} = \frac{1}{2a}[4\nu+\beta] \quad (\delta \neq \epsilon),$$

$$M_{\delta}{}^{\epsilon}|_{\delta}{}^{\epsilon} = \frac{1}{2a}[\alpha+4(\lambda+\mu)] \quad (\delta \neq \epsilon).$$

M' est donné par la relation (2.22). La restriction sur la somme permet d'écrire comme il n'y a que deux atomes par maille :

$$M'_{\alpha}{}^{\gamma}|_{\beta}{}^{\delta} = v \sum_{\epsilon\zeta} L(1)^{\gamma}_{\alpha\epsilon}\, \underset{2}{G}(11)^{\epsilon\zeta} L(1)^{\delta}_{\zeta\beta}.$$

$\underset{2}{G}(11)$ est défini par l'équation (2.22 bis). C'est la matrice inverse de Γ^0 où on a enlevé les trois lignes et les trois colonnes correspondant à la valeur j ou $k = 2$. C'est donc l'inverse de la matrice $\Gamma^0(11)$.
On a donc

$$M'_{\epsilon}{}^{\gamma}|_{\zeta}{}^{\delta} = -\frac{v}{4\alpha}\sum_{\kappa} L(1)^{\gamma}_{\epsilon\kappa}\, L(1)^{\delta}_{\kappa\zeta}.$$

Le calcul de $L(1)$ est immédiat (équation 2.21).

$$L(1)^{\gamma}_{\delta\epsilon} = -\frac{2a\beta}{v} \text{ si tous les indices sont différents.}$$

$$= 0, \qquad \text{dans tous les autres cas.}$$

D'où les valeurs de M'

$$M'_{\delta}{}^{\epsilon}|_{\epsilon}{}^{\delta} = M'_{\delta}{}^{\epsilon}|_{\delta}{}^{\epsilon} = -\frac{\beta^2}{2a\alpha}.$$

On aura donc les valeurs des coefficients

$$N_1{}^1|_1{}^1 = N_2{}^2|_2{}^2 = N_3{}^3|_3{}^3 = \frac{\alpha+8\mu}{2a},$$

$$N_2{}^2|_1{}^1 = N_3{}^3|_1{}^1 = N_1{}^1|_2{}^2 = N_1{}^1|_3{}^3 = N_2{}^2|_3{}^3 = N_3{}^3|_2{}^2 = \frac{\beta+4\nu}{2a},$$

$$N_2{}^3|_2{}^3 = N_3{}^1|_3{}^1 = N_1{}^2|_1{}^2 = N_3{}^2|_3{}^2 = N_1{}^3|_1{}^3 = N_2{}^1|_2{}^1 = \frac{1}{2a}\left[\alpha - \frac{\beta^2}{\alpha} + 4(\lambda+\mu)\right]$$

$$N_3{}^2|_2{}^3 = N_1{}^2|_2{}^1 = N_3{}^1|_1{}^3 = N_2{}^3|_3{}^2 = N_2{}^1|_1{}^2 = N_1{}^3|_3{}^1 = \frac{1}{2a}\left[\beta - \frac{\beta^2}{\alpha} + 4\nu\right].$$

Tous les autres coefficients sont nuls. Les N sont bien au nombre de quatre et différents en général.

Ils ne dépendent pas du paramètre τ, c'est-à-dire qu'il n'était pas nécessaire de supposer la symétrie des coefficients $C_{\alpha\beta}$ pour assurer l'équilibre de deux parties A et B du cristal. Les coefficients d'élasticité statique Λ (ou C) seront donc :

$$C_{11} = N_1{}^1|_1{}^1 = \frac{\alpha+8\mu}{2a},$$

$$C_{12} = N_1{}^1|_2{}^2 = \frac{\beta+4\nu}{2a}, \tag{3.8}$$

$$C_{44} = \frac{N_3{}^2|_2{}^3+N_3{}^2|_3{}^2}{2} = \frac{1}{4a}\times$$

$$\times\left[\alpha-\frac{2\beta^2}{\alpha}+4(\lambda+\mu+\nu)+\beta\right].$$

et la compressibilité aura la valeur :

$$\frac{1}{K} = \frac{1}{3}(C_{11}+C_{12}) = \frac{1}{3}\,\frac{\alpha+8\mu+2\beta+8\nu}{2a}. \tag{3.9}$$

(c) *Relations entre les divers coefficients*

Si on avait borné le calcul aux premiers voisins, on aurait pu établir la relation :

$$N_2{}^2|_3{}^3 N_3{}^2|_3{}^2 = (N_2{}^2|_3{}^3+N_1{}^1|_1{}^1)N_2{}^3|_3{}^2$$

c'est-à-dire

$$4\mathcal{C}_{11}(\mathcal{C}_{11}-\mathcal{C}_{44}) = (\mathcal{C}_{11}+\mathcal{C}_{12})^2.$$

C'est la relation de Born.

En tenant compte des deuxièmes voisins on pourra écrire :

$$\frac{3}{K}-(\mathcal{C}_{11}+\mathcal{C}_{12}+\mathcal{C}_{44}) = \frac{1}{2a}\,\frac{\beta^2}{\alpha}, \tag{3.10}$$

équation qui relie la compressibilité aux coefficients dynamiques. α doit être positif car il correspond à la fréquence Raman. On en déduit que

$$\frac{1}{K} \geqslant \frac{1}{3}(\mathcal{C}_{11}+\mathcal{C}_{12}+\mathcal{C}_{44}).$$

(d) *Spectre de vibration et fréquence Raman*

Pour obtenir ce spectre il faut résoudre l'équation séculaire (2.12). Le paramètre τ va cependant intervenir explicitement sauf pour des directions privilégiées qui sont [100] et [111].

Il est aisé de voir que si σ tend vers 0, l'équation (2.12) admet trois racines tendant vers zéro, formant les branches acoustiques et trois racines tendant vers $8\alpha/\mu A$, formant les branches optiques. Ces trois dernières racines correspondent à la fréquence Raman, et on aura :

$$\omega_R = \sqrt{\left(\frac{8\alpha}{\mu_A}\right)}. \tag{3.11}$$

Pour toute valeur de σ, en général, existeront six racines, qui correspondront à trois vibrations optiques et trois vibrations acoustiques elliptiques qu'on peut considérer comme formées de 2 pseudolongitudinales et 4 pseudotransversales.

VOL. 5 1958

4. APPLICATIONS

(a) *Diamant*

(1) *Détermination des paramètres de forces.* Nous possédons pour ce corps cinq grandeurs : la fréquence Raman, la compressibilité, et les trois constantes élastiques $\mathcal{C}_{11}$, $\mathcal{C}_{12}$, $\mathcal{C}_{44}$.

Nous pouvons donc en principe déterminer les cinq paramètres de force : α, β, λ, μ, ν. La grandeur connue avec le plus de précision est la fréquence Raman.

D'après ROBERTSON *et al.*[4] elle vaut 1332 cm^{-1} soit

$$\omega_R = \sqrt{\left(\frac{8\alpha}{\mu_A}\right)} = 2{,}51\cdot 10^{14}$$

ce qui conduit à $\alpha = 0{,}157\cdot 10^6$ dynes/cm.

La compressibilité mesurée par ADAMS[5] et WILLIAMSON[6] est en moyenne $0{,}17\cdot 10^{-6}$ par megabar ce qui permet d'écrire :

$$\frac{1}{K} = \frac{1}{6a}[\alpha+8\mu+2\beta+8\nu] = 5{,}9\cdot 10^{12}\ \text{dynes/cm}^2.$$

La situation est moins claire en ce qui concerne les constantes élastiques. Trois déterminations ont été réalisées : l'une par étude aux rayons X par PRINCE et WOOSTER[7], les deux autres par mesure de la vitesse du son. La plus ancienne est due à

BHAGAVANTAM et BHIMASENACHAR[8] l'autre très récente à MCSKIMIN et BOND[9].

Le tableau ci-dessous donne les trois résultats exprimés en dynes/cm²

	PRINCE et WOOSTER[7]	BHAGAVANTAM et BHIMASENACHAR[8]	MCSKIMIN et BOND[9]
$\mathcal{C}_{11}$	$11{,}0\cdot10^{12}$	9,5	10,76
$\mathcal{C}_{12}$	3,3	3,9	1,25
$\mathcal{C}_{44}$	4,4	4,3	5,76

On voit que les valeurs de MCSKIMIN et BOND sont en désaccord avec les autres valeurs déterminées.
La relation :

$$\frac{3}{K}-(\mathcal{C}_{11}+\mathcal{C}_{12}+\mathcal{C}_{44})=\frac{\beta^2}{2a\alpha} \qquad (3.10)$$

conduit pour les valeurs de BHAGAVANTAM et MCSKIMIN à $\beta=0$.

Les valeurs de PRINCE et WOOSTER conduisent à β^2/α négatif, mais si au lieu de prendre la moyenne des compressibilités, on utilise celle d'Adams, $6{,}3\cdot10^{12}$ dynes/cm², β^2/α est positif et très voisin de zéro. On prendra donc pour l'ensemble des valeurs $\beta=0$. Dans le diamant $2a=3{,}56$ Å;
Et au total les paramètres de forces seront :

	Constantes élastiques (10^6 dynes/cm) utilisées mesurées par :		
	PRINCE et WOOSTER	BHAGAVANTAM et BHIMASENACHAR	MCSKIMIN et BOND
α	0,157	0,157	0,157
β	0	0	0
λ	−0,0294	−0,0236	−0,0163
μ	0,0293	0,0226	0,0282
ν	0,0343	0,0365	0,0312

Malgré la dispersion expérimentale, les valeurs des constantes de forces ne diffèrent pas énormément.

(2) *Discussion.* Les constantes élastiques statiques et dynamiques ne dépendent pas du paramètre τ. Il n'en est pas de même pour les valeurs de la pulsation ω en général. Nous allons essayer de déterminer τ par l'intermédiaire d'une hypothèse *physique* sur la nature des forces entre deuxièmes voisins et discuter les résultats obtenus ci-dessus, ainsi que les valeurs expérimentales des constantes élastiques. Nous pourrons également comparer les conclusions de cet article avec celui de SMITH.[3]

La théorie de LAVAL n'existant pas à l'époque de son travail SMITH confond les coefficients statiques et dynamiques. De plus elle admet que les coefficients $C\binom{m-p}{j\ k}_{\alpha\beta}$ sont symétriques en α et β. Ceci lui permet de négliger le paramètre τ et dans la relation $1/K=1/3(C_{11}+2C_{12})$ d'utiliser les valeurs des constantes dynamiques. Cette dernière relation est bien vérifiée pour les valeurs de BHAGAVANTAM et pour celles de PRINCE. Cette coincidence est fortuite, bien que ces valeurs montreraient soit que le cristal est très voisin des relations de Cauchy $\mathcal{C}_{11}=2\mathcal{C}_{12}=2\mathcal{C}_{44}$, soit que les forces sont presque centrales. Le désaccord devient important avec les valeurs de MCSKIMIN. Celui-ci s'en étonne dans son article, mais on ne peut conclure que ses mesures soient erronées ou que la compressibilité soit inexacte, puisque ces grandeurs ne sont pas en contradiction avec la relation (3.10) que nous avons établie.

La confusion entre coefficients statiques et dynamiques ne laisse plus à SMITH que quatre relations.

Pour pouvoir calculer les constantes de forces autres que α et β elle suppose que les forces entre seconds voisins sont centrales et choisit :

$$\mu=\nu \qquad \lambda=0.$$

Ce choix détermine en réalité des forces centrales très particulières. En effet les forces centrales les plus générales dépendent d'un potentiel $V(r)$ et on peut écrire :

$$C\binom{m-p}{\substack{j\ k\\ \alpha\ \beta}}=\phi\binom{m-p}{j\ k}\delta_{\alpha\beta}+\psi\binom{m-p}{j\ k}\times$$
$$\times(m^\alpha-p^\alpha+j^\alpha-k^\alpha)(m^\beta-p^\beta+j^\beta-k^\beta).$$

$\delta_{\alpha\beta}$ est l'indice de Kronecker et

$$\begin{cases}\phi\binom{m-p}{j\ k}=\dfrac{1}{r}\dfrac{dV\binom{m-p}{j\ k}}{dr}.\\[2ex] \psi\binom{m-p}{j\ k}=\dfrac{1}{r}\left[\dfrac{d}{dr}\left(\dfrac{1}{r}\dfrac{dV\binom{m-p}{j\ k}}{dr}\right)\right].\end{cases}$$

Les forces centrales les plus générales entre seconds voisins dépendent de deux paramètres λ et ν par exemple, τ est nul et

$$\mu = \nu + \lambda.$$

Pour choisir $\lambda = 0$, SMITH s'appuie sur une propriété établie par Born, qui a montré que dans le cas des forces centrales un cristal cubique à faces centrées obéit aux relations de Cauchy.

Cette relation n'est valable que pour un cristal *mono-atomique*, où chaque atome est centre de symétrie. La supposition de SMITH revient à négliger les premiers voisins.

On peut montrer ce fait en considérant l'équation de stabilité du cristal abandonné à lui-même,

$$\sum_{p\,jk} B^{m-p}_{\substack{j\ k \\ \alpha}} (m^\gamma - p^\gamma + j^\gamma - k^\gamma) = 0,$$

ce qui dans le cas des forces centrales s'écrit :

$$\sum_{p\,jk} \phi^{m-p}_{j\ k} (m^\alpha - p^\alpha + j^\alpha - k^\alpha)(m^\gamma - p^\gamma + j^\gamma - k^\gamma) = 0. \tag{4.1}$$

Si on admet qu'il n'y a de forces qu'entre seconds voisins cet ensemble d'équations conduit directement à $\lambda = 0$.

Mais en fait cette équation doit s'appliquer à l'ensemble des forces du cristal. Si l'on suppose que *toutes* les forces sont centrales et en se bornant aux forces entre premiers et seconds voisins, cette équation devient :

$$\alpha - \beta + 8\lambda = 0, \tag{4.2}$$

Cette équation est identique à celle obtenue en égalisant les valeurs des coefficients statiques et dynamiques :

$$\alpha - \beta + 4\lambda + 4\mu - 4\nu = 0,$$

qui se réduit à (4.2) puisque $\mu = \nu + \lambda$.

En égalisant les coefficients statiques et dynamiques on suppose les forces centrales, mais les valeurs obtenues pour $\mathcal{C}_{12}$ et $\mathcal{C}_{44}$ restent différentes, la relation de Cauchy ne pouvant être satisfaite puisque le réseau n'est pas mono-atomique.

Avec son hypothèse, SMITH établit une relation à laquelle doivent obéir les constantes élastiques, mais elle constate que cette relation est encore plus mal vérifiée que la relation de Born, qui néglige les forces entre deuxièmes voisins. Pour pouvoir néanmoins calculer μ, elle est conduite à modifier, d'une manière appréciable, $\mathcal{C}_{44}$. Cette modification ne peut aller sans une modification concomitante de $\mathcal{C}_{11}$ et $\mathcal{C}_{12}$. Cette conclusion est à rapprocher de la variation que l'on constate pour ces valeurs, dans les mesures de PRINCE et WOOSTER et de MCSKIMIN.

Pour déterminer le paramètre τ nous allons faire l'hypothèse que les forces entre seconds voisins peuvent être considérées comme formées d'une force centrale (de type Van der Waals par exemple) et d'une force due à la variation des angles de liaison. On peut montrer aisément que dans la matrice C^0, la partie due à ces dernières forces est

$$C^0_\theta = \begin{vmatrix} \rho & \rho & 2\rho \\ \rho & \rho & 2\rho \\ -2\rho & -2\rho & -4\rho \end{vmatrix},$$

celle due aux forces centrales est :

$$C^0_c = \begin{vmatrix} \epsilon - \eta & \epsilon & 0 \\ \epsilon & \epsilon - \eta & 0 \\ 0 & 0 & -\eta \end{vmatrix},$$

on en tire :

$$\mu = \rho + \epsilon - \eta,$$
$$\nu = \rho + \epsilon, \qquad \tau = 2\rho.$$
$$\lambda = -4\rho - \eta,$$

c'est à dire, avec les valeurs expérimentales :

	Constantes élastiques (10^4 dynes/cm) utilisées mesurées par :		
	PRINCE et WOOSTER	BHAGAVANTAM et BHIMASENACHAR	MCSKIMIN et BOND
ρ	0,61	0,242	0,332
ϵ	2,82	3,408	2,787
η	0,50	1,39	0,293
ϵ/η	5,6	2,45	9,5

La valeur de ϵ/η si l'on suppose des forces de Van der Waals entre seconds voisins est 4. Il est assez

VOL. 5 1958

Tableau 3.

	Constantes elastiques (10^6 dynes/cm) utilisees determines par :			Valeurs calculées par SMITH d'apres les constantes de BHAGAVANTAM et modification de C_{44}
	PRINCE et WOOSTER	BHAGAVANTAM et BHIMASENACHAR	MCSKIMIN et BOND	
α	0,157	0,157	0,157	0,157
β	0	0	0	0,104
λ	−0,0294	−0,0236	−0,0163	0
μ	0,0293	0,0226	0,0282	0,0226
ν	0,0343	0,0365	0,0312	0,0226
τ	0,0122	0,0048	0,0066	0

surprenant que ce soit la valeur de PRINCE et WOOSTER qui en soit la plus voisine.

L'ensemble des résultats est consigné sur le Tableau 3 ainsi que les déterminations de SMITH.

Revenons maintenant à la conclusion $\beta = 0$, qui est la plus surprenante et en contradiction formelle avec la détermination de SMITH.

La force entre premiers voisins déterminée ici est dirigée suivant l'axe joignant les deux atomes, c'est une force très particulière qui matérialise en quelque sorte la liaison carbone-carbone.

On peut la supposer formée de la combinaison d'une force centrale générale et de la force venue de la déformation des angles de liaison, qui entre premiers voisins conduit à une matrice de la forme :

$$\begin{vmatrix} 8\rho & -4\rho & -4\rho \\ -4\rho & 8\rho & -4\rho \\ -4\rho & -4\rho & 8\rho \end{vmatrix},$$

cette combinaison conduisant à $\beta = 0$. En fait vue la précision expérimentale on doit conclure que β est petit devant α de l'ordre $\frac{1}{10}\alpha$ par exemple.

(b) *Silicium et germanium*

On ne connaît pas la fréquence Raman pour ces deux corps. De plus la valeur de la compressibilité du silicium donnée dans les tables est vraisemblablement trop faible d'un facteur trois. Il est légitime d'en conclure que la compressibilité donnée est la linéaire. Moyennant cette hypothèse on trouve pour le silicium et le germanium une valeur de β^2/α faiblement négative.* On en conclut que $\beta = 0$.

Pour déterminer la constante α on pourrait, comme la majorité des auteurs, admettre que la fréquence du premier pic d'absorption infra-rouge se confond avec la fréquence Raman. Cependant les vibrations des réseaux de type diamant sont en théorie inactives en infra-rouge et il est hasardeux d'admettre cette identification. Le cas du diamant lui-même se complique du fait que l'on connaît deux types de diamant de ce point de vue. Le type II possède son premier pic d'absorption vers 2010 cm^{-1}, le type I vers 1390 cm^{-1}. Cette deuxième valeur, voisine de la fréquence Raman, est due à des impuretés; la véritable absorption intrinsèque a lieu a 2010 cm^{-1}.

Pour le silicium et le germanium, les premiers pics ont lieu à 625 cm^{-1} et 345 cm^{-1}. Celui du silicium varierait avec les impuretés et pourrait être considéré comme étant la bande fondamentale; mais, mis à part le fait que le réseau est en principe inactif, cette bande continue d'exister pour du silicium de très haute pureté et il paraît délicat de la confondre avec la fréquence Raman. La conclusion est identique pour le germanium, la bande à 345 cm^{-1} étant peu sensible aux impuretés.

Pour déterminer la fréquence Raman, il faut calculer α, nous ferons donc l'hypothèse qui nous a permis de calculer τ, et dans l'impossibilité de

* Pour une discussion de ces bandes voir LAX et BURNSTEIN,[10] et DE LAUNAY.[11]

Les coefficients d'élasticité ont été mesurés par J. MCSKIMIN *et al.*,[12] la compressibilité de Si par RICHARDS *et al.*[13]

Tableau 4. *Valeurs de la fréquence Raman en* cm^{-1}.

	ε/η								
	2,45	4	5,6	9,5	SMITH	HSIEH*	Exp.	Abs.I.R.	Temperature de Debye θ_D
Diamant	1332	1332	1332	1332	1332	1515†	1332	2010‡	1360‡
Silicium	448	383	341	308	—	860	?	625‡	460‡
Germanium	253	215	200	167	—	400	?	345‡	250‡

* Calcul fait avec les hypotheses de HSIEH.[14]

† Ce calcul est fait a partir des constantes élastiques de BHAGAVANTAM et de l'hypothèse de SMITH sans modifier C_{44}.

‡ D'apres LAX et BURNSTEIN[10] DE LAUNAY[11] donne pour θ_D dans le diamant : 1293 cm^{-1}.

trancher entre les différentes valeurs du rapport ϵ/η obtenues pour le diamant nous les avons toutes utilisées. Les résultats sont reportés dans le Tableau 4.

5. CONCLUSIONS

Il paraît difficile de choisir entre les diverses hypothèses faites pour le rapport ϵ/η. Le rapport 2,5 déterminé à partir des mesures de BHAGAVANTAM conduit à la valeur la plus proche de la température de Debye pour la fréquence Raman. Le rapport 5,6 déduit des mesures de PRINCE et WOOSTER est le plus voisin de celui que l'on obtiendrait pour des forces de Van der Waals.

Les valeurs de MCSKIMIN semblent les moins satisfaisantes, et C_{12}, a priori, est trop petit. Ce point n'a pas échappé à cet auteur, qui est surpris du désaccord de ses valeurs avec la relation $1/K = 1/3(C_{11}+2C_{12})$.

Nous avons vu que cette relation ne peut être appliquée aux coefficients dynamiques et qu'on ne peut en conclure que les mesures de MCSKIMIN sont fausses. Ce dernier a fait une critique soignée de ses déterminations, et a pris un grand nombre de précautions qui militent en faveur de ses mesures. La critique qu'il donne des mesures de BHAGAVANTAM et convaincante. Quant à celles de PRINCE et WOOSTER elles sont par nature assez imprécises car elles sont déduites de mesures aux rayons X.

Il n'est d'ailleurs pas certain que les lois de forces dans le germanium et le silicium soient analogues à celles du diamant car les distances atomiques sont nettement plus grandes. Quoiqu'il en soit, on peut affirmer que les fréquences Raman ne sont pas les fréquences d'absorption infra-rouge déterminées dans le silicium et le germanium, elles seraient respectivement voisines de 400 et 200 cm^{-1}. On constatera également que les forces entre seconds voisins sont approximativement des forces centrales, les forces de déformation des angles de liaison restant faibles. Avec l'hypothèse de $\epsilon/\eta = 9,5$, les forces entre seconds voisins dans le germanium sont assez voisines de l'hypothèse de SMITH. Mais le résultat $\beta = 0$ ou $\beta \ll \alpha$ reste la conclusion marquante de cet article.

Note added in proof: La valeur de la fréquence optique ω_R du germanium a été determinée par PELAH I., EISENHAUER C. H., HUGHES D. J., et PALEWSKY H., (*Phys. Rev.* **108**, 1091 (1957))—Elle vaut 0,034 eV cequi correspond à 275 cm^{-1}. Cette valeur est voisine de la température de Debye.

On entire les valeurs des constantes élastiques, exprimée en dynes/cm.

$\alpha = 4,03 \cdot 10^4$, $\beta = 0$, $\lambda = -7,30\ 10^3$, $\mu = 4,05\ 10^3$
$\nu = 8,17 \cdot 10^3$.
Avec les hypotheses faits ci-dessies on determine $\tau = 1,59 \cdot 10^3$ et $\varepsilon/\eta = 1,79$.

BIBLIOGRAPHIE

1. LAVAL J. Cours au Collège de France (non publié); *Comptes rendus du Congrès Solvay* p. 273 (1952); *J. Phys. Rad.* **18,** 289, 369 (1957).
2. LE CORRE Y. *Bull. Soc. franç Minér* **77,** 1363 (1954); **78,** 33 (1955).
3. SMITH HELEN J. *Phil. Trans.* A**829,** 105 (1948).

4. Robertson R., Fox J. et Martin A. *Phil. Trans.* A**232,** 463 (1934); *Proc. Roy. Soc.* A**157,** 579 (1936).
5. Adams L. F. *Wash. Acad. Sci.* **11,** 45 (1921).
6. Williamson E. F. *Franklin Inst.* **193,** 491 (1922).
7. Prince E. et Wooster W. *Acta. Cryst.* **6,** 450 (1953).
8. Bhagavantam S. et Bhimasenachar J. *Nature Lond.* **154,** 546 (1944); *Proc. Roy. Soc.* A**187,** 381 (1948).
9. McSkimin H. et Bond W. *Phys. Rev.* **105,** 1, 116 (1957).
10. Lax M. et Burnstein E. *Phys. Rev.* **97,** 39 (1955).
11. de Launay J. *Solid State Physics* Vol. 2 p. 219 Academic Press, New York (1956).
12. McSkimin H. *et al. J. Appl. Phys.* **24,** 988 (1953).
13. Richards, Stull et Bonnet *Publ. Carneg, Instn.* **76,** (1907).
14. Hsieh Y. *J. Chem. Phys.* **22,** 306 (1954).

PAPERS TO BE PUBLISHED IN FUTURE ISSUES

V. L. Ginzburg and A. P. Levanyuk: Light scattering near second-order phase transition and Curie points.

R. W. Keyes: Effects of electron–electron scattering on the electrical properties of semiconductors.

O. Flint and J. H. O. Varley: On the mechanism of oxide film formation on zirconium.

M. Ya. Azbel' and E. A. Kaner: Cyclotron resonance in metals.

A. Ascoli, M. Asdente, E. Germagnoli and A. Manara: Activation energies for production and migration of vacancies in platinum.

G. Bogner und E. Mollwo: Über die Herstellung von Zinkoxydeinkristallen mit definierten Zusätzen.

H. Rupprecht: Über Konzentration und Beweglichkeit von Elektronen in Zinkoxydeinkristallen mit definierten Zusatzen.

J. M. Whelan and G. H. Wheatley: The preparation and properties of gallium arsenide single crystals.

G. Heiland: Feldeffekt und Photoleitung an ZnO-Einkristallen.

A. Smakula and J. Kalnajs: Oxygen impurity in silicon single crystals.

R. E. Schlier and H. E. Farnsworth: Structure of epitaxed copper deposited by evaporation onto a clean (00·1) face of a titanium crystal.

J. L. Birman: Calculation of coulomb crystal potentials.

J. I. Pankove: Radiative surface effect in germanium.

H. Fritzsche: Resistivity and Hall coefficient of Sb-doped germanium at low temperature.

D. G. Worden and G. C. Danielson: Electrical resistivity of thin films of potassium at 100°K.

D. H. Roberts and J. E. Baines: Photoconductivity in chemically deposited films of lead selenide.

J. B. Goodenough: An interpretation of the magnetic properties of the Perovskite-type mixed crystals $La_{1-x}Sr_xCoO_{3-\lambda}$.

P. G. de Gennes: Neutron scattering by antiferromagnets above the Néel-point.

B. K. Agarwal and M. P. Givens: Soft X-ray absorption by manganese and manganese oxide.

T. A. Sandenaw and R. A. Gigney: The electrical resistivity and thermal conductivity of plutonium metal.

C. S. Fuller and J. M. Whelan: Diffusion, solubility and electrical behavior of copper in gallium arsenide.

W. Paul and D. M. Warschauer: Optical properties of semiconductors under hydrostatic pressure—III Silicon–germanium alloys.

L. P. Kao and E. Katz: Phenomenological theory of anisotropic isothermal galvanomagnetic effects.

G. Leibfried und Chr. Lehmann: Gittertheoretische Behandlung einer Schraubenversetzung in Alkalimetallen.

E. Daniel: Influence du potentiel du reseau et contribution des couches a l'annihalation du positon dans le cuivre.

R. A. Oriani and W. K. Murphy: Thermodynamics of ordering alloys—III Energies of transformation of the $Au_{1/2}Cu_{1/2}$ phases.

A. Taylor and R. M. Jones: Constitution and magnetic properties of iron-rich iron–aluminum alloys.

W. Low and D. Shaltiel: Paramagnetic resonance spectrum of gadolinium in single crystals of thorium oxide.

A. H. Mones and E. Banks: Ferromagnetism in the system Na_2O–ZnO–Fe_2O_3.

R. Nathans, M. T. Pigott and C. G. Shull: The magnetic structure of Fe_3Al.

C. H. L. Goodman: The prediction of semiconducting properties in inorganic compounds.

U. Gonser and B. Okherse: The question of radiation induced phase changes.

R. A. EPPLER and H. G. DRICKAMER: The effect of pressure on the spectra of the Te^+ ion alkali halide lattices.

D. F. C. MORRIS: The instability of some dihalides of copper and silver.

E. SCHLÖMANN: Ferromagnetic resonance in polycrystalline ferrites with large anisotropy.

E. MOOSER and W. B. PEARSON: The crystal structure and properties of the group VB to VIIB elements and of compounds formed between them.

A. B. LIDIARD: Anion diffusion in alkali halide crystals.

E. SCHLÖMANN: Spin wave analysis of ferromagnetic resonance in polycrystalline ferrites.

E. O. KANE: The influence of exchange on the effective mass formation.

R. T. BATE and C. V. HEER: Some optical and magnetic properties of irradiated LiF.

R. F. WALLIS and H. J. BOWLDEN: Theory of impurity photoionization spectrum of semiconductors in magnetic fields.

F. S. HAM: Theory of diffusion-limited precipitation.

C. R. VASSEL: L'effet des elements de la première longue période sur la résistivité du cuivre et de l'aluminium.

G. A. ALERS and J. R. NEIGHBORS: The elastic constants of zinc between 4·2° and 670°K.

W. DESORBO and G. E. NICHOLS: A calorimeter for the temperature region 1° to 20°K—The specific heat of some graphite specimens.

J. C. BOWMAN and J. A. KRUMHANSL: The low temperature specific heat of graphite.

K. KOMATSU: Particle size effect of the specific heat of graphite at low temperatures.

PIERRE BRISSONNEAU: Contribution a l'etude quantitative du trainage magnetique de diffusion du carbonne dans le fer α.

W. D. JOHNSTON, R. R. HEIKES and D. SESTRICH: The properties, crystallography and magnetic properties of the $Li_zCo_{(1-z)}O$ system.

HELMUT BROSS und ALFRED SEEGER: Elektronentheoretische Untersuchungen über Fehlstellen in Metallen—VI Der elektrische Widerstand von Doppelleerstellen in ein wertigen Metallen.

G. F. NEWELL: Extreme frequencies of lattice vibrations for disordered binary alloys.

J. BROSER und R. BROSER-WARMINSKY: Über den Mechanismus der Energiewanderung in Kadmiumsulfid-Kristallen.

E. F. WESTRUM and D. M. GRIMES: Low temperature heat capacities and thermodynamic properties of zinc ferrites—II Effect of thermal history and metallic additives.

W. MARSHALL: The antiferromagnetism of $CuCl_2 2H_2O$.

G. J. DIENES: The temperature dependence of the elastic moduli of vitreous silica.

GERALD W. SEARS: Strength of lithium fluoride whiskers.

NILS BÄCKLUND: Electrical resistance of some metal alloys at the temperatures of liquid helium.

N. T. MELAMED: Energy transfer in Zn : S : Cu : Cl phosphors.

MANUEL CARDONA and WILLIAM PAUL: A quadratic photoelectromagnetic effect in germanium.

MAURICE GOLDMAN: Résonance nucléaire des protons dans l'acide trichloroacétique.

G. MEIJER: Infra-red fluorescence of copper-activated zinc sulphate phosphors.

VOL. 5 1958

DL.
5
958